

An International
Forum For
The AE Science
and Technology

JOURNAL OF ACOUSTIC EMISSION

Vol.17, No.1-2/January-June 1999



**E-GLEA 1; PRIMER ENCUENTRO DEL GRUPO
LATINOAMERICANO DE EMISIÓN ACÚSTICA
(The First Meeting of Latin American Group on
Acoustic Emission) at Buenos Aires, ARGENTINA**

Endorsed by
AEWG, AEWGI
CARP and
EWGAE

Published by
Acoustic Emission Group
Los Angeles, CA

JOURNAL OF ACOUSTIC EMISSION

Editor: Kanji Ono

Associate Editors: A. G. Beattie, T. F. Drouillard, F. C. Beall and M. Ohtsu

1. Aims and Scope of the Journal

Journal of Acoustic Emission is an international journal designed to be of broad interest and use to both researcher and practitioner of acoustic emission. It will publish original contributions of all aspects of research and significant engineering advances in the sciences and applications of acoustic emission. The journal will also publish reviews, the abstracts of papers presented at meetings, technical notes, communications and summaries of reports. Current news of interest to the acoustic emission communities, announcements of future conferences and working group meetings and new products will also be included.

Journal of Acoustic Emission includes the following classes of subject matters;

A. Research Articles: Manuscripts should represent completed original work embodying the results of extensive investigation. These will be judged for scientific and technical merit.

B. Applications: Articles must present significant advances in the engineering applications of acoustic emission. Material will be subject to reviews for adequate description of procedures, substantial database and objective interpretation.

C. Technical Notes and Communications: These allow publications of short items of current interest, new or improved experimental techniques and procedures, discussion of published articles and relevant applications.

D. AE Literature section will collect the titles and abstracts of papers published elsewhere and those presented at meetings and conferences. Reports and programs of conferences and symposia will also be presented.

Reviews, Tutorial Articles and Special Contributions will address the subjects of general interest. Nontechnical part will cover book reviews, significant personal and technical accomplishments, current news and new products.

2. Endorsement

Acoustic Emission Working Group (AEWG), European Working Group on Acoustic Emission (EWGAE), Committee on Acoustic Emission from Reinforced Composites (CARP), and Acoustic Emission Working Group of India have endorsed the publication of Journal of Acoustic Emission.

3. Governing Body

The Editor and Associate Editors will implement the editorial policies described above. The Editorial Board will advise the editors on any major change. The Editor, Professor Kanji Ono, has the general responsibility for all the matters. Associate Editors assist the review processes as lead reviewers. Mr. T.F. Drouillard is responsible for the AE Literature section. The members of the Editorial Board are selected for their knowledge and experience on AE and will advise and assist the editors on the publication policies and other aspects. The Board presently includes the following members:

S.H. Carpenter	(USA)
D.A. Dornfeld	(USA)
P. Fleischmann	(France)
L. Golaski	(Poland)
M.A. Hamstad	(USA)
H.R. Hardy, Jr.	(USA)
R. Hill	(UK)
I.V. Ivanov	(Russia)
P. Jax	(Germany)
T. Kishi	(Japan)
O.Y. Kwon	(Korea)
J.C. Lenain	(France)
S.L. McBride	(Canada)
W. Morgner	(Germany)
C.R.L. Murthy	(India)
H. Niitsuma	(Japan)
A.A. Pollock	(USA)
T.M. Proctor, Jr.	(USA)
I. Roman	(Israel)
C. Scala	(Australia)
C. Scruby	(UK)
A. Vary	(USA)
E. Waschkies	(Germany)
M. Wevers	(Belgium)
J.W. Whittaker	(USA)
B.R.A. Wood	(Australia)

4. Publication

Journal of Acoustic Emission is published quarterly in March, June, September and December by Acoustic Emission Group, PMB Suite 106, 16350 Ventura Blvd, Encino, CA 91436. It may also be reached at 6531 Boelter Hall, University of California, Los Angeles, California 90095-1595 (USA). tel. 310-825-5233. FAX 818-990-1686. e-mail: ono@ucla.edu

5. Subscription

Subscription should be sent to Acoustic Emission Group. Annual rate for 1999 is US \$96.00. For surface delivery, add \$8 in the U.S. and \$11 for Canada and elsewhere. For air mail delivery to South America, add \$18, Western Europe, add \$25 and add \$30 elsewhere. Overseas orders must be paid in US currencies with a check drawn on a US bank. VISA/MC accepted. Inquire for individual (with institutional order) and bookseller discounts.

For year 2000 and beyond, changed format/rates will apply. Please read announcement on page i of this issue.

6. Advertisement

No advertisement will be accepted, but announcements for books, training courses and future meetings on AE will be included without charge.

New Format for *Journal of Acoustic Emission*

We are pleased to announce a new format for the publication of *Journal of Acoustic Emission*. Since 1982, we have used the standard paper-based publication format on a quarterly schedule each year. With the advances of electronic media, we have decided that the time has arrived for a change to the electronic publication, although we will retain at least for the present a paper-based format as well for those who must have printed copies. We believe this will best serve the international AE community as more technical content can be delivered to the readers with no increase in cost.

Specifically, we will modify the mode of publication in the following manner:

1. Each article will be available to the subscribers as a pdf file on a new World Wide Web page for the Journal immediately upon the completion of review. Password and software for reading the pdf files will be provided.
2. Abstracts of all the articles will be provided free on the Journal web page.
3. One (or more) CD-ROM will be sent to the subscribers at the end of year.
4. For those requiring printed copies, these will be sent along with CD-ROMs.

With this switch to the electronic media, additional activities will be incorporated.

1. Data files for waveforms and various digital data, such as transducer calibration curves and transfer functions of propagation media, can be attached to a technical paper.
2. Raw AE data can be incorporated in tutorial articles so that readers can use it for self-training at own laboratory (or at home).
3. Theses and reports (on any language) can be made available through the internet connection or can be provided on the Journal web page.
4. Depending on demands, back issues and articles will become available on the Journal web page.
5. Subject to Editor's acceptance, papers can be made available on the Journal web page prior to review on author's request.
6. Technical presentation from conferences (e.g., in Powerpoint file format) will become accessible on the Journal web page.

Subscription rate schedule has been changed as follows for year 2000.

Volume 18	2000	\$104	including air shipping to anywhere
		\$136	with printed copy shipped surface

Subscription order should be sent to (VISA/Master Card accepted):

ACOUSTIC EMISSION GROUP

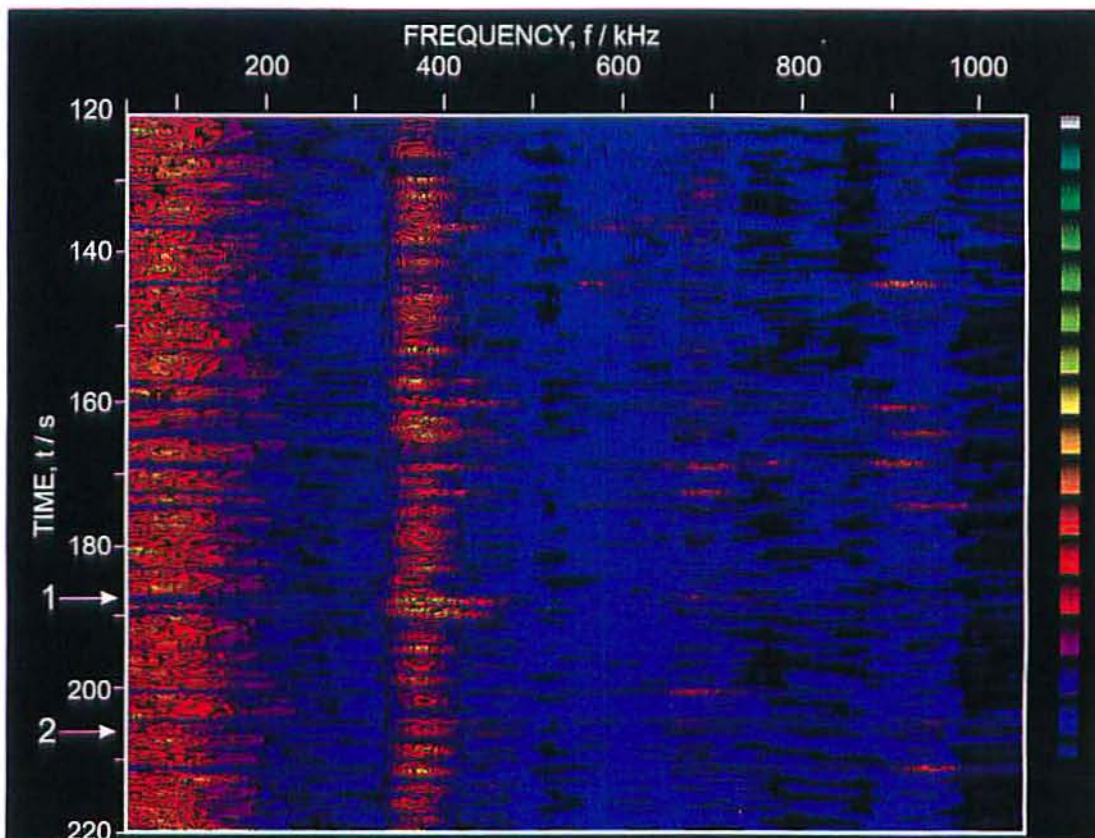
16350 Ventura Bl, PMB Suite 106, Encino, Calif 91436 USA

Phone: 1-310-825-5233; FAX Number: 1-818-990-1686;

e-mail address: ono@ucla.edu



Founding members of GLEA, Grupo Latinoamericano de Emisión Acústica. From l to r: Rosa Piotrkowski, Tulio Palacios, José Ruzzante, M. Isabel López Pumarega, María Armeite; front, Pedro Feres Filho, Miguel Angel Sabio Montero. (Missing from the photo is C. D'Attellis.)



Color plate for Figure 8 on page 9.

Classification of Acoustic Emissions in Metallic Glasses

A. Vinogradov

Abstract

A complex statistical and spectral analysis of acoustic emission (AE) during the plastic flow of metallic glasses (MGs) is performed with the aim of classification of AE sources in this kind of disordered media. The ideas of optimization and enhancement of reliability of AE analysis are described in terms of factor and cluster analysis over a wide range of AE parameters in both time and frequency domains. It is shown that the AE signals in MGs naturally fall into two categories (clusters) differed by their amplitude and spectral characteristics. This allowed to conclude that two different mechanisms of inhomogeneous plastic flow, i.e. two AE sources, exist in MGs. One mechanism is simply associated with shear band formation, while identification of the other mechanism is not quite straightforward. A possible nature of that unknown mechanism of plastic deformation of MGs is discussed and argued that it could be a nucleation of shear bands inside the amorphous body.

1. Introduction

1.1 Plastic Deformation of Metallic Glasses

Plastic deformation of metallic glasses (MGs) was the focus of numerous experimental and theoretical investigations in the last two decades. It was found that depending on testing conditions one of two flow modes occurs: *inhomogeneous* flow which is highly localized in the slip bands similar to those in crystalline metals or *homogeneous* viscous flow which does not reveal any signs of strain localization (Masumoto and Maddin, 1975; Alekhin and Khonik, 1992). Despite many efforts and a variety of speculative models the nature of inhomogeneous plastic deformation of MGs remains unclear. Difficulties of direct structural investigations have led to a fairly large number of structural models, which are employed to describe a thermal stability, mechanical behavior and other properties of MGs. One approach comprises several dislocation-disclination models and their modifications (Gilman, 1973; Morris, 1979; Zaichenko and Borisov, 1982). This concept is based on

experimental results indirectly showing a possibility of the inhomogeneous flow by the formation and motion of linear defects with long-range stress fields. Alternative understanding is possible, however, if one takes into account the existence of a large fraction of the excess free volume in MGs, which can significantly facilitate atomic mobility and provide strain localization upon loading (Alekhin and Khonik, 1992; Argon, 1979; Spaepen, 1977). Neither of the models is commonly accepted today and more experimental evidence is needed for verification of the mechanism of plastic flow in MGs.

Localization of plastic deformation in the narrow shear bands of less than 1 mm width at sufficiently low temperatures is typical for most MGs. The structure and properties of shear bands have been studied and reviewed in Donovan and Stobbs (1981) Zielinski and Ast., (1983) and Noskova et al. (1985). Shear plastic deformation in MGs is accompanied by rather powerful AE as has been found in former studies (Leksovskii et al., 1986; Braginskii et al., 1986; Vinogradov et al., 1988; Vinogradov et al., 1989; Vinogradov and Leksovskii, 1996; Khonik et al., 1997). The present work is directed towards further clarification of AE origin in amorphous metallic alloys. This is supposed to shed some light on the microscopic mechanism of their inhomogeneous flow.

1.2 AE during Plastic Deformation of Metals and AE Signal Processing

Although it has long been recognized that the AE signal contains information about the dynamics of defect motion (Fleischmann and Rouby, 1979), the problem of AE analysis is still how to extract this information. Early AE studies related to plastic deformation of metals had a simple descriptive character, trying to establish some qualitative correlation between the AE signal and macroscopic stress-strain behavior. The situation is still very puzzling in attempts to relate acoustic emissions and micro-structural characteristics of materials and their defects. A progress achieved in this area is largely due to the works of Kishi et al (1981), Enoki and Kishi (1991) and also Wadley et al. (1981) and Scruby et al. (1986), for example. They have developed a quantitative approach for AE source characterization by a source function, which was determined by the deconvolution technique. This way is particularly effective for evaluation of fracture processes, but it has obvious

Received 10 April 1998; in final form, 15 September 1998. The author was affiliated with Department of Mechanical Systems Engineering, Kanazawa University, Kanazawa 920-8667, Japan. He is now with Faculty of Engineering, Osaka City University, Osaka, Japan.

difficulties in application to plastic deformation, where up to now we have no uniform approaches to both the AE data processing and interpretation.

Fundamental theoretical aspects of AE caused by various dislocation reactions have been considered by Natsik and Chishko (1972, 1978, 1982) within the framework of continuous mechanics. They have shown that different sources produce different AE in the wave zone. This could serve as a fundamental physical basis for source identification. However, precise verification and application of their calculations is still difficult even when a well calibrated measuring system is used, because activating a single AE source in a real crystal is quite rare and the sensitivity of the available measuring AE equipment is limited (especially for the broad-band one).

AE is always a random process (Lucia and Redondi, 1976). The arbitrary AE appearance reflects the stochastic nature of the defect movement during the plastic deformation. This is not surprising, because AE is always associated with the movement of a great number of atoms in random stress fields of microscopically inhomogeneous media. Thus, it seems obvious that the statistic methods developed in the theory of random processes and random data are natural for quantitative characterization of AE fluxes. Four main quantities are commonly used to describe the basic properties of random data: mean square values, probability density functions, auto-correlation functions and power spectral densities. All these quantities have been utilized elsewhere for AE description. However, since AE can be regarded as a multi-variate process the problem of the "most informative" parameter arises. A total AE count, peak and root mean square (RMS) voltage, energy and many other time-domain parameters are often measured using different equipment that provides insufficient information about AE sources and makes it extremely difficult to compare and rationalize the results obtained by different investigators unless the same conditions of data recording and treatment have been met. More detailed information on the AE sources can be derived, in principle, from the power spectral density function if the broad-band apparatus is used and if a special attention is paid to calibration of the measuring system. Although the shape of AE spectra is affected by many experimental factors such as the specimen geometry, sensor characteristics and location, etc. (Ono and Ucisik, 1976), we should always bear in mind that for the stationary data its spectral presentation is equal to the time domain picture by Wiener-Khinchine theorem (Priestley, 1981) and the problems of spectral analysis are just masked but not solved in time domain. Moreover, many of the above-mentioned factors can be taken into account by calibration and proper filtering in spectrum analysis (Lucia and Redondi, 1976). Successful examples of the AE source discrimination by means of Fourier spectral analysis are given by Graham and Alers (1974) and Egle et al. (1981). In both cited works the sources were a priori known and

acted at significantly different instants of time. Woodward and Harris (1977) applied statistical treatment to the array of AE spectra, showing that there were three distributions of amplitude spectra in zirconium. This allowed the authors to conclude about the presence of three kinds of AE mechanism such as twin initiation, twin broadening and slip.

The Fourier transform is fast, vivid and, therefore, convenient for AE depiction. However, other kinds of spectral orthogonal expansions or data representation can be equally (or even more) useful to explore the AE structure. During the past decade, the impressive development of the pattern recognition technique has provided new opportunities for classification and identification of AE signals. For example, the wavelet transform with further nearest neighbor clustering, autoregressive analysis and neural networks applications were shown to be very effective for this problem (Ono and Wu, 1996; Suzuki et al., 1996; Grabec, 1995; Grabec and Sachse, 1989).

Thus, the purpose of the present work is two-fold. At first, we focus ourselves on quantitative discrimination between the AE sources during the plastic deformation of such a complicated material as a metallic glass, anticipating further identification of emitting defects. Secondly, we aimed at showing that the systematic use of mathematical statistics provides a powerful tool for quantitative AE source discrimination without any *a priori* assumptions on the nature of emitting defects. To achieve this purpose we employ the complex data treatment involving general descriptive statistics, Fourier analysis of individual pulses, factor and cluster analyses. The details of data processing are given below.

2. Experimental

2.1 Specimens and Mechanical Testing

Ribbon shaped $\text{Co}_{57}\text{Fe}_{5}\text{Ni}_{10}\text{Si}_{11}\text{B}_{17}$ MG (15 μm thick, 14 mm width) was obtained by standard melt-spinning technique. This glass was chosen because its mechanical behavior has been extensively studied in a wide temperature range (Khonik et al., 1997). Thin foil transmission electron microscopy was used to ensure an amorphous structure. The sample gage length was 120 mm. A total number of the specimen tested is 18. The tensile tests were performed on an Instron-type screw-driven testing machine at the constant strain rate $(7.0 \pm 0.4) \times 10^{-5} \text{ s}^{-1}$ and $(373 \pm 5) \text{ K}$ temperature. This temperature is much lower than the crystallization temperature of the given glass (Khonik et al., 1997). The specimen was heated to the testing temperature at a rate of 10 K/min. The elevated temperature was used to facilitate formation of shear bands during inhomogeneous plastic flow. As has been reported in Khonik et al., (1998) for the glass under investigation, the AE activity correlating with a number of shear bands attains its maximum value at about 373 K. This provides a large enough number of AE

events within a single realization; this is important for further statistical treatment. The surface of the deformed specimens was observed with a help of scanning microscopy.

2.2 AE Apparatus

AE monitoring was carried out using a computer-controlled AE setup, which is schematically shown in Fig. 1. A miniature broadband (50-1000 kHz) AE sensor AE-900M (3 mm in diameter) made by NF Electronic Instruments was securely mounted on the specimen surface 15 mm from the lower grip. The sensor frequency response is shown in Fig. 1. The AE signal was amplified by 60 dB with a low-noise broadband preamplifier followed by the 20-1000 kHz bandpass filter together with the 40-dB main amplifier and built-in integrating circuit for RMS voltage measurements.

A part of installation, which is responsible for acquisition of AE parameters, contains two synchronized channels: one is for recording *slow* AE-parameters such as RMS voltage (U_{RMS}) and activity m (a number of pulses per unit time) and the other is for high-speed AE sampling.

In the first (slow) channel, we used a 12-bit analog-to-digital converter (ADC) (Datel PC412A), which also contains a built-in 16-channel multiplexor and 12-bit digital-to-analog converter (DAC). This ADC was also used for recording of external experimental parameters such as strain, stress, temperature, etc. The sampling rate could be chosen by software, but mostly we took a set of 20 samples of every parameter at every 0.1 s and stored their mean values.

In the second (fast) channel for high-speed AE sampling, we used a Datel PC414D 12-bit ADC with a sampling rate up to 4 MHz and on-board FIFO memory of 16 ksamples. To gain a pre-triggering mode of operation we added an extra home-made circuit with an analog comparator. The threshold reference signal for the comparator is taken from the PC412 DAC and can be changed by software. In the case of continuous AE, which has no pronounced peaks of amplitude, the ADC can be periodically started by a computer timer. The threshold was set of 2 dB higher than the peak noise level. The system was carefully grounded to minimize an electrical noise. About 100 noise events were detected before each test. Calculation of spectral and time-domain parameters followed by statistical treatment described below allows to obtain a representative *image* of the noise events in terms of its waveform, power spectral density and cluster of calculated parameters. This noise *image* was used during data processing for further identification of *false* signals, which must be excluded from analysis and for subtraction of noise spectral density from the spectra of *true* AE events. The digital oscilloscope Kenwood OR1400 is used for a real-time monitoring of

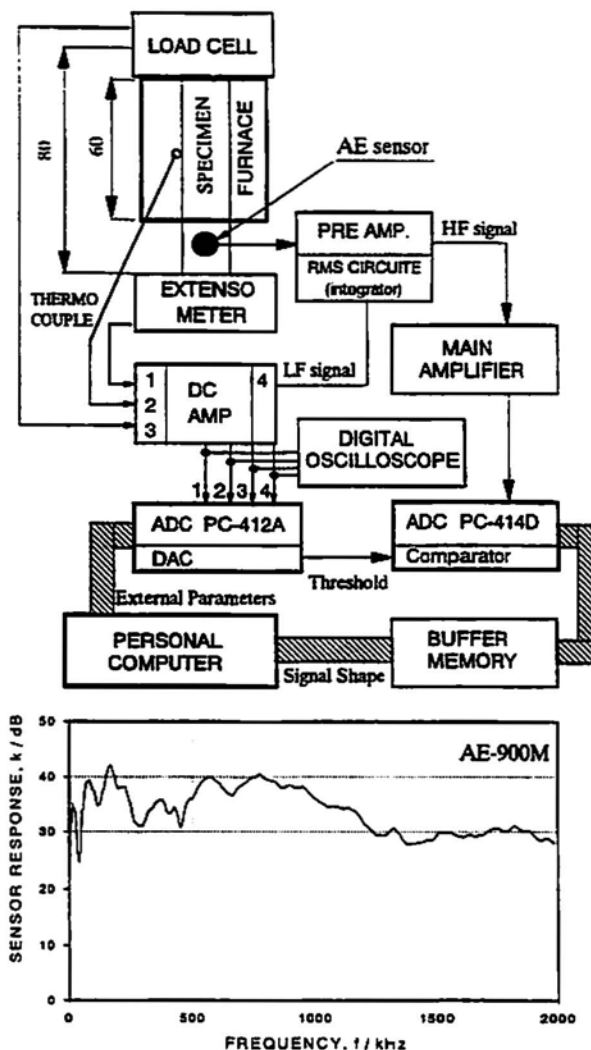


Fig. 1 Experimental set-up and AE sensor frequency response.

stress-strain behavior together with AE RMS voltage or other *slow* parameters.

2.3 Data Processing

The simplified outline of data processing used in the present work is shown in Fig. 2. Let us briefly comment on the basic steps of data analysis, omitting the technical details that can be found elsewhere. As a caution, we should stress that the improper use of statistical algorithms can be misleading and the reliability and limitations of conclusions drawn from statistical results is of primary importance (Bendat and Piersol, 1966).

1) At first, time histories of various time-domain parameters are obtained and plotted with the stress-strain curve. By visual evaluation of the recorded realizations one can determine the type of AE events: continuous, burst or

mixed. In the case of burst type AE, we plot an activity m and peak amplitude $U_p(t)$ as a function of time (or strain) while for continuous AE the plot of $U_{RMS}(t)$ appears to be an almost unique characteristic of the AE flux in time domain.

2) During the next step, we determine general statistical properties of AE fluxes. Since the way of data treatment depends on the type of process, a test of stationarity should be conducted. If the process can be regarded as a stationary one, then it is natural to describe it via probability distribution functions of peak amplitudes $h(U_p)$, time intervals between pulses $h(t)$, etc. Otherwise, we should use some special methods developed for non-stationary processes; this is much more formidable mathematical task (Lu and Rendoli, 1976; Priestley, 1981; Bendat and Piersol, 1966).

3) The details of AE spectral analysis have been reported in Egle et al. (1981) and Vinogradov et al. (1995). The standard 4096-points digital fast Fourier transform of the AE signal gives a periodogram, which is not a consistent estimate of the power spectral density $G(f)$. By windowing, one can significantly decrease the variance of this estimate. A rectangular smoothing window is used in the present work with a spectral width from 1 to 20 kHz. The spectral density of electrical noise is subtracted before calculation of spectral parameters. From the power spectral density function, the following characteristics are computed numerically after noise spectrum subtraction: E is the total energy measured as an integral of $G(f)$ over a whole frequency range of 50-1000 kHz, f_c is the fundamental frequency corresponding to the maximum of $G(f)$, $G_{max} \equiv G(f_c)$ is the magnitude of spectral density at the fundamental frequency, f_{med} is the median frequency and f_{eff} is the effective width of spectra, which equals to the width of imaginary rectangular spectra with the maximum density G_{max} and the total energy E , i.e. $E = G_{max} \cdot f_{eff}$. With the time domain parameters such as U_p and U_{RMS} they form a complete set of descriptive variables that we used. In principle, one can expand this set by adding extra parameters such as a rise time, duration of pulse, etc., but this is not necessary for the purpose of the present work.

4) Since we measure many parameters to describe the same AE phenomenon, the problem of how to reduce a number of variables becomes important. Apparently, AE parameters correlate with each other. This provides the possibility to choose the *less correlated* variables for optimal description of AE. It seems impossible to say *a priori* which variables are to be used. We employ a principal component analysis as a data reduction method. The fundamentals of factor analysis can be found in Cooley and Lohnes, (1971) and Harman, (1967). The question is how many factors to extract? Although the nature of this decision is arbitrary in general case, it is reasonable to suppose that for the purpose of the present work the number of factors should be two because all variables differ substantially in two respects: those which are measured in time domain (U_p , U_{RMS} , E , rise time, duration of pulse, etc.) and those, which are related

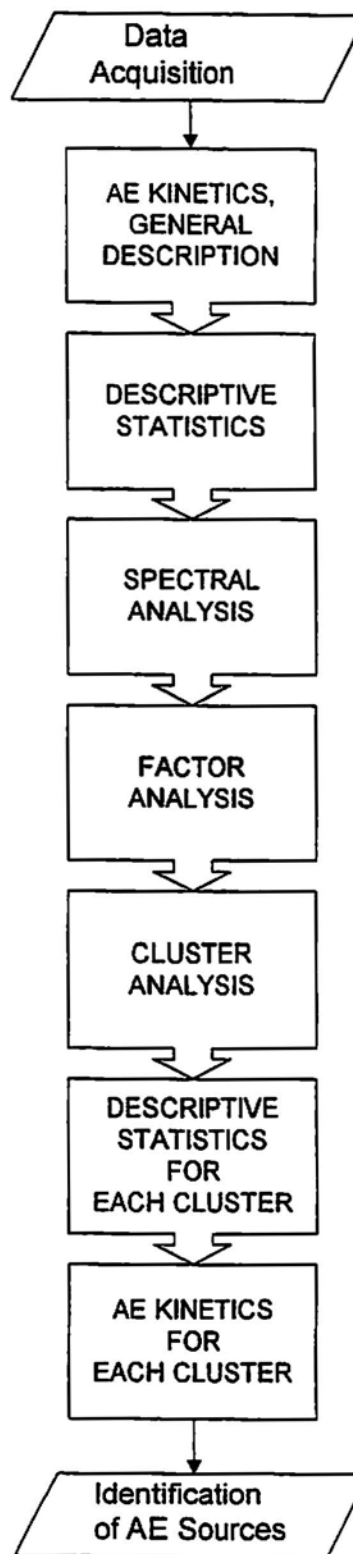


Fig. 2 A flow-chart showing the main steps of data processing.

to the shape of spectrum in frequency domain (G_{max} , f_{med} , f_c , f_{eff} , etc.). Further analysis will confirm this idea because extracting more than two factors does not significantly change variability.

5) The goal of clustering is to reduce the amount of data by categorizing or grouping similar data items together. The so-called partitional clustering attempts to decompose the data set into a set of disjoint clusters. The criterion function that the clustering algorithm tries to minimize may emphasize the local structure of the data, as by assigning clusters to peaks in the probability density function, or the global structure. Typically the global criteria involve minimizing some measure of dissimilarity in the samples within each cluster, while maximizing the dissimilarity of different clusters. A commonly used partitional clustering method is the so called K-means clustering (MacQueen, 1967; Hartigan, 1975) where the criterion function E_K is the average squared distance of the data items x_k from their nearest cluster centroids, m_c ,

$$E_K = \sum_k |x_k - m_{c(x_k)}|^2 \quad (1)$$

where $c(x_k)$ is the index of the centroid that is closest to x_k .

6) After clustering, one can obtain statistical descriptions for the populations of signals belonging to different clusters. Estimating the distribution functions and their parameters is supposed to be useful for conclusions about the nature of emitting defects and for further comparison with theoretical models of AE.

7) Once each signal has been associated with a certain cluster it is not difficult to separate contributions of signals from different clusters to resultant AE. One can plot a time history for individual clusters to see how do different AE mechanisms behave with time (or strain).

3. Experimental Results

3.1 AE Appearance in Metallic Glasses

The stress-strain curve of MG under investigation at room temperature is almost linear. Typical AE time-history is shown in Fig. 3 as an activity (number of pulses per unit time) (a) and an amplitude (b) versus strain. Although AE starts long before failure, the stress corresponding to the AE onset is fairly large. The AE behavior displayed in Fig. 3 is common for a wide range of MGs (Leksovskii et al., 1986; Braginskii et al., 1986; Vinogradov et al., 1988; Vinogradov et al., 1989; Vinogradov and Leksovskii, 1996; Khonik et al., 1997). In contrast to continuous emission in pure single- and poly-crystals, AE in MGs is of burst type that reflects a strongly localized character of plastic flow at low temperatures. Let us note that for any AE time-history in MGs it is possible to find some parts, which can be treated as weakly self-stationary processes. All results discussed below refer to this kind of behavior.

The amplitude distribution is shown in Fig. 4. It does not differ substantially from that usually observed in MGs (Braginskii et al., 1986). This distribution cannot be fitted by a simple statistical function because of a long tail in

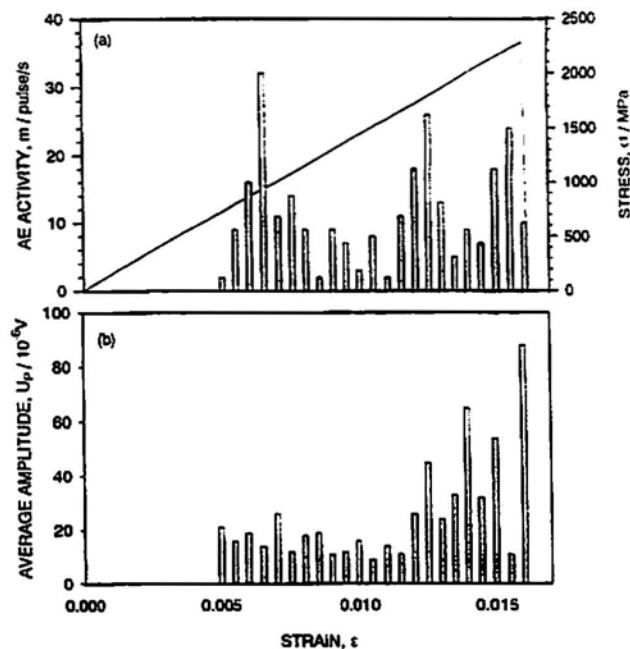


Fig. 3 Typical AE activity (a) and amplitude (b) as functions of strain in metallic glasses (AE time-history in terms of activity and peak voltage).

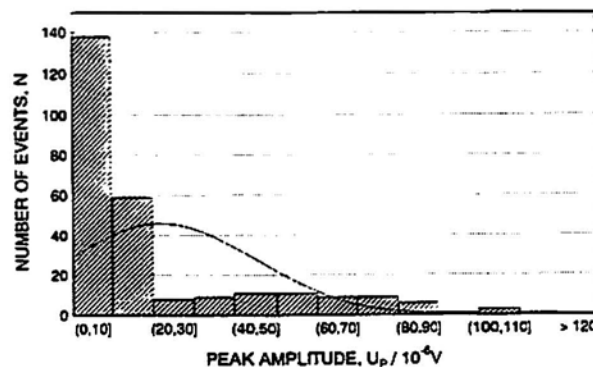


Fig. 4 Typical amplitude distribution of AE signals and its fit by normal law (solid line). No simple fit by ordinary statistical functions can be accepted for a given AE record.

high-amplitude region. One can suspect that the U_p distribution is bimodal and consists of a low-amplitude fraction and a high-amplitude fraction, which are produced by different sources. In some glasses, the second mode in the amplitude distribution is more clearly pronounced (Braginskii et al., 1986; Vinogradov et al., 1988). Even so, a simple amplitude discrimination is not effective enough for source characterization neither in general case nor in particular case of metallic glasses because of ambiguity in the discrimination threshold and in the statistical significance. The features of AE fluxes on different stages of deformation of MGs have been discussed in details in the above cited pa-

pers, whereas in the present work we deal predominantly with the AE sources.

3.2 Shear Bands as AE Sources in MGs

Using direct in-situ AE monitoring with simultaneous SEM image recording we have shown that the shear bands such as those shown in Fig. 5 produce elastic waves during inhomogeneous plastic deformation (Vinogradov and Leksovskii, 1996). Formation and growth of these bands are accompanied by the release of elastic energy from local plastically deforming regions, resulting in the AE pulse of a specific shape. The in-situ experiments have also revealed that some signals appear, while no changes in the surface morphology could be noticed within the limits of SEM resolution. Moreover, the shape and amplitude of these signals were different than those of the signals coming from the shear bands. Taking into account that the first AE events are usually observed at the stresses much lower than those required for the formation of the first shear bands, one can suppose that two kinds of AE source may operate in MGs during inhomogeneous plastic flow. Digitizing individual waveforms makes it possible, in principle, to distinguish precisely between these two kinds of signal and to trace their behaviors separately.

3.3 Shapes and Spectra of Individual Signals

Zaichenko and Braginskii (1990) have found two characteristic frequencies in power spectra of MGs: a low frequency maximum of 10-30 kHz and a high frequency peak of 500 kHz. These authors have used a disclination-dislocation model (Zaichenko and Borisov, 1982) to account for their experimental results. They pointed out that the low-frequency component could be associated with an

nihilation of network disclinations during the step growth at a free surface while the high frequency component was assigned to dislocation emergence from the ribbon. This attractive interpretation was, however, criticized in Vinogradov and Leksovskii, (1996b) where it was underlined that a thorough examination of some experimental factors such as a sample geometry and sensor position is absolutely required because of their great importance for the shape of spectrum (Ono and Usicik, 1976). It was shown that the low-frequency component of 10-30 kHz is due to a longitudinal sample resonance similar to that of the stretched string. For this reason we limit the lowest frequency of our analysis at 50 kHz.

All signals were visually evaluated in both time and frequency domain. This resulted mainly in two distinct types of signals. Typical waveforms and power spectra of AE in MGs are represented in Figs. 6 and 7. The signals do not overlap usually and the burst type AE is evident. Type-1 signals are characterized by a sharp initial rise and decaying waveform of high peak amplitude and clearly pronounced high-frequency components of 640 kHz and higher. The number of type-1 signals is much smaller than the number of type-2 signals. Compared to the type-1 signals, the type-2 events have smaller amplitudes, shorter duration and more flat noise-like spectra with dominant low- and medium-frequency components of 100 and 300 kHz. We should notice that although most peaks are attributable to the features of the sensor frequency response, their relative heights are different in different kinds of signals. This results in significant difference in spectral characteristics (median frequency, in particular).

To compare the shapes of spectra, the normalized spectral density, G^* , for each signal was computed as $G^*(f) = G(f)/E$. The contour map of the normalized power



Fig. 5 Shear bands on the surface of the $\text{Co}_{57}\text{Fe}_5\text{Ni}_{10}\text{Si}_{11}\text{B}_{17}$ metallic glass deformed in tension. These bands are identified to be one source of AE in MGs (type 1).

spectral density in time (or strain) -frequency coordinate is shown in Fig. 8. The spectral features such as characteristic frequencies peculiar to individual signals can be seen from the color change. No significant evolution of spectral components with time (or strain) is revealed. The shapes of spectra of individual signals at the end of deformation are essentially the same as those at the beginning. Thus, the process meets requirements of the weakly self-stationary random process and, therefore, can be simply treated in terms of distribution functions, means and variances of respective variables.

Such a visual classification is useful, but it is a time consuming task, providing only qualitative information in general case. As we examine a fairly large number of specimens and signals, the use of semi-automatic data processing (Fig. 2) is more rigorous and convenient.

3.4 Factor and Cluster Analysis

The correlation matrix for variables, which are listed in Table 1, is given in Table 2. It shows that some correlations are of substantial magnitude (for example, $E-U_{RMS}$ are correlated at the level of 0.85) while other are just weakly cor

related ($f_{med}-U_p$). In the calculation of eigenvalues (Table 3, see Harman, (1967) for details about computational algorithms) for each variable, two factors are to be extracted with respect to the Kaiser criterion (Harman, 1967). This Kaiser criterion states that we have to retain only factors with eigenvalues greater than 1. These two factors cover 78% of total variance (Table 3) and their loadings are presented in Table 2. Factor loadings can be interpreted as correlation between the respective variables and factors, providing most important information for the understanding of factors. Factor 1 is marked by the highest loadings for amplitude-related parameters such as U_p , U_{RMS} and E while, in contrast, Factor 2 shows the highest loadings for frequency domain items such as f_{med} , f_c and f_{eff} and the lowest for U_p , U_{RMS} and E . Choosing two variables with the highest loadings for Factor 1 and Factor 2 correspondingly, we reduce the number of measured parameters to a pair of most representative ones (U_p-f_{med}), which promises to give the clearest description of the AE structure in MGs. Further, we shall use only this pair for AE characterization. We should notice that the attempt to call a greater number of variables for better AE description does not change the results of analysis, but it substantially complicates both calculation and interpretation.

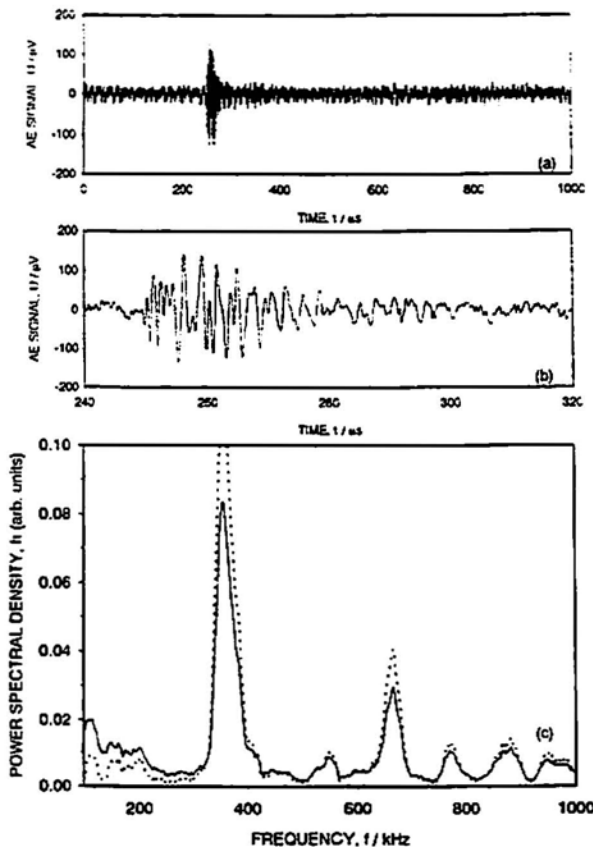


Fig. 6 Representative waveform (a), (b) and power spectral density (c) of AE in a metallic glass - a type-1 signal; (a) a whole single realization; (b) a part of realization. Dashed line (c) shows the spectral density prior to noise removal.

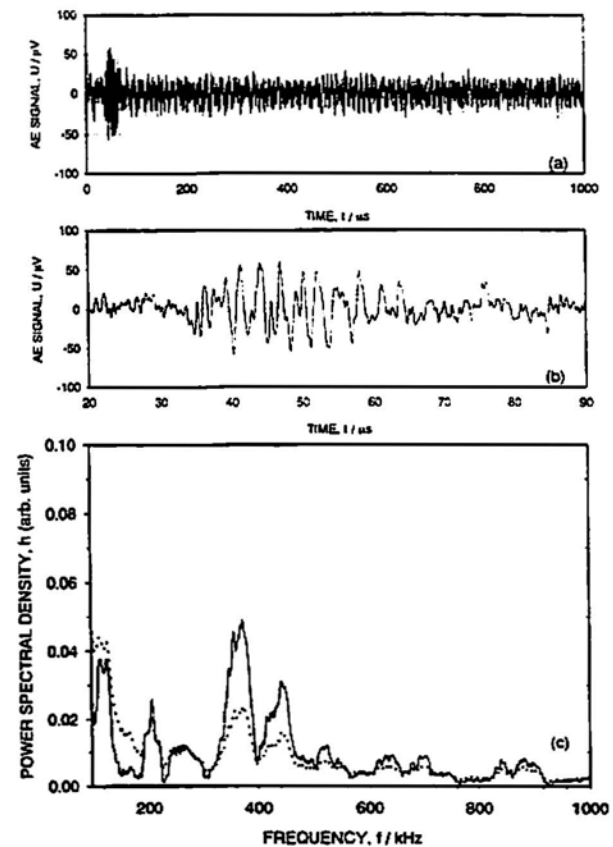


Fig. 7 Representative waveform (a), (b) and power spectral density (c) of AE in a metallic glass - a type-2 signal; (a) a whole single realization; (b) a part of realization. Dashed line (c) shows the spectral density prior to noise removal.

Table 1 Statistical parameters of AE signals in the metallic glass under load.

Parameter	Total AE, N=167		Cluster 1, N=11		Cluster 2, N=156	
	Mean	Std.Dev.	Mean	Std.Dev.	Mean	Std.Dev.
$U_p, \mu V$	94	155	630	118	56	52
$U_{RMS}, \mu V$	9.6	32.6	17.1	13.2	6.3	5.6
$E, \mu V^2s$	2800	15150	35520	45580	320	1960
f_c, kHz	324	150	610	130	304	120
f_{med}, kHz	390	84	620	100	374	53
f_{eff}, kHz	142	48	170	30	140	47

Table 2 Correlation matrix and factor loadings for some AE parameters.

Variable	U_p	U_{RMS}	E	f_c	f_{med}	f_{eff}	Factor Loadings	
							Factor 1	Factor 2
U_p	1	0.78	0.65	-0.02	-0.01	-0.59	0.89	-0.25
U_{RMS}	0.78	1	0.85	-0.07	-0.06	-0.46	0.81	0.2
E	0.65	0.85	1	-0.17	-0.24	-0.47	0.82	-0.42
f_c	-0.02	-0.07	-0.17	1	0.48	0.04	-0.04	0.81
f_{med}	-0.01	-0.06	-0.24	0.48	1	0.24	-0.27	0.87
f_{eff}	-0.59	-0.46	-0.47	0.04	0.24	1	-0.71	0.42

Table 3 Eigenvalues for 6 factors (number of factors equals to the number of variables measured). Eigenvalues for the factors to be retained are shown in bold.

Factor	Eigenvalue	% total Variance	Cumulative Eigenvalue	Cumulative %
1	3.4	57	3.4	57
2	1.3	21	4.7	78
3	0.63	11	5.33	89
4	0.34	6	5.67	95
5	0.21	3	5.88	98
6	0.12	2	6	100

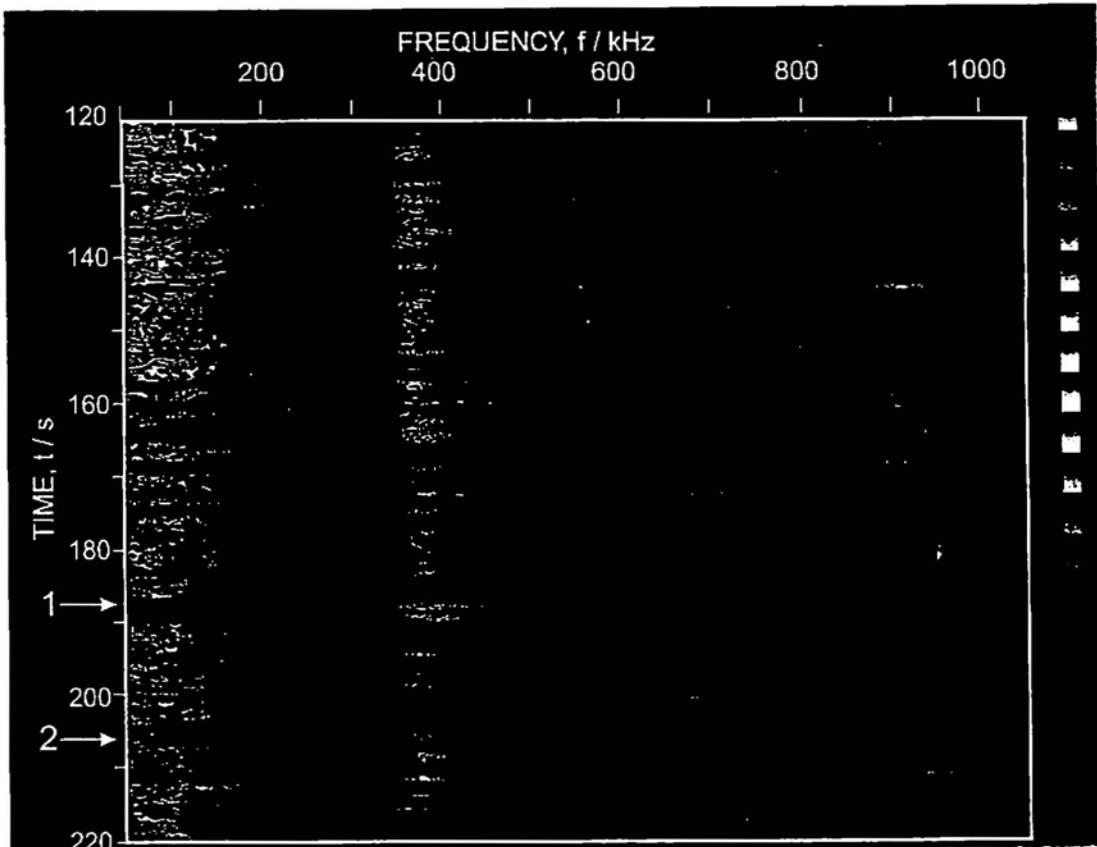


Fig. 8 Contour map showing the normalized average power spectral density as a function of time (strain). No change in the averaged spectrum shape is visible with deformation. Arrows 1 and 2 indicate the map cross sections where the two typical examples of AE events have been taken and shown in Figs. 6 and 7, respectively. See Page ii for the same figure with color.

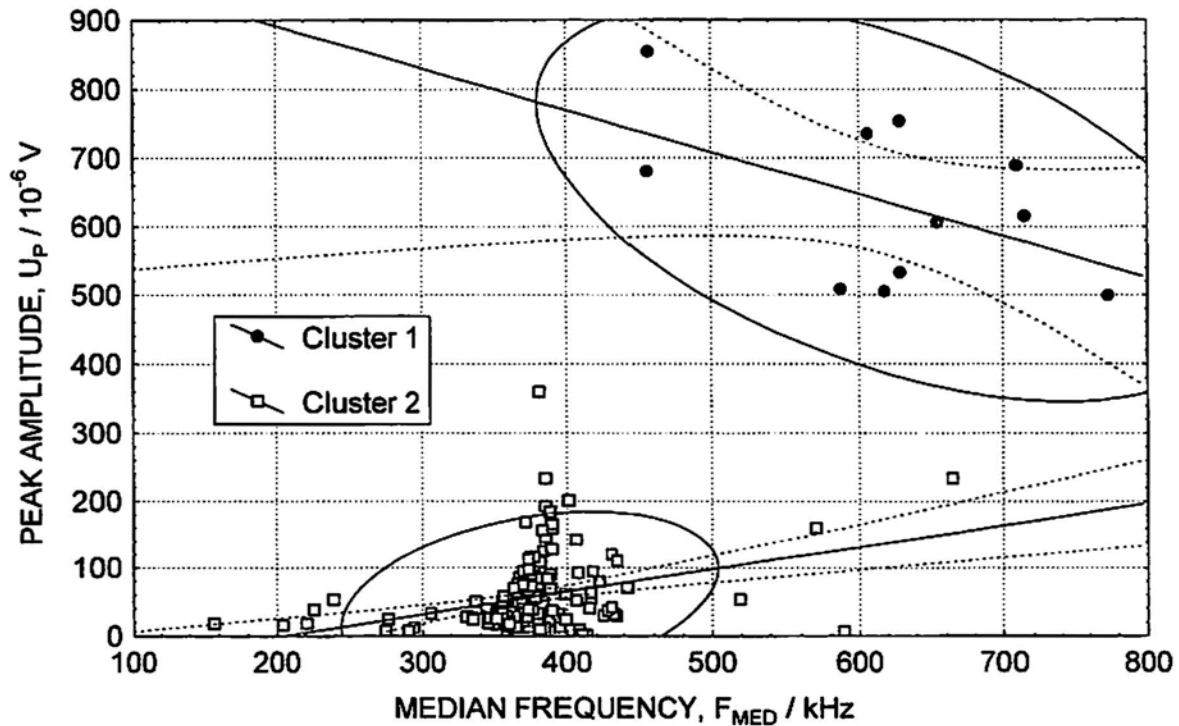


Fig. 9 Example of AE scatter-plot in U_p - f_{med} (peak amplitude versus median frequency) coordinate after K-means clustering. Cluster 1: filled circles; Cluster 2: open squares. Scattering ellipses, regression lines and confidence bands are shown.

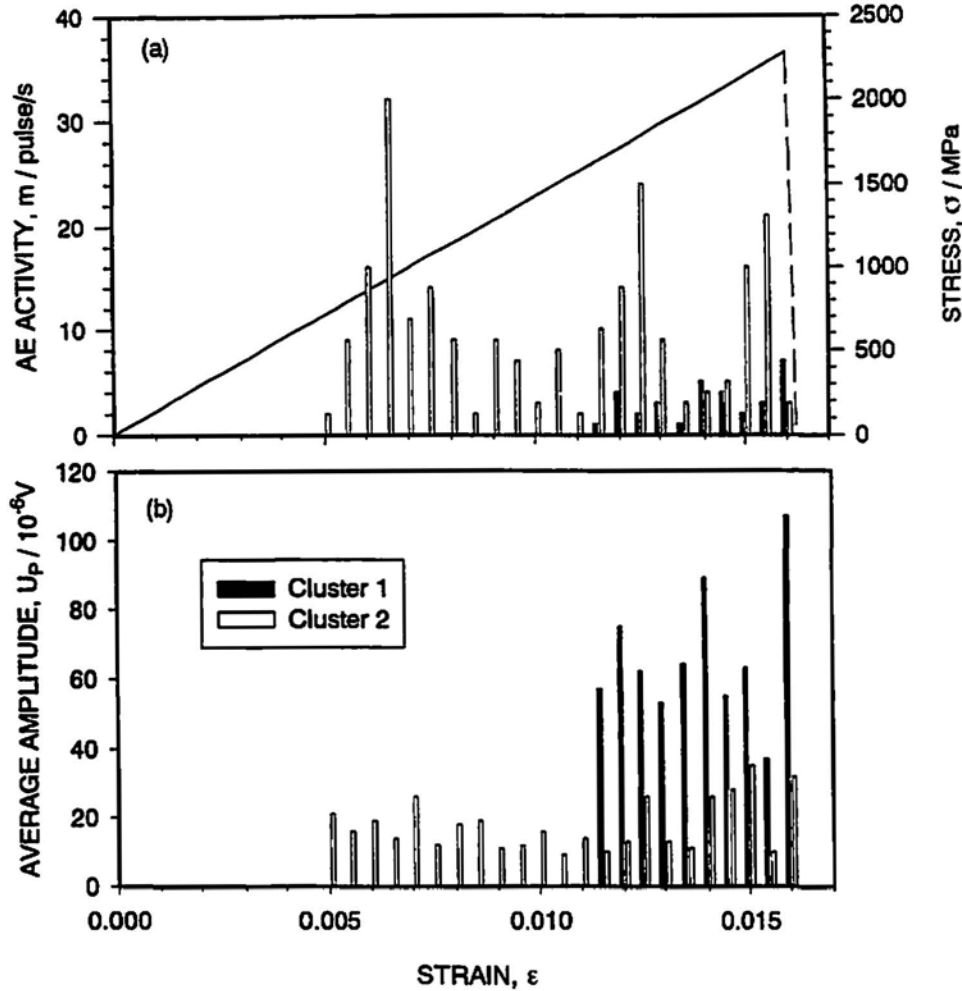


Fig. 10 AE time-history (Fig. 3) is redrawn in this figure after signal classification into two clusters. The signals of Cluster 2 appear earlier than the signals of Cluster 1.

Applying K-means clustering algorithm to the array of AE records from the same specimen, one can find that all signals naturally fall into two categories with respect to their peak amplitudes and median frequencies. Clustered structure of AE data can be easily recognized from the scatter-plot in U_p - f_{med} coordinate, as seen in Fig. 9. Cluster 1 consists of signals with relatively high amplitudes and high median frequencies whereas Cluster 2 includes low amplitude signals with high median frequency. Mean values and standard deviations of both clusters are given in Table 1. Let us notice that the signals are nearly normally distributed within each cluster as is proved by the Kolmogorov-Smirnov test of normality for a fairly large number of AE records. This classification agrees with qualitative visual evaluation by signal and spectral shape discussed above: the type-1 signals form Cluster 1 and the type-2 signals belong to Cluster 2. The similar, but not the same, classification procedure was adopted earlier by Woodward and Harris (1977) and also by Muravin and co-authors (1989, 1996a,b).

4. Discussion

We have experimentally shown that the resultant AE $\{X(t)\}$ is caused by two random stationary processes $\{X_1(t)\}$ and $\{X_2(t)\}$ characterized by their own distribution functions and different shapes of waveforms and power spectra of their constitutive events. Thus, we deal with a typical example of the additive random process:

$$\{X(t)\} = \{X_1(t)\} + \{X_2(t)\}. \quad (2)$$

Having a certain type of cluster assigned to each signal, we obtain the AE time history as a sum of these two processes as shown in Fig. 10. Thus, the structure of the AE flux shown in Fig. 3 becomes clearer. One can see that firstly AE in MGs appears as a flux of type-2 signals. The activity of this flux may attain its maximum and then another process comes into play. The latter process is easy to identify: Cluster 1 is formed by the signals coming from the shear bands (see Secs. 3.1 and 3.2). Interpretation of the other

type of signals (Cluster 2) is much more complicated since no direct structural investigations can help resolve this problem. For this reason AE appears as a powerful tool, which may shed some light on the mechanisms of plastic flow of amorphous metals and alloys. The results of AE studies undoubtedly show that inhomogeneous plastic deformation of MGs cannot be entirely associated with the shear bands visible on the surface. The other mechanism, which acts in addition to shear banding is expected. In the literature, a few arguments exist in favor of possible presence of some plastically deformed regions with significantly smaller scale than the shear bands. For example, in line with our observations, Zielinski and Ast (1983) showed that irreversible plastic deformation started long before the first shear band could be noticed during bending of Ni75Si8B17 MG. Rolling MGs up to 30-40% may not reveal any shear bands on relatively wide regions of the surface while the microhardness of these regions is higher than that of initial material (Alekhin and Khonik, 1992). The nature of such a mechanism of inhomogeneous plastic flow as an additional source of AE is not clear yet and is a subject of further investigation. However, that mechanism must meet at least the following requirements:

- (1) it cannot be identified by direct surface observations;
- (2) it should be localized and should act during a relatively short time to ensure necessary conditions for AE;
- (3) it should be of a smaller scale than the shear bands.

Presumably, it seems plausible to suppose that the small shear events may nucleate inside the amorphous ribbon. This can occur at a relatively low applied stress because the strong heterogeneity of microscopic structure of multi-component MGs results in the significant non-uniformity of internal stress fields. These stresses are arbitrary distributed within the sample and as they attain the magnitude high enough for shear band nucleation, the shearing occurs in the small local volumes of the ribbon. The stress relaxation with the rapid latent energy release causes a flexural elastic wave detected as an acoustic emission. The shearing does not necessary reach a free surface due to the same structural heterogeneity, which plays a dual role in plastic deformation: on one hand, it assists shear initiation but, on the other hand, it provides high stress barriers to be overcome during shear band propagation. Thus, the propagation of shear requires much higher stresses than nucleation. Indeed, the nucleation precedes propagation and type-1 signals appear always after type-2 signals. The small area swept during shearing inside the ribbon leads to the smaller amplitudes and energies of AE signals.

5. Summary and Conclusions

A complex statistical and spectral analysis of acoustic emission (AE) during the plastic flow of metallic glasses (MGs) is performed with the aim of classification of AE sources. A special attention is paid to quantitative characterization of AE features peculiar to individual sources. AE is considered as a multivariate stochastic process. Factor

analysis is employed to optimize a set of descriptive variables. The algorithm of AE data processing is described. Two parameters were found to be most representative for the purpose of this study: peak amplitude measured in time domain and median frequency obtained from power spectral density. With a help of cluster analysis it is shown that the AE signals in MGs fall into two categories (clusters) differed by their amplitude and spectral characteristics. This allowed us to conclude that two different mechanisms of inhomogeneous plastic flow, i.e. two AE sources, operate in MGs. One mechanism is associated with shear band formation during inhomogeneous deformation, while identification of the other mechanism is incomplete. A possible nature of that unknown mechanism of plastic deformation of MGs is discussed and argued that it could be a nucleation of shear bands inside the amorphous body.

Finally, let us note that the method of data processing used in the present work is not limited to metallic glasses and can be widely used for various materials and engineering constructions both in laboratory experiments and in practical non-destructive testing. The simplicity and the lack of arbitrary decisions during data processing allows full automation of the calculations involved. It makes this approach effective for AE source identification. For instance, it can be employed for reliable identification of noise signals that is of importance in most AE problems and, particularly, non-destructive inspection.

Acknowledgements

The author is grateful to Professors K. Kitagawa, S. Hashimoto and V. Khonik for their stimulating interest and encouragement. Financial support is provided by the Ministry of Education, Science and Culture of Japan, grant-in-aid 09650715.

References

- A.P. Alekhin and V.A. Khonik (1992), *Structure and Physical Regularities of Deformation of Amorphous Alloys*, Metallurgiya, Moscow, (in Russian).
- A.S. Argon (1979), *Acta Metall.*, **27**, 47.
- J.S. Bendat and A.G. Piersol (1966), *Measurement and Analysis of Random Data*, J. Wiley & Sons.
- A.P. Braginskii, A.Yu. Vinogradov, A.M. Leksovskii and B.M. Medvedev (1986), *Sov. Tech. Phys. Lett.*, **12**, 459.
- W.W. Cooley and P.R. Lohnes (1971), *Multivariate Data Analysis*, Wiley and Son, New York.
- P.E. Donovan and W.M. Stobbs (1981), *Acta Metall.*, **29**, 1419.

- D.M. Egle, C.A. Tatro and A.E. Brown (1981), *Mater. Evaluation*, **38**, 1037.
- M. Enoki and T. Kishi (1991), *Acoustic Emission. Current Practice and Future Directions*, eds. W. Sachse, J. Roget and K. Yamaguchi, STP 1077, ASTM, Philadelphia, p. 47.
- P. Fleischmann and D. Rouby (1979), *Strength of Metals and Alloys*, (eds. P. Haasen, V. Gerold and G. Kostorz) vol. 1, Pergamon Press, New York, p. 559.
- J.J. Gilman (1973), *J. Appl. Phys.*, **44**, 675.
- I. Grabec (1995), *Proc. of Neural, Parallel and Scientific Computations*, vol. 1, p. 172.
- I. Grabec and W. Sachse (1989), *J. Acoust. Soc. Am.*, **85**, 1226.
- V.A. Khonik, K. Kitagawa, V.M. Mikhailov and A.Yu. Vinogradov (1998), *J. Appl. Phys.* (in press).
- L.J. Graham and G.A. Alers (1974), *Mater. Evaluation*, **32**, 31.
- H.H. Harman (1967), *Modern Factor Analysis*, Chicago University Press, Chicago.
- J.A. Hartigan (1975), *Clustering Algorithms*, Wiley & Sons, New York.
- V.A. Khonik, V.M. Mikhailov and A.Yu. Vinogradov (1997), *Scripta Mater.*, **37**, 377.
- T. Kishi, K. Ohno and K. Kuribayashi (1981), *Journal of JSNDI*, **30**, 911 (in Japanese).
- A.M. Leksovskii, A.Yu. Vinogradov and V.V. Smirnov, *Sov. Tech. Phys. Lett.*, **12** (1986) 265.
- A.C. Lucia and G. Redondi (1976), *Trans. ASME Ser. J (USA)*, **98**, 199.
- J. MacQueen (1967), *Proc. of the Fifth Berkeley Symposium on Mathematical Statistics and Probability*, vol. I, eds. L.M. Le Cam and J. Neyman, California University Press, Los Angeles, p. 281.
- T. Masumoto and R. Maddin (1975), *Mat. Sci. & Eng.*, **19**, 1.
- R.C. Morris (1979), *J. Appl. Phys.*, **50**, 3250.
- G.B. Muravin, Ya.V. Simkin and A.I. Merman (1989), *Sov. J. Nondestruct. Test.*, **25**(4), 239.
- G. Muravin, L. Lezvinsky, B. Muravin and Y. Canetti (1996a), *Progress in Acoustic Emission VII*, eds. T. Kishi, Y. Mori, Y. Higo and M. Enoki, The Japanese Society for NDI, Tokyo, p. 255.
- G. Muravin, L. Lezvinsky and B. Muravin (1996b), *Progress in Acoustic Emission VII*, eds. T. Kishi, Y. Mori, Y. Higo and M. Enoki, The Japanese Society for NDI, Tokyo, p. 261.
- V.D. Natsik and K.A. Chishko (1972), *Sov. Phys. Solid State*, **14**, 2678.
- V.D. Natsik and K.A. Chishko (1978), *Sov. Phys. Solid State*, **20**, 264.
- V.D. Natsik and K.A. Chishko (1982), *Sov. Phys. Acoust.*, **28**, 225.
- N.I. Noskova, N.F. Vildanova, Yu.I. Filipov and A.P. Potapov (1985), *phys. stat. sol. (a)*, **87**, 549.
- K. Ono and H. Ucisik (1976), *Mater. Evaluation*, **34**, 32.
- K. Ono and J.-Yu Wu (1996), *Progress in Acoustic Emission VII*, eds. T. Kishi, Y. Mori, Y. Higo and M. Enoki, The Japanese Society for NDI, Tokyo, p. 237.
- M.B. Priestley (1981), *Spectral Analysis and Time Series*, vol. 1, Academic Press, New York.
- C.B. Scruby, K.A. Stacey and G.R. Baldwin (1986), *J. of Physics D*, **19**, 1597.
- F. Spaepen (1977), *Acta Metall.*, **25**, 407.
- H. Suzuki, T. Kinjo, M. Takemoto and K. Ono (1996), *Progress in Acoustic Emission VII*, eds. T. Kishi, Y. Mori, Y. Higo and M. Enoki, The Japanese Society for NDI, Tokyo, p. 47.
- A. Vinogradov, M. Nadtochiy, S. Hashimoto and S. Miura (1995), *Mater. Trans., JIM*, **36**, 426.
- A.Yu. Vinogradov., A.M. Leksovskii, V.A. Bershtein, V.M.Egorov and V.V.Smirnov (1988), *Sov. Phys. Solid Stat.*, **30**, 314.
- A.Yu. Vinogradov, A.M. Leksovskii, Yu.V. Milman and V.P. Ovcharov (1989), *Phys.Met*, **11**, 66.
- A. Vinogradov and A. Leksovskii (1996a), *Materials Science Forum*, **210-213**, 549.
- A.Yu. Vinogradov and A.M. Leksovskii (1996b), *Progress in Acoustic Emission VII*, eds. T. Kishi, Y. Mori, Y. Higo

and M. Enoki, The Japanese Society for NDI, Tokyo, p. 153.

H.N.G. Wadley, C.B. Scruby and G. Shrimpton (1981), *Acta Metall.*, **29**, 399.

B. Woodward and R.W. Harris (1977), *Acustica*, **37**, 190.

S.G. Zaichenko and V.T. Borisov (1982), *Doklady AN SSSR*, **263**(3), 622 (in Russian).

S.G. Zaichenko and A.P. Braginskii (1990), *Metallofizika*, **12**(4), 15 (in Russian).

P.G. Zielinski and D.G. Ast (1983), *Phil. Mag. A*, **48**, 811.

MEETING CALENDAR

24th EWGAE Meeting (EWGAE 2000)

May 24-26, 2000; at CETIM, Senlis (40 km N of Paris), France; Program Chairs: C. Rigault and M. Cherfaoui (christel.rigault @cetim.fr)

AE in structural and advanced materials (metals, concrete, rock, FRP, ceramics,...)
AE in structures (pressure vessels, pipelines, reactors, aircraft, bridges, offshore platforms, buildings, ...)
AE in manufacturing process monitoring (welding, machining, casting,...)
AE in diagnostics (leak detection and monitoring, plant maintenance, wear, machine condition...)
AE instrumentation and signal processing; Standards and codes of practice
Seizmoacoustics (dams, geotechnics)

Contact the Program Chairs to request Call for Papers.

43rd Meeting of AEWG

July 17-20, 2000; Seattle, WA; Program Chair: Allen T. Green (ATGreen1@aol.com)

July 17: 2000 Primer

July 18: Technical Presentations, AEWG business meeting

July 19: Technical Presentations, Awards Banquet

July 20, morning: Tour of Boeing Engineering Labs

July 21-22: ASME Pressure Vessels and Piping Meeting (separate registration needed)

15th International AE Symposium (IAES-15)

September 11-14, 2000; The International House of Japan, Tokyo, Japan; <http://home.att.ne.jp/green/iaes15>

Symposium Organizing Committee Co-Chairs: T. Kishi and Y. Higo; Program and Papers Committee Chair: M. Ohtsu; Secretary Committee Chair: S. Yuyama (e-mail : aeyuyama@sh0.po.ijnet.or.jp)

- (1) Advanced overview: Review and future aspects of AE technology, Standards and codification,
- (2) Sensors: Calibration, New development, Standardization etc.
- (3) AE instrumentation and AE analysis: System calibration, Signal processing, Time- and frequency-domain analysis, etc.
- (4) AE in materials and source-materials characterization: Ceramics, FRP, FRM, Metals, Concrete, Rock, Wood, etc.
- (5) Applications to structures: Pressure vessels, Reactors, Pipelines, Aerospace, Transportation, Offshore structures, etc.
- (6) Manufacturing process monitoring: Wear, Contact, Tribology, Machining, Welding, Casting, etc.
- (7) Applications to medical fields: Implant, Heart, etc.
- (8) Applications to geo-structures and civil engineering: Landslide, Underground development, Mining, Microseismics, Geothermal development, Maintenance of infrastructure, etc.
- (9) Novel applications:

The deadline for submission of abstract (100 - 200 words with key words in English, 4 copies): January 31, 2000.

March 31, 2000 Notification of acceptance and instructions for authors.

May 31, 2000 Deadline for final text. Registration and remittance of registration fee.

June 30, 2000 Second announcement and program.

Acoustic Emission Characteristics of Soil and Sand in Response to Simulated Root Growth

C. Divaker Durairaj, L. Okushima and S. Sase

Abstract

Detecting root growth with acoustic emissions (AE) caused by root-soil interaction has potential applications in greenhouses. In this study, root growth was simulated by pushing a probe into the soil at preset rates using a mechanical simulator developed for this purpose. The investigation was conducted under noise proof environment on soil and sand at various moisture levels with the simulated root growth varied at 3 levels from 0.5 to 1.33 mm/h. AE were detected by an array of three sensors connected to conventional AE instrumentation. The results showed that the emissions were very weak in the soil consisting of 0.4 mm particles, but the growth rate could be inferred based on the rate, at which these emissions are generated. In sand, wet or dry, the emissions were of high intensity and periodic. Spectral methods were used to recognize the pattern of hit distribution. When AE measurements from real root growth were analyzed using spectral methods, it was possible to detect the change in real root growth rate, by way of correlating it with those of the simulated study.

1. Introduction

The physiological state of plants in greenhouses should be assessed accurately, so that the in-house environmental attributes could effectively be controlled to obtain high quality crop production. This, in turn, will lead to just-in-time market delivery of produce and conservation of water and other inputs. From this viewpoint, non-destructive sensing of individual plants in greenhouses is needed. AE is an interesting method for the said purpose. In particular, the study of AE patterns, generated by root growth in soil, is of great interest towards developing a root growth monitoring system for greenhouses. In an effort to detect AE caused by real root-soil interaction, Okushima et al. (1994) experimented with different types of sensors, including a simple condenser microphone and studied their response to the generated AE signals from different soils. Okushima et al. (1996) showed that under real root growth, sand emitted higher AE hit counts than a culture soil containing humus.

Received 19 August 1998. C. Divaker Durairaj is affiliated with Department of Farm Machinery, Tamil Nadu Agricultural University, Coimbatore 641 003, INDIA, L. Okushima (limi@nkk.affrc.go.jp) and S. Sase are with Department of Land Improvement, National Research Institute of Agricultural Engineering, 2-1-2 Kannondai, Tsukuba 305, JAPAN.

Their studies revealed the range of AE signals generated from root-soil interaction for sand and culture soils. AE due to root-soil interaction, involve a high degree of complexity, since the medium in question, is so complex in characteristics. Many factors, such as the type and size of soil particles, the moisture content of the soil, the presence of humus (Okushima et al., 1996), the level of compaction, and the limiting stresses of the soil surface boundary, affect the nature of AE signals generated. The key factor, which is of interest, is the rate at which the root grows and its influence on the pattern of AE hit distribution over time. The rate of real root growth varies drastically from 0.25 to 1.4 mm/h over different stages of its growth (Shimotashiro et al., 1998). Our objective is to recognize the pattern of AE hit occurrence and correlate it with that of the root growth rate. Towards this end, the pattern of AE generated at constant root growth rates need be ascertained first. Since it may not be possible to maintain a constant root growth rate in a real plant, our study attempted to simulate the root growth itself using a mechanized simulator and acquire AE data for each level of growth rate. The data was ultimately used for recognizing the pattern of hits generated for each growth rate.

2. Experimental Setup

The root growth simulator (Fig. 1) was just a mechanism, which pushed a probe into the soil at the required rate of root growth, thus simulating the growing root tip. It consisted of a stepper motor and allied circuitry for generating the stepper signals. Since the stepper motor is a discrete device and steps through its rotation, directly driving the probe by the motor may cause discrete motions to the simulating probe. Hence, to make the simulations realistic, a gearbox of reduction as high as 2730:1 was used between the motor and the probe movement. This way, the stepper motor could be driven at higher speeds, thus masking its discrete motion. A sliding barrel receiving motion from the gearbox, converts it to a linear motion. To isolate the simulator's noise and vibration from the soil itself, a hydraulic transmission was added as the final drive element. It was a simple assembly of two injection syringes connected mouth to mouth through a flexible hose and filled with water devoid of air bubbles. One of these syringes was mounted beneath the slider so that it pushes on the plunger at the set rate. The movement gets transmitted to the other syringe's plunger, which held the probe simulating the root. The

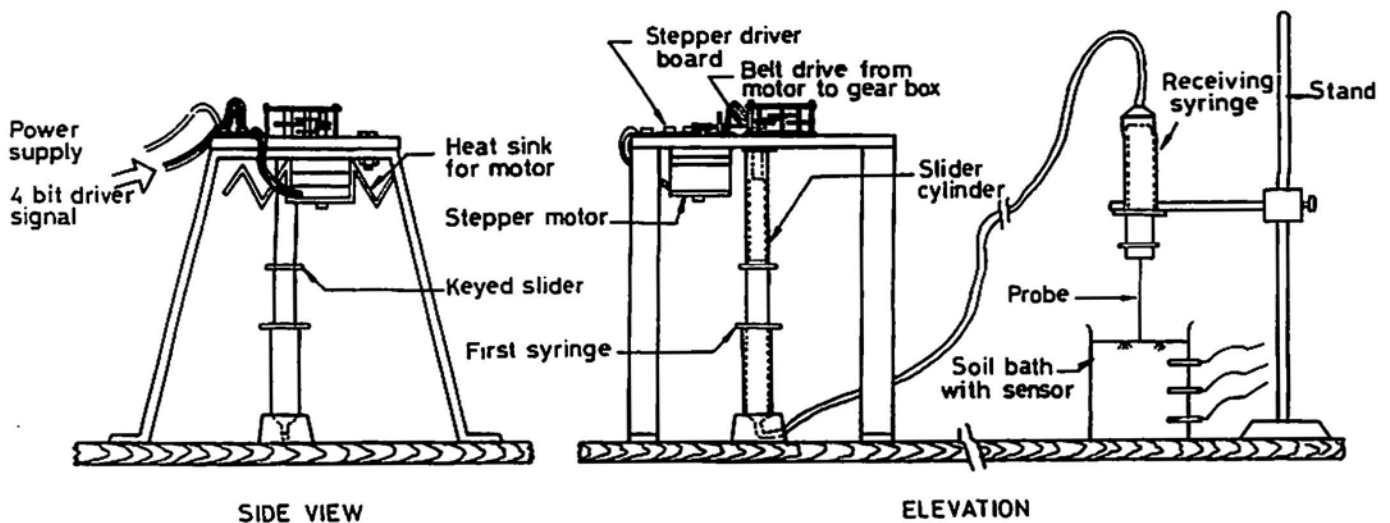


Fig. 1 Construction of the root simulator.

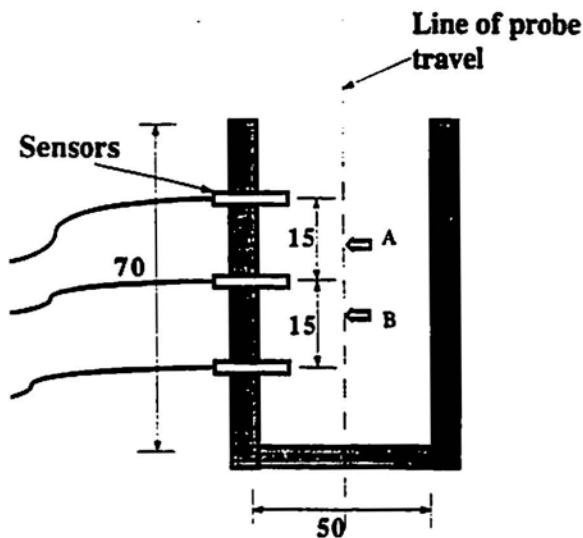


Fig. 2 Arrangement of sensors in the soil bath.

second syringe with the probe was clamped on a stand over the soil surface at the required position. To exactly simulate root growth, a real root tip itself of 0.8 mm diameter was used as inserted on to a 0.2-mm metal pin. The bulbous tip eliminated any abrasion of the metal probe's periphery with soil, since its diameter is larger than the metal probe itself.

Figure 2 shows the arrangement of sensors in the soil bath. In an effort to study the relationship between the AE hits received by different sensors placed at different locations, an array of three sensors were used in the soil bath. This provided for analyzing the influence of the medium and its condition on the propagation of AE. The sensors were accelerometers (CR-03C-0030, Fuji Ceramics Co.) whose main detecting band of frequencies was 3–15 kHz with resonance at 9 kHz. Preamplifiers of 40 dB gain were used to amplify the sensor outputs. 40 dB gain and 35 dB threshold levels were set on the AE monitor (LOCAN 320, Physical Acoustics Corp.). The probe simulating the root

was made to traverse from point A to B (Fig. 2). The soil bath itself was a plexiglass (PMMA) cylinder of 50 mm diameter and 70 mm depth. It had circular marks around its periphery at equal intervals of 10 mm, so that the soil could be loaded in layers, ensuring the same level of compaction all over and maintaining the bulk density of the soil at the required level. Two root growth media were considered for the study, which were,

- i. a fine beach sand consisting of uniformly sized 0.4 mm particles,
- ii. Akadama soil (a lower layer soil of Andosols), which was ground and sieved to acquire particle sizes ranging from 0.3 to 0.4 mm.

Sand was tested when it was dry and at 10% moisture and soil was tested at three levels of moistures, namely dry, 20% and 30% moisture. During all the trials, soil and sand, whether dry or moist were loaded into the bath at bulk densities of 1.2 and 1.5 g/ml, respectively. The travel rate of the simulator's probe (growth rate) was varied at three levels of 0.5, 1.0 and 1.33 mm/h on each treatment and measurements replicated thrice. AE was logged for 24, 12 and 8 h, respectively for 0.5, 1.0 and 1.33 mm/h growth rates and hence the net travel made by the probe's tip ('AB' in Fig. 2) was 12 mm in all the cases. The trials were conducted inside a noise proof growth chamber to eliminate spurious hits due to external noise. The hits as accumulated over particular time intervals were analyzed for any possible patterns of distribution with respect to time. Different time intervals of 5 min, 15 min and 30 min were tried for obtaining the discrete samples of hit data. It was found that the distributions sampled at larger time intervals were "aliases" of the periodicity of distributions obtained at smaller time intervals. For convenience and also to obtain a higher degree of freedom for any statistical analysis, the hit distribution sampled over 0.25 hr was considered for pattern recognition. The sampling rate was hence kept constant, while analyzing all the hit distributions pertaining to different

Table 1 ANOVA on the number of hits as influenced by probe travel rate and position in dry sand.

Growth rate	Count	Sum	Average	Variance
0.5 mm h ⁻¹	12 2285	190.4167	6536.992	
1.0 mm h ⁻¹	12 2264	188.6667	4795.879	
1.33 mm h ⁻¹	12 1702	141.8333	5076.697	

ANOVA

Source of Variation	SS	df	MS	F	P-value	F crit
Displacement of Probe, mm	72039.64	11	6549.058	1.328341	0.273815	2.258517
Growth rate, mm h ⁻¹	18227.06	2	9113.528	1.84849	0.181112	3.443361
Error	108465.6	22	4930.255			
Total	198732.3	35				

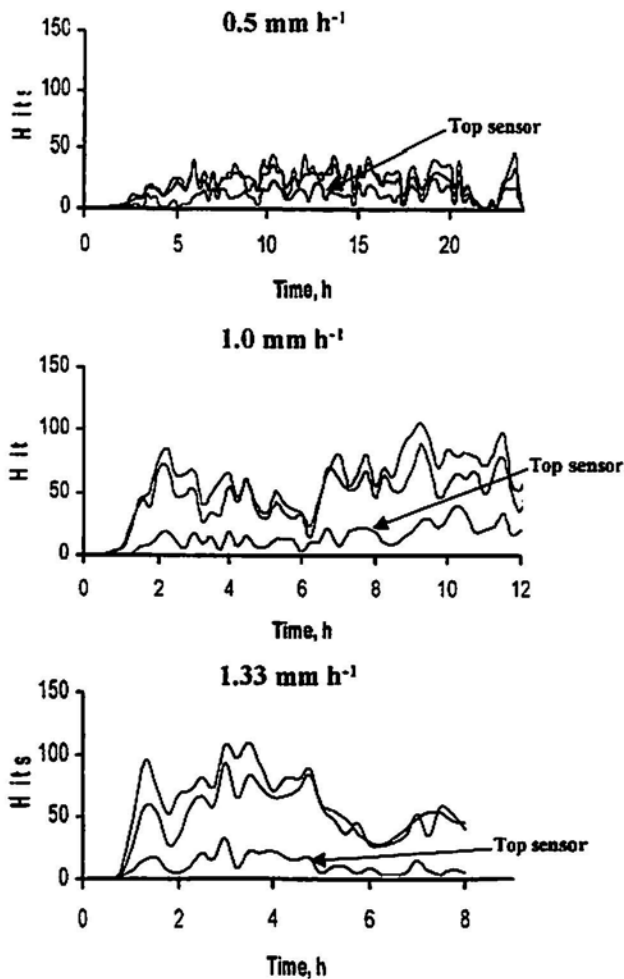


Fig. 3 Distribution of AE hits in dry sand.

growth rates. Hence, the Nyquist critical frequency, which is the reciprocal of twice the sampling time interval, was constant for the whole analysis.

3. Results and Discussion

3.1 Acoustic Emissions of the Sand

The AE activity in dry sand was to a maximum of 125 hits per 0.25 h. To explore whether the number of hits themselves could be used to deduce the simulated growth rate (probe travel rate), an Analysis of variance (ANOVA) was attempted on the number of hits, with the displacement of probe (time) itself as one factor and the probe travel rate as another. The ANOVA (Table 1) on dry sand showed that both of the factors were insignificantly affecting the number of hits detected. This implied that the number of hits as such, could not be used for correlating it with growth rate.

As seen from the hit distributions, a periodicity was present. Since the hits were observed at equal interval of time, the data was analyzed as a time series. Figure 3 shows the data series with respect of dry sand, when the probe rates were 0.5, 1.0 and 1.33 mm/h. The auto-correlation function (acf) of the AE hit series, acquired by the three sensors, showed that hits received by all the three were almost of the same pattern since they have received the same hits simultaneously. The acf clearly showed that the data series was non-stationary. Making Polynomial regressions to the hit data distribution effected the required de-trending. The regressions were of the form as detailed below.

$$Y = 77.94 - 56.63777x + 17.70994x^2 - 2.469692x^3 + 0.1737567x^4 - 0.00600871x^5 + 0.000080896x^6;$$

$$r^2 = 42\% \text{ for } 0.5 \text{ mm/h}$$

$$Y = -132.91 + 229.6816x - 102.3444x^2 + 20.93684x^3 - 2.151279x^4 + 0.1087562x^5 - 0.00216329x^6;$$

$$r^2 = 33\% \text{ for } 1.0 \text{ mm/h}$$

$$Y = -59.635 + 230.5496x - 211.9526x^2 + 97.79892x^3 - 22.31707x^4 + 2.405202x^5 - 0.09786581x^6;$$

$$r^2 = 70\% \text{ for } 1.33 \text{ mm/h,}$$

where 'Y' is the number of hits and 'x' is time in hour.

After de-trending the data, it showed that the distribution had periodical seasonality. Therefore, the method of Dominant Frequencies was used to do spectral analysis on the distribution as a time series. Rather than using a fast Fourier transform method, this method uses the maximum-entropy (or all poles) method. The maximum-entropy method represents the data in terms of a finite number (N) of complex poles of discrete frequency. By contrast, the fast Fourier transform essentially fits the power spectrum to a polynomial and is better for data whose spectrum is smoothly varying. Figure 4 shows the power spectrum of the hit distribution pertaining to the three simulated probe travel (root growth) rates. The frequency is in units of the Nyquist critical frequency (the reciprocal of twice the time interval between the data points) and the power expressed in arbitrary units. The number of complex poles (N) was 4 for calculating the spectrum. The distinct peaks indicated that the AE hit distribution had dominant frequencies of periodicity in relation to the simulated root growth rate. To further verify whether the time series had common frequency components, a coherence analysis was made between the time series pertaining to each pair of growth rates. The coherence analysis proved that the frequencies at which the hits occurred were distinctly dissimilar for each simulated growth rate.

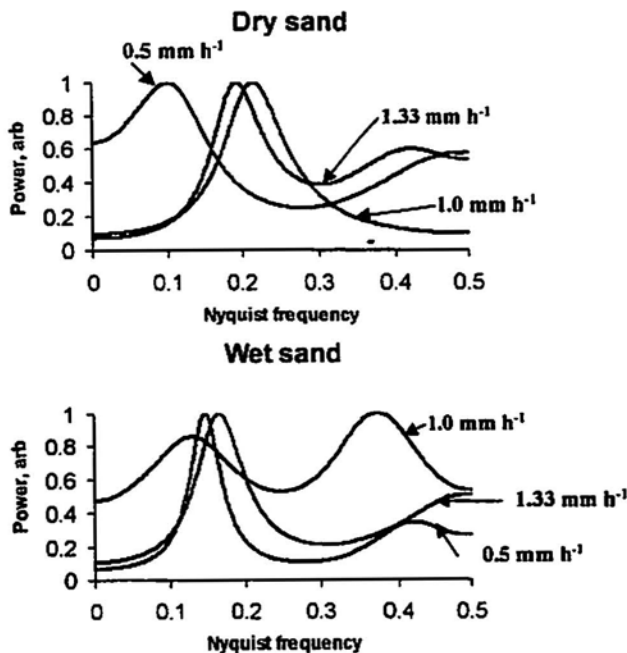


Fig. 4 Dominant frequencies at simulated growth rates.

In wet sand, the hit rates were to a maximum of 400 hits per 0.25 h (Fig. 5). The higher hits were due to the lower acoustic impedance of the wet sand transmitting even weak hits to the sensors. The ANOVA (Table. 2) shows that both the factors were significant, which was unlike of the dry sand. This provides for the possibility of using the number of hits themselves to detect the growth rate of the root. Since the hit distribution of wet sand also had distinct periodicity, spectral analysis was carried out. The distributions showed the presence of a trend, which was removed using polynomial regression, which were in the form of,

$$Y = 51.74 - 86.46x + 43.0799x^2 - 8.122728x^3 + 0.7323735x^4 - 0.03189654x^5 + 0.00053952x^6;$$

$$r^2 = 47\% \text{ for } 0.5 \text{ mm/h}$$

$$Y = 1283.01 - 1096.99x + 426.6945x^2 - 83.19402x^3 + 8.634029x^4 - 0.4549649x^5 + 0.00951093x^6;$$

$$r^2 = 82\% \text{ for } 1.0 \text{ mm/h}$$

$$Y = -463.019 + 1560.2739x - 1101.103x^2 + 363.8607x^3 - 61.64478x^4 + 5.145188x^5 - 0.1673926x^6;$$

$$r^2 = 88\% \text{ for } 1.33 \text{ mm/h,}$$

where 'Y' is the number of hits and 'x' is the probe displacement.

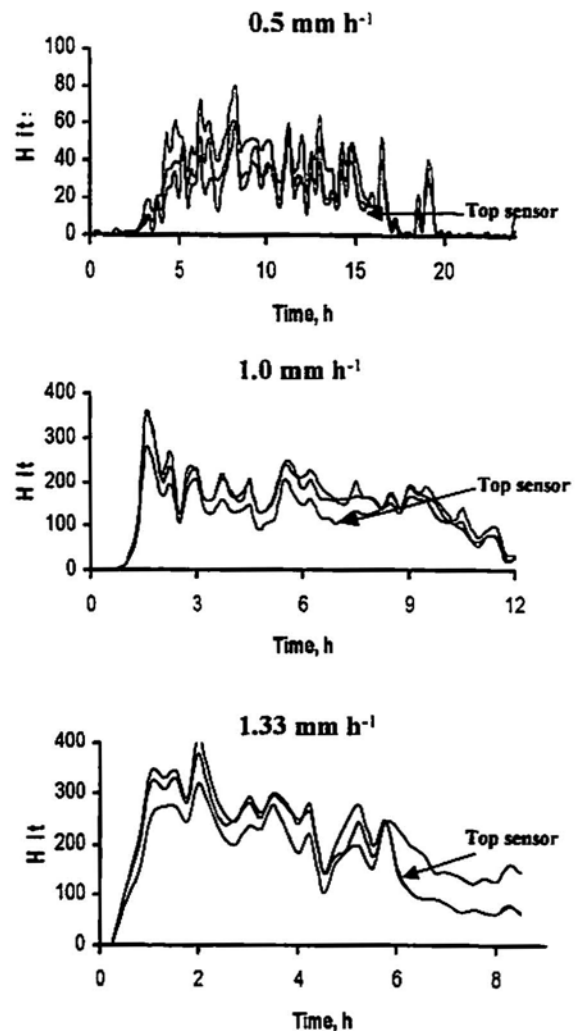


Fig. 5 Distribution of AE hits in wet sand at 10% moisture.

Table 2 ANOVA on the number of hits as influenced by probe travel rate and position in wet sand (10%).

Growth rate , mm h ⁻¹	Count	Sum	Average	Variance
0.5 mm h ⁻¹	12	3596	299.6667	12163.7
1.0 mm h ⁻¹	12	7451	620.9167	53748.63
1.33 mm h ⁻¹	12	5695	474.5833	30285.72

ANOVA

Source of Variation	SS	df	MS	F	P-value	F crit
Probe position, mm	776125.2	11	70556.84	5.503394	0.000342	2.258517
Growth rate, mm h ⁻¹	620843.4	2	310421.7	24.21272	2.76E-06	3.443361
Error	282053.3	22	12820.6			
Total	1679022	35				

The power spectrum (Fig. 4) indicated distinct peaks in the distribution. Here also, the coherence analysis proved that the frequencies at which the hits occurred were distinctly dissimilar for each simulated growth rate.

3.2 Acoustic Emissions of Soil

AE hits in soil were not many and the reason was basically due to the absence of abrasive particles (Okushima et al., 1996). Moreover, soil as a porous medium, attenuates whatever weak AE being emitted. The AE hits as acquired from loose dry soil of 0.4 mm particle size exhibited very minimal counts and were practically of no use. However, the AE hits from moist soils, though weak and sparse, were generally in the range of 1 to 5 at various intervals of time depending on the probe travel rate. Increasing the gain of AE instrumentation, was attempted, but noise and spurious hits were excessive and the experiment was aborted. So the experiment was continued with the same gain and the hit distribution was analyzed as such. Since the hit distributions did not have any periodicity, a spectral analysis could not be made. However, the intervals, at which the hits occurred in terms of the probe displacement, were analyzed for an underlying pattern.

As for the wet soil 20% moist, when the probe travel was 0.5 mm/h (Fig. 6), the hits occurred at approximately every 0.6 to 0.8 mm of probe displacement. But when the probe entered deeper layers, a slight periodicity in hit distribution was observed. However the number of hits ranged only up to a maximum of 6. When the penetration rate was increased to 1.0 mm/h, AE hits decreased. There was AE activity only when the probe was directly in front of the sensor. The reason may be that the AE generated at this

penetration rate consisted of a band of frequencies, which did not fall into the frequency band of the sensor or they were being attenuated by the medium completely. When the penetration rate was increased further to 1.33 mm/h, the AE activity was higher, but they occurred at every 3-4 mm movement of the probe. This rate of movement could have caused localized compression zones building up pressure, until released by particle movement at longer intervals.

When the soil was made 30% moist, the hit distributions (Fig. 7) were different from those of the drier soils. At a penetration rate of 0.5 mm/h, hits occurred every 0.8 to 1.4 mm movement of the probe. The sensor located at deeper layers was not registering hits, whereas the sensor at the top layer was sensing hits. This was specific to the soil at 30% moisture. There is a possibility that the soil particles, instead of moving locally at the probe tip, rise as single mass at the top, causing AE activity there. When the penetration rate was taken up to 1.0 mm/h, AE activity decreased very much like in the drier soil with 20% moisture. The penetration rate of 1.33 mm/h, offered a similar response as that at 0.5 mm/h, but here the hits occurred every 2 - 3 mm movement of the probe. From the analysis, it seems that there is a possibility of detecting the growth rate based on the interval, at which the hits occur.

3.3 Influence of the Medium on Hit Detection

The hit data was also analyzed whether the attenuation of sound in porous media posed problems in detection of AE generated by root growth. Dry sand, anticipated to be the most attenuating medium, did not cause any problems, since the AE activity is at least 10 folds higher than that of plain soil. But plain soil, especially the dry one, may cause

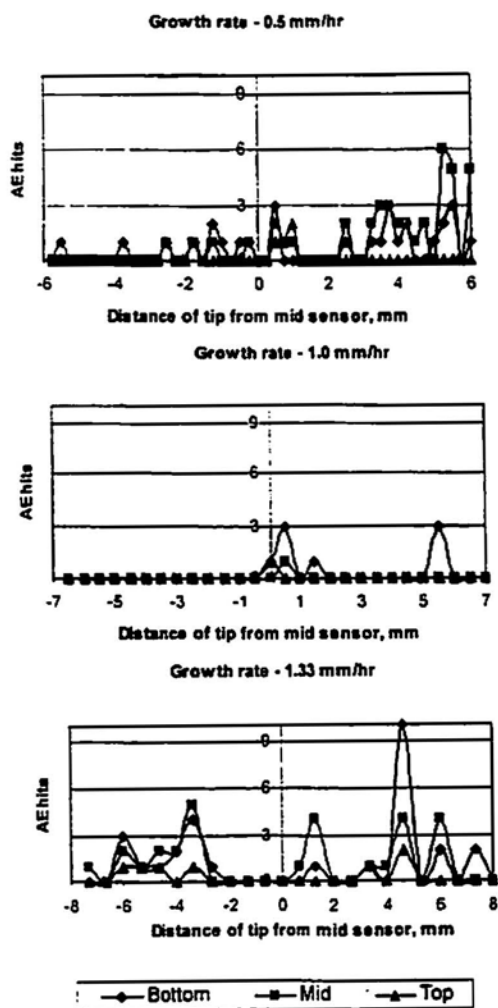


Fig. 6 AE hit distribution of wet soil at 20% moisture.

AE detection problems. Increasing the gain and threshold of AE sensor and associated circuitry may cause problems of noise and spurious signals being picked up.

The auto-correlation functions of the hit distributions against time indicated that all the sensors detected the same hits. But the hit distribution itself (Fig. 3) showed that the sensor placed near the soil surface (top) logged far lesser hits than those of the other two. This could only mean that the acoustic impedance of the dry sand near the surface was higher than the rest and had mollified the hits arriving at that sensor. Dry sand seems to vary its impedance based on its looseness of packing. Even when the probe tip was between the top and the middle sensors, the hit rate was weak on the top sensor. However, this phenomenon was absent in wet sand (Fig. 5). All the sensors detected the hits simultaneously and had more or less the same number of hits per unit time. In regard to soil, the sensor near the soil surface also had problems detecting the hits, when the medium was relatively drier (20% moisture). However, the number of hits observed in soil was very low in all the sensors and the difference could not be discerned clearly. These observa-

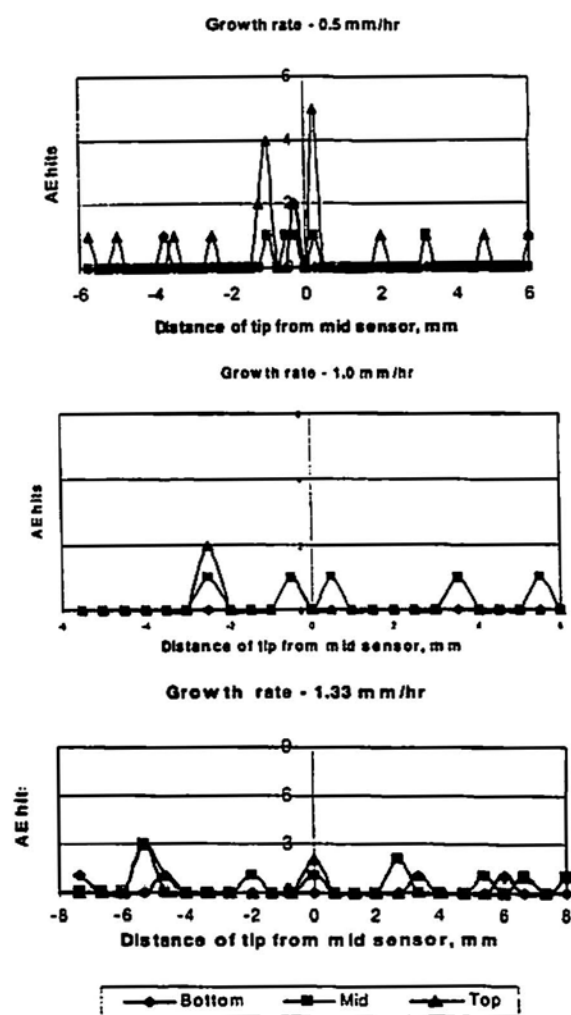


Fig. 7 AE hit distribution of wet soil at 30% moisture.

tions indicate that the sensor placement becomes critical when the medium is dry.

3.4 AE from Real Root Growth

A germinated maize seed with a root length of 2 mm was sown in the bath (Fig. 2) having wet sand at 10% moisture. AE caused by real root growth was measured for 3 days. The hits accumulated over 0.25 h interval were analyzed. The data series was found to be non-stationary and carrying periodicity. The 72 h data series was segmented into distributions pertaining to consecutive 12 h periods and each segment analyzed as a separate time series. Each was in turn de-trended using polynomial regression over time and, dominant frequencies at four complex poles were determined (Fig. 8). Comparing Figs. 8 and 4, the dominant frequencies at the first 12 h period of real root growth were similar to that of the simulated growth at 1.0 mm/h. The dominant frequencies at 12 - 24 h period peaked at about 0.2 Nyquist frequency (Fig. 8), which was similar to that at the simulated growth rate of 0.5 mm/h (Fig. 4).

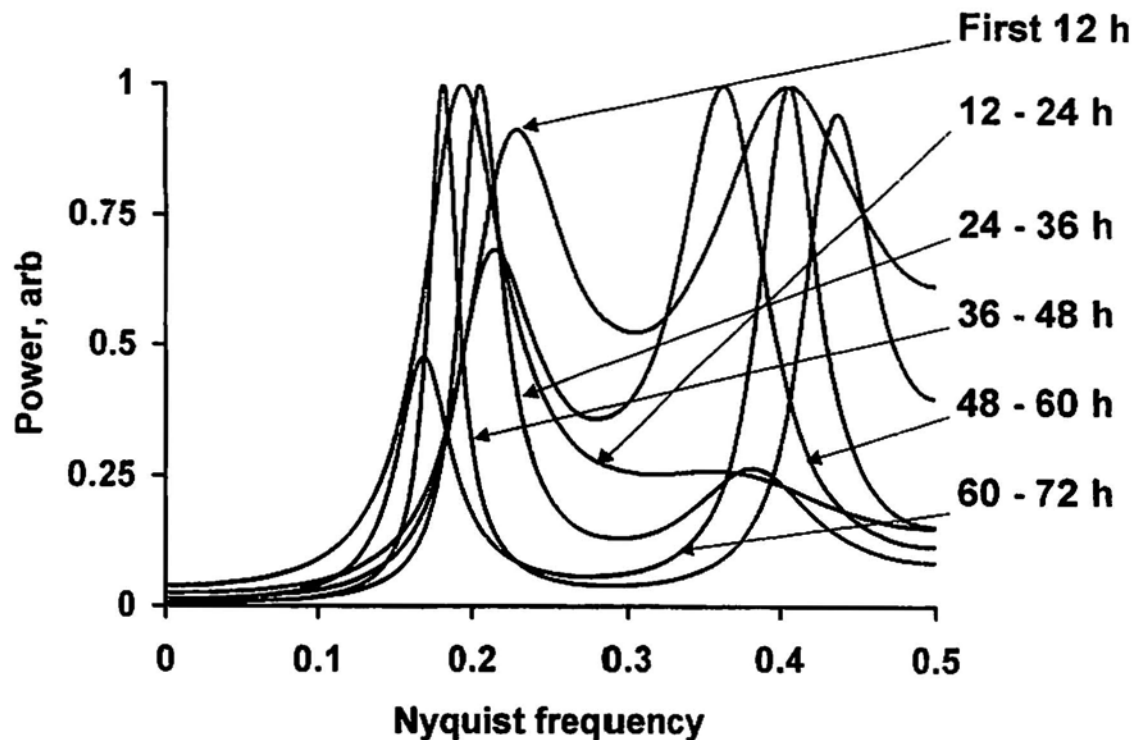


Fig. 8 Power spectrum of hits caused under real root growth.

Similarly, the 36 - 48 h period showed a drop in the dominant frequency (Fig. 8), which was alike as that of the simulated growth at 1.33 mm/h. The total root growth in 72 h was 70 mm, as measured after removing the seed out of the sand. This corresponded approximately with that of the sum of predicted growth proposed by the simulated data. Though the real root growth rate could not be exactly discerned yet, the analysis showed possibilities of using the hit distribution for predicting the real root growth rate. This would be possible if data on more number of simulated growth rates are available for analysis.

4. Conclusions

In sand, wet or dry, the AE was high at 400 hits per 0.25 h. Since they are periodic, spectral analysis could effectively be used to differentiate the patterns, towards deducing the growth rate. The results showed that the emissions were very weak in soil, but the root position and growth rate could still be inferred based on the rate at which these emissions are generated. AE measurements from real root growth were analyzed using spectral methods and possibilities were found to exist for detecting the real root growth rate, by way of correlating it with those of the simulated study. But the simulations must be extended to other growth rates also, so that the acquired database could be used for accurate predictions. The acoustics of the porous medium itself is of much concern towards effective deduction of the emission. Much more studies should be directed at the influence of the medium on the attenuation

of AE. This would facilitate decisions on the proper placement of the sensor in the real greenhouse environment.

Acknowledgements

This study was supported by a short term fellowship of the Japanese Science and Technology Agency awarded to the first author, through the Japanese International Science and Technology Exchange Center, Tsukuba, Japan. We acknowledge the support offered by the staff of the National Research Institute of Agricultural Engineering, Tsukuba, Japan, where the work was carried out.

References

- L. Okushima, M. Shimojo and Y. Higo (1994), "Acoustic emission sensor for detecting of plant root growth", *Progress in Acoustic Emission VII*, eds. T. Kishi et al., Japanese Society for NDI, Tokyo, p. 131.
- L. Okushima, M. Shimojo, Y. Higo, T. Ohtani and S. Sase (1996), "Possibility of root growth measurement underground by Acoustic emission sensor", *Progress in Acoustic Emission VIII*, eds. T. Kishi et al., Japanese Society for NDI, Tokyo, p. 339.
- T. Shimotashiro, S. Inanaga, Y. Sugimoto and H. Dokai (1998), "Non-destructive measuring for distribution of root number on vertical soil plane using AE method", *Plant Production Science*, 1, 25-29.

Program and Abstracts of the 42nd AEWG Meeting

June 15, 16, 1999 at Nassau Inn, Princeton, NJ; S.J. Vahaviolos, Program Chair.

TUESDAY, JUNE 15, 1999

Detection and Evaluation of Acoustic Emission due to Rock Failure

Tomoki Shiotani, Masayasu Ohtsu and Shigeru Miwa, Research Institute of Technology, Tobishima Corporation and Department of Civil Engineering and Architecture, Kumamoto University

It is well known that acoustic emission (AE) waves strongly attenuate during propagation inside geotechnical materials. To detect AE waves clearly, therefore, AE sensors of lower frequency characteristics and deformation-related wave-guides should be applied to the detection. In the case of monitoring rock failure, it is further difficult to completely take into account the state of the pre-existing crack properties, although several surveys to examine rock characteristics and crack conditions are performed prior to the monitoring. Thus, it is necessary to develop an effective method for detecting AE waves which is not dominantly influenced by the existing cracks. One prospective method for a wave-guide is replacing excavated holes with cementitious materials of the same mechanical properties as rock. When rock-mass moves along the cracks, the filler replaced in the holes would behave coincidentally with rock, and AE waves produced from the filler are expected to be of the same signal-patterns as those from rock. Then, it suggests that the local failure of the rock could be observed by AE activity from the filler. By evaluating the AE activity of various fracture tests in the laboratory, fracture state of the rock could be estimated by AE activity of the filler. In the case that the filler already contains many cracks, there is another problem to be solved. Because AE attenuation characteristics of the filler with many cracks are possibly identical to those of actual rock, it may result in the difficulty to detect AE signals effectively. To solve this problem, a steel bar is installed into an excavated We with AE sensors. AE signals subsequent to the local motion would be detected until final rock failure. These AE waves may have no relation with the fracture, because they result from friction between the filler and the steel bar.

A series of studies were conducted for detecting and evaluating of AE signals from this type of wave-guides. In the laboratory, AE characteristics due to fracture of the filler were experimentally studied by bending and shear load tests. Thus, AE parameters effectively characterizing failure-state were extracted. In situ slope monitoring was carried out by applying the proposed techniques. AE source location was performed, and then locations were compared with actual cracks observed by a borehole-camera. AE waves were examined on their parametric characteristics, taking into account the results laboratory experiments. Thus, the applicability of the technique to detecting and evaluating of AE signals for rock failure is verified,

Quantitative Evaluation of Fracture Processes in Concrete by the Use of Improved b-Value.

Shigenori Yuyama, NPA; Tomoki Shiotani, Tobishima Corporation; T. Okamoto, Taiheiyo Cement Co.; Masayasu Ohtsu, Kumamoto University

Improved b-value, an effective parameter to describe state of fractures, has been proposed by the authors. This parameter is obtained as gradients of cumulative amplitude distributions calculated for a constant number of the most updated AE data (hits), determining statically the range of amplitudes. In the present study, the improved b-value analysis is applied to the fracture processes of a reinforced concrete (RC) beam with a single reinforcement, an RC rigid frame under repeated loadings, a center notched concrete beam, and the same beam reinforced with CFRP sheet. Moment tensor analysis, a quantitative AE waveform analysis based on the moment tensor modeling of cracks, has been applied to classify crack types and to determine crack orientations in the fracture processes of these specimens. Comparison of the results from the moment tensor analysis and those from the improved b-value analysis demonstrated that the latter is very useful for quantitative evaluation of fracture processes as a practical method based on the extracted AE features.

Quantitative Analysis. of Fracture Process in RC Column Foundation by Moment Tensor Analysis of Acoustic Emission. Shegnori Yuyarna, Zheng-wang Li, NPA; Yoshihiro Ito, Masaki Arazoe, Sato Kogyo Co.

Detection of Defects in Gears by Acoustic Emission Measurements

N. Tandon and S. Mata

Abstract

Acoustic emission (AE) measurements have been performed on test gears, without defect and with defects of different diameters in one of the teeth, on a gear test rig. The defect, simulating a pit, was produced on gear tooth by spark erosion and the size of this defect was successively increased after each measurement. Acoustic emission (ring-down) counts, peak amplitude and energy and the distribution of events versus AE counts and peak amplitude were measured. Overall vibrations of the gear were also measured simultaneously. The results indicated that the AE measurements were successful in detecting defects in gears and could detect smaller defect sizes as compared to vibration measurements. The distribution of AE counts and peak amplitude becomes broader because of the presence of a defect in the gear.

1. Introduction

The wear caused by mechanical deterioration in rotating machines almost always manifests itself in terms of changes in the levels of vibrations and acoustic emissions at different points of machine. As the machine deteriorates it vibrates more and more, and the mechanical stresses and strains have a tendency to cause further deterioration. Acoustic emissions (AE) are in the frequency range from 100 kHz to 2 MHz as opposed to vibrations which are in 0-20 kHz range. The classic source of acoustic emissions are defect-related deformations. The sudden movements at the source produce stress waves, which radiate out into the structure. As the stress in the material is raised, many of these emission are generated. The most commonly used AE signal measurement parameters are AE events, AE (ring-down) counts, energy and peak amplitude. The distribution of events versus any other of these parameters is also sometimes measured. Acoustic emission measurements have been applied to the condition monitoring of machinery for at least a quarter of a century and has consistently been found to be sensitive to distress and degradation in a wide range of machinery. The application of AE to condition monitoring has been growing steadily, albeit slowly for

many years. Clearly there is a large gulf between research on a test rig under controlled condition and routine applications within industry as part of a predictive maintenance strategy. However, the signs are that AE has stood the test of time and is poised to emerge as a major player in condition monitoring over the coming years.

The most common failure modes of gears are pitting and scoring. Pitting failure is a fatigue effect, which occurs due to higher Hertzian contact stresses than the surface can withstand. Gears under load produce repeated surface and sub-surface stresses and if the loads are high enough, chunks of metal will fatigue from the surface producing pits. Initial pitting usually occurs near the pitch line, in the region where the oil film is thin. Vibration and noise analysis is the most common means of gear monitoring and diagnostics (Umezawa et al., 1982; Fujita et al., 1983; Nicks, 1990; Muralidharan et al., 1994; Choy et al., 1996). Gear vibration is affected by the faults in gear teeth. It has been shown (Fujita et al., 1983) that pitting failures and tooth breakage due to pitting failures could be predicted by monitoring the change in tooth profile and changes of dynamic characteristics such as vibration and noise and also the tooth root strains.

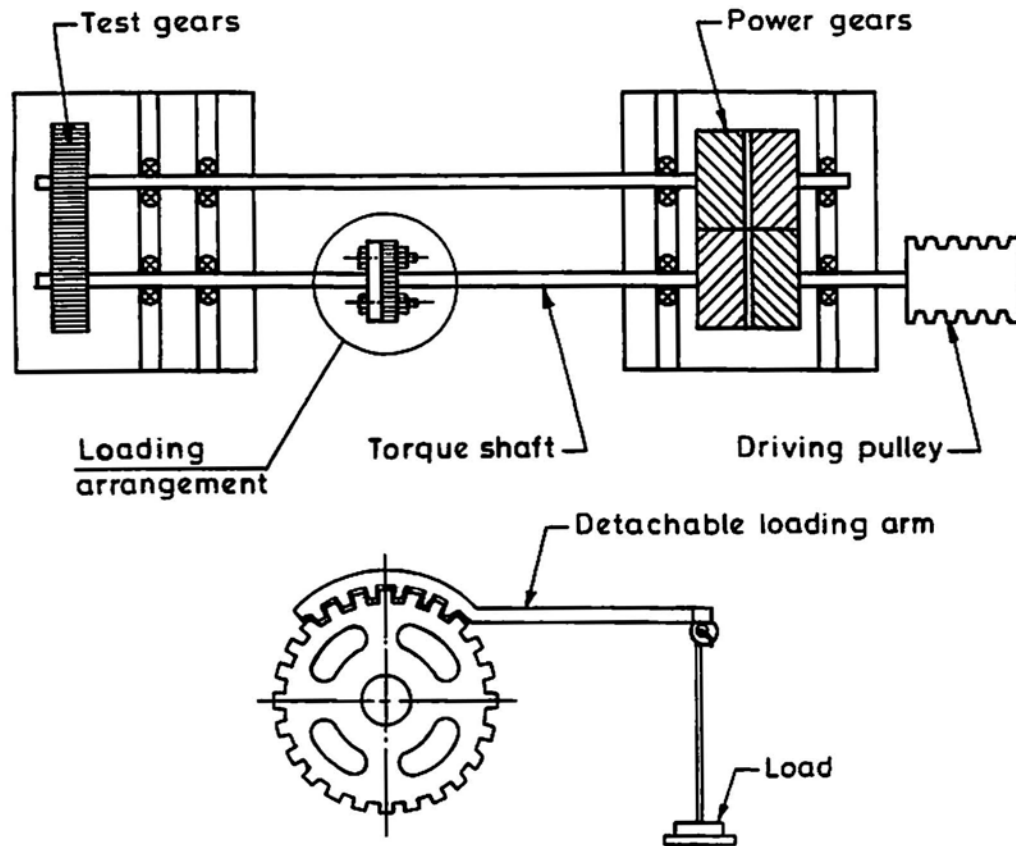
Some studies on the AE measurements for the detection of defects in bearings have been carried out (Tandon and Nakra, 1990; Yoshioka and Fujiwara, 1984). Acoustic emission is also expected to increase when a defect in the form of a pit is present in a tooth of a gear. So in the present investigation, AE measurements were performed on gears without defect and with intentionally introduced defects by spark erosion. The size of these defects, simulating pits, was also changed to determine the smallest defect size that could be detected by AE measurements for the gears tested.

2. Experimental Setup

2.1 Test Rig and Gears

The investigation was carried out on IAE gear lubricant testing machine. A schematic diagram of the gear test rig is shown in Fig. 1. The machine basically consists of test head and power return gearbox mounted on a bed plate and coupled together by a torque shaft. The test head assembly consists of two test gear spindles mounted on anti-friction

Received 2 April 1998. The authors are affiliated with ITMME Centre, Indian Institute of Technology, Hauz Khas, New Delhi 110016, India. (ntandon@itmmec.iitd.ernet.in)



Side-view of loading arrangement

Fig. 1 A schematic diagram of the gear test rig.

bearings. The front cover of the test head assembly is easily removable and behind this cover is the spigot for locating the test gears. The test gears are lubricated by a jet of oil. Load on the test gears can be applied by an arm onto which weights can be added.

The measurements were performed on hardened and ground spur gears supplied along with the test rig. The gears had involute profile with a pressure angle of 20° . The face width of the gears was 5.1 mm (0.2") and diametral pitch 5. The gear and the pinion had 16 and 15 teeth, respectively.

2.2 Measuring Instruments

Acoustic emissions were detected using a piezoelectric transducer (AET AC375). The acoustic emission transducer had a resonant frequency of 375 kHz and was followed by a preamplifier (AET 160) with an appropriate plug-in filter (FL-25). The preamplifier had a gain of 60 dB. The signal was post-amplified before being analyzed in AET 5000 mainframe AE processor. The first elements in the mainframe are main amplifiers and thresholds, which are adjusted to determine the test sensitivity. The main amplifier provides additional gain up to 40 dB to boost the signal further prior to analysis. The analog wave that comes out of

the main amplifier can be displayed on an oscilloscope. A microcomputer is interfaced with the mainframe processor for recording the AE data.

Burst type acoustic emission event is usually separated from the continuous activity by the use of a threshold. Only AE events or AE counts that exceed thresholds are allowed to be processed. Since the noise level may vary, a floating or automatic (rather than fixed) threshold is used in order to improve the resolution of the burst event. Each AE signal is measured by hardware circuits, which are contained in the mainframe and measured parameters are passed through the central microcomputer to a disc file of signal descriptions. During or after the data recording, the main system extracts the data for graphic display.

Overall vibration acceleration was measured using an accelerometer (B&K 4368) and a charge amplifier (B&K 2635). The undamped natural frequency of the accelerometer is 39 kHz and its sensitivity is 4.30 mVs/m. Overall rms vibrations in 0.2 Hz to 10 kHz frequency range were measured.

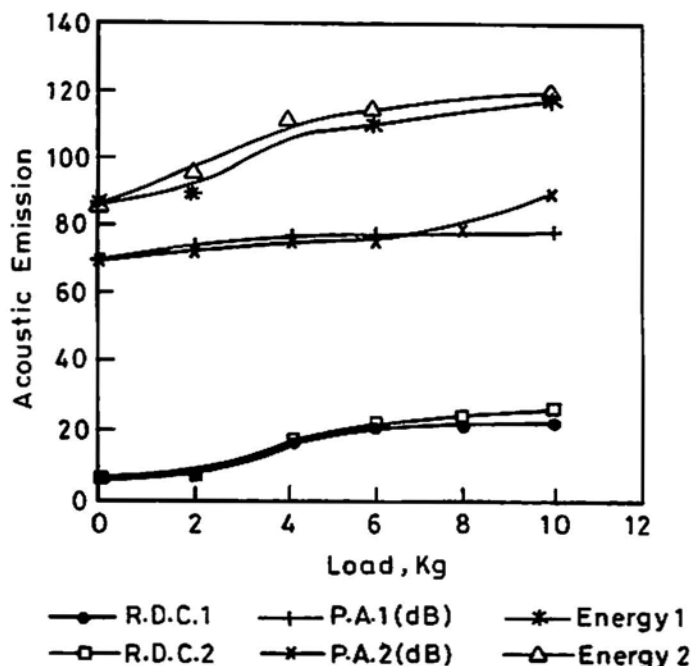


Fig. 2 Repeatability of AE measurements on a defective gear. RDC = AE counts; PA = peak amplitude.

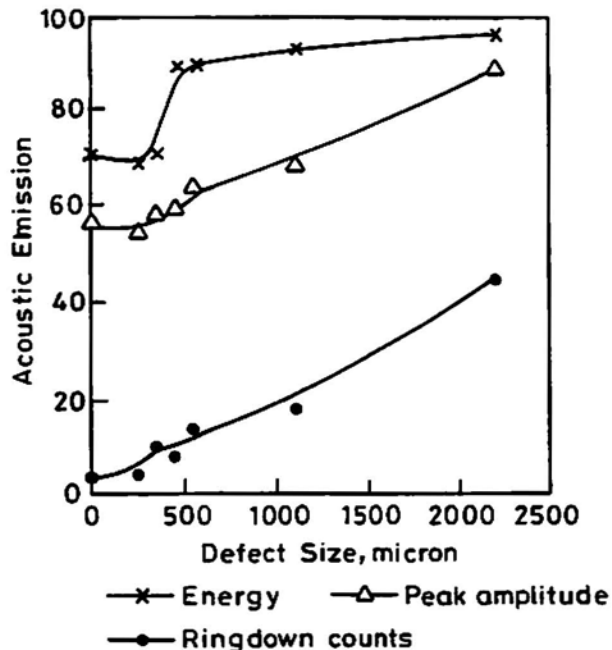


Fig. 4 AE measurements of gears at 6 kg load.

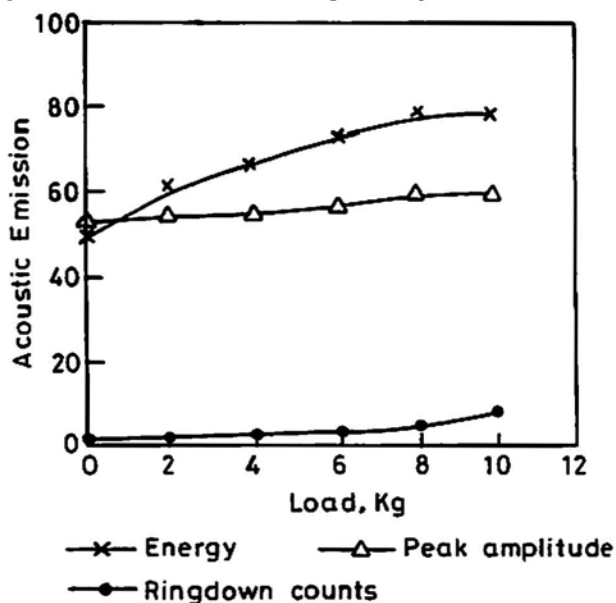


Fig. 3 AE measurements of non-defective gears.

3. Measurement Method

The AE signal was measured close to the bearings of the test gear box. Vibrations (generated mainly at gear teeth mesh frequency and its harmonics) were also measured simultaneously, for the purpose of comparison. All the tests were carried out at 1000 rpm. The AE measurements were performed when there was no defect in the gear and when the gear was removed and a defect in the form of a pit was produced on a tooth on the gear pitch line, by spark erosion. The defect diameter was increased after each test on the same gear. Defects of 250, 350, 450, 550, 1100 and 2200

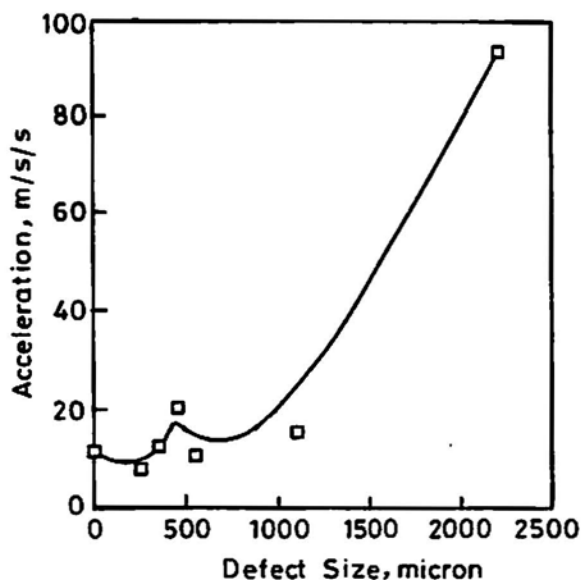


Fig. 5 Overall vibrations of gears at 6 kg load.

μm diameters with a constant depth of 500 μm were produced.

In order to provide maximum discrimination between the signal and the background noise, and at the same time, to maintain the sensitivity of the AE monitoring system, appropriate threshold level of detection and the level of post amplification were set up. These levels were kept constant for all the measurements. The AE parameters measured were energy, peak amplitude and AE counts. The distribution of AE events versus AE counts and peak amplitude was also measured. The repeatability of AE measurements

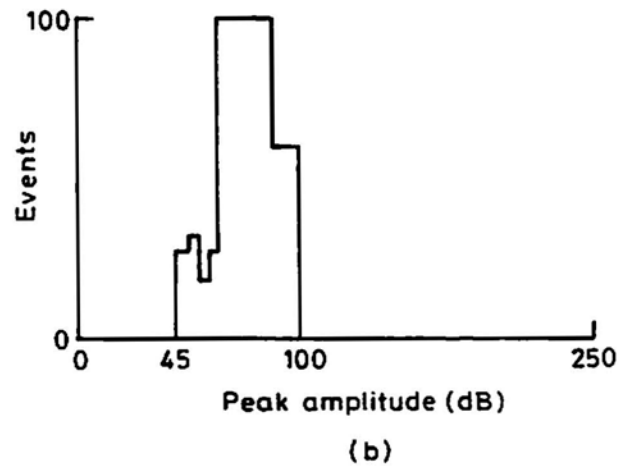
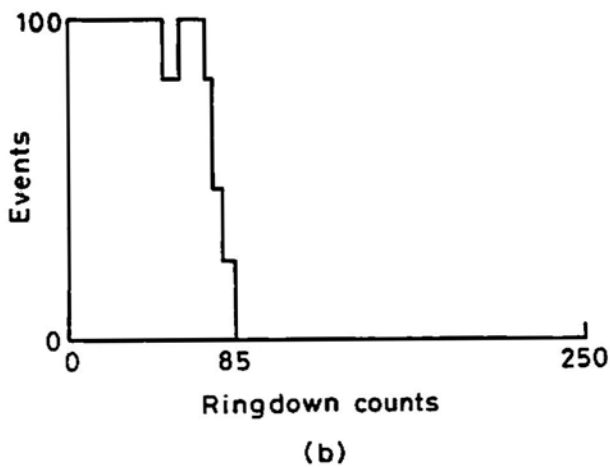
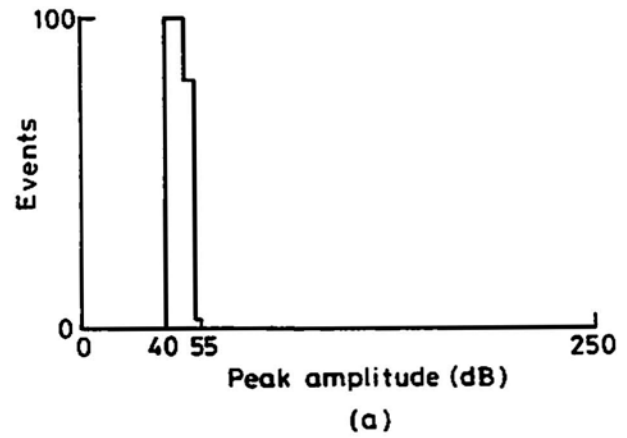
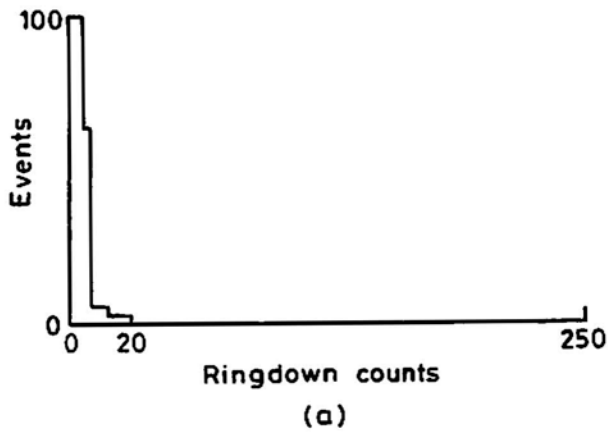


Fig. 6 The distribution of AE events vs. AE counts for the good gear (a) and for the gear with 1100- μm size defect (b) at 6 kg load.

Fig. 7 The distribution of AE events vs. peak amplitude for the good gear (a) and for the gear with 1100- μm size defect (b) at 6 kg load.

was also checked on a defective (having some pitting marks) gear set.

4. Results and Discussion

The AE parameters - AE (ring-down) counts, peak amplitude and energy were measured at two different times on a gear, which had some pitting marks, to study the repeatability of these measurements. The results are shown in Fig. 2. All the three parameters measured show quite good repeatability. The variation of acoustic emission parameters with load was investigated on the test gear set without defect. The results shown in Fig. 3 indicate that there is some increase in acoustic emissions with an increase in load.

The variation in AE parameters measured for different sizes of defects in test gear tooth for 6 kg load are shown in Fig. 4. The results show that there is an increase in the AE parameters measured, with increase in defect size. This shows that AE measurements can be used for condition monitoring of gears. The increase in AE is marked when the defect size is around 500 μm or greater in diameter with

reference to acoustic emissions at zero defect. AE (ring-down) counts show slightly better results as compared to energy and peak amplitude. The vibration measurements, which were performed simultaneously for the purpose of comparison, indicate that distinct increase in vibration levels is measured when the defect size is more than 1000 μm (Fig. 5). This indicates that the AE measurements are better than overall vibration measurements for the detection of defects in gears, because they can detect defects earlier (smaller defects) as compared to overall vibration levels.

The distribution of AE events and AE counts and peak amplitude for the good gear and for the gear with 1100- μm size defect, at 6 kg load, are shown in Figs. 6 and 7. It is seen that, in general, the distribution becomes broader because of the presence of defect in the gear. The AE event count goes to zero for AE counts of 20 and 85 for the gear without defect and with 1100- μm size defect, respectively (Fig. 6). Figure 7 shows that for the maximum events, the peak amplitude is centered around 50 dB for good gear and around 75 dB for gear with 1100- μm size defect.

5. Conclusions

The AE measurements can be successfully used for the detection of defects in gears. The AE measurement results are better than overall vibration measurements for the detection of defects in gears because the defects of smaller size could be detected by AE measurements. The distribution of AE events versus AE (ring-down) counts and peak amplitude becomes broader with the presence of defect in the gear tooth.

References

F.K. Choy, V. Polyshchuk and D.P. Townsend (1996), "Analysis of the effect of surface pitting and wear on the vibration of a gear transmission system", *Tribology International*, **29**, 77-83.

K. Fujita, A. Yoshida and K. Ota (1983), "On the possibility of early detection of gear tooth failures by noise and vibration", *Proceedings Sixth World Congress On Theory of Machine and Mechanisms*, pp. 668-672.

J. Nicks (1990), "Evaluation of vibration analysis for fault detection using gear test rig", *Proceedings I. Mech. E., First International Conference on Gear Box Noise and Vibration*, pp. 165-172.

M.K. Muralidharan, N. Tandon and B.C. Nakra (1994), "Condition monitoring of gears by noise analysis", *Proceedings Intl. Conf. COMADEM 94*, New Delhi, pp. 427-439.

N. Tandon and B.C. Nakra (1990), "Defect detection in rolling element bearings by acoustic emission method" *J. Acoustic Emission*, **9**, 25-28.

K. Umezawa, K. Handa, H. Kawarada and H. Kamei (1982), "On prognosis of gear surface failures using sound of gear", *Bull. JSME*, **25**, 834-841.

T. Yoshioka and T. Fujiwara (1984), "Application of acoustic emission technique to detection of rolling bearing failure", *Acoustic Emission Monitoring and Analysis in Manufacturing*, ed. D. A. Dornfeld, ASME, New York, pp. 55-75.

42nd AEWG Meeting

After the great Hanshin earthquake, numerous studies have been made to evaluate damage levels, toughness and deformation characteristics of reinforced concrete (RC) columns exposed to the earthquake shock. In the present study, RC columns are subjected to simulated seismic lateral loading under different axial loads. Acoustic emission (AE) is monitored to characterize the seismic behavior of column foundation. AE is shown to be very sensitive to detect cracks generated in the foundation. An AE moment tensor analysis is applied to analyze the fracture process quantitatively. Experimental results demonstrate different fracture behavior, depending on the different axial loads. It is also shown that the moment tensor analysis is very useful for quantitative evaluation of the fracture process.

Pipeline Testing Experience in Russia. Victor V. Shemyakin, PAC-Russia (No abstract available)

Cold Header Machine Process Monitoring Using an Acoustical Approach.

Henrique Reis, D. Brad Cook, and Aaron C. Voegelé, NDT and E Research Lab., University of Illinois

In cold heading manufacturing processes, a partial fracture of the punch pin recess tip leads to production of out-of-tolerance parts. A process monitoring system was developed to assure that out-of-tolerance parts do not contaminate the batch of acceptable parts. A four-channel data acquisition system was assembled to collect and store the acoustic signal during the manufacturing process. A genetic algorithm was designed to select the smallest subset of waveform features necessary to develop a robust artificial neural network that could differentiate among the various cold heading machine conditions. The developed monitoring system is able to terminate production within seconds of punch failure using only four waveform features. Both complete and partial fracture modes can be detected using the developed process monitoring system.

Acoustic Emission Monitoring of Plasma Sprayed Ceramic Thermal Barrier Coatings

David W. Prine, Jennifer R. Mawdsley, and Katherine T. Faber, Northwestern University

Acoustic emission monitoring techniques are providing a practical tool to evaluate the mechanical performance of plasma sprayed ceramic coatings. Test specimens are fabricated with Small Particle Plasma Sprayed 7% (weight) yttria partially stabilized zirconia deposited on 1018 carbon steel substrates to a thickness of 3 to 6 mils. These materials show considerable promise as thermal barrier coatings that can survive severe mechanical deformation.

AE is being used to monitor performance of the test specimens in a 4-point bend test. Both single cycles that exceed the elastic limit of the substrate and fatigue tests with several thousand cycles have been monitored. Other workers in the field have attempted to apply AE to this problem but have typically not given sufficient attention to the elimination of non-valid AE resulting from either the test machine or the test fixture. For these tests a simple three channel linear array with source location is used to suppress background noise from the test fixture. Both narrow band resonant and broad band sensors are being used. Special sensor coupling shoes were constructed to eliminate coupling variations resulting from extreme changes in curvature of the test specimen as it undergoes bending.

Conventional event based AE as well as digital waveform data is recorded. This paper will discuss in detail the experimental results obtained to-date. The specimens are remarkable for their lack of AE. The presence of porosity and microcracking in the coating apparently prevents or suppresses the growth of large brittle failures. Large numbers of very low amplitude events that probably result from frictional and microcrack sources characterizes the AE from a good specimen. The waveform data clearly shows several classes of AE events distinguishable in both the time and frequency domains. Good correlation has been obtained between AE and changes in the process parameters.

Waveform Evaluation of Acoustic Emission Signals from Electroplating

Kanji Ono, UCLA and Tsutomu Morikawa, Osaka Pref. Industrial Research Inst.

Takano and Ono reported 25 years ago that AE signals from crack formation during electroplating can be detected and are distinguishable from those due to hydrogen bubble evolution and collapse. Few studies have been done since, although AE is now a standard technique in monitoring the adhesion of plated/coated films in conjunction with scratching. We recorded AE signals during electroplating of copper, nickel and chromium on copper and stainless steel sheets, by varying the conditions of plating (solution composition, pH level, temperature and current density). AE waveforms (using a PAC WD sensor and a MISTRAS board) exhibit distinct plate-wave characteristics, with cracks giving strong extensional modes and hydrogen bubbles having mostly flexural waves. Waveform- or frequency-based discrimination can be easily performed to separate the two signal types. Signal amplitude can also be

Acoustic Emission Signals in Thin Plates Produced by Impact Damage

William H. Prosser, Michael R. Gorman and Donald H. Humes

Abstract

Acoustic emission (AE) signals created by impact sources in thin aluminum and graphite/epoxy composite plates were analyzed. Two different impact velocity regimes were studied. Low-velocity (less than 0.21 km/s) impacts were created with an airgun firing spherical steel projectiles (4.5 mm diameter). High-velocity (1.8 to 7 km/s) impacts were generated with a two-stage light-gas gun firing small cylindrical nylon projectiles (1.5 mm diameter). Both the impact velocity and impact angle were varied. The impacts did not penetrate the aluminum plates at either low or high velocities. For high-velocity impacts in composites, there were both impacts that fully penetrated the plate as well as impacts that did not. All impacts generated very large amplitude AE signals (1-5 V at the sensor), which propagated as plate (extensional and/or flexural) modes. In the low-velocity impact studies, the signal was dominated by a large flexural mode with only a small extensional mode component detected. As the impact velocity was increased within the low velocity regime, the overall amplitudes of both the extensional and flexural modes increased. In addition, a relative increase in the amplitude of high-frequency components of the flexural mode was also observed. Signals caused by high-velocity impacts that did not penetrate the plate contained both a large extensional and flexural mode component of comparable amplitudes. The signals also contained components of much higher frequency and were easily differentiated from those caused by low-velocity impacts. An interesting phenomenon was observed in that the large flexural mode component, seen in every other case, was absent from the signal when the impact particle fully penetrated through the composite plates.

1. Introduction

Damage from impact is a serious hazard to aircraft and spacecraft. During takeoff and landing, impact threats include runway debris and birds. Ice created on spacecraft from the exposure of humid air to the cold of cryogenic propellants may break off during launch and cause impact damage. There are also numerous in-flight sources of impact

damage including birds, projectiles used against military aircraft, and collisions with other aircraft or spacecraft. For spacecraft, there is another hazard, which is the impact of micrometeoroids and space debris. These on-orbit collisions occur at velocities exceeding 10 km/s, and at these velocities, even very small particles can create significant damage. The seriousness of the threat of this type of impact damage to spacecraft is reflected in the titles of two government reports; "Space Program: Space Debris is a Potential Threat to Space Station and Shuttle" (GAO, 1990) and "Space Station: Delays in Dealing with Space Debris May Reduce Safety and Increase Costs." (GAO, 1992)

Acoustic emission (AE) monitoring has been proposed as one method for structural health monitoring to detect, locate, and assess impact damage. Lempriere (1987) and Nelson and Lempriere (1987) discussed such applications of AE for spacecraft. The advantages of such a monitoring system are that the number of post-flight inspections can be minimized or eliminated. This can lead to a tremendous cost savings while at the same time providing enhanced safety. For long-term orbiting space platforms such as the proposed Space Station, routine inspections for impact damage are particularly difficult. Extra-vehicular activity (EVA) is expensive and dangerous, and there are limited space-tested tools and techniques for damage inspection and assessment. A recent example demonstrating this point is the inability to find the leak in a Mir Space Station Module, caused by a collision with another spacecraft, even after several EVA inspections.

In this research, AE signals from impact sources in plates were detected with broad band, high fidelity sensors and digitized for analysis. Impact events were studied in both isotropic aluminum, and anisotropic graphite/epoxy. Both materials are widely used on aircraft and spacecraft. Low-velocity impacts were created with a pump airgun, firing spherical steel projectiles at velocities less than 0.21 km/s. Varying the number of times the airgun was pumped made it possible to study the effect of velocity variation within the low velocity regime. The effect of the angle of the plate on the observed signal was also evaluated. High-velocity impacts were generated in these plates with a two-stage light-gas gun. The velocity was varied over the range of 1.8 to 7 km/s. A smaller nylon projectile was used. Again, the angle of impact was varied. For the composite materials, by varying the velocity in the high-velocity re-

Received 30 June 1998. William H. Prosser (w.h.prosser@express.larc.nasa.gov) and Donald H. Humes are affiliated with NASA Langley Research Center, Hampton, VA 23681-0001, and Michael R. Gorman is with Digital Wave Corp., Englewood, CO 80111.

gime, impacts that fully penetrated the plate were produced as well as those that did not.

For all conditions of impact studied in this research in both the aluminum and graphite/epoxy composite plates, the detected AE signals were of very large amplitude. At the relatively short distances of propagation (less than 20 cm) in this work, attenuators, rather than preamplifiers, were used in some cases. This was necessary to reduce the signal amplitudes to a sufficiently low level for digitization. All signals contained propagating plate mode (extensional and/or flexural) components. Although location results are not presented in this paper, the large amplitude signals (and thus large signal-to-noise ratios) made it possible to obtain excellent impact location agreement with that measured directly on the plate.

For low-velocity impacts, the flexural plate mode was predominant. As the projectile velocity was increased within the low-velocity regime, the overall amplitude of the modes increased and the amplitude of higher frequency components in the flexural mode increased. Previous research (Gorman, 1990; Gorman and Prosser, 1991; Prosser, 1991) showed the effect of the direction of source motion on the relative amplitudes of plate modes. This was the motivation for varying the angle of impact. In contrast to the previous studies, no clear effect of varying the trajectory on the relative amplitude of plate modes was observed.

For high-velocity impacts, the extensional mode amplitude was much larger than for low-velocity impacts and comparable to that of the flexural mode. The signals contained much higher frequency content. Again, the effect of varying the impact angle produced no change in the relative amplitudes of the plate modes. The flexural mode was entirely absent in every case where full penetration of the composite plate occurred. Further study of this effect is warranted as this could provide a useful discriminator for the detection of spacecraft-hull penetration.

In previous research, attempts were made to use acoustic detectors to characterize the micrometeoroid environment. Examples of this work are described by Konstantinov et al. (1969), Alexander et al. (1962), and Kapinsinsky (1978). Laboratory experiments were used to characterize the sensitivity of the devices and such acoustic detectors were widely flown on balloons, sounding rockets, satellites, and lunar and deep-space probes. However, much like AE testing of structures, the reliability of the data from these on-board acoustic sensors has often been questioned because extraneous noise was not identified or eliminated. Thus, the rates of impacts determined from acoustic signals were unrealistically high in comparison to other measurement systems such as capacitive discharge detectors. The extraneous noise signals were attributed to both electromagnetic interference and noise caused by thermal expansion of the spacecraft.

Laminated composite materials offer considerable weight savings for aircraft and spacecraft, but are particularly susceptible to impact damage. As such, there has been considerable study on acoustic waves generated by impact sources (Gardiner and Pearson, 1985; Weems et al., 1991; Takeda et al., 1981). However, these studies have focused primarily on impact sources of very low velocity such as dropped projectiles or weights dropped onto impact tups. The signals acquired in these experiments are in agreement with the results from the low-velocity impact testing in this study in that small amplitude extensional mode components followed by much larger flexural mode components can be identified. In addition, a number of authors including Moon (1973), Sun and Lai (1974), Datta et al. (1992), Karim (1991), and Mal and Lih (1992) have investigated theoretical approaches for predicting acoustic waves in composite laminates generated by impact sources.

More recently, Nelson and Lempriere (1987) evaluated AE signals generated by impact sources in metallic plates for the development of AE technology for the Space Station. Although they successfully demonstrated the detection and location of impacts, an AE monitoring system was not included in later plans for the Space Station. It is believed that the infant state of the waveform-based technology used, combined with severely limited development funds, led to the curtailment. In their study, they detected and digitized signals with broadband sensors for low-velocity impacts created with an air gun and spherical projectiles. They also collected signals from a very limited number of high-velocity impacts, but the results were not discussed in detail. AE signals propagating as plate modes were also observed in both cases and considerable discussion focused on the ability to locate sources with these dispersive waves. However, they tested only metal specimens representative of space-station materials and only considered normal impact. They also suffered problems with their digitizing instrumentation causing high frequency spikes that distorted some signals. Furthermore, differences between penetrating and non-penetrating high-velocity impacts were not evaluated. Thus, a more extensive study was conducted and the results are detailed below.

2. Low-Velocity Impact

A pump air gun (Daisy model 880) was used to produce low-velocity impacts. Spherical, steel balls with a diameter of 4.5 mm were used. The velocity of the projectiles was not measured in these experiments. The nominal maximum muzzle velocity for this model gun, as obtained from the manufacturer, is 0.21 km/s when the gun is pumped to its full capacity of 10 pumping. At this velocity, the estimated kinetic energy ($mv^2/2$) of the projectile is 8.2 J.

The target plate was 2024 aluminum sheet with a thickness of 3.175 mm and 50.8 cm square. For safety, the target plate with attached sensors was placed inside a chamber of 76-mm thick high density foam. The plate was placed on a fixture that allowed the angle of impact to be varied from normal to the plate (90°) down to 10° grazing incidence in 10° steps.

Heavily damped, 3.5 MHz ultrasonic transducers for thickness gaging (Panametrics model V182) were used to detect the signals produced by these low-velocity impacts. Operated far off their resonance in the low-frequency AE range (less than 1 MHz), these sensors provide flat with frequency, high-fidelity, displacement response. This was demonstrated (Prosser, 1991) by comparison of their response against that of a calibrated laser interferometer. In addition, Papadakis (1980) discussed why such transducers make ideal high-fidelity AE sensors. This sensor has a diameter of 1.27 cm. This large aperture leads to problems with phase cancellation across the sensor face at higher frequencies. To reduce this effect, a smaller diameter sensor (Digital Wave Corp., model B1025) was used in the high-velocity impact studies, which were conducted later. Even though these two sensors have similar response curves as a function of frequency except for the aperture effects, exact comparisons of the low- and high-velocity impact generated AE signals are not made. This is particularly true for the higher-frequency extensional mode and the higher-frequency component of the flexural mode. However, gross differences of these signals, particularly of the relative amplitudes of the plate modes between low-velocity and high-velocity impacts are noted and will be discussed.

For these experiments, four sensors were placed in a rectangular array around the anticipated impact spot. They

were all located at a nominal distance of 15.2 cm from the impact. In repeated test firing, the impact position did not vary more than 1.27 cm in any direction from the desired impact position. As the amplitudes of the AE signals produced by these impacts were so large, no preamplifiers were used. The output of the sensors were put directly into a transient recorder (LeCroy model 6810) which had a 12-bit vertical resolution. A sampling frequency of 2 MHz was used and 1024 points were acquired for each waveform.

A typical signal captured from an impact, in which the gun had been pumped five times is shown in Fig. 1a. The extensional and flexural mode components of this signal are identified in this figure. The extensional mode propagates with a faster velocity and suffers little dispersion, while the flexural mode travels more slowly with dispersion such that higher frequencies arrive earlier in the signal. The peak amplitude of the signal is quite large, and again, this is without any amplification. The flexural mode is dominant and the extensional mode is barely observable in comparison. This is as expected since the impact produces a large out-of-plane source motion and thus generates a large bending moment. For these impacts, the projectile did not penetrate the plate but did produce a significant crater. The crater diameter was approximately the same diameter as the spherical projectile.

A signal from an impact, in which the gun was only pumped twice is shown in Fig. 1b. The velocity (and energy) of the projectile for this case is smaller, which leads to a smaller peak amplitude. Again, the flexural mode is dominant with very little extensional mode signal present. Not only is the amplitude different for the signals from different impact velocities, but the frequency content changes as well. As can be seen in the time domain signals of Fig.

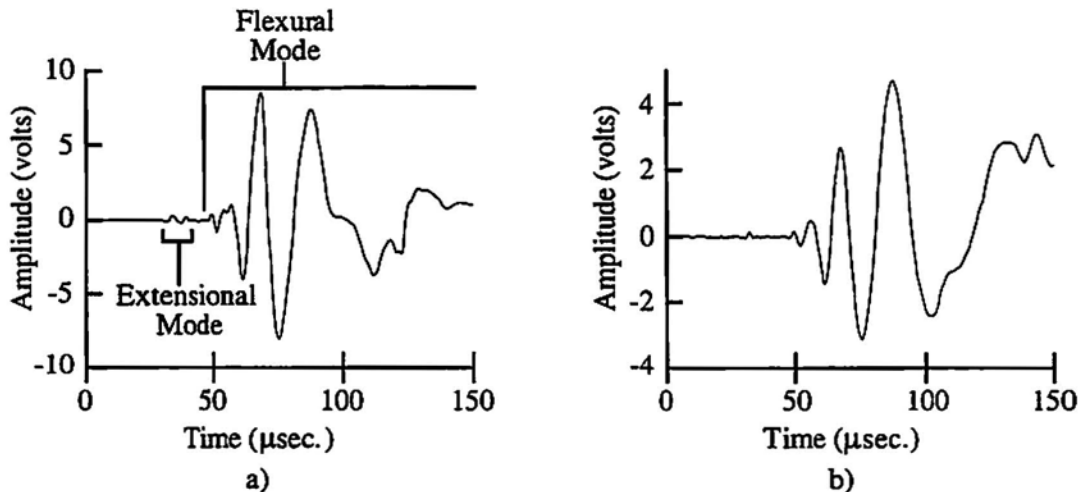


Fig. 1 AE signals produced by low-velocity impact on aluminum plate with: a) air gun pumped 5 times, and b) air gun pumped 2 times.

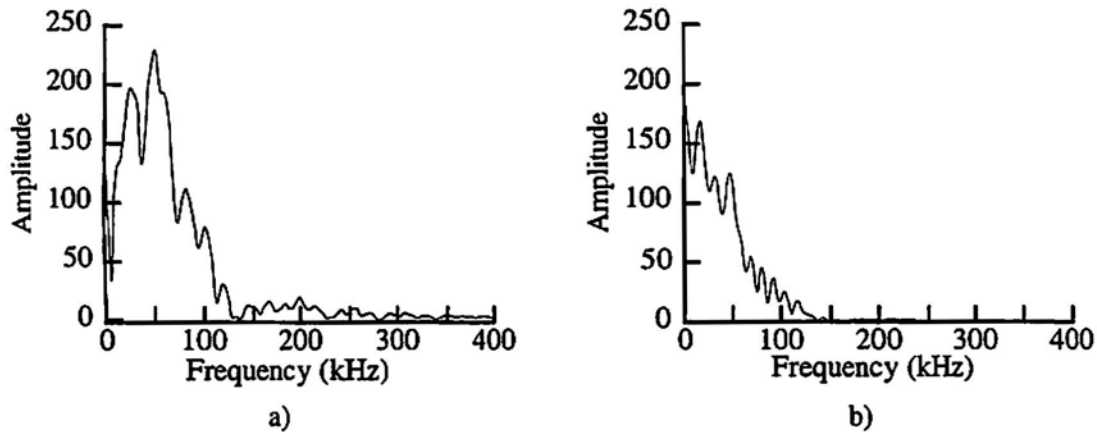


Fig. 2 Magnitude of FFT of AE signals in Fig. 1 produced by low-velocity impact on aluminum plate with: a) air gun pumped 5 times, and b) air gun pumped twice.

1, and even more clearly in their frequency response curves in Fig. 2, the high-frequency content increased in the signal from the higher-velocity impact.

No effect of impact-angle variation on the relative amplitudes of the two plate modes was observed. As mentioned previously, earlier research (Gorman, 1990; Gorman and Prosser, 1991; Prosser, 1991) had demonstrated a strong relationship between the directionality of the source motion and the relative amplitudes of plate modes. In this previous work, the simulated AE sources (pencil-lead breaks) were all applied at the mid-plane of the plate as the source angle was varied. Impact sources, however, occur on, or near the surface of the plate. This off-mid-plane source always creates a large bending moment, and thus large flexural mode. The variation in the angle of impact produced frequency content and overall amplitude (of both modes) changes similar to those produced by varying the velocity. This is because the normal component of the impact velocity changes, as the angle is varied. These effects, as well as signal dispersion effects due to slight variation in the propagation distance from shot to shot, all contributed to further mask any possible effect on relative amplitudes of plate modes that might have been caused by impact angle variations. Further study is needed to determine the feasibility of impact trajectory assessment through AE signal analysis.

3. High-Velocity Impact

A two-stage light-gas gun was used for high-velocity impact experiments. These high-velocity impacts cause damage, which more closely simulates that caused by hypervelocity impacts of micrometeoroids and space debris on spacecraft. The first stage of this gun consisted of a Swift 5.59-mm caliber rifle, which fires a nylon piston. The barrel for this first stage is pressurized with hydrogen prior to the shot. As the 5.59-mm diameter nylon piston is fired down the barrel in the first stage, it further compresses the

hydrogen until the high pressure ruptures a polymer membrane at the muzzle end of the first stage. The piston is caught in a large steel capture block prior to reaching the end of the first stage. The pressurized hydrogen then propels a much smaller projectile down an evacuated chamber at velocities, for this gun, up to 7 km/s. More details about the operation of such guns are given by Crozier and Hume (1957) and more recently by Schneider and Stilp (1990).

The velocity is controlled by a number of factors including the projectile size and weight, the amount of powder charge in the first stage, and the original pressure of the hydrogen gas in this stage. For these experiments, the impact projectiles were nylon cylinders with diameter of 1.5 mm and length of 1.25 mm. The velocity was measured with an optical system. Using mirrors, the path of a He-Ne laser beam was manipulated so that it passed twice through the intended path of the projectile at known, fixed distances between passes. The laser beam then impinged on a photo-detector. As the impact projectile traveled down the chamber, each time it passed through the laser beam, it temporarily blocked the light from arriving at the photo detector. The photo-detector output signal could then be used to determine the time required for the particle to travel the distance between the two beam paths. This time, with the known distance, was then used to determine the velocity of the projectile, which in our experiments ranged from 1.8 to 7 km/s. Over this velocity range, the calculated kinetic energy of the projectile ranges from 4.1 J to 61.7 J. Thus, even though the velocities are much higher than those used in the low-velocity study, the energy of the projectile is of the same order of magnitude.

Both aluminum and graphite/epoxy composite plates were impacted at high velocities. The 2024 aluminum plates had the same nominal thickness and lateral dimensions as those used for low-velocity experiments. Two

different graphite/epoxy composites were used. The first was 8 plies of IM7/8552, which had a nominal thickness of 1.27 mm. The lateral dimensions of these plates varied but was 25.4 x 25.4 cm or larger. The second was 24 plies of IM7/977-2 with a nominal thickness of 3.56 mm. The lateral dimensions of these plates were 35.6 x 35.6 cm. Both laminates were quasi-isotropic lay-ups, the first being $[0, 45, 90, -45]_8$ and the second being $[0, 45, 90, -45]_{24}$. For the composites, only impact normal to the plate was studied, while for the aluminum, the impact angle was varied again from normal (90°) down to 10° in 10° steps.

As mentioned previously, different sensors (Digital Wave Corp. model B1025) were used for the high-velocity experiments. These were similar to those used in the low-velocity impact study in that they are highly damped ultrasonic sensors operating far off resonance to provide a flat frequency response. However, they have a smaller diameter, which minimizes aperture effects thus providing better fidelity at the higher frequencies in the extensional mode and the early portion of the flexural mode. Again, four sensors were used in an array around the impact site. However, in this case, they were not equidistant from the impact site. For the aluminum plates, the nominal sensor positions were as shown in Fig. 3. For the composite plates, similar sensor spacing was maintained, but because the lateral dimensions of the plate were different, the positions relative to the plate edges were different. Also, as illustrated in this figure, there was slightly larger variability of the impact site from shot to shot.

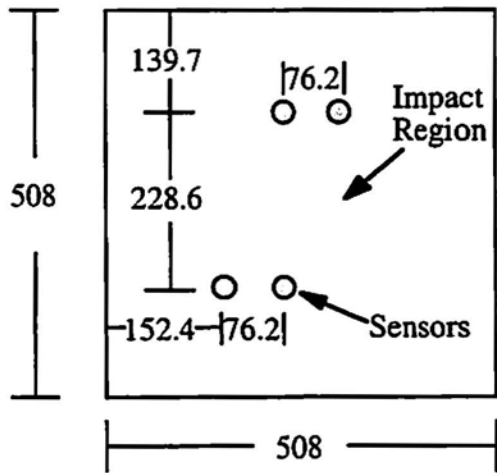


Fig. 3 Illustration of sensor positions for high-velocity impact in aluminum plate. Dimensions in mm.

A different signal recording system (Digital Wave Corp. model 4012 Fracture Wave Detector) was used for these experiments. It also had 12-bit vertical resolution, but the sampling frequency was 10 MHz. The signal was bandpass filtered from 20 kHz to 1.5 MHz. Because the input range of this digitizer was limited to ± 0.5 V, an attenuating preamplifier (Digital Wave Corp. model 2040

G/A) was used to provide 20-dB attenuation. For the signals presented in this paper, the amplitudes have been multiplied by 10 to correct for this attenuation and provide the voltage output from the sensor. This allows direct comparison of these signals against those recorded from the low-velocity impact study. However, the differences in type of sensors and filtering must be considered when making such comparisons. Thus, only significant differences in wave shape and modal content will be discussed between these two impact conditions.

Figure 4a shows the signal produced in an aluminum plate from a high-velocity impact. The velocity of the impact particle was 4.2 km/s and the aluminum plate was not penetrated. In fact, for the range of velocities tested, no projectiles penetrated the aluminum plates. The propagation distance to the sensor was 14.7 cm. Because of the significant high-frequency components in this signal, it is more difficult to clearly identify the extensional and flexural mode components. A 500 kHz low-pass filter was applied with the results shown in Fig. 4b. Here the plate mode components are more readily identified. In comparing these signals to the low-velocity impact signals in Fig. 1, it is noted that the shift in arrival times of these signals, and others to be presented later, are due to differences in trigger timing. Two significant differences are readily apparent when comparing signals caused by high-velocity impact to those caused by low-velocity impact. The first, which was clearly demonstrated by the need to use a low-pass filter to identify the modes, is that there is much higher frequency content in signals produced by high-velocity impact. It is suspected, although not verified by signal analysis, that higher order Lamb modes may be present in this high-frequency signal. This higher frequency content is not unexpected due to the source mechanism at much higher velocity. An increase in high-frequency content was also observed even for the slight velocity increase in low-velocity impact (cf. Fig. 2).

The second significant difference between the low- and high-velocity impact signals is the much larger extensional mode component for high-velocity impacts. It has an even larger amplitude than the flexural mode for this signal. A qualitative explanation for this difference can be offered based on an examination of the type of deformation produced by impacts at these different velocities. As discussed previously, low-velocity impact produces a crater, which is of similar diameter to the projectile diameter. For high-velocity impact, however, the diameter of the crater is several times larger than the diameter of the projectile. Thus, there is significant in-plane deformation as the crater expands in the high-velocity impact event. It seems likely that this in-plane deformation from crater expansion accounts for the large extensional plate mode component in high-velocity impact signals.

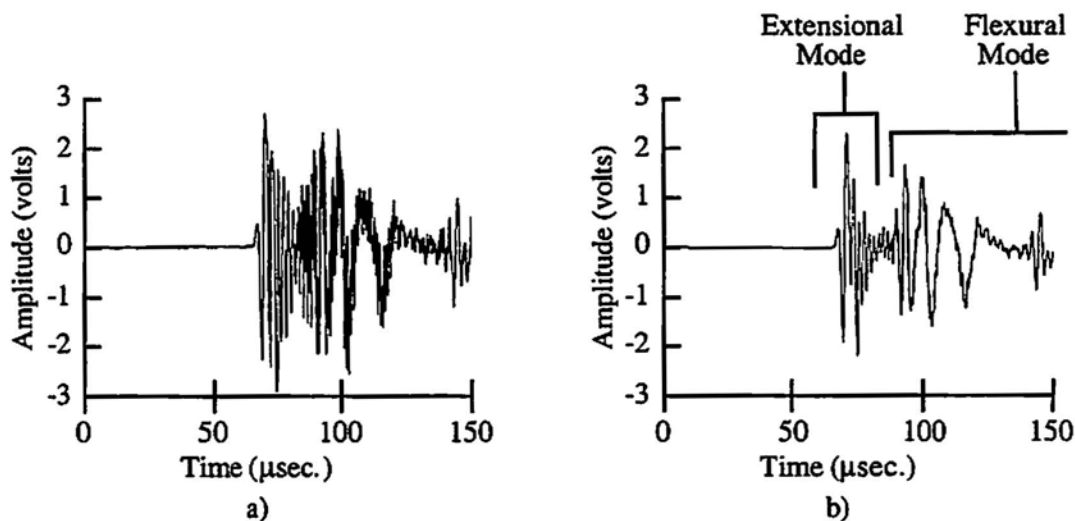


Fig. 4 a) AE signal produced by high velocity impact on aluminum plate; b) same signal as a) except after filtering with 500-kHz low-pass filter.

Again, no clear difference in the relative amplitude of the plate-mode components was detected as a function of the angle of impact. As the angle was decreased from normal impact, overall decreases in signal amplitude were observed as the normal component of the velocity decreased. However, the larger variations in the actual impact spot relative to the sensor positions made it difficult to investigate this effect. The apparent amplitudes of the modes change with propagation distance, especially for the flexural mode because of its high dispersion. Further, more controlled tests, in which either the propagation distance varied less, or amplitude changes due to propagation distance variations are compensated, are required. This will allow a better determination of whether information about impact trajectory is also contained in AE signals.

For high-velocity impacts in composite plates, the impact projectile fully penetrated the plate in most cases, except when the projectile was at the low end of the velocity spectrum (less than 2 km/s). Figure 5 shows the signal from an impact event, in which the projectile did not penetrate the composite plate. The velocity for this impact was 1.8 km/s. The plate in this experiment was the 8-ply IM7/8552 material. The distance of propagation was only 7.2 cm in a direction at a small angle (approximately 1.5°) from the 0°-fiber direction in this quasi-isotropic material. Again, similar to the signal from high-velocity impact in aluminum, there are large amplitude extensional and flexural mode components. However, the very high-frequency components that were present in Fig. 4a, are missing. This is most likely due to the much higher attenuation at higher frequencies that is typical of composites.

A different result was obtained when the composite plate was penetrated. Figure 6a shows a signal for such a case in the 8-ply material where the projectile velocity was 6.6 km/s. The propagation distance was 14.1 cm in a direc-

tion of 51.4° with respect to the 0°-fiber direction. For this signal, the flexural mode component is not present. The signal is composed only of the extensional mode and its reflections from the plate edges. A similar result is shown in Fig. 6b for the 24-ply laminate. The velocity in this case was 5.2 km/s. The propagation distance was 13.0 cm along a 54.3° propagation direction.

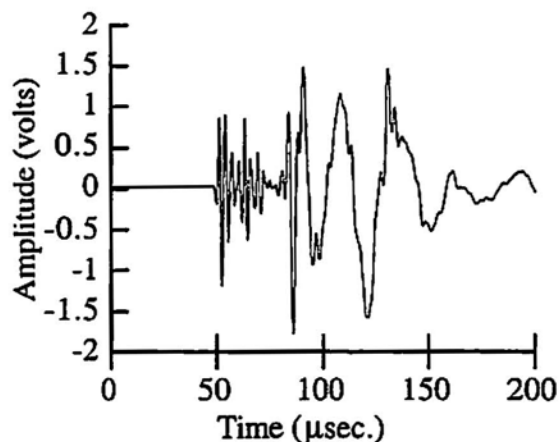


Fig. 5 AE signal produced by non-penetrating high-velocity impact on 8-ply graphite/epoxy composite plate.

4. Summary

In this study, AE signals generated by impact were detected with broadband, high fidelity sensors. A wide variety of impact conditions were studied including both low- and high-velocity impact, and varied impact trajectory in metal and composite targets. In the composite plates at high velocities, both penetrating and non-penetrating impacts were generated. In all cases, the AE signals had very large amplitude and propagated as plate modes.

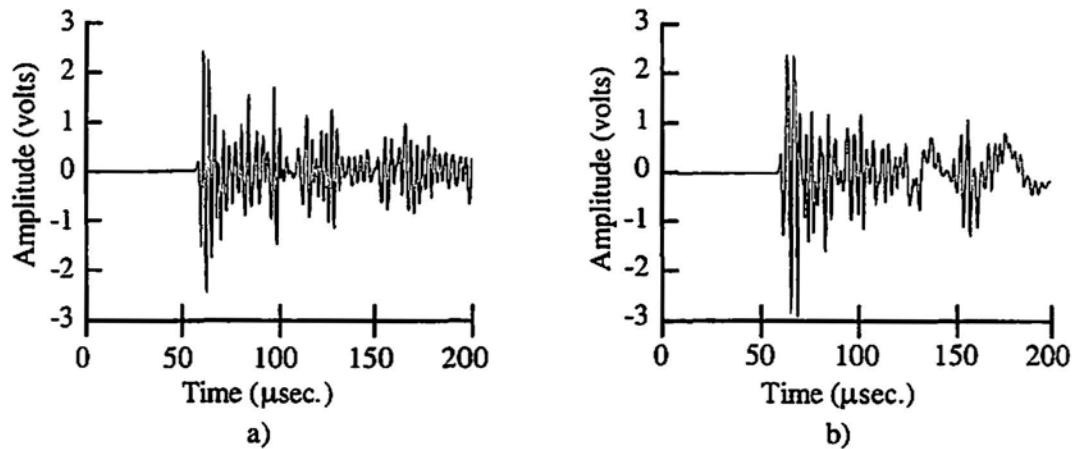


Fig. 6 AE signals produced by penetrating impact in composite plates; a) 8-ply laminate, and b) 24 ply laminate.

AE signals from low- and high-velocity impacts were easily differentiated from their frequency content and modal analysis. Low-velocity impacts produced signals with little extensional mode and large flexural mode components. For variations in velocity over the low-velocity regime, effects on both the amplitude and frequency content of the AE signals were observed. High-velocity, non-penetrating impacts also produced AE signals with large flexural modes. However, these signals had large extensional mode components of comparable amplitude to the flexural mode. The large extensional modes may be due to the in-plane crater deformation caused by impacts at these velocities. When high-velocity impacts fully penetrated the composite plates, the flexural mode was absent from the AE signal. Variations in the impact trajectory had no discernible effect on the modal content of the AE signals at either high or low velocities. The only signal variation was a change in overall amplitude, which was attributed to simple changes in the normal velocity component as a function of impact angle.

These results demonstrate the feasibility for using AE to not only detect and locate impact events on aircraft and spacecraft, but also provide information about the nature of the damage. The very large signal amplitudes for the impacts studied indicate that relatively large sensor spacing might be used for practical, economical, implementation. This, of course, depends on a number of factors such as the minimum allowable undetected impact damage, and the structural complexity of the region to be monitored, which can significantly affect the propagation of AE waves. The observed variation in signal characteristics with impact parameters such as velocity suggests that quantitative information about the impact parameters could be obtained. Such information could be used to remotely assess damage, which is of particular importance for long-term orbiting spacecraft. Likewise, the ability to

differentiate penetrating and non-penetrating impact events would be critical for assessing damage in spacecraft, particularly on pressurized components such as habitat modules and tanks.

However, further study will be necessary to develop and implement a full-scale AE impact-monitoring system for a given application. A wider range of impact velocities, projectile size and materials, and propagation distances, which are representative of those expected for the particular application should be tested. Also, realistic specimen geometry again representative of the aircraft or spacecraft to be monitored should be studied. This will allow the effects of wave propagation such as reflections or attenuation through complex geometry to be evaluated. Such effects can be significant and are often ignored when attempting to extend laboratory AE results to monitor real structures. And finally, as with any AE application, considerable attention needs to be paid to evaluating and eliminating potential noise sources. The development of accurate models to predict AE signals from impact sources will also be of tremendous benefit. Such simulations could help minimize the high expense required for experimentally testing a wide variety of impact conditions, and can be used to help understand and interpret results from actual events.

References

- W. M. Alexander, W. W. McCracken, L. Secretan, and O. E. Berg (1962), "Review of Direct Measurements of Interplanetary Dust from Satellites and Probes," NASA TN D-1669, pp. 39-60.
- W. D. Crozier, and W. Hume (1957), "High Velocity Light Gas Gun," J. Appl. Phys., 28, 892-894.

- S. K. Datta, T. H. Ju, R. L. Bratton, and A. H. Shah (1992), "Transient Response of a Laminated Composite Plate," *Review of Progress in Quantitative Nondestructive Evaluation*, 11, 145-151.
- GAO (1990), "Space Program: Space Debris is a Potential Threat to Space Station and Shuttle," GAO Report # GAO/IMTEC-90-18.
- GAO (1992), "Space Station: Delays in Dealing with Space Debris May Reduce Safety and Increase Costs," GAO Report # GAO/IMTEC-92-15.
- D. S. Gardiner and L. H. Pearson (1985), "Acoustic-Emission Monitoring of Composite Damage Occurring Under Static and Impact Loading," *Experimental Techniques*, 9, 22-28.
- M. R. Gorman (1990), "Plate Wave Acoustic Emission," *J. Acoust. Soc. Am.*, 90(1), 358-364.
- M. R. Gorman and W. H. Prosser (1991), "AE Source Orientation by Plate Wave Analysis," *Journal of Acoustic Emission*, 9(4), 283-288.
- I. Kapinsinsky (1978), "On the Reliability of the Acoustic Method of Micrometeoroid Detection," *Bulletin of the Astronomical Institutes of Czechoslovakia*, 29(6), 326-330.
- M. R. Karim (1991), "Impact Response of a Unidirectional Composite Laminate," *JSME International Journal*, 34(4), 496-504.
- B. P. Konstantinov, M. M. Bredov, E. P. Mazets, V. N. Panov, R. L. Aptekar, S. V. Golenetskii, Y. G. Guryan, and V. N. Il'inskii, (1969), "Micrometeors in Circumterrestrial Space Observed by Kosmos-163," Translated from *Kosmicheskie Issledovaniya*, 7(6), 817-821.
- B. M. Lempriere (1989), "Nondestructive Evaluation of Composite Structures in Space," Boeing Report # D180-31598-1.
- A. K. Mal and S. S. Lih (1992), "Wave Field Produced in a Composite Laminate by a Concentrated Surface Force," *Review of Progress in Quantitative Nondestructive Evaluation*, Vol. 11, 137-144.
- F. C. Moon (1973), "Wave Surfaces Due to Impact on Anisotropic Plates," *Journal of Composite Materials*, 7, 62-79.
- J. M. Nelson and B. M. Lempriere (1987), "Space Station Integrated Wall Design and Penetration Damage Control," Final Report for NASA Contract NAS8-36426.
- E. P. Papadakis (1980), "Broadband Flaw Detection Transducers: Application to Acoustic Emission Pulse Shape and Spectrum Recording Based on Pulse Echo Response Spectrum Corrected for Beam Spreading," *Acoustica*, 46, 293-298.
- W. H. Prosser (1991), "The Propagation Characteristics of the Plate Modes of Acoustic Emission Waves in Thin Aluminum Plates and Thin Graphite/Epoxy Composite Plates and Tubes," NASA Technical Memorandum 104187.
- E. Schneider and A. Stulp (1990), "Acceleration of Particles in Light Gas Guns for Micrometeoroid/Space Debris Simulation," *Proceedings of the International Symposium on Environmental Testing for Space Programs - Test Facilities and Methods*, Sponsored by ESA, eds. T. Guyenne and J. Hunt, Noordwijk, Netherlands, June 22-29, pp. 385-388.
- C. T. Sun and R. Y. S. Lai (1974), "Exact and Approximate Analyses of Transient Wave Propagation in an Anisotropic Plate," *AIAA Journal*, 12(10), 1415-1417.
- N. Takeda, R. L. Sierakowski, and L. E. Malvern (1981), "Wave Propagation Experiments on Ballistically Impacted Composite Laminates," *Journal of Composite Materials*, 15, 157-174.
- D. Weems, H. T. Hahn, E. Granlund, and I. G. Kim (1991), "Impact Detection in Composite Skin Panels Using Piezoelectric Sensors," *American Helicopter Society 47th Annual Forum Proceedings*, 1, 643-652.

Reflections of AE Waves in Finite Plates: Finite Element Modeling and Experimental Measurements

W. H. Prosser, M. A. Hamstad, J. Gary and A. O'Gallagher

Abstract

We investigated the capability of a three-dimensional dynamic finite element method for predicting far-field acoustic emission (AE) signals in thin plates of finite lateral extent, including their reflections from the plate edges. A lead-break (Hsu-Neilsen) source to simulate AE was modeled and used in the experimental measurements. For the thin plate studied, the signals were primarily composed of the lowest order symmetric (So) and antisymmetric (Ao) Lamb modes. Experimental waveforms were detected with an absolutely calibrated, wideband, conical element transducer. The conditions of lead fractures both on the surface of the plate as well as on the edge of the plate were investigated. Surface lead breaks preferentially generate the Ao mode while edge lead breaks generate the So mode. Reflections of developed plate waves from both normal and oblique incidence angles were evaluated. Particularly interesting for the case of the lead break on the plate edge were So waves produced by the interaction of a Rayleigh wave with the plate corner and those produced by a bulk shear wave mode that converted at the side edge. The Rayleigh wave, in this case, propagated along the specimen edge. For all cases considered, the experimental measurements were in good agreement with the predictions of lateral plate boundaries.

1. Introduction

Gary and Hamstad (1994) previously validated a dynamic finite element method (DFEM) for predicting simulated AE signals in thin plates. Experimental measurements were shown to be in excellent agreement with predictions from a two-dimensional, cylindrically symmetric, finite element model. The effect of varying finite element parameters such as cell size was investigated. Other variables such as source rise time and diameter, as well as sensor

aperture were also evaluated in this work. Later, Hamstad et al. (1996) extended this approach in developing a three-dimensional DFEM for predicting AE signals in thick plates. Again, experimental measurements with a calibrated wideband sensor were used to confirm the finite element models. More recently, Hamstad et al. (1998a) and (1998b) have applied the DFEM for predicting AE signals from more realistic source configurations such as buried dipole sources. Prosser et al. (1998) also compared the DFEM approach to plate theory predictions of AE signals for both isotropic and anisotropic plates. In all of this previous work on predicting AE waveforms with the DFEM, only the direct signal arrivals have been studied.

However, a major advantage of the DFEM in comparison to other methods for predicting AE signals is the ability to model AE signals in realistic specimen geometries. This, of course, includes predicting reflections from lateral plate boundaries. Because of the complexity of the problem, most theoretical treatments of Lamb waves for AE or ultrasonics assume the plate to be of infinite lateral extent. Examples of this are given by Guo et al. (1996) and references contained therein. Exceptions to this are works by Gorman and Prosser (1996), Prosser et al. (1998), and Huang (1998). However, the normal mode solution to plate theory used in these studies is applicable only to limited simple geometries such as rectangular and circular plates. Also, these plate theories predict only the extensional plate (lowest order symmetric Lamb) mode and flexural plate (lowest order anti-symmetric Lamb) modes and thus are not useful when the AE signals contain higher order Lamb modes.

This research validated the capability of the DFEM to predict AE signals in finite plates including reflection components. Simulated AE sources (lead breaks or Hsu-Neilsen sources) were modeled in rectangular aluminum plates, 3.175 mm thick. Experimental measurements of waveforms from lead-break sources were then obtained with an absolutely calibrated, wideband, conical element sensor for comparison. The lead-break source was positioned on either the plate surface or the plate edge near the mid-plane. As discussed by Gorman (1991) and Gorman and Prosser (1991), lead breaks on the surface preferentially generate the Ao mode while lead breaks on the plate edge generate signals with dominant So-mode components. For these two source configurations, plate specimens with different source and receiver positions were used to examine

Received on 30 June 1998. W. H. Prosser is affiliated with NASA Langley Research Center, Hampton, VA 23681-0001 (w.h.prosser@express.larc.nasa.gov), M.A. Hamstad is with University of Denver, Denver, CO 80208 and National Institute of Standards and Technology, Boulder, CO 80303, and J. Gary, and A. O'Gallagher are with National Institute of Standards and Technology, Boulder, CO 80303. This is a contribution of the U.S. National Institute of Standards and Technology; not subject to copyright in US.

signals containing reflections from both normal and oblique angles of incidence.

For the lead break on the plate edge, two particularly interesting reflection signals were theoretically predicted and observed experimentally. The first was due to a Rayleigh wave, which was generated by the edge lead-break source and propagated along the plate edge. After interacting with the plate corner, it propagated back to the receiver on the plate surface with a velocity corresponding to the S_0 mode. Another apparent mode conversion was due to a wave propagating to the plate edge at the bulk-mode shear velocity, mode converting with a change in angle appropriate for shear-to-longitudinal mode conversion, and then returning to the receiver as the S_0 mode. For all cases considered, including these apparent mode converted reflections, excellent agreement between DFEM predictions and experimental measurements was observed.

2. Dynamic Finite Element Method

The DFEM used in this research has been reported by Gary and Hamstad (1994) and Hamstad et al. (1996). Only the details relevant to this study are repeated herein. Both a two-dimensional, cylindrically symmetric model and a three-dimensional model have been developed. The two-dimensional model, although requiring less memory and computational time, has limited applications. It can be used only for isotropic materials and limited source/specimen geometries (round plate with axisymmetric source at the center). The three-dimensional model was required for this work to predict reflections in plates with noncircular geometries, and to model the in-plane lead-break source on a plate edge.

In the finite element method, a leapfrog approximation in time and linear elements in space was used. Stress-free boundary conditions were assumed along the top and bottom surfaces as well as along the outer edges of the plate. A source function with temporal variation to approximate that of a lead break as determined by Breckenridge et al. (1990) was used. An amplitude of 1 N was used, which is in good agreement with that produced by the fracture of a 0.3-mm diameter Pentel 2H lead. A density of 2700 kg/m^3 , longitudinal elastic wave speed of 6320 m/s, and shear wave speed of 3100 m/s, which were obtained from Kolsky (1953) for aluminum, were used in the model calculations. For all cases, a plate thickness was taken to be 3.175 mm.

As discussed previously by Gary and Hamstad (1994), the DFEM also models the source as the application of a force with the time history of a lead break at the position of interest. However, the force condition for the experimental lead break is actually the release of a force with that time response at the given position. Thus, the measured signal is 180° out of phase with that theoretically predicted. In agreement with this previous work, the experimental signals

were inverted in this study for comparison to the theoretical predictions of DFEM.

In order to produce situations, in which one or two reflections could be observed without significant superposition with the arrival of the direct signal or other reflections, plates with relatively large lateral dimensions were required for the finite-element model and experiment. Plates with two different lateral dimensions were used. The first was $26.7 \times 63.5 \text{ cm}$ and the second was $38.1 \times 50.8 \text{ cm}$. Because of these large lateral dimensions and the large memory requirements of the three-dimensional DFEM, the minimum finite-element cell dimension that could be used was $1/12$ of the plate thickness or approximately 0.26 mm. The cells had an aspect ratio of unity. This relatively large cell size led to a source diameter that was much larger than experimental conditions. For the experiment, a 0.3 mm lead was used. In reality, the source diameter is probably much smaller than this as the lead was held at an angle with respect to the surface, causing a smaller point of contact. Gary and Hamstad (1994) demonstrated that for a step-function input source in the DFEM, the source diameter must be at least four times larger than the cell dimension to avoid high frequency numerical transient noise. In these models with the lead-break source, which has a slower rise time and a smoother start and finish, a source diameter of two times the cell dimension was used. No high frequency numerical transients were observed and good agreement with experimental measurements was obtained.

3. Experimental Measurements

Simulated AE signals were produced by the fracture of 0.3-mm, Pentel 2H lead on 6061-T6 aluminum plates. To preferentially generate S_0 -mode AE signals, the lead was fractured on a plate edge near the plate mid-plane. For the A_0 mode, the lead was fractured on the plate surface. In agreement with the DFEM models, the two plates were 3.175 mm thick with one having lateral dimensions of $26.7 \times 63.5 \text{ cm}$ while the second was $38.1 \times 50.8 \text{ cm}$. A National Institute of Standards and Technology (NIST) standard reference AE sensor was used to detect the simulated AE signals. It was coupled to the aluminum plate specimens with Apiezon M grease. This sensor was a wideband, absolutely calibrated, conical element type sensor. The response of this sensor is flat with frequency from nearly 20 kHz to above 1 MHz. The calibration factor used to convert the voltage output of the sensor to surface displacement was 5.623 nm/V .

The theoretical and experimental signals were band-pass filtered by digital signal processing software with four-pole, Bessel filters. However, the low-pass and high-pass cutoff frequencies were different in the surface lead break experiments from those used in the edge lead break experiments. Two factors necessitated this filtering scheme to allow a comparisons of the DFEM predictions with experi-

ment. The first was that the sensor used for experimental measurements was flat with frequency only from around 20 kHz to just above 1 MHz. The second motivation for filtering was so that the reflected signals of interest could be more clearly observed. For the Ao mode created by surface lead-break sources, the amplitude of the signals becomes increasingly larger at lower frequencies, which arrive later in the signal because of their slower velocity. In this case, the signals reflected from the plate edges were superimposed on the low-frequency, large-amplitude components in both the theoretical and experimental signals. A 50-kHz high-pass cutoff frequency was used for the studies of Ao mode to reduce these component of much lower frequencies and to more clearly show the reflected signals. A 1000-kHz low-pass cutoff frequency was used because of the limited sensor response above this frequency.

For the edge lead-break sources, even though great care was used in positioning the source, it was impossible to exactly center it at the mid-plane of the plate. Thus, a component of the Ao mode was always generated, which was not present in the DFEM predictions. Since this mode contains predominantly lower-frequency components than the So mode, the discrepancy between theory and experiment was minimized with the high-pass filtering. A high-pass cutoff frequency value of 100 kHz was necessary to adequately reduce the Ao mode. Also, in contrast to the Ao mode, the So mode has very high frequency components that travel more slowly and superimpose with the reflected signals. A lower value of low-pass cutoff frequency of 750 kHz was used to reduce these high-frequency components to more clearly see the reflections.

For comparing the amplitudes of the experimental signal and the theoretical prediction of DFEM, only the NIST-sensor calibration factor was used. However, the experimental signal had to be adjusted in time for comparison with the model because the experimental data acquisition was not triggered by the lead-break source. The arrival of the wave at the experimental sensor location triggered data acquisition, with digital pre-trigger acquisition used to record the earliest arrival of the signal. In all cases, the experimental waveform was shifted in time so that the first peak of the symmetric mode arrival coincided with the DFEM prediction

4. Surface Lead-break Source

Several different AE source and receiver positions were used to investigate AE signals of Ao-Lamb mode and their reflections generated by pencil-lead breaks on the plate surface. For the first case, the source and receiver were positioned as shown in Fig. 1a to allow observation of the direct arrival and normal incidence reflection of the Ao mode. As illustrated in that figure, the 38.1 x 50.8 cm plate was used and the propagation distance for the direct arrival (illustrated as path 1) was 7.62 cm. The total propagation

distance for the signal reflected off of the plate back edge (path 2) was 25.4 cm. The DFEM and experimental signals are shown in Fig. 1b. Both were bandpass filtered from 50 to 1000 kHz. For the Ao mode, out to the 150 μ s time period shown in Fig. 1b, only the direct arrival and the back-wall reflection are observed. Excellent agreement between the theoretical prediction and experimental measurement was obtained for the Ao mode and its reflection.

Even though the surface lead-break source preferentially generated the Ao mode, a very small So-mode component is seen in Fig. 1b prior to the anti-symmetric mode arrival. Because of the faster velocity of the So mode, the signals also contain multiple reflections of this mode. However, they are much smaller in amplitude than the dominant anti-symmetric mode and were not examined in detail. The So mode and its reflections were studied with edge lead-break sources, which are discussed later in this paper.

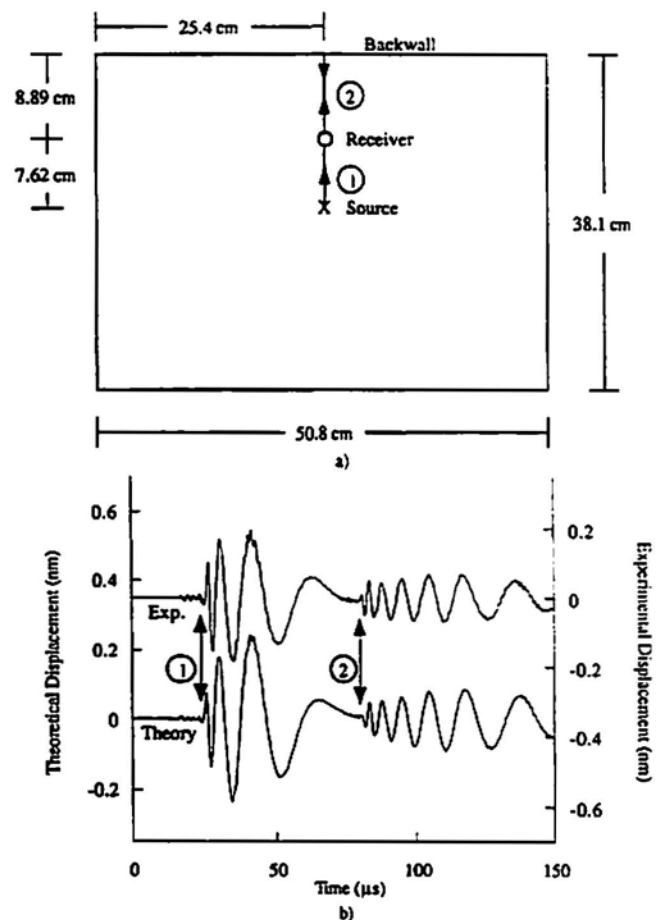


Fig. 1 Direct arrival and normal incidence reflection of Ao-Lamb-mode AE signal generated by surface lead-break source; a) Plate geometry and source/receiver locations, b) Filtered experimental and DFEM-predicted waveforms.

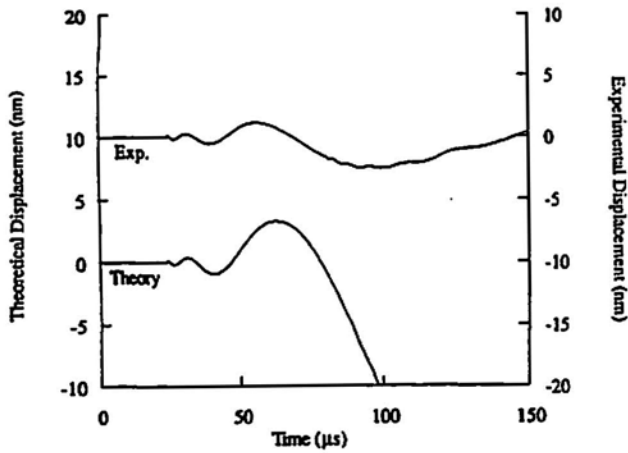


Fig. 2 Unfiltered theoretical and experimental signals for plate, source, receiver geometry shown in Fig. 1a.

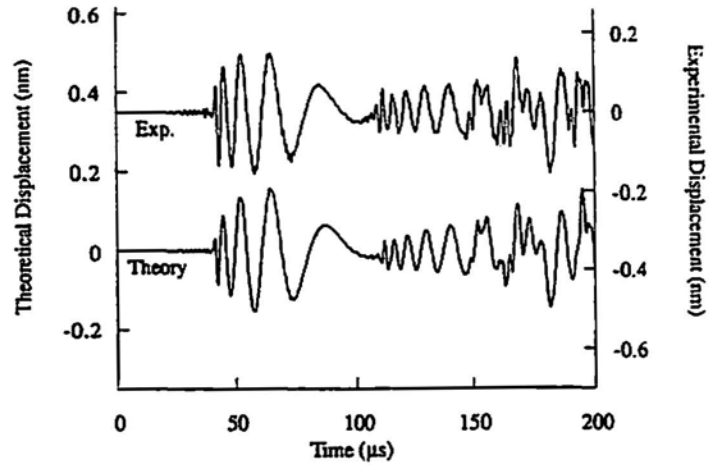


Fig. 4 Theoretical and experimental signals from Fig. 3b over longer time scale showing agreement for arrival of multiple reflections.

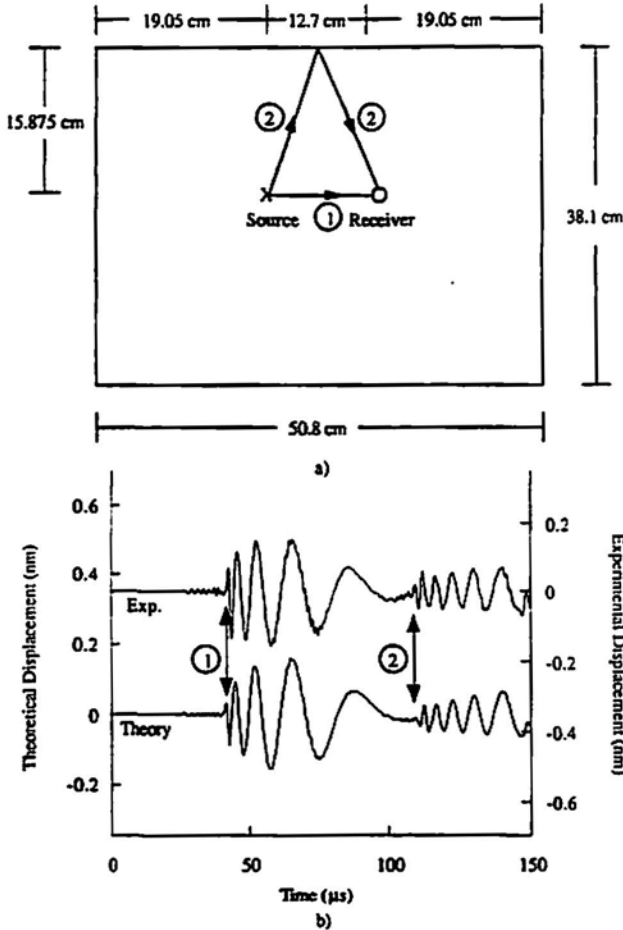


Fig. 3 Direct arrival and oblique incidence reflection of Ao-mode AE signal generated by surface pencil lead-break source; a) Plate geometry and source/receiver locations, b) Filtered experimental and DFEM-predicted waveforms.

The necessity of filtering is illustrated by examining the unfiltered theoretical and experimental signals from Fig. 1b which are shown in Fig. 2. Because of the increasing amplitude of the Ao mode at longer times, which corresponds to the lower frequency arrivals, the reflections are not even apparent. The 50-kHz high-pass filter enables the observation of the reflections. The lack of agreement between the experimental signal and the DFEM prediction at longer times in Fig. 2 is caused by the lack of low-frequency response of the sensor below 20 kHz.

The case of oblique incident reflections of the Ao mode generated by a surface lead break was studied next. The source, receiver, and plate geometry are shown in Fig. 3a. These were chosen such that, after filtering, the direct arrival (path 1) and reflected signals (path 2) were not superimposed. Again, the 38.1 x 50.8 cm plate was used. The source to receiver distance was 12.7 cm, and they were equidistant (15.9 cm) from the plate edge. The total propagation distance for the reflected signal was calculated to be 34.2 cm. As illustrated in the figure, the angle of incidence (and reflection) with respect to a normal to the plate edge was 21.8°. The bandpass filtered DFEM and experimental waveforms are shown in Fig. 3b. Again, good agreement was observed. Figure 4 shows the comparison of the theoretical and experimental signals at even longer times. Additional reflections from the other plate edges begin to arrive after 145 μ s. The agreement is still quite good for these superimposed reflections.

The final surface lead-break case considered was again oblique incident reflection. However, in this case, the dimensions were chosen such that the direct arrival and the reflected signal were superimposed. Figure 5a shows the plate geometry, and the source and receiver positions. The 26.7 x 63.5 cm plate was used and the source to receiver

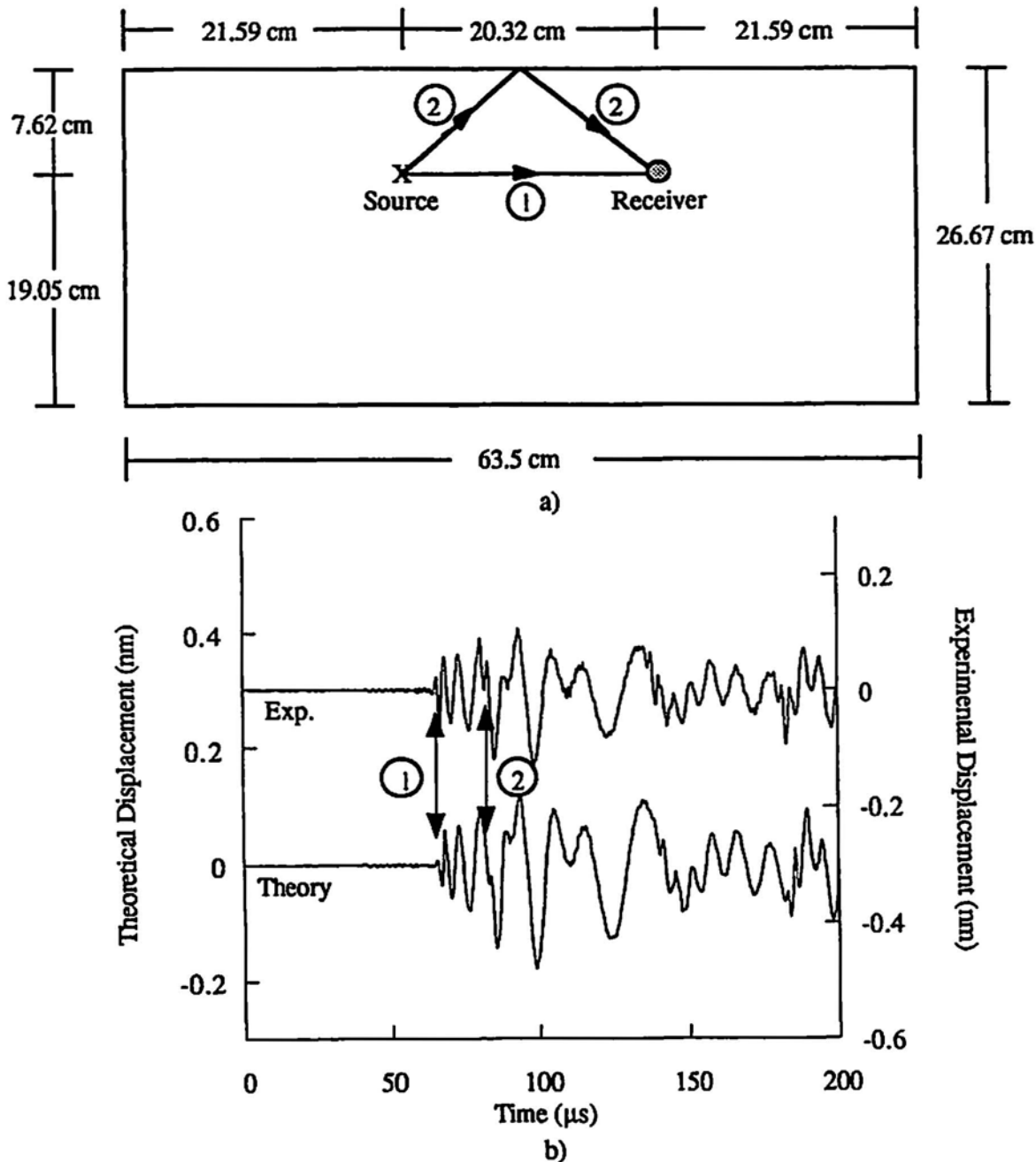


Fig. 5 Direct arrival and oblique incident reflection of Ao-Lamb-mode AE signal generated by surface lead-break source; a) Plate geometry and source/receiver locations, b) Filtered experimental and finite element predicted waveforms.

distance was 20.3 cm. The source and receiver were positioned 7.62 cm from the plate edge, which produced a propagation distance of 25.4 cm for the reflected signal. The angle of incidence and reflection was 53.1° . The theoretical and experimental signals are shown in Fig. 5b. In this figure, the direct arrival and reflected signals are indicated with arrows labeled 1 and 2, respectively. Additional reflected signals from other plate edges appear in the signal beyond 135 μs . Again, there is good agreement between the theoretical and experimental waveforms.

5. Edge Lead-break Source

Edge lead-break sources were used to preferentially generate AE signals of So-Lamb mode and to investigate their reflections. As before, two different plate dimensions were used along with different source and receiver positions to observe the particular reflections of interest. The first case studied was a normal incident reflection. The 26.7 x 63.5 cm plate was used with the source positioned mid-plate along the longer edge. The positions of the source and receiver with respect to the plate dimensions are shown in Fig. 6a. Likewise, the ray paths for the direct and reflected

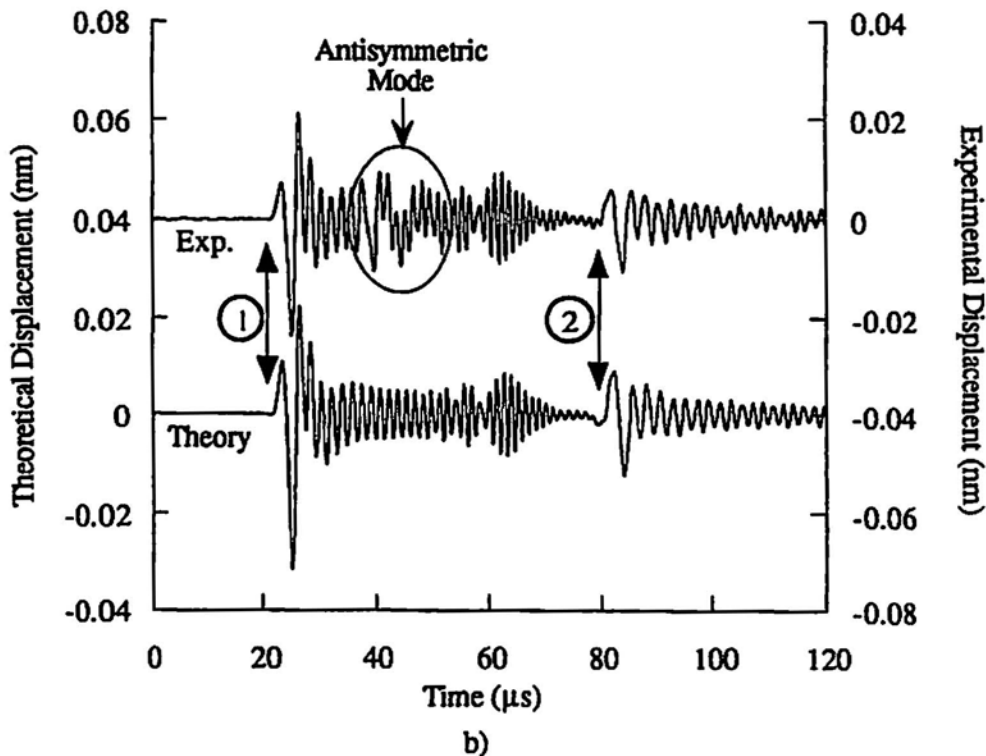
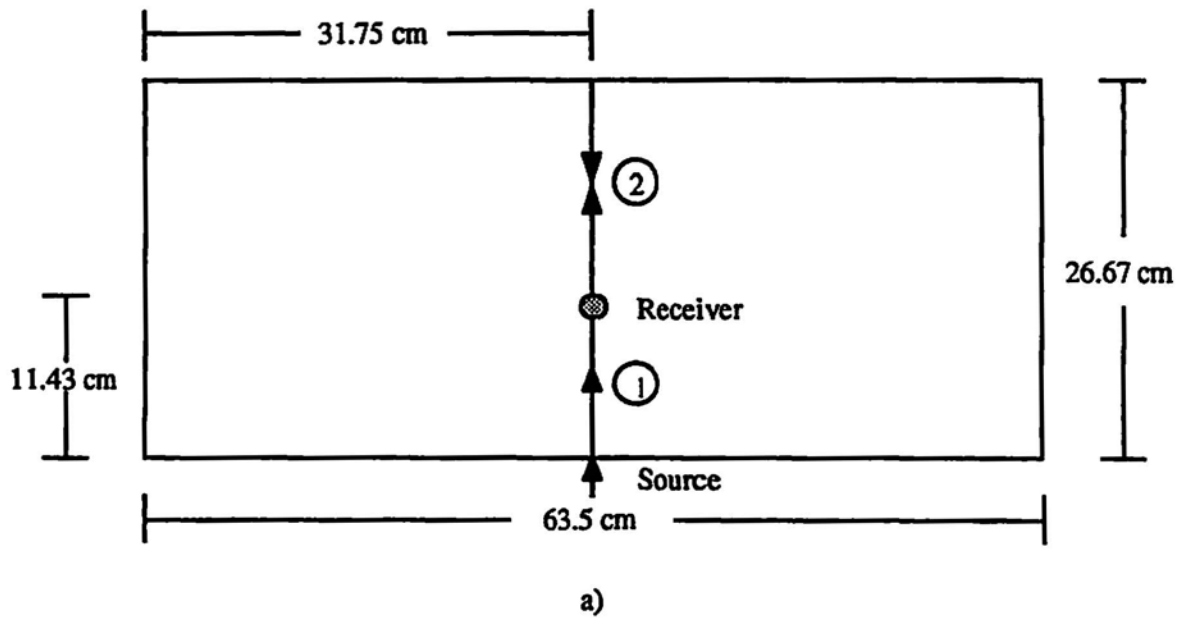


Fig. 6 Direct arrival and normal incident reflection of So-Lamb-mode AE signal generated by edge lead-break source; a) Plate geometry and source/receiver locations, b) Filtered experimental and DFEM-predicted waveforms.

signal are indicated in this figure as 1 and 2, respectively. The propagation distance for the direct signal was 11.4 cm, with the propagation distance from the backwall reflection being 41.9 cm. The bandpass filtered (100 - 750 kHz) theoretical and experimental signals are shown in Fig. 6b with the direct and reflected signal arrivals indicated by 1 and 2, respectively. As can be seen, the signals are in good agreement with the exception of the circled Ao component in the experimental waveform, which is discussed below. Figure 7 shows the same two waveforms with an expanded time

scale so that the excellent agreement of the reflected components is more clearly seen.

As mentioned previously, it was impossible to exactly center the edge lead-break source at the mid-plane of the plate. A magnifying glass and a fine rule scale on the plate edge were used to more closely position the source at the mid-plane. However, an Ao-mode component was always detected in the experimental signal. A number of lead-breaks were performed for all of the edge lead-break ex-

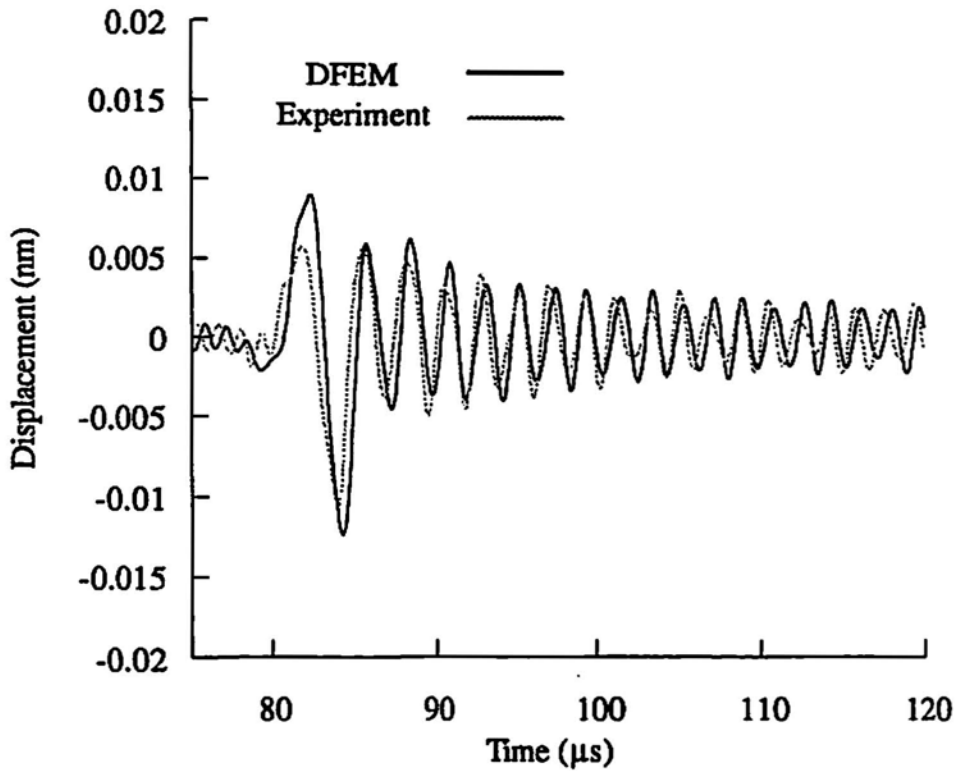


Fig. 7 Signals from Fig. 6 with expanded time scale to show comparison of reflected signal.

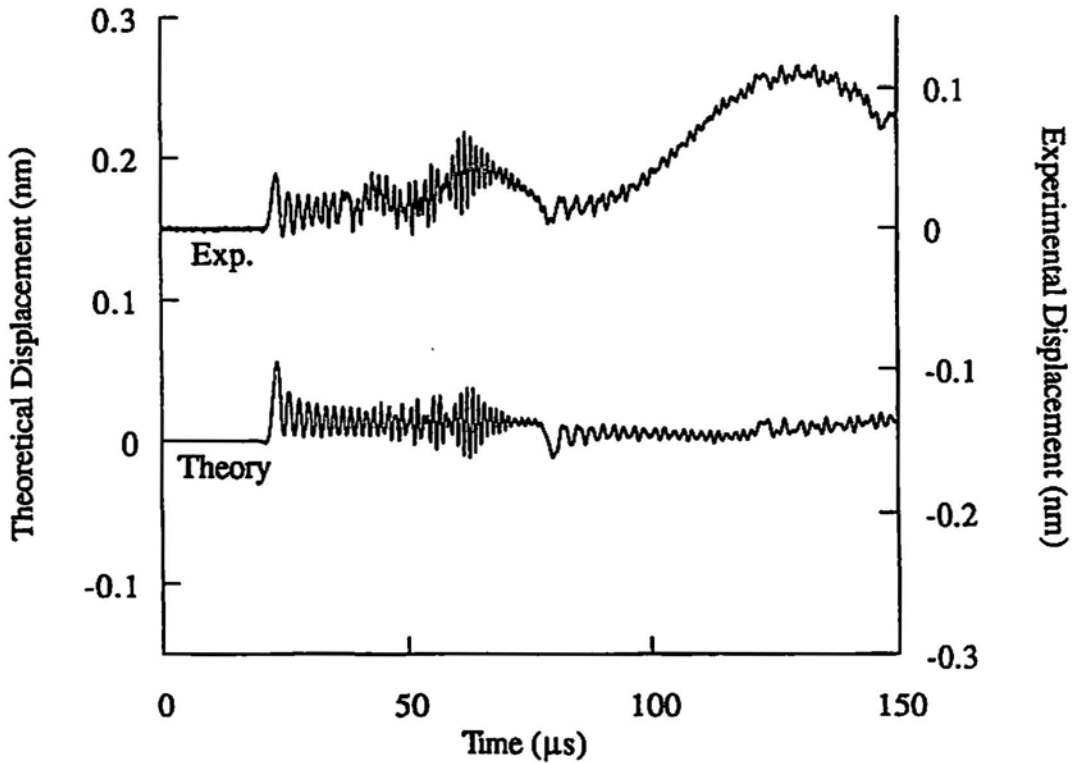


Fig. 8 Theoretical and experimental waveforms of Fig. 6 without bandpass filtering.

periments and ones chosen with a minimum of this anti-symmetric mode component. The 100-kHz high-pass filtering then eliminated most of this mode. However, as seen in the circled region of the experimental waveform in Fig.

6b, the A_0 mode does contain higher frequencies which were not filtered. These are superimposed on the direct arrival of S_0 mode. Other signals from edge lead-break sources shown later in this paper also show this effect.

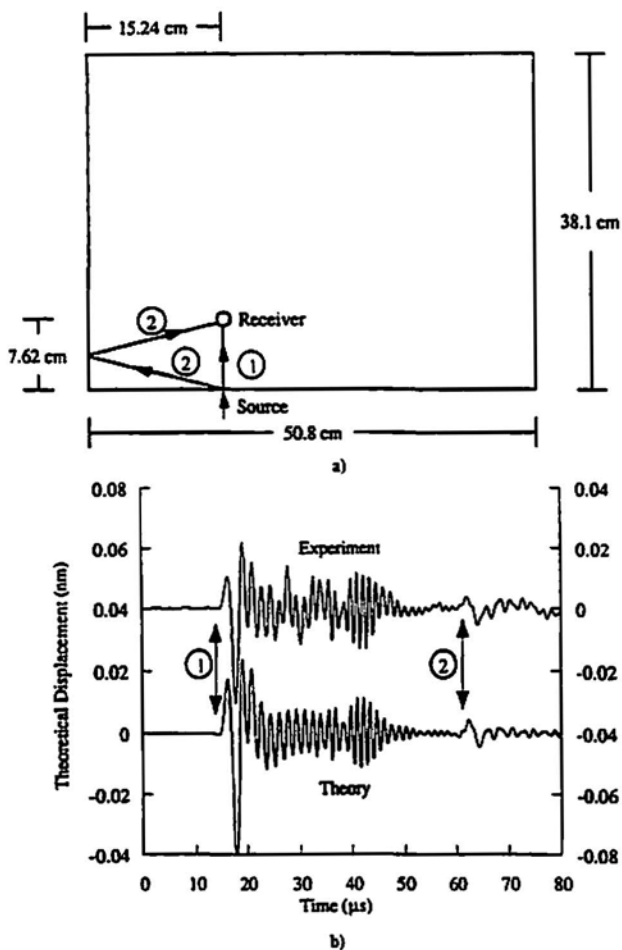


Fig. 9 Direct arrival and oblique incident reflection of symmetric Lamb-mode AE signal generated by edge lead-break source; a) Plate geometry and source/receiver locations, b) Filtered experimental and DFEM-predicted waveforms.

Since the DFEM allowed the source to be positioned exactly at the mid-plane, a corresponding anti-symmetric mode component in the theoretical signal is not observed. Figure 8 shows the unfiltered experimental and theoretical waveforms for the source, receiver, and plate geometry shown in Fig. 6a. The unfiltered, larger-amplitude A_0 mode in the experimental signal is clearly seen.

For the case of oblique incident reflection of the S_0 -Lamb mode, we used an edge lead-break source on the 38.1 x 50.8 cm plate. As shown in Fig. 9a, the source was positioned at 15.2 cm from one corner. This position was used so that the reflection from only one side could be obtained unobstructed by reflections from the backwall or other side. Also shown in Fig. 9a are the positions of the source and the ray paths for the direct (1) and reflected (2) signals. The source-to-receiver distance for the direct arrival was 7.62 cm and for the reflected signal, it was 31.4 cm. The angle of incidence and reflection for this reflection with respect to the normal to the plate edge was 14° . The band-pass-filtered experimental and DFEM predicted waveforms

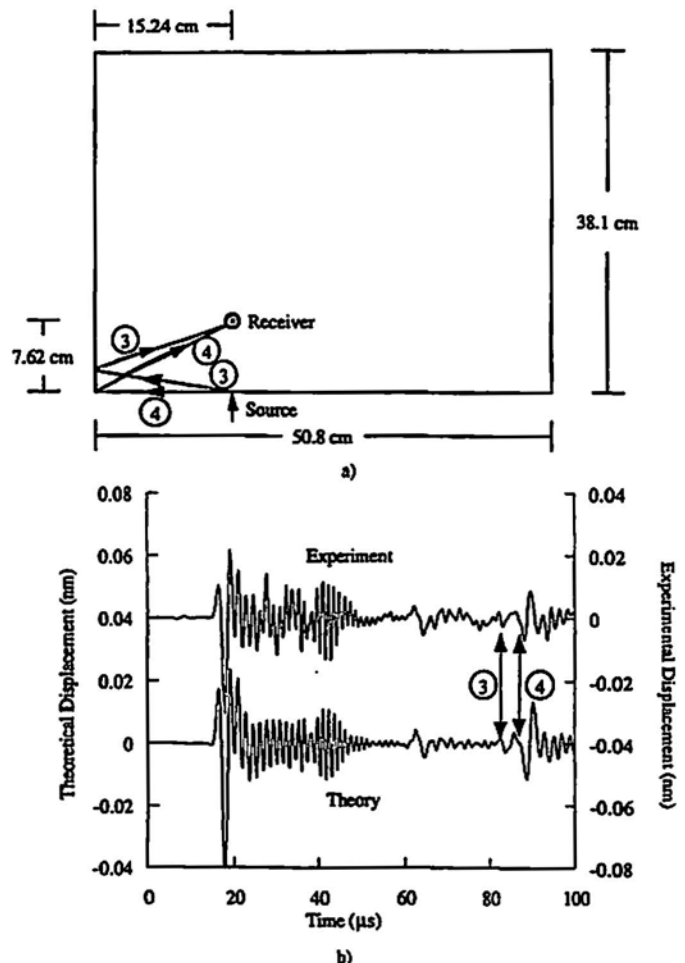


Fig. 10 a) Plate geometry, source/receiver locations, and propagation paths for mode-converted Rayleigh and shear waves, b) Filtered experimental and DFEM-predicted waveforms.

are shown in Fig. 9b. This figure shows the signals out to a point in time, during which only these two arrivals (direct wave and sidewall reflection) are present. Very good agreement between the DFEM and experimental waveforms is demonstrated. The discrepancy of the presence of some higher frequency components of the A_0 mode of the experimental signal is again noted.

When the time scale for Fig. 9b is expanded as shown in Fig. 10b, two additional signal arrivals are noted and are labeled 3 and 4. The arrival times for signals 3 and 4 were found to be too early to have been created by reflections from either the back edge or the far side edge of the plate. These two signal arrivals are particularly interesting in that they appear to be reflected signals with paths as shown in Fig. 10a, which have been mode-converted at the edge and corner of the specimen, respectively. Several aspects of the DFEM signals were examined to reach this conclusion. These included the arrival times and amplitudes of signals 3 and 4 at different sensor locations as well as the in-plane displacement components for positions along the propagation paths to the edge and the corner.

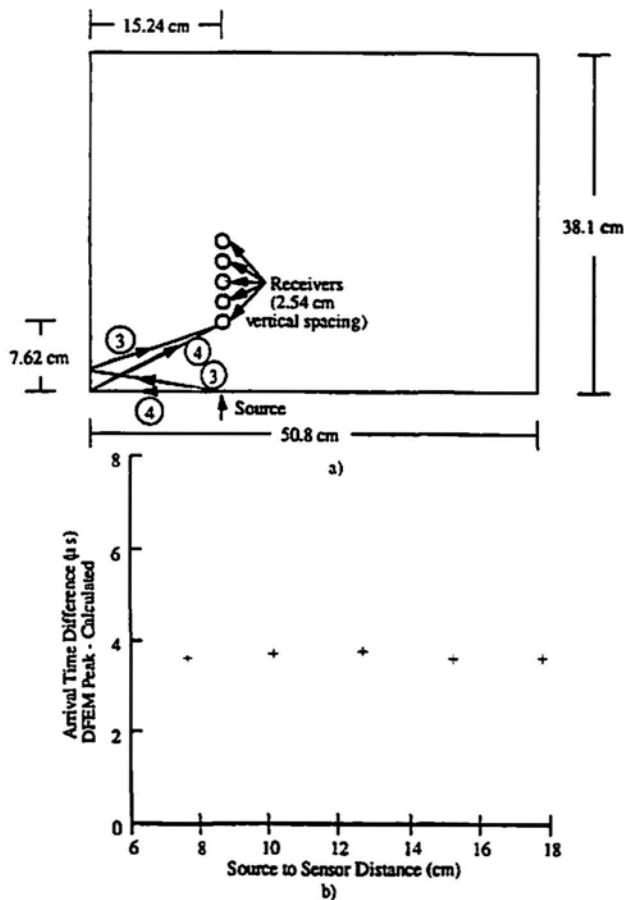


Fig. 11 a) Source and receiver positions for arrival time measurements to evaluate propagation paths for arrivals of mode-converted reflection, b) Difference in arrival time between that determined from peak of signal 3 (DFEM) and calculated from shear/longitudinal mode-converted propagation path using shear and extensional plate velocities.

The sensor locations, for which the arrival times and amplitudes were measured from the DFEM signals (equivalent to those of signals 3 and 4 in Fig. 10b), are shown in Fig. 11a. They were such that the direct path from the source to the sensor ranged from 7.62 cm to 17.8 cm in 2.54 cm intervals. Because of the smaller amplitude of arrivals 3 and 4 and their superposition with higher frequency components of other weaker signals, it was not possible to determine their exact first arrival time. Instead, the arrival times of the peaks of signals 3 and 4 were measured at the different locations. These arrival times were compared to those calculated using the known shear (3100 m/s) and Rayleigh velocities (2894 m/s), and the plate theory extensional velocity (5403 m/s) which serves as an approximation for the velocity of So-mode first arrival. In comparison with the calculated arrival times, it was expected that the values measured from the peaks of the DFEM signals 3 and 4 would be slightly later. However, this time difference between measured and calculated arrival times should be constant for the different sensor locations. For signal 3, the

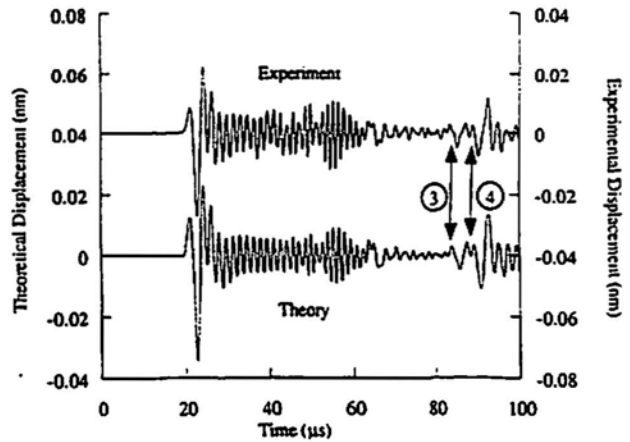


Fig. 12 Filtered experimental and DFEM-predicted waveforms for source, receiver, and plate geometry as in Fig. 10a except with receiver positioned at 10.2 cm propagation distance from source.

propagation path and modes, which gave such a constant arrival-time difference between calculated and measured values for the different sensor locations, was that of a bulk shear wave propagating out to the edge, mode-converting to a longitudinal wave with the appropriate change in angle, and then returning to the receiver as the So mode. Figure 11b shows the time difference between the measured peak of signal 3 arrival time, and the calculated arrival time for this mode-converted reflection. Other possible paths considered include (a) shear and Rayleigh waves propagating along the edge, which affects the mode conversion at the corner, and returning as the So mode, and (b) a shear mode, which is mode-converted at the edge without the expected change in angle of reflection. None of these gave expected arrival times consistent with those measured for signal 3 at the different sensor locations.

In addition to the arrival time, the amplitude of this signal component was also measured at the various source-to-sensor distances. These were examined and compared to expected changes in amplitude for mode-converted longitudinal waves as a function of the angles of incidence of the shear mode as discussed by Graff (1991). At the 7.62-cm distance used for the signals in Fig. 10b, the angle of incidence for the shear mode with respect to the normal to the edge is 9.34° , and the angle of reflection for the mode-converted wave is 18.55° . The total propagation distance is 31.5 cm. The amplitude of this mode-converted reflection is quite small and barely noticeable. However, when the signal is examined with the sensor at a distance of 10.2 cm from the source on the edge, the amplitude of this reflection is larger as shown in Fig. 12. In this case, the angle of incidence is 12.37° and the angle of reflection is 24.10° with a total propagation distance of 32.3 cm. Although not shown here, it was confirmed that the amplitude of this mode-converted signal continues to increase when the sensor-to-

source distance, and thus angle of incidence of shear mode, is increased. This increase of signal amplitude as a function of increasing angle of incidence is consistent with the amplitude relations for the mode conversions from bulk shear waves to bulk longitudinal waves. Another factor, which might also be contributing to this increase in amplitude for more distant sensor positions, is the shape of the radiation patterns for shear modes from a point monopole source, as discussed by Scruby (1985).

For such a mode conversion to occur at the plate edge, it is noted that the shear wave must be polarized vertically with respect to the plate edge. This shear wave is also polarized horizontally with respect to the plane of the plate. The in-plane displacements, perpendicular to the propagation direction, were also examined in the DFEM calculation to evaluate the existence of a shear mode with horizontal (with respect to the plane of the plate) polarization. These were examined at the modeled sensor locations, as well as at positions along the path of the shear wave, which would propagate out to the plate edge, be mode-converted and return to the sensor at 7.62 cm distance from the source. For the DFEM signals, which propagated along a direct path to the modeled sensor locations, no transverse, in-plane displacements corresponding to a shear mode arrival were observed. This is to be expected if the radiation patterns, as discussed by Scruby (1985), for shear modes from a point monopole type source are considered. Shear modes from such a source radiate out at angles with respect to the direction of the monopole with no component propagating directly along the direction of the monopole force (i.e., directly ahead of the source). The transverse, in-plane displacements for propagation along the direction of the shear wave to the edge did show an arrival that corresponded to the shear wave arrival time. However, analysis of these in-plane displacement components was complicated because of other shear modes with different polarizations, and their interactions with the plate surfaces.

A similar analysis of the arrival times of the waves designated as signal 4 in Fig. 10b and 12 at different propagation directions was completed. From this, the path and modes of signal 4 were found to be consistent with a Rayleigh wave propagating away from the source on the plate edge, which was mode-converted at the plate corner and propagated to the modeled sensor location as the So mode. The in-plane (and normal to the plate edge) displacement from the DFEM model was examined at multiple locations along the plate edge to verify the existence of a Rayleigh wave. Figure 13 shows the in-plane displacement component for a position at the mid-plane of the plate and on the edge at a distance of 7.62 cm from the edge lead-break source. The large amplitude Rayleigh wave is clearly present in this signal. The dynamics of this mode conversion at the corner are not as well understood. However, the agreement between the DFEM and experiment is again good for these mode-converted reflections.

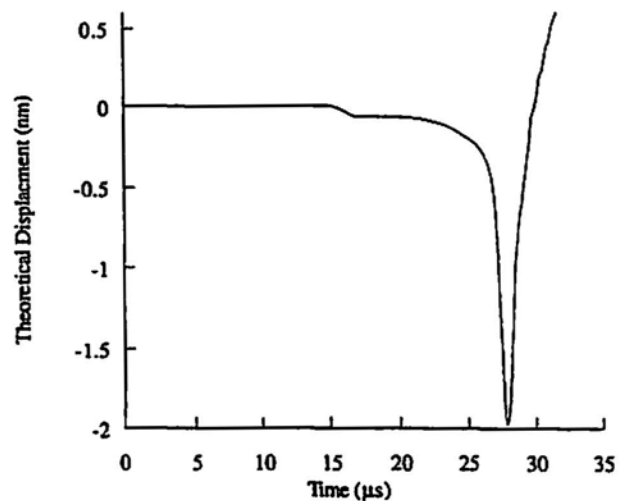


Fig. 13 Theoretical in-plane displacement for position at mid-plane of plate edge at a distance of 7.62 cm from edge break source showing the arrival of Rayleigh wave component.

6. Summary and Conclusions

The results of this study validate a three-dimensional dynamic finite element method (DFEM) for predicting AE waveforms in finite plates including reflection components. Simulated AE sources (lead breaks) were modeled and used for the experimental confirmation. Both lead breaks on the surface and the edge of thin aluminum plates were considered. In thin plates, surface lead breaks preferentially generate the Ao-Lamb mode while lead breaks on the edge near the mid-plane of the plate preferentially generate the So mode. It was demonstrated theoretically and experimentally that the edge break source also generates a Rayleigh wave, which propagates along the plate edge. This Rayleigh wave interacts at the plate corner to produce a mode converted So wave. Also observed theoretically and experimentally was a mode-converted reflection caused by shear waves generated by the edge lead-break source. These waves were mode-converted at the sides of the plate upon reflection to longitudinal waves, which then propagated through the thin plate as the So mode. An absolutely calibrated, wideband sensor was used for all experimental measurements. In all cases, good agreement was obtained between the DFEM predictions and experimental measurements.

The validation of the DFEM for predicting the reflections of AE signals in plates is an important step toward making it a useful tool for predicting AE waveforms in real practical structures. In such structures, signal reflections are often a significant contribution to the waveform because of structural complexities such as holes, free edges, welds, joints, etc. The effect of reflections on AE waveforms is even more pronounced in laboratory specimens such as coupons, which usually have very small lateral dimensions. Further work is necessary, however, to validate the model for predicting waveforms in other practical situations that

include specimens with thickness changes, welds, varying and/or anisotropic material properties.

References

F. Breckenridge, T. Proctor, N. Hsu, S. Fick, and D. Eitzen (1990), "Transient Sources for Acoustic Emission Work," *Progress in Acoustic Emission V*, eds. K. Yamaguchi et al., JSNDI, Tokyo, pp. 20-37.

J. Gary and M. A. Hamstad (1994), "On the Far-field Structure of Waves Generated by a Pencil Lead Break on a Thin Plate," *J. Acoustic Emission*, 12(3-4), 157-170.

D. Guo, A. Mal, and K. Ono (1996), "Wave Theory of Acoustic Emission in Composite Laminates," *J. Acoustic Emission*, 14(3-4), S19-S46.

M. R. Gorman (1991), "Plate Wave Acoustic Emission," *J. Acoust. Soc. Am.*, 90(1), 358-364.

M. R. Gorman and W. H. Prosser (1991), "AE Source Orientation by Plate Wave Analysis," *J. Acoustic Emission*, 9(4), 283-288.

M. R. Gorman and W. H. Prosser (1996), "Application of Normal Mode Expansion to Acoustic Emission Waves in Finite Plates," *J. Appl. Mech.*, 63(2), 555-557.

K. F. Graff (1991), *Wave Motion in Elastic Solids*, Dover Publications Inc., New York.

M. A. Hamstad, J. Gary, and A. O'Gallagher (1996), "Far-field Acoustic Emission Waves by Three-Dimensional Finite Element Modeling of Pencil-Lead Breaks on a Thick Plate," *J. Acoustic Emission*, 14(2), 103-114.

M. A. Hamstad, J. Gary, A. O'Gallagher (1998a), "On Wideband Acoustic Emission Displacement Signals as a Function of Source Rise-Time and Plate Thickness," *J. Acoustic Emission*, 16, S251-S259.

M. A. Hamstad, J. Gary, A. O'Gallagher (1998b), "Modeling of Buried Acoustic Emission Monopole and Dipole Sources with a Finite Element Technique," to be submitted.

W. Huang (1998), "Application of Mindlin Plate Theory to Analysis of Acoustic Emission Waveforms in Finite Plates," to be published in the *Proceedings of the Review of Progress in Quantitative Nondestructive Evaluation*, 17.

H. Kolsky (1953), *Stress Waves in Solids*, Dover Publications Inc., New York.

W. H. Prosser, M. A. Hamstad, J. Gary, and A. O'Gallagher (1998), "Comparison of Finite Element and Plate Theory

Methods for Predicting Acoustic Emission Waveforms," Submitted to the *Journal of Nondestructive Evaluation*.

C. B. Scruby (1985), "Quantitative Acoustic Emission Techniques," *Nondestructive Testing*, Vol. 8, Academic Press, Inc., London, pp. 141-208.

42nd AEWG Meeting

used to discriminate weak AE signals from the bubbles, which were originally detected during corrosion by Rettig and Felson.

Zonal and Database Match Approach: A Potential Method for AE Source Location on Water Filled Tank, H. Warren Shen and Adrian A. Pollock, Physical Acoustics Corporation

The traditional zonal approach assumes that the AE source should fall within the zonal area where the first triggered sensor is located. However, in the railroad tank test that involves water, the above is not always true. We found in our study that many sensors were first triggered by water-borne AE signals generated on the other side of the tank. The Zonal and Database Match approach looks at the entire tank for possible sources of the triggering pattern observed from the 12 channels.

The tank surface is first divided into 12 hexagons where each hexagon contains a sensor. Each hexagon is further divided into 6 triangles (A, B, C, D, E, F) and each triangle contains 2 median triangles (Left and Right). Four small right triangles (1, 2, 3, and 4) are then further divided from a Left and a Right median triangle respectively. In that case, the entire tank car has 576 small triangles, and each small triangle can now be uniquely identified. For example 4DL1 indicates Sensor #4, D Triangle, L median triangle, small triangle #1. Each one of the 576 small triangles should cover an area ranging from 313 in 2 (for a 10,000-gallon Railroad Tank Car) to 634 in (for a 29,000-gallon Railroad Tank Car).

The Zonal and Database Match approach considers each of these 576 triangles as a possible source zone for an observed AE hit-set. For each zone, the computer can calculate the possible range in arrival times of four kinds of waves (extensional, flexural, water-borne direct and waterborne reflected) at each of the twelve sensors. This theoretical pattern of arrival time range is unique for each small triangle. When an AE signal hits the system, the computer will try to compare the real hit pattern with each of the theoretical patterns and locate one small triangle out of the 576 with the best match. In simple terms, we will have the computer calculate the arrival time range patterns for all the 576 small triangles, and then in order to process an AE hit-set the computer will look at its arrival time pattern and see which of the 576 small triangles gives a good fit. This is the Zonal and Database Match approach.

AE Source Location with Dual-wave Mode Method, Maochen Ge, GE Acoustics Technology

The dual-wave mode method refers to an AE source location method that utilizes two different types of wave arrivals with distinctive travel velocities. From a practical point of view, extensional and flexural arrivals are the main concern of these two different wave types. In the case of liquid filled tanks, they may be metal borne extensional waves and liquid borne waves. The need of the dual-wave mode method is due to a number of practical and theoretical reasons. First, the arrivals that can be used for AE source location is highly mixed. Practical experiences have indicated that it is almost equally possible for both extensional and flexural wave triggering in an automated arrival timing system. The traditional AE location methods are limited to handle a single type of arrivals and, therefore, have to face one of two following choices: assuming all arrivals as extensional waves or simply using one type of arrivals. In the first case, it would introduce large and systematic errors into the input data, which has been a primary reason responsible for the poor AE location accuracy in the past. In the second case, it would lead to a tremendous loss of original data.

With the dual-wave mode method, one could use both extensional and flexural wave arrivals from the same sensor. Therefore, the second advantage of the dual-wave mode is that one could double the location information with the same hardware configuration. This is particularly important when a monitoring system consists of the very limited number of channels or when the manual analysis is needed to analyze those critical AE events.

The third important reason to use a dual-wave mode method is due to the location mechanisms. The location mechanisms for methods using one type and two types of arrivals are different. In general, the methods using a single type of arrivals have a good accuracy control in the central areas between sensors, but poor control in the areas near the sensors and the areas outside the array. However, when two types of arrivals are used simultaneously, it adds another location mechanism by increasing the accuracy control in the radial direction. Therefore, one would normally have the better location accuracy with a dual-wave mode method. In this presentation, ample practical cases will be used to demonstrate how our dual-wave mode method has dramatically improved AE source location accuracy.

Classification of Acoustic Emission Signatures Using a Self-organization Neural Network

Tinghu Yan, Karen Holford, Damian Carter and John Brandon

Abstract

Acoustic emission (AE) testing is a promising technique for use in structural health monitoring. A critical factor for the successful implementation of this technique in both laboratory and field is the ability to achieve reliable source identification, which can be best achieved through adoption of pattern recognition techniques. In particular, there is a need for discrimination of AE signals from fatigue crack growth and extraneous AE in order to quantitatively evaluate fatigue crack growth. This paper presents a waveform descriptor-based classification of AE signals during laboratory fatigue testing of a full-scale steel bridge girder using a self-organization neural network. The pitfalls of AE signal classification based on automatically extracted waveform features are demonstrated through the consideration of typical signals from individual sources and the complications during the AE signal acquisition and waveform feature extraction process. Careful interpretation of the classification results is emphasized in order to identify the likely origin of AE data contained within each class.

1. Introduction

Acoustic emissions (AE) or stress waves are generated during irreversible processes either external or internal to a material. The stress waves can be detected and monitored by sensors to yield information about source location and source characteristics, which in turn can aid damage assessment. The detection and evaluation of fatigue crack growth in steel structures by the AE technique has been of great interest for practical non-destructive testing (NDT) applications since the early 1970s (Pollock and Smith, 1972; Gong et al., 1992; Sison et al., 1996; Yoon et al., 1997). Many approaches have been proposed to correlate fatigue crack growth behavior with AE parameters, including AE events, counts, amplitude and energy. AE count rate has been found to be quite useful for modeling fatigue crack growth (Harris and Dunegan, 1974; Morton et al., 1974; Sin-

clair et al., 1977; Bassim, 1987; Bassim et al., 1994). However, the successful application of these quantitative results *in situ* relies on the reliable detection and identification of AE of interest, i.e., elimination of extraneous noise from sources other than fatigue crack growth.

Perhaps noise is the most difficult problem of AE monitoring both in the laboratory and in the field (Gong et al., 1992; Hamstad and McColskey, 1997). It has been reported that extraneous AE can make up more than 98% of detected AE when monitoring a steel railroad bridge in the field (Gong et al., 1992). A wide range of potential noise sources may occur in practical AE monitoring, which include mechanical noise, such as load causing vibration and rubbing of structural components; environmental noise, such as rain, wind, and air-borne acoustic noises from other acoustic activities; and electrically induced noise, such as electromagnetic interference (EMI). Using modern integrated pre-amplifiers, differential transducers, proper grounding and screening of AE equipment, the problem of EMI has been virtually eliminated. For continuous monitoring of large structures in the field, environmental noise still presents a problem, to which careful attention must be paid (Gong et al., 1992).

Mechanical noises of vibration generally present AE events of long rise time, which are located in a lower frequency band. This noise may be eliminated by the proper choice of operating frequency to attenuate low frequencies, or filtered out through time-domain feature analysis as well as through high-pass filters. However, it has been observed that mechanical noises from rubbing of moving parts and fretting of crack faces present high-frequency signals, which are similar to the AE signals emitted from fatigue crack growth (Gong et al., 1992). It is then difficult to eliminate this type of noise through frequency filtering without losing the AE signals of interest from crack propagation.

Mechanical noises, such as vibration and rubbing of moving parts, may also be stopped at the source during laboratory testing by using damping materials between specimen and jig contact point, or eliminated by space discrimination through the use of guard sensors and spatial filtering. A guard sensor is an AE transducer placed at a location outside the mounting area. Any signal that first intercepts this sensor will be considered an invalid signal and will be discarded. For spatial filtering, two sensors

Received 9 January 1999. Tinghu Yan is affiliated with Department of Mechanical Engineering, Southeast University, Nanjing 210096, P. R. China. Karen Holford (Holford@cardiff.ac.uk), Damian Carter and John Brandon are with Cardiff School of Engineering, University of Wales Cardiff, Queen's Buildings, The Parade, PO Box 685, Cardiff CF2 3TA, UK.

are placed so that if the signal is emitted from a crack at a known location, the differences of the arrival time at two sensors would fall in a particular "window" and all plausible background noise sources would give arrival-time differences outside the "window". These techniques are quite successful where a noise source is separated from the known monitoring area. In addition, meticulous mounting of AE sensors and careful attachment of cables also help reducing other types of mechanical noises caused by the vibration of electrical connections and cables.

For laboratory cyclic fatigue testing, a combination of source location and load-controlled gating techniques provide a further means for discrimination of AE from fatigue crack activities (including both crack propagation and crack surface fretting) and other extraneous noises. As a crack is a concentrated source from a fixed location, only AE signals originating from a tightly clustered location need be considered, while randomly scattered AE signals can be ignored. In addition, fatigue crack growth usually occurs only under peak tension loading cycles. In this case, the load-controlled gating technique can be used to record AE signals only when the load approaches its peak level, thus eliminating a large amount of noise events produced by frictional rubbing at the crack surfaces during intermediate loading cycles.

In the field, the elimination of extraneous AE signals other than those from fatigue crack growth is much more complicated. The location of a crack, if it exists, is unknown prior to testing, and due to the dispersion of the AE waves originating from either fatigue crack growth or extraneous AE sources at various distances and the poor accuracy of arrival time-based source location techniques used in a typical fixed-threshold AE system, the means of guard sensors, spatial filtering, and/or source location may not be so effective. Furthermore, in field testing, the unpredictable fatigue-load spectrum rather than smooth sinusoidal pattern used in the laboratory, makes it difficult to apply the load-gating technique to record AE signals only during the peak load.

In this paper, waveform descriptor-based classification using a self-organization neural network for AE signals from EMI, fatigue crack growth, and crack surface fretting during a cyclic tensile loading of a full-scale bridge girder in a laboratory environment is investigated. The pitfalls of AE signal classification based on automatically extracted waveform features are demonstrated through an important consideration of the typical signals from individual sources. The complications during AE signal acquisition and waveform feature extraction process are reported, resulting in a recommendation for careful interpretation of the waveform descriptor-based classification results.

2. Experimental Procedure

The measurement of AE signals was conducted using a LOCAN 320, which is a multiple channel commercial AE system from PAC (Physical Acoustics Corp., USA). Resonant transducers R15D and R15I (PAC) of 150 kHz nominal center frequency were mounted on the web of a full-scale steel bridge girder, coupled with silicon grease. Pre-amplification of the sensor signal with 40 dB gain was made with integral internal preamplifiers for the R15I sensors and using external PAC 1220A preamplifiers for the R15D sensors. The threshold used for AE signal acquisition was 45 dB, and system timing parameters; Peak Definition Time (PDT), Hit Definition Time (HDT), and Hit Lockout Time (HLT) of 500, 1000 and 1000 μ s, respectively, were implemented. Three-point bending cyclic fatigue testing was conducted at a stress range of 10-262 MPa, load range of 10-230 kN, and frequency of 1.5 Hz, using a Dartec 500 hydraulic fatigue machine.

Figure 1 shows the geometry of the girder and the experimental set-up and Fig. 2 shows the photograph of a typical girder after testing. The girder was fabricated from grade 43C steel plate by metal-inert gas (MIG) welding with approximately 6 mm fillet welds. To minimize distortion and residual stresses, the components of the girder (flanges, webs and stiffeners) were initially tack welded at the corners and centers of each panel. Continuous welds were then run between the tacks, following as closely as possible the methods used typically in the bridge construction industry.

Seven AE signal parameters as well as time, load and channel number were measured in real time by the PAC LOCAN 320 AE data acquisition system, and the AE signal waveforms were recorded using a PAC TRA 212 with the PAC LOCAN 320. A sampling rate of 5 MHz and data length of 4096 was used for acquisition of signals from crack activities, and 2048 for EMI signals. The AE waveform descriptors examined in this study include Rise time (RT, μ s), AE Counts (CNTS), Energy (ENRY), Duration (DUR, μ s), Peak amplitude (AMP, dB), Average frequency (AVF, kHz), and Counts-to-peak (CNTP).

3. Pattern Recognition Analysis of AE Signals

AE signals provide information concerning the source of the emission and the material or structure under examination and generally one can recognize visually the existence of certain waveform categories and correlate them to underlying source mechanisms (Ono, 1997). Although this can be very time consuming as the number of AE signals is often large, especially in continuous monitoring, manual waveform classification has to be done in some cases (Hamstad and McColskey, 1997). With modern pattern recognition analysis techniques, the

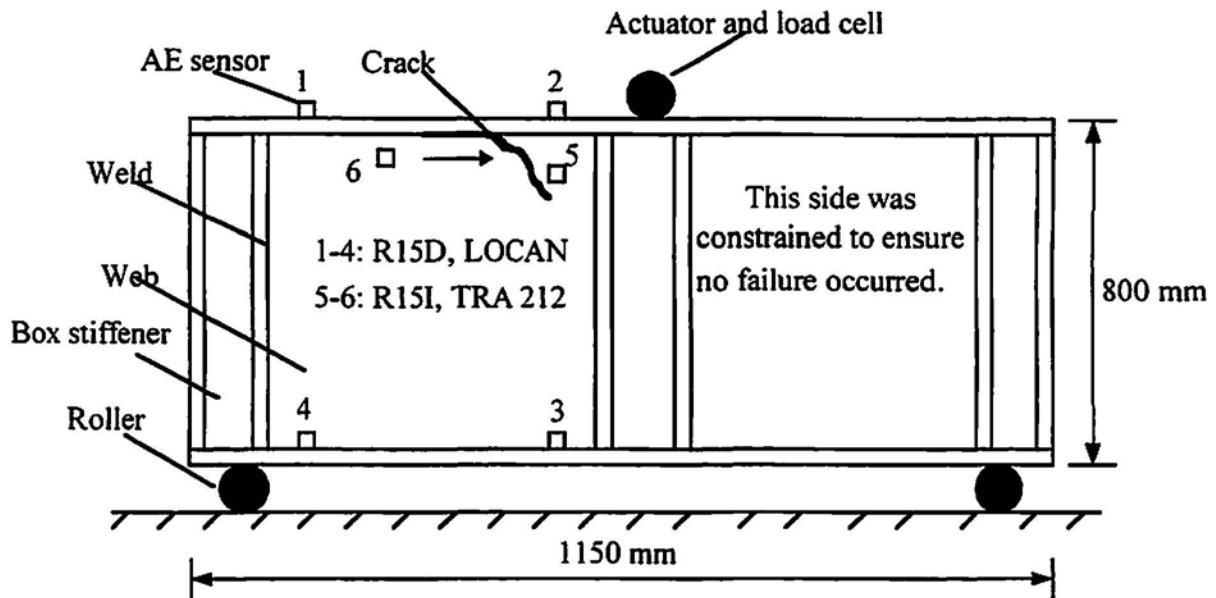


Fig. 1 The experimental set-up.

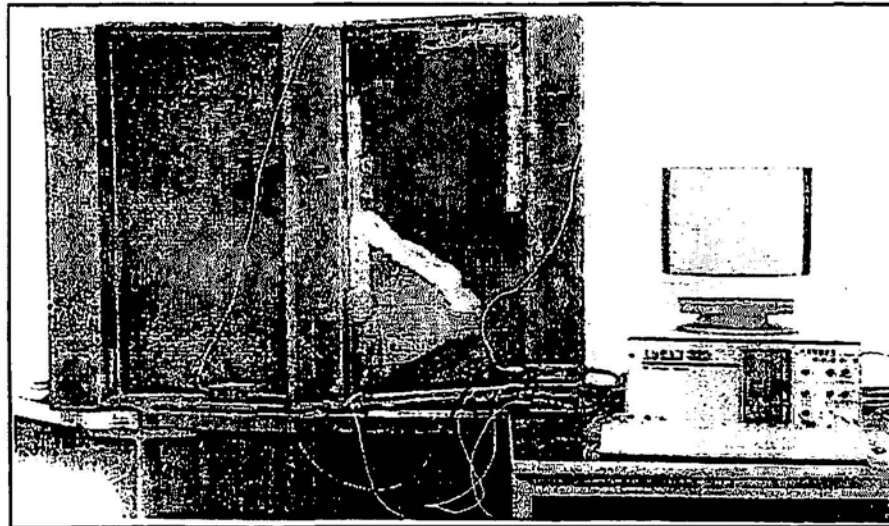


Fig. 2 Photograph of typical tested girder.

classification of AE signals has become less labor intensive.

Most recently, commercial software packages designed for classification or for noise discrimination of AE signals have become available, such as ICEPAK (Tektrend International Inc., Canada) and PAC-PARS (Physical Acoustics Corp., USA), which include standard statistical and error back-propagation neural network classifiers; and Visual Class™ (Vallen Systeme GmbH, Germany), which performs classification based on multiple FFT (Fast Fourier Transform) of the signals in staggered time windows. All of these are very useful for classification of AE signals and, of these methods, the k-nearest neighbor classifier has been proved most effective (Ono, 1997). In addition, in composite material testing, a clustering method based on the combination of max-min distance and modified Forgy

algorithms has been successfully applied for characterizing different failure mechanisms of glass fiber/epoxy specimens during tensile loading through the classification of detected AE signals (Anastassopoulos and Philippidis, 1995), and more recently, a clustering algorithm based on learning vector quantizer (essentially a self-organization neural network) has been employed for recognizing the different damage modes of carbon/carbon laminates during tensile loading through the clustering of similar AE signals (Philippidis et al., 1998). A number of other authors have also investigated the potential of neural networks in AE source identification. An adaptive Resonance Theory (ART) family of neural networks has been utilized to analyze AE signatures of loose parts within a nuclear reactor coolant system and to classify the patterns of AE signals associated with different masses and impact energies of the loose parts (Keyvan and Nagaraj, 1996; Keyvan

and Pickard, 1997). An error back-propagation neural network has been utilized to solve the inverse problem in AE, i.e., determining the information of the AE source waveform, which is independent of the propagation media, the AE sensor and the AE measuring system, from the detected AE signal. It was demonstrated that the appropriate source waveform associated with mode I crack extension can be effectively determined by a trained multi-layer neural network (Yuki and Homma, 1996). Again, it has been demonstrated that an error back-propagation neural network can locate AE sources in the aluminum plate and bolted channel structures (with and without damping material between the joints) far more accurately than the classical time difference method, especially in structures with discontinuities where the wave velocity is no longer constant in all directions (Venkatesh and Houghton, 1996).

However, classification and interpretation of AE signals based on AE waveform descriptors must be conducted carefully, as many factors may influence the waveform features of AE signals. These include the characteristics of source itself and material, the path and distance from the source to the AE transducer, geometrical factors of the structural members, frequency response of the AE sensor, as well as the set-up of AE measuring system, such as threshold and system timing parameters. Thus, the waveform features of AE signals from a certain source may change in both the frequency and the time domain, depending on the structural factors and processing methods. This makes unsupervised classification methods more suitable than supervised classification methods for AE signal classification in practical structure monitoring, as the trained patterns for supervised classification methods are usually obtained from testing of model specimens. In doing so, one presumes the existence of similarity between the generated AE signals and the propagation characteristics of each failure mechanism in the model specimen and the actual structure *in situ*, and the coherence of AE sensors, pre-amplifiers, the AE measuring system as well as their corresponding set-ups.

Another aspect of AE signal classification is that it is being recognized that waveform-based analysis of AE signals obtained using either resonant or wideband sensors offers advantages to traditional AE waveform descriptors based classification methods for discrimination of extraneous AE (Hamstad and McColskey, 1997; Keyvan and Pickard, 1997; Suzuki et al., 1996; Kinjo et al., 1997), and that the wavelet transform (WT) is becoming another powerful tool for AE signal discrimination. WT allows the determination of the frequency spectrum as a function of time with optimized resolutions both in time and frequency domains using width-variable wavelets as the basic functions. The resultant wavelet transform coefficients in the time-frequency plane provides more informative charac-

terization of transient signals than the power density spectra obtained from the traditional Fourier transform. WT has been successfully applied to classify the AE signals emitted during tensile loading of a longitudinal glass-fiber reinforced composite specimen and four types of visually observed WT spectrograms have been correlated to the known fracture modes excellently (Suzuki et al., 1996). Furthermore, in order to classify the WT spectrograms automatically, Kinjo et al. (1997) examined three 3-D image classification methods, i.e., classical matched filtering of given images (MF), matched filtering of Laplacian images (MF-LI), and Fourier phase correlation (FPC), and it was found that the FPC method was superior to the other two methods in its higher classification counts and discrimination capability.

The current study focuses on the investigation of waveform-descriptors based classification for AE signals using a self-organization neural network, while the AE waveform-based analysis using wavelet transform for discrimination of extraneous AE signals during the fatigue testing is investigated further in the forthcoming publication by the authors.

4. Self-organization Neural Network

The self-organization neural network was introduced by Kohonen in 1981 (Kohonen, 1989). It consists of two fully connected layers (input-output) of neurodes, and the connections arriving to neurode j in the output layer bear weights that collectively form the coordinates for the cluster center at neurode j . The input layer is commonly arranged in a linear or rectangular array, while the output layer may be configured in rectangular or hexagonal arrays. The geometry chosen to represent the output layer determines the configuration of the "neighborhood" of each output neurode (Fig. 3). The topology of self-organization neural network (SONN) used in this paper is illustrated in Fig. 4.

Initial cluster center coordinates are randomly picked through the generation of random connection weights. When an input pattern is presented to the input layer, each Euclidean distance between the input pattern and the corresponding connection weight vector from the input neurodes to a particular output neurode j is calculated and compared to produce a single winning output neurode with minimum Euclidean distance. The winning output neurode indexes the cluster center, whose coordinate weight vector matches the input pattern most closely.

Once the winning output neurode is found, the weights of each connection arriving to output neurodes in the neighborhood of the winner are adjusted by

$$\Delta w_{ji} = \eta(t) d_{ji} \quad (1)$$

where $\eta(t)$ is a learning rate decreasing with time, $0 < \eta(t)$

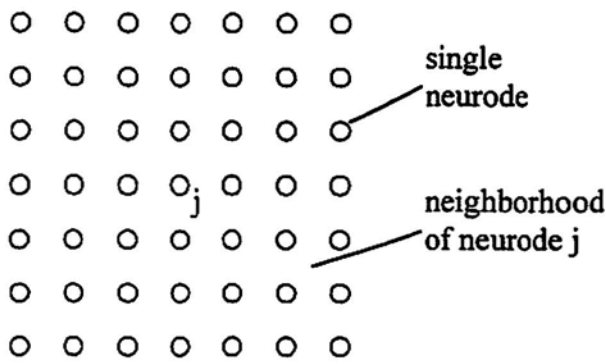


Fig. 3 Neighborhood of neurone in rectangular array.

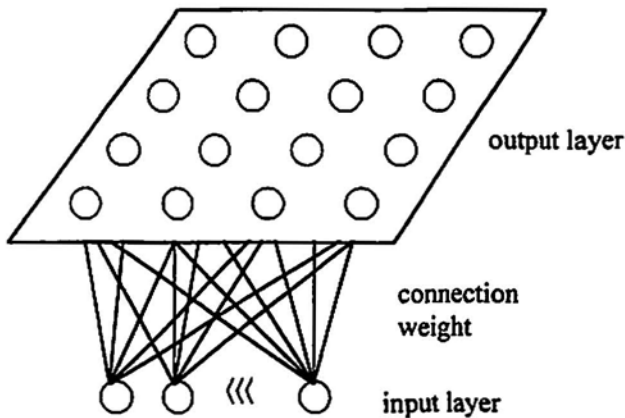


Fig. 4 Self-organization (Kohonen) neural network (SONN) topology.

$i = 0, 1, \dots, n$, n is the number of input neurones, $j > 0$, the index of output neurones; t is the iteration number increasing upon the introduction of all input patterns; and w_{ji} is the i -th coordinate difference between the corresponding weight vector of output neurone j and the input pattern. The learning rate function is generally defined as

$$\eta(t) = \eta_0(1 - t/T) \quad (2)$$

where η_0 is the initial learning rate constant, T is the time interval, during which the learning rate decreases to zero.

All input patterns are sequentially presented to the input layer of SONN, and the process of calculating Euclidean distances, finding the winning output neurone, as well as adjusting the connection weights of output neurones

in the neighborhood of the winner is repeated for an appropriate predefined number of iterations. The result is that the values of the weights form clusters, which reflect the probability density of the input patterns, while the output neurones that are in topologically near each other react similarly to similar input patterns (Eberhart and Dobbins, 1990).

5. Results and Discussion

In the classification experiment, 122 samples from sensor 5, including 58 crack growth and 64 crack surface fretting AE, were extracted using a combination of information on source location, load cycle occurrence, expertise of the general signal characteristics from different sources and their associated waveforms; another 21 spurious AE signals from electromagnetic interference (EMI) were introduced by interfering with the transducer cables without cyclic loading. The 143 samples were amalgamated in random order to a single data file for subsequent classification by the SONN.

Figure 5 shows the SONN classification topology result with 9 output neurones. The figure shows how four significant classes of data are recognised by the SONN, containing 16, 56, 41, and 30 input patterns, respectively. The typical waveform feature data characteristics of these four classes are listed in Table 1.

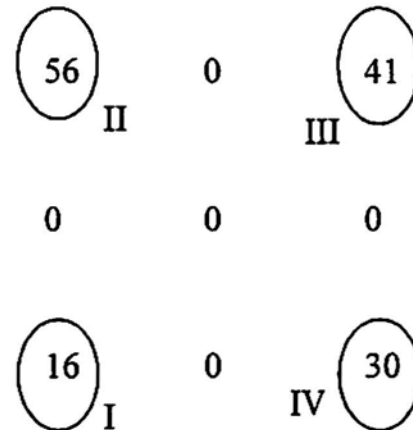


Fig. 5 SONN classification topology result for 143 AE with 9 output neurones.

Table 1 Typical characteristics of the four classes of AE identified by the SONN

Class No	Patterns	RT (μ s)	CNTS	ENRY (V·s)	DUR (μ s)	AMP (dB)	AVF (kHz)	CNTP
I	16	1-27	1-71	2-4	2-86	45-56	278-822	1-13
II	56	5-210	1-36	1-42	12-358	52-80	48-167	1-23
III	41	26-204	98-119	230-706	756-819	80-95	125-154	3-27
IV	30	354-756	105-123	255-576	818-819	80-87	128-150	51-106

Consideration of the relative associated waveform feature data from the four classes can provide a hypothesis as to their likely identities and corresponding waveform characteristics. However, identification and interpretation of AE waveform descriptor-based SONN classification results may not be so simple. Determination of the source contents of these classes is less straightforward and requires an understanding of the nature of the individual source events and the implications of the AE signal acquisition and waveform feature extraction process. The complications are best demonstrated through a consideration of typical signals from the individual sources.

AE from fatigue crack growth can arise from a multiplicity of sources, including plastic zone expansion, inclusion fracture and ductile tearing. Figure 6 illustrates four typical AE signals associated with fatigue crack growth and highlights several critical considerations. The first point to note is that the emission category broadly termed "crack growth" can embrace two basic types of source behaviour. The waveform in Fig. 6(a) illustrates a "classic" crack growth event, which has well defined peak and decay characteristics, and is of short duration and fast rise time. The lower signals in Figs. 6(b), (c) and (d) also show three waveforms from crack growth and demonstrates an apparently unique property; its ability to produce cascaded bursts of emission in rapid temporal succession with individual bursts having similar waveform feature properties to those of the isolated crack growth event. The "rapid cascaded burst" phenomenon is highly significant since it presents an opportunity for crack growth source identification based on an event rate criterion, and the time lapse between bursts may also offer an insight into the activity level of a crack. However, this relies on the assumption that the AE hardware and software is capable of resolving such rapid bursts of AE and correctly identifying the signal as being composed of separate hits of AE.

In defining a hit, the AE system uses three user-predefined timing parameters for AE waveform measurement, i.e., Peak Definition Time (PDT), Hit Definition Time (HDT), and Hit Lockout Time (HLT). Consider the case where the PDT, HDT and HLT were set at 500, 1000 and 1000 μ s, the AE signals of Fig. 6(b), (c) and (d) will be recorded as a single hit respectively by the AE system and treated accordingly by the waveform feature extraction routine. This can result in measurement of erroneous waveform feature values, since under the current system timing parameters set-up, the software cannot unambiguously isolate the individual bursts into separate hits. Consequently, measured values of rise time, counts, duration, energy, peak amplitude, counts-to-peak and average fre-

quency may be misleading and adversely affect the classification process. It is clearly unreliable for further identification based on the extracted waveform features.

However if the PDT, HDT and HLT are set at more appropriate values to cope with the type of cracking AE, for example, HDT=200 μ s, then this may corrupt the measurement of waveform features from longer duration signals. Figure 7 shows two typical signals from crack surface fretting. Two observations are significant. Firstly, both signals are relatively "flat" in comparison with crack growth emissions, consequently their peaks are less well defined and the two waveforms will yield significantly different measurements of rise time and counts-to-peak, which may affect classification reliability. Secondly, both waveforms occupy the entire window length, which, in hindsight, is inappropriately short for fretting signals and limits the maximum duration to approximately 820 μ s due to the adopted sampling rate (5 MHz) and data length (4096).

Evidently, there is a problem in defining these hit timing parameters. In order to identify and describe the burst-type crack growth AE, short HDT and HLT are desirable; however, this adversely affects measurement of the long-duration fretting signals.

The complications of AE data acquisition and feature extraction process are not confined to crack growth and fretting signals. Figure 8(a) illustrates a typical EMI signal, while Fig. 8(b) shows a rapid and intense EMI signal, which can produce high measured values in energy, counts, duration as well as amplitude. Another important point to note is that, although crack growth is a potentially unique mechanism of rapid burst emission, it is not the only source that can give rise to the detection of "rapid burst" phenomena. Figures 8(c) and (d) illustrate that EMI may also replicate this behavior and produce similar waveform features to the AE signals arising from crack growth.

Thus, it would not be always reliable to classify AE signals based on automatically extracted waveform features. The limitations behind the technique to produce these waveform feature data must be considered, especially as, due to inappropriate values of HDT and HLT, rapid bursts of cracking AE or EMI signals may be recorded as a single hit, resulting in measurement of erroneous waveform feature values and adverse affects on the classification. Returning to the waveform descriptor-based classification results of the SONN, it is evident that some confusion of the number and identity of sources can occur.

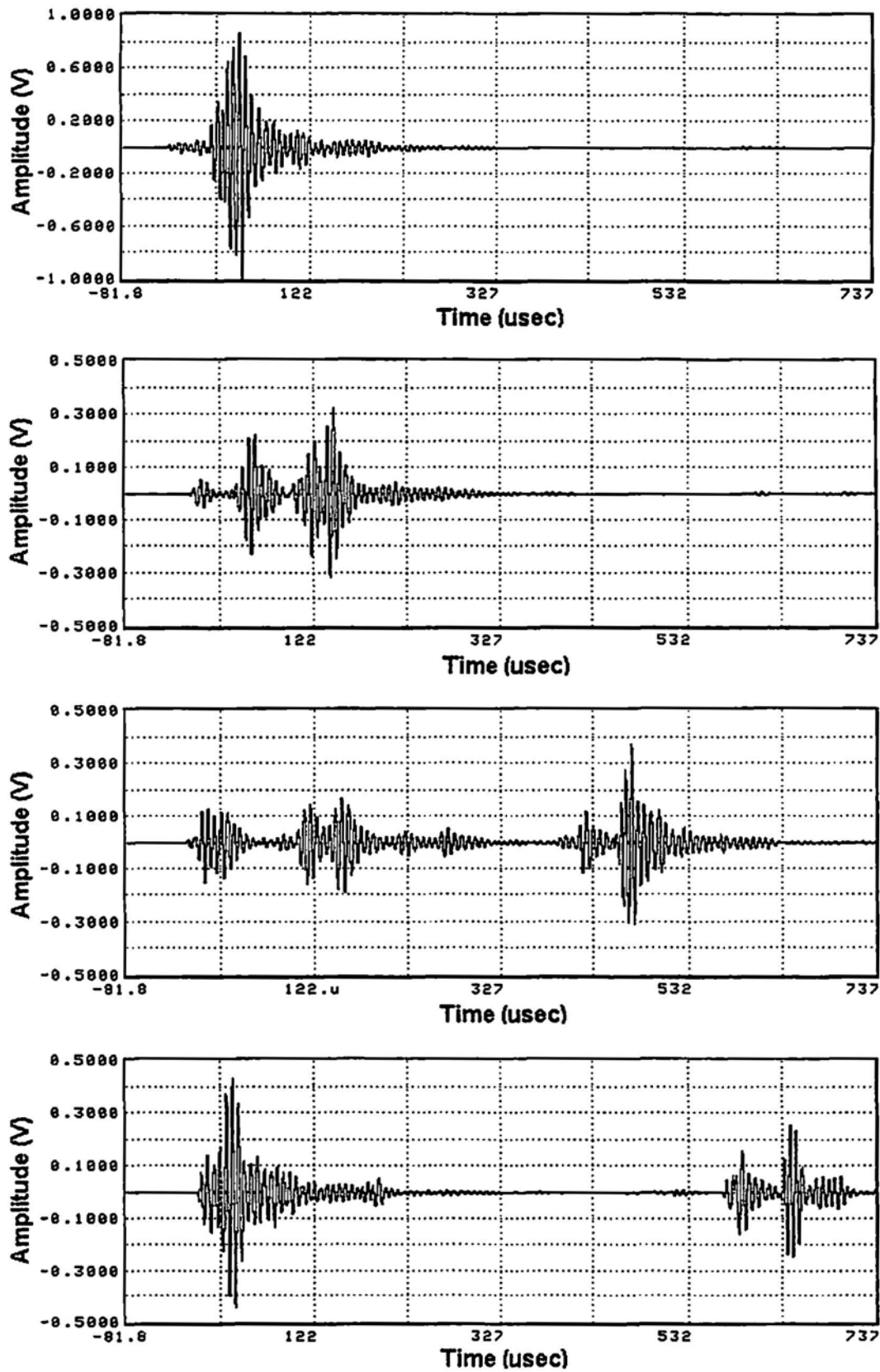


Fig. 6 AE signals from crack growth. (a) Classical crack growth AE (top). (b)-(d) Burst type of crack growth AE (1-3).

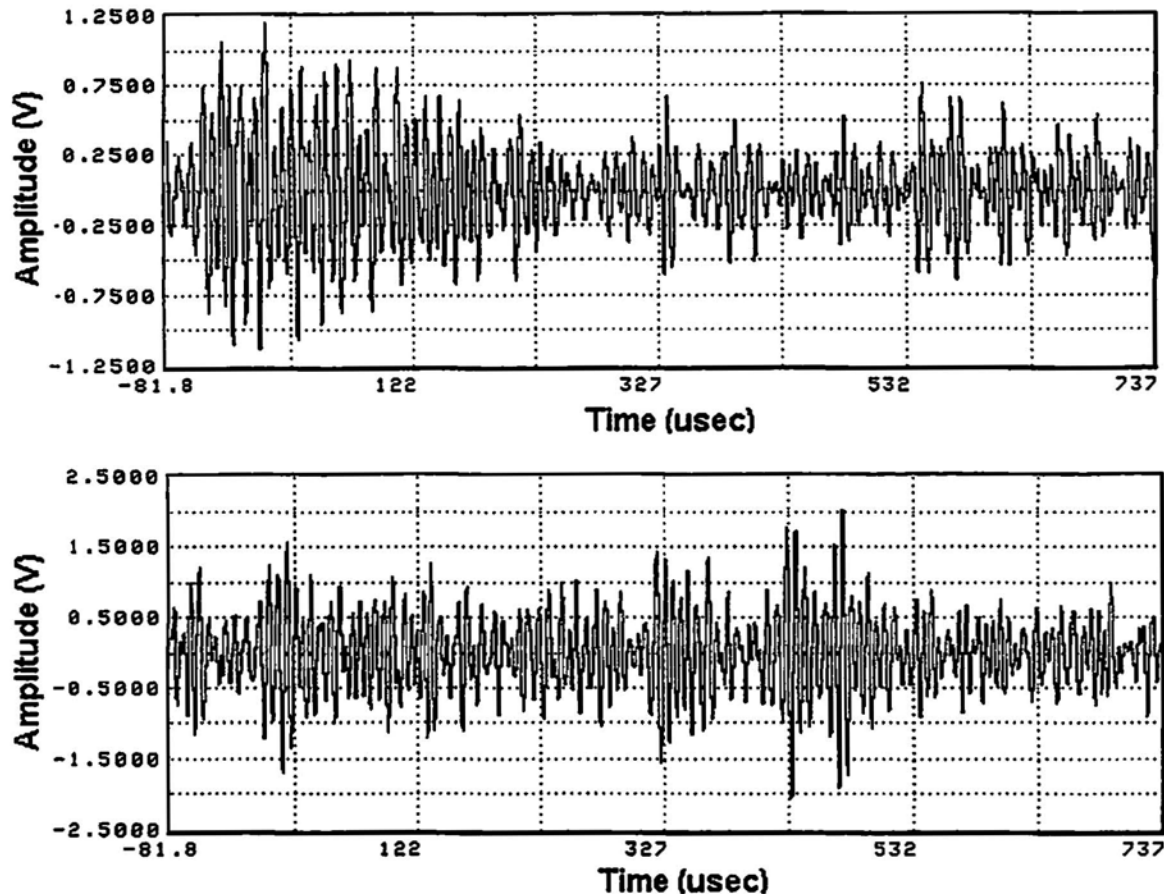


Fig. 7(a) and (b) Crack surface fretting AE (1) and (2).

The 16 patterns of class I can readily be identified as EMI signals due to their low measured values of energy and amplitude and, most significantly, their very high average frequency. Unlike other AE signals, EMI is not the result of excitation of the resonant transducer element via a mechanical coupling, but is the result of an induced current in the transducer-to-AE-system cables and is therefore not bounded by resonant behavior of the element, yielding measured values of average frequency, which cannot be attained by the narrow-band resonant transducers used in this experiment. This phenomenon also produces low amplitudes since the EMI signals may not be amplified by the integrated preamplifiers inside the AE sensors. However, due to the complexity of EMI signals as shown in Fig. 8, the measured values of rise time, counts, duration and counts-to-peak may not be small.

The 41 patterns of class III and 30 patterns of class IV can be identified as mainly crack surface fretting signals, due to their very high measured values of duration, energy, counts and amplitude. Whilst the measured values of rise time of this emission category may occupy a wide range as shown in Fig. 7(a) and (b), so may the measured values of counts-to-peak. An important phenomenon of this category of signal is that they are the result of excitation of the

resonant transducer element and thus the measured values of their average frequency may be bounded around the transducer resonance frequency (in this experiment, i.e., 150 kHz). Another important phenomenon is that the duration of this category of signal may be as long as the user predefined HDT. Although crack surface fretting signals are mainly contained in class III and IV, some overlap with rapid burst-type crack growth and/or intense EMI signals may also occur according to their waveforms as shown in Figs. 6 and 8, as these signals may produce much higher measured values of rise time, counts, energy, and duration than a single "classic" crack growth or a typical EMI signal.

Careful attention must be paid to the interpretation of the 56 patterns contained within class II. It is most likely that this class is primarily comprised of "classic" and "burst-type" crack growth AE, although some overlap with EMI may also occur. Further examination of the waveform feature data associated with their corresponding waveforms reveals that three subclasses of AE contained within class II and their typical waveform feature data characteristics are listed in Table 2.

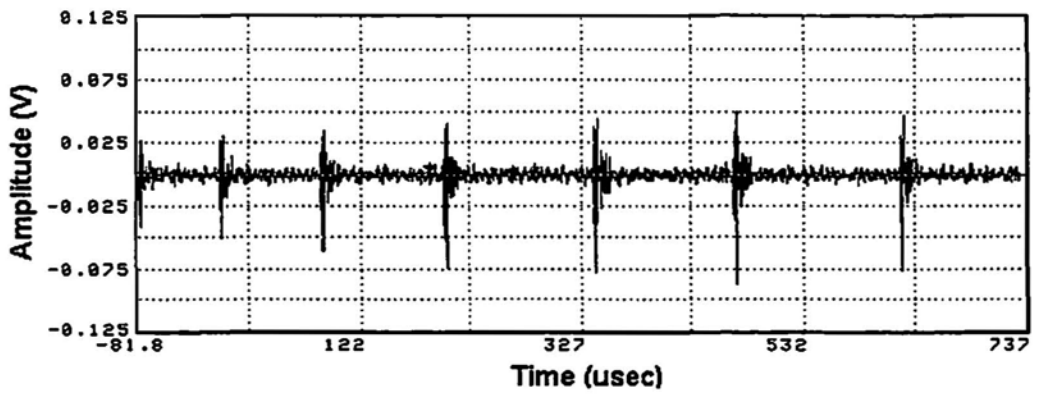
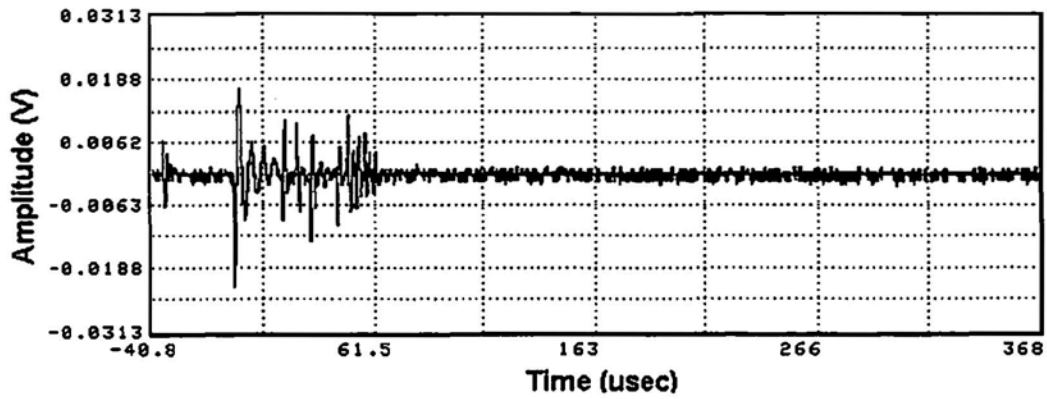
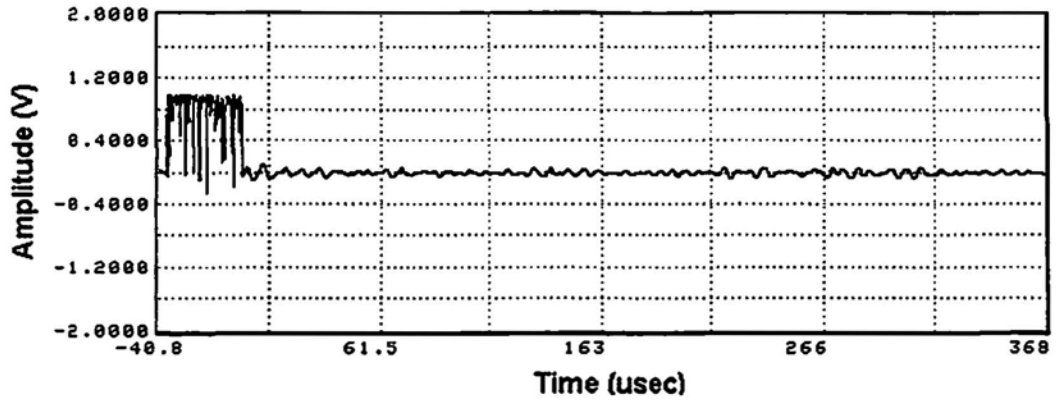
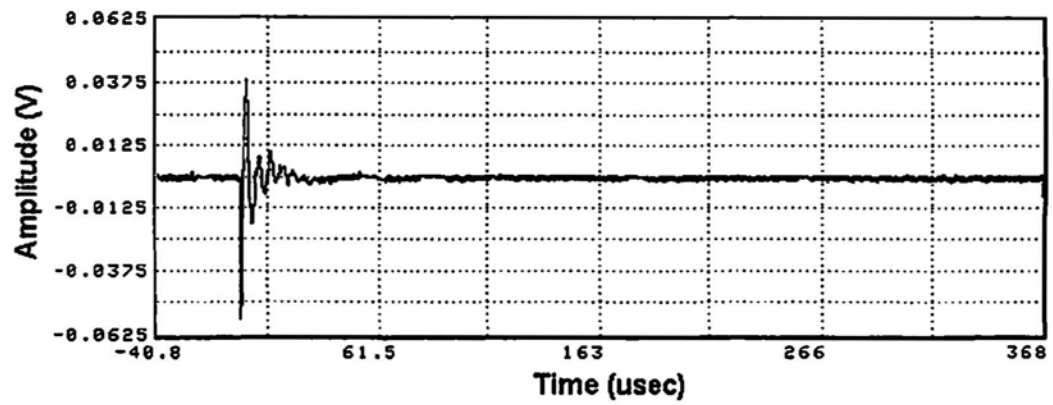


Fig. 8 EMI signals. (a) Typical EMI signal (top). (b) Rapid and intense EMI signal. (c) and (d) Rapid bursts of EMI (1) and (2).

Table 2 Typical characteristics of waveform feature data of the three subclasses in class II.

Patterns & Identity	RT (μ s)	CNTS	ENRY	DUR (μ s)	AMP (dB)	AVF (kHz)	CNTP
3 EMI	1	7	2	294	54	24	1
45 classic crack growth AE	5-84	1-32	1-42	12-276	52-80	80-167	1-13
8 burst-type crack growth AE	10-210	13-36	7-29	207-358	61-76	48-122	1-23

Table 3 Distribution of input patterns in each identified class.

Identity of input patterns	SONN identified classes				Total number
	I	II	III	IV	
EMI	16	3	0	2	21
Crack growth	0	53	3	2	58
Fretting	0	0	38	26	64

Obviously, due to the inherent disadvantages associated with waveform descriptor-based classification, some confusion of the number and identity of sources was unavoidable, although the SONN is able to give good value classification results. Table 3 summarizes the distribution of original 143 AE signals of known source identities in each SONN class identified, based on the waveform feature data in this classification experiment.

6. Conclusions

It is shown that difficulty exists in unambiguously identifying individual AE sources by consideration of waveform-descriptor feature values alone, unless considerable care is taken over AE waveform acquisition and feature extraction, which requires adequate knowledge of the behavior of AE sources in the specimen or structure under investigation. Absolute feature values are highly specific to a particular test configuration, AE source and specimen geometry, and this factor can seriously prejudice the validity of supervised classification procedures in arbitrary applications. However, if these considerations are duly addressed, significant potential for AE signal classification by the self-organization neural network (SONN) technique exists; for example, in assisting the practitioner in establishing the likely number and identity of AE sources present, and careful consideration of the relative properties of distinct classes identified by the SONN technique may provide a useful insight into the origin of acoustic emission in an arbitrary application.

Acknowledgements

The authors wish to express their gratitude to HEFCW for their financial support of this research and to the Royal Society for its support of the Royal Fellowship programme. Laboratory testing was performed in the Structural Engineering Laboratory, Cardiff School of Engineering, University of Wales Cardiff. The assistance of Dr. A.W. Davies and the technical staff of the divisions of Civil,

Structural and Mechanical Engineering is also gratefully acknowledged.

References

- A.A. Anastassopoulos and T.P. Philippidis (1995), "Clustering Methodology for the Evaluation of Acoustic Emission from Composites", *Journal of Acoustic Emission*, 13(1/2), 11-22.
- M.N. Bassim (1987), "Macroscopic Origins of Acoustic Emission", *Non-destructive Testing Handbook*, 2nd ed., Vol. 5, Acoustic Emission Testing, eds. R.K. Miller and P. McIntire, American Society for Non-destructive Testing, Columbus, OH, pp. 46-61.
- M.N. Bassim, S.S. Lawrence and C.D. Liu (1994), "Detection of the Onset of Fatigue Crack Growth in Rail Steels Using Acoustic Emission", *Engineering Fracture Mechanics*, 47(2), 207-214.
- C. Eberhart and R.W. Dobbins (1990), *Neural Network PC Tools*, Academic Press, London.
- Z. Gong, E.O. Nyborg and G. Oommen (1992), "Acoustic Emission Monitoring of Steel Railroad Bridges", *Materials Evaluation*, 50(7), 883-887.
- M.A. Hamstad and J.D. McColskey (1997), "Wideband and Narrowband Acoustic Emission Waveforms from Extraneous Source During Fatigue of Steel Samples", *Journal of Acoustic Emission*, 15(1-4), 1-18.
- D.O. Harris and H.L. Dunegan (1974), "Continuous Monitoring of Fatigue Crack Growth by Acoustic Emission Techniques", *Experimental Mechanics*, 14(2), 71-81.
- S. Keyvan and J. Nagaraj (1996), "Pattern Recognition of Acoustic Signatures Using ART2 - a Neural Network", *Journal of Acoustic Emission*, 14(2), 97-102.

S. Keyvan and R.G. Pickard (1997), "Feature Extraction of Metal Impact Acoustic Signals for Pattern Classification by Neural Network", *Journal of Acoustic Emission*, 15(1-4), 79-87.

T. Kinjo, H. Suzuki, N. Saito, M. Takemoto and K. Ono (1997), "Fracture-mode Classification Using Wavelet Transformed AE Signals from Composite", *Journal of Acoustic Emission*, 15(1-4), 19-32.

T. Kohonen (1989), *Self-organization and Associative Memory*, 3rd ed., Springer-Verlag, Berlin, New York.

T.M. Morton, S. Smith, and R.M. Harrington (1974), "Effect of Loading Variables on the Acoustic Emissions of Fatigue Crack Growth", *Experimental Mechanics*, 14(5), 208-213.

K. Ono (1997), "Recent Development in Acoustic Emission", *Journal of Acoustic Emission*, 15(1-4), S95-S102.

T.P. Philippidis, V.N. Nikolaidis and A.A. Anastassopoulos (1998), "Damage Characterisation of Carbon/Carbon Laminates Using Neural Network Techniques on AE Signals", *NDT&E International*, 31(5), 329-340.

A.A. Pollock and B. Smith (1972), "Stress-wave Emission Monitoring of a Military Bridge", *Nondestructive Testing International*, 5(6), 348-353.

A.C.E. Sinclair, D.C. Connors and C.L. Formby (1977), "Acoustic Emission Analysis During Fatigue Crack Growth in Steel", *Materials Science and Engineering*, 28(2), 263-273.

M. Sison, J.C. Duke, G. Clemens and M.G. Lozev (1996), "Acoustic Emission: a Tool for the Bridge Engineer", *Materials Evaluation*, 54(8), 888-900.

H. Suzuki, T. Kinjo, Y. Hayashi, M. Takemoto, K. Ono and Y. Hayashi (1996), "Wavelet Transform of Acoustic Emission Signals", *Journal of Acoustic Emission*, 14(2), 69-84.

V. Venkatesh and J.R. Houghton (1996), "Neural Network Approach to Acoustic Emission Source Location", *Journal of Acoustic Emission*, 14(2), 61-68.

D.J. Yoon, S.S. Lee, P. Park, S.H. Kim, S.H. Lee and, Y.J. Park (1997), "Acoustic Emission Monitoring of the Fatigue Crack Activity in Steel Bridge Members", *Journal of Acoustic Emission*, 15(1-4), S11-S18.

H. Yuki and K. Homma (1996), "Estimation of Acoustic Emission Source Waveform of Fracture Using a Neural Network", *NDT&E International*, 29(1), 21-25.

42nd AEWG Meeting

Source Location Studies on a Tank Car, Yajai Promboon, The University of Texas at Austin

The paper presents preliminary results from a study of source location methods for a steel tank car. Two types of artificial sources were used in the study; pencil lead breaks and bending of a steel bar welded to the tank. For the initial part of the study, wide band sensors were used to capture the waveform. Tests were performed on an empty tank car and then on the tank car filled with water. On an empty tank, source location based on the frequency at the group velocity yielded very promising results. On the full tank, source location is accomplished by using a low frequency signal. The paper also presents the algorithm used to triangulate the source called simplex optimization. Current work is focussing on use of a sensor with multiple resonant frequencies, and on source location for tanks under pressure. Results from a pressure test with air will be presented. Research continues on the more difficult problem of a liquid filled tank.

A New Method for Lamb-Wave Source Location of Impact on CFRP Plates.

Hirokazu Yamada, Yoshihiro Mizutani, Hideo Nishino, Mikiyo Takemoto, Aoyama Gakuin University and Kanji Ono, UCLA.

This study reports the development of a new source location method using Lamb waves of impact on carbon-fiber reinforced plastic (CFRP) plates. We monitored Lamb waves produced by pencil-lead breaks and steel-ball impacts using four resonant-type AE transducers mounted on 300-mm square corners within 500-mm-square plates and determined arrival time of 65 kHz Ao-Lamb waves, extracted by using a wavelet transform. Source location was first estimated into one of four quadrants by the arrival time differences of the Lamb waves. Next, the source location in the previously identified quadrant was determined by iteration. Here, the measured arrival-time differences were matched with those computed by moving a virtual source position in 0.5 mm steps. We developed an algorithm providing automatic determination of arrival times and coordinate computation. It takes 17 s for each source-location identification. Orientation dependence of Lamb waves for CFRPs are experimentally measured and included in the algorithm. Accuracy of the source location for a unidirectional-CFRP plate is less than 10 mm within the 300 x 300 mm square. The maximum error of 6.5 mm and the average error of 2.1 mm were obtained for a (0/45/-45)s CFRP plate.

PLENARY INVITED LECTURE

Quantitative Analysis of AE Source Parameters by SIGMA Procedure.

Masayasu Ohtsu and Mitsuhiro Shigeishi, Kumamoto University

Previously, the source characterization of AE was performed by the deconvolution analysis, which could provide information only on crack kinetics. Recently, it is realized that the moment tensor analysis of AE can provide quantitative information on kinematics of crack motion in materials. By applying SIGNIA procedure developed, AE sources are classified into tensile cracks and shear cracks. The direction of crack motion is derived from the eigenvectors of the moment tensor.

In the present study, to characterize AE sources further, a relation between the damage parameter in the damage mechanics and the moment tensor is investigated. Thus, a procedure to determine the damage parameter from the SIGMA-AE analysis is developed. In uniaxial compression tests of the plate specimens with a center slit, the damage evolution is estimated as the accumulation of the damage parameter for concrete and mortar materials. Further, the procedure leads to quantitative estimation of the crack volumes in the case that absolutely calibrated sensors are employed. As a result, the crack volumes are quantitatively estimated in concrete and mortar plates. From these results, it is found that both the damage parameter and crack volume of mortar are larger than those of concrete. It demonstrates the effect of crack arrest due to aggregate in the process of microfracturing in cementitious materials.

AEWG Business Meeting/Banquet

Wednesday, June 16, 1999

Martensitic Transformation Dynamics of Cu-Al-Ni Shape Memory Alloy Single Crystals by Acoustic Emission Methods. Kenichi Yoshida, S. Kihara, K. Sakamaki, Tokushima University

Cu-Al-Ni shape memory alloy exhibits a super-elasticity which shows perfect recovery of plastic deformation. The super-elasticity used in this paper results from a perfectly reversible martensitic transformation. The martensitic

Discussion of the Log-Normal Distribution of Amplitude in Acoustic Emission Signals

M. I. López Pumarega, R. Piotrkowski and J. E. Ruzzante

Abstract

In this paper, we study from a statistical point of view, the acoustic emission (AE) produced by deformation and crack propagation in steel samples from seamless tubes. The most convincing result was obtained by correlating the histogram of burst amplitudes with the log-normal distribution. This result is interpreted according to the Central Limit Theorem. It can be assumed that in the process of plastic flow and crack propagation, the incremental damage sustained between any two stage of the process is a random proportion of the total damage existing at the preceding stages. Because the measurable characteristic of the material, in this case the deformation arriving at the AE sensor, is the product of a large number of underlying causes, which are independent random variables, the Central Limit Theorem applies.

1. Introduction

The acoustic emission (AE) waves represent the propagation of elastic energy coming from different sources, such as deformation and crack propagation in materials, when they are submitted to stresses. The elastic waves are detected at the surface by means of piezoelectric transducers that transform the mechanical pulses into electric signals.

The electric signals are discrete packets, named bursts, immersed in a background of continuous noise. The bursts are asymmetric and are characterized by their amplitude (A), duration (D) and rise-time (R). Due to the complex nature of the whole phenomenon, the subject is usually treated statistically. Up to now, the property, for which better results have been obtained, is the amplitude. Nevertheless, different distributions have been employed by several authors; such as power law models, log-normal and Weibull distributions (Erlenkamper, 1979; Pollock, 1973, 1981; Ono et al., 1978).

Received 20 July 1998. M.I. López Pumarega (lopezpum@cnea.edu.ar) and J.E. Ruzzante are affiliated with Grupo Ondas Elásticas, U. A. ENDE, Comisión Nacional de Energy Atómica (CNEA), CAC, Av. Gral. Paz 1498, (1650) Pcia. de Buenos Aires, Argentina. R. Piotrkowski (piotrkow@cnea.edu.ar) is with Escuela de Ciencia y Tecnología, Universidad Nacional de General San Martín, Calle 91, No. 3391, (1652) Pcia. de Buenos Aires, Argentina.

Earlier, López Pumarega et al (1996) presented results concerning the analysis of AE signals coming from steel tubes. The log-normal distribution is shown to be adequate to describe the results. In the present paper, we continued the analysis of these signals and the results are explained according to the Central Limit Theorem (CLT).

2. Procedures

2.1 Materials and Methods

Test samples were rings obtained by transversal cut from seamless steel tubes, with 14 cm outside diameter, 1 cm thickness and 2 cm width. A section with a chord length of 6 cm was eliminated from each ring in order to introduce it in a device, which, by opening it, introduced a distribution of stresses. Force was manually exerted through a screw. Figure 1 shows a photograph of the experimental setup and Fig. 2 shows the block diagram of the detection system.

A total of 11 samples were employed, 10 of them corresponding to the same steel (type 1) in Table 1, while the composition of the remaining one (type 2), was slightly different and its thickness was greater so as to be able to bear a fatigue-produced initial crack.

Table 1 Metallurgical and geometrical characteristics of type 1 samples.

Composition (in wt. %): C 0.16, P 0.042, S 0.001, Si 0.26,
Mn 0.67, V<.05, Nb<0.03, Ti<0.05
Hardness: 75 Rockwell B scale
Grain size: 15 μ m
Thickness: 1 cm; Width: 2 cm; Outside Diameter: 14 cm

Three AE transducers were attached to each sample. Two of them with a resonance frequency of 200 kHz, acted as guard sensors to eliminate the noise produced at the holding points. The third one, put on the top of the ring, where the maximum degree of deformation occurred, was a wideband (300-800 kHz) sensor. A wideband sensor was selected in order to perform the frequency analysis of the signals in future work. The signals were pre-amplified and then amplified and processed with the AE AEDOS system. The force to open the ring was applied by hand and was measured with a load cell. The end opening of the ring was

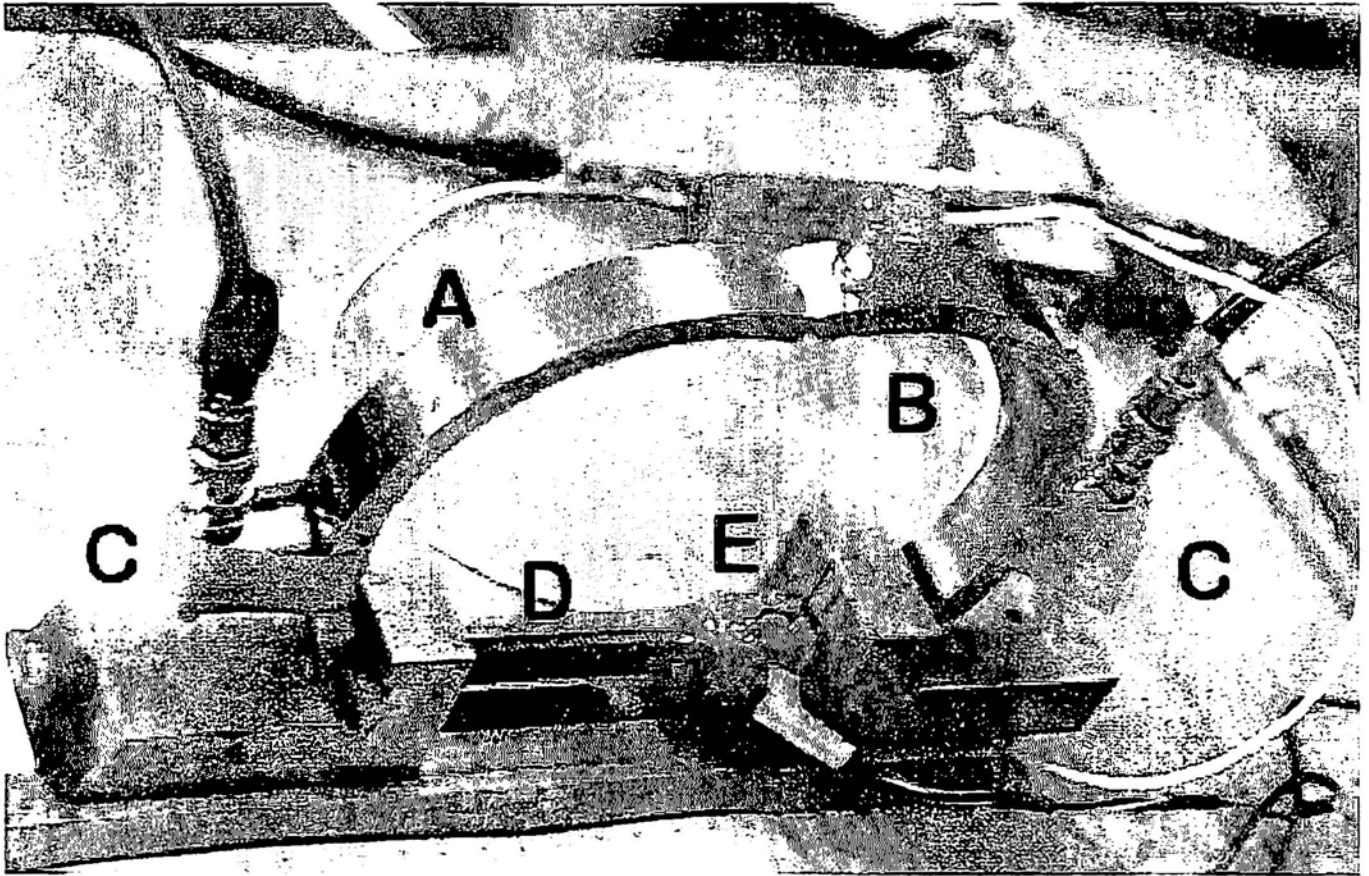


Fig. 1 Experimental setup. A: sample, B: wideband sensor, C: guard sensors, D: screw, E: load cell.

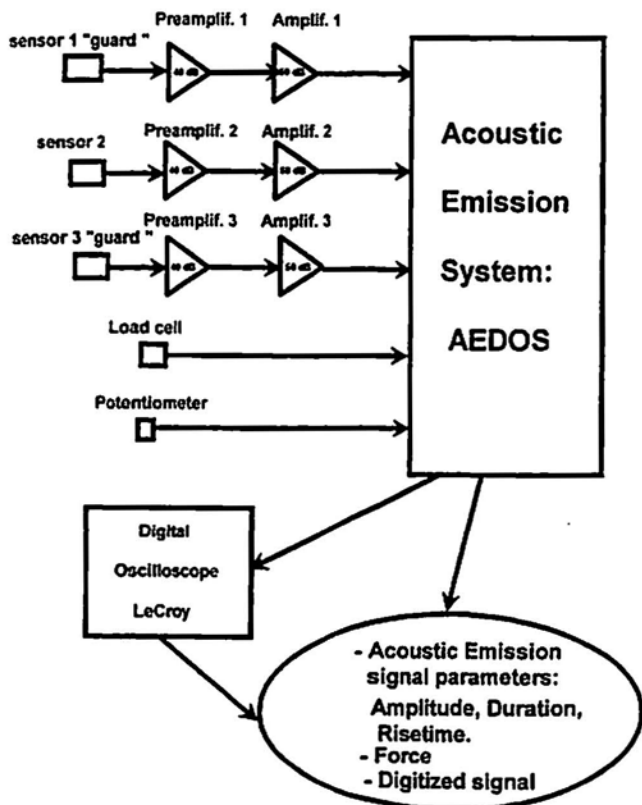


Fig. 2 Block diagram of the detection system.

Table 2 Characteristics of experiments

Name	Material	Notch	Thinning	Oxide	Initial crack	Experiment type
CEL8	1	Yes	-	-	-	β
CEL9	1	Yes	-	-	-	β
CEL11	1	Yes	-	-	-	β
CEL10	1	Yes	-	Yes	-	β_1
CEL12	1	-	Yes	-	-	α
CEL13	1	-	Yes	-	-	α
CEL14	1	-	Yes	-	-	α
CEL15	1	-	Yes	Yes	-	α_1
CEL16	1	-	Yes	Yes	-	α_1
CEL17	1	-	Yes	Yes	-	α_1
AROF1	2	Yes	-	-	Yes	γ

measured with a potentiometer. Both the force and the opening were recorded by the AEDOS system.

Four different types of rings were prepared from the 10 type-1 samples. Some of them had a triangular inside notch at the top in order to promote crack propagation; others were thinned out in the same region in order to favor de-

formation. The tubes were oxidized in their natural state. Some samples were tested with their oxide layer and in others, this layer was eliminated. Table 2 shows the characteristics of experiments.

In the CEL12, CEL13 and CEL14 experiments, (α -type), due to the previous thinning, the fundamental process induced by stresses is deformation. In the CEL15, CEL16 and CEL17 experiments (α_1 -type) added to deformation is the oxide layer break-down. In the CEL8, CEL9, CEL11 experiments (β -type) and AROF1, (γ -type), due to the prior notch and initial crack, the crack propagation process is expected to play the fundamental role. In the CEL10 (β_1 -type) experiment the oxide breakdown is added.

2.2 Experimental Results

The mean values of the parameters A, D and R together with the total number of AE events (N) for each experiment were obtained. The results are summarized in Table 3, which shows that for the oxidized samples (α_1 -, β_1 -type) both the number of bursts and the mean value of the amplitude (A) take high values and those of rise-time (R) take low values. The mean D and R values are very different for the α - and β -type experiments. For this reason, they can be used to identify the events in a general experiment.

Table 3 Typical values of the N, A, D and R parameters.

Type	α	α_1	β	β_1	γ
N	21-27	141-332	17-65	214	64
A (mV)	970-1265	2425-3390	703-1273	1629	1800
D (μ s)	21-143	203-266	229-376	102	775
R (μ s)	15-35	16-23	59-85	19	258

2.3 Statistical Analysis of Signals

Statistical studies were performed on the signal parameters and the total number of events for each experiment. With this aim, the distribution function, which better fits the histograms, was selected. Until now, the more convincing results refer to the amplitudes data. As the histograms are asymmetric, the exponential, Gamma, Chi-squared, Weibull and log-normal distributions were compared. Assuming a significance level of 0.05, and using Pearson Chi-square and Kolmogoroff goodness-of-fit tests,

log-normal distributions could not be rejected; besides, looking at the histograms themselves, with log-normal distribution we obtained the best fits. In Figs. 3-5, three examples of fits for both Weibull and log-normal distributions are shown; the figures themselves are self explanatory. This occurred for all the experiments that are in Table 2, which means that the involved phenomena share a common essential property.

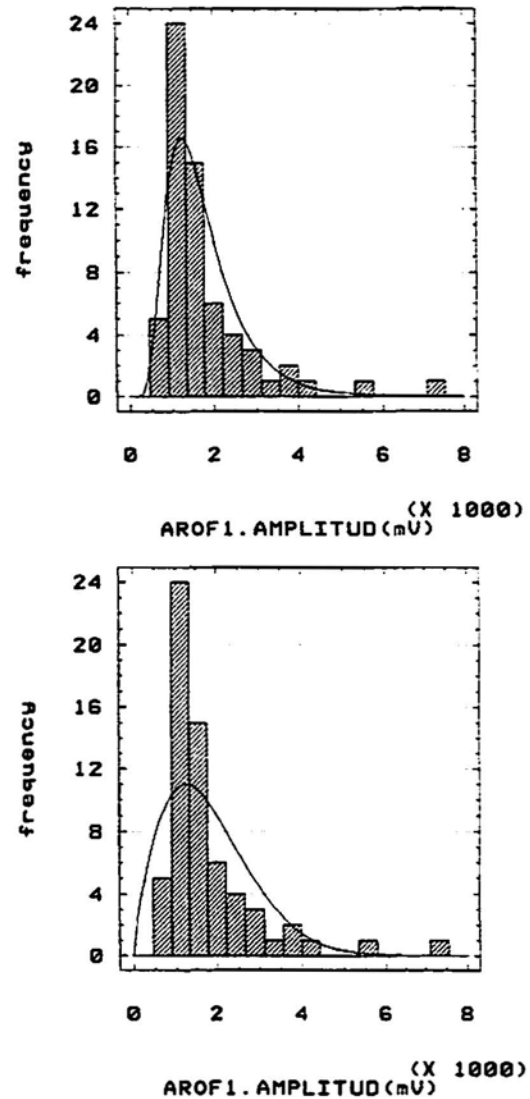
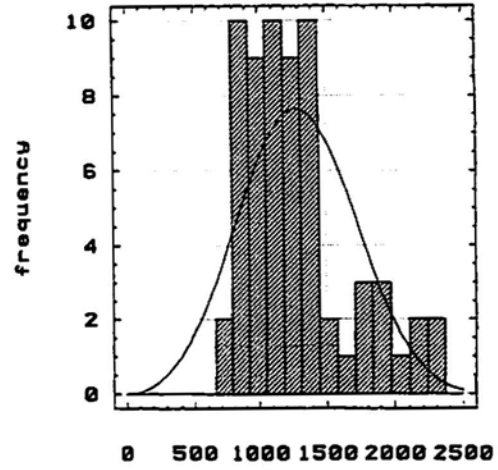
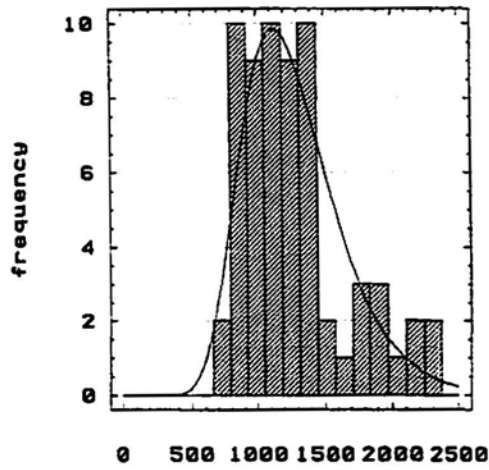


Fig. 3 Comparison of the amplitude histograms with log-normal (above) and Weibull (below) distribution for AROF1 sample.

2.4 Influence of the Detection System

A burst is the transducer response $r(t)$ to the mechanical excitation $s(t)$, that arrives coming from different points, where accumulated elastic deformation energy was produced. In the following, we analyze the influence of the detection system on the output signal in two extreme cases with (a) resonant transducer, and (b) wideband transducer. In both cases we assume that the amplification stage behaves linearly.



CEL11. AMPLITUD (mV)

CEL11. AMPLITUD (mV)

Fig. 4 Comparison of the amplitude histograms with log-normal (left) and Weibull (right) distribution for CEL11 sample.

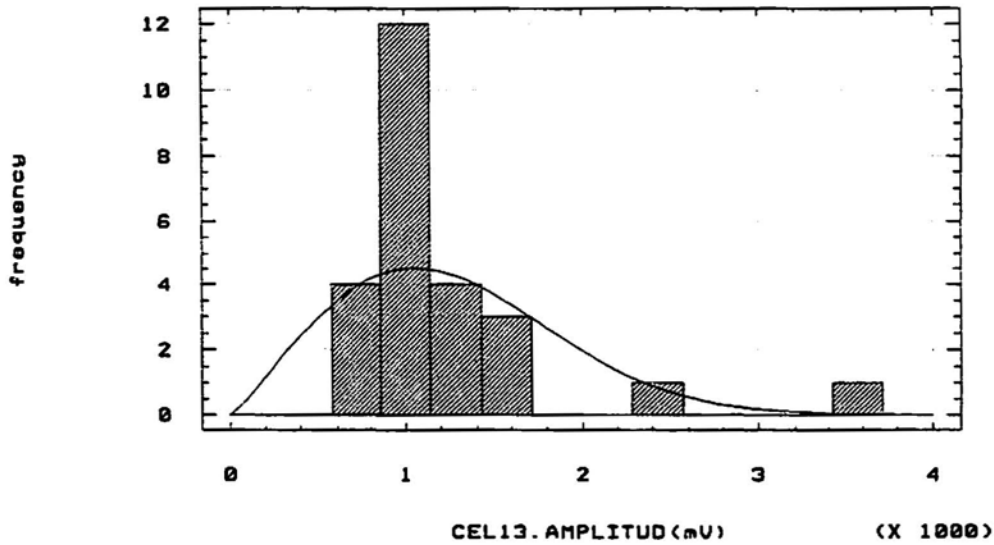
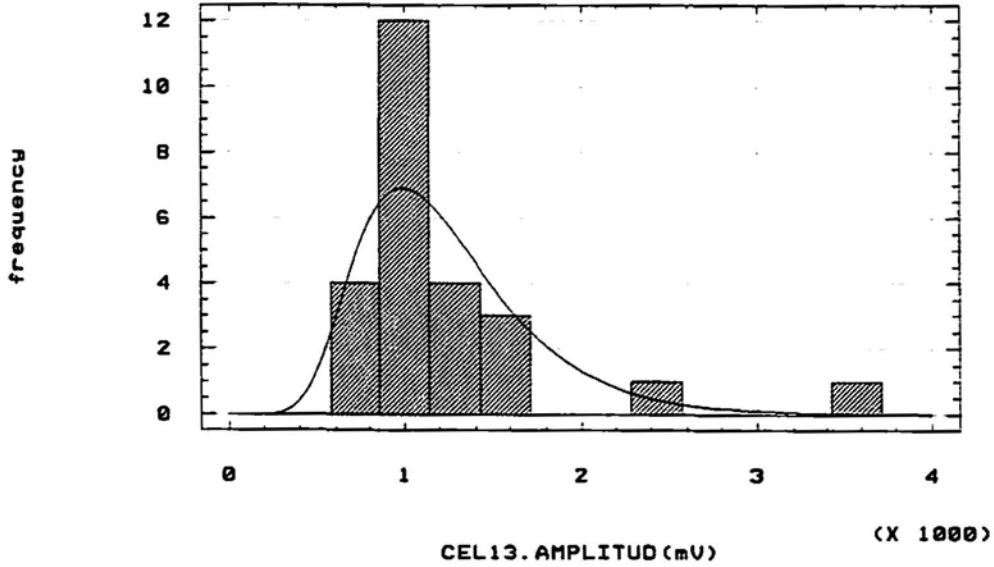


Fig. 5 Comparison of the amplitude histograms with log-normal (left) and Weibull (right) distribution for CEL13 sample.

Following Ono et al. (1978), we suppose that rectangular pulses with amplitude S and duration T reach the sensor:

$$s(t) = S[u(t) - u(t-T)] \quad (1)$$

where $u(t)$ is the unit step function. The transducer response to this stimulus, $r(t)$, is the convolution of $s(t)$ with the transducer response $v(t)$ to a mechanical impulse $\delta(t)$,

$$r(t) = \int_{-\infty}^t s(\lambda) v(t-\lambda) d\lambda = s(t) * v(t) \quad (2)$$

For a resonant damped transducer with resonant frequency ω_0 and damping decay constant β (case (a)), Ono et al. (1978) found that:

$$v(t) = \exp(-\beta t) \exp(i \omega_0 t) u(t) \quad (3)$$

from which we obtain for $t \geq T$ the solution:

$$r(t) = \frac{S (e^{\beta T} - 1) e^{-\beta t} \exp(i \omega_0 t)}{\beta - i \omega_0} \quad (4)$$

When $r(t)$ is expanded in Taylor series for $t = T$, and $\beta T \ll 1$, the result is that the maximum $r(t)$ value is proportional to S , putting thus in evidence the proportionality between the amplitude of the transducer response A , and the amplitude of the arrived mechanical excitation S .

For a wide band transducer (case (b)), considered as a low-pass filter with cut-off frequency ω_c , it holds:

$$H(\omega) = \begin{cases} e^{-i\omega t_0} & |\omega| < \omega_c \\ 0 & |\omega| > \omega_c \end{cases} \quad (5)$$

where $H(\omega)$ is the transducer transference function and t_0 is an arbitrary initial value.

From (2)

$$F[r(t)] = F[v(t)] \times F[s(t)] = H(\omega) \times F[s(t)] \quad (6)$$

where F means Fourier Transform. So we obtain

$$F[r(t)] = H(\omega) \times S \times \int_0^T \exp(-i\omega t) dt = g(\omega) \quad (7)$$

and

$$r(t) = F^{-1}[g(\omega)]. \quad (8)$$

To solve (8) it is necessary to expand the exponential. Assuming for simplicity, $t_0 = 0$, and $(t - T) \ll 1/\omega_c$, we obtain

$$r(t) = S \omega_c T / \pi. \quad (9)$$

Therefore, the amplitude of the transducer response is again proportional to the amplitude of the mechanical excitation S .

These are very important results. The proportionality between both amplitudes, S (mechanical impulse) and A (AE signal Amplitude), permits to infer that the statistical distribution of both parameters is the same.

In another work of our group, Pérez et al. (1997) presented a mathematical model to simulate the AE events. The detection system was adequately represented by a fourth-order differential equation. If impulses enter the system, burst signals emerge, characterized by A , D , and R parameters, where A is proportional to the input amplitude. The output signals for impulse inputs, with amplitude log-normally distributed, were burst type with the same amplitudes distribution. Moreover, the output signals resulted similar to the experimental events, including D and R parameters. This shows that D and R parameters are strongly influenced by the detection system, and this is not the case for the A parameter, for which a linear relation holds. In the actual case, the input signals are not impulses; nevertheless the referred results show the strong and complicated influence of the detection system on the D and R parameters, for which proportionality between input and output values cannot be postulated.

In the following, the proportionality between the amplitudes of the input mechanical impulse and output electric signals (AE) is assumed.

2.5 Log-normal Distribution

We apply to our case the analysis performed by Cramer (1961) to decide the conditions leading to the fact that a given random function can be described by the log-normal distribution.

If the causes that originate a given amplitude of deformation, s , inside the material do not act by simple addition but are sequentially connected, they would give rise to an asymmetric distribution.

Let us suppose that there are n stress values (ξ_1, \dots, ξ_n) that act in the order indicated by their sub-indexes. These stresses are then considered as independent random variables. We designate as s_i the total deformation produced by the set of stresses (ξ_1, \dots, ξ_i). It can be supposed that the additional deformation produced by the following stress, ξ_{i+1} , is proportional to both ξ_{i+1} and to a certain function of the deformation reached until the prior step, $h(s_i)$:

$$s_{i+1} = s_i + \xi_{i+1} h(s_i) \quad (10)$$

from which

$$\xi_1 + \dots + \xi_n = \sum_{i=0}^{n-1} \frac{s_{i+1} - s_i}{h(s_i)} \quad (11)$$

If each stress gives place to a minute contribution of the total deformation, the transition to continuous calculation can be performed and the sum is replaced by an integral.

$$\xi_1 + \dots + \xi_n = \int_{s_0}^s \frac{dt}{h(t)} = I(s) \quad (12)$$

where $s = s_n$ represents the total deformation.

As by hypothesis ξ_1, \dots, ξ_n are independent variables and n is a large number, it can be deduced that the function $I(s)$ of the random variable s , which appears in the second member of (14) follows a normal distribution. If the simplest case, $h(t) = t$ is considered, it holds:

$$\xi_1 + \dots + \xi_n = \int_{s_0}^s \frac{dt}{t} = \ln s - \ln s_0 \quad (13)$$

In order to gain generality we consider $\ln(s - a)$ instead of $\ln(s)$, "a" being the initial deformation value. We also consider $s_0 = 1$, which means that deformations are measured in s_0 units. From (15), it is $\ln(s - a)$, which follows a normal distribution, with m and σ parameters, and the result is:

$$g_{m, \sigma}(\ln(s - a)) = \frac{1}{\sigma \sqrt{2\pi}} \exp\left(-\frac{(\ln(s - a) - m)^2}{2\sigma^2}\right) \quad (14)$$

which is valid for $s > a$, while $g = 0$ for $s < a$. It then holds that the variable s follows a log-normal distribution f :

$$f_{m, \sigma}(s) = \frac{1}{\sigma(s - a)\sqrt{2\pi}} \exp\left(-\frac{(\ln(s - a) - m)^2}{2\sigma^2}\right) \quad (15)$$

As stated previously, the "a" parameter represents the shift of the curve along the abscissa; that is to say, the initial value of deformation. The parameter m represents the arithmetic mean of the variable $\ln(s - a)$. So, from the last value, the geometric mean value of $(s - a)$ can be obtained.

As a conclusion, the distribution of amplitudes of the deformation pulses that arrive at the detection system is log-normal, and this result is according to the CLT.

3. Discussion and Conclusions

The mean values of the parameters A, D and R seem to act as indicators of the main source of AE signal; that is to say, if they are originated in crack propagation, deformation or layer breakdown, as can be deduced from Table 3. This is an encouraging result and it induces the performing of a larger number of future experiments. In particular, the difference between the mean values of the parameters D and R for the experiments α and β is outstanding. The N and A values are very high for the oxidized samples. All these facts deserve an adequate theoretical explanation.

A good fit was obtained between the amplitudes histograms and the log-normal distribution for all our experiments in this work. This result could be explained accord-

ing to the CLT. The underlying physical meaning is that the detected AE signal is the complex consequence of a great number of random independent sources, to which individual effects are linked.

There are several antecedents of using asymmetric distribution functions, specially log-normal and Weibull distributions, in materials science.

Stranadel and Jonsta (1994) found Weibull distribution to represent the carbide size distribution in spheroidized steels. Ono et al. (1978) found that the distribution of AE amplitudes in HSLA steels could be described by the Weibull distribution, and assigned the AE source to the decohesion of a great number of MnS inclusions present in these steels, sizes of which are Weibull distributed. In that case, samples were round tensile specimen submitted to tensile tests, and they had near twice nominal Mn composition compared with our samples. The effect of short-transverse tensile stress orientation made the decohesion of the inclusions the most important source of AE compared with deformation.

Satora (1978) showed that carbide size distributions in steels fit the log-normal distribution. The log-normal function is frequently used to describe the distribution of grain sizes in polycrystals. While the normal distribution occurs as a result of the additive effect of random events, the log-normal distribution results from effects that are multiplicative. This has been used by Vaz and Fortes (1988) as a justification for the applicability of the log-normal function to describe the sizes of recrystallized grains, which nucleate at random and grow at a rate that depends on their size. Bury (1975) stated that the incremental damage produced between any two stages of plastic flow or crack propagation, is a random proportion of the total damage existing at the preceding stage, and the magnitude of the relevant observable failure criterion (percentage elongation, rupture strength, etc.) is then log-normally distributed. Since damage processes are irreversible, their states are functions of time. It follows that the statistical models of material properties should be based on a theory of stochastic processes in time and space relating external conditions to atomic and molecular changes at various locations in the solid.

Summarizing, it is possible to assume that only two important mechanisms exist as sources of AE signals: creation and propagation of dislocations, and creation of new surfaces by cracks or inclusions decohesion. Plastic flow and crack propagation essentially constitute irreversible damage processes. It can be assumed that damage is a multiplicative process; that is, the incremental damage sustained between any two stages of the process is a random proportion of the total damage existing at the preceding stages.

If we suppose that the measurable characteristic of a material is the result of causes that cannot be readily measured themselves, and if:

- i) the measurable characteristic is a multiplicative effect of underlying causes,
- ii) the causes are independent random variables, and
- iii) there is a large number of causes,

then the Central Limit Theorem (CLT) is applicable.

In our case, the log-normal distribution was adequate to describe the total number of experiments. This could be because the phenomena of dislocation movements and crack creation and propagation present in different proportion in all experiments have the same behavior from the statistical point of view.

Acknowledgements

The authors would like to record their appreciation of the very helpful discussions with Dr. Kanji Ono during his visit to their Laboratory.

References

K.V. Bury (1975), *Statistical Models in Applied Science*, John Wiley & Sons, New York, pp. 295-591.

S. Erlenkamper (1979), "Time and Amplitude of Acoustic Emission Signals in Fracture Mechanism Experiments", *Acoustic Emission*, Proc. Deutsche Gessellschaft für Metallkunde eV, pp. 165-188.

M.I. López Pumarega and J.E. Ruzzante (1996), "Acoustic Emission Signal Analysis from Steel Tubes", *Proc. 14th World Conference on Non-Destructive Testing (14th WCNDT)*, Vol. 4, pp. 2493-2496, New Delhi, India, (December 1996).

K. Ono, R. Landy and C. Ouchi (1978), "On the Amplitude Distribution of Burst Emission Due to MnS Inclusions in HSLA Steels", *Proc. The Fourth AE Symposium*, High Pressure Institute of Japan, Tokyo, pp. 4-33/4-45.

L.V. Perez, M. Armeite, M.I. López Pumarega and J.E. Ruzzante (1997), "Modelo Matematico para la Simulacion de Eventos de Emision Acostica", *Actas Congreso Regional de Ensayos No Destructivos, CORENDE*, pp. 299-303, Mendoza, Argentina, 27-30 Oct.

A.A. Pollock (1973), "Acoustic emission amplitudes", *Non-destructive Testing*, October, pp. 264-269.

A.A. Pollock (1981), "Acoustic Emission Amplitude Distributions", *International Advances in Non-Destructive Testing*, 7, 215-239.

K. Satora (1988), "Size distribution and carbides dispersion in bearing steel", *Kutnik (Katowice)*, 55(11-12), 319-321.

B. Stranadel and Z. Jonsta (1994), "Distribution of dimple sizes of the fracture surface of spheroidized steel in the transition region", *Eng. Fract. Mech.*, 48(6), 863-871.

M. Vaz and M.A. Fortes (1988), "Grain Size Distribution: The Log-Normal and the Gamma Distribution Functions", *Scripta Metallurgica*, 22, 35-40.

42nd AEWG Meeting

transformation used is from D03 structure to 18R transformation which can be observed in-situ by an optical microscope during tensile deformation at room temperature. Therefore, the dynamics of martensite plate such as the nucleation and the growth was examined in detail. Acoustic emission behaviors during the stress-induced martensitic transformation have been investigated using two types of specimens of Cu-Al-Ni shape memory alloy single crystal ([100](001) crystallographic orientation), each of which have different stress concentration coefficients, K_t , 1.01 in large round shaped notches and 2.65 in rectangular notches. The difference of dynamical martensitic transformation behavior has been compared with that of acoustic emission behavior using these specimens. Small martensites occur far before yielding near the notched bottom of the latter specimen. The generation of these martensites which consist of two or three-kinds of habit planes has been considered as the sources of lower amplitude, shorter rise time and shorter duration time acoustic emission. On the other hand, sporadic martensites occur near yielding near the bottom of the former specimen. The acoustic emission activity also is lower and more sporadic. As a result, it is made clear that the acoustic emission event rate and the amplitude distribution are associated with the nucleation and the growth of martensite plate during loading or the disappearance and the shrinkage of them during unloading. After nucleation at the center of the specimens, the martensite plates grow to three directions, that is, length, width and thickness directions. Comparatively higher amplitude acoustic emission occurs during growing to the length and the thickness directions. When the coalescence of the martensite plates and the growth passing through the specimen thickness occur, we can observe the highest amplitude acoustic emission. Otherwise, it was made clear that acoustic emission total event counts generated during martensitic transformation did not depend on the specimen volume, sequential change of the acoustic emission waveforms during deformation was different in two types of specimens because of difference of these martensite plate shapes, and the martensitic transformation rate obtained by acoustic emission waveform analysis increased with increase of fatigue damages.

Acoustic Emission Monitoring of Noisy Materials.

Timothy J. Fowler, The University of Texas at Austin

Composites, concrete, some aged metals, and carbon are among a group of noisy materials that give copious emission on initial loading. The pattern of emission is unpredictable. Sometimes it occurs as bursts, with intervening periods of low emission, other times it is continuous. Emission may start early in the load cycle, reach a peak rate, and then decrease at higher loads. Other times the rate of emission will increase with increasing load. The large amount of noise on first loading makes it difficult to conduct meaningful acoustic emission tests on new equipment and structures. In addition, monitoring the first loading may create the misleading impression that the structure is defective, when it is not.

The problem caused by the large quantity of emission on first loading is well recognized. Most of the standard test procedures specify less stringent evaluation criteria for emission from first loading than for emission from subsequent loadings. Some test procedures, such as the American Society of Mechanical Engineers Code for fiber reinforced plastic (FRP) pressure vessels, allow data from the first loading to be disregarded. Other procedures, such as the American Society for Nondestructive Testing Recommended Practice for balsa core FRP highway tankers, compare emission from multiple loadings.

A large quantity of emission during initial loading is not necessarily bad. Rather it is a consequence of the internal structure of the material. The presentation will discuss the problem of noisy materials, the source of this noise, and various approaches for dealing with it. Data from recent experimental work will be used to illustrate some of the evaluation techniques used to interpret emission from noisy materials.

Acoustic Emission Testing of Hoist Brake Components at the Waste Isolation Pilot Project.

Alan Beattie, PAC

The Waste Isolation Pilot Plant (WIPP) was developed to store low level radioactive waste in chambers carved out of rock salt. The storage area is some 2000 ft. below the floor of the desert in south eastern New Mexico near the town of Carlsbad.. Three separate hoists are operated at the site to convey cargo and passengers to and from the storage area. Safety considerations dictate that two of the hoists be operational at all times. These hoists are of different sizes with passenger capacities ranging from four to over sixty persons. The two smaller hoist systems are quite old, the middle sized one having been built around 1925. All hoists have emergency brakes on the cable drums to stop the cages in the event of system failures. The emergency braking systems on the two smaller hoists have had their components tested with AE for the last six years. These tests are novel in that the actual testing time is approximately one second. The rods driving the emergency brakes are instrumented with AE sensors and the cage is

Unsupervised Pattern Recognition Techniques for the Prediction of Composite Failure

T. P. Philippidis, V. N. Nikolaidis and J. G. Kolaxis

Abstract

An unsupervised pattern recognition procedure is presented for the discrimination of acoustic emission (AE) signals from glass-fiber/polyester (GRP) coupons stressed in tension to failure. The laminated composites consist of unidirectional and bidirectional stitched glass fabrics stacked at various sequences. The purpose of the analysis is to identify AE from specific layers in a laminate and to relate clusters of similar signals to characteristic load stages, thus enabling failure prediction of laminates of any stacking sequence. The multivariate unsupervised classification method presented in this work, based mainly on artificial neural system (ANS) algorithms, achieves classifications that can be used as a means to predict coupon failure by performing clustering on the union of several AE data sets produced in different experiments and using principal component projection. Class size ratios, of selected classifications, are used to create criteria linked to coupon failure and the schema is stabilized via a simple supervised classifier to apply the criteria on unknown coupon AE data.

1. Introduction

For practical applications of AE monitoring where there is no *a priori* knowledge of signal characteristics and simulation of AE generating mechanisms is difficult, e.g. failure modes of composite materials, unsupervised pattern recognition (UPR) techniques (Anastassopoulos et al., 1995) were introduced to assist in discriminating signals from various different sources. In a series of projects, UPR procedures were used to successfully identify signals emitted from different damage mechanisms of various composite systems based either to conventional PR algorithms (Anastassopoulos et al., 1996; Anastassopoulos et al., 1998a, 1998b) or to artificial neural systems (ANS), (Philippidis et al., 1998). The method was successfully applied to material coupons and structures as well.

Typical primary composite structures made of glass-fiber reinforced polyester matrix (GRP) composites consist of a number of basic building layers, which are stacked in laminates of varying thickness and content. One of the

problems one has to deal with in an eventual application of acoustic emission (AE) monitoring on such a structure is the identification of AE signals emitted from various sources, i.e. damage modes exhibited by different layers. Furthermore, it is of great practical importance to correlate clusters of identified similar signals to specific load stages, or life fractions for fatigue loading, thus enabling failure prediction of the structural component.

The materials investigated in this study consist of GRP constructions typical of wind-turbine rotor blades. More specifically, two basic building layers are used; a unidirectional (UD) and a bidirectional (BD) layer stitched glass fabric consisting of an equal proportion of fibers oriented at $\pm 45^\circ$. The two basic layers are laminated in two different stacking sequences. A number of tensile tests is performed on coupons made either of UD or BD layers and, based on AE data processing results from these tests, identification of signals emitted during loading of multidirectional (MD) laminates made of the aforementioned layers is attempted.

An unsupervised ANS scheme similar to the Learning Vector Quantizer (LVQ)-based methodology used successfully in carbon/carbon (C/C) composite coupon AE data (Philippidis et al., 1998), is applied on AE data recorded during experiments of GRP coupons under tension. Four groups of GRP specimens are considered, varying on fiber lay-up specifications.

While recorded under similar experimental constraints, specific GRP AE differs from C/C AE in several ways. Even at low sensitivity settings, the GRP coupons produce a much larger number of AE records. Typical data sets contain an average of 11250 AE records, up to the maximum load reached, for each MD and BD coupon, 25030 for each UD coupon, and 17630 for MD coupons of different stacking sequence (MDN). Being much larger than the average 3670 records recorded per C/C coupon experiment, the data-set sizes themselves call for a different classification approach. Furthermore, unlike C/C AE where extreme-valued records could be used to predict failure, in GRP experiments a significant number of records with high AE signal characteristics consistently appear during all load stages.

The original method of performing classification on AE data from each experiment separately, (Anastassopou

Received 15 September 1998. The authors are affiliated with Mechanical & Aeronautics Engineering Dept., University of Patras, P.O. Box 1401, Patras 265 00, Greece. (philippidis@tech.mech.upatras.gr)

los et al., 1995), handicaps the results in respect to their generalization power, since the produced classes are bound to be unique for the experiment. Classes of particular interest need to appear in all classifications; otherwise, the information provided by the class properties cannot be used in a generalized remaining-life prediction schema. Being affected by singularities in each data set, such as outliers or different number of "natural" clusters, similar classes within different classifications are difficult to identify, methods such as the Rand statistic (Rand, 1971) are used, if they exist at all.

The above constraints indicate that a different approach needs to be taken in order to achieve classifications of any explorative value on GRP AE data, i.e. classifications that can be used as a means to predict failure. The methodology discussed here involves clustering performed on the union of several AE data sets (produced in different experiments) using principal component projection. Questions about the use of mathematical clustering evaluation criteria for selecting the best classification amongst several are raised and an alternative approach based on amplitude distributions is suggested. With the number of natural clusters in the data being unknown, the clustering algorithm needs to be applied for a different number of requested classes, and thus classification selection is of major importance in unsupervised AE data exploration. Based on selected classifications, class-size ratio criteria are created and linked to the coupon's remaining life. Finally, it is shown that the results of the unsupervised analysis can be used to train a simple supervised classifier enabling the application of the prediction criteria to new AE data.

2. Experimental Procedure

Four E-glass fiber reinforced polyester laminates of different stacking sequence are considered. All laminates are INTERCHEM CHEMPOL 80 THIX polyester resin hand lay-ups, E-glass from AHLSTROM GLASSFIBRE, cured at room temperature. Two fabrics are used in manufacturing the above mentioned laminates. The first is mainly unidirectional, of 700 g/m² total weight, with parallel continuous fibers. A number of glass fiber strands, 30 g/m², are laid transversely to the main portion of fibers and stitched together to allow fabric handling. The second glass fabric

weighs 450 g/m² in total and contains equal proportion of continuous fibers in the (+45°) and (-45°) directions with respect to the loading axis stitched together. The stacking sequences of the four laminate types are [0₃]_T, [(±45)₃]_T, [0/(±45)₂/0]_T, and [(±45)/0₂/(±45)]_T, for UD, BD, MD, and MDN, respectively (see Table 1).

From each laminate, four straight edge coupons of 250 mm length and 25 mm width are cut using a diamond wheel and are prepared in accordance to ASTM D 3039-76. Aluminum tabs are glued to all coupon ends, resulting on 160 mm of free coupon length. Double edge notches of 5 mm length each are cut normal to the loading axis at the coupon's mid-length. Sixteen tensile tests, four from each laminate type, are carried out using a screw-type tensile machine under displacement control mode. In all experiments, displacement rate is kept constant at 1 mm/min.

During all tests described above, AE activity was monitored using a SPARTAN 2000AT of Physical Acoustics Corporation (PAC). A single AE transducer PAC R15, resonant at 150 kHz, is firmly attached to each coupon at a 45 mm distance from the notches, using ultrasonic couplant (Krautkraemer ZG). AE signals are amplified by a PAC 1220A filter-preamplifier set at 40 dB pre-amplification and 100-300 kHz band-pass filtering. The SPARTAN signal analyzer settings are set at 45 dB threshold, 20 dB gain, 50 μs peak definition time (PDT), 150 μs hit definition time (HDT), and 300 μs hit lock-out time (HLT). Data sets consisting of SPARTAN AE records containing seven signal descriptors are recorded during each experiment. The descriptors are Rise Time (RT), Counts (CNTS), Energy (ENE), Duration (DUR), Amplitude (AMP), Average Frequency (AVF), and Counts-to-Peak (CNP).

3. Data Preprocessing

Twelve out of the sixteen tensile experiments performed are used for the AE analysis via the unsupervised classification schema. Experiments using MDN coupons are excluded from the unsupervised classification stage since they will be used as unknown data in the supervised schema to be presented later. For each of the twelve experiments, data items recorded past the last maximum load value recorded are dropped out of further consideration. A

Table 1 Stacking sequences for the four laminate types.

Number of Experiments	Laminate Abbreviation	Laminate Description	Stacking Sequence			
			0°	±45°	±45°	N/A
4	UD	Unidirectional	0°	0°	0°	N/A
4	BD	Bi-directional	±45°	±45°	±45°	N/A
4	MD	Multidirectional 1	0°	±45°	±45°	0°
4	MDN	Multidirectional 2	±45°	0°	0°	±45°

series of steps is then taken to form the final data set, on which clustering will be performed: Each data set is filtered to eliminate outliers and false recordings. These filters eliminate records for which $CNTS \leq CNP$, $DUR \leq RT$, $CNTS \geq 1000$ and $AVF \geq 500$. The last two filters are justified by data plots indicating that only a negligible number of records have these properties and the values are far from the recorded average.

Two additional "empirical" filters are applied on the data. The first eliminates records x , for which

$$|(d - \langle d \rangle)/s| \geq 70,$$

where d the Euclidean distance of x to the mean vector of the set, $\langle d \rangle$ the mean of all such distances, and s the standard deviation of all such distances. Similar in concept, the second filter eliminates all records, for which some descriptor x takes values satisfying $|(x - \langle x \rangle)/s| \geq 50$, where $\langle x \rangle$ and s the descriptor's mean and standard deviation in the set, respectively. Being applied last and with very high threshold, the two filters did not eliminate more than a few records in each data set.

The union of the filtered sets forms a new set, which is standardized by subtracting the mean value and dividing by the standard deviation of each corresponding descriptor in the data set. Data is then projected on a new set of axes found via Principal Component Analysis (PCA), (Anderberg, 1973; Johnson et al., 1992), which allows the reduction of the data set dimension by utilizing statistical properties of the data. The method implemented here calculates the eigenvectors of covariance matrix to expose a set of orthogonal axes (principal components - PCs) on which the data reaches maximum variance. Using PCs, the clustering can be performed on a space of limited dimensionality, to which all descriptors have contributed according to their separability power. The PC direction can also be used to select the most powerful subset of the original data set descriptors in an approach similar to the original (Anastassopoulos et al., 1995), where dimensionality reduction is performed by dropping descriptors of high correlation via Wilk's λ or complete link criteria. This, however, is not the approach taken here, where data is projected and clustering is performed on PC axes. In analyzing the results of clustering performed in PC-space, the one-to-one correspondence of original and projected vectors is used to determine class properties in terms of physical signal characteristics. Combined with the above data normalization, the covariance matrix of the standardized set equals the correlation matrix of the original, while its eigenvalues equal the new variances of the data projected to the corresponding new axes (Anderberg, 1973). To select the number of new axes used, a degree of fit is given by the ratio of the sum of selected new variances with the sum of all new variances. For the clustering results presented later, this ratio was valued at 0.98 for 5 PCs.

4. Clustering Method

Work presented here uses a classification schema based on Learning Vector Quantizer artificial neural system (LVQ ANS). The LVQ is a two-layer (input-output) ANS presented by Kohonen in 1981. The unsupervised single winner LVQ ANS (Kohonen, 1988; Lippmann, 1987; Simpson, 1990), upon which this clustering schema is based, determines cluster reference vectors, centers, by a series of iterative steps that classify each input vector, via an embedded parallel Euclidean nearest-neighbor classifier, to one of the initial cluster centers and then uses the input-to-center distance to adjust the winner cluster center itself. The cluster-center adjustment is inversely proportional to the number of iterations performed forcing the algorithm to stabilize. The maximum number of encoding iterations to be performed is user-defined, the iteration counter increases upon the presentation of the entire data set, and no other converge criterion is used to terminate the encoding (cluster-center adjustment) stage.

In this form, the LVQ suffers from non-deterministic behavior caused by the initialization of cluster centers to random values and the effect of data-item encoding order in the cluster centers created. Taking these disadvantages into account, a modified LVQ schema (M-LVQ) was previously introduced for classification of AE records from C/C composites (Philippidis et al., 1998). The M-LVQ selects initial cluster centers from a small subset of the data set that contains most-distant vectors. The pair of vectors of greater in-between distance is first added to the initially empty set, then the vector, whose total distance from those already in the set is maximum. This step is repeated until the set size becomes equal to the number of requested classes and thus contains enough vectors to initialize the LVQ. This selection and initialization method first detects extreme vectors, lying usually at the ends of the data envelope and then, possibly, vectors inside the data envelop, which progressively splits the data in zones. To fix the presentation order during the encoding stage of the M-LVQ scheme, data vectors were presented according to their Euclidean distance from the data set's mean, with vectors closest to mean were presented first.

The M-LVQ applied on individual AE data sets from C/C composite experiments successfully identified small critical classes at the very last stage of the coupon's life. At the same time, the scheme produced classifications rating very low on the R separation measure (Davies, 1979; Anastassopoulos et al., 1995), which is assumed to be a suitable method for selecting classifications on this type of data. However, the M-LVQ-scheme presentation ordering step proved too time-consuming for the size of the GRP AE data sets analyzed in this work, and was not used.

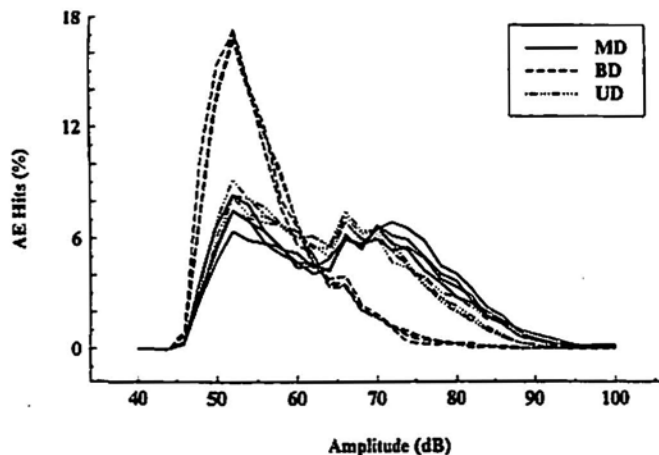


Fig. 1 Amplitude distributions for all data files used in UPR analysis.

Summarizing, the LVQ-based schema used for GRP AE clustering had a learning rate constant set to 0.8, run for 2500 encoding iterations, with initial cluster-reference vectors set to the most distant data-set items, and operated on a 5-PC space. No algorithmic ordering of the data was applied for encoding. This “relaxed” M-LVQ schema will be referred to as RM-LVQ. The data set was reordered so that experiments from MD coupons are presented first at each encoding cycle, followed by BD and UD. This is an arbitrary decision, partially justified by the fact that, unlike UD and BD, MDs contain both 0° and $\pm 45^\circ$ fiber layers, but did result in the most interesting classifications that will be shown below. The clustering schema run for 2 to 20 classes. Classification results are to be discussed later.

5. Results and Discussion

5.1 Clustering Selection

The final, preprocessed, data set consists of 147752 records projected into PCs. The set is a union of all AE signal descriptor vectors, recorded during 4 MD, 4 BD, and 4 UD coupon tensile experiments. Focusing on the amplitude distributions of signals recorded on each coupon type, it is seen that the presence of 0° fibers, i.e. in the loading direction, gives a distinguishable signature on the frequency distribution plots, as shown in Fig. 1. The MD and UD data sets exhibit a multi-modal distribution of amplitudes peaking around 52, 66, and 74 dB, while BD amplitudes are mostly distributed around 52 dB. Amplitude distribution analysis has been a trusted tool in detecting AE sources (Pollock, 1981). Practical AE approaches suggest that failure modes produce mostly unimodal amplitude distributions, thus in this case at least three amplitude-separable failure modes take place in the experiments. Therefore, when evaluating a clustering of such data, it would be desirable that these modes are distinguishable as individual clusters preferably having a unimodal amplitude distribution.

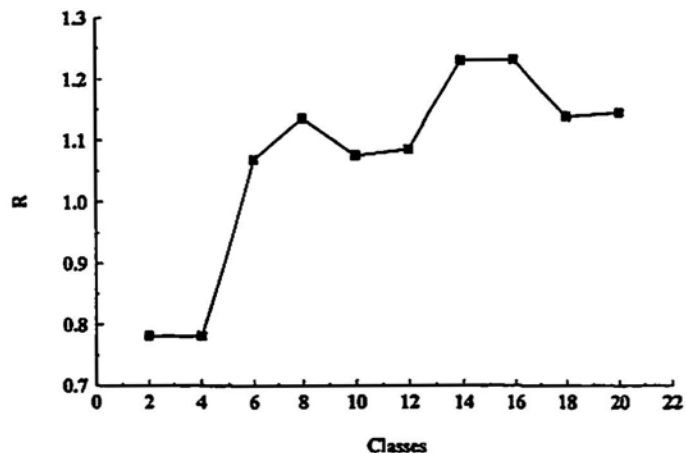


Fig. 2 R-criterion values for RM-LVQ classifications of 2 to 20 classes.

However, common mathematical clustering evaluation criteria such as the R-criterion, which has proven some reliability with respect to AE clustering (Anastassopoulos et al, 1995; Philippidis et al., 1998), cannot take into account such qualifying factors. Indeed, for evaluating the set of RM-LVQ classifications of variable output size, number of classes, in the 2 to 20 range, the R separability measure is of little use since it does not produce any significant minimization, which would indicate a particularly “good” clustering, from the engineering point of view.

More specifically, the minimal R value, taken for the preprocessed items in principal component space and valued at 0.781537 (Fig. 2), is found at the 4 class classification, which produced classes sized 40, 1630, 145952, and 130 records each. This clustering placed most AE signals in one class, Class#2, and created two classes too small to be of any interest. The remaining class, labeled Class#1 and sized 1630 records, whose amplitude distribution (Fig. 3), indicates to be of some significance, contains very high amplitude records, around 85 dB, from all experiments. However, with the GRP coupons producing high amplitude signals at early load, the class is distributed around all load stages and thus cannot be used to make assumptions about the coupon’s remaining strength or life. Figure 4 shows the distribution of AE records classified in this class over the load normalized per experiment.

10-Class RM-LVQ Classification Results

Conversely, by moving on to classifications rating higher, worse on the R-criterion, the 10-class classification shows some interesting properties. The clustering placed 69% of the entire AE data set to Class#7, a class of records with mostly low signal characteristics, as seen in Table 2. However, the mean counts, energy, duration and amplitude values for Class#7 are very close to the mean recorded values of BD experiments; see Table 3. Additionally, the overall amplitude distribution of the class, as shown in Fig. 5, is

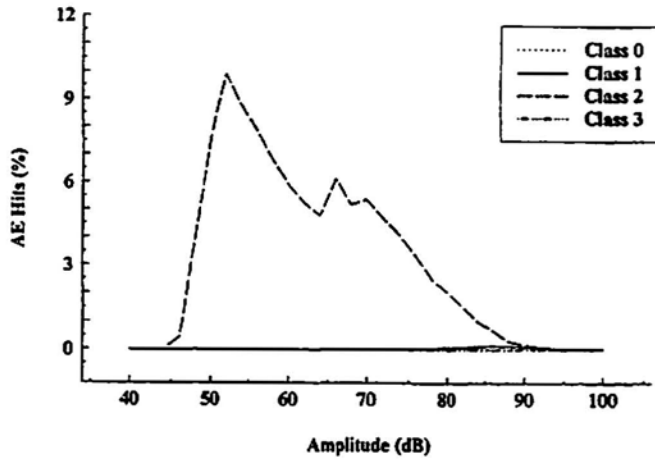


Fig. 3 Amplitude distribution for RM-LVQ 4-class classification.

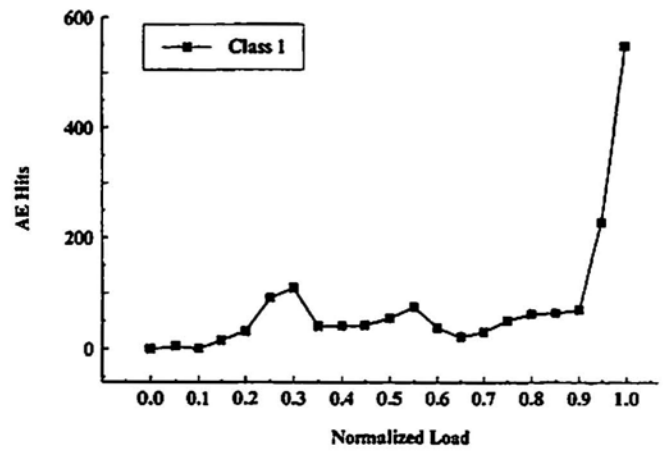


Fig. 4 Load distribution for class#1 of RM-LVQ 4-class classification.

Table 2 Descriptor ranges for RM-LVQ 10-class case.

ID	Size		RT	CNTS	ENE	DUR	AMP	AVF	CNP
0	31	min	1	447	361	3438	81	106	1
		max	99	844	2829	7550	100	157	13
		mean	18.38	649.70	1350.77	4822.61	96.58	135.03	6.41
1	752	min	1	67	48	594	65	73	1
		max	177	265	436	2522	100	238	28
		mean	33.24	129.23	201.07	1047.28	86.76	124.04	6.88
2	12104	min	0	26	17	173	55	45	1
		max	76	127	222	1189	100	205	14
		mean	24.42	49.06	65.52	374.95	78.50	133.27	4.33
3	11688	min	14	3	3	46	45	16	2
		max	231	221	182	1182	96	307	39
		mean	65.29	25.00	15.88	179.40	60.23	141.99	11.54
4	19858	min	1	9	5	66	52	48	1
		max	105	119	226	1048	98	277	15
		mean	37.14	35.71	31.50	252.05	69.99	145.17	7.78
5	931	min	1	3	3	9	57	52	2
		max	48	75	62	490	100	333	13
		mean	8.91	29.60	22.79	212.86	80.38	145.44	8.36
6	113	min	1	156	104	1358	64	82	1
		max	143	396	838	3765	100	169	22
		mean	27.35	259.77	447.68	2058.28	91.16	126.92	6.99
7	102226	min	0	2	1	5	44	8	1
		max	85	51	47	634	100	444	13
		mean	20.95	12.75	7.83	97.07	56.70	134.30	4.05
8	2	min	246	236	818	1904	98	104	41
		max	312	339	1027	3240	99	123	51
		mean	279.0	287.5	922.5	2572.0	98.5	113.5	46.0
9	47	min	1	304	352	2319	78	112	1
		max	104	596	1140	4965	100	159	23
		mean	26.14	414.89	756.65	3035.36	93.31	137.17	6.95

similar to the one displayed by individual BD data subsets, given in Fig. 1.

These are indications that the AE classified in this class is caused by mechanisms not related to the presence of 0°-fibers. Classes#2, 3 and 4 are also of significant size. These classes show a trend towards unimodal amplitude distribution, with Class#4 peaking at the originally predicted 74

dB, and Class#2 peaking at 83 dB. The latest can be used to identify the presence of 0°-fibers in the coupons. Containing records with above-average valued counts, energy, duration, and relatively high amplitude, Class#2 contains 8.6 % of all UD AE, 13.2 % of all MD, and only 0.89 % of BD AE. Similarly, focusing on two of the smaller-sized classes, namely 0 and 9, both are characterized by high energy and duration records. Each of these classes contains AE from all

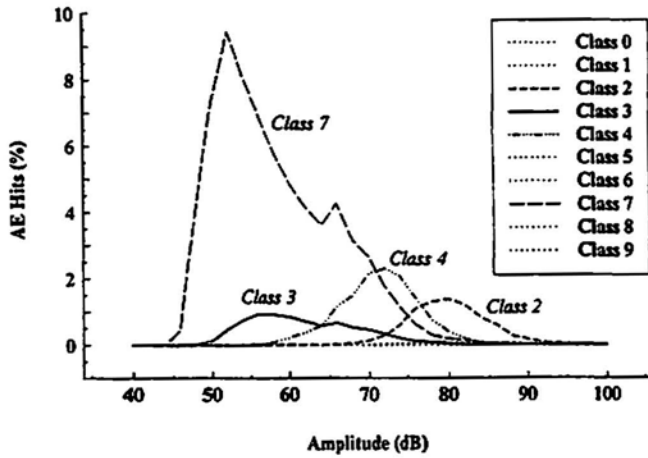


Fig. 5 Amplitude distributions for RM-LVQ 10-class classification.

MD and UD experiments, with no BD record classified in them.

20-Class RM-LVQ Classification Results

Following the same procedure, the 20-Class RM-LVQ classification rated worse on the R-criterion. The trend towards mostly unimodal amplitude distributions per class continues in this classification as well, as shown in Fig. 6. The clustering consists of eight larger sized classes, as

shown in Table 4. The twelve smaller classes were not analyzed further since they did not contain AE from all experiments. Figure 7 shows the distribution of the larger classes on load, normalized independently for each experiment. Once again, due to the nature of GRP AE, most classes contain AE that was recorded at all load stages, and cannot directly be used for failure prediction. The percentage, however, of records gained by some of the classes appears to vary depending on the load stage.

This property can be exploited to predict the remaining life of the coupon via ratios of class sizes per load stage, i.e. ratios of the number of AE records recorded during the period under consideration and classified in the classes used by the criteria. Indeed, application of such criteria gave interesting results, and proved quite fit to purpose, especially in cases where 0° fibers were used, i.e. UD and MD coupons.

One of the criteria created splits the experiment in three stages : not critical, less critical, and critical. The stages are characterized by three score numbers n_1, n_2, n_3 as follows:

Not Critical (1) $n_1 = s_5 / (s_4 + s_{15})$
 Less Critical (2) $n_2 = s_4 / (1 + s_{15})$
 Critical (3) $n_3 = (s_3 + s_4 + s_{15}) / (1 + s_{15})$

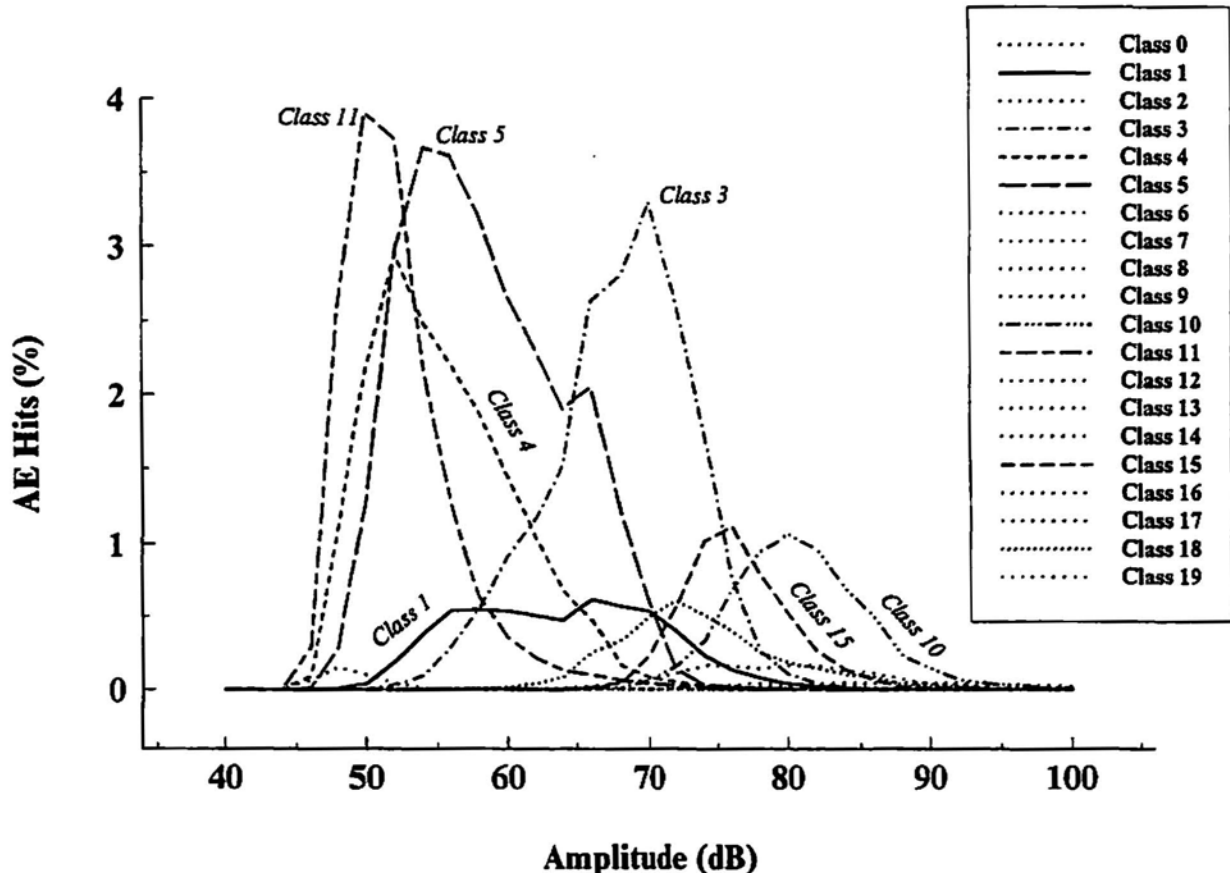


Fig. 6 Amplitude distributions for RM-LVQ 20-class classification.

Table 3 Signal characteristic values recorded during GRP tension experiments.

AE Source (Coupon Type)		RT	CNTS	ENE	DUR	AMP	AVF	CNP
UD	mean	24.93	20.48	18.16	150.08	61.88	139.66	5.06
	std. dev.	15.24	19.74	32.92	151.12	9.93	34.33	2.82
BD	mean	29.20	13.66	8.12	97.93	54.64	137.25	5.24
	std. dev.	18.99	11.54	11.30	78.62	6.61	41.22	3.52
MD	mean	29.34	28.11	27.32	219.08	64.07	128.09	5.52
	std. dev.	18.44	29.93	55.24	229.39	11.08	31.89	3.01
All Types (MD UBD UUD)	mean	26.92	20.93	18.32	156.20	60.90	136.29	5.21
	std. dev.	17.08	22.02	37.56	168.56	10.21	35.65	3.03

Table 4 Descriptor ranges for the larger-sized classes of RM-LVQ 20-class clustering.

ID	Size		RT	CNTS	ENE	DUR	AMP	AVF	CNP
1	8625	min	22	5	5	63	46	36	4
		max	211	113	123	768	96	307	36
		mean	68.84	28.17	18.71	200.26	62.28	143.16	12.47
3	27994	min	0	5	3	26	50	103	1
		max	63	65	59	401	87	298	16
		mean	30.18	27.20	19.22	173.58	66.65	158.96	6.84
4	24848	min	0	2	1	8	44	129	1
		max	45	39	26	215	83	280	12
		mean	16.04	9.04	4.97	53.78	54.02	171.05	3.26
5	38283	min	0	3	2	24	45	16	1
		max	97	61	39	541	76	166	14
		mean	30.45	14.76	8.07	119.23	56.93	124.56	5.32
10	8713	min	0	26	18	173	57	64	1
		max	45	113	222	1163	100	201	11
		mean	22.86	48.54	66.78	369.26	79.14	133.09	3.99
11	22828	min	0	2	1	14	44	8	1
		max	75	55	27	615	81	142	8
		mean	14.13	5.63	4.12	67.58	50.84	90.40	2.04
15	7053	min	23	25	12	181	60	89	1
		max	85	81	147	479	91	208	13
		mean	37.07	42.40	47.99	303.36	74.72	140.28	7.16
18	5276	min	0	2	2	14	56	18	1
		max	52	57	64	840	100	166	12
		mean	10.56	23.43	18.03	208.35	72.14	113.28	4.70

where s_k is the number of items classified in class k for the period under consideration. The stage can then be determined by comparing the above listed ratios for a selected load period and finding the largest. If, for example, at any given load stage, z , only AE signals recorded in the period $0 \dots z$ are considered, the overall n -scores are shown in Fig. 8a, and 8b. The values displayed in Fig. 8a are sums of the calculated n -score values of each experiment with load normalized to the experiment's maximum load. Figure 8b

shows the percentage of each n -score over the sum of all n -scores for the period under consideration. The overall trend shows the prevalence of n_1 values in up to 13% of critical load, n_2 in 13% to 60%, and n_3 in the last 40% of the coupon's life. To verify that this still applies to AE from each individual experiment, Figs. 9 and 10 show the n -score percentage for each MD and UD AE data separately. Despite some fluctuation, the figures do show that the schema generally performs properly.

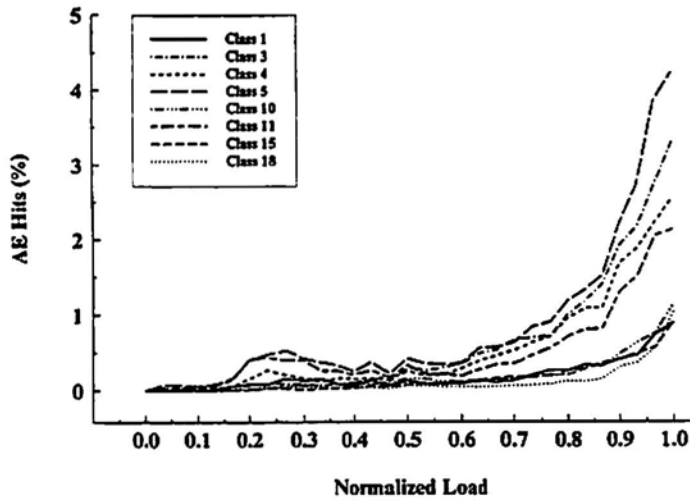


Fig. 7 Load distribution of RM-LVQ 20-class classification.

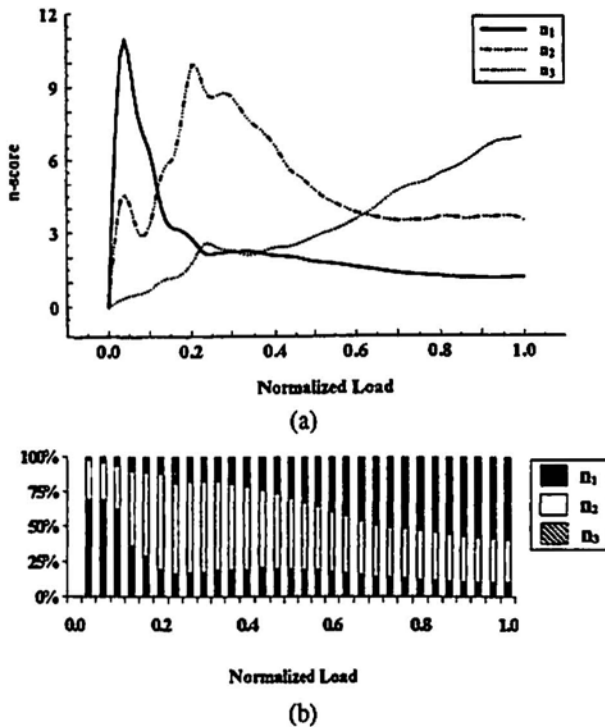


Fig. 8 (a) and (b) n-scores and overall performance for entire AE data set: AE period = (0..z).

The same n-score definitions are applicable even if only AE recorded during a shorter period, not the entire AE history, of the experiment is considered. For example, splitting each experiment in 30 load periods, and using only AE recorded in each period, the n-scores can still be used to hint about the loading history of the coupon. The overall performance of the schema is, in this case, shown in Figs. 11a, and 11b. Once again, the sum of n-scores for AE recorded in periods equal to 1/30-th of each experiment's load is displayed in Fig. 11a, while Fig. 11b shows the percentage over the sum of all such scores for the given period.

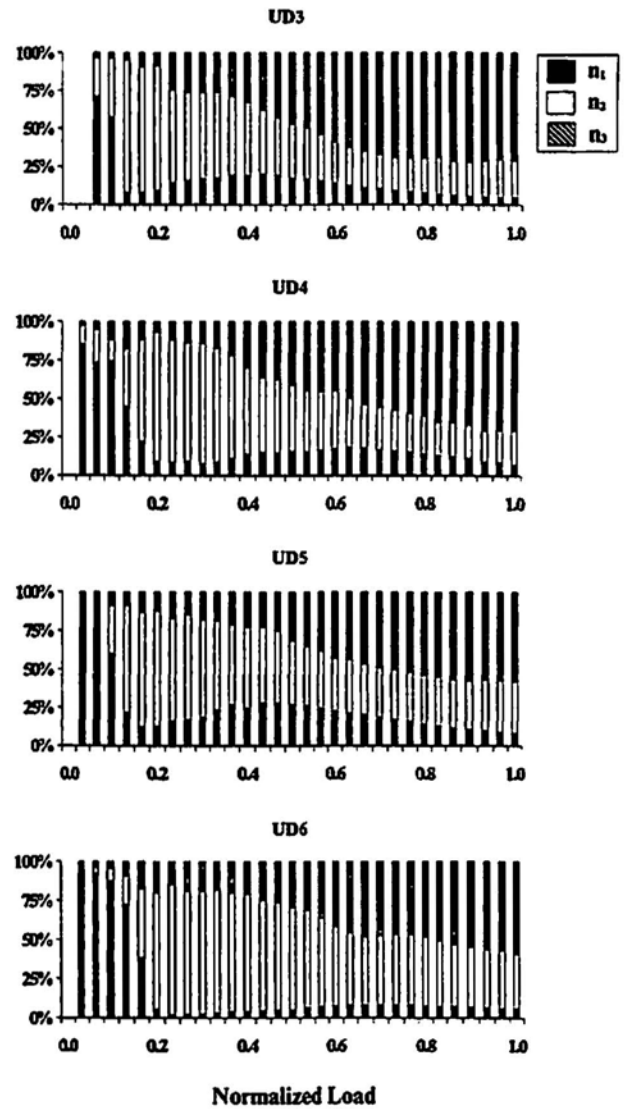


Fig. 9 n-scores, performance on UD coupon AE: AE period = (0..z).

The overall trend can be verified by looking at the individual AE subsets from each experiment separately, as shown in Figs. 12 and 13 for UD and MD experiments, respectively. The figures give strong evidence that by using AE recorded at a later stage in the experiment, enough information is still revealed to enable a remaining-life or strength prediction mechanism.

Notably, the above described scheme is only one of several possible. Another similar criterion uses:

$$n = (s_3 + s_{15}) / (s_1 + s_{11})$$

to determine if the coupon has entered the last half of its remaining life. The criterion can be applied for the problem of prediction using AE acquired during particular load stage periods. Once again, periods equal to 1/30-th of the total load per experiment are used for the evaluation. Overall, n takes values shown in Fig. 14, indicating that $n > 1$ can be associated with load around 50% of the failure load.

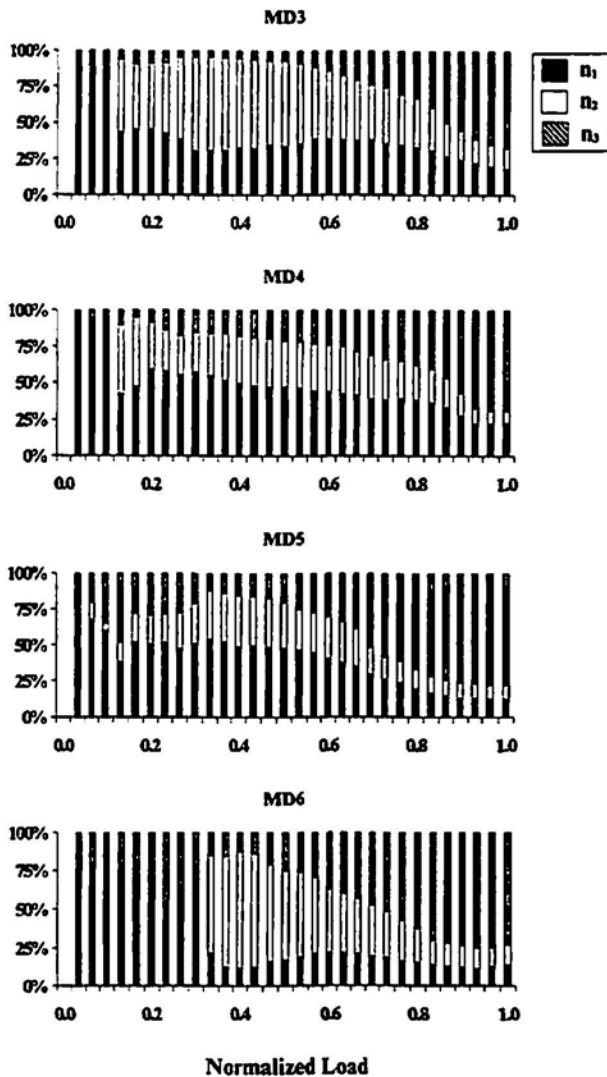


Fig. 10 n-scores, performance on MD coupon AE: AE period = (0..z).

5.2 Applying the Criteria on Unknown AE Data

In an attempt to evaluate the aforementioned criteria schemes in an online-like situation where AE is recorded and failure criteria are applied while the test is in progress, four new tension experiments were performed using materials similar, but not identical, to the ones already used for the RM-LVQ data set. The four coupons, identified MDN, are MD-type specimens with $[\pm 45/0_2/\pm 45]_T$ glass fiber lay-up, different from the $[0/(\pm 45)_2/0]_T$ MD, whose AE was included in the RM-LVQ data set.

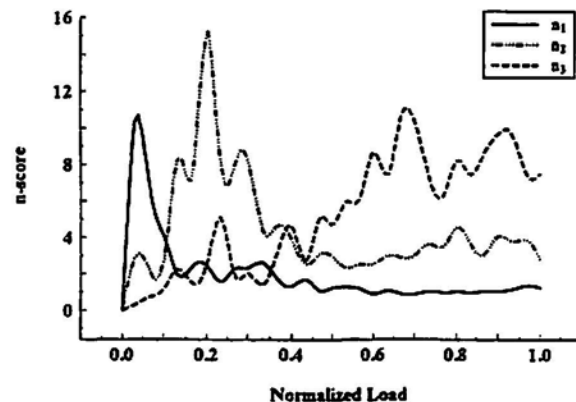
The schema created uses an Euclidean distance nearest neighbor classifier (NNC) to classify incoming AE to 20 classes of similar properties to those created by RM-LVQ while repeatedly applying the criteria to determine the load criticality. The 1-NNC, (Tou and Gonzales, 1974), is the simplest form of supervised classifier and requires a set of pre-calculated fixed class prototypes to compare with incoming AE vectors. These cluster centers are never modi-

fied by NNC, thus no new information is revealed by the algorithm. Here, the NNC class-prototype vectors are set equal to the mean vectors of RM-LVQ classes viewed in regular descriptor space; i.e., with AE data filtered and standardized but not projected in PC-space.

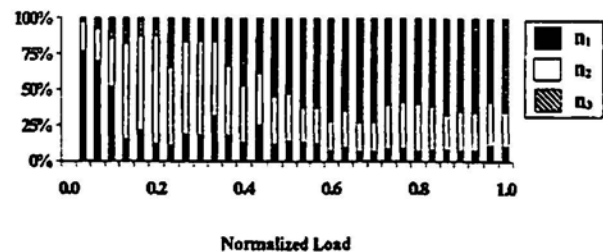
Performing only on-line capable operations, the new AE is standardized using the mean and standard deviation of the original RM-LVQ data set, and all filters except empirical ones are applied. For each new AE data set, NNC is used to classify the AE data recorded during a limited load stage and the class-size criteria are calculated. Overall, the NNC classification of new data creates classes with similar physical properties to those produced by RM-LVQ, which is verified by Fig. 15. In testing the online applicability of the criteria, two cases are considered:

(a) using NNC-created classes of all AE recorded from the no-damage state to current load.

This involves NNC classification of all AE from the beginning of the test. At any point, the NNC classes can be used to calculate the n-score criteria, which would predict the level of damage that has occurred so far. The overall evolution of the first n-score criteria calculated in such manner can be visualized by Figs. 16a, and 16b where the sum of n-scores over the load normalized to the maximum reached, per experiment, is displayed. Once again, at any



(a)



(b)

Fig. 11(a) and (b) n-values and overall performance for entire AE data set: AE period = (1/30-th).

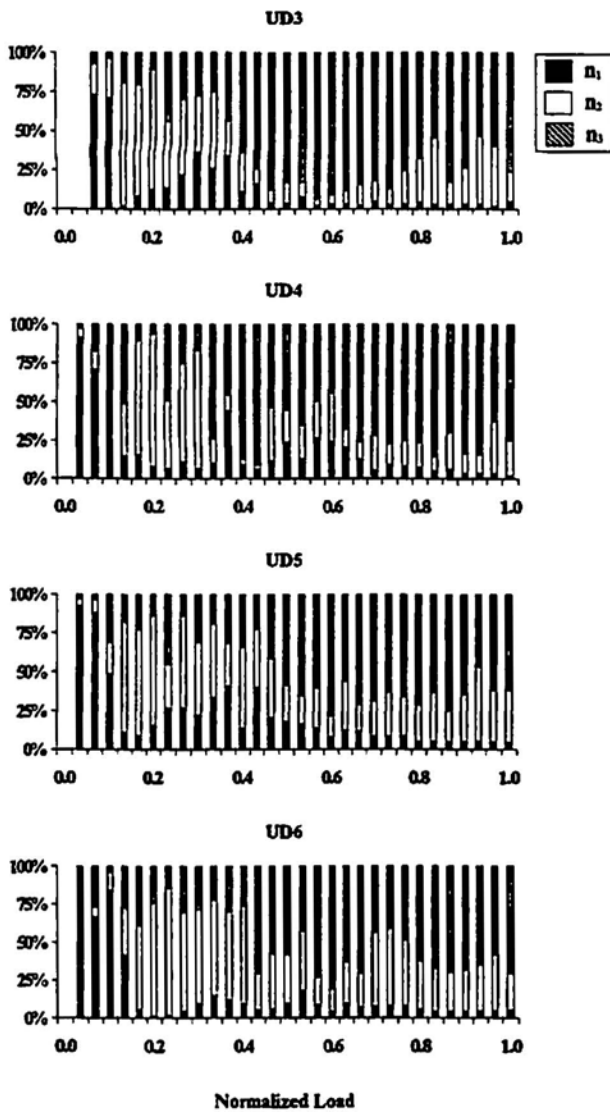


Fig. 12 n-scores, performance on UD coupon AE: AE period = (1/30-th).

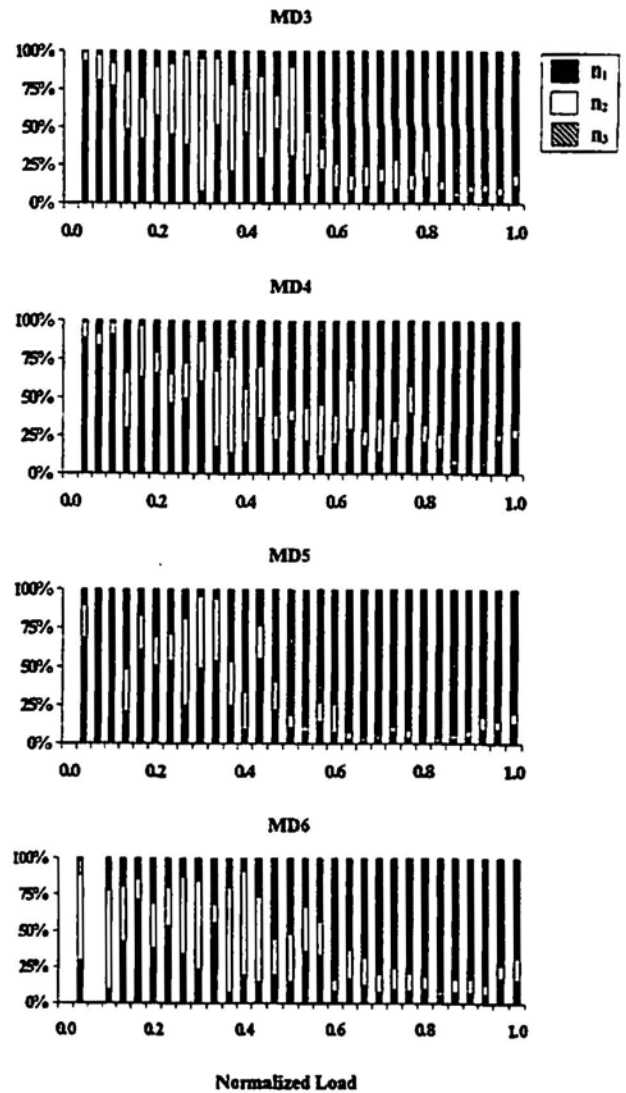


Fig. 13 n-scores, performance on MD coupon AE: AE period = (1/30-th).

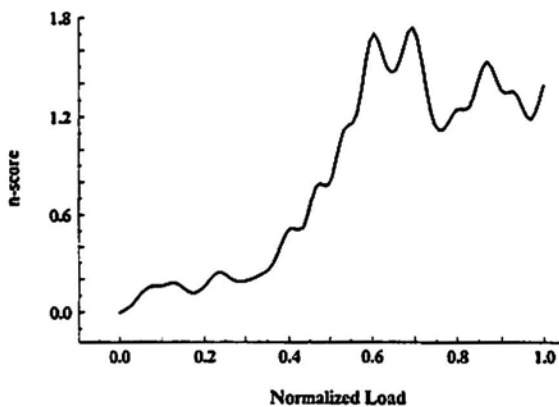


Fig. 14 Overall values for second criterion (AE period = (1/30-th).

load stage, the classes used to calculate the n-scores depicted in the figures consist of AE from 0 to current load stage. The overall trend is repeated for individual experiments as is evident in Fig. 17, showing that the criteria could still be applied on an on-line mode of operation.

(b) using NNC-created classes of a limited number of past AE records.

This case simulates a situation where pre-loading has been applied to the coupon but no AE history is available. Based on very limited AE records (whose rate of emission varies with load), this is the hardest of all cases considered. To test the applicability of the criteria-based schema, the NNC is applied to sequential subsets of 300 AE records and the criteria are calculated using the classification of these records only. The classes which are created and used to

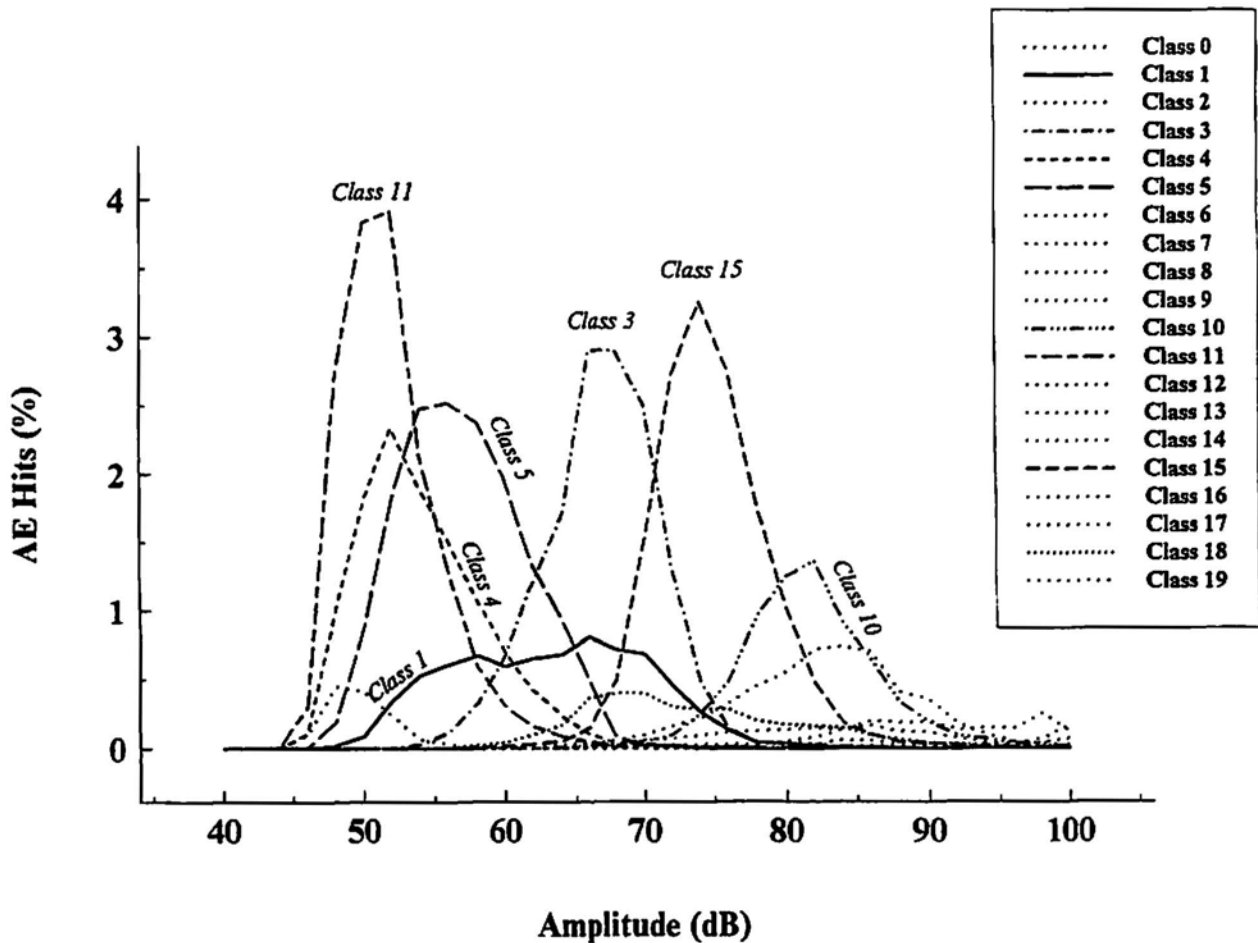
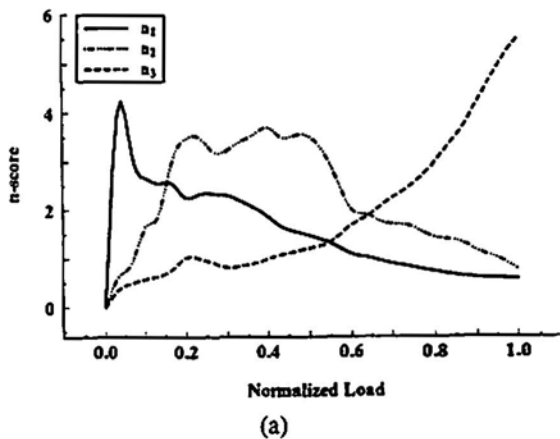
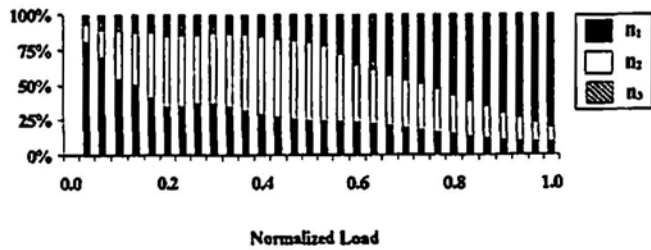


Fig. 15 Amplitude distributions for NNC 20-class classification (overall MDN AE data).



(a)



(b)

Fig. 16(a) and (b) n-scores using NNC, overall performance on all MDN AE: AE period = (0..z).

calculate the class size ratios are subsets of the 300 AE record sets. With such a small number of AE records considered, there are periods where very few elements are classified in the classes used for the criteria; this creates discontinuities in the ratios and makes results fluctuate. Still, as indicated by Fig. 18 with results from coupon MDN2, showing the progress of n-score values for the criteria applied on MDN coupons and the average normalized load for the period, whose AE is used, n_1 and n_2 still generally prevail during the less critical periods of the experiment while n_3 tends to dominate the last loading stages.

6. Conclusions

An AE study of GRP tensile failure behavior when subjected to loading is presented along with an unsupervised, ANS-based, pattern recognition procedure, which can be used to predict remaining strength or life of the GRP.

The principal-component projection proved useful in the clustering of similar signals, eliminating the need for extensive experimentation in descriptor selection. Classification performed on a union of AE from experiments of all different coupon types allowed the creation of classes with

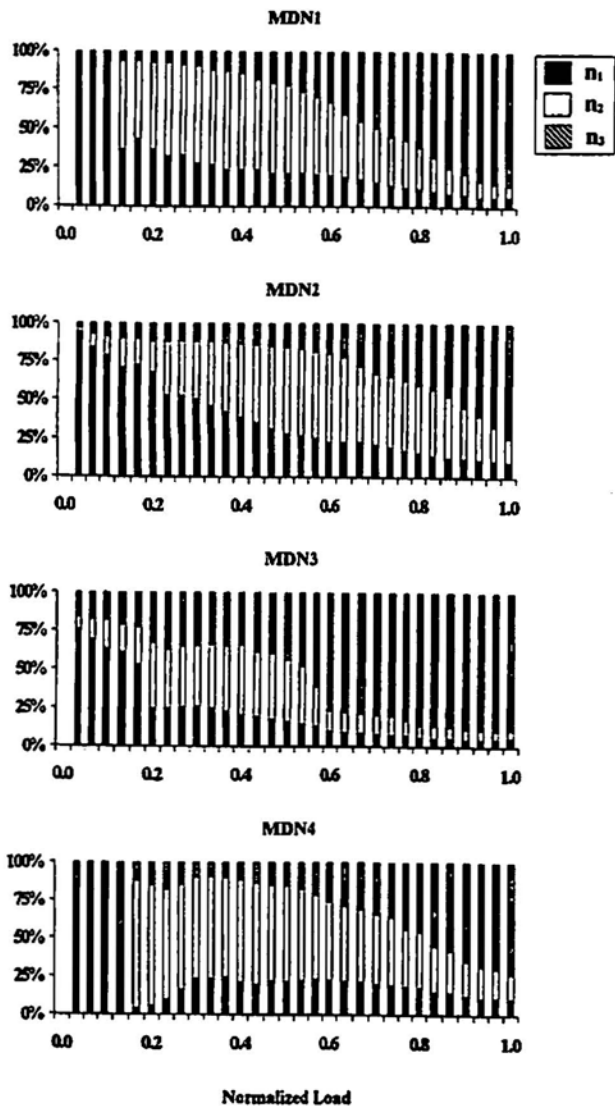


Fig. 17 n-scores performance using NNC classifications on MDN coupon AE: AE period = (0..z).

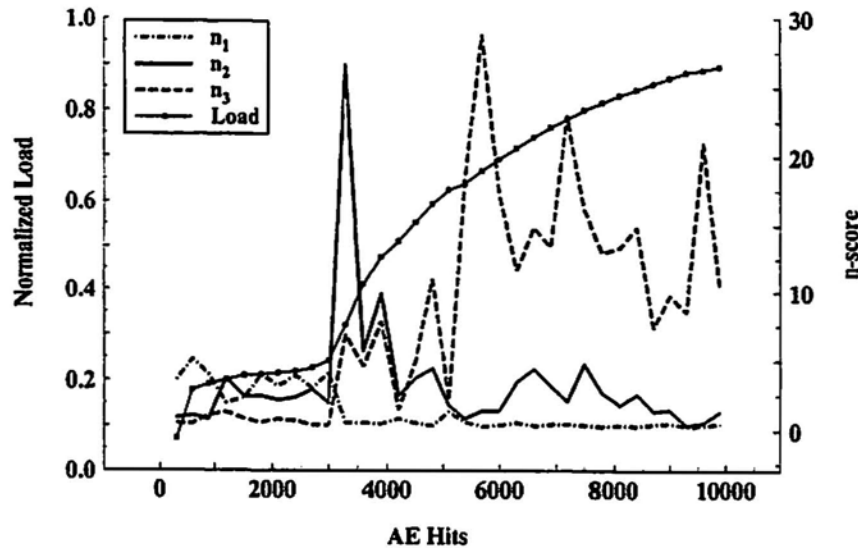


Fig. 18 n-scores and performance on MDN2 coupon AE: AE period=300 Hits.

properties of uniform validity. Focusing on classifications of classes with unimodal amplitude distributions also proved suitable.

The unsupervised classification procedure presented in this work shows that for these AE data sets such clustering is advantageous, producing valid results and raising questions about the use of mathematical clustering-evaluation criteria as a method of selecting the best classification amongst several - as needs to be done since the number of natural clusters in the data is unknown - and suggests an alternative approach based on class amplitude distributions.

Working along these lines, interesting classifications are revealed. There is strong evidence that a classification exists, in which grouping of AE caused by 0° fibers and AE unrelated to 0° fibers occurs in two amplitude-distinguishable classes. Furthermore, the classes tend to obtain AE records at different rates depending on the load criticality. This observation, expressed as a set of three class-size ratios, is used to form a criterion linking AE to the percentage of remaining coupon strength or life. The criterion proved successful in all coupons tested, allowing the creation of a supervised, trained, schema where load stage is successfully predicted using new AE not considered in the original unsupervised analysis.

Although the study is limited to small coupon testing, where damage occurs very close to the AE sensor, it verifies the strong potential of unsupervised AE analysis.

All preprocessing, classification and pattern recognition methods used in this work were performed using a custom pattern recognition software package, VPR, running under Win32. Text-only versions of the software are available for other operating systems. The program is available from the authors upon request.

References

A.A. Anastassopoulos and T. P. Philippidis (1995), "Clustering Methodologies for the Evaluation of AE from Composites", *J. Acoustic Emission*, **13**(1/2), 11-22.

A.A. Anastassopoulos, T. P. Philippidis and S. A. Paipetis (1996), "Failure Mechanism Identification in Composite Materials by Means of Acoustic Emission. Is it Possible?", *Non Destructive Testing*, eds Van Hemelrijck and A.A. Anastassopoulos, Balkema, Rotterdam, pp. 143-149.

A.A. Anastassopoulos and T. P. Philippidis (1998a), "Pattern Recognition Analysis of AE from Composites", *Proc. 23rd European Conference on Acoustic Emission Testing*, Vienna, Austria, pp. 15-20.

A.A. Anastassopoulos, S. J. Vahaviolos and J. C. Lenain (1998b), "Signature Recognition of Acoustic Emission from FRP Structures", *Proc. 7th European Conference on Non Destructive Testing (ECNDT)*, Copenhagen, Denmark.

M. R. Anderberg (1973), *Cluster Analysis For Applications*, Academic Press, New York.

D. L. Davies and D. W. Bouldin (1979), "A Cluster Separation Measure", *IEEE Transactions on Pattern Analysis and Machine Intelligence PAMI-1*, pp. 224-227.

R. A. Johnson and D.W. Wichern (1992), *Applied Multivariate Statistical Analysis*, Prentice-Hall International, New York.

T. Kohonen (1988), *Self-Organization and Associative Memory*, Springer-Verlag, Berlin.

R. P. Lippmann (1987), "An Introduction to Computing with Neural Nets", *IEEE ASSP Magazine*, **14**, 4-22.

T. P. Philippidis, V. N. Nikolaidis and A. A. Anastassopoulos (1998), "Damage Characterization of Carbon/Carbon Laminates Using Neural Network Techniques on AE Signals", *NDT&E International*, **31**(5), 329-340.

A.A. Pollock (1981), Acoustic Emission Amplitude Distributions, *International Advances in Nondestructive Testing*, **7**, 215-239.

W.M. Rand (1971), "Objective criteria for the evaluation of clustering methods", *J. Am. Stat. Association*, **66**, 846-850.

P. K. Simpson (1990), *Artificial Neural Systems*, Pergamon Press, New York.

J. T. Tou and R. C. Gonzalez (1974), *Pattern Recognition Principles*, Addison-Wesley, Reading, MA.

42nd AEWG Meeting

allowed to go into free fall. When the maximum allowed velocity is reached, the emergency brakes are applied. All detected AE is carefully examined and the approximate source locations determined. A written procedure with failure criteria has been established. For the first five years, no AE indications of flaws were seen. On a test in October 1998, a large AE burst was seen at the peak load. A retest with sensors concentrated in the suspected region confirmed the finding. The braking system was disassembled and an inclusion inside a main pivot pin was found in the general position indicated by the AE analysis.

Fast Fracture Source for Quantitative AE Simulation: Laser break-down of Silicone in a Crack. Kanji Ono, UCLA; Ryuji Masaki, Mikio Takemoto, Aoyama Gakuin University

We propose a new artificial fracture source for quantitative acoustic emission (AE) characterization. The source utilizes dipole forces produced by the break-down of silicone (or other liquids) placed inside a slit (or a crack). We irradiated a focused Q-switched Nd-YAG laser beam (5 ns duration, 20 to 90 mJ) on the silicone in a 0.3-mm wide slit. The slit was machined on the distal plane of a 70-mm diameter cylindrical block. The out-of-plane displacement produced by the resultant bulk waves was monitored on the outside surface using a heterodyne-type laser interferometer. Quantitative source simulation to the displacement revealed that the silicone break-down produces dipole forces to slit walls (equivalent to Mode-I fracture with the direction of motion normal to the wall). The source had a rise time of 0.18 μ s, which was unaffected by the level of laser beam energy. However, the source opening volume increased with laser beam energy. This source has the rise time shorter than that of a pencil-lead break source and allows the calibration of a sensor-structure system to several MHz range. Next, this break-down source was employed to determine the transfer function of a broadband AE transducer and the propagation medium. Using the transfer function determined, we estimated the source function of a compression-type PZT element coupled to two half-cylinders and excited by a pulse. The source function agrees with that measured directly by a laser interferometer, confirming the utility of the break-down source. This experiment also verifies that such an arrangement of a PZT element and structural shapes can be a good AE source for simulation and calibration. Other combinations of sources, structural shapes and AE transducers are also examined and results will be discussed. For example, we monitored AE signals from delayed fracture in a dual-phase stainless steel and successfully studied the source kinetics by the waveform simulation technique developed here.

Studying AE from Carbon Fiber Reinforced Silicon Carbide for use in re-entry Component Health Monitoring System (HMS). Richard Nordstrom, Hartmut Vallen, Vallen-Systeme GmbH; Jan Werner, Andreas R. Meyer, Technical University Munich; Arnd Reutlinger, R. Graue, Kayser-Threde

Carbon fiber/SiC matrix material is being developed for use in the nose of the X-38 as a thermal protection system. Within this context it is desired to exploit AE generated from the C/SiC as part of a health monitoring system (HMS) strategy. The project has begun with material and simulation testing and later will be implemented in actual flight. The HMS including AE has the status of an experiment on the X-38.

The first steps of this program are laboratory material testing and developing in-flight monitoring capability. The basic understanding gained from AE measurements on C/SiC with a high end AE system (AMSY4) provides some guidelines for specifying the in-flight system. The in-flight HMS program and X-38 design place more specific constraints on the in-flight AE monitoring instrument.

Initial testing is described wherein mechanical and thermal material tests were performed. Tests where controlled variation of loading rate, load program, stress concentration and temperature were carried out. Most tests were carried out on a laminate consisting of 16 unidirectional plies, however a C/SiC weave was also tested. The C/SiC composites generated a great deal of AE in all test variations performed. The trend seen first in simple static bend testing was repeated in various test programs: many AE measurements increase toward failure in a steady process, most notably: peak amplitude, energy, rms/ASL, and number of hits/events. Load program, load rate and specimen geometry are parameters varied in initial testing. Damage observations are made in-test and microscopy is performed post test to help characterize damage. Specific results are presented for various test configurations. Transient recording of AE signals and pattern recognition of AE signal type are further tools used to analyze the initial testing.

The in-flight AE monitoring system is to provide data for the HMS acquisition system. The acquisition speed for all subsystems is set within the HMS specification (1 Sample/ms); the total monitoring time period is set by re-entry flight characterization. The AE monitoring system is designed so that multiple AE acquisition modules can be attached to each AE sensor, each module providing a characteristic of the AE per millisecond. A data reduction

Real-Time Tool Condition Monitoring in Cold Heading Machine Processes Using an Acoustic Approach

Henrique L.M. dos Reis, David B. Cook and Aaron C. Voegelé

Abstract

In cold heading manufacturing processes, complete or partial fracture of the punch-pin leads to production of out-of-tolerance parts. An on-line process monitoring system has been developed to assure that out-of-tolerance parts, caused by failure of the punch pin, do not contaminate the batch of acceptable parts. A four-channel data acquisition system was assembled, and corresponding software developed, to collect and store the acoustic signal generated during the manufacturing process. Waveform features were extracted from the acoustic signal. A genetic algorithm was designed to select the smallest subset of waveform features necessary to develop a robust artificial neural network that could differentiate among the various conditions of the punch pin, i.e., no failure, complete fracture, and partial fracture of the punch pin. For the particular part being manufactured, the developed monitoring system is able to terminate production within seconds of punch pin failure using only four waveform features of the acoustic signal.

1. Introduction

Cold heading is a manufacturing process used to produce complex shaped components from metal rod or wire. This process utilizes interchangeable punch and die tools in a versatile high-speed multi-step manufacturing system. Through a progressive series of deformations, manufacturing of complex parts, once achieved only through multiple turning, milling, and drilling stages, can now be manufactured in a cold header. The advantages of cold heading processes over traditional manufacturing methods including higher strength parts, better surface properties, higher production speed, and lower manufacturing costs (Carlson, 1987; Dallas, 1980; Browne, 1985). However, the realization of these advantages is dependent on both the reliability of the cold heading machine during operation and the skill of the operator during setup and during production of the manufactured parts (Ghostline, 1992; Crum, 1996; Brankamp, 196; Terzyk, 1996).

An example of the manufacturing progression of a panhead fastener produced by a double-blow, single-die cold heading is shown in Fig. 1. Part production begins as

the raw wire is drawn from a spool and forced to pass through a series of feed rollers. The wire is fed through a cut-off bar until it reaches the required length gauge. This gauge determines the amount of material in the final part. The cut-off bar shears the material and a pair of transfer fingers moves the sheared piece of wire into alignment with the die; then, a moving ram assembly pushes the work piece into the die. The first blow punch is rotated into alignment with the die by the rotating head on the end of the ram. After the first deformation step, i.e., first punch, is completed, the second deformation step, i.e., second punch, takes place. As the second punch reaches the front dead center of its movement, the knock out pin advances to push out the part as the ram recedes. The finished part is pushed free of the die and drops to the bottom of the machine into a collection bin. The process repeats itself as the next cut-off bar comes into alignment with the die. The intermediate step in the deformation sequence is similar for a wide variety of panhead fasteners; the cone-shaped head is produced by impacting the bar blank with a straight punch pin. The second step, i.e., the second punch, of the process is unique to each type of fastener produced; for the panhead part shown in Fig. 1-a, the Tamper Resistant Torx T-20 recess punch pin shown in Fig. 2, is used.

To achieve lower costs for cold header manufactured parts, machine down time, setup time, and tool replacement frequency needs be minimized; as a result, quality control has had an increasing economic impact on cold header manufacturing processes (Terzyk, 1996; Reis and Cook, 1997; Reis and Voegelé, 1997). For example, the primary customers of the precision fastener sector of cold header manufacturing use assembly-line robots to attach fasteners quickly and precisely to their products. The influence of one out-of-tolerance part stopping the production of an entire automated assembly line has a severe cost penalty. The four main causes for out-of-tolerance fasteners are material inconsistencies, inadequate lubrication, punch pin wear, and punch pin fracture. Each of these four failure modes causes unacceptable part production, but becomes critical at significantly different rate. The first three causes tend to affect part quality over a long period of time; this extended amount of time gives the operator the opportunity to observe the progression to failure, and take corrective action at the appropriate time. In these slow progressive failure modes, 'failure' is defined at the discretion of a skilled operator to maximize the efficient operation of the cold heading process. The fourth cause, namely, punch pin fracture,

Received 30 June 1999. The authors are affiliated with Department of General Engineering, University of Illinois at Urbana-Champaign, Urbana, Illinois 61801. (h-reis@uiuc.edu)

Table 1 Data acquisition parameters.

	High Pass (kHz)	Low Pass (kHz)	Amplification (dB)	Buffer Length	Sampling Rate (kHz)
Channel 1	0.3	12	7	4096	195
Channel 2	12	40	14	4096	195
Channel 3	40	90	24	8192	781
Channel 4	90	150	30	8192	781

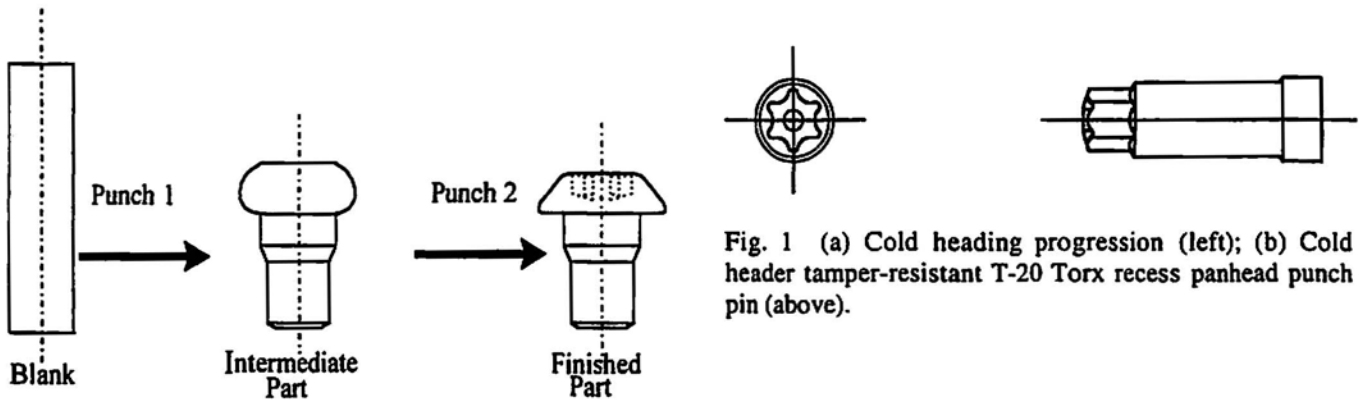


Fig. 1 (a) Cold heading progression (left); (b) Cold header tamper-resistant T-20 Torx recess panhead punch pin (above).

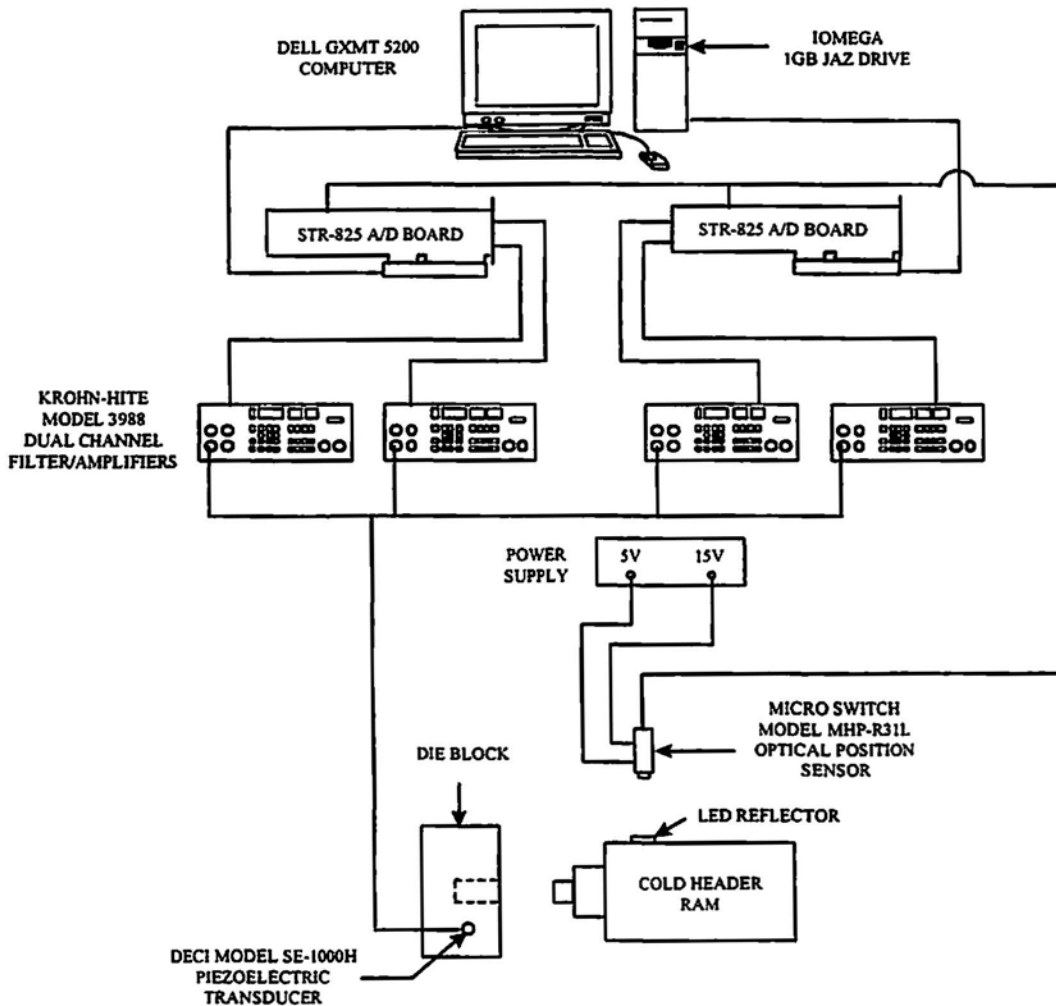


Fig. 2 Hardware components for the four channel data acquisition system.

cases an abrupt change in the condition of the cold header, which can not be detected by the operator in time to prevent poor quality parts from being produced.

A common quality control method used to decrease the risk of unrecognized punch pin fracture consists in placing part count limits on the life of the punches based on previous failure rates. However, the number of parts produced before failure of the punch pin varies considerably for different runs; therefore, the part count limit must be set at very low percentages of the maximum attainable life. While part limits do prevent a large quantity of out-of-tolerance parts, the premature replacement of the punch pin results in significant unrealized production along with increased machine downtime. In an attempt to prevent poor quality parts from leaving the manufacturing facility, the sequential batch containment is also common practice in industry; here, a bin is placed at the cold header exit chute which collects parts as they are produced. The operator periodically checks the quality of the part by verifying its critical dimensions; if the critical dimensions are within tolerance, the operator empties the bin into a finished part container. If the sampled parts do not meet specifications, the machine is shut down, and the parts contained in the bin are scrapped.

Current on-line machine condition monitoring methods attempt to determine when changes occur in the quality of either the part being produced or the production machine during operation. However, current methods are only partial successful in detecting complete fracture of the punch pin, and a high incidence of false calls is observed which leads to unacceptable excessive machine down time (Reis and Cook, 1997; Reis and Voegle, 1997). This paper presents a potentially robust, real-time cold header machine condition monitoring methodology that would allow the production of out-of-tolerance parts due to punch pin fracture to be detected before the parts exit the cold header. Because the punch pin used in the second punch fails more frequently than the punch pin used in the first punch, failure of punch pin during the second punch is the main cause of out-of-tolerance parts. As a consequence, monitoring the condition of the punch pin during the second punch is the primary goal of this paper. The proposed methodology has the potential to monitor the cold heading machine process condition, and automatically stop the manufacturing process at the moment of incipient failure.

2. Experimental Procedure

Figure 2 shows the developed four-channel data acquisition system (Reis and Cook, 1997). The main components of the system include a directional piezoelectric transducer (DECI, Model SE-1000H), four eight-pole dual-channels filter/amplifiers (Krohn-Hite Model 3988), two dual-channel data acquisition A/D boards (SONIX, STR-825), an optical trigger, a personal computer, and a remov-

able hard drive. The SE 1000-H directional transducer exhibits slightly resonant response characteristics near 7 kHz, and has a relatively flat response from approximately 10 kHz to 250 kHz. The transducer was mounted to the cold header die block. The transducer output signal was divided into the four channels of the data acquisition system. Four eight-pole filter/amplifiers (Krohn-Hite Model 3988) were used to independently adjust the bandpass filtering and the necessary amplification on each data acquisition channel, as shown in Table 1.

An optical sensor (Micro Switch Model MHP-R31L), mounted on the cold header frame near the moving punch, was triggered using a reflective tape strip mounted to the moving punch ram. The sensor mounting-bracket was adjustable to allow the time between the initiation of the sensor output signal and the physical contact of the punch with the material blank to be varied. A Pentium personal computer, equipped with an IOMEGA internal 1GB JAZ drive, was used.

The software for the four-channel data acquisition system was also developed; it included in a command menu, which among other options, allowed the user to independently configure the parameters for the two A/D data acquisition boards. From all the collected files, the percentage of files saved permanently from the first portion of the test run depended on the total number of files collected for the run. If fewer than 400 files were collected, all of them were saved permanently. If more than 400 but less than 3,000 files were collected, the final 400 were saved sequentially but only every other file of the remaining files was saved. If more than 3,000 but less than 6,000 files were collected, only every third file was saved. If more than 6,000 but less than 1,000 files were collected, only every fourth file of the remaining files was collected. If more than 10,000 but fewer than 15,000 files were collected, only every sixth file of the remaining files was saved. This progressive scheme allowed data collection runs of varying lengths to be saved in approximately the same storage space, yet containing the vital information recorded at the end of each test run near the location of the cold header condition variation, including failure of the punch pin. For an in-depth description of the data acquisition system, the reader is referred to references (Reis and Cook, 1997; Reis and Voegle, 1997).

The tests were conducted during production runs of the panhead tamper-resistant Torx fastener, see Fig. 1. The production runs had an average production rate of 2.97 parts per second. Eight production runs were monitored regarding the condition of the cold header including failure of the punch pin used during the second punch (Reis and Cook, 1997; Reis and Voegle, 1997). The parts manufactured during these runs were characterized as well as the time of failure of the corresponding punch pins used during the second punch; complete fracture of the punch pin was

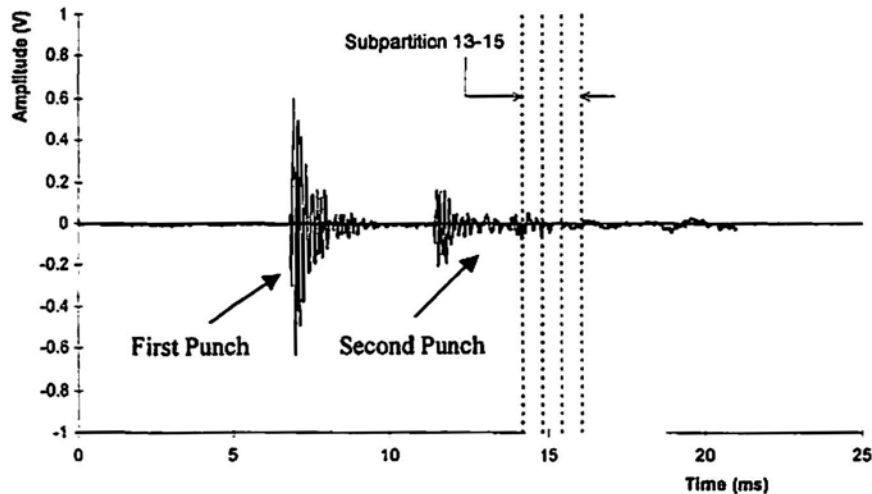


Fig. 3 Location of 128 point time domain sub-partitions 13, 14, and 15 in the first channel for the typical impact sound waveform.

observed during six production runs, and partial failure of the punch pin was observed during two production runs.

3. Experimental Results and Analysis of Data

For each of the eight runs, waveform features were calculated for the waveforms stored in each of the four channels (one waveform per channel) using a time-based partitioning scheme as shown in Fig. 3. For the first and second channel, twenty partitions of 128 points long were used while, because of their higher sampling rate, channels three and four only used the last twelve partitions. A total of 289 waveform features per time domain sub-partition were calculated in the time, frequency, cepstral, auto-correlation, and cross-correlation domains. Furthermore, the ratios between two features, such as the area under the power spectral density curve, extracted from two time-equivalent sub-partitions from two different channels were also calculated. For a complete list of the waveform features (Wu and Du, 1996; Hay and Chan), the reader is referred to references (Reis and Cook, 1997; Reis and Voegle, 1997). The data was organized into waveform feature trends with each trend containing one waveform feature versus file number, i.e., time.

By plotting the amplitude of a single feature versus time, distinct trends were observed in certain features, which corresponded to changes in the cold header during production runs. However, because of the overabundance of data, an automated procedure was developed to identify waveform features that were sensitive to punch pin failure. For each trend, two regions defined by a starting and ending file number (a file number corresponding to a manufacturing part) were selected based upon the file collected when punch pin failure was detected. A gap of 100 files was placed on either side of the recorded failure point to account

for any delay between actual and detected failure. The regions were defined as three hundred points before and after the failure gap, as shown in Fig. 4. The procedure involved the calculation of the average and the standard deviation for each of the waveform features within the two selected boundaries. The difference between the lower standard deviation and the upper standard deviation boundary was evaluated and used to rank the waveform feature trends; the larger the difference, the easier the detection and the higher the rank (Reis and Cook, 1997; Reis and Voegle, 1997), see Fig. 4. Other changes in the stress-wave feature trends, such as slope changes, were found not to be sensitive to punch failure.

By keeping trends with positive differences in two or more trial runs, the large number of waveform feature trends was reduced to 70. Some of these trends showed large variations during the cold header start up. By eliminating trends that displayed significant start up noise or possessed some type of discontinuity not related to punch pin failure, the list of waveform features was further reduced to twenty; these remaining waveform features consistently showed changes with respect to failure of the punch pin for every trial. The waveform feature trends were then normalized by dividing each of the trend data points by the average of one hundred points collected at the beginning of the corresponding run, i.e., beginning at point one hundred. Several of these trends showed strong linear correlation with each other ($R > 0.90$) indicating a strong linear dependence. Reducing the number of waveform features, β , as input would result in significant computational savings. Four of the twenty normalized feature trends that showed the smallest correlation with each other were linearly combined as shown in equation (1) below:

$$\beta = \tau + \rho + \eta + \kappa - 3 \quad (1)$$

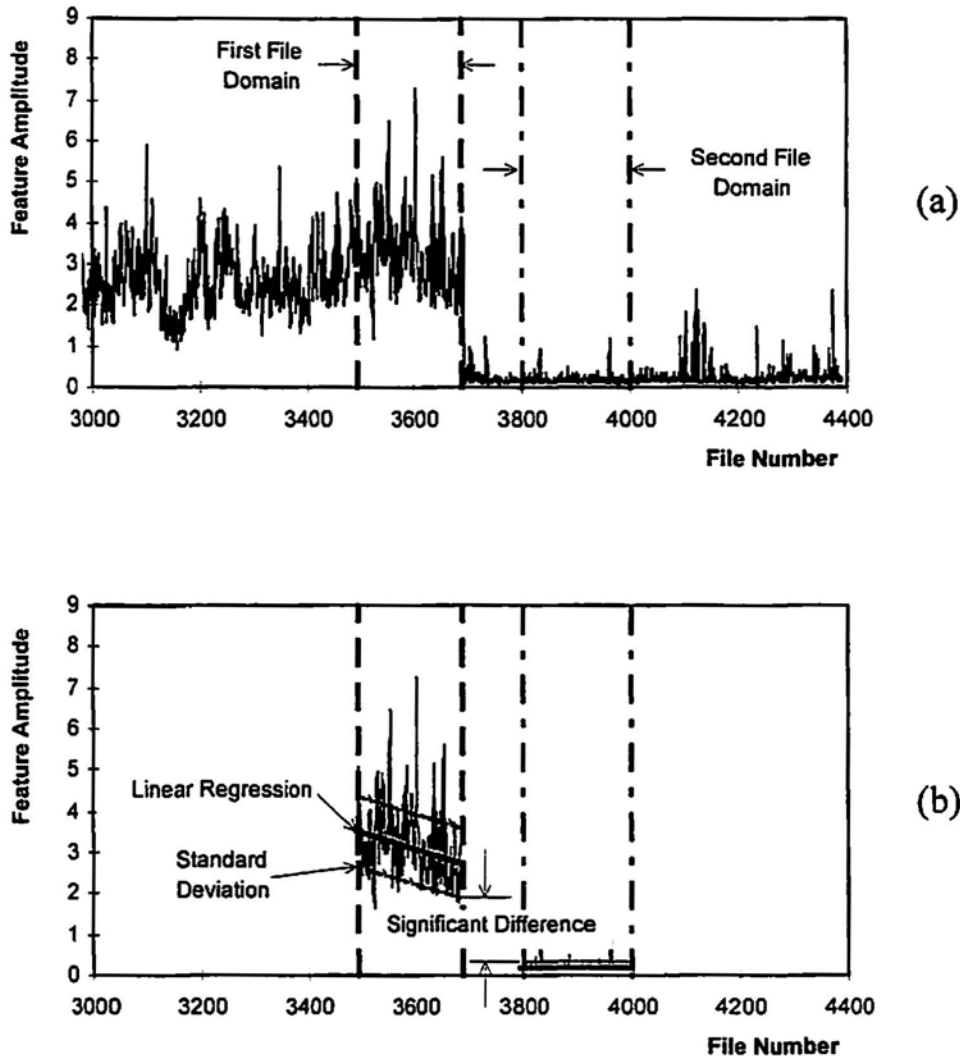


Fig. 4 Parameters for typical automated trend analysis showing (a) file domain regions for trend comparison and (b) significant feature amplitude difference between the two file regions.

In equation (1), τ represents the ratio of the normalized energy in time domain sub-partition 13 for the channels one and two, ρ represents the ratio of the normalized energy in time domain sub-partition 14 for the channels one and two, η is normalized energy in the cepstrum of the time domain sub-partition 15 for the channel one, and κ is the normalized rectified area of the auto correlation of the time domain sub-partition 15 for the channel one.

Figure 5 shows the amplitude variation of the combined waveform feature β as a function of file number, i.e., time, for trial run number eight. Figure 5-a shows the variation of β without any filter being used, and Figs. 5-b and 5-c show the variation of β with a three point and a five point median filter, respectively. These figures show that a distinct change in the amplitude of dimensionless combined waveform feature β occurs with the experimentally observed failure of the punch pin. Similar results were also

observed for the other trial runs (Reis and Cook, 1997). The results shown in Fig. 5 indicate that this procedure has the potential of being used to determine when failure, i.e., fracture, of the punch pin occurs during the operation of the cold header.

This empirical methodology could serve as a simple failure criteria for a single cold heading machine. However, the problem is messy in the sense that the selected waveform feature set will vary for different cold headers, and for each cold header, it will vary for each die/punch combination that are used for different manufactured parts. Therefore, there is a need to develop an adaptive failure criteria methodology for the cold heading manufacturing processes. The monitoring system needs to be automated in order to self-adapt to new cold heading machines that may require different waveform feature trends. In order to provide an adaptive process control, an approach based upon a

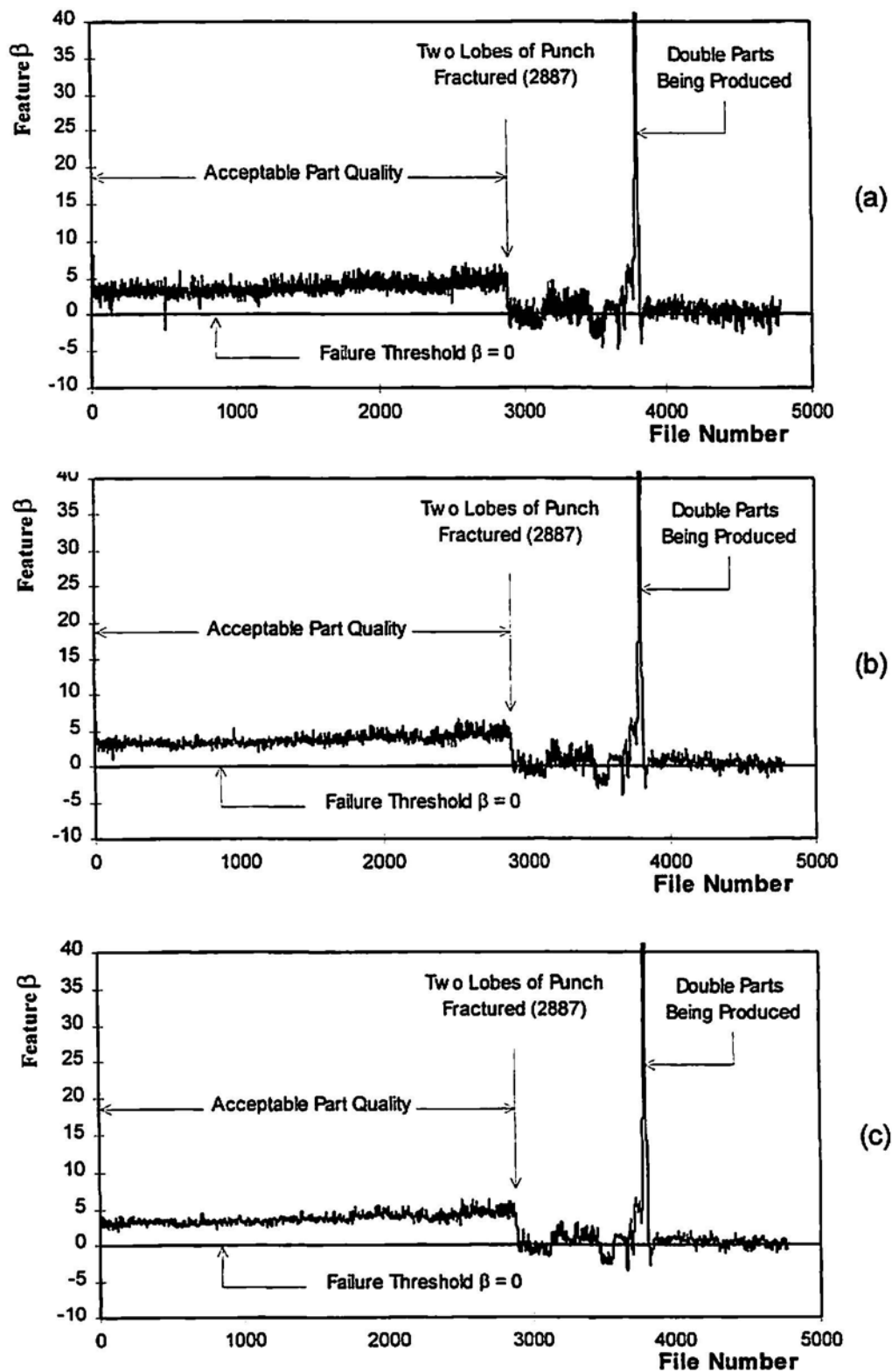


Fig. 5 Feature β for punch test number eight vs. file number with (a) no filter applied, (b) a three point median filter applied, and (c) a five point median filter applied.

genetic algorithm designed neural network monitoring system is proposed (De Jong, 1975; Goldberg et al., 1993; Goldberg, 1996, 1989).

4. The Neural Network Monitoring System

Genetic algorithms are robust search procedures based on the Darwinian principle of natural selection and genetics

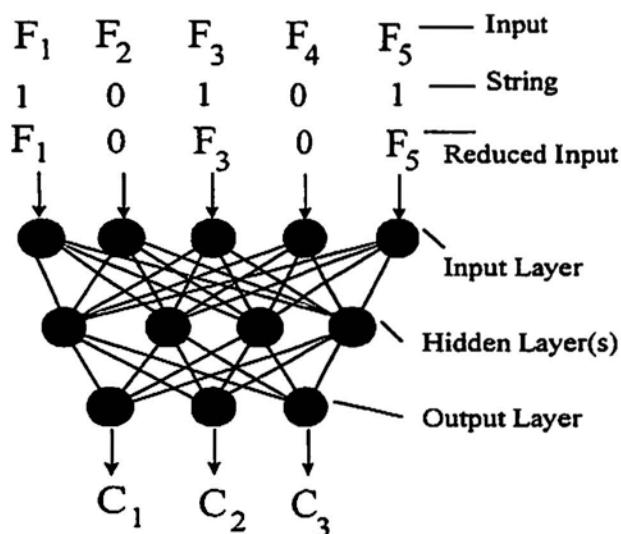


Fig. 6 Neural network and genetic algorithm design interface.

(Goldberg, 1989). Genetic algorithms work by relating binary strings to a performance or fitness estimate (Reis and Voegle, 1997), a single number that summarizes the overall performance of the designed neural network. The first step towards the genetic algorithm designed neural network was to encode the binary strings for the artificial neural network simulation (Wilson and Lehr, 1990; Anon., 1994; Zurada, 1992; Masters, 1994; Hassoun, 1995; Haykin, 1994). To control which impute features were introduced into the neural network, a binary filter mechanism was used as shown in Fig. 6. Using one bit assigned to each waveform feature, a string with a length of twenty bits was used to represent the impute layer structure; to include a feature, the bit was set to one while a setting of zero removed the input. The

filtering, which was carried out by multiplying the input feature vector by the filter vector for each exemplar on each epoch, leads to a reduced input vector which includes only the desired features. While the network contains twenty inputs and all twenty inputs receive a signal, the input nodes of the excluded features receive a zero signal. The hidden layer network input features are then calculated by counting the number of active features. Please note that to use this methodology in other cold heading machine processes, a longer binary string may be needed; the length of the binary string depends upon the waveform features selected by the automated trend analysis to be sensitive to punch pin failure.

The output layer contains three modes, i.e., no failure, partial failure, and complete failure of the punch pin. However, the process monitoring system requires only the evaluation of system failure or non-failure. This was accomplished by output signal filtering. This filtering was accomplished by setting the output of a node to zero if the original output signal is less than 0.65. The level of 0.65 was chosen because if a signal output is below 0.65, the network does not have strong confidence in the classification. Furthermore, a second filtering level uses a five-point minimum filter, which requires a minimum of five failure calls for the system to identify failure of the punch pin. This conservative approach significantly reduces the chances of nuisance shutdowns due to spurious responses. Using a normal production rate of 2.97 parts per second, the network with a five-point minimum filter has an inherent delay of 1.7 seconds; this requires a conveyor belt to provide the necessary delay time between part production and deposit in the collection bins. A relatively small conveyor belt is a small price to pay for nuisance shutdowns (Reis and Voegle, 1997).

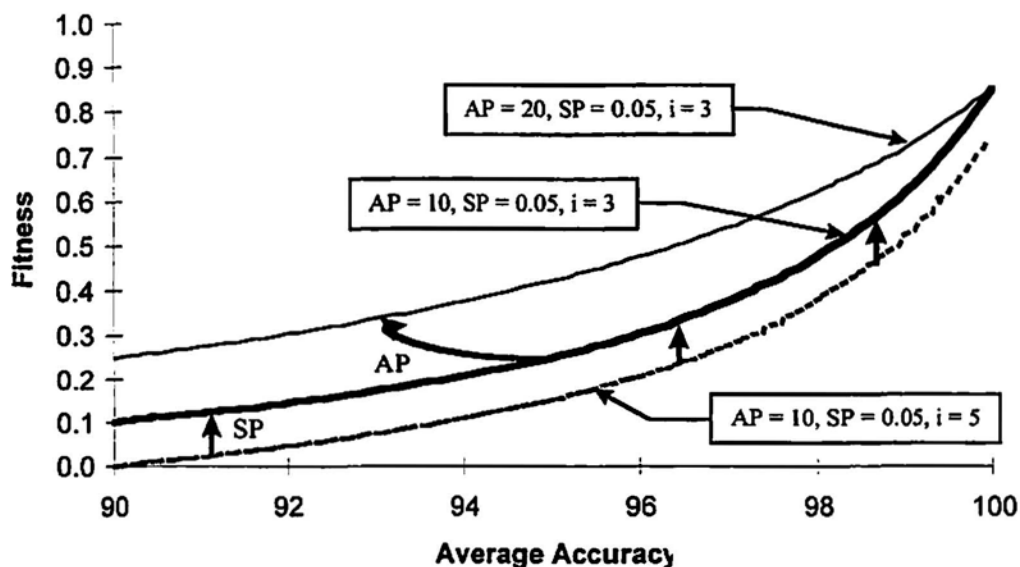


Fig. 7 Accuracy and size penalty relationship.

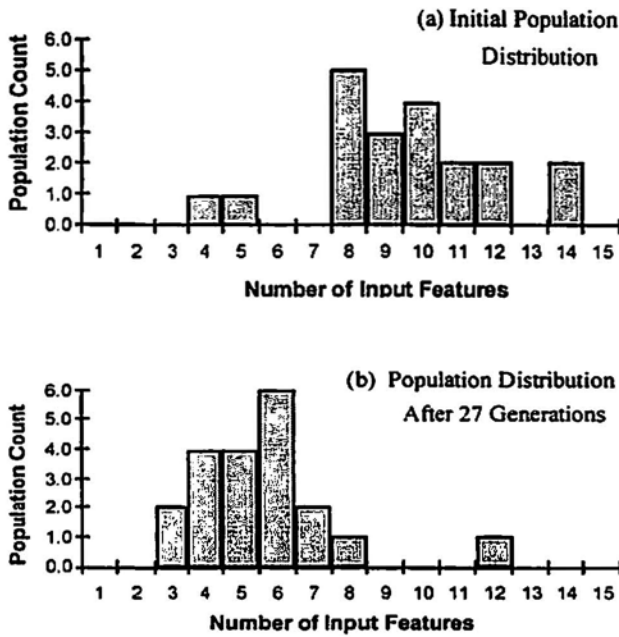


Fig. 8 (a) Initial population histogram; (b) Twenty-seventh generation population histogram.

The main objective of the genetic algorithm search procedure is to select the smallest number of waveform features in the input layer that maintains the required accuracy. Accuracy is evaluated as a direct measure of the percentage of correct calls for each used output class. An accuracy penalty and a size penalty are introduced to allow one performance measure to be balanced against the other. Equation (2) shows the used fitness relationship, where AP and SP represents the accuracy and size penalties, respectively, and the variable “i” represents the number of active inputs to the neural network.

$$f = \frac{AP}{[(AP + 100k) - A_{Class1} - A_{Class2} - \dots - A_{Classk}]} SP(i-1) \quad (2)$$

Equation (2) has two terms; the first term incorporates the accuracy while the second introduces the size of the network. The denominator adjusts to a wide variety of inputs; the first term has a maximum value of one when the input accuracy for each class is 100% and decreases asymptotically to zero. Here, three classes (k=3) were used, namely, no failure, partial failure, and complete failure of the punch pin. The accuracy and size penalties act together in order to balance each other. An accuracy penalty value of 10 and a size penalty value of 0.05 were used in this study, as shown by the middle line in Fig. 7, which shows the effects of the various penalty values on fitness for two different size input sets.

The genetic algorithm was capable of starting with a random initial population and evolving the network designs by striving for constant improvement. Artificial innovation was observed as the algorithm produced neural network

designs with fewer and fewer active inputs. The genetic algorithm process was found to be robust and insensitive to crossover, mutation, population, accuracy penalty, and size penalty parameters, and proved capable of reaching the desired objectives without human intervention. For a better discussion of the genetic algorithm designed neural network the reader is referred to Reis and Voegle (1997).

Figure 8-a shows the initial population histogram created by using a random number generator to assign either the value of zero or one to each bit in every string. Figure 8-b shows the population histogram for the generation number twenty-seventh. Figure 8-b shows that by the time of the twenty-seventh generation, the algorithm has focused on networks with a very small number of active input waveform features. The average number of active input waveform features is about five, with several models attempted a number as small as four or three inputs. The network performance for later generations did not further reduce the number of input features; the algorithm continued to work with similar size distribution of input features (Reis and Voegle, 1997). The early generations provided sporadic and usually poor results; however, as the number of new generations progressed, the number of networks with four and five active features increased, as did the fitness. After twenty-seven generations, see Fig. 8, while there is still variation, the amount present is far less that in earlier generations. The genetic algorithm is able to introduce new combinations that maintain accuracy while requiring fewer input features. For later generations, the genetic algorithm recommended about half of the networks with input feature sets of five waveform features and the other half of the networks with input feature sets of four active waveform features.

In production runs number 6 and 7, complete and partial punch pin fracture, respectively, were observed. Data collected in these runs was used in the neural network training. Two hundred data points corresponding to good part production, i.e., no punch failure, were collected from each of these two runs for a total of four hundred data points and labeled “no failure.” Four hundred data points corresponding to complete fracture of the punch pin were extracted from run number 6 and labeled “complete fracture,” and seven hundred eighty two data points were extracted from run number 7 and labeled “partial fracture.” These class samples were selected randomly throughout the process. Once selected, the data set was combined by randomly sorting the data in the training file, which contained the classification string and twenty possible inputs for each exemplar. The network was able to accurately separate all three classes. Table 2 shows the accuracy resulting from a set of four waveform features used as impute to the neural network. The smaller networks, i.e., networks with four-feature input set, converged quickly and proved to be very stable; the neural network training always converged in fewer than 250 epochs. Several sets of four waveform fea

Table 2 Training accuracy results for the four-feature input set.

	Good Punch	Partial Failure of Punch	Complete Failure of Punch	Accuracy
Good Punch	394	5	1	98.5%
Partial Failure of Punch	6	770	6	98.5%
Complete Failure of Punch	0	2	398	99.5%

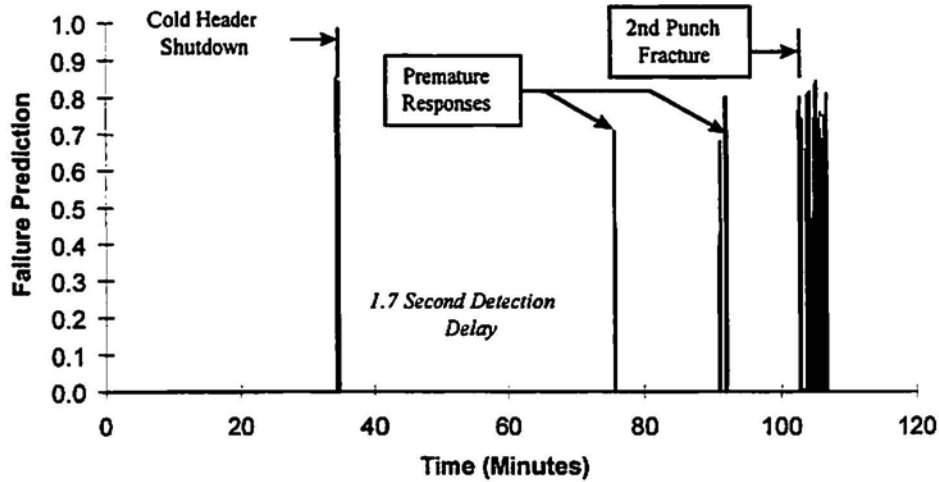


Fig. 9 Evaluation of Trial 1 – Case of complete failure.

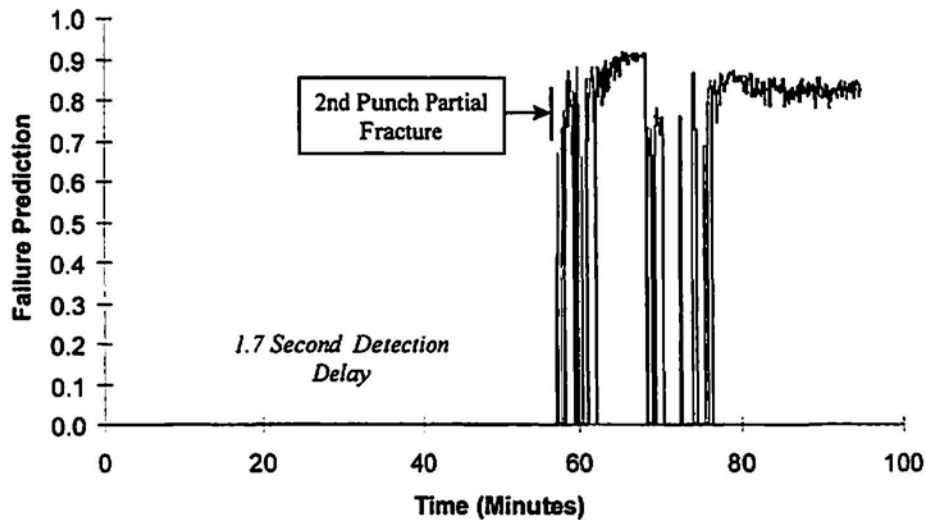


Fig. 10 Evaluation of Trial 8 – Case of partial failure.

tures, including the one used in Equation (1), see Fig. 8-b, worked well for the input of the neural network. All the selected waveform features were extracted from the later portion of the waveform; this strongly points to the conclusion that the critical information occurs in the last half of the second impact punch (Reis and Voegle, 1997).

5. Process Monitoring System Evaluation

The remaining six runs were used to evaluate the neural network. Figure 9 shows the neural network response for the first trial run. There are three failure predictions before the second punch pin actually completely fractured.

The complete fracture was detected 1.7 seconds after it occurred, which is a result of inherent delay in the system due to filtering. While, the premature responses at first glance appear to be false calls by the network, other possibilities exist for these early failure indications. The first failure indication correlates to a shutdown cycle. While the second, third, and fourth early failure predictions do not have any known attributable cause, it is possible that the neural network may be detecting early partial fractures of the punch pin that do not change part performance, but lead to eventual punch failure. The second early failure indication occurs twenty minutes before the complete fracture, and the third, and fourth indications occur only about ten minutes before complete fracture.

Figure 10 shows the evaluation response for trial number eight, when the punch pin partially fractured after a period of time. Figure 10 confirms that the genetic algorithm designed neural network is able to separate the good from the partial failure class. Although the failure prediction is a combined response for both the partial and complete fracture failure, a close examination of the minimum filtered data shows accurate prediction of failure and that the network is capable of differentiate between the two types of failure, i.e., partial and complete failure. Failure of the punch pin for the other production runs was successfully detected with similar performance (Reis and Voegle, 1997).

6. Conclusions

A monitoring system is presented to detect punch pin failure in cold heading machine processes. Four waveform features were linearly combined to provide an accurate and stable failure detection criterion for the punch pin failure in cold heading manufacturing process of a precision fastener. A robust genetic algorithm designed neural network is also presented to serve as the monitoring system. The genetic algorithm designed neural network, using four waveform features as the input layer, also proved to be able to detect both partial and complete fracture of the punch pin for a cold heading machine process. The proposed genetic algorithm designed neural network methodology allows the development of monitoring systems that are adaptable to different cold heading machines as well as different die-punch combinations within the same cold header. It was observed that all the selected waveform features were extracted from the later portion of the waveform, which strongly suggests that the critical information appears in the last half of the second impact punch. The proposed genetic algorithm designed neural network has the potential of being self-adaptable to other cold heading machine processes.

Aknowledgements

The authors would like to acknowledge the support provided by Elco-Textron, Inc. and by Camcar-Textron, Inc.

References

- Anon. (1994), "NeuroSolutions, Manual" vol. I, Version 2.1, NeuroDimension Inc. Gainesville, FL.
- K. Brankamp and T. Terzyk (1996), "Monitoring Forces and Acoustic Emission in Cold Forming," *Wire*, 46(5), 334-335.
- T. Browne and N. Tepovich (1985), "Cold Header Rod: A Quality Approach," *Wire Journal International*, 18(6), 55-61.
- K. Carlson (1987), "More Precision and Variety from Cold Heading," *Machine Design*, 59(18), 99-103.
- T.H. Crum (1996) "Surprising Answers- Results of a Condition Monitoring Program Survey," *Proc. Twentieth Annual Meeting of the Vibration Institute*, Willowbrook, IL. pp. 197-201.
- D.B. Dallas (1980), "New Innovations in Cold Forming," *Manufacturing Engineering*, pp. 96-99.
- S. Ghostline and P. Bebeck (1992), "Inspection Of Ferromagnetic Wire in A Cold Heading Operation," *Wire Journal International*, 25(7), 61-65.
- D.E. Goldberg (1989), *Genetic Algorithms in Search, Optimization, and Machine Learning*, Addison-Wesley Publishing, Reading, MA.
- D.D. Goldberg, K. Deb, and D. Thierens (1993), "Toward a Better Understanding of Mixing in Genetic Algorithms," *Society of Instrument and Control Engineers Journal*, 32(1), 10-16.
- D.E. Goldberg (1996), "Toward a Mechanics of Conceptual Machines," *Proc. Eighteenth Southeastern Conf. on Theoretical and Applied Mechanics*, vol. 18, pp. 1-9.
- M.H. Hassoun (1995), *Fundamental of Artificial Neural Networks*, MIT Press, Cambridge, MA.
- R.D. Hay and R.W.Y. Chan (1993), "ICEPAK Intelligent Classifier Engineering Package Theory of Operations," Techtrend International Inc., Montreal, Quebec.

S. Haykin (1994), *Neural Networks: A Comprehensive Foundation*, Macmillan, New York, NY.

De Jong, K. A. (1975), "An Analysis of The Behavior of a Class Of Genetic Adaptive Systems," *Doctoral Dissertation*, University of Michigan, dissertation Abstracts International, 36(10), 5140B, University Microfilms No. 76-9381, Ann Harbor, MI.

T. Masters (1994), *Advanced Algorithms for Neural Networks: A C++ Sourcebook*, John Wiley and Sons, N.Y.

H.L.M. dos Reis and D.B. Cook (1997), "Real-Time Tool Condition Monitoring in Cold Heading Processes Using an Acoustic Approach," Technical Report UILU ENG 97-3003, University of Illinois at Urbana-Champaign, Urbana, Illinois.

H.L.M. dos Reis and A.C. Voegle (1997), "Cold Header Process Monitoring Using a Genetic Algorithm Designed Neural Network Approach," Technical Report UILU ENG 97-3004, University of Illinois at Urbana-Champaign, Urbana, Illinois.

T. Terzyk and F. Opper (1996) "Force And Acoustic Monitoring in Cold Forming," *Wire Industry*, 63(752), 622-623.

B. Widrow and M.A. Lehr (1990), "30 Years of Adaptive Neural Networks: Perceptrons, Madaline, And Backpropagation," *Proceedings of the IEEE*, 78(9), 1415 - 1442.

Y. Wu and R. Du (1996) "Feature Extraction and Assessment Using Wavelet Packets for Monitoring of Machine Processes," *Mechanical Systems and Signal Processing*, 10(1), 29-53.

J.M. Zurada (1992), *Introduction To Artificial Neural Systems*, West Publishing, New York, NY.

42nd AEWG Meeting

strategy for analysis/interpretation goals can then be described based on the monitored values. Details of this monitoring strategy are subject to change. From here, more realistic simulations are to be performed. Temperature, fatigue and vibration tests are currently underway. Scheduled first in-flight use is the first X-38 re-entry flight in the year 2001.

Nondestructive Evaluation of Radial Track Tires using AcoustoUltrasonics.

Henrique L. Reis, Nondestructive Testing & Evaluation Research laboratory (No abstract available)

Laboratory Scale Testing in AE. Richard Nordstrom, Vallen-Systeme GmbH

Whereas specimens and loading rigs have been developed specifically for studying elasticity and fracture properties of materials in the laboratory, most laboratory scale testing in Acoustic Emission use no specialized test, rather they rely on the tests developed for elasticity and fracture mechanics. This is despite the fact that they are designed to characterize altogether different physical properties of materials than the quantities that are important for AE in use: damage indicators, integrity analysis indicators, and the like. There are certain materials tests where single damage mechanisms predominate, here these tests are called single dominant damage mechanism (SDDM) tests. SDDM tests performed on composite materials include tests on model composites (e.g., single fiber fragmentation test, SFFT), single mode fracture tests (e.g., Mode I delamination in the double cantilever beam specimen, DCB), and tests merely developed to study a specific phenomenon (e.g., matrix splitting in static tensile tests on double-edge notched specimens, DEN) or specific parameters (e.g., tensile tests to determine the limiting monotonic strength, LMS). AE from tests beyond coupon testing are considered for comparison. The results of these tests are not analyzed for damage type which is largely determined, but for quantity, progression and variance within each test type. The question of how well each SDDM test can be used to characterize specific types of AE and which features are most desired for an AE analysis within laboratory scale testing will be discussed. How different -choices in laboratory scale testing effect the usefulness of AE results for generalization and scaling will be discussed.

Wavelet-based Acoustic Emission Techniques.

Gary Qi, Department of Mechanical Engineering, University of Memphis

Wavelet transform, introduced in the area of applied mathematics and signal processing in the early 1980's, was applied to an arbitrary square summable real function and transformed into a series of shifted and dilated sum of wavelets. It has been shown to be a powerful tool in all areas dealing with analysis of transient signals. The concept of wavelet analysis has been studied extensively for the past 15 years. Recent research activities have dealt with developments of new wavelet basis, performing fast computing algorithmic transforms, and new applications.

In the study of material fracture behavior, carbon and glass fiber composites (CFR & GFR) are examined- It is found that the exponential constant M value (used to determine the relationship between stress and stress intensity factor) is well correlated with the wavelet level energy compared relatively to the classical fracture mechanics. The conventional and wavelet-based AE techniques are both presented to show the advantage of wavelet-based methods. The results verify that the wavelet-based method better approximates residual strength, using classical fracture mechanics as the base line. Data compression is one of the major applications of wavelet analysis technique. The AE signal is decomposed into different 'wavelet levels. These levels contain information that can be minimized. To achieve the maximum compression ratio, the amplitude-based criterion and signal energy are computed and compared. It is found that the compression ratio can be as high as 7 with the distortion only 0.6% using the thresholding algorithm introduced by the author.

The wavelet analysis is also applied to the failure mode identification of composites. A general trend is observed by investigating the energy distribution of decomposed AE signals. This trend indicates that the energy in the AE signals is concentrated in three levels (levels 7, 8, & 9) representing frequency ranges of 50-150 kHz, 150-250 kHz, and 250-310 kHz, respectively. Furthermore, the energy percentages in these levels are 8%, 15%, and 75%, respectively. These are speculated to be associated with different failure modes of CFR composites. At last, AE body wave attenuation is studied. The wavelet-based method is able to provide the waveform energy distribution. The analysis presents that level approximation energy attenuation is dominated by lower scales, whereas, level detail energy attenuation is dominated by median scales. In summary, the wavelet analysis is powerful tool and it is an effective method to be applied in the acoustic emission area.

Visualizing Acoustic Emission by Visual AE. Jochen Vallen, Vallen-Systeme GmbH (No abstract available)

Prototype Multiplexing System for AE Acquisition. W.H. Prosser, Daniel F. Perey, NASA Langley Research; Edgar F. Scales, Analytical Services and Materials; Michael R. Gorman, Digital Wave Corporation

Over the last decade, advances in waveform based AE instrumentation and Modal AE analysis have led to improvements in AE technology. More accurate source location, and better noise discrimination and source identification are now possible. These advances have resulted in a renewed interest in developing AE for *in-flight* structural health monitoring of aerospace vehicles. AE is being evaluated for a wide range of aerospace vehicles including the X-33 and Reusable Launch Vehicle, F-15, Joint Strike Fighter (JSF), as well as commercial aircraft. For *in-flight* monitoring, these programs have all identified a requirement to significantly reduce the cost, mass, size, and power requirements of AE instrumentation.

To help address this requirement, a prototype AE multiplexing (AEMUX) circuit for waveform acquisition was built and evaluated. This prototype circuit multiplexed the output from eight sensors into two acquisition channels, eliminating the need for six A/D channels. The system was designed such that the eight sensors being monitored formed a linear array. When a trigger event was detected from any one of the sensors, the AEMUX rapidly (< 1 ps) switched, passing the signal from two sensors in the array to the two acquisition channels. The switching was configured so that the two acquired signals were from the sensors on either side of the trigger sensor. The rationale for this was to take advantage of the propagation delay so that the earliest arrivals of the signal are still acquired on each channel. These first signal arrivals are critical for accurate source location. If the signal from the trigger sensor is acquired, which is the case if the trigger sensor was at either end of the array, then the pre-trigger signal arrivals are lost. The AEMUX circuit also identified which channels were acquired with digital encoding on the signals. The location of the source could then be determined relative to positions of the acquired sensor pair and the overall sensor array. This prototype AEMUX system was evaluated using pencil lead break (Hsu-Neilsen) sources on an aluminum plate. It performed as designed providing rapid, low noise, trigger based switching, with encoded channel identification. This multiplexing approach is not limited to linear arrays, but can be easily extended to monitor sensors in planar or three-dimensional arrays. Likewise, the multiplexing ratio is not limited to that of (8:2) used for this prototype, but can be optimized for the application of interest.

Investigation of Auto Sensor Test-Self Test Mode for AE System Performance Verification. James R. Mitchell, Peter Finkle, PAC

An electronic means to determine the performance of an AE instrument has been developed. The technique, known as Auto Sensor Test -Self Test Mode (AST-STM) utilizes a voltage pulse to excite a sensor's crystal and the structure to which the sensor is attached. After excitation, the sensor output is measured. Instrumentation performance, including efficiency of the coupling, can be determined by comparing the waveform duration and energy to minimum values established using a sensor and instrumentation channel that is known to be operating properly on the same structure. The AST-STM method is compared with the pencil lead break method for a variety of sensor frequencies, couplant types, couplant efficiency factors, structural geometry and plate thickness.

Smart Sensors & Instruments for AE Testing. Harold L. Dunegan, Dunegan Engineering Consultants Inc. (No abstract available)

Commercial Presentations

AVAILABLE BOOKS ON ACOUSTIC EMISSION

Journal of Acoustic Emission, Vol. 1 - 3 (1982 - 84) \$ 50 per volume; Vol. 4 - 8 (1985 - 89) \$ 90 per volume;
Vol. 9 - 16 (1990, 91/92, 93-98) \$ 96 per volume (+ shipping of \$8 US/\$11 others per vol.)

Progress in Acoustic Emission IX (1998), The Proc. of the 14th International AE Symp./5th WMAE; \$120 + shipping
Available from **Acoustic Emission Group**, 16350 Ventura Blvd., Encino, CA 91436 USA
Send credit card (Visa/MC) order by FAX to 1-818-990-1686; e-mail: ono@ucla.edu

ASNT NDT HANDBOOK (2nd Edition), Vol. 5, Acoustic Emission Testing (1988)

Eds. R.K. Miller and P. McIntire. 650 pages. \$110.25

Third to Sixth Int'l Symposium on AE from Composite Materials (1989, 1992, 1995, 1998)

Available from Book Dept., ASNT, PO. Box 28518, Columbus, OH 43228. Also call (800) 222-2768.

Third-Fifth Conf. on AE/Microseismic Activity in Geologic Structures and Materials (1982),

(1989), (1991); Eds. Hardy & Leighton. Available from Trans Tech Publications, 16 Bearskin Neck, MA 01966.

ASTM-STP's:

Acoustic Emission, Current Practices and Future Directions (1991), STP-1077.

Acoustic Emission Testing of Aerial Devices and Associated Equipment used in the Utility Industries (1992),
STP-1139. Available from ASTM, 1916 Race St, Philadelphia, PA 19103.

Progress in Acoustic Emission IV (1988), V (1990), VI (1992), VII (1994), VIII (1996),

The Proceedings of the 9th-13th International AE Symposium. These volumes are \$150 plus shipping.

Available from JSNDI, Natsume BLDG No. 5, 4th fl, Kanda Sakumagashi 67, Chiyoda, Tokyo 101 JAPAN

22nd European Conf. on AE Testing, Aberdeen, Scotland, May 1996; Available from Univision, Robert Gordon

University, Kepplestone, Queen's Road, Aberdeen, AB9 2PG, UK; fax (44) 1224 263323

Acoustic Emission -- Training Guide; How to Ensure an Accurate and Valid Acoustic Emission Test,

Jim Leaird, ISBN 1-890545-007, list price \$125. Available through Amazon.com and ASNT.

Short Courses

Acoustic Emission Short Courses for the requirements of ASNT's TC-1A led by Dr. Richard A. Nordstrom will be offered by Acoustic Technology Group. Dates and venues are:

December 6-10, 1999: the Oregon Graduate Institute, Hillsboro (Portland suburb), Oregon.

March 20-24, 2000: Northwestern University Infrastructure Technology Institute, Evanston (Chicago suburb), Illinois.

1999 SUBSCRIPTION RATE

Base rate for one year (combined issues)	\$ 96.00
Add Postage of U.S. - Book rate	\$ 8.00
All others - Surface	\$ 11.00
Western Europe/S. America - Air mail rate	\$ 25.00
All others - Air mail rate	\$ 30.00

For 2000, there will be substantial changes in format and rates. Please see page i of this issue.

VISA and Mastercard orders accepted.

Payment must be in U.S. dollars drawn on a U.S. bank.
Bank transfer accepted. (Account No. 080-03416470) at
California Bank and Trust
San Fernando Valley Office
15250 Ventura Blvd,
Sherman Oaks, CA 91403-3262

One volume of four issues per year. Index included in the last issue. Back issues available at \$50 per volume for

Vols. 1-3, \$90 per volume for Vols. 4-8, \$96 per volume for Vols. 9-16. US surface postage \$8 per volume. For Canada and overseas surface delivery, add \$11 and for air mail, add \$30 per volume (shipping charges will be adjusted for multi-volume order).

All orders should be sent to (or Fax 1-818-990-1686):
[Please note the addition of **PMB** in address. This is a new US Postal Regulation and mails won't arrive without it.]

Acoustic Emission Group
PMB Suite 106, 16350 Ventura Blvd.
Encino, CA 91436 USA

For inquiry through Internet, use the following address:

ono@ucla.edu
Editor-Publisher Kanji Ono Tel. (310) 825-5233
Cover Design Robin Weisz (UCLA Publications)
Production Pace Publication Arts

Publication Date of This Issue (Nos. 1 and 2): 30 September 1999.

Notes for Contributors

1. General

The Journal will publish contributions from all parts of the world and manuscripts for publication should be submitted to the Editor. Send to:

Professor Kanji Ono, Editor - JAE
6531 Boelter Hall, MSE Dept.
University of California
Los Angeles, California 90095-1595 USA
FAX (1) 818-990-1686
e-mail: ono@ucla.edu

Authors of any AE related publications are encouraged to send a copy for inclusion in the AE Literature section to:

Mr. T.F. Drouillard, Associate Editor - JAE
11791 Spruce Canyon Circle
Golden, Colorado 80403 USA

All the manuscripts will be reviewed upon submission to the Editor. Only papers not previously published will be accepted. Authors must agree to transfer the copyright to the Journal and not to publish elsewhere, the same paper submitted to and accepted by the Journal.

A paper is acceptable if it is a revision of a governmental or organizational report, or if it is based on a paper published with limited distribution.

An abstract of about 200 words is needed for Research and Applications articles, while it should be shorter than 100 words for other articles.

The language of the Journal is English. All papers should be written concisely and clearly.

2. Page Charges

No page charge is levied. Twenty-five copies of off-prints will be supplied to the authors free of charge.

3. Manuscript for Review

Manuscripts for review need only to be typed legibly; preferably, double-spaced on only one side of the page with wide margins and submitted in duplicate.

The title should be brief. Except for short communications, descriptive heading should be used to divide the paper into its component parts. Use the International System of Units (SI).

References to published literature should be quoted in the text citing authors and the year of publication. These are to be grouped together at the end of the paper in alphabetical and chronological order. Journal references should be arranged as below. Titles for journal or book articles are helpful for readers, but may be omitted.

H.L. Dunegan, D.O. Harris and C.A. Tatro (1968), *Eng. Fract. Mech.*, 1, 105-122.

Y. Krampfner, A. Kawamoto, K. Ono and A.T. Green (1975), "Acoustic Emission Characteristics of Cu Alloys under Low-Cycle Fatigue Conditions," NASA CR-134766, University of California, Los Angeles and Acoustic Emission Tech. Corp., Sacramento, April.

A.E. Lord, Jr. (1975), *Physical Acoustics: Principles and Methods*, vol. 11, eds. W. P. Mason and R. N. Thurston, Academic Press, New York, pp. 289-353.

Abbreviations of journal titles should follow those used in the ASM Metals Abstracts. In every case, authors' initials, appropriate volume and page numbers should be included. The title of the cited journal reference is optional.

Illustrations and tables should be planned to fit a single column width (87 mm or 3.3") or a double width (178 mm or 7"). For the reviewing processes, these need not be of high quality, but submit glossy prints or equivalent with the final manuscript. Lines and letters should be legible.

4. Review

All manuscripts will be judged by qualified reviewer(s). Each paper is reviewed by one of the editors and may be sent for review by members of the Editorial Board. The Board member may seek another independent review. In case of disputes, the author may request other reviewers.

5. Electronic Media

In order to minimize typographical error, the authors are encouraged to submit a floppy disk copy of the text. We can read Macintosh and IBM PC formats. On the INTERNET, you can send an MS Word file or the text portion to "ono@ucla.edu". This will greatly shorten the time of communication.

6. Color Photograph

We can print color photographs needed to enhance the technical content of an article. Because of the cost, the author is asked to pay \$200 per page.

Contents

Page i	Announcement: New Format for <i>Journal of Acoustic Emission</i>
Page ii	Founding members of GLEA, Grupo Latinoamericano de Emisión Acústica Color plate for Figure 8 on page 9.
Page 1-13	Classification of Acoustic Emissions in Metallic Glasses A. Vinogradov
Page 15-21	Acoustic Emission Characteristics of Soil and Sand in Response to Simulated Root Growth C. Divaker Durairaj, L. Okushima and S. Sase
Page 23-27	Detection of Defects in Gears by Acoustic Emission Measurements N. Tandon and S. Mata
Page 29-36	Acoustic Emission Signals in Thin Plates Produced by Impact Damage William H. Prosser, Michael R. Gorman and Donald H. Humes
Page 37-47	Reflections of AE Waves in Finite Plates: Finite Element Modeling and Experimental Measurements W. H. Prosser, M. A. Hamstad, J. Gary and A. O'Gallagher
Page 49-59	Classification of Acoustic Emission Signatures Using a Self-organization Neural Network Tinghu Yan, Karen Holford, Damian Carter and John Brandon
Page 61-67	Discussion of the Log-Normal Distribution of Amplitude in Acoustic Emission Signals M. I. López Pumarega, R. Piotrkowski and J. E. Ruzzante
Page 69-81	Unsupervised Pattern Recognition Techniques for the Prediction of Composite Failure T. P. Philippidis, V. N. Nikolaidis and J. G. Kolaxis
Page 83-93	Real-Time Tool Condition Monitoring in Cold Heading Machine Processes Using an Acoustic Approach Henrique L.M. dos Reis, David B. Cook and Aaron C. Voegelé
	Conferences and Symposia
Page 14	Meeting Calendar
Page 22-95	42 nd Meeting of The Acoustic Emission Working Group
Page 96	Available Books on Acoustic Emission/Short Courses

An International
Forum For
The AE Science
and Technology

JOURNAL OF ACOUSTIC EMISSION

Vol.17, No.3-4/July-December 1999



Australian AE Testing of Chemical Plant Start-up in lieu of Hydro-test

Endorsed by
AEWG, AEWGI
CARP and
EWGAE

Published by
Acoustic Emission Group
Los Angeles, CA

JOURNAL OF ACOUSTIC EMISSION

Editor: Kanji Ono

Associate Editors: A. G. Beattie, T. F. Drouillard, F. C. Beall and M. Ohtsu

1. Aims and Scope of the Journal

Journal of Acoustic Emission is an international journal designed to be of broad interest and use to both researcher and practitioner of acoustic emission. It will publish original contributions of all aspects of research and significant engineering advances in the sciences and applications of acoustic emission. The journal will also publish reviews, the abstracts of papers presented at meetings, technical notes, communications and summaries of reports. Current news of interest to the acoustic emission communities, announcements of future conferences and working group meetings and new products will also be included.

Journal of Acoustic Emission includes the following classes of subject matters:

A. Research Articles: Manuscripts should represent completed original work embodying the results of extensive investigation. These will be judged for scientific and technical merit.

B. Applications: Articles must present significant advances in the engineering applications of acoustic emission. Material will be subject to reviews for adequate description of procedures, substantial database and objective interpretation.

C. Technical Notes and Communications: These allow publications of short items of current interest, new or improved experimental techniques and procedures, discussion of published articles and relevant applications.

D. AE Literature section will collect the titles and abstracts of papers published elsewhere and those presented at meetings and conferences. Reports and programs of conferences and symposia will also be presented.

E. AE Program and Data Files: Original program files and data files that can be read by others and analyzed will be distributed in CD-ROM.

Reviews, Tutorial Articles and Special Contributions will address the subjects of general interest. Nontechnical part will cover book reviews, significant personal and technical accomplishments, current news and new products.

2. Endorsement

Acoustic Emission Working Group (AEWG), European Working Group on Acoustic Emission (EWGAE), Committee on Acoustic Emission from Reinforced Composites (CARP), and Acoustic Emission Working Group of India have endorsed the publication of Journal of Acoustic Emission.

3. Governing Body

The Editor and Associate Editors will implement the editorial policies described above. The Editorial Board will advise the editors on any major change. The Editor, Professor Kanji Ono, has the general responsibility for all the matters. Associate Editors assist the review processes as lead reviewers. Mr. T.F. Drouillard is responsible for the AE Literature section. The members of the Editorial Board are selected for their knowledge and experience on

AE and will advise and assist the editors on the publication policies and other aspects. The Board presently includes the following members:

S.H. Carpenter	(USA)
D.A. Dornfeld	(USA)
P. Fleischmann	(France)
L. Golaski	(Poland)
M.A. Hamstad	(USA)
H.R. Hardy, Jr.	(USA)
R. Hill	(UK)
P. Jax	(Germany)
T. Kishi	(Japan)
O.Y. Kwon	(Korea)
J.C. Lenain	(France)
S.L. McBride	(Canada)
C.R.L. Murthy	(India)
H. Niitsuma	(Japan)
A.A. Pollock	(USA)
T.M. Proctor, Jr.	(USA)
I. Roman	(Israel)
C. Scala	(Australia)
C. Scruby	(UK)
A. Vary	(USA)
E. Waschkies	(Germany)
M. Wevers	(Belgium)
J.W. Whittaker	(USA)
B.R.A. Wood	(Australia)

4. Publication

Journal of Acoustic Emission is published annually in CD-ROM by Acoustic Emission Group, PMB Suite 106, 16350 Ventura Blvd, Encino, CA 91436. It may also be reached at 6531 Boelter Hall, University of California, Los Angeles, California 90095-1595 (USA). tel. 310-825-5233. FAX 818-990-1686. e-mail: ono@ucla.edu

5. Subscription

Subscription should be sent to Acoustic Emission Group. Annual rate for 2000 and 2001 is US \$104.00 including CD-ROM delivery, by priority mail in the U.S. and by air for Canada and elsewhere. For additional print copy, add \$32. Overseas orders must be paid in US currencies with a check drawn on a US bank. VISA/MC accepted. Inquire for individual (with institutional order) and bookseller discounts.

6. Advertisement

No advertisement will be accepted, but announcements for books, training courses and future meetings on AE will be included without charge.

Modeling of Buried Monopole and Dipole Sources of Acoustic Emission with a Finite Element Technique

M. A. Hamstad, A. O'Gallagher and J. Gary

Abstract

The requirements for dynamic finite-element modeling of the source dynamics and wave propagation of buried acoustic-emission point sources were examined. Maximum permissible source and cell sizes for point sources were determined as a function of the minimum wavelength for frequencies of interest. These wavelengths were calculated from the source rise-times. For both buried monopoles and dipoles, finite-element predictions for both plates and half-spaces were compared with published results obtained from other approaches. The modeled signals were evaluated from the epicenter to a distance of 15 plate thicknesses for plates with a thickness of ≤ 25 mm. The finite-element method provided accurate results and a practical means to analyze finite specimens, unlike most alternate approaches.

1. Introduction

This paper is a third publication validating the use of dynamic finite-element modeling (DFEM) to predict acoustic emission (AE) displacement fields. The first publication (Gary and Hamstad, 1994) reported the experimental validation of an axi-symmetric two-dimensional code; the second (Hamstad et al., 1996) extended the experimental validation to a three-dimensional code. In both of these papers, a short-rise-time surface force was used as the AE source to accomplish an experimental validation. Since, in general, a real AE source is a buried transient dipole, the axi-symmetric DFEM method has been extended to include this more complicated case in this work. First, we examined the necessary resolution and other requirements for convergence of the DFEM results for buried point sources. Then, since it was not easy to carry out an experimental validation, we compared our results with other, previously published, independent analytical results (Scruby et al., 1983; Pao et al., 1979; and Hsu, 1985). Since this effort is to be coupled with an experimental program, the DFEM results generally extend to significant distances from the source (i.e., 15 or more plate thicknesses from the source).

Received 5 November 1999. The authors are affiliated with National Institute of Standards and Technology, Boulder, CO 80303, USA. M. A. Hamstad is also with University of Denver, Denver, CO 80208, USA. This is a contribution of the U.S. National Institute of Standards and Technology; not subject to copyright in the United States.

2. Finite Element Model Summary

Since the model has been discussed previously (Gary and Hamstad, 1994), only its new aspects are fully described here. The DFEM method was based on a leapfrog approximation in time and linear elements in space. Where the specimen configuration involves surfaces, stress-free boundary conditions were used. To model a buried dipole, two closely spaced body forces were applied simultaneously along opposite directions. As a consequence of the finite aspect of the finite-element (FEM) approach, each of these body forces was actually distributed uniformly over a small region. Thus, the dipole was equivalent to two small but finite, simultaneous monopole sources in close proximity. The dipole strength was determined by multiplying the force of each of the equal (and opposite) monopoles by the small distance (dipole spacing) between the centers of the two monopoles. The temporal form of the applied body forces was step-like in nature. The exact time dependence of the step-like loading was a variable that will be described in more detail later. The axi-symmetrical code was used for most of this study since it enabled us to increase the resolution without overwhelming our computing resources.

3. Buried Source Resolution Requirements

Analytical approaches to modeling AE signals usually have not been concerned with the source size since, by definition, the sources are point sources. To compare DFEM results with analytical point-source results, it was necessary to consider the requirements for a finite source to accurately approximate a point source. From the literature dealing with seismology (Aki and Richards, 1980), we found a requirement that the wavelengths of the signals of interest must be much longer than the source dimensions. Another requirement was that the point where the signal is observed must be at a distance D (from the source) that is much greater than the source dimensions (Scruby et al., 1983). In addition, DFEM modeling requires that the cell size must be smaller than the smallest wavelength of interest, and the time step must satisfy a stability condition called the Courant-Friedrichs-Lewy (CFL) condition (Strikwerda, 1989). In our case the CFL condition required the time step to be less than the time required for the bulk longitudinal wave to traverse a single cell. We took the normalized time to traverse a single cell as 1, hence the CFL value must be < 1 .

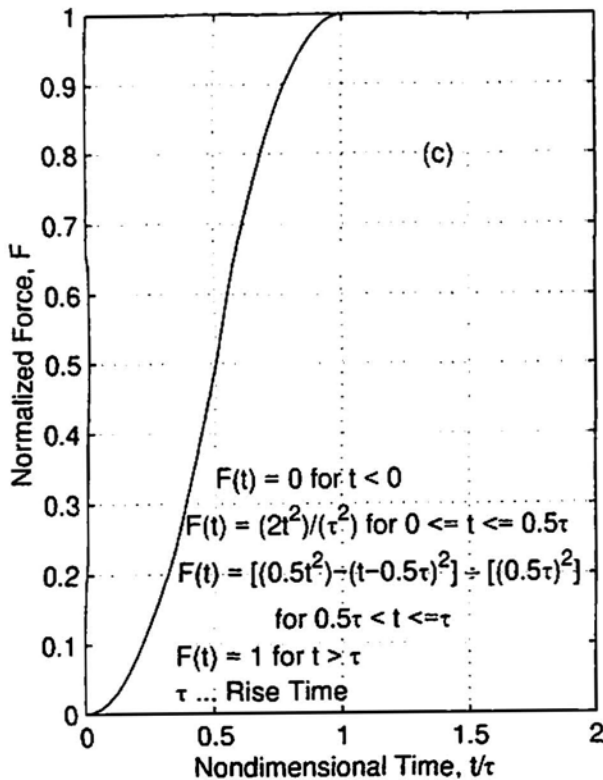
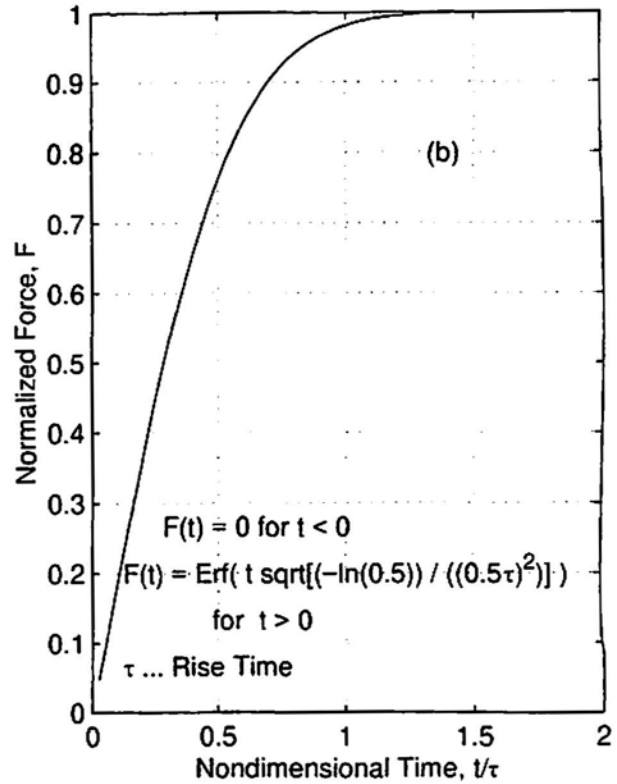
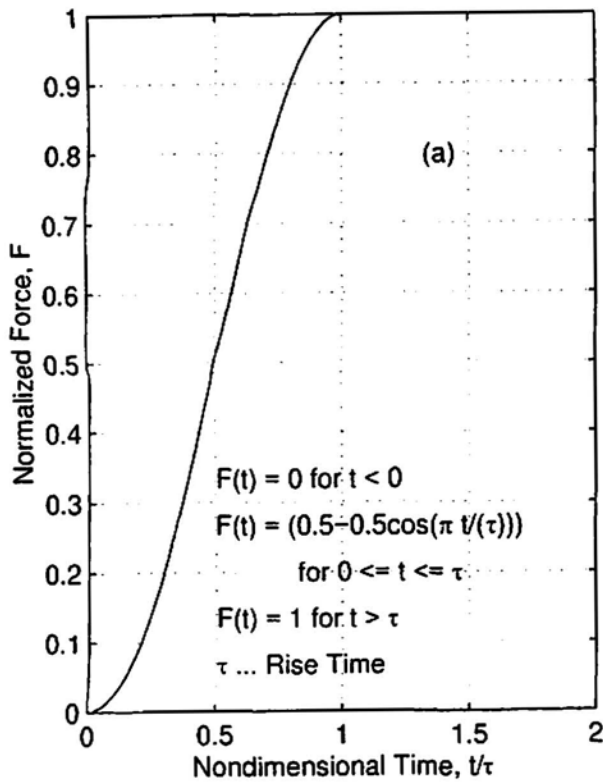


Fig. 1 Source temporal characteristics: (a) "cosine bell", (b) half-width Gaussian, (c) parabolic.

The DEFM requirements for a dipole to be considered a point source are more difficult (assuming limits on computing resources) to meet than those of a monopole because of the increased source size. Hence, our considerations

focus on dipoles. The minimum wavelength (λ_m) is one of the most important parameters, and it must be determined in a consistent manner. We used the equation

$$\lambda_m = c_s / f = c_s \tau, \quad (1)$$

where c_s is the bulk shear velocity, τ is the source rise time, and f is the maximum frequency (taken as the reciprocal of the source rise time). To determine how much bigger than the source size the minimum wavelength must be, we examined the convergence of the DFEM results as a function of the parameter λ_m/s , in which s was the dipole source size. The dipole size was calculated along the axis of the dipole force from the dimension (height) of each monopole (of the dipole) along with the dimension of the cell(s) separating the two monopoles. For these calculations the temporal source function, $T(t)$, was a "cosine bell" given by

$$\begin{aligned} T(t) &= 0 && \text{for } t < 0 \\ T(t) &= 0.5 - 0.5\cos(\pi t/\tau) && \text{for } 0 \leq t \leq \tau \\ T(t) &= 1 && \text{for } t > \tau. \end{aligned} \quad (2)$$

Figure 1 demonstrates this temporal dependence along with other temporal functions that are used later in this work. Figure 2 shows as a function of λ_m/s the normalized peak amplitude (for a constant dipole strength) of the out-of-plane displacement at distances of 1h, 5h and 15h (h is plate thickness) from the epicenter. These are for a midplane vertical dipole in a steel plate 25 mm thick (bulk longitudinal velocity of 5940 m/s; shear velocity, 3220 m/s; and density, 7800 kg/m³). Results at the epicenter, 2h, and 10h were similar and are not shown. The scale for normalized peak amplitude was created by setting the peak amplitude equal to one for the smallest source size. This plot (Fig. 2) is a convenient way to examine the convergence of the DFEM

Table 1 Finite-element parameters for λ_m/s runs with the two-dimensional code.

Cell size (cs), mm	0.031							
$\lambda_m/(cs)$	51.9							
CFL	0.9							
Source rise time, μs	0.5							
Run no.	2506	2505	2499	2498	2268	2278	2492	2493
Source size (s), mm	1.313	0.938	0.75	0.563	0.375	0.281	0.156	0.094
Minimum* D/s	9.5	13.3	16.7	22.2	33.3	44.5	80.1	133
λ_m/s	1.23	1.72	2.15	2.86	4.29	5.73	10.32	17.2

*At epicenter where D = 12.5 mm

Table 2 Finite-element parameters for D^\dagger/s runs with the two-dimensional code.

Cell size (cs), mm	0.031			
$\lambda_m/(cs)$	20			
CFL	0.9			
Source rise time, μs	0.2 (cosine bell)			
Run no.	2510	2509	2508	2507
Source size (s), mm	0.531	0.281	0.156	0.094
λ_m/s	1.18	2.22	4	6.68
D/s	3.78	7.14	12.9	21.4

† The distance D is calculated from the center of the dipole to the epicenter on the surface of the half-space.

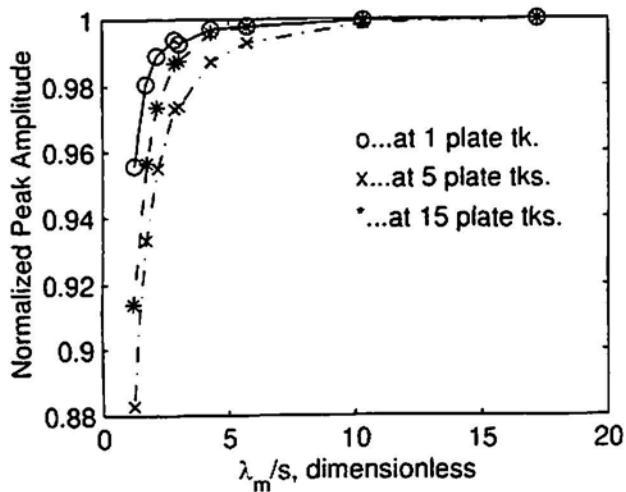


Fig. 2 Normalized peak amplitude of out-of-plane displacement at 15-plate thickness versus λ_m/s for a 25-mm thick steel plate with a midplane vertical dipole.

results as the source size becomes small relative to the minimum wavelength. Table 1 gives other parameters of the DFEM calculations for the "cosine-bell" sources with 0.5- μs rise time. This table confirms (in some cases from numbers determined later in this paper) that the other requirements for DFEM modeling of point sources were met or exceeded. From Fig. 2, the value of λ_m/s required for convergence was determined. We chose a value of $\lambda_m/s \geq 2$, to be satisfactory, even though it leads up to a 5% error in the peak amplitudes. We consider this to be an acceptable

error for DFEM modeling of dipole AE sources for two reasons: first, the peak amplitude error is only 0.5 dB; second, as Fig. 3 shows, the signal for $\lambda_m/s = 2.2$ is very similar to that for $\lambda_m/s = 17.2$ in both its time and frequency domains for 1h and 15h. The similar results at other distances are not shown.

We also examined the requirement that the distance D to the observation point be much greater than the source sizes. In practice, the distance of propagation is almost always much greater than the source size, but for completeness we wanted to establish a specific value for D/s. We chose to examine the effect of the D/s ratio on convergence for the epicenter displacement on a half-space representation that had the center of the vertical dipole source located just 2 mm below the surface. The rise time of the cosine-bell source was reduced to 0.2 μs (to allow us to more clearly distinguish bulk arrivals). Figure 4 shows the normalized out-of-plane peak amplitude of the signal (for constant dipole strength) as a function of the ratio D/s. The normalized peak amplitude scale was created by setting the peak amplitude equal to one for the smallest source size. Table 2 provides a record of other finite-element parameters for these results. This table confirms that the other requirements for DFEM modeling of point sources were met or exceeded. The relevant material constants for aluminum (bulk longitudinal velocity of 6250 m/s, shear velocity 3125 m/s, and density 2700 kg/m³) were used. Figure 5 shows the calculated signals (out-of-plane displacement at the epi-

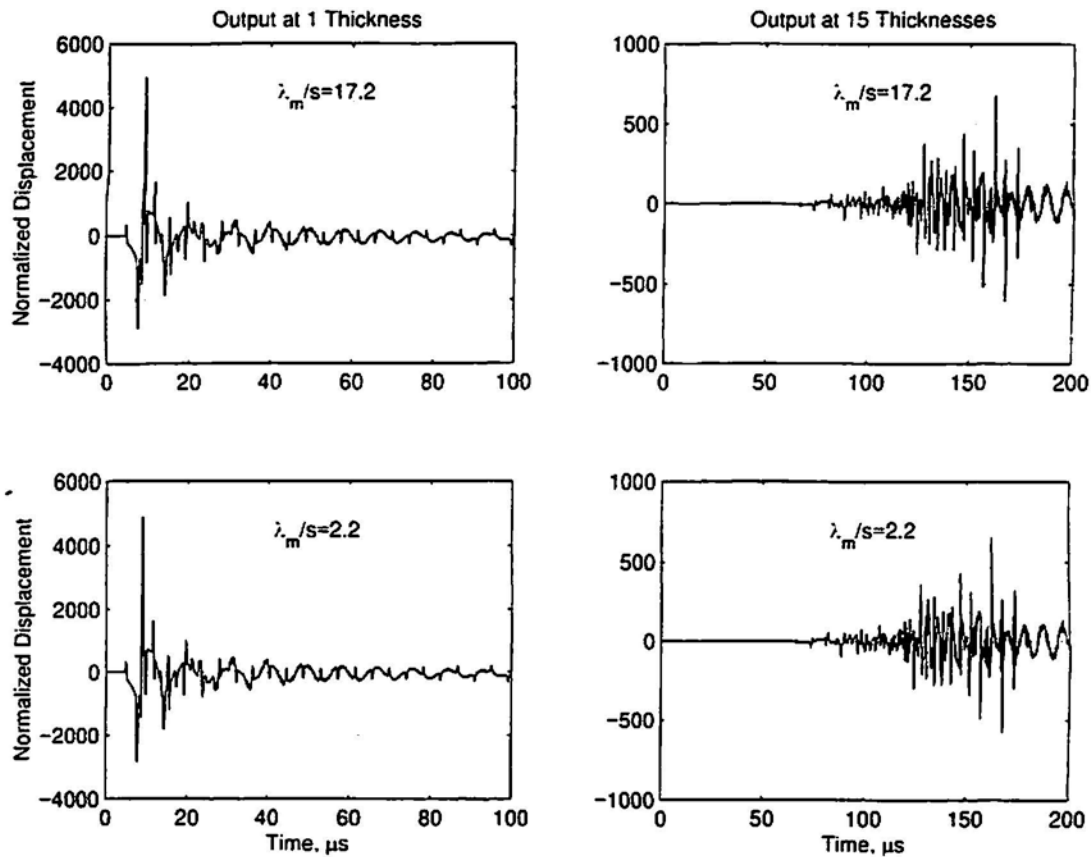


Fig. 3(a) Comparison of normalized out-of-plane displacement signals with $\lambda_m/s = 2.2$ versus $\lambda_m/s = 17.2$. Note the normalized displacement scale has units of $m/(N \cdot m)$, since the displacement has been divided by the dipole strength.

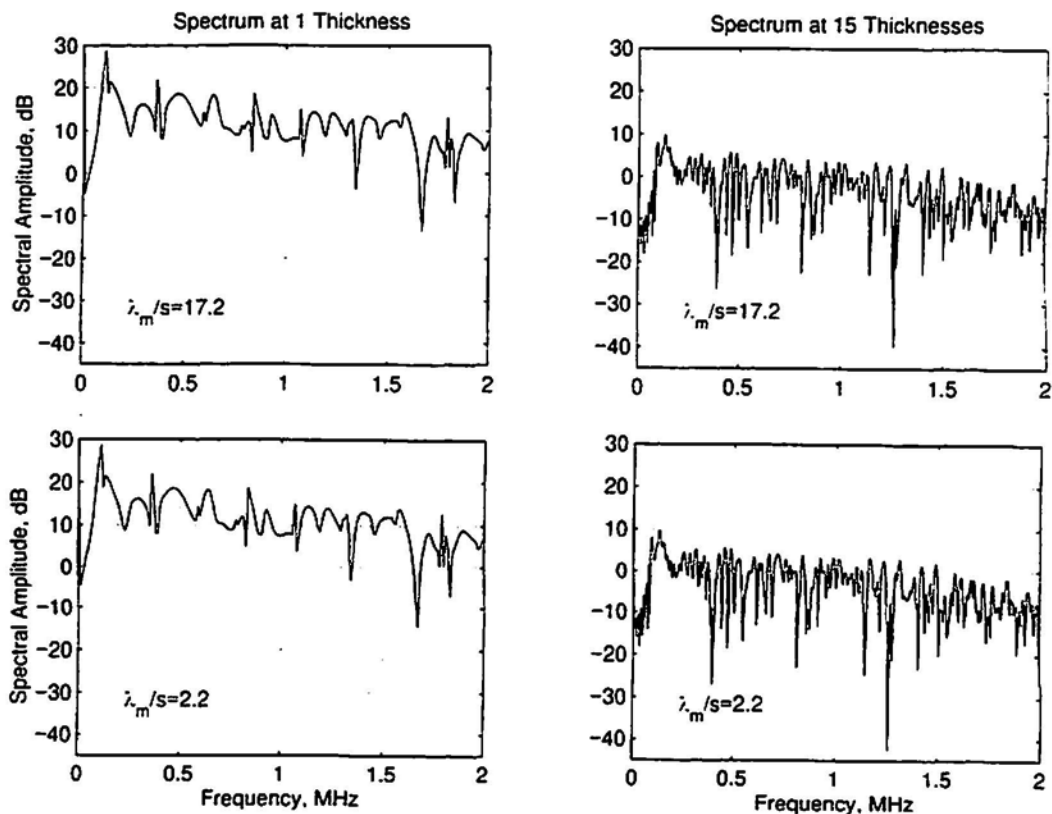


Fig. 3(b) Comparison of the spectrums of normalized out-of-plane displacement with $\lambda_m/s = 2.2$ versus $\lambda_m/s = 17.2$.

Table 3 Finite element parameters for $\lambda_w/(cs)$ "restart" runs except reference high-resolution run no. 2519.

CFL	0.9						
Source rise time, μs	1						
Dipole strength $N \cdot m$	4.2×10^{-2}						
s , mm	0.156						
Minimum* D/s	75.3						
λ_w/s †	20.6						
Run no.	2519	2544	2523	2524	2520	2525	2521
Cell size (cs) ††, mm	0.052	0.104	0.208	0.313	0.417	0.521	0.625
$\lambda_w/(cs)$ ††	62	31	15.5	10.3	7.7	6.2	3.9

* At epicenter when $D = 12.5$ mm.

† Defined by high resolution run number 2519.

†† In lowest resolution region.

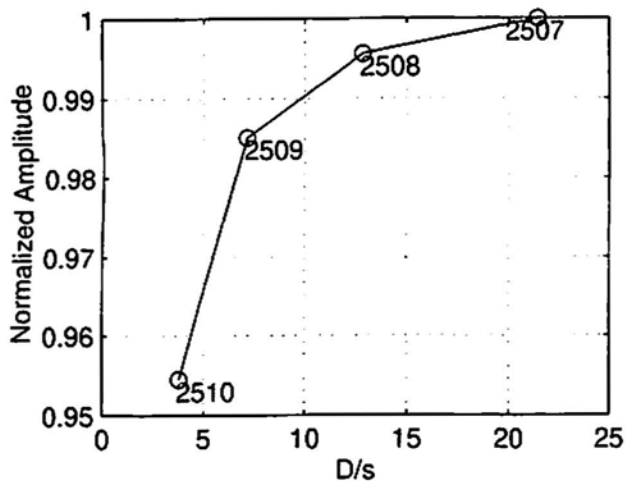


Fig. 4 Normalized out-of-plane peak amplitude at the epicenter versus D/s (run numbers shown).

center) for three of the cases. The vertical scale has been normalized by the dipole source strength to result in units of $m/(N \cdot m)$. The peak amplitude used to create Fig. 4 corresponds approximately to the beginning of a bulk shear wave arrival (See Fig. 2 in Tirbonod, 1992, for a complete discussion). The small "bump" at about $0.5 \mu s$ corresponds approximately to the end of the bulk longitudinal arrival. These arrivals are only approximations due to the presence of near-, intermediate- and far-field terms, all contributing to the displacement field (Aki and Richards, 1980; Tirbonod, 1992) for this model geometry. The reader should note the small degradation in peak amplitude and in the clarity of the initial "bump" in Fig. 5 as D/s decreases. Based on the results shown in Figs. 4 and 5, we chose $D/s > 7$ to be satisfactory for convergence.

The study of convergence of FEM results as a function of the cell size is complicated by the fact that the minimum source size also changes as the cell size changes. What is needed is a way to study the effect of cell size (relative to the minimum wavelength of interest) alone. Due to the range of cell sizes we chose to examine, we could not sim-

ply adjust the number of cells in the source to keep the source size constant. Thus, we used a previously developed technique (Hamstad et al., 1996) based upon two separate two-dimensional code FEM runs in 25-mm thick steel (same material constants as before) plates. In this numerical experiment, we first carried out a high-resolution run for a midplane vertical dipole source ($1 \mu s$, cosine bell) where the requirement for λ_w/s was well satisfied. From the results of this run we extracted the displacements (as a function of time) at an imaginary cylindrical surface in the plate located at a 75-mm radius from the dipole source. Next, we computed far-field results for a series of lower-resolution runs for a cylindrical plate with a disk of 75-mm radius removed from the center. For the lower-resolution runs at each time step, the displacements (u , v) were specified along the vertical boundary at 75 mm by using the results from the first higher-resolution run. Then, the final results from "restarted" (lower-resolution) runs were compared with a higher-resolution run over the entire domain of interest (solid plate with no hole). This comparison of out-of-plane displacement took place at 5h, 10h, and 15h from the source. Figure 6 shows the displacement signals at 15h as a function of $\lambda_w/(cs)$; the cell size (cs) of the lower-resolution domain was used except for the run at higher resolution over the entire domain. The dipole strength was $4.2 \times 10^{-2} N \cdot m$. Table 3 shows relevant finite-element parameters for the runs leading to Fig. 6. This table confirms that the other requirements for DFEM modeling of point sources were met or exceeded. As Fig. 6 shows, a resolution equivalent to $\lambda_w/(cs) \geq 15$ is probably acceptable for AE finite-element modeling since this signal is very close to that with $\lambda_w/(cs) = 62$. Clearly, for $\lambda_w/(cs) = 6.2$ the signal convergence is significantly degraded. The results for 5h and 10h lead to similar conclusions with respect to the required value of $\lambda_w/(cs)$. It is interesting to note how $\lambda_w/(cs) \geq 15$ compares to the $\lambda_w/s \geq 2$ requirement for the case when the dipole is of minimum size (i.e., 3 cells, 1 each for the monopoles with 1 cell space between). In this case, substituting $s = 3(cs)$ results in $\lambda_w/s = 5$, which meets the previously established criteria.

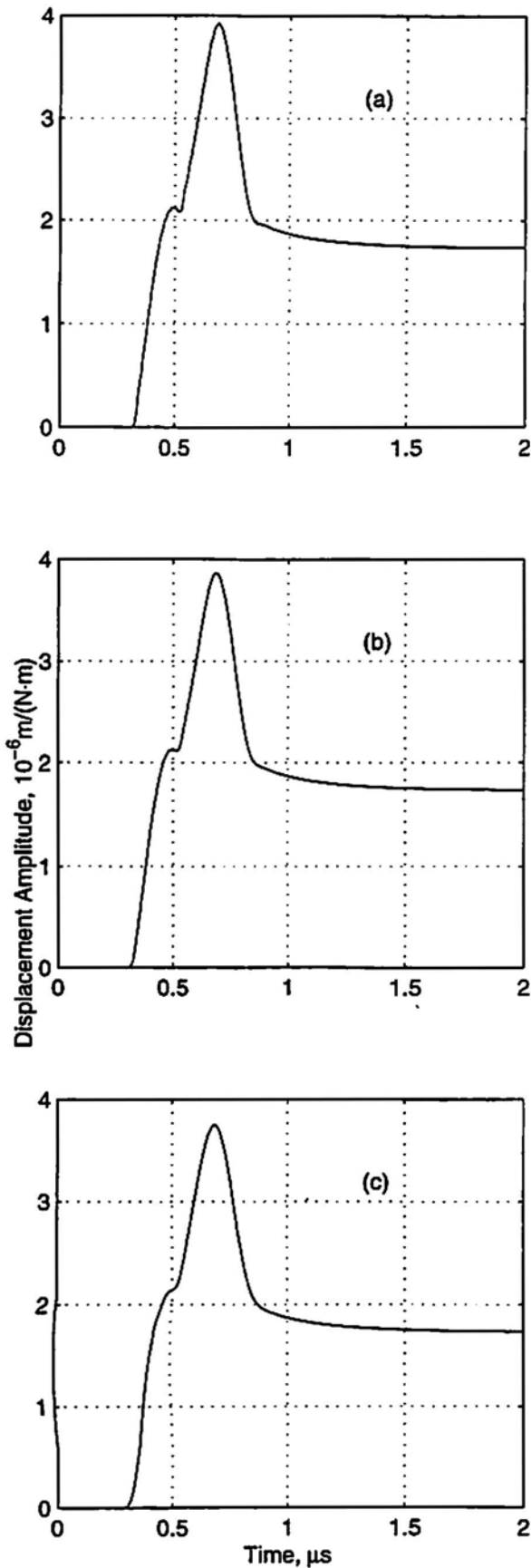


Fig. 5 Out-of-plane epicenter displacement normalized by dipole source strength. D/s equals to (a) 21.4, (b) 7.1, (c) 3.8.

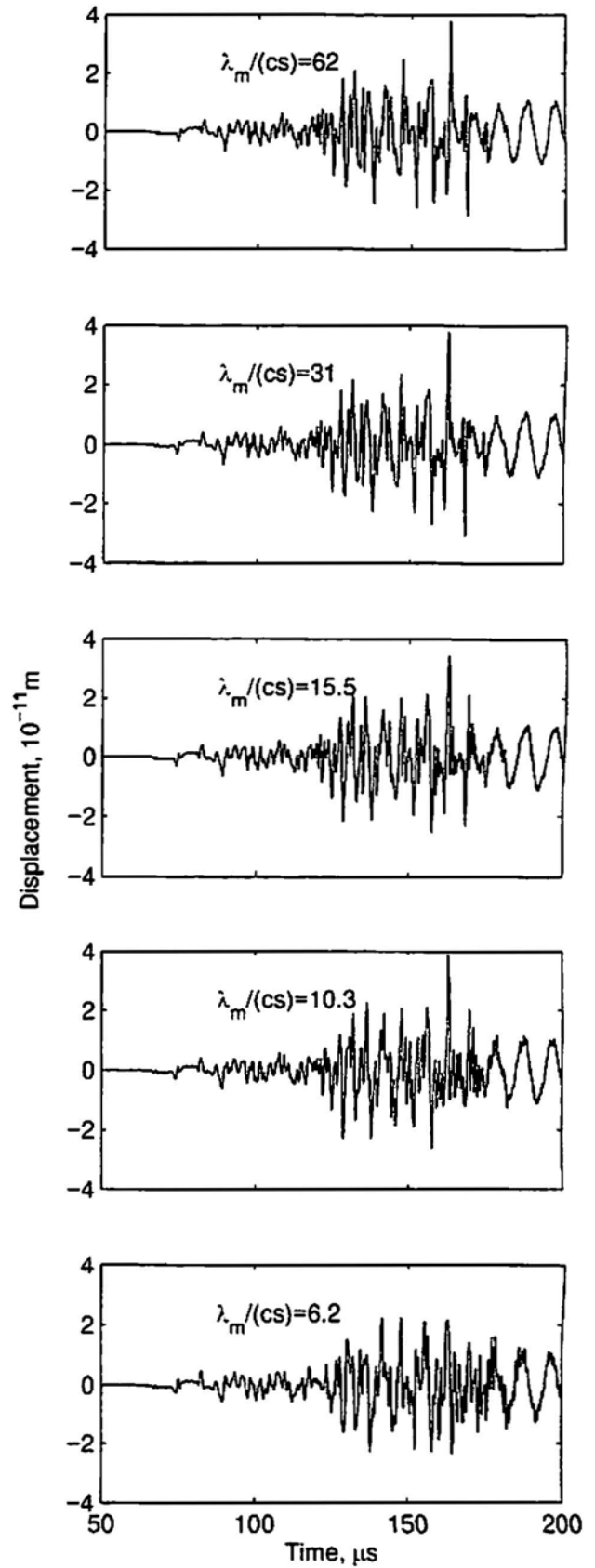


Fig. 6 Comparison of out-of-plane displacement signals at 15h as a function of $\lambda_m/(cs)$ for "restarted" runs. The case for $\lambda_m/(cs) = 62$ is not a "restarted" run. Dipole strength equals $4.2 \times 10^2 \text{ N}\cdot\text{m}$.

Table 4 Conditions of finite-element runs for comparisons with the results of others.

Figure	Run	Rise time, μs	Cell size (cs), μm	Source size (s), μm	Plate thickness, mm	Source location	Longitudinal and shear velocities, m/s
7	2586	0.3	65.1	260.4	25	midplane	5940, 3220
8	2607	0.5	65.1	130	25	midplane	5940, 3429
9	2639	0.03	6.25	43.8	NA*	25 mm below surface	6250, 3125
10(a)	2644, 2645	1	50	200	25	midplane	5940, 3220
10(b)	2643	1	50	500	25	midplane	5940, 3220
11(b)	2646	2.566	66	397	25.4	midplane	5940, 3429

* Not applicable

Table 5 Values of key parameters for the finite-element runs of table 4.

Run	λ_m/s	$\lambda_m/(cs)$	Minimum D/s	CFL	Density, kg/m^3	Shear modulus, N/m^2	Source force, N	Dipole spacing, m
2586	3.7	14.8	192	0.9	7800	8.09×10^{10}	1	NA*
2607	13.2	26.3	385	0.9	7800	9.17×10^{10}	100	NA*
2639	2.2	15	571	0.9	2662	2.6×10^{10}	1	2.5×10^{-5}
2644, 2645	16.1	64	250	0.9	7800	8.09×10^{10}	1	NA*
2643	6.44	64	100	0.9	7800	8.09×10^{10}	1	3×10^{-4}
2646	22.1	133	128	0.9	7800	9.17×10^{10}	1	2.65×10^{-4}

* Not applicable

4. Comparison with Results of Other Approaches

4.1 Buried Monopoles

We used Hsu's code (Hsu, 1985) based on a Green's-function approach to provide one comparison with the DFEM. Results from both models were compared for a vertical monopole AE source located at the midplane of a steel plate 25 mm thick. The source was again a "cosine-bell" shape with a rise time of 0.3 μs . Since such a source could not be modeled directly using Hsu's code, results were obtained from the convolution of the results from a "unit step" calculation (obtained with a 12.5 ns time step) with the first derivative of the "cosine-bell" source function. All the previously developed requirements for the DFEM calculation of a point source were met. Tables 4 and 5 list the parameters for this calculation, identified as Fig. 7, as well as those for other further comparisons. Figure 7 directly compares the out-of-plane displacement of the two approaches at two horizontal distances (measured from the epicenter position) 2h and 5h from the source. In this figure, the normalized displacement, d_n , is given by

$$d_n = \pi d G h / F, \quad (3)$$

where d is actual displacement (m), G is the shear modulus (N/m^2) and F is the monopole force (N). The normalized time, t_n , is given by

$$t_n = t V_s / h, \quad (4)$$

where t (in second) is time and V_s is the shear velocity (m/s).

A second comparison was made with published results (for a plate with a midplane vertical monopole with a step rise-time. Analytical results based on a ray method (Pao et al., 1979) were presented with the restriction that the longitudinal velocity be $\sqrt{3}$ times the shear velocity. The FEM results were calculated with a "cosine-bell" source with a rise time of 0.5 μs . For this rise time, all the necessary DFEM requirements were met for the plate of 25 mm thickness. Tables 4 and 5 list key DFEM parameters for this calculation associated with Fig. 8, which directly compares the out-of-plane (u_z) and in-plane (u_x) displacements at 2h, 4h, and 6h from the source. The ordinate axis was non-dimensionalized by the same expression as equation 3; the abscissa was normalized by equation 4a,

$$t_n = t V_L / h, \quad (4a)$$

where V_L is the longitudinal velocity (m/s).

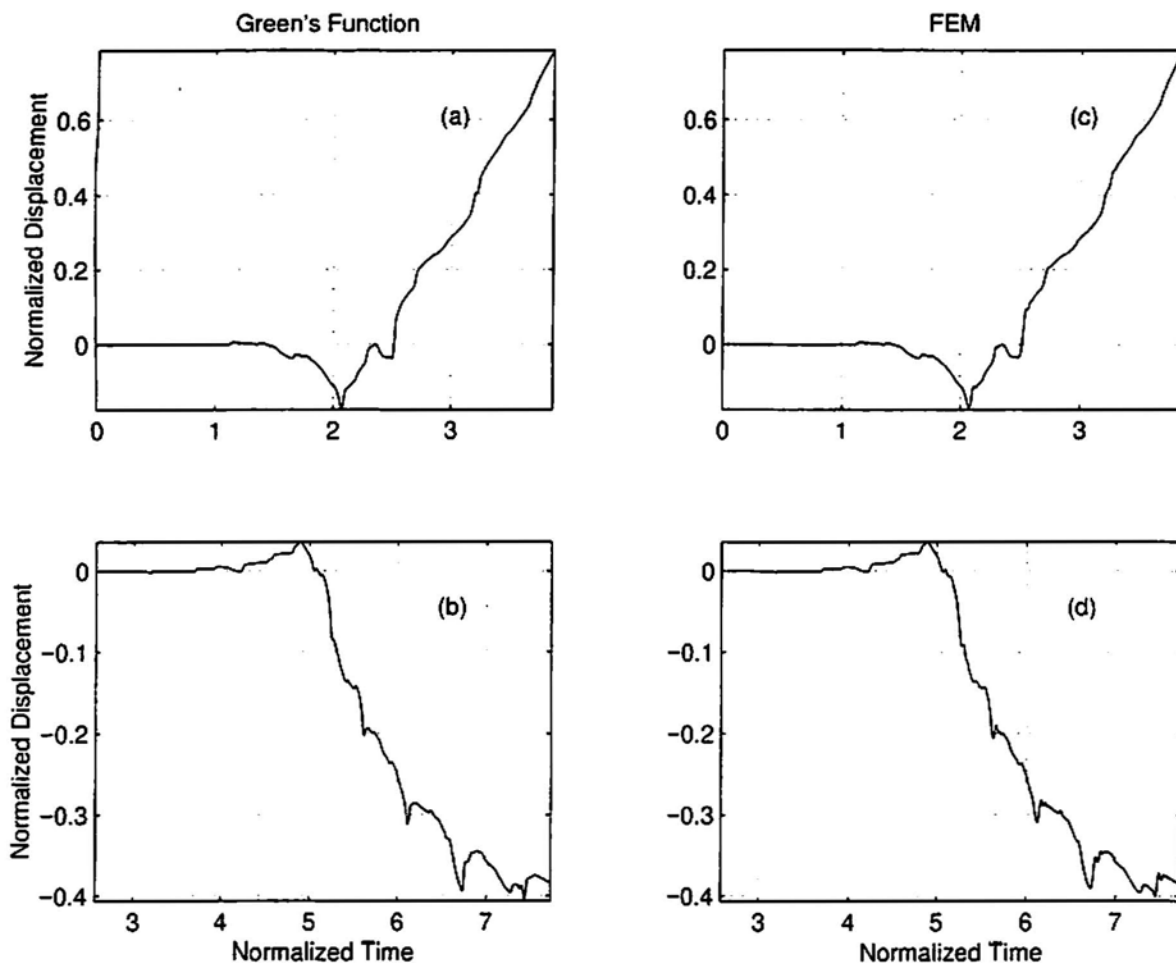


Fig. 7 Buried monopole comparison of out-of-plane displacement signals at 2h and 5h for FEM versus Green's function code (Hsu, 1985). Note (a) and (c) at 2h and (b) and (d) at 5h.

For both cases considered above, the DFEM results clearly match the amplitude and shape of the alternate calculations. For the second case, this result is, at first, surprising since the $0.5\text{-}\mu\text{s}$ rise time does not match the step rise for the other approach. The step rise results were not available in a form that would allow convolution to be performed. However, good agreement was still obtained, as the signals are dominated by the high amplitude of the low-frequency displacement owing to the non-equilibrated monopole force. A better comparison of the two approaches could be made by using a high-pass frequency filter and then comparing the results. Since the step source result is not available in a form that would enable such a comparison, the models were evaluated below for dipoles where the self-equilibrating source forces result in signals without a steady increase in displacement in one direction. Hence, the higher-frequency aspects can be more directly compared.

4.2 Buried Dipoles

Four comparisons were made for buried vertical dipoles where the rise time and shape of the DFEM source were the same as those for the independent approaches as described below. The first comparison was for the out-of-

plane displacement at the epicenter position 25 mm above the $0.03\text{-}\mu\text{s}$ rise time source occurring in a half-space (Scruby et al., 1983). The temporal shape of the source was one-half a Gaussian curve, as shown in Fig. 1b. The DFEM results were calculated with conditions meeting the necessary requirement (see Tables 4 and 5, Fig. 9). Figure 9 shows results that are nearly identical except for a small 2.2 dB difference in peak amplitude. To match the vertical axis in the previously published result, the out-of-plane displacement in μm was divided by the dipole strength in $\text{N}\cdot\text{m}$. The abscissa is real time. The DFEM result was filtered by a 30 MHz (based on the spectrum in Scruby et al., 1983) low-pass six-pole Bessel filter to remove some oscillations due to the very small rise time.

The second comparison was made by using Hsu's code (Hsu, 1985) to form the difference of two vertical monopoles centered about the midplane of a 25-mm thick plate. One monopole was centered at 12.65 mm below the top of the plate and the other at 12.35 mm. (Note that if these two monopoles are viewed as a dipole, then the dipole spacing and the source size are 0.3 mm.) The Green's function for a "unit step" (calculated with a 5 ns time step) of each monopole was convolved with the first derivative of

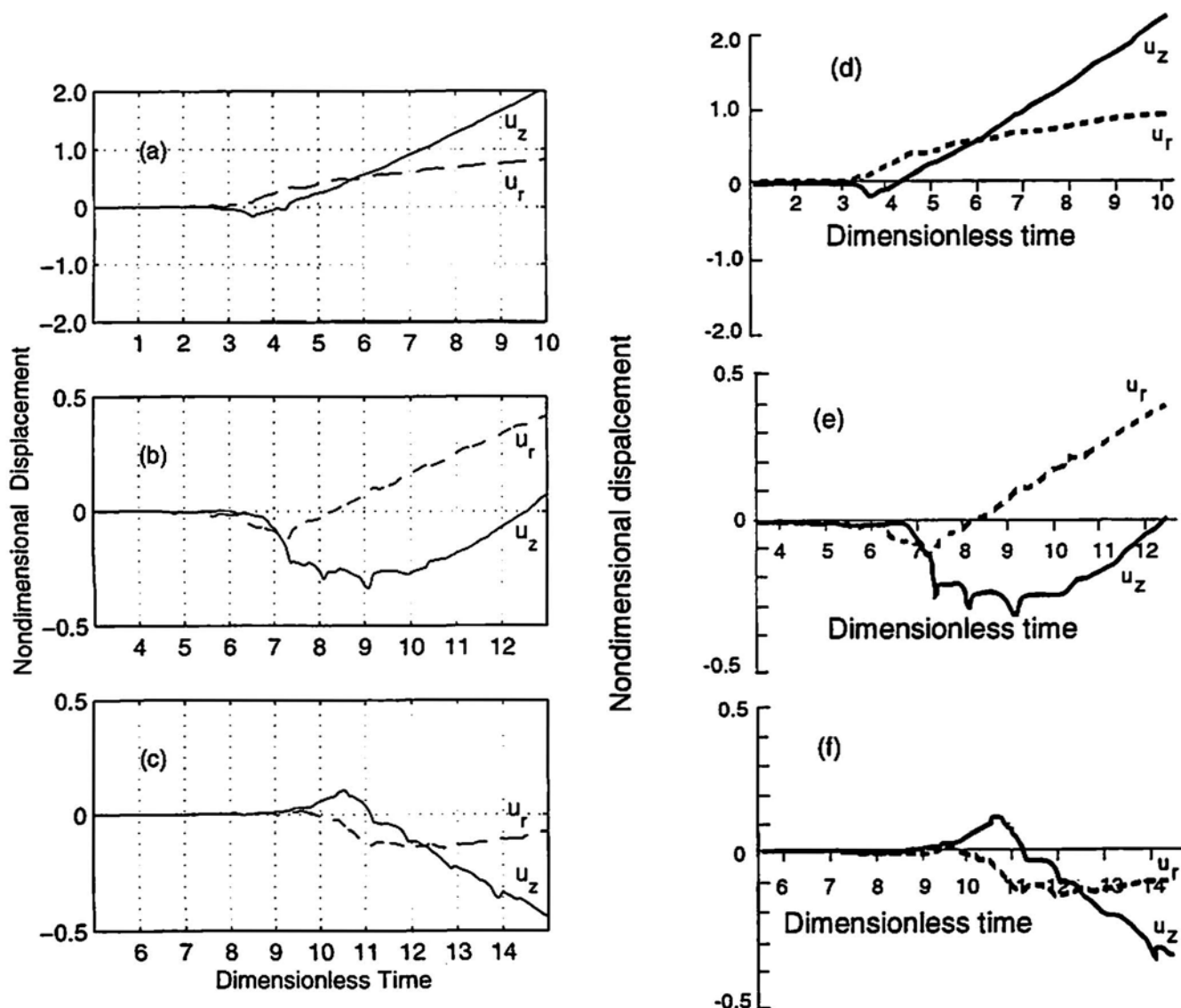


Fig. 8 Buried monopole comparison of both in-plane and out-of-plane signals at 2h, 4h, and 6h (top to bottom) for FEM [(a)-(c)] versus ray-method [(d)-(f)] approach (Pao et al., 1979). Out-of-plane: u_z ; in-plane: u_r .

the "cosine-bell" temporal source with a rise time of $1 \mu\text{s}$. Then, the result for a dipole (strength of $0.3 \text{ N}\cdot\text{mm}$) was obtained by subtracting one convolved monopole result from the other. The corresponding DFEM result was also formed by adding two vertical monopoles (with opposite direction forces and $1 \mu\text{s}$ cosine bell rise time) also centered about the midplane. The FEM calculation satisfied convergence requirements; the parameters are given in Tables 4 and 5 for Fig. 10(a). Figure 10(a) compares the results at 2h. The ordinate axis for results of both the Green's function and FEM methods was normalized by using equation 3 with the plate thickness replaced by the plate thickness squared and the monopole force replaced by the dipole strength (in $\text{N}\cdot\text{m}$). Since the source size for the "summed dipole" was very small, both summed results met the requirements for a point source when the rise time is $1 \mu\text{s}$.

A third comparison used the previously mentioned Hsu's code (Hsu, 1985) for a midplane vertical dipole in a 25-mm thick plate. As in the above case, the rise time was $1 \mu\text{s}$ and the shape was the "cosine bell" function. The result for the dipole was obtained by convolution of the Green's function result for a "unit step" source (obtained with a 5 ns time step) with the first derivative of the "cosine bell" function with a $1\text{-}\mu\text{s}$ rise time. The results are shown in Fig. 10(b) at the same position and with the same material properties as those in Fig. 10(a). The DFEM midplane vertical dipole result shown in Fig. 10(b) met the required convergence properties with the parameters shown in Tables 4 and 5 for Fig. 10(b). The same normalization was used in Fig. 10(b) as was used in Fig. 10(a).

The final comparison was also made for a midplane vertical dipole in a plate. In this case, the rise time was the

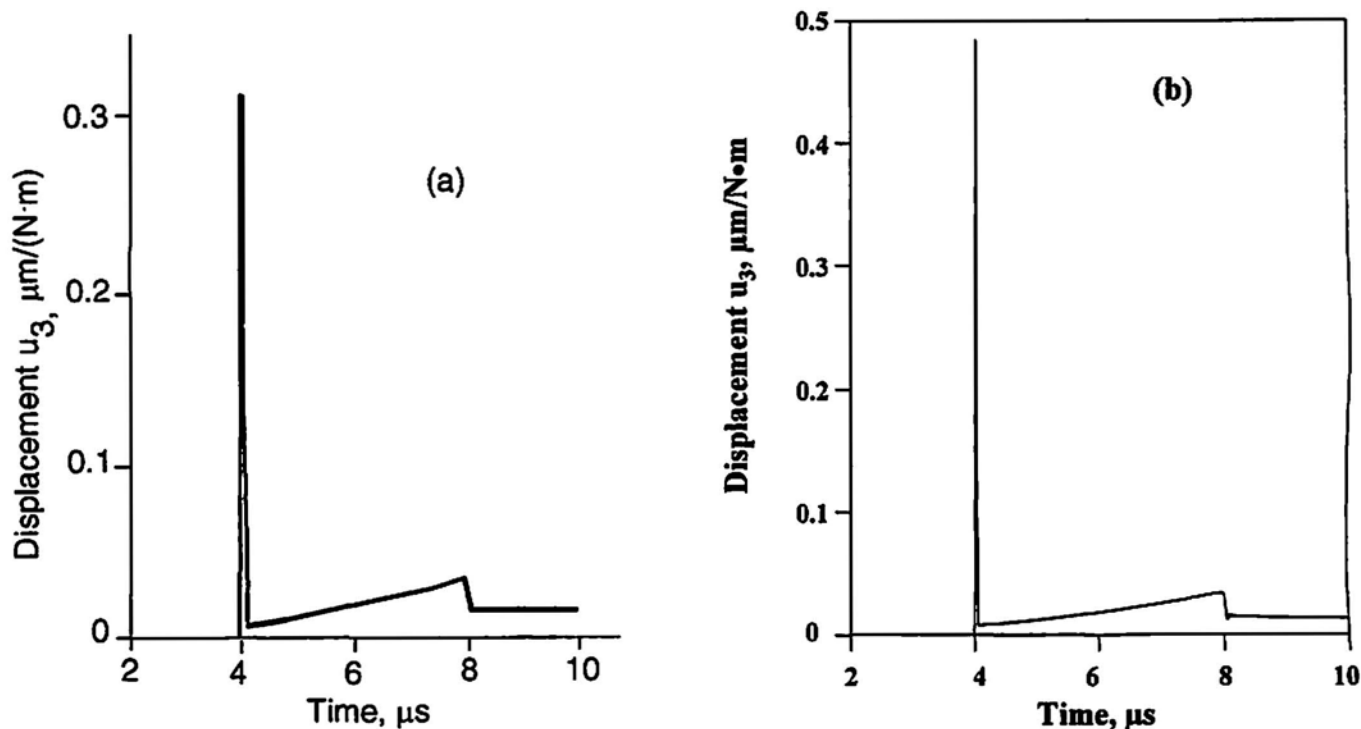


Fig. 9 Comparison of epicenter out-of-plane displacements between (a) alternate approach (Scruby et al., 1983) and (b) FEM approach. Displacement shown is per unit source strength.

"parabolic ramp" (see Fig. 1(c)) originally used in the analytical work (Pao et al., 1979) with a rise time value that corresponds to $2.56 \mu\text{s}$ for the plate thickness of 25 mm used in the DFEM calculation. Again, the calculated DFEM result met convergence requirements with the parameters shown in Tables 4 and 5 for Fig. 11. Figure 11(a) and (b) compare the out-of-plane displacements at 2h, 4h, and 6h positions on the top surface of the plate. The abscissa was normalized by using equation 4a. The ordinate normalization is given by

$$d_n = \pi d G h^2 / F s_m, \quad (5)$$

where s_m is the spacing of the monopoles (m).

Figures 7 through 11 clearly show that the DFEM results nearly match the independent analytical results with two exceptions. In the first of these, the result calculated by using Hsu's code for the midplane dipole does not match the DFEM waveform (see Fig. 10(b)), but the peak amplitude is nearly the same. Upon closer examination of the first part of the displacement (DFEM and Hsu results), we determined that the match was exact until the first direct ray reflection arrived from the bottom plate surface at the point where the displacement was calculated (at $10.68 \mu\text{s}$ in the Hsu result in Fig. 10(b)). The reflected ray displacements differed from the DFEM result in sign. This difference probably leads to the differences observed between the two approaches, as seen in Fig. 10(b). Note that with the DFEM code the effects of reflections are calculated without any

direct code changes regardless of whether the source is a surface force or a buried body force monopole or dipole. Another evidence that the dipole result obtained by using Hsu's code (Hsu, 1985) is not correct is the following: the result of using the Hsu code to calculate a dipole by summing two monopoles does exactly match the DFEM result (i.e., Fig. 10(a) [Green's function] versus 10(b) [DFEM]).

The second case where the DFEM result does not match is the dipole result (Pao et al., 1979) shown in Fig. 11. In this case, the major difference (contrary to that illustrated in Fig. 10) is the scale of the normalized displacement axis. We have not been able to resolve this difference in scale factor. The waveforms match quite closely, particularly at positions near the epicenter. Further from the epicenter, there is a small difference in one region of the waveforms calculated by the two methods. Note that (1) the DFEM result exactly matches the amplitude for the ray approach for a buried monopole (by the same authors Pao et al., 1979, see Fig. 8) and that (2) the DFEM code is the same as that validated previously with experimental results (Hamstad and Gary, 1994; Hamstad et al., 1996).

Recently, another independent study validated the DFEM approach for buried dipoles (Mal et al., 1998). In this case, at 5h, 10h, and 15h, the DFEM and independent results matched both in amplitude and in waveform for a 300 ns "cosine-bell" rise-time source. The match was nearly perfect until shortly after the peak of the AE signal. After

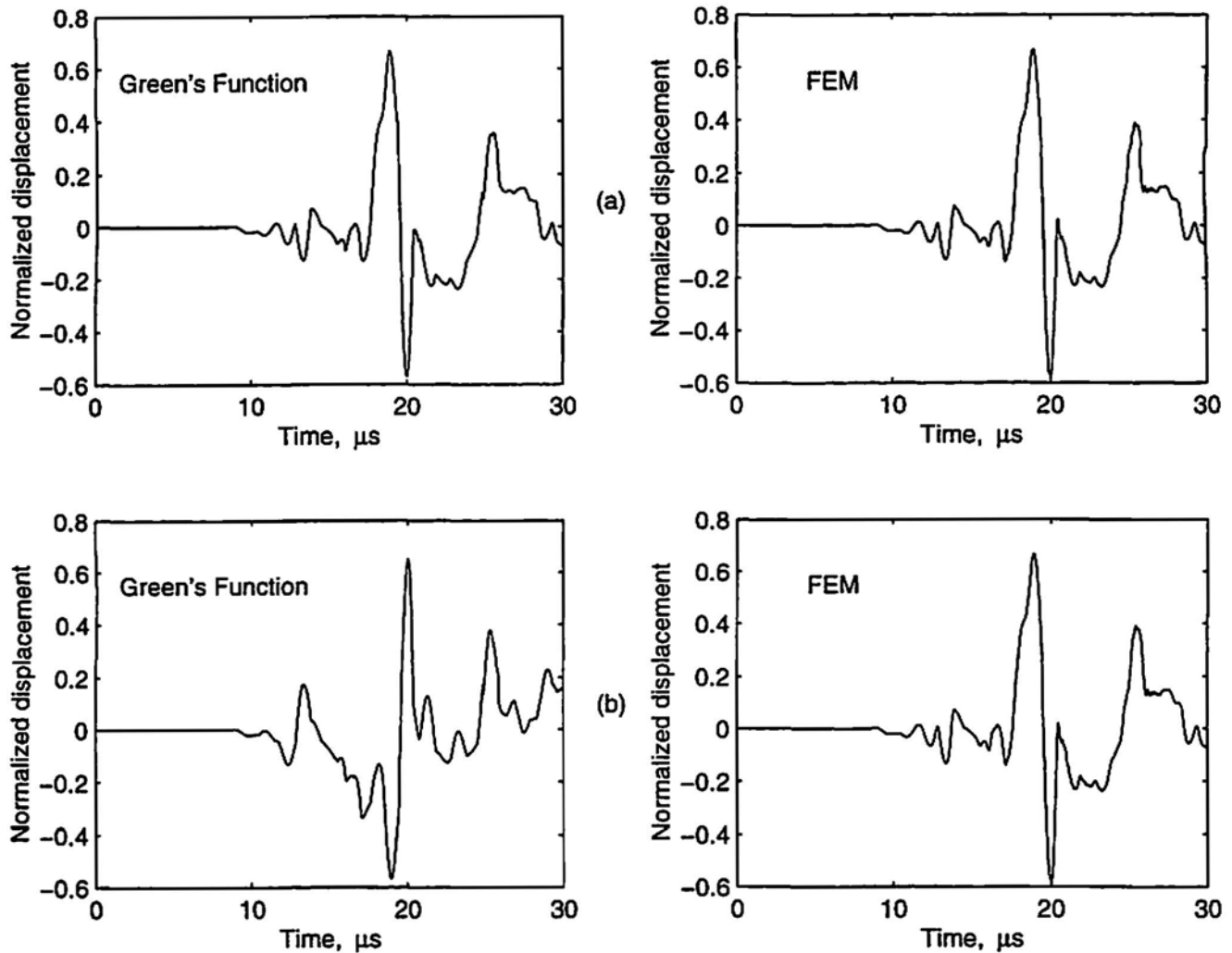


Fig. 10 Midplane vertical dipole comparisons of Green's function approach versus FEM approach. Out-of-plane displacement is shown at 2h for top (a) dipoles formed by summing two monopoles and bottom (b) dipoles.

the peak, the waveforms differed slightly owing to the artificial damping present in the independent approach.

5. Resources Required for Three-Dimensional Modeling

Since in the future we are interested in modeling three-dimensional buried-dipole cases in up to 25.4-mm thick plates out to 15h, we evaluated whether our current computing capability will be adequate to meet the established requirements. For this calculation, we used a 2.3- μ s rise time "cosine bell" source in steel with the same material constants used in Figs. 1 and 2 and our current maximum of 51 cells were distributed across the thickness of a 25.4 mm x 929 mm x 929 mm domain. The out-of-plane displacement was calculated with the three-dimensional DFEM code. Result on the top surface of the plate at 15h is shown in Fig. 12(a), while Fig. 13 shows the geometry for this calculation. We note that this domain is adequate for one quadrant, 0° to 90° of a first quadrant, of the radiation pattern using both the large domain size and a partially effective

non-reflecting boundary condition (Higdon, 1990) to eliminate significant reflections for up to 200 μ s. The displacement shown in Fig. 12(a) is the result along 22.5° radiation angle. The result in Fig. 12(a) was the same as that at 0°, 45°, 67.5°, and 90° radiation angles. These are all in the first quadrant having the source center located at $x = 345.4$ and $y = 345.4$ mm and being 7.7 mm below the plate top surface, except for minor changes from the ideal of 15h (due to constraints imposed by the cell size). Figure 12(b) shows the displacement result at the same position with 408 cells (identical to a 204 cell result not shown) across the thickness for the vertical dipole using the two-dimensional code with a domain radius of 1067 mm about the central source. Looking at two key parameters, λ_w/s and $\lambda_w/(cs)$, we can see reasons for the small difference between those two runs. For Fig. 12(a), λ_w/s is 5 and $\lambda_w/(cs)$ is 14.9; for Fig. 12(b), λ_w/s is 10 and $\lambda_w/(cs)$ is 119. Clearly, the three-dimensional code results could be slightly improved (in the region of the peak amplitude) if the resolution could be increased to 101 cells across the thickness, as shown in Fig.

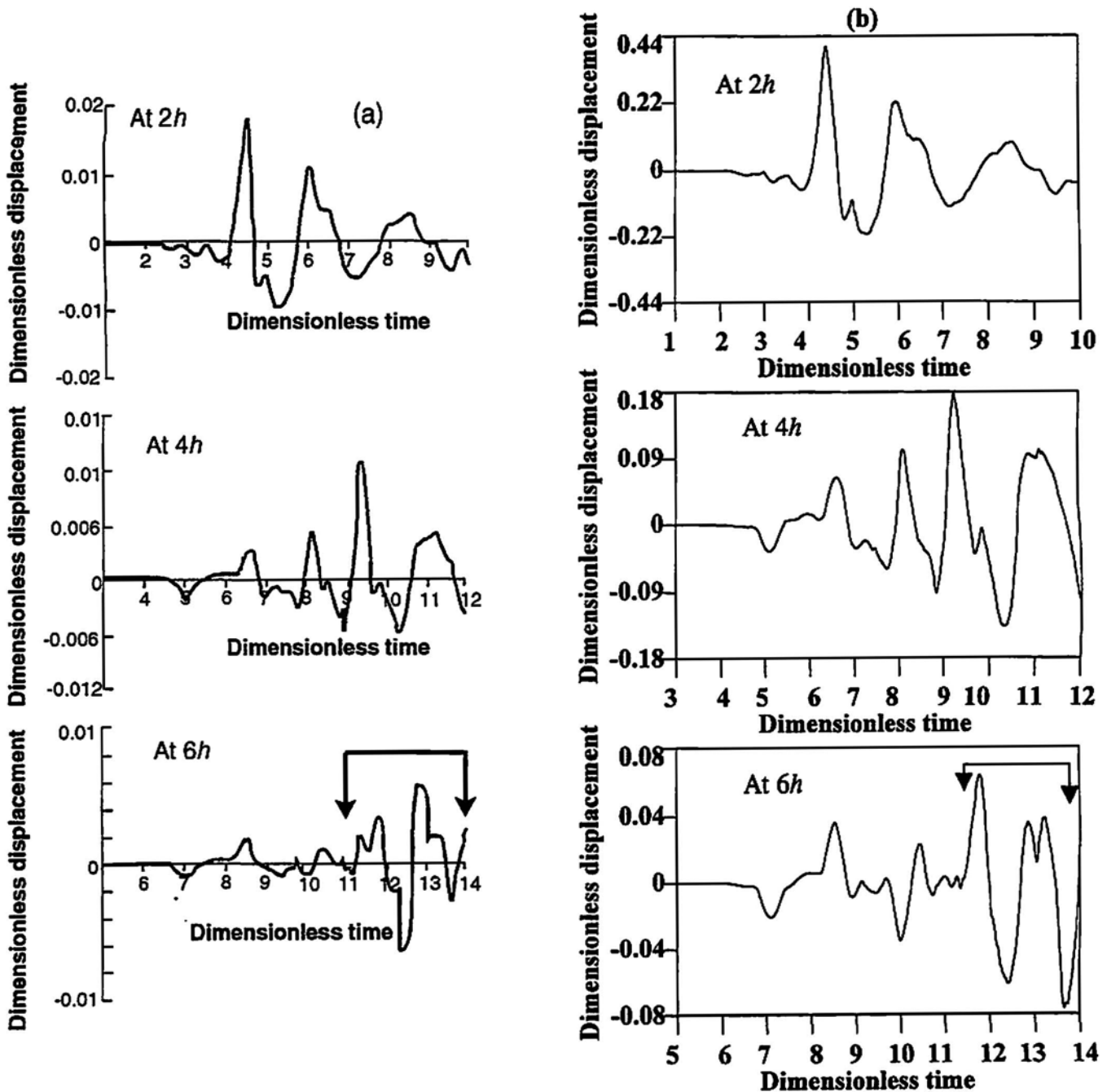


Fig. 11 Out-of-plane displacement at 2h, 4h, and 6h from a midplane vertical dipole. Analytical results (Pao et al., 1979) are shown in (a) and FEM results in (b). Regions between arrows show primary differences in signal-shape.

12(c) for the two-dimensional code. In this case, the above two key ratios are 5 and 29.7. The current three-dimensional case mentioned above leads to a run with the mesh of $52 \times 1867 \times 1867$ points for a total of 2651 time steps. Each time step requires about 480 floating-point operations per mesh point. This problem requires about 4.4×10^9 bytes of memory. The processor used for this computation required about $2.6 \mu\text{s}$ to advance each mesh point one time step. The total computation required about 240 hours of computer time. The code runs at very high efficiency on a parallel computer so an eight-processor machine could reduce the wall clock time to 30 hours. We

believe that this code would run efficiently on a distributed-memory parallel computer with 32 to 128 processors. We think that the 51 cell results are adequate for initial explorations of three-dimensional radiation patterns and more complicated dipole sources, but we hope our computing resources will be capable of modeling 101 cells for a 25.4-mm thick plate in the not too distant future. This increased resolution would allow more accurate modeling at the $2.3\text{-}\mu\text{s}$ rise time or similar accuracy modeling but with a rise time of down to $1.15 \mu\text{s}$. In order to most accurately examine three-dimensional cases with rise times less than $1.15 \mu\text{s}$, additional computing capability will be required.

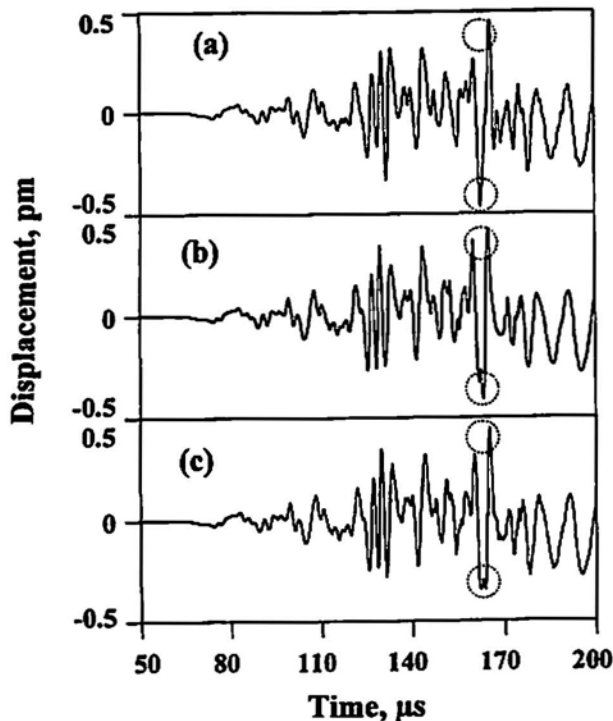


Fig. 12 Out-of-plane displacement at $15h$ for a $2.3\text{-}\mu\text{s}$ rise time "cosine bell" dipole source: (a) three-dimensional code with 51 cells through the thickness; (b) two-dimensional code with 408 cells through the thickness; (c) two-dimensional code with 102 cells through the thickness. Dotted circles show regions of small differences in the signals.

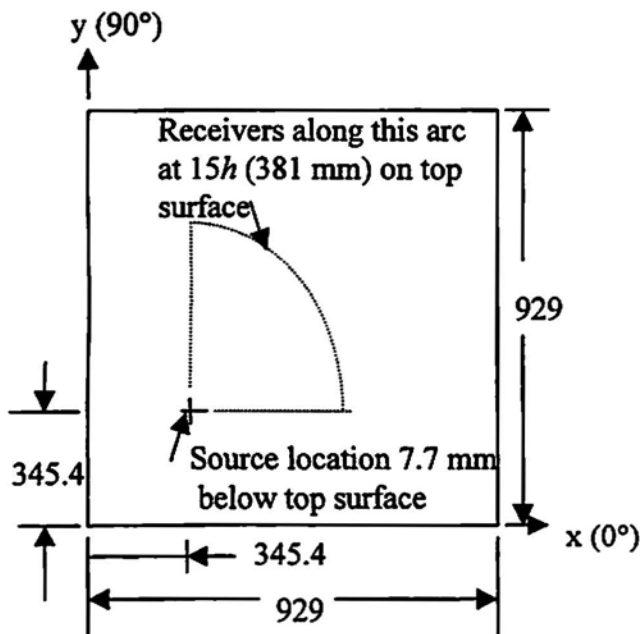


Fig. 13. Domain for three-dimensional DFEM result shown in Fig. 12(a). Dimensions in mm.

However, as we recently observed (Hamstad et al., 1998), relating results modeled with small rise times to experimental results requires high sensitivity, wideband sensors with a flat frequency response to higher frequencies than that typically available in current sensors.

6. Contrasts Between DFEM Modeling and Alternate Analytical Approaches

A key difference between DFEM and the alternate analytical approaches is the fact that with DFEM finite plate samples with edge reflections can be modeled as well as the infinite plates, to which the other analytical techniques typically are limited. The DFEM method has been validated experimentally for both normal and oblique edge reflections (Prosser et al., 1999). Further, in principle, the DFEM can also model AE in geometry more complex than a simple plate or half-space and provide for both near- and far-field results within the same computation. Finally, the DFEM method can provide spatial displacements at selected times after the operation of the AE source.

7. Conclusions

Key finite element parameters have been determined for finite element modeling of buried monopole and dipole AE point sources with a "cosine bell" source: λ_m/s and $\lambda_m/(cs)$. Here, λ_m is the minimum wavelength of interest, s is the source size, and cs is the cell size. Our study indicated that adequate results are obtained for $\lambda_m/s \geq 2$ and $\lambda_m/(cs) \geq 15$. Very good results can be obtained if both of these numbers are doubled.

Comparisons with independent analytical methods show that the FEM results are accurate. Results also demonstrate that three-dimensional cases (with a $2.3\text{-}\mu\text{s}$ rise time and a 25.4-mm thick plate) can be effectively modeled with the FEM code to obtain displacements up to a distance of $15h$ by using our current computing resources.

References

- Keiiti Aki and Paul G. Richards (1980), *Quantitative Seismology Theory and Methods*, Vol. II, W.H. Freeman, New York, pp. 802–803.
- John Gary and Marvin Hamstad (1994), "On the far-field structure of waves generated by a pencil break on a thin plate," *J. Acoust. Emission*, 12(3–4), 157–170.
- M.A. Hamstad, J. Gary, and A. O'Gallagher (1996), "Far-field acoustic emission waves by three-dimensional finite element modeling of pencil-lead breaks on a thick plate," *J. Acoust. Emission*, 14(2), 103–114.

M.A. Hamstad, J. Gary, and A. O'Gallagher (1998), "Wideband acoustic emission displacement signals as a function of source rise-time and plate thickness," *Progress in Acoustic Emission IX*, Acoustic Emission Working Group and Acoustic Emission Group, Los Angeles, CA, pp. IV-48-IV-57.

Robert L. Higdon (1990), "Radiation boundary conditions for elastic wave propagation," *SIAM J. Numer. Anal.*, **27**(4), 831-870.

N.N. Hsu (1985), "Dynamic Green's functions of an infinite plate—a computer program," NBSIR 85-3234, available through NTIS, PB86-143856/AS.

Ajit K. Mal, Dawei Guo, and Marvin A. Hamstad (1998), "AE wavefield calculations in a plate," *Progress in Acoustic Emission IX*, Acoustic Emission Working Group and Acoustic Emission Group, Los Angeles, CA, pp. IV-19-IV-29.

Yih-Hsing Pao, Ralph R. Gajewski, and Ahmat N. Ceronoglu (1979), "Acoustic emission and transient waves in an elastic plate," *J. Acoust. Soc. Amer.*, **65**(1), 96-105.

W. H. Prosser, M.A. Hamstad, J. Gary and A. O'Gallagher (1999), "Reflections of AE waves in finite plates: finite element modeling and experimental measurements," *J. Acoust. Emission*, **17**(1-2), 37-47.

C.B. Scruby, H.N.G. Wadley, and J.J. Hill (1983), "Dynamic elastic displacements at the surface of an elastic half space due to defect sources," *J. Phys. D: Appl. Phys.*, **16**, 1069-1083.

John Strikwerda (1989), *Finite Difference Schemes and Partial Differential Equations*, Wadsworth and Brooks/Cole, Pacific Grove, CA.

B. Tirbonod (1992), "Acoustic emission sources modeled by dislocations," *International J. of Fracture*, **58**, 21-53.

Numerical Assessment of the Quality of AE Source Locations

Gang Qi and Jose Pujol

Abstract

In this article, we examine the factors affecting the quality of acoustic emission (AE) source locations and introduce numerical indicators that can be used to establish whether an AE location can be considered reliable or not. The locations discussed here were computed using location software based on well-established earthquake location techniques. Assuming that the specimen, in which AE occurs, is approximately isotropic and homogeneous, the two major sources of possible location errors are noise and the distribution of sensors that record an event. The distribution of sensors plays a critical role. This is demonstrated with results obtained when the recording sensors form a planar array, in which case there was a "blind zone" for events in a position symmetric with respect to the position of the sensors. The effect of noise is studied using simulated noisy data generated for known source locations. By comparison of the locations obtained using these data and the actual locations the effect of noise can be assessed. The effect of the sensor distribution is quantified by the condition number of a matrix of partial derivatives involved in the computations. Low condition numbers indicate that the locations are well constrained, while high condition numbers indicate that the locations may be unreliable. Regarding the effect of noise, in our case an error level of 1% or less does not introduce significant distortion, while a 5% error level is close to the maximum acceptable level.

1. Introduction

Although the acoustic emission (AE) technique is widely used in various areas to evaluate the mechanical behavior of materials and to provide early warnings and health monitoring, algorithms for the determination of the location of AE sources (or cracks) involving denoising and numerical assessment of the reliability of the computed results have not been investigated. In fact, in reviewing the published literature, only a limited number of research papers are available in the area of AE source location. For instance, 2D and 3D AE source location techniques were introduced in the Nondestructive Testing Handbook (ASNT, 1987), while Grosse et al. (1997) developed Hypo^{AE} (a derivative of earthquake location software) to per-

form AE source location computations. In their work, not only the source location was discussed, but the mechanism of the source was studied as well. Similar work was found also in Buttle and Scruby (1990) and Scruby et al. (1986). Although other researchers used AE location techniques, most of their work used no more than three-channel AE systems on planar settings. In the practice of AE source location, there are several factors preventing the advancement of the technique. One likely major factor is the presence of noise in the measured AE signals due to the complex nature of the AE experiments. Another possible factor is the number and distribution of sensors recording an event, which in some cases may not be adequate to properly constrain the locations. In any case, the AE technique has been criticized as being unpredictable and unreliable. To address these questions, the authors used a two-step approach. First, they developed a simple but effective location method (Qi et al., 2000) using ideas borrowed from well-established earthquake location techniques (Lee and Stewart, 1981). The method was tested with data generated in a simple specimen, which allowed a preliminary assessment of the quality of the computed crack locations. In the second step, described here, the authors performed a computer simulation of the effects of internal noise, studied sensor distribution, and introduced several numerical indicators that allow an objective quantification of the quality of the locations. These indicators are directly related to the singular values of the matrix of partial derivatives that arises when setting the equations for the location problem. An important aspect of this work, which also follows ideas used in earthquake location, is that it allows an assessment of the quality of the results that can be expected for a given distribution of sensors when the location of the sources are assumed to be known. In other words, if there is reason to believe that the AE source will have a preferred location, then a proposed distribution of stations can be tested to determine its expected performance.

2. Experimental

2.1 Material

Compact tension specimens were prepared for the tests. The specimens were made of Palacos R (Smith & Nephew, Memphis, TN). The composition of the Palacos powder is given in Table 1 (Lewis, 1997).

Received 27 December 1999. Gang Qi (gangqi@memphis.edu) is affiliated with Department of Mechanical Engineering, and Jose Pujol is with Center for Earthquake Research and Information, The University of Memphis, Memphis, TN 38152-6576 USA.

Table 1 Constituents of Palacos cement.

BPO	Z ₂ O ₂	Chlorophyll	P(MMA/MA)	N, N-DMPT	Hydroquinone	MMA
0.5-0.6	14.85	200 ppm	83.55-84.65	2.13	64 ppm	97.87 ppm

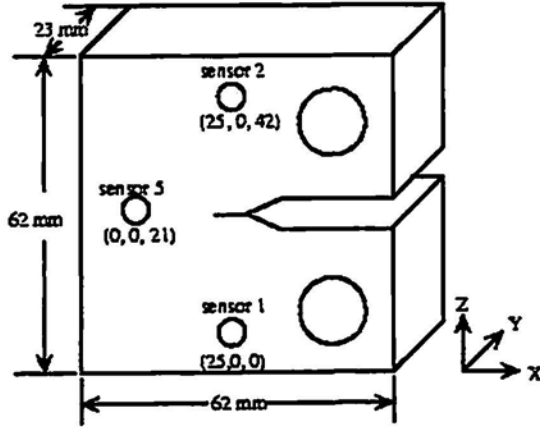


Fig. 1 Specimen dimensions and sensor locations.

2.2 Instruments and Test Setup

The instrumentation used in the tests is listed below.

- PAC AEDSP 32/16 PC-based data acquisition board (highest sampling frequency 20 MHz, six-channel system).
- PAC 1220A preamplifier (100 – 300 kHz).
- PAC PICO wide band piezoelectric AE transducer (bandwidth 100 kHz - 1 MHz).
- Silicon grease couplant.

The parameters for the instrument setup are listed in Table 2.

Figure 1 shows the geometry of the specimen and the locations of three of the six AE sensors (see also Table 3). The AE sensors were taped to the specimens¹. The acquired signals were conditioned with preamplifiers. The conditioned signals (with gain of 40 dB) were fed to the main data acquisition boards. Fatigue tests were performed with a stress ratio of zero. During the tests, the following AE parameters were monitored and recorded: time, AE counts, AE events, amplitude, energy, and frequency. The time sequence AE data were recorded according to the order of hit time at each individual sensor. This time sequence AE data was used with the location algorithm referred to above.

¹ It was found that the sensors became loose from time to time during the fatigue test period of four to five hours. As a result, the AE signal became temporarily quite noisy.

Table 2 Test parameter setup.

Parameter Type	Instrument set values
Threshold type	Fixed
Threshold value	40 dB
Peak Definition time	200 μ s
Hit definition time	400 μ s
Hit lock time	300 μ s
Sample rate	2 MHz
Filter on board (low)	10 kHz
Filter on board (high)	1.2 MHz
Pre-trigger	20 μ s
Hit length	1 k
Cycle count threshold	0.4 V
Delta-T front end filter	Yes
Front end filter	No

3. 3-D AE Source Location Algorithm

The location algorithm has been introduced in Qi et al. (2000) and is based on a standard technique used to locate earthquakes (e.g., Lee and Stewart, 1981). The basic features of the algorithm are as follows:

1) Assume that the medium is homogeneous and isotropic, so that the velocity of wave propagation is a constant, and that a crack occurs at time T_0 at point (x_0, y_0, z_0) . The waves generated by the crack reach the sensor j at time t_j . In principle, the crack generates both compressional (or P-) waves and shear (or S-) waves, and the following equations apply to both types of waves provided that the appropriate velocity is used.

2) The origin time t_0 and location (x_0, y_0, z_0) of the crack are derived from the arrival times t_j recorded at N sensors as follows. The arrival time t_j is equal to

$$t_j = T_0 + \tau_j(x_0, y_0, z_0) \quad j = 1, 2, \dots, N \quad (1)$$

where τ_j is the travel time from (x_0, y_0, z_0) to the j -th sensor. As the system of equations (1) is nonlinear, it is solved in two steps. First, it is linearized using a Taylor expansion and then the corresponding system is solved by iteration. Let i indicate iteration number. Then, equation (1) is replaced by

$$r_{ji} = dT_0 + \nabla \tau \cdot dv \quad (2)$$

where r_{ji} is the difference (residual) between the observed arrival time and the arrival time computed in the previous iteration

$$r_{ji} = t_j - [T_0^{i-1} + \tau_j(x_0^{i-1}, y_0^{i-1}, z_0^{i-1})] \quad (3)$$

Table 3 Sensor locations.

Sensor number	Coordinates (mm)		
	X-coordinates	Y-coordinates	Z-coordinates
1	25	0	0
2	25	0	42
3	25	23	0
4	25	23	42
5	0	0	21
6	0	23	21

For the first iteration an initial estimate for the solution must be given. Symbol ∇ denotes the gradient operator, and dv is the vector $(dx, dy, dz)^T$. In matrix form, equation (2) becomes

$$\bar{R} = A d\bar{x} \quad (4)$$

where

$$\bar{R} = (r_{1i}, r_{2i}, \dots, r_{Ni})^T \quad (5)$$

$$A = \begin{pmatrix} 1 & \nabla\tau_1 \\ 1 & \nabla\tau_2 \\ \vdots & \vdots \\ 1 & \nabla\tau_{N-1} \\ 1 & \nabla\tau_N \end{pmatrix} \quad (6)$$

$$d\bar{x} = (dT_0, dv)^T \quad (7)$$

Equation 2 is solved using a damped least-square technique. The iterative process stops when one of the following three conditions are satisfied:

(i) The average root square residual

$$ARSR = \frac{\sqrt{\sum_{i=1}^n R_i^2}}{N} < \epsilon_r \quad (8)$$

where ϵ_r is a cut-off value;

(ii) $|\delta r_i| \leq \epsilon_r$ and $|\delta r_j| \leq \epsilon_r$, where ϵ_r and ϵ_r are cut-off values;

(iii) the number of iterations exceeds a pre-set value.

This algorithm was implemented in a Matlab toolbox that includes a search for arrivals times from the same event. The results described here were obtained using this toolbox and P-wave arrivals. The P-wave velocity was determined using pencil lead breaks (Qi et al., 2000). Usually, convergence to a solution required 2 to 4 iterations.

4. Factors Affecting the Quality of the AE Source Locations

Assuming that the specimen, in which AE occurs is fairly homogeneous, there are two possible major sources of error in the computed locations. One is noise and the other is the distribution of the sensors that record an event. They are described below.

4.1 Noise

Noise can have a detrimental effect on the quality of AE experiments, especially on the computed AE source locations. Three types of potential AE noise are recognized: environmental, internal and special. Environmental noise is that generated by external factors such as load train, electronic instrumentation, and other unknown sources generated outside of the tested material. The internal noise originates in waves other than the direct P- and S-waves, such as reflected and refracted waves. Their importance will depend, to a large extent, on the nature of the specimen investigated; the more heterogeneous the model the higher the likelihood that this kind of noise will be a problem. Special noises are those associated with particular aspects of mechanical tests and are generated by surface touching during the tests. An example of this type of noise is the fretting between fatigued surfaces associated with fatigue tests. The fretting noise is one of the most difficult to be eliminated/reduced.

Presently, the techniques to remove noise are limited to the use of threshold values for quantities such as amplitude, energy, and frequency content. Environmental noise has been satisfactorily removed in material characterization tests and usually will not be a significant source of error for AE source location computation. The special noise, on the other hand, may or may not introduce errors in AE source location computations depending on the specific nature of each mechanical test. For example, in a mechanical fatigue test, AE signals are commonly associated with fretting noise. It is not an easy task to remove this noise. Generally, the crack-tip region is the place where most fretting occurs. As a result, the physical contact between the fatigued surfaces can enhance the AE signal from the region of interest. It must be noted that the special noise is not any form of stress/strain energy release during loading. Therefore, it is of no interest to include the special noise in the AE material characteristic evaluation.

In an AE source location test, the internal noise deserves further consideration. First of all, since the internal noise is in the form of wave energy released during the

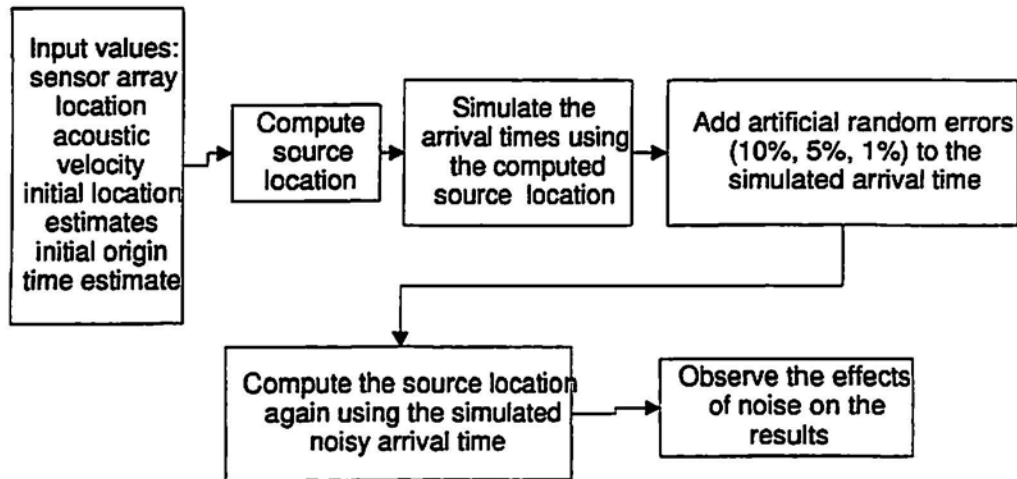


Fig. 2 Computer simulation of noise effect.

loading process, it is safe to say that the effect of internal noise on a typical AE material characteristic test or process monitoring is very limited. However, this type of noise can be a significant source of error when locating AE sources. In AE location computations, the internal noise will interfere with the direct waves if they arrive at a sensor at approximately the same time. The nature of the interference can be complicated and will depend on which signal arrives first and on the polarity and amplitude of the signals. For example, if the noise arrives before the direct signal, the onset of the latter may be affected, thus introducing some error in the estimated arrival time, which may affect the quality of the computed locations. In this paper, it is the intention of the authors to limit the discussion to the effects of the internal noise on the quality of the computed source locations. It is assumed that the environmental noise can be eliminated or reduced to a level such that it will not have significant effects on the determination of the AE source location. As in routine AE tests the output of the detection algorithm is an arrival time, there is no *a-priori* way to tell whether it corresponds to a direct P- or S-wave, or to estimate how much error may affect it. To find out, it is necessary to search for a group of arrivals to the different sensors within an expected time window, to use those arrivals to locate the source, and to use the results of the location algorithm to estimate the quality of the location. In order to investigate the effect of errors in the arrival times, the authors used simulated times computed for given source locations. These locations are determined using actual data and then computer generated uniformly distributed random errors are added to the simulated times to make the signal noisy. The noisy simulated data are then used with the location algorithm. By comparison of the results obtained with the actual and the simulated data, it is possible to get an idea of the effect of noise on the locations. This simulation process is illustrated in Fig. 2. An example of application of this approach is given in the next section

4.2 Distribution of Sensors

Even for perfect experimental data, if the distribution of the sensors that recorded an AE event is not appropriate, the location of the event may be affected by a significant amount of error. Interestingly, the average residual (see equation 8) may be very small and yet the location may be grossly inaccurate. For this reason, we investigated the use of the condition number of the matrix A given in equation 6 to assess the quality of the location. The condition number of any matrix is the ratio of the largest singular value to the smallest one (Noble and Daniel, 1977). Condition numbers are important because they give an indication of the linear dependence, or independence, of the columns of a matrix. If one of the singular values is equal to zero, then one of the columns of A will be linearly dependent on the other ones and a unique solution does not exist. If the smallest singular value is nonzero but considerably small, the columns may be close to linearly dependent and the matrix is said to be ill-conditioned. As a result, small errors in the data may be "magnified" into large errors in the vector solution. Therefore, AE source locations, for which the condition number of A matrix is very large, should be considered unreliable even if the average residual is small. Examples given in the next section illustrate the relation between condition number, sensor distribution and event locations.

5. Results and Discussion

The fatigue tests performed in this research were continuously monitored. The first 14,400 cycles constitute the initial stage of the test. In the second stage, the maximum load was increased to 800 N. For details, see Qi et al., (2000). In this paper, only one time period was selected to investigate the factors affecting the accuracy of the computed results. In this section, it will be shown that some of the computed locations occur near where they are expected, which makes it possible to estimate location errors. Other computed locations, on the other hand, are not well con-

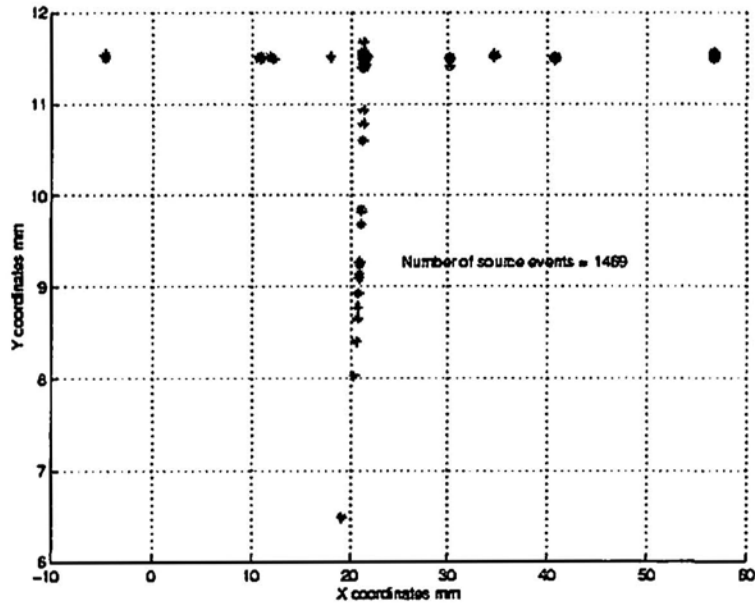


Fig. 3 x-y projection of crack locations for fatigue cycles 17,280 to 17,720 using a location close to sensor 3 as initial estimates.

strained as a result of an unfavorable distribution of sensors. As a consequence, one of the coordinates cannot be determined uniquely. The reason for this fact is discussed in detail later in the paper.

5.1 Estimated Location Errors

Figure 1 shows a detailed view of the sensor locations. Notice the location of the tip of the notch, given by $x = 19$, $0 < y < 23$ and $z = 21.5$. It is expected that AE activity will take place along this tip. Figure 3 shows the computed source locations for fatigue cycles 17,280 to 17,720. Note that there is a concentration of activity centered at about $y = 11.5$ and $x = 21.5$. The corresponding value of z is 21. Comparison of the coordinates of the tip of the notch with the computed locations shows that the inferred source of AE activity is close to the expected location. To estimate the error in the computed locations, the difference between the coordinates of the crack tip and the coordinates of the average of the source locations was computed. This gives $21.5 - 19 = 2.5$ mm, zero, and $21 - 21.5 = -0.5$ mm in the x-, y- and z-directions, respectively. Notice that the physical size of a PICO sensor is 5 mm in diameter. Therefore, the accuracy of the computed results is well within the limitations introduced by the instrumentation. There is a slightly curved line with a length of less than 4 mm, possibly related to activity along the crack tip, and several concentrations of activity along $y \cup 11.5$. The latter have a range of values for the x coordinate, some of which place the AE sources well outside of the specimen. This obviously indicates that at least some of these locations must be incorrect. To investigate the reliability of the locations, the condition number of the matrix of derivatives in the last iteration and the

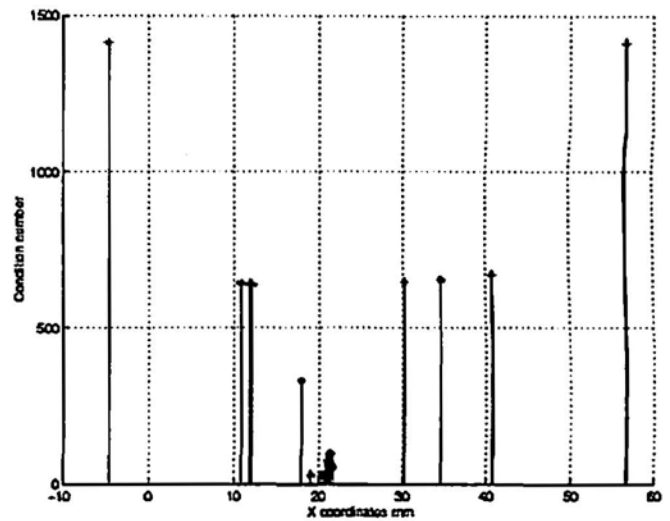


Fig. 4 Condition number vs. x coordinate for fatigue cycles 17,280 to 17,720.

average residual were computed (Figs. 4 and 5). For the events with $x \cup 21.5$ and the events on the curved segment the condition number is less than 100 and 50, respectively. These condition numbers can be considered to be relatively small values and they indicate that the computed locations are well constrained. As a result, these locations are reliable. On the contrary, for all the other computed locations, about half of the total computed locations, the condition numbers are significantly larger, which indicates that the matrices of derivatives are not well conditioned. Therefore, the corresponding computed locations cannot be considered reliable. In fact, as discussed next, they might well be part

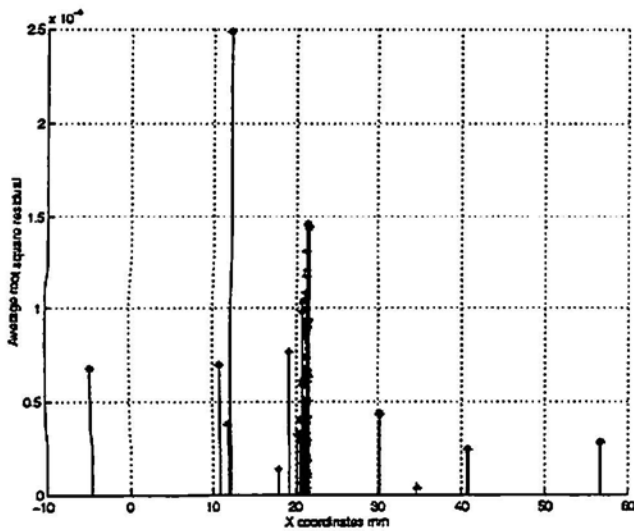


Fig. 5 ARSR value vs. x coordinate for fatigue cycles 17,280 to 17,720.

of the concentration of events at $x = 21.5$, although there is no way to prove, or disprove, this statement.

5.2 Effect of Sensor Distribution

As a general rule, the distribution of sensors should be such that it surrounds the potential AE sources, and the number of sensors should be as large as possible to provide sufficient constraints. However, even in cases where the sensor distribution appears to be adequate, as in the present experiment, it may happen that the amplitude of the AE signals is not strong enough to be recorded by all the sensors. This reduces the actual number of sensors hit, and changes the geometry of the sensor distribution.

The results described in the previous section were obtained with the initial estimate of each source location very close to the location of sensor 3. The initial origin time for each event was the earliest arrival time. When the initial estimate was changed to the average of the locations of the sensors that recorded the event, the computed locations clustered primarily at $x = 21.5$ and $x = 25$, as shown in Fig. 6. Note that there is no activity at $x = 25$ in Fig. 3. The locations in Fig. 6 look better than those shown in Fig. 3 because none of them are outside of the specimen and a large part of them occur where they are expected. However, in view of the large condition numbers discussed above, it was suspected that the events at the locations other than $x = 21.5$ were not well constrained, and that the dependence of the final locations on the initial locations was the result of an unfavorable distribution of recording sensors. This was indeed the case, as it was found that these non-unique locations were associated with the events recorded by sensors 1, 2, 3 and 4 only. From Fig. 1 and Table 3, it can be seen that these four sensors form a symmetric planar array with center at $y = 11.5$ and $x = 25$. As the main source of AE activity happens to occur around $y =$

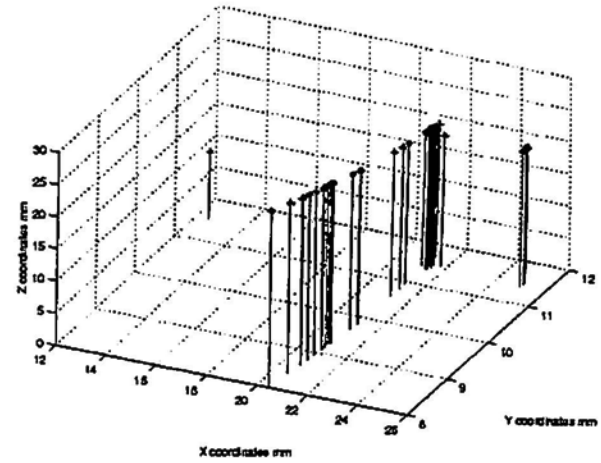


Fig. 6 3D crack locations for fatigue cycles 17,280 to 17,720 using the average sensor array location as the initial estimates.

11.5, the locations of the events recorded by these four sensors do not constrain the x coordinate. The locations with $x = 25$, in particular, were suspected to be an artifact. To verify this hypothesis the locations were recomputed with the initial value of the x coordinate set equal to 15. The corresponding final locations for the events recorded only by sensors 1, 2, 3, and 4 had x coordinate equal 15. These numerical experiments, as well as several others the authors carried out, demonstrate that, in a way, this planar four-sensor distribution has a "blind zone" along the x-axis. As can be seen from equation 6, one of the columns of matrix A is made of ones. If all of the columns of Δt as in the original are not a multiple of the first column, then A will be well-conditioned and a unique solution will exist. When one or more of the columns of Δt as in the original become linearly dependent or close to multiples of a column of ones, then A will become ill-conditioned. This situation occurs for a symmetrical planar sensor distribution with respect to the potential source and parallel to a coordinate plane (in this case parallel to y-z plane). As a consequence, there is not enough information to constrain the values of the four unknowns and the technique becomes "blind". For instance, the computed value of x in this paper will depend on the initial value of x and there will be a trade-off between the values of x and origin time. A similar trade-off is sometimes observed in earthquake seismology, where the location of an event (a point in 3-D space) must be inferred from the arrival times recorded by sensors arranged on the surface of the earth (which can be assumed to be plane for distances of a few hundreds of kilometers). Generally speaking, the "blind zone" effect is rarely seen in practical tests because the geometric shape of the test subjects is not necessarily symmetrical, as in the case of the standard compact tensile specimen studied here.

Our results also show that the locations of the events recorded by five or six sensors are not affected by the selection of the initial locations. In general, this fact means that the computed locations are well constrained, and can be used as a criterion to establish the reliability of the locations. Therefore, in addition to the condition number discussed above, it is possible to assess the quality of the locations by comparing the results obtained for different initial locations. However, this approach may not be feasible if real-time results are expected, in which case the condition number will be the only quality indicator. The average residual, on the other hand, may have limited value when the noise level is low, as in the case discussed in this paper, and the number of recording sensors is small. This can be seen clearly from Figs. 4 and 5; the events with the largest condition numbers have residuals that are among the smallest of all.

5.3 Effect of Noise

As discussed before, the internal noise is a possible major source of error affecting the accuracy of the AE source location. To investigate the effect of internal noise the computer simulation process was used as described in Sec. 4.1 and Fig. 2. The locations used to compute the simulated times are those shown in Fig. 3. With these locations it is possible to see the effect of noise under well-constrained and poorly-constrained conditions. To compare the results, several levels of noise were studied. The initial locations were always close to sensor 3.

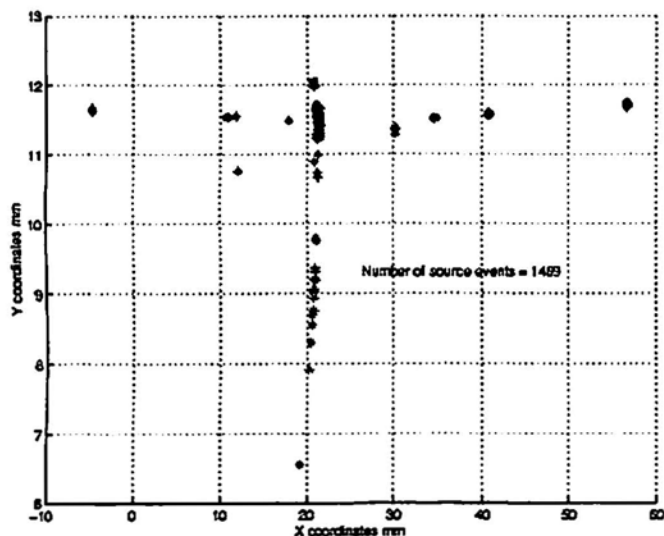


Fig. 7 Locations obtained using simulated data for the locations shown in Fig. 3. Error level 1%.

Figure 7 shows the results for a noise level of 1%. The computed locations differ little from the “clean signal”. Correspondingly, the condition number and the ARSR are almost identical to those in Figs. 4 and 5. Figure 8 shows the results for a noise level of 5%. Comparison of this figure with Fig. 3 shows several differences. First, the original

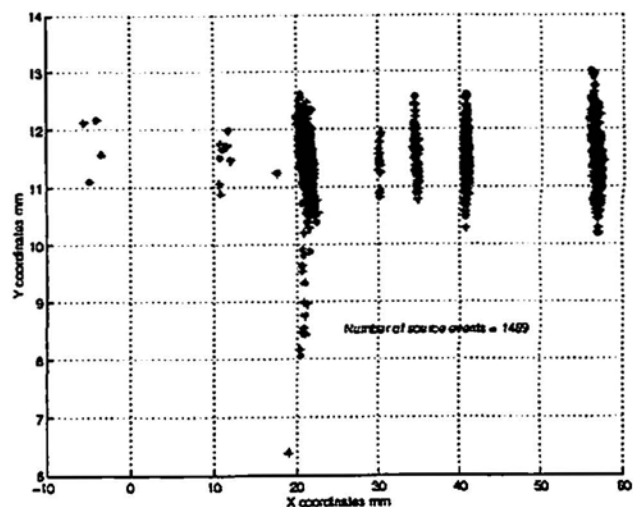


Fig. 8 Locations obtained using simulated data for the locations shown in Fig. 3. Error level 5%.

clusters along the x axis at $y = 11.5$ become linear features along the y direction. The original values of x changed by a small amount only, although it is clear that the thickness of the linear features is larger than the width of the clusters. The net result is a somewhat distorted picture of the actual size of the source of AE activity. On the other hand, the curvilinear feature at the expected source location is fairly well recovered. The condition numbers (Fig. 9) remain comparable to those obtained in the original computations. The ARSR value (Fig. 10), however, does not provide much information. These statements regarding condition numbers and ARSR also apply when the error level is 10% (Figs. 11 and 12), but not to the computed locations. At this error level, the resulting pattern is quite different from that obtained for the previous error level. The clusters along the x axis are barely recognizable, with a large spread in the computed locations. Figure 13 shows clearly that the linear feature exhibited in the previous error level no longer exists. When the error level is increased further the clusters tend to merge together.

These results suggest that the internal noise may indeed have a significant effect on the accuracy of the computed AE source location. In our case, the effect will be minimal when the error level is below 1%. At this error level, the accuracy of the noisy signal is close to that of the “clean signal”. Therefore, in our case a 1% error will not affect the locations significantly, while the 5% error is probably the highest that can be acceptable for AE source location.

6. Conclusions

The 3-D AE source location software package developed by the authors has the capability to assess the reliability of computed locations. The most useful indicator of the quality of a solution is the condition number of the matrix of partial derivatives A. A small condition number corre-

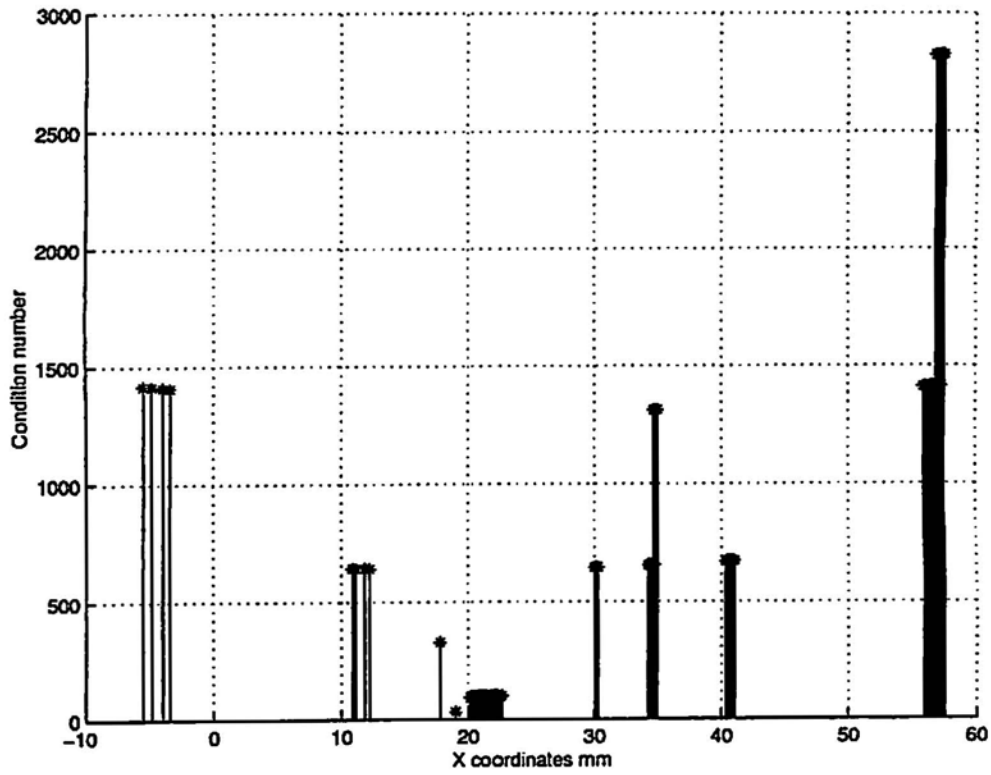


Fig. 9 Condition number vs. x coordinate for the locations shown in Fig. 8.

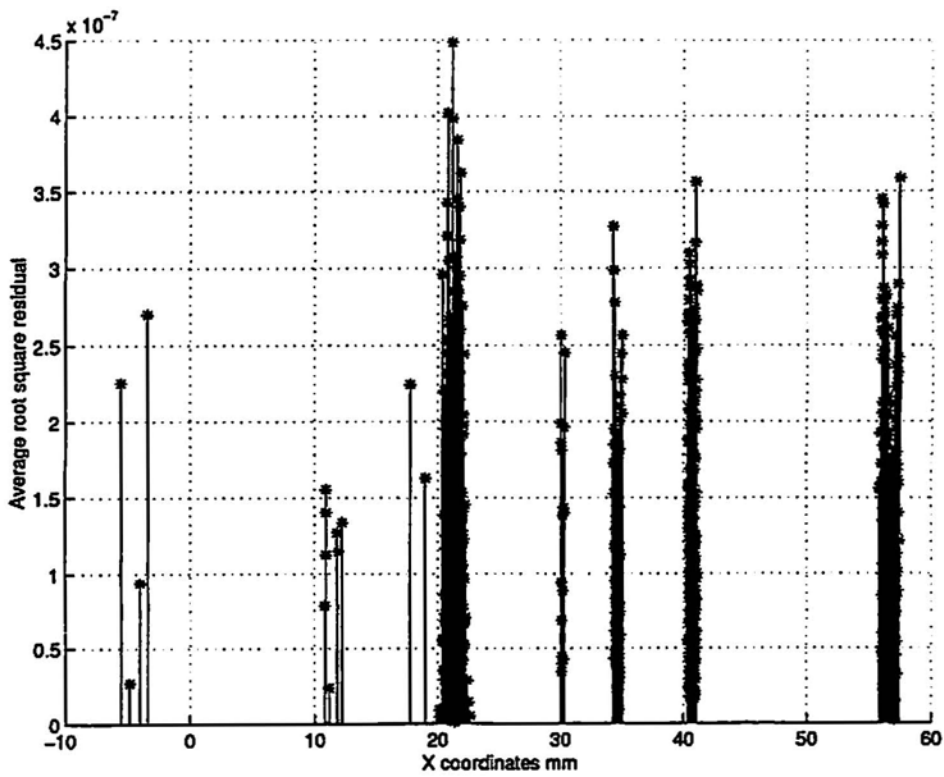


Fig. 10 ARSR value vs. x coordinate for the locations shown in Fig. 8.

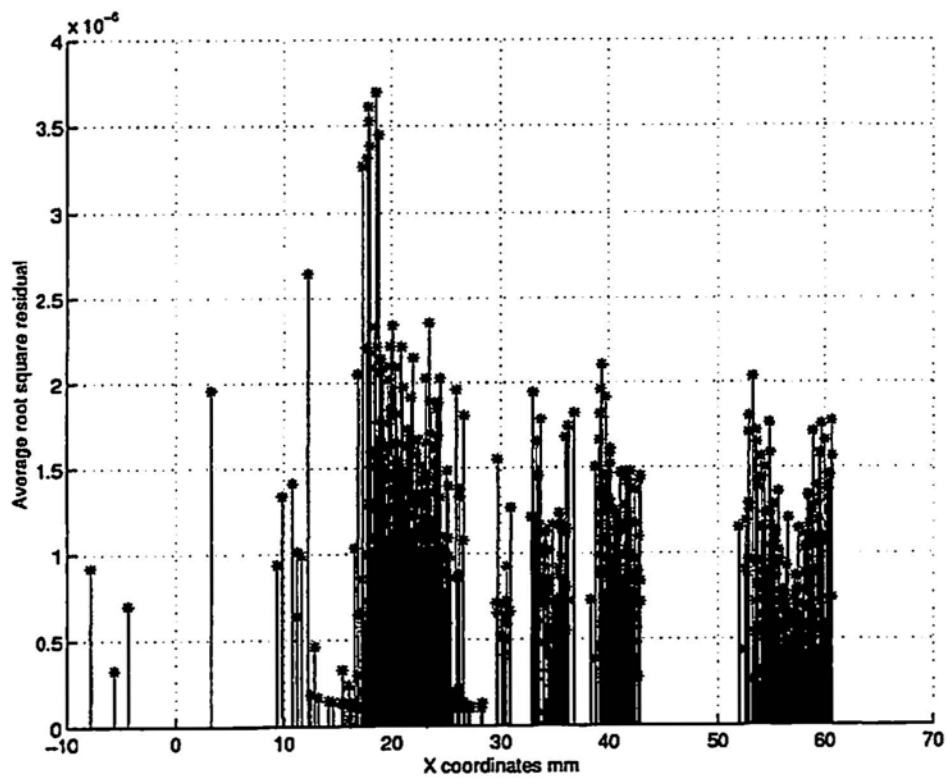


Fig. 11 ARSR value vs. x coordinate for the simulated data with an error level of 10%.

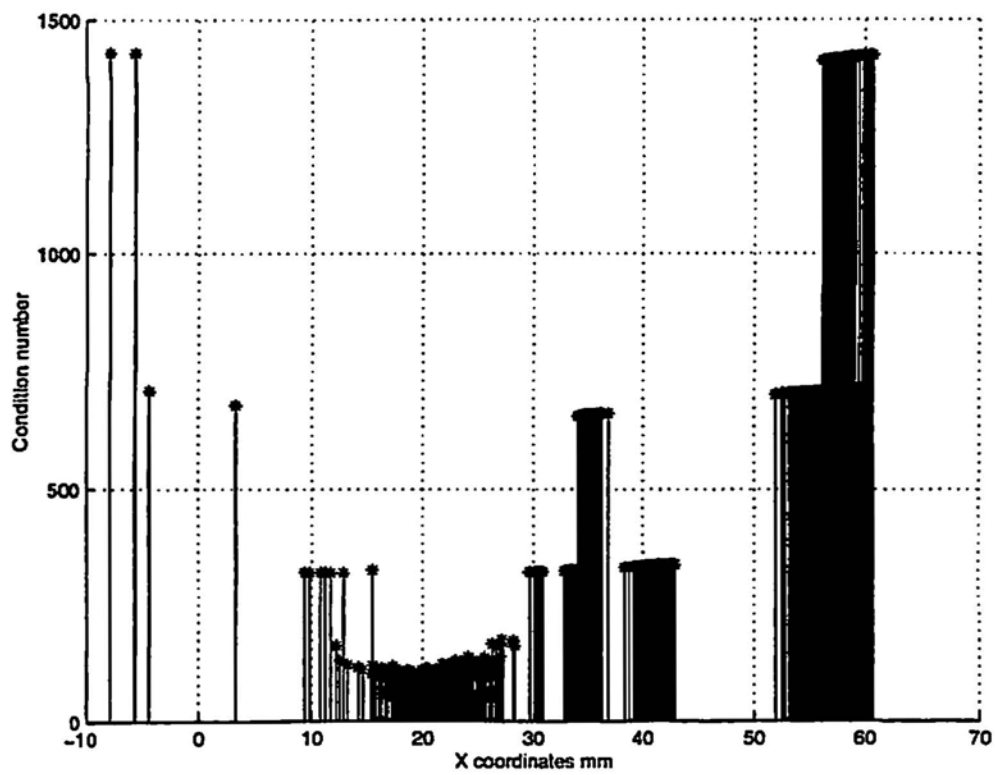


Fig. 12 Condition number vs. x coordinate for the simulated data with an error level of 10%.

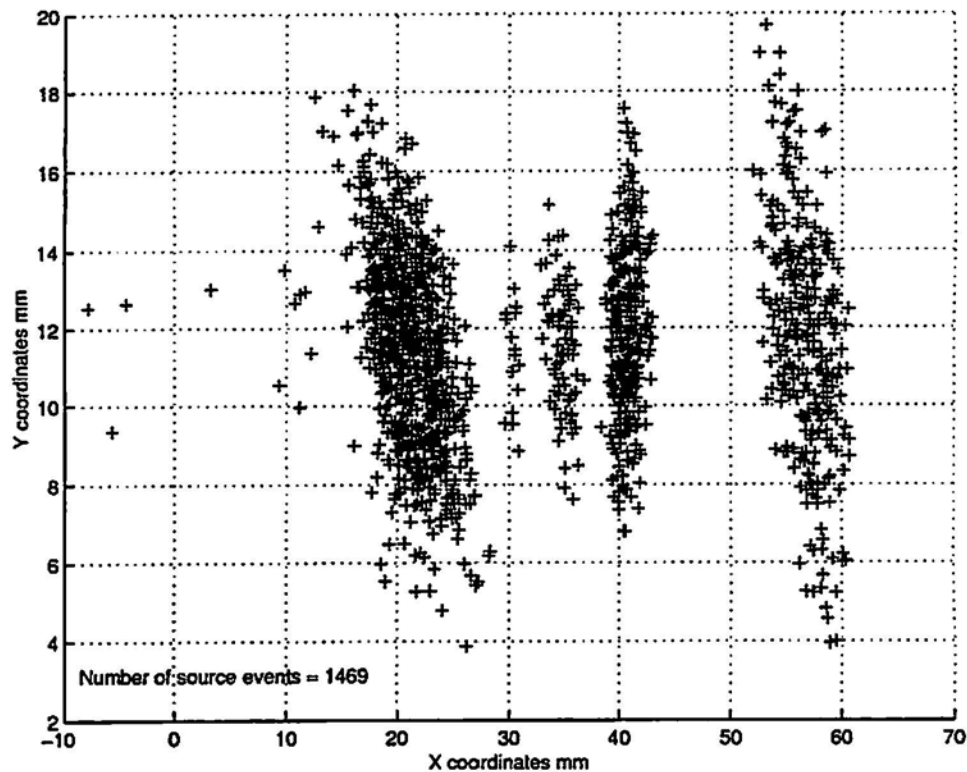


Fig. 13 Locations obtained using simulated data for the locations shown in Fig. 3. Error level 10%.

sponds to a well-constrained solution, while a large one indicates that the solution may not be reliable. A simple way to find out whether a solution is reliable or not is to change the initial estimate. If the computed location depends on the initial estimate, the location is unreliable. The vector R is a reasonable indicator of solution quality only when it can be assured that a solution is well constrained. Large condition numbers are associated with unfavorable sensor distributions. For the data presented here, the well-constrained locations agree very well with the expected location of AE activity. The poorly-constrained locations, on the other hand, are the result of a planar distribution of sensors in a symmetric position with respect to the point of AE activity. This resulted in a blind zone for the x coordinate, which could not be determined. Therefore, when designing an AE experiment it is important to make sure that the distribution of sensors is such that the condition number of matrix A is as small as possible. This can be done before the experiment is actually carried out using simulated data generated for expected AE sources locations.

Acknowledgement

CERI contribution No. 399.

References

ASNT (1987), *Nondestructive Testing Handbook*, 2nd Edition, American Society for Nondestructive Testing, Columbus, OH.

D. J. Buttle and C. B. Scruby (1990), "Characterization of fatigue of aluminum alloy by acoustic emission, Part I - identification of source mechanism", *J. Acoustic Emission*, 9(4), 243.

C. Grosse, H. Reinhardt, and T. Dahm (1997), "Localization and classification of fracture types in concrete with quantitative acoustic emission measurement techniques", *NDT & E International*, 30(4), 223.

W. Lee and S. Stewart (1981), *Principles and Applications of Microearthquake Networks*, Academic Press, New York.

G. Lewis (1997), "Properties of acrylic bone cement: state of the art review", *J. Biomedical Materials Research*, 38, 155-182.

B. Noble, and J. Daniel (1977), *Applied Linear Algebra*, Prentice-Hall, Upper Saddle River, NJ.

G. Qi, J. Pujol, and Z. F. Fan (2000), "3D AE visualization of bone cement fatigue crack locations", *J. Biomedical Materials Research*. (in press)

C. B. Scruby, K. A. Stacey, and G. R. Baldwin (1986), "Defect characterization in three dimensions by acoustic emission", *J. Physics: D Applied Physics*, 19, 1597-1612.

Structural Integrity and Remnant Life Evaluation Using Acoustic Emission Techniques

Brian R. A. Wood, Robert W. Harris and Elizabeth L. Porter

Abstract

The present industrial community which, in many countries, has been permitted to operate under a self-regulation criteria, in some instances, has demonstrated a tendency to use economic and convenience constraints to determine their operating scenarios. The desire to make manufacturing plants and structures more productive has sometimes resulted in them being operated under conditions which can exceed those envisaged during the initial design. While these plants and structures still operate efficiently and safely, the real structural integrity and remnant life evaluation is really unknown. This report discusses the application of acoustic emission techniques, which can provide an estimate of both present structural integrity and the remaining safe operational life of the structure being monitored.

1. Introduction

It is now in excess of 30 years since modern acoustic emission (AE) techniques have been generally employed in industry. In that period, great advances have been made in both AE instrumentation development and applications including basic functions such as defect/leak/source detection and location, and some source identification. Acoustic emission techniques have been used in a variety of applications in industrial plant. The special techniques we developed can provide real time defect location, generally identify processes and procedures damaging pressurized equipment, provide a structural integrity evaluation, and after a number of tests and analysis operations provide an estimate of remnant life of the structure monitored.

2. Basic Theory

When a material or object is placed under stress, any defect, which is activated, will act as a source of elastic waves. The resultant surface wave can be detected by an appropriate transducer, which produces an electrical pulse that may be analyzed to provide a framework to determine much of the information contained in a signal. The detected pulse will be different from that generated by a source as a consequence of: the microstructure of the material; the de-

tails of the elastic wave propagation between source and transducer; and the characteristics of the transducer and monitoring equipment. Simple analysis of the detected pulses may not always give results with a high degree of credibility for both source location and identification, so the interpretative procedures must take into account as many factors as possible.

In an analysis in the frequency domain, the power spectral density (PSD) of a source can be estimated if some knowledge about the transfer functions operating in the chain of events between source and transducer is available. Simple pattern recognition applied to the experimentally measured PSD's can provide further information about source attributes, however this does require a wide-band response and also critical spatial positioning of the transducers, so that the approach is impractical for large transducer separations. The results of the various analysis techniques applied to the detected AE signals form a knowledge base, which is used to extract information about the nature of these signals.

A desirable end-point for all of the processing is to present the data in ways which will readily provide a real time indication of structural integrity. One parameter called Indicative Energy is used in the analysis procedures. It can be derived from the peak amplitude distributions of the detected pulses. Provided that all the equipment and the transducer locations remain the same, then valid comparisons both within a test and between tests are possible on the same structure. An indication of structural integrity can be gained from the indicative energy values if plotted as a function of an appropriate activity/stimulus factor producing what has been termed a localized energy graph. These indicative energy values can be plotted as a function of time to predict maintenance requirements and estimate the remnant life of the structure. Alternatively the data can be plotted and continuously updated during a monitoring period so that areas of probable significant activity can be readily identified as the test progresses. This is a very valuable tool when monitoring a plant or structure start-up operation.

3. Philosophy of AE Monitoring

The use of AE techniques to monitor structures often employs a 10 hour monitoring program, which is about 0.02% of the life of a vessel in operation for 5 years. The

Received 15 November 1999. Authors are affiliated with Metacoustics Pty. Limited, P.O. Box 6042, Blacktown, New South Wales, 2148, Australia. aetteam@metacoustics.com.au

results of such a program have been used to provide a current evaluation of structural integrity and so gain certification for future operation. If the monitoring becomes an annual occurrence then the testing time rises to around 0.1% of the operating period. The use of continuous or periodic AE monitoring, consideration of the plant material characteristics and test procedures which recognize the Kaiser effect, make it now feasible to use AE assessment as the basis for continuous plant operation (no statutory shut-downs). This is especially so when coupled with other NDT techniques and if there are realistic plant operating conditions. Prior to start-up, any plant or structure should be in a new condition. On start-up the plant or structure is placed under considerable stress, both localized and overall (particularly if it is a high-temperature, high-pressure vessel). This traumatic experience often results in significant damage being done to the plant or structure. It is possible that up to 60% of the operational degradation may be initiated by transient operating conditions specifically in the first 48 to 72 hours of operation, although other mechanisms such as fatigue and creep will both initiate and produce defect growth during plant operation. The growth of any defect or AE source will be dependent on the material properties and the plant operating conditions. Under "normal" plant operation the source/defect activity which may be connected with mechanisms such as fatigue, creep, stress corrosion etc, is usually associated with sustained long-term deformation. Since any defect/source activity will vary depending on the surrounding stress it is not possible to get a definite measure of the damage/degradation of the structure. A number of plant monitoring programs and separate tests where vessels and samples have been stressed to failure indicate that there is a relationship between Indicative energy 1 and Indicative energy 2 which produces a local and/or overall indication of relative damage. The Relative Damage Index can be plotted as a function of a number of parameters including test time, operating period, or applied load and is usually depicted on a logarithmic scale. A typical form of the relative damage curve

versus log time graph is given in Fig. 1. The exact nature of the regions of inflection and the approximately linear sections of the graph will vary for different situations.

After a prescribed period (typically 3 to 10 years depending on the structure and its operating conditions), there will be a statutory shut-down and maintenance program to restore the plant or structure to a near new or defect-free condition. The next start-up will again cause degradation and so the cycle continues. AE monitoring during start-up and preferably also during operation will highlight and assess the severity of any source activity, so that operational conditions detrimental to structural integrity will be determined. Historical AE data will allow the determination of a cumulative indication of remnant life. This analysis can be applied to data obtained during a test program and may be related to both the whole structure, or to specific areas of interest for that test program providing a short-term evaluation of integrity, stability and failure. It may also use data from several tests on the same structure, employing the same transducer locations over an extended period of time to provide a long term estimate of the operation, integrity and remnant life for both specific areas of interest or the entire structure.

4. Structural Integrity Evaluation

The AE data was analyzed and interpreted with respect to individual surveillance areas or to structures as complete units for a number of structures. The results of the analyses were progressively up-dated during the tests so that a continuing series of results were obtained, which also provided trends related to individual conditions in the structure. An evaluation of the structural integrity of the areas monitored provided an indication of the localized conditions at various stages during the test programs. The Structural Integrity Index is a computed value from the acoustic emission data recorded from each transducer. A Structural Integrity Index

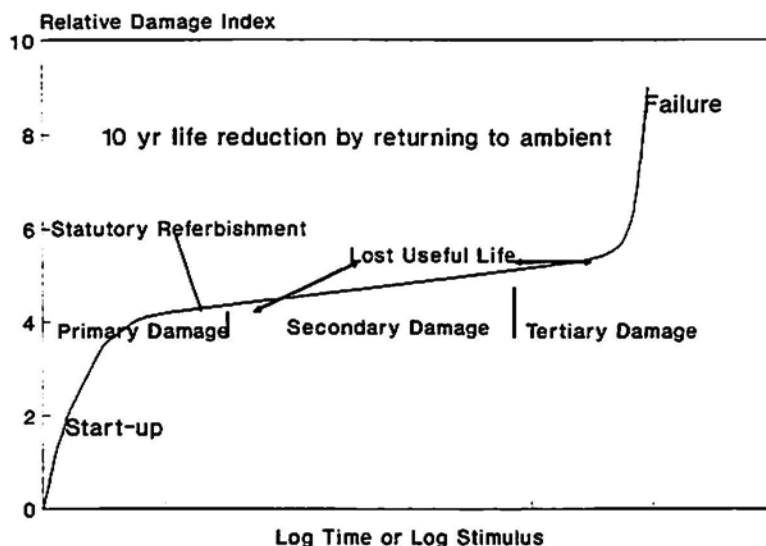


Fig. 1 Relative damage curve.

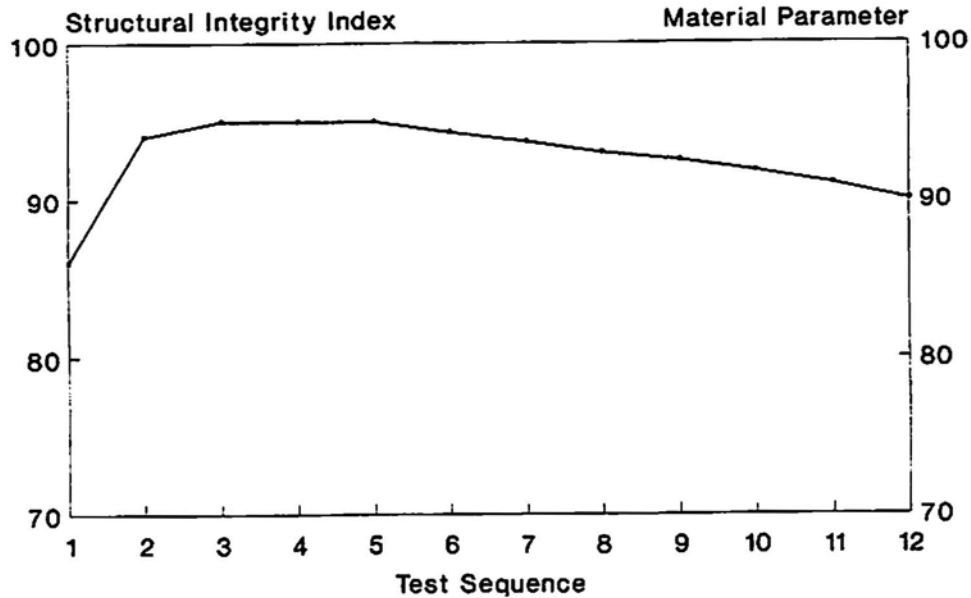


Fig. 2 Structural integrity index vs. test sequence (time or stimulus)

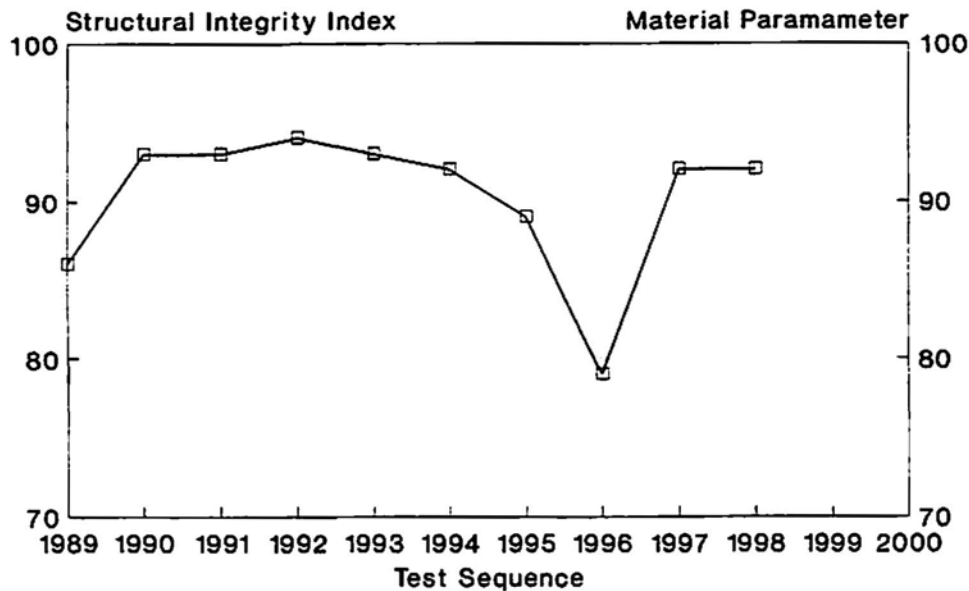


Fig. 3 Structural integrity index variations from annual monitoring.

of 100 is the highest level of structural integrity. Depending on the material and the geometry of the structure, a Structural Integrity Index above:

- 90 for Fiber-reinforced plastics
- 90 for Geologic/Concrete-type materials and
- 80 for structural steel,

indicates a good structure. An idealized structural integrity graph is shown in Fig. 2.

5. Typical Test Results

The analysis techniques are based on laboratory research on various materials used in structures such as pipelines, pipe structures, tanks, pressure vessels, bridges and

dams. The data is combined with the physical properties of these materials and the waveform analysis of AE data recorded during the field test to derive the Structural Integrity Index. The laboratory and field test data also better define the index value associated with material failure, and thus the structure's operational safety criteria can be estimated.

Successive test monitoring has demonstrated the gradual degradation of vessels/structures, and the associated material, from the start of service life to the time of current monitoring. This allows the scheduling of maintenance and identifies any specific area exhibiting material degradation. If any repair has been fully successful, the results of subsequent AE tests on the vessel/structure will demonstrate a

return to a high level of structural integrity and thus safe service life. Likewise areas of inadequate repair will be identified.

This AE test technique has been applied to many different structures and operating conditions. The technique can be modified to accommodate many test/operating criteria, which include the following conditions usually encountered in modern plant operating programs.

5.1 Regular Time-Based Monitoring

A number of vessels were monitored annually over a number of years. The results shown in Fig. 3 demonstrate the change in the Structural Integrity Index of one vessel, initially through normal aging/degradation and then the accelerated deformation resulting from a detrimental change in plant operating conditions. The vessel was repaired in 1996 and the return of structural integrity is apparent.

5.2 AE Testing in Lieu of Hydro-Testing - During Plant Start-up.

There is some debate about the use of a hydro-test on pressure equipment and many alternatives have been explored. Acoustic emission techniques offer a valid alternative and have been successfully used in lieu of a hydro-test in the start-up of a new chemical plant.

The data were recorded and analyzed during the start-up operations, and many defects located. Each defect was classified and most were repaired. This is shown in Fig. 4 where the Structural Integrity Index falls as there is a step in the applied stress, and then it levels out as the structure stabilizes.

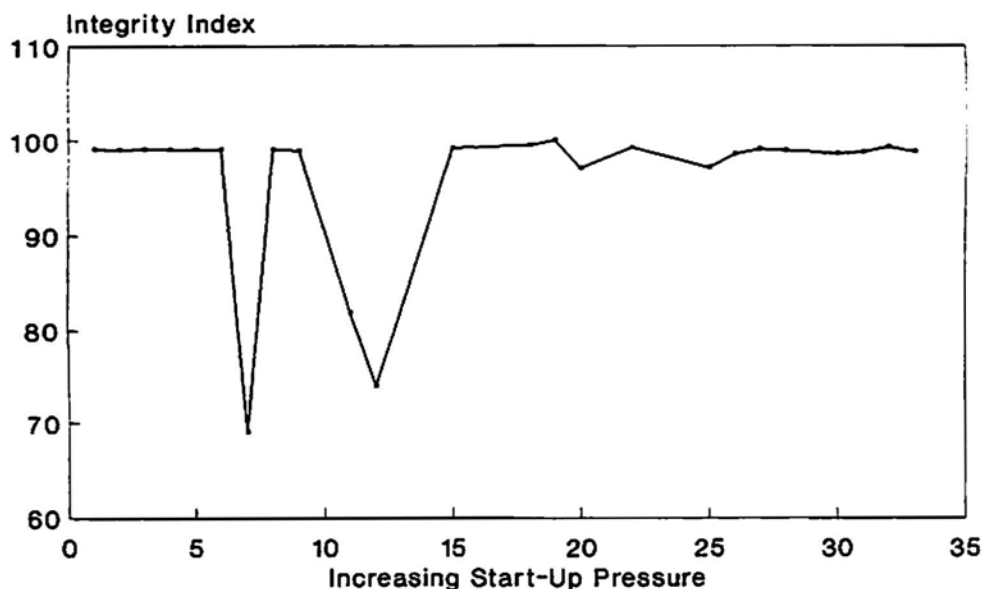


Fig. 4 Plant Start-up Monitoring.

5.3 Continuous Plant Monitoring

Continuous plant monitoring is a very expensive technique and so is not frequently employed. However semi-continuous monitoring, where a plant or a section of plant is instrumented and monitored both frequently and regularly, can have very significant advantages to plant owners/operators. Using these techniques, it is possible to plot the progress of an entire plant or only a small segment of a structure, which may require specific attention. Many structures have been taken out of service because a defect has been identified. Some, but certainly not all, of these defects may not have been in areas subjected to significant operating stresses, and the structure may have been capable of continued safe operation without adversely affecting the integrity of the structure. While this concept may cause some concern, it can also provide significant re-assurance of a structure's safety for continuing operation while preparations are made for repair and/or replacement of the apparently defective structure. The graph shown in Fig. 5 shows the results of intensive monitoring of one section of a pressure vessel where a known defect existed. This area was significantly stressed during the plant start-up operation, which is shown early on the graph. From this point on, the known defect was activated by some plant operating conditions. These were identified and controlled/modified, thus allowing continued plant operation, in this case for some months, while a new piece of equipment was manufactured, tested and then the defective component was replaced.

5.4 Remnant Life Evaluation

As structures and plants are being required to operate at or near the design criteria, the need to know and understand the real structural integrity of plant equipment is a necessity. Laboratory tests on the base material used to build

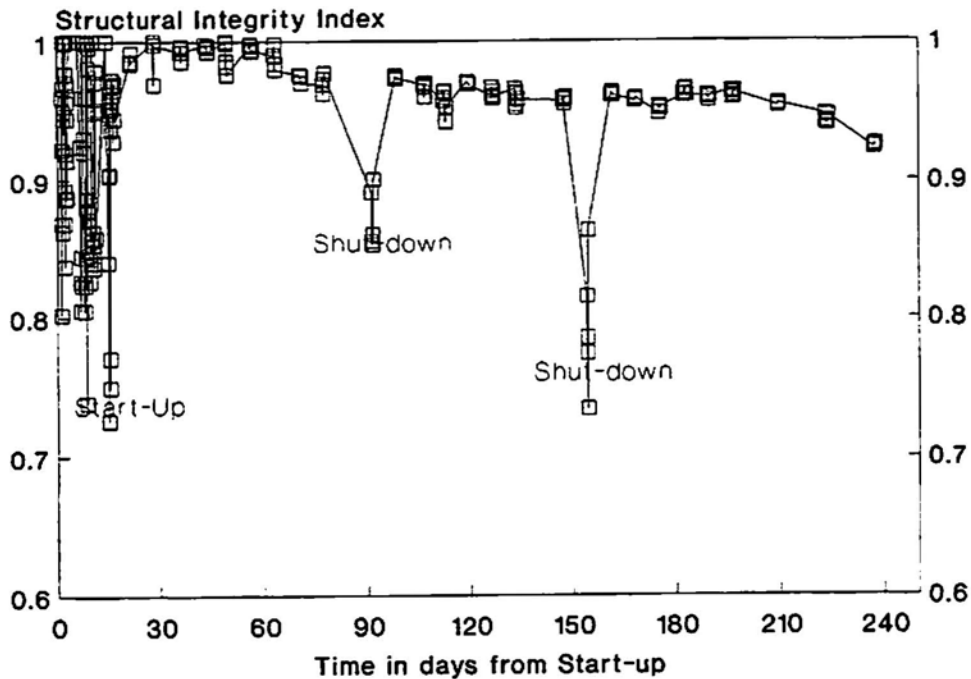


Fig. 5 Continuous AE monitoring of a defect area during plant operations.

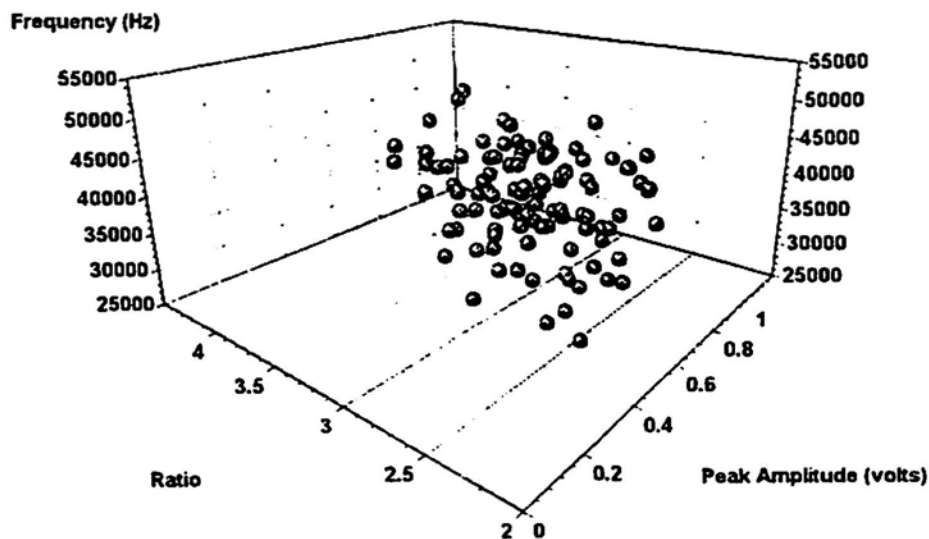


Fig. 6 Pattern recognition plot of AE activity from an operating plant.

a structure are made to determine a series of physical parameters. These parameters are then used to determine the critical values reported in section 5 of this report. As the Structural Integrity Index calculated in each test program is evaluated, it is possible to make an indicative prediction of the time required for the structure integrity index to reach the calculated critical value of the base material. In the early stages of the life of a structure/vessel, the predicted remnant life will usually be large and approximate, however as the structure/vessel approaches failure, this estimate becomes realistic and a valuable safety tool which can also be used to plan plant maintenance schedules and component replacement.

5.5 Pattern Recognition Analysis

A goal of any field investigation is to estimate the range of different types of signals being received by the transducers, and so some form of pattern recognition is required. The investigator requires both uniqueness and robustness in the analytical techniques used, which in practice cannot be totally achieved. There also should be some physical basis behind the choice of parameters rather than simply an elegant mathematical algorithm with no relevance to the physics and material science involved. Patterns in the parameters derived from the detected signals need to be determined, so samples of digitized raw data are

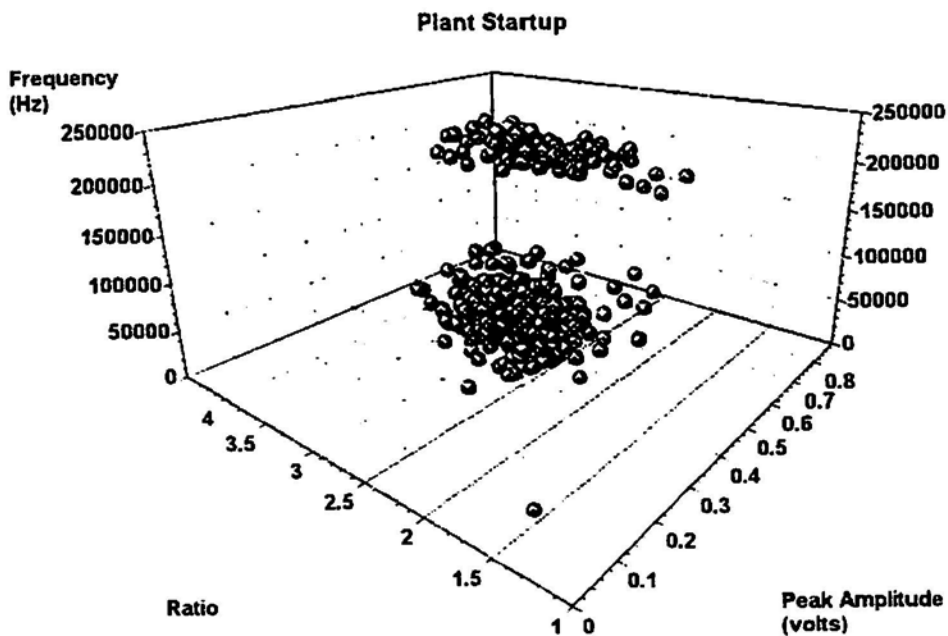


Fig. 7 Pattern recognition plot from a damaged plant.

required. The first question that should be asked is whether the samples selected are good representations of the general population. These samples of digitized raw data generally exhibit a bias since the larger amplitude signals are preferentially captured. Hence, predominantly events arising from the more deleterious sources are being stored for analysis, meaning that a pessimistic view of the mechanical integrity would be deduced using this data on its own. This in itself is not an unsatisfactory result since safety of a structure must always be of supreme importance. When acquiring data for analysis by sampling and digitizing signals, the restrictions placed by such a process must be considered. The Nyquist criterion requires that the sampling frequency should be at least twice the highest frequency inherent in the signal being sampled. Since the conversion is being carried out by an analog-to-digital converter having only a certain number of bits in the result, the possibility of quantization errors must be considered. Laboratory and field investigations have shown that this approach to pattern recognition has greatly assisted in delineating different groupings of events. Figure 6 is a typical plot of data recorded during plant operation. While this data is a mixture of process noise and AE from the structure monitored, the tight single cluster is indicative and may be termed normal operating conditions. Data recorded from an operating plant, which has both known and unknown defects, produces two obvious groupings of activity as shown in Fig. 7, which highlights material degradation as a totally independent set of AE data due to the plant operation.

6. Conclusions

There is still much work required to determine what happens at a microstructural level and the detailed nature of

the associated stress distribution generating AE pulses. The current technology is biased towards engineering and electronics and a significant input relating to the physics and materials science aspects of AE is needed to advance the technology. At present, we have developed a monitoring and analysis technique which it has been demonstrated can classify the structural integrity of pressure equipment along with other structures and predict the remnant life and maintenance requirements of the structure or plant item being monitored. The addition of signal analysis, waveform and pulse analysis to the already viable collection of AE techniques forms part of the testing regime required to both detect and validate AE data. Universally, most of the information available from AE monitoring is not used, because of the short-term economic considerations controlling both monitoring equipment and techniques. The need to validate data and its interpretation has never been so important. The correct detection of AE data and the simultaneous analysis of that data using a portfolio of techniques is necessary to ensure the safe and efficient use of industrial plant and structures.

Acknowledgments

The authors wish to express their appreciation to the other members of the Metacoustics Acoustic Emission team who participated in both the laboratory and field test work associated with this report.

The data were obtained from a large number of field test programs, which are commercially confidential. However, the assistance and cooperation of the many companies that worked with Metacoustics on these projects is both acknowledged and appreciated.

Selected Papers from

International Conference

Acoustic Emission '99

Held at Brno, Czech Republic, 15-17 June 1999

**In commemoration of the 100th anniversary
of Brno University of Technology**

International Conference Acoustic Emission '99

Report on International Conference Acoustic Emission '99, at Brno, Czech Republic, 15-17 June 1999.

Pavel Mazal and Václav Svoboda

On the occasion of celebrations of the 100th anniversary of Brno University of Technology (VUT) (Czech Republic), a successful international conference dedicated to the development and possibilities of using the technology of acoustic emission was organized by the Institute of Design. The Conference AE'99 took place from 15 to 17 June 1999 at Faculty of Mechanical Engineering, Brno University of Technology. Czech Society for Non-destructive Testing and Brno branch of the Association of Mechanical Engineers of the Czech Republic were co-organizers. The conference was steered by a scientific committee consisting of:

Jean-Claude LENAIN, EPA SUCY en Brie, France
Eckhard PRIDÖHL, FI Dresden, Germany
Lubomír SODOMKA, CVUT Praha, Czech Republic
Václav SVOBODA, CNDT Praha, Czech Republic
Josef SIKULA, CVUT Brno, Czech Republic
Oldrich TARABA, CVUT Praha, Czech Republic
Peter TSCHELIESNIG, TÜV Wien, Austria

More than 80 participants from 10 countries registered at the conference and nearly 50 contributions were presented. They were divided into a session aimed to theoretical problems and into several sessions solving practical problems connected with AE applications, especially in mechanical engineering and civil engineering. The level of most of the contributions was very high, the evidence of what was a number of wide-ranging discussions. An exhibition of experimental technology was a very important part of the conference. The most modern appliances by Vallen-Systeme, Euro Physical Acoustics, Energovyzkum Brno, AED Laboratory Brno, ADA Pízen, and others were demonstrated. The participants of the conference had an opportunity to take part in rich accompanying program, including an evening social party on a steamer at the Brno Lake, a visit of caves in the Moravian Karst National Park and a visit to a museum at fortress Äpilberk, etc.

The international conference provided a very good overview of contemporary state of development of AE method and its use in technical practice in the Czech Republic and in a number of top workplaces abroad. As far as the Czech Republic is concerned, theoretical problems of acoustic emission are being developed especially in the Academy of Science of the Czech Republic (especially the Institute of Thermomechanics and at some Technical Universities (CVUT Praha, VUT Brno, TU Liberec, etc.). As for practical applications, acoustic emission is standard method used in a number of power stations for analyzing and control of various parts of energetic devices (Opatovice Electric, CEZ Detmarovice, JE Temelín, etc.) and in applications in mechanical engineering (namely, aircraft industry) and in civil engineering. Several domestic

firms introduced themselves at the conference, that (on commercial basis) ensure non-destructive testing by help of AE for foreign firms. AE applications by evaluation of the condition of pressure vessels, containers, and eventually the entire construction (especially energetic) systems and searching for leaks of various media are quite common. Other potential uses of acoustic emission are gradually being developed, e.g. in the area of machining, evaluation of mechanical qualities of materials (especially by cyclic loading of advanced materials). Prompt editing of a very interesting proceedings of all contributions, edited by Pavel Mazal, was positive side of the conference, too. Selected papers are presented in this issue. List of the entire contributions in the proceedings of the conference AE'99 is given below (Page numbers are listed for the papers included in this issue.):

J. Blaha, K. Sláma, M. Svetlík (ADA Akustická emise, s.r.o. Plzen, Czech rep.)
Accurate localization of defects in the welds of a header with a set of pipes

T. Boczar (TU Opole, Poland) Identification of fundamental forms of partial discharges **S7**
based on the results of frequency analysis of their acoustic emission

T. Boczar, M. Lorenc (TU Opole, Poland) Measurements of acoustic emission
generated by basic forms of partial discharges and calibration sources

G. Budenkov, O. Nedzvetskaya (TU Izhevsk, Russia) The calculation program
of acoustic fields of growing cracks

G. Budenkov, O. Nedzvetskaya, E. Bulatova (TU Izhevsk, Russia) Technical possi- **S13**
bilities of the non-contact acoustic emission method at testing hollow articles integrity

K. Chandrashekar, A. Ramachandra (S.J. College of Engineering, Mysore, India)
Experimental investigation and analysis of universal machinability index using AE

M. Cerny, P. Mazal, V. Suba (Mendel UAF Brno + Brno UT, Brno, Czech rep.) **S20**
Method of AE and possibilities of corrosion degradation detection

N.G. Chausov, S.A. Nedoseka, N.D. Gakh (IPP Kiev, Ukraine) Accelerated strength
check by the acoustic emission method for concrete with additives

F. Chmelík, P. Lukác (Charles University Praha, Czech rep.) Application of acoustic **S29**
emission in metal physics and materials science

S. Constantinescu, O. Mitoseriu, A. Ciocan, T. Radu, A. Chiriac (University of Galati,
Romania) Hot-rolled plates surface defects

J. Crha, K. Würfl (Vitkovice, Czech rep.) Life time estimation and quality assessment
by acoustic emission method

F. Dusek (AED Lab. Brno, Czech rep.) Acoustic emission analyzers of series AED FTA

J. Dvoráček, J. Petrás, D. Kolár (Brno UT, Czech rep.) Description of AE signals
in the course of the contact fatigue test method

- L. Golaski, P. Gebiski, I. Baran, Kanji Ono (Kielce UT + FRI Krakow, Poland and Univ. of California, USA) Waveform analysis of acoustic emission during pressurization of glass-fiber composite pipes **S37**
- F. Havlíček, J. Crha (TU Ostrava, Vítkovice a.s. Ostrava, Czech rep.) Acoustic emission monitoring during solidification processes **S45**
- F. Helebrant, J. Ziegler, L. Hrabec, J. Dedrle (TU Ostrava, Czech rep.) Certifikace odborné způsobilosti osob v ATD CR (in Czech)
- M. Korenská, L. Pazdera, J. Smutny (Brno CVUT, Czech rep.) Determination of propagation wave velocity in solid state by means of electric discharge spark
- A. Kotolomov, G. Budenkov, O. Nedzvetskaya (Izhevsk TU, Russia) Radiation of B. acoustic emission waves during stress corrosion cracking of the metal **S51**
- M. Landa, M. Chlada, Z. Prevorovsky (ITCAS Praha, Czech rep.) NDE of phase transformations in Cu based shape memory alloys by ultrasonic techniques **S57**
- J.C. Lenain (EPA Sucy en Brie, France) Structural integrity assessment of pressure vessels with MONPAC/IPAC technology
- M. Lorenc (TU Opole, Poland) Selection of calibration method of measuring systems used in the acoustic method of estimating electric discharges
- O. Matal, J. Zaloudek, T. Simo (Energovyzkum, spol. s.r.o. Brno, Czech rep.) VVER steam generators and acoustic emission **S65**
- O. Matal, J. Zaloudek (Energovyzkum, spol. s.r.o. Brno, Czech rep.) Application of acoustic emission in valve diagnostics
- P. Mazal, J. Richter (Brno UT, Czech rep.) Application of acoustic emission technique on fatigue testing machine Rumul **S70**
- L. Moraru, A. Ciocab, S. Constantinescu, C. Tudose (University of Galati, Romania) Crystallite size and microstrain of aluminium solidified in ultrasonic field
- O. Nedzvetskaya, G. Budenkov, A. Kotolomov (Izhevsk TU, Russia) Definition of growing cracks depth using Rayleigh waves
- J. Nuffer, D. Lupascu, J. Rödel (UT Darmstadt, Germany) Acoustic emission and state of fatigue of ferroelectric $\text{Pb}(\text{Zr}_x\text{Ti}_{1-x})\text{O}_3$ ceramics **S78**
- L. Pazdera, J. Smutny (Brno UT, Czech rep.) Possibility to location of an acoustic emission sources
- R. Pensec, M. Cherfaoui, C. Herve, A. Laksimi (UT Compiègne and CETIM, France) Monitoring of defects evolution in pressure vessels. Application to the improvement

of the AE detection criteria

V. Svoboda, J. Petrusek, A. Proust (Elektrárny Opatovice a.s. and Preditest s.r.o. Praha, Czech rep.) Application of AE method at pressure tests of boiler header **S83**

V.I. Petrov, V.E. Gromov, I.S. Lobova, N.D. Kalyukina, E.S. Kuchumova, S.N. Gorlova (Siberian TU, Novokuznetsk, Russia) The use of acoustic emission in heat engineering

I. Polajnar (University of Ljubljana, Slovenija) AE during resistance spot welding

V. Poppeová, S. Fogelton, J. Uríček (TU Zilina, Slovakia) Vyuzitie AE pri hodnotení procesu obrábania kovov (in Slovak)

Z. Prevorovsky, M. Chlada, M. Landa, M. Blaháček (Institute of Thermomechanics, CAS, Czech rep.) Simulation and identification of AE sources in anisotropic structures

F. Rauscher (TUV Vienna, Austria) Acoustic emissions of vessels with partially penetrated longitudinal seams **S92**

L. Sodomka (CTU Praha, Czech rep.) Acoustic emission of composites

L. Sodomka (CTU Praha, Czech rep.) Acoustic emission and mechanoluminescence

L. Sodomka (CTU Praha, Czech rep.) Acoustic emission on dislocation

J. Sikula, B. Koktavy, I. Kosiková, J. Pavelka, T. Lokajček (Brno UT, Czech rep.) Electromagnetic emission from polycrystalline solids **S100**

J. Sikula, J. Pavelka, K. Koktavy, K. Hájek, M. Dobes, L. Ostry (Brno UT, Czech rep.) Acoustic emission of ballscrews

R. Stastny, C. Holecek (Elektrárna Detmarovice, Czech rep.) Experience from stationary equipment operation used for leak detection by means of AE on boiler pressure units of Detmarovice power station

O. Taraba, M. Murla (ELTEC Praha, Czech rep.) The characteristic of the acoustic emission generated by leaks when gas or liquid medium is transported

O. Taraba, M. Murla (ELTEC Praha, Czech rep.) The acoustic emission generated by an electrical polarisation of a dielectric and a magnetic polarization of some magnetic materials

P. Tscheliesnig, J. Liöka (TUV Vienna, Austria and SKODA Plzen, Czech rep.) The testing of LPG vessels with acoustic emission examination **S108**

Z. Weber, M. Korenská, L. Pazdera (Brno UT, Czech rep.) Structural integrity evaluation of reinforced concrete crossbeam by acoustic emission method

K. Zehnula, P. Benes (Brno UT, Czech rep.) Utilization of AE for the flow measurement

Abstracts

M. Dabrowski, K. Karbowski (Cracow UT, Poland) The investigation into wear of TiN coating on tool steel considering the signal of AE

I. Kolarov (HST, Sofia, Bulgaria) A model investigations of AE in rolling bearings

R. Novak (CTU Praha, Czech rep.) AE application to monitoring of hard coatings failures

D. Sajdl (VSCHT Praha, Czech rep.) Development of a new laboratory calibration source for AE

J. Zizka, M. Novák, V. Prukner, V. Gabriel (TU Liberec, Czech rep.) AE for cutting process monitoring

Limited number of Proceedings from the conference is still available at the organizers of the conference and it is possible to buy it for price US\$70, (mailing and packing included) from the conference organizer at the address below:

Pavel Mazal,
Institute of Design,
Brno University of Technology,
Technick-2,
CZ 616 69 BRNO, Czech Republic

fax: +420-5-4114-3231, e-mail: mazal@cms.fme.vutbr.cz

Received 15 October 1999. Pavel Mazal is affiliated with Brno University of Technology, Faculty of Mechanical Engineering, Brno, CZ 616 69 Czech Republic (mazal@cms.fme.vutbr.cz) and Václav Svoboda is with Preditest, s.r.o., Praha, Czech Republic.

Next EWGAE Meeting

In 2002, EWGAE meets at Praha, Czech Republic. It is tentatively scheduled for the second week of September.

Cover Photograph

Metacoustic team of Australia used over 170 transducers simultaneously to monitor a chemical plant during its start-up in 1997. This test was used successfully in place of the hydro-test that is normally employed to evaluate such a plant prior to start-up.

**IDENTIFICATION OF FUNDAMENTAL FORMS OF PARTIAL DISCHARGES BASED
ON THE RESULTS OF FREQUENCY ANALYSIS OF THEIR ACOUSTIC EMISSION**

BOCZAR TOMASZ

**DEPARTMENT OF ELECTRICAL ENGINEERING AND AUTOMATIC CONTROL
TECHNICAL UNIVERSITY OF OPOLE**

Abstract

The paper presented the spectral analysis of acoustic emission pulses generated by a sort of discharges on indeterminate-potential particles moving in liquid dielectric materials. Amplitude and power density spectra for the pulses was computed, followed by the derivation of their descriptors characterizing the discharges in a synthetic way. Some interesting properties of the discharges were extracted from the descriptors, contributing to possible use of the method in diagnostics of insulating systems in electric power facilities.

Keywords:

AE-acoustic emission, PD – partial discharges

1. PROBLEM STATEMENT

In recent years the development of the AE method has been conditioned by improving measuring systems employing the achievements of electronics and computer technology, and has been connected with the application of digital signal processing procedures. Increasingly, the problem is not the recording of AE generated by PD but the proper analysis and interpretation of the achieved measurement results.

An important issue consists in defining and determining the parameters characterizing AE pulses, referred to as descriptors, which should be combined with the condition of the measured insulation and should contain indispensable information for PD form identification. To date, in order to characterize PD, a group of parameters determined in a course of time run transformations of the measured AE signals has been mainly used. These variables are not always sufficient to characterize the processes that are accompanied by AE activity. Digital processing of AE signals enables the discrimination of parameters characterizing the spectra paths of the measured AE pulses. Determining descriptors' values in the time-domain and evaluating them in respect to their usefulness in detection, location and PD measurement is a current issue and requires further research. Moreover, the issue is also the possibility of PD form identification, based on the knowledge of frequency spectra generated by this AE pulse discharge. These issues have been discussed in Refs. [1, 2, 3, 4, 5].

In the research conducted, the following two theses have been put forward:

- a) various PD forms are accompanied by AE generation of characteristic frequency spectra and descriptors connected with these spectra,
- b) identification of the form of discharges based on the knowledge of frequency spectra of AE pulses and descriptors connected with them, at the present state of science, is possible only in the case of single-source discharges of one kind.

2. SELECTION OF PD GENERATED TYPES AND THEIR CHARACTERISTICS

In publications on PD, depending on the approach, we can encounter various criteria for their classification. The most common is the energy-type criterion. We can also encounter classification based on the variation of PD intensity in time. There is also classification based on the geometry of the flaw and on the sort of dielectric material in which PDs are generated. In this paper, a classification is adopted which makes it possible to differentiate the most important forms of PD occurring in the insulation of high-power transformers during their operation. We thus classify the discharges as follows: discharges of the type "spike-plate" in oil, surface discharges in oil, discharges in gas bells generated in oil, discharges on indeterminate-potential particles moving in oil.

Spark gap sketches of each of the listed forms of discharges have been built for the generation. They have been characterized in Refs. [1, 2, 3, 4, 5].

3. SELECTION OF DESCRIPTORS CHARACTERIZING AE PULSES GENERATED BY PD

In AE measurements it is very important to determine the descriptors of pulses containing the most essential information for PD evaluation. So far, when determining the detrimental effects of PD on insulation, time-domain descriptors have been used. These variables are not always sufficient to characterize PD processes, which are accompanied by AE activity. Moreover, they have not been used to identify generated types of PD. Theoretically, around 50 various descriptors can be used in the AE method, only 20 of which, however, are of metrological value. In this paper have been analyzed and determined the values of the following descriptors, which in the frequency-domain characterize the measured AE pulses, generated by PD: maximum value, frequency for the maximum value of the spectrum, medium value, RMS value, peak factor, variance, median frequency, standard deviation, ranges of dominant frequencies for the assumed discrimination threshold. Formulas defining the above-listed parameters have been taken from the theory of signals. The values of the above-defined descriptors have been calculated separately for the amplitude spectrum, which presents the dependence of the Fourier transform module on frequency, and for the energy density spectrum, determined as a square of the module of this transform. These values have been determined for all registered AE paths generated by each of the matched PD forms.

4. SELECTION OF CONDITIONS OF PD GENERATION, MEASURING SYSTEMS AND THE MEANS OF DETERMINING THE SPECTRA OF THEIR AE PULSES

The value of voltage of discharge generation, at which the generated AE pulses were registered, for all four systems was 80% U_p (breakdown voltage). For each of the PD generation systems the recording of AE pulses was performed ten times. The time of each measurement was 1s, which ensured the recording of AE pulses in 50 periods. To determine what influence a change of the value of voltage of discharges generation for PD generated in the system with particles of indefinite potential has on the frequency analysis results, AE pulses measurements at the voltage of 60% and 70% U_p were performed. In order that the results of measurement and analysis of AE pulses generated by the selected PD forms may be of general value and be comparable, they were given as relatives referred to the values of the breakdown voltage U_p . To measure and analyze the frequency spectra of AE pulses generated by the defined PD types, a standard diagnostic system by the firm Bruel & Kjaer was used that consists of the following parts: a wide-band contact

piezoelectric transducer (type 8312), an amplifier with a filter (type 2638), a measuring card (TAD-05) provided with a 12-bit A/D converter, placed in a computer.

Frequency analysis of AE pulses generated by typical PD forms was performed for time periods of various lengths in the range from a few ms to several dozen μ s. The sequences of AE pulses coming from all discharges generated during consecutive half-cycles, and also single discharges separated from these series were taken into consideration. Frequency analysis was performed separately for AE impulses emitted during the positive and negative half-cycles of the supplying voltage.

For each measurement the following AE characteristics have been drawn: time plot, amplitude spectrum and spectrum of energy density that have been presented in Refs. [1, 2, 3, 4, 5].

5. ANALYSIS OF THE POSSIBILITIES OF IDENTIFYING PD FORMS BASED ON A KNOWLEDGE OF THE SPECTRA OF AE PULSES AND DESCRIPTORS THAT CHARACTERIZE THEM.

The results of the performed analyses presented in Refs. [1, 2, 3, 4, 5] proved that the generation of each of the four tested PD forms is accompanied by AE of characteristic plots of frequency spectra. The length of the analyzed time periods and the value of generation voltage in the range from striking voltage to the value of 80% Up for the tested PD forms did not influence the plots of their amplitude spectra and energy densities. In Fig. 1 and 2 the averaged amplitude spectra plots obtained for the four considered PD forms have been presented. The characteristics have been drawn, using spline interpolation, separately for AE impulses generated in positive (Fig.1) and negative (Fig.2) half-cycles of the voltage. The length of time for which the characteristics were designated was 4.096 ms. In order to distinguish between the plots of particular spectra, letter assignments have been introduced that indicate consecutively the graphs corresponding with the following forms: a - PD generated in oil in "spike-plate" system, b - PD generated in oil system with gas bells, c - surface PD in oil, d - PD generated in oil with indeterminate-potential particles. Comparing the designated frequency characteristics, a clear difference in their plot should be noted, dependent on the kind of PD.

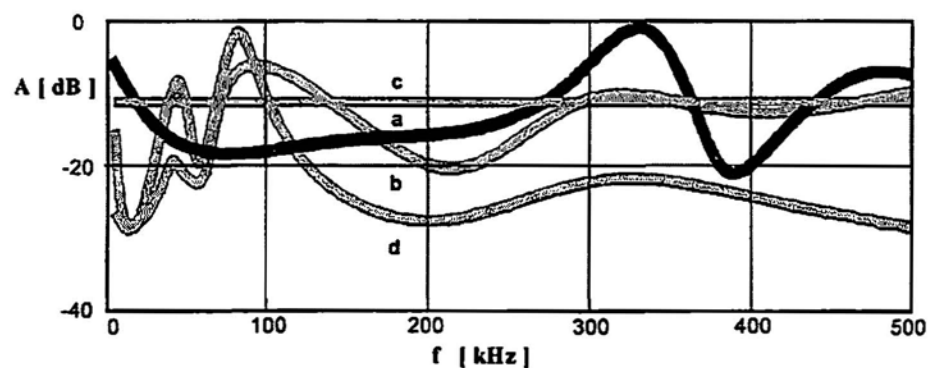


Fig.1 Averaged amplitude spectra plots of the four PD forms during the positive half-cycle, for the time period 4.096 ms

For each of the analyzed PD forms, characteristic values of descriptors designated for frequency spectra of their AE have been received. In Fig. 3 and 4 the average values of median frequency have been compiled for both half-cycles, separately for the amplitude spectrum (Fig. 3) and energy density spectrum (Fig. 4).

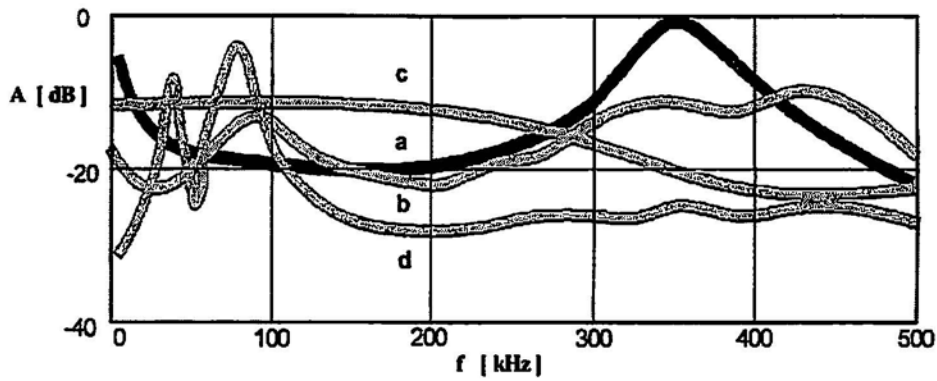


Fig. 2 Averaged amplitude spectra plots of the four PD forms during the negative half-cycle, for the time period 4.096 ms

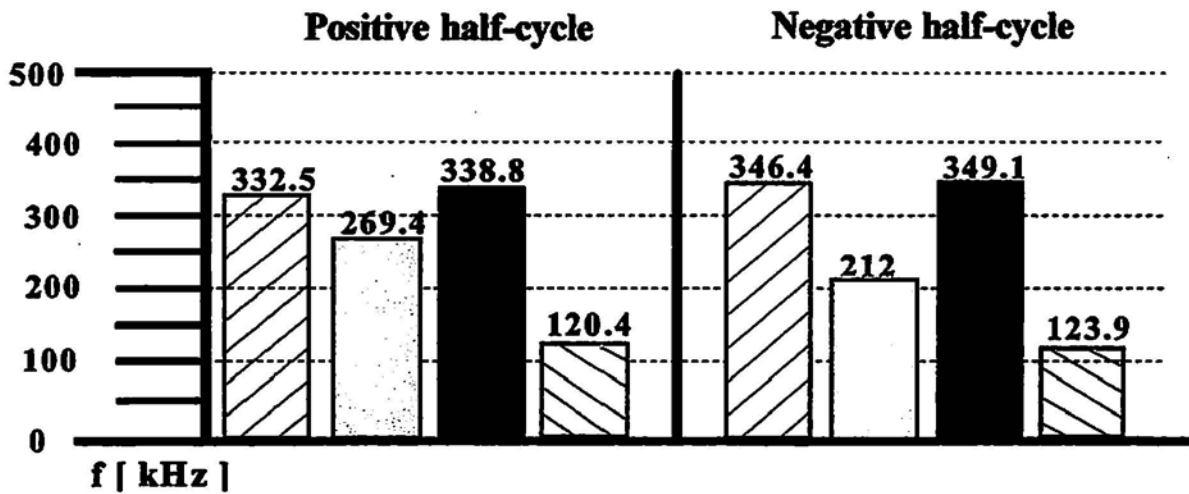


Fig. 3 Compilation of average values of median frequency calculated for the amplitude spectrum for the four tested PD forms

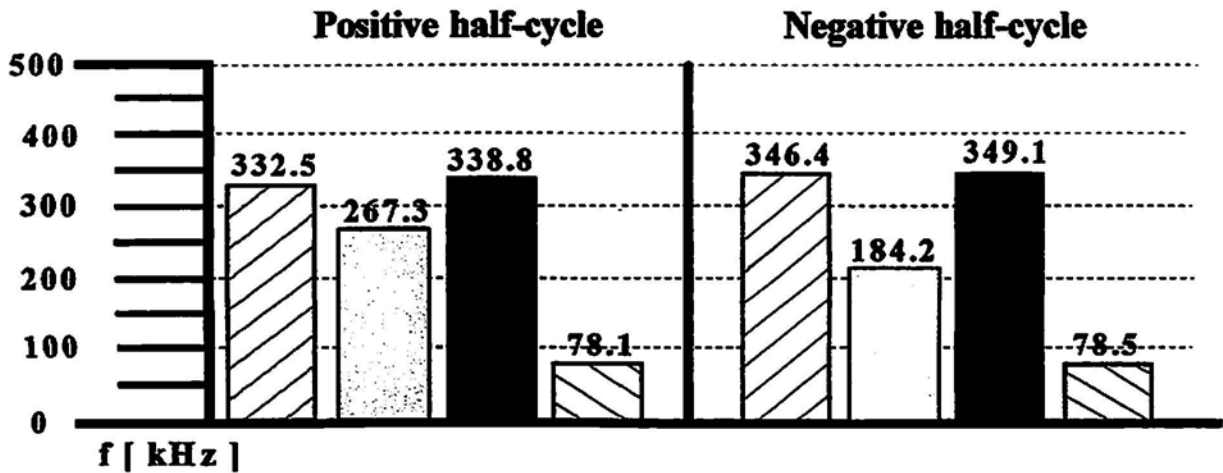


Fig. 4 Compilation of average values of median frequency calculated for the energy density spectrum for the four tested PD forms

Explanations:

-  - oil discharges in "spike-plate" system
-  - surface discharges in oil
-  - discharges in oil system with gas bells
-  - discharges generated in oil with indeterminate-potential particles

Chart 1 Compilation of ranges of dominance frequencies for the four tested PD forms

PD type	Bandwidth of dominance frequencies [kHz]	
	PD generated during the positive half-cycle	PD generated during the positive half-cycle
a	0-30 ; 230 - 370 ; 420 - 500	0-30 ; 260 - 450
b	60 - 160 ; 260 -500	70 -110 ; 290 - 350
c	"flat spectrum"	250 - 500
d	30 - 50 ; 60 -100	30 - 40 ; 60 -100

The designated values are mathematical averages calculated each time from the values obtained for three time periods. In Chart 1 are listed the ranges of bandwidths of dominance frequencies in the spectrum, which have been determined for each of the tested PD forms, at the same discrimination threshold equal -100 dB. They have been determined separately for the positive and negative voltage polarization.

6. CONCLUSIONS AND SUMMING UP

- a) Characteristic frequency spectra plots of AE pulses and descriptor values that characterize them have been obtained for the tested PD forms.
- b) On the evidence of frequency spectra plots, the ranges of bandwidth of dominance frequencies and the value of the median frequency, compared simultaneously, it is possible to identify PD forms. However, it refers only to one-point discharges, single and of one type. The open issue remains the possibility of identifying a few PD forms occurring simultaneously, or discharges of one type but repeated ones and additionally in more complex insulation systems. Moreover, it is not possible to uniquely identify PD forms exclusively on the basis of the value of one, selected descriptor.
- c) Frequency analysis of AE pulses from PD should be conducted regarding the polarization of the supplying voltage.
- d) Designated limits (boundaries) of bandwidths of dominance frequencies for particular PD forms indicate the necessity of using of measuring equipment and performing the analysis of the measured AE pulses in the range of at least 500 kHz.

In this paper the values of descriptors characterizing the measured AE pulses in the

frequency-domain have been defined and determined. It has been shown which descriptors, in some cases, can be used to identify the generated PD forms.

The results of the performed frequency analysis confirm the possibilities of PD form identification knowing the frequency spectra and descriptors determined for them. This can be of practical significance in evaluating the condition of insulation systems of such electrical power facilities as high power transformers, high voltage measuring transformers, insulators and power capacitors. However, PD occurring in industrial conditions have multiple source, are repeated and are of various types, therefore it is necessary to carry out further research, which would supplement the state of knowledge in Frequency analysis of AE pulses generated by multi-point PD of various types.

REFERENCES

- [1] Boczar T., Analiza widm impulsów akustycznych emitowanych przez niepełne wyładowania powierzchniowe, ZN Pol. Op. Nr 219, z. 44 Elektryka, Opole 1996, str. 125 - 136.
- [2] Boczar T., Analiza częstotliwościowa sygnałów emisji akustycznej generowanej przez wyładowania elektryczne, Prace 20 SPETO, 1997, str. 441 - 445.
- [3] Boczar T., Możliwości identyfikacji formy wyładowania na podstawie widma częstotliwościowego jego emisji akustycznej, VI EUI'97 Zakopane, 23 - 25.10.1997, str. 35 - 40.
- [4] Boczar T., Badanie widm częstotliwościowych impulsów emisji akustycznej generowanych przez wyładowania niepełne, IV IW - 98, Poznań - Kiekrz, 1998, str. 51-57.
- [5] Skubis J., Boczar T., Spectrum of acoustic emission pulses generated by electric slide surface discharges in oil, Archives of Electrical Engineering, No 1, Vol. XLVII, 1988, pp.25-38

TECHNICAL POSSIBILITIES OF THE CONTACTLESS ACOUSTIC EMISSION METHOD AT TESTING HOLLOW ARTICLES INTEGRITY

Prof., Dr.Tech.Sc. G.Budenkov,

Ass. Prof., PhD O.Nedzvetskaya, Ass. Prof. E. Bulatova

Izhevsk State Technical University

Studencheskaya st., 7, Izhevsk, Russia, 426069,

E-mail: root imi.udmurtia. SU, Tel. (3412) 588852; Fax (3412) 588852

***ABSTRACT.** Technical possibilities of the contactless acoustic emission method at testing hollow articles using ultrasonic leak detector «GERMES-2 » are presented. The possibilities of the quantitative estimation of leakage output in articles working with gauge pressure and quantitative estimation of the sizes of hollow articles through defects are shown. The recommendations for development of techniques and means of a ultrasonic leak detective method are given.*

***KEYWORDS:** integrity, tightness, contactless acoustic method, leakage, output, through defects.*

INTRODUCTION

In order to insure reliable work of systems of transportation and keeping of liquids and gases, working both with gauge pressure (pipelines, high pressure vessels), and without it (sectional coolers, cabins and automobile interiors, the containers for products keeping, etc.), the requirements of tightness or impenetrability and air-tightness and leak-proofness are necessary. The reason of loss of tightness are more often through defects, which look like voids, burn- through, cracks, fusion, local channels. Tightness is estimated by leak detective method. Leak-tested methods are made the rather high requirements on sensitivity remotability, productivity and maintenance of safety The majority of modern leak-tested methods with a high threshold of sensitivity (mass-spectrometer method $5 \cdot 10^{-13}$ W, luminescent method - 10^{-10} W, halogen method - 10^{-7} W) have practically up to zero remotability, low , productivity and require the special preparation of a surface.

In this aspect the contactless acoustic leak-tested method is notable for high remotability and operations and can be effectively used for the control of articles on tightness at low requirements to threshold of sensitivity.

The contactless acoustic leak-tested method is based on registration and analysis of parameters of acoustic waves generated by leakage into environmental atmosphere and allows to define a leakage location and to estimate its parameters.

CONTACTLESS ACOUSTIC LEAK-DETECTOR "GERMES-2»

The portable ultrasonic leak detector «GERMES-2 » (Fig.1) is developed in Izhevsk State technical university. The device is intended for:

- Detecting gas leakage in systems with gauge pressure;
- Definition of leakage location;
- Estimation of leakage output and volume of following gas for a unit of time;
- Detecting and estimation of tightness loss places of closed volumes.
- Detecting discharge in power electrical circuits.

The action of the device is based on registering acoustic waves of an ultrasonic range, which are radiated during gas outflow through small through holes under pressure large than 0,3 atmospheres, and also accompany the discharge processes. The frequency spectrum of such waves can extent from sound range frequencies up to several megahertz and consequently can't be always heard by the operator (in absence of the device).

In order to detect site of tightness loss of closed volumes the generator of ultrasonic waves including as a set of the device with periodically deviating frequency is located inside of the article. The site of tightness loss are defined with the help of the receiver-display block, recording the maximum signals in such sites.

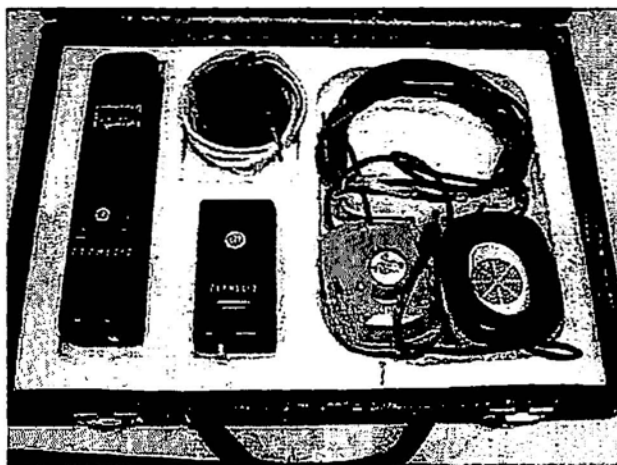


Fig.1. Foto of contacless acoustic leak-detector"Germes-2».

The basic technical characteristics of leak-detector "Germes-2» are listed in table 1.

Table 1

Technical characteristics	Value
1. Transmitter operating frequency, kHz	40±2
2. Wave stress of the transmitter block, Pa	2
3. Sensitivity of the receiver-display block (min. sound stress, registered by the device on operating frequency), Pa	10 ⁻⁵
4. Sensitivity of the the receiver-display block to an airflow in a leak-tested regime, W	10 ⁻³
5. Indication: Sound (dynamic loudspeaker and head telephones), frequency, kHz	1,5-3
Pointer type indicator	
6. Power source: Receiver-display block, V	+6

Time of continuous work without boost charge, hour	10
Ultrasound transmitter block, V	+5
Time of continuous work without boost charge, hour	50
7. Sizes, mm	
Receiver-display block	250x55x46
Ultrasound transmitter block	120x55x35
Weight, kg	
Receiver-display block	0,52
Ultrasound transmitter block	0,28
Article in packing	2,5

ESTIMATION OF LEAKAGE OUTPUT BY ACOUSTIC EMISSION METHOD

As was told above, gas (liquid) outflowing through leakage at superfluous pressure is accompanied by radiation of acoustic waves into an environmental atmosphere or by acoustic emission (AE).

The true gas leakage output W is defined by product of gauge pressure P on volume of outflowing gas V for a time unit t :

$$W = \frac{PV}{t} \quad (1)$$

The energy of acoustic waves, radiated by leakage for unit of time (leakage acoustic output W_A) makes up a part of general output W . The acoustic and true leakage outputs are connected by some coupling coefficient k :

$$k = \frac{W}{W_A} \quad (2)$$

Coefficient k depends on a number of the factors (sizes and geometry of the hollow, pressure differential, temperature etc.). It can be determined from the experimental graph, constructed according to the technique given in [1]. To estimate true (general) output of leakage quantitatively it is necessary to know the coupling coefficient k and the output of acoustic waves W_A , radiated by leakage into an atmosphere.

Consider a way of determination of acoustic waves output W_A using the leakage detector «GERMES-2» described above, receiving acoustic waves in a narrow frequency bandwidth about 40 kHz.

The threshold intensity in a wave I_0 registered by the device receiver (power of sound energy, transferring through an unit area, perpendicular to the propagation direction) is defined as

$$I_0 = \frac{p_0^2}{2\rho c} \quad (3)$$

where $p_0 = 2 \cdot 10^{-5}$ Pa – the threshold of sensitivity of the device on pressure (Table 1), $\rho c = 430$ Pa*c/m – wave resistance of propagating environment (atmosphere). At such value of receiving pressure the device pointer deviates on half of indicator scale. Calculations according with the formula (3) give for $I_0 = 4,6 \cdot 10^{-13}$ W/m². Thus the minimum value of ultrasound intensity (threshold of sensitivity) has been found, it can confidently register by the device. The distance r between the leakage source and device

receiver-display block, on which the indicator pointer deviates on half of scales at the maximum sensitivity, is the radius of half-sphere, on which the intensity of acoustic wave radiated by the leakage source is equal I_0 . (Here the leakage is assumed to be a point source of ultrasound, forming a spherical wave). Then the complete power of sound energy in a spherical wave, radiated by leakage source in operating frequency band of the device (acoustic leakage power), is defined:

$$W_A = I_0 \cdot S = I_0 \cdot 2\pi r^2 \quad (4)$$

In the paper [1] the results of measurements of true and acoustic leakage outputs depending on gauge pressure are given, coupling coefficient k and threshold of sensitivity to to gas and gas-liquid leakage is estimated.

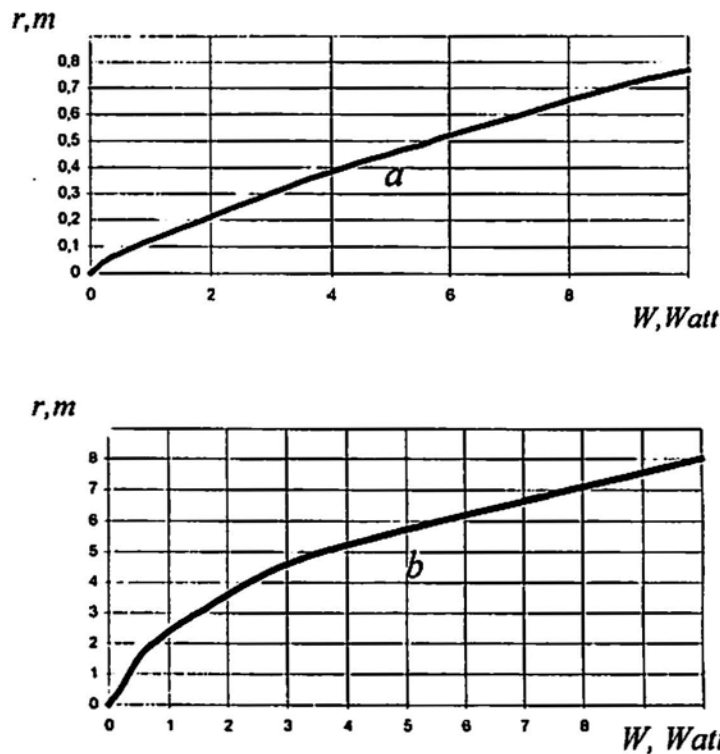


*Fig.2. The dependencies of leakage output W on the distance r :
a- without using the attenuator, b- using the attenuator.*

The dependencies of leakage output W on the distance r between the leakage source and device receiver-display block are submitted on Fig.2 as an example of the estimation of leakage output (without using the attenuator - Fig.2a, using the attenuator - Fig. 2b). (The attenuator is used in conditions of external noises of sound range, and also if necessary to reduce the device sensitivity for estimating the leakages of great output). The submitted dependencies are received experimentally at gauge pressure 0,1-0,3 MPa.

The accuracy of the estimation of leakages output depends on geometry of the gas outflow channel and the presence of a moisture and oil in outflow area. The latter can result in essential

overestimate of measured leakage output.

The knowledge concerning leakage true output, allows us to make a conclusion about flow rate of the product (gas) outflowing for a certain time interval, that is to estimate product losses, gassing of industrial premises and living accommodation, etc.

For example the gas flow rate will make $1,05 \text{ m}^3/\text{year}$, if the leakage output is equal to $0,25 \text{ W}$ and gauge pressure is equal to 75 atm. ; and the gas flow rate will make $1040 \text{ m}^3/\text{year}$, if the leakage output is equal to 10 W and gauge pressure is equal to 3 atm. The leakage with higher output as a rule radiate waves in a sound frequency range and can be detected by the operator without the device.

Thus, contactless acoustic leak-tested method allows

- To detect the leakage in systems with gauge pressure;
- To define the leakage location;
- To estimate the leakage output and volume of following gas for a unit of time.

TESTING OF HOLLOW ARTICLES INTEGRITY BY CONTACTLESS ACOUSTIC METHOD

The contactless acoustic method testing of hollow articles on the presence of through defects is following. The source of in a frequency range of $30 - 60 \text{ kHz}$ is located inside of hollow articles. The ultrasonic waves, penetrating through a hole with the size more than $\sim 0,01 \lambda$ (λ is the wave length), can be fixed by acoustic receiver-display block of the device outside the testing article.

However the walls of the controllable articles can be also transparent for the ultrasonic waves at the certain angles of incidence, determined by a rule of coincidence

$$\alpha = \arcsin(C_v/C_m), \quad (5)$$

where C_v is the wave velocity in air, C_m is the velocity of the Lamb wave mode a_0 , excited in a wall of the article. Therefore acoustic devices alongside with a useful signal (ultrasonic waves, penetrated through the hole), will also register noise (ultrasonic waves caused by the acoustic transparency of the walls of the testing articles).

The authors investigate experimentally the dependencies of a useful signal and noise on parameters of through defect, elastic properties of a material and article wall thickness. The contactless acoustic leak-detector "Germes-2" was used in researches as measuring-acoustic device.

The acoustic fields of holes, simulating through defects, with diameters of $0,08-0,22 \text{ mm}$ in a steel and aluminium plates with the thickness $0,8-4 \text{ mm}$, and also acoustic transparency of the plates (noises) are investigated on the base of technique described in [2].

In Fig. 3 the dependencies of acoustic pressure in the wave, penetrating through the hole on the hole cross-section area (Fig 3a) and on the hole length, referred to its diameter (Fig.3b) are shown.

It is assumed that the ultrasonic waves penetrating through the hole are the point source of ultrasound, forming a spherical wave.

Therefore the acoustic pressure in the wave is determined by the formula

$$P = \frac{A}{r_0} \cdot e^{-\delta r_0}, \quad (6)$$

where $A = \frac{P_0 \cdot r}{e^{-\delta r}}$, r is the distance r between the through hole and device receiver-display block, on which the indicator pointer deviates on half of scales at the maximum sensitivity, that corresponds to pressure in registered wave $P_0 = 2 \cdot 10^5 \text{ Pa}$ (Table 1); r_0 is equal for example to 1 cm (the distance

between the through hole and device receiver-display block, on which signal was reliably registered).

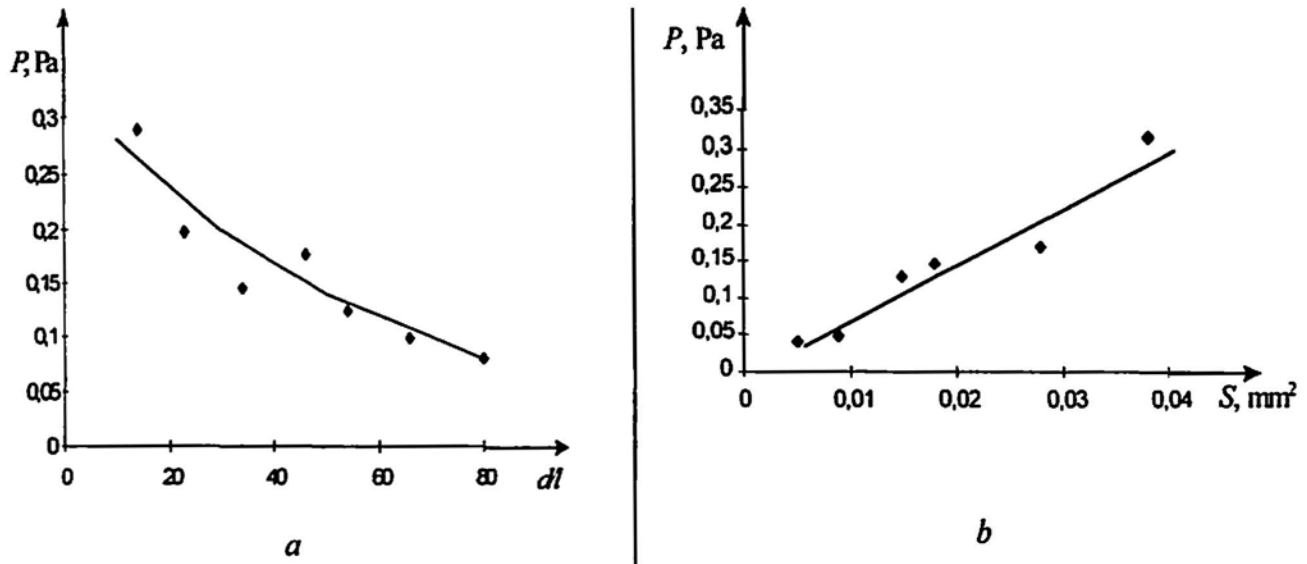


Fig. 3. The dependencies of acoustic pressure in the wave on the hole cross-section area (a) and on the hole length, referred to its diameter (b).

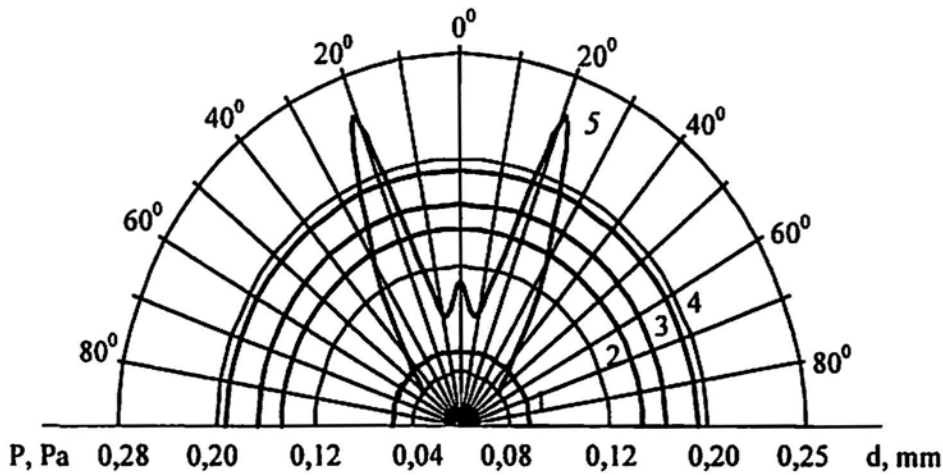


Fig.4. Spatial distributions of wave pressure amplitudes, radiated by a through holes with the diameters of 0,11 mm (curve 1), 0,14 mm (curve 2), 0,15 mm (curve 3), 0,19 mm (curve 4), and radiated by the steel plate with thickness of 2,1 mm (curve 5).

As an example experimentally obtained spatial distributions of wave pressure amplitudes, radiated by the steel plate with thickness of 2,1 mm are represented on Fig. 4. It is the results of research acoustic transparency of the steel plate walls (noise). The lines of acoustic pressure level P in waves, radiated by a through holes with the diameters of 0,11-0,19 mm are put also there.

From figures 3-4 it is visible, that detectability of the through defects depends on their sizes (diameter and length), and also from acoustic transparency of the controllable article walls. On the one hand, the amplitude of a useful signal is directly proportional to the through defect area and decreases with increase of its length (wall thickness). On the other hand, its acoustic transparency (noise)

decreases with increase of wall thickness. Thus the relation of the useful signal to noise is increased. The increase of noise most occurs in directions of the maximal transparency, that are defined by the coincidence rule (5) for Lamb wave mode a_0 .

The method sensitivity may be increased owing to orientation of the acoustic device in the directions of the least transparency of the article wall. Besides the acoustic noise at testing is possible to reduce by damping of article material in the field of testing.

The sensitivity of the method is larger at testing articles made of materials with large impedance.

The sensitivity of the given method in some cases is rather high. So, in a steel plate of 4 mm thickness a defect with the diameter of 80 microns has been found. For revealing such a defect by means of the echo-pulse method using angle probe (transversal waves) the working frequency 18 МГц, would be required, no control on which practically is realised.

As the device can be calibrated in absolute values of acoustic pressure the possibility of the quantitative estimation of through defect parameters (length and area) is following from the Fig.3. Thus estimation of through defect sizes is more unambiguous, than in the case of the estimation of leakage output.

Thus, the results obtained can be used as a basis for development of techniques of contactless acoustic emission control of articles on tightness:

- for the estimation of leakage output in the systems with gauge pressure;
- for the control and estimation of integrity of hollow articles in the systems without pressure.

REFERENCES

1. G.A. Budenkov, O.V. Nedzvetskaya, E.G. Bulatova. Technical possibility of contactless acoustic method of leakage finding. - Defektoskopiya, 1996, № 12, p. 48-53 (in Russian).
2. G.A. Budenkov, E.G. Bulatova, O.V. Nedzvetskaya, Grebenshikov S.P. Contactless acoustic method for through type defect discovering in hollow articles. - - Defektoskopiya, 1996, № 11, p. 43-48 (in Russian).

METHOD OF ACOUSTIC EMISSION AND POSSIBILITIES OF CORROSION DETECTION DEGRADATION

Michal Černý*, Pavel Mazal**, Viktor Šuba**

* Mendel University of Agriculture and Forestry of Brno

** Brno University of Technology

Introduction

Corrosion is a type of material damage, that is an important problem in both production and user area of industry. It represents an important heavy drain of the economy and it influences safety, working life, ecology etc.

For above mentioned reasons, the corrosion laboratory of Institute of Basic Technology and Repair MZLU in Brno, together with Institute of Construction VÚT FS Brno decided to start research program aimed not only to better understanding of parallel phenomenon of corrosion degradation, but especially to early detection of corrosion attack of steel construction materials by the method of non-destructive control (NDK). Endeavour should be directed to corrosion attack control in situ, which is not very persuasive by many NDK methods (electrochemical noise measuring, roentgenologic, laser, ultrasonic method). In many cases, it is only stating of surface corrosion attack, which means that of square of local character. The effort should be aimed to those types of local corrosion, that are the most feared and the most perfidious - point corrosion, selective corrosion and intercrystalline corrosion.

AE is comparatively new method of non-destructive control, which is quickly developing at present. It should not only be an efficient laboratory tool, as the results from periodical controls of integrity of equipment and components but even one of the most advantageous methods for analysing and following of equipment degradation during periodical stopping or even by following the damage during operation. AE enables to make quick diagnosis even in noisy operational conditions. This type of control represents considerable economic savings taking into consideration that the continuity of production process is not interrupted.

1 Acoustic emission phenomenon

AE is a phenomenon when, due to internal local micro movement of material, transition elastic waves appear [1]. It is noticed as an electric signal with help of piezoelectric sensing unit, that transforms elastic waves emitted by material into electric signal. It is increased, filtered and processed in such a way that it will enable to determine characteristics that were sought after. (Chart 1)

Chart 1a: A list of potential AE sources (incomplete)

Metal materials	Plastic deformation, co-operative movement of dislocation, twinning, slip on grains bounds, emergence of Lüders bands... Fracture of decohesion of precipitates of inclusions appearance and/or spreading of cracks by static or dynamic stress, fatigue or stress corrosion, embrittlement by hydrogen Diffusionless phase transformation (martenzite) Local corrosion (point, slit corrosion)
-----------------	--

Chart 1b: The influence of application and configuration on AE

Secondary or external sources	hydrogen release friction of sidewalls of the crack mechanical shock, friction, wear, abrasion leakage of gas or liquid cavitation, boiling, erosion, crystallisation electric discharge (coronary effect)
-------------------------------	---

Many parameters exist, that can be characterised in order to be able to establish the character of the source, to localise it and to measure its activity: time delay of signal, length of signal lasting, transconductance, maximum amplitude, frequency, impulse dose energy, time behaviour of signal *etc.* It can be done by registering of changes or maximum values in the cycle batch or by counting of them. There are many procedures for their analysis: space analysis (localisation) spectrum analysis, time analysis, statistics, respectively multivariable analysis.

It is inevitable that the followed mechanism is irreversible. The source has satisfactory capacity and frequency zone of the sensing unit and its sensitivity correspond with the followed phenomenon. The emissivity of the material depends on many parameters, connected with its characteristics (microstructure, mechanical characteristics, way of possible degradation, structure transformation *etc.*). The influence of the „size“ of signal is especially important for measuring in situ due to compensation of, in many cases unfavourable, conditions of acoustic noise background.

2 AE using in the area of corrosion

Of many NDK methods, main method of electrochemical noise has spread in last few years. There are few works that effectively make use of AE and they have not been, except for several of them e.g. /2/ significantly applied in industry. The reason is probably in a low intensity of the source of emission by corrosion attack (initiation and spreading of point corrosion and intercrystalline corrosion) in comparison with other sources during operation of the part. Many works take into account AE by evaluation of surface corrosion in connection with hydrogen release or with changes of presence of corrosion products inside the material/5/.

Mastering measuring technology and computer processing of signal, that has been gained during measuring of fatigue qualities of construction materials at UK VÚT FS was motivation for research in the area of point and intercrystalline corrosion, that takes into account especially the influence of growth of corrosion products in the amount of material as the source of acoustic voltage surge by polymorphic distortion of material lattice.

3. Measuring

Tested material has been chosen with consideration to coincidence of inter-crystalline corrosion and of extended application as well. Steel 17242 (0.25%C,18%Cr,9%Ni,2%Mn) serves the purpose very well; it represents basic construction material in chemical and manufacturing industry. It has not been alloyed by titanium and niobium and that is why it is significantly subject to inter-crystalline corrosion as a result of deprivation of areas on boundaries of grains by Cr, which is connected with carbide precipitation Cr₂₃C₆ (Cr₇C₂) on boundaries of grains under suitable diffusion conditions (temperature). This perfidious corrosion type, together with embrittlement mean localisation for mechanical defect, especially by welded and heat formed steels.

Tested samples: the shape of sample has been influenced by standard ČSN 420321 (for case of proving existence of inter-crystalline corrosion by traction test). The dimensions of sample of rolled metal sheet : 200x20x1mm (Figure 1). Etalons, certain for sensing of basic acoustic echo were carefully polished and passivated. Tested samples were only polished. For general comparison with different type of corrosion, material 11373, which has been exploited paralelly, proves important tendency to surface corrosion.

Corrosion environment: chloride environment is very unsuitable for austenitic steel 18/9; it led to choice of corrosion solution - 10% NaCl solution. The temperature of the solution as an activator and corrosion accelerator was 40°C. The sample was immersed into solution in constant depth of draft about 50 mm. By measuring 2b, 3b, solution 33% H₂SO₄ was chosen for clear degradation of material (Figure2).

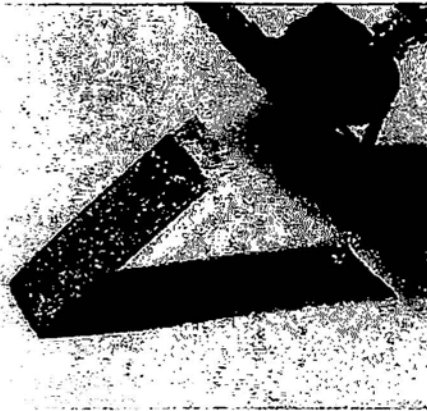


Fig. 1 Sample with fixed probe solution

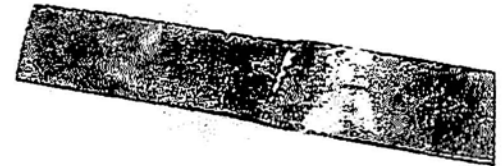


Fig. 2 Sample from measuring in H₂SO₄

Measuring system: 2-channel analyser AED 10C with pre-amplifier without arranged filters has been used for orientation measuring. In further measuring 1 and by measuring 2, 2B, 3, 3b, the main configuration was formed by 15-channel analyser AED FTA 16. Two to three probes in the same time, pre-amplifier, recording, and analysing unit PC (Figure3).



Fig. 3 Workplace with AED FTA 16 analyser, with probes, pre-amplifiers and PC

4 Measuring

Measuring itself has been done in three stages

First stage - verifying: during these preliminary tests, acoustic activity was followed on corroding samples in time intervals, both on AED 10C and AED FCA 16. It was consequently compared with acoustic activity from passivated etalons. Furthermore, growth of activity by individual measuring of steels 17242 and 11373 has been followed.

Second stage- long-lasting measurement has been done in two environments, in solution of NaCl and H₂SO₄.

II a - sample was fully fixed on a board and immersed (50mm) in 10% solution of NaCl. Measurement conditions - strengthening 28dB, frequency range 30kHz - 1,5mhz, reference level 100mV. Period of measuring 60s (1440 measuring /day). Measuring was done for 144 hours (Figure 4,5).

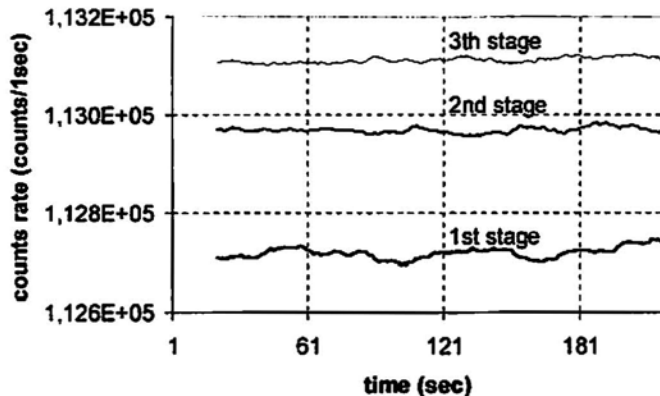


Fig. 4: The dependence of signal frequency on time in NaCl solution

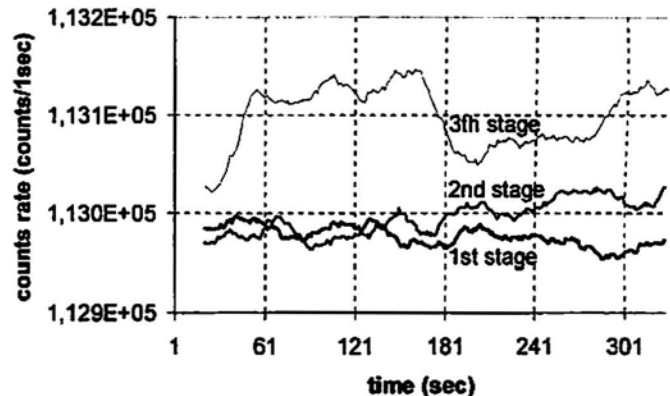


Fig. 5: Frequency of signals as a function of time by steel 11373

II b - checking of acoustic signals record in comparison solution H₂SO₄ - by intensive attack (etching) of the surface by acid. There is a prerequisite that the degradation from the point of view of acoustic echo should have been analogy of surface corrosion (material - steel 11373).

3 stage - measuring for comparison of activity of sources is represented by measuring in NaCl, H₂SO₄ and in the atmosphere (etalon) and it was aimed to direct comparison of frequency of signals and the importance of damage followed in the end of the test. AE sensing from etalon enabled to eliminate appeared artefacts during measuring from the reason of electric noise in the net. Analysis of corrosion damage has been done by method of light microscopy - following of inter-crystalline damage on metalographic samples. Samples were processed mechanical - chemically and they were followed both as polished and with visible structure (structure caused by Vilela-Bain and Nital mixture 1:1). Parameters of measuring equipment: amplifying - pre-amplifier 40dB, analyser amplifier 28 dB, reference level, and frequency level are the same. Time 2160 hours.

5 Results

I stage - measuring proved the importance of tuning of piezoelectric sensing units to the same level of amplifying for all channels, which must be done by means of characteristics of individual sensing units, used for identical formula (value of tolerance ± 2 dB quoted by producer importantly influences value of sensed dependencies). The dependency in Figure 6 show growth in values of summary frequency by individual taking offs with time distances 14 to 21 days. Taking into account the corrosion extent (initial stadium of inter-crystalline corrosion) the growth of frequency is slow. Information concerning creating of passivating layer (immediately after immersing the sample into the solution) its failure and initial corrosion development is missing. Completing measuring on steel 11373, that corrodes on the surface shows gradual growth as well. The number of recorded signals is more considerable than by steel 17242

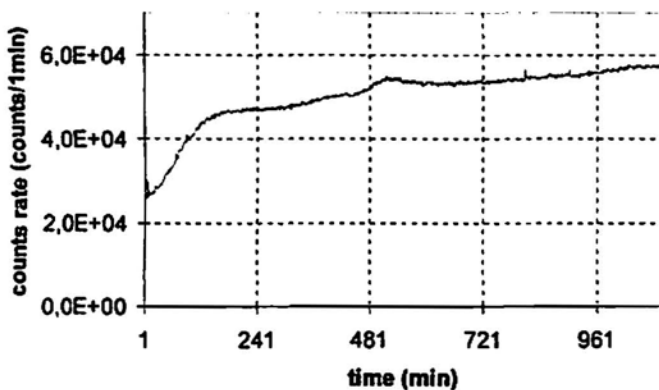


Fig. 6: Growth of frequency by long lasting test (17242 - NaCl)

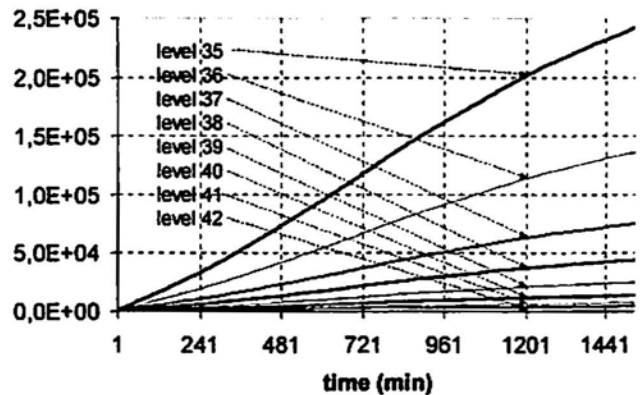


Fig. 7: Share of individual levels in total sum of signal (NaCl)

II stage - Evaluation has been aimed to search of levels, which significantly prove on total growth of signal frequency. Figure 7 shows the highest activity on levels 35, 36 and less on level 37 dB. By samples degraded in solution H₂SO₄, the activity of levels is divided better-proportioned into individual levels 35 to 48 and it is naturally bigger (Figure 8). Figure 9 shows gradual growth in AE frequency in time steps 100 min. By the sample H₂SO₄ the initial growth is steeper and than the activity corresponds with all-surface degradation of the metal by etching (Figure 10).

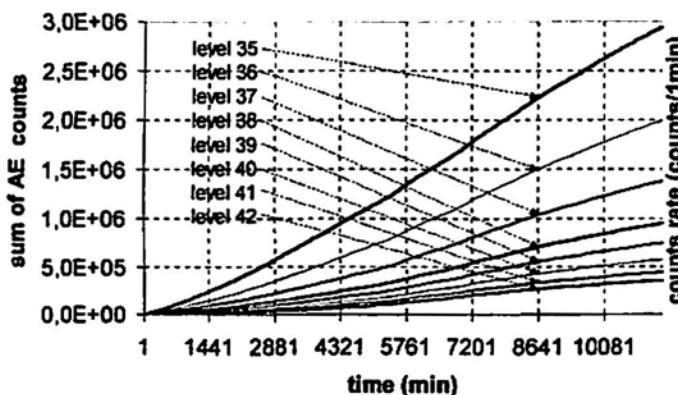


Fig. 8: Share of individual in total sum of levels by H₂SO₄

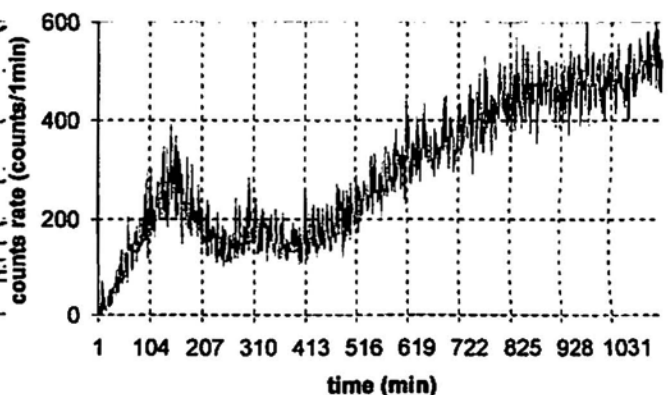


Fig. 9: Development of inter-crystalline corrosion by steel 17242

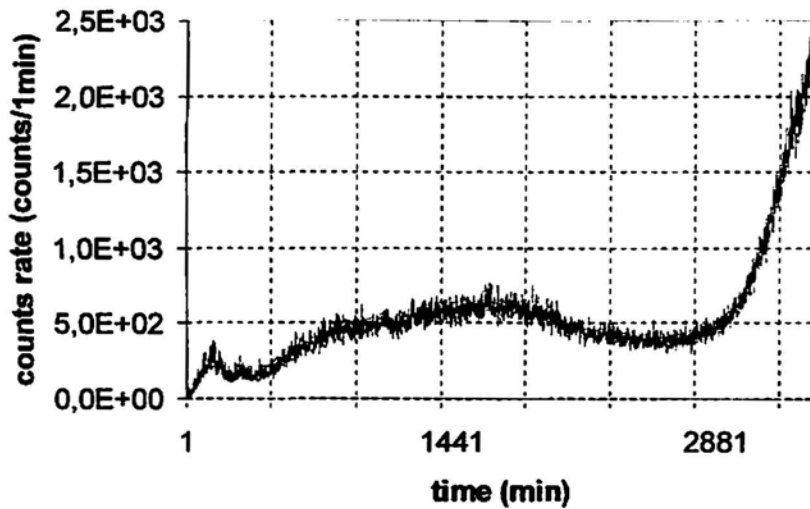


Fig. 10: Damage of steel surface 11373 by acid

III. stage records made in the last days of the test of the third stage show growth of frequency both in the area of corrosion attack and in its further progress (development) in both environments (NaCl, H₂SO₄) (Figure 11). The activity of corrosion action inside the material and on the surface of the material is in contrast with stabilised emitivity of the etalon (Figure 12). The extent of inter-crystalline damage are shown in metalographic snaps (Figures 13-15), where we can see progressive development of attack and destruction of grain borders by inter-crystalline corrosion and the placement of carbides Cr by individual take offs. Individual extensions can be, with some approximation, classified to results from measuring of acoustic echo of material.

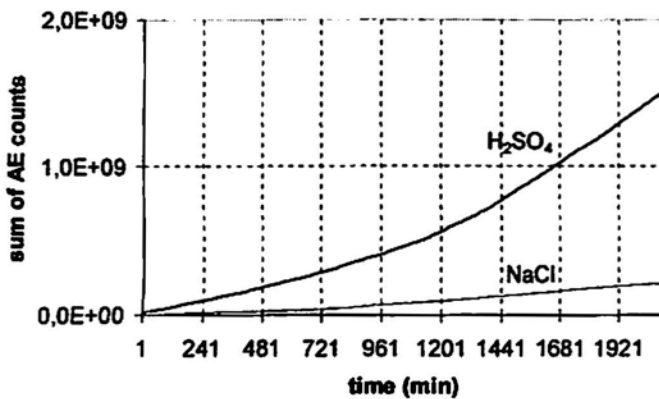


Fig. 11a: Growth of frequency in initial phase of third stage by NaCl/H₂SO₄

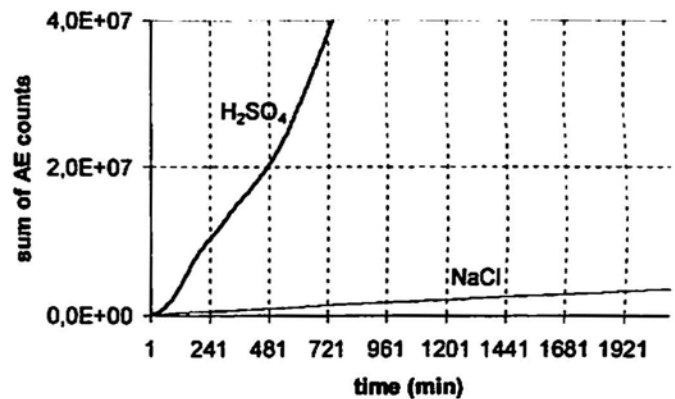


Fig. 11b: Growth of frequency in ending of third stage by NaCl/H₂SO₄

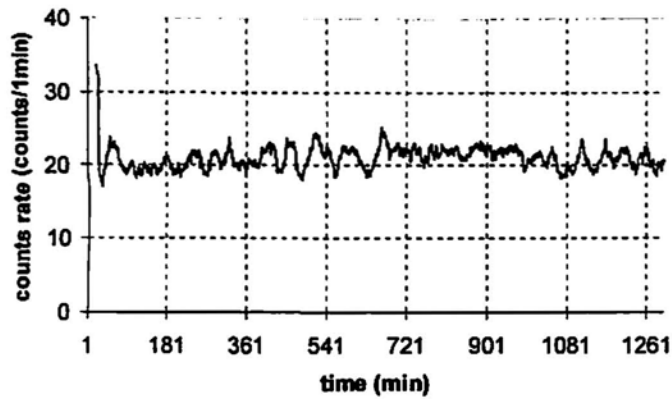


Fig. 12: Sleeping average of signal frequency by etalon



Fig. 13: First traces of inter-crystalline corrosion development in sample also of after 21 days after immersing into NaCl

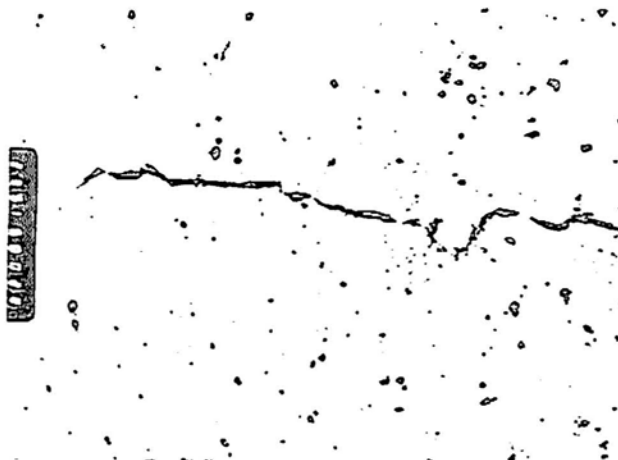


Fig. 14: Inter-crystalline damage and placing of carbides Cr

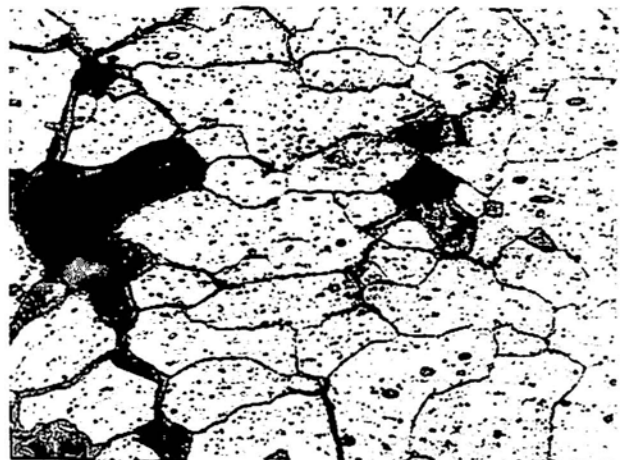


Fig. 15: Significant inter-crystalline damage after about three months of NaCl solution performance

Conclusion

The contribution represents entry part of research project of above-mentioned workplaces MZLU and VUT FS in Brno. Described applied method of acoustic emission is in this entry part charged with insufficient experience with elimination of considerable noise of background. AE sources in course of development of corrosion attack have been sufficiently described neither in domestic nor in foreign literature so far.

That is why effort to set quantitative relation between the number of recorded signals and the extent of damage followed in the end of the test (stage III) is expressed in the introductory part. Comparison of linear relationship between frequency of signals by inter-crystalline corrosion of steel 17242, surface corrosion by steel 11373 and „etching“ of the same steel in H₂SO₄ is a contribution. We can say that AE method seems to be sensitive and reliable enough.

In further research, our attention will be aimed to localisation of damage, time progress of signal in individual corrosion stadium and the fact, that acoustic emission in corrosion progress probably appears in sequence waves in connection with further local micro sources. Some areas can become active again after several hours (days) of latency. Both this and further facts significantly charge the evaluation of short-term measuring. The file of AE measurement should mouth into ensuring of continual total acoustic activity. Especially degradation is concerned, where no other NDK can be used (in the same price relations). Significant savings can be reached by periodic controls of static device. Enabling to control it by AE method requires still much research effort.

Literature

- /1/ Association Française de Normalisation. Vocabulaire utilisé en émission acoustique, AFNOR, NFA 09-350
- /2/ D. L. Parry. Detection of corrosion pitting in pipelines using acoustic emission technology. Conference on Non Destructive Evaluation, Proc., April 1983, p. 388-402
- /3/ T. V. Rettig, M.J. Felsen. Acoustic Emission Method for Monitoring Corrosion Reactions. Corrosion, Vol. 32, No. 4, 1976, p. 121-126
- /4/ F. Mansfeld, P. J. Stocker. Acoustic Emission from Corroding Electrodes. Corrosion, Vol. 35, No. 12, 1979, p. 514-544
- /5/ R. H. Jones, M. A. Freisel. Acoustic Emission during Pitting and Transgranular Crack Initiation in Type 304 Stainless Steels. Corrosion, Vol. 48, No. 9, 1992, p. 751-758

APPLICATION OF ACOUSTIC EMISSION IN METAL PHYSICS AND MATERIALS SCIENCE

FRANTIŠEK CHMELÍK and PAVEL LUKÁČ

Department of Metal Physics, Charles University, Ke Karlovu 5, 121 16 Praha 2, Czech Republic

Abstract

Acoustic emission (AE) is a value *in situ* method to study various processes in metals and metal matrix composites, particularly if combined with other experimental techniques. Few examples are given, showing the AE applicability to structure changes induced by thermal and/or mechanical loading. The effect of precipitation on the Portevin - Le Châtelier effect in an AlLi alloy, microstructure evolution in Mg-based metal matrix composites due to internal thermal stresses and phase transitions in the CuAu system (dental gold) will briefly be discussed.

Key words: acoustic emission, alloys, Portevin - Le Châtelier effect, metal matrix composites, thermal stresses, phase transitions.

1. INTRODUCTION

Acoustic emission (AE) stems from transient elastic waves generated within a material due to sudden localized irreversible structural changes [1]. In metallic materials, AE responds to the dislocation glide, twinning and microstructural damage. In metal matrix composites, damage in the ceramic phase and interface decohesion are additional sources of AE. The objective of this paper is to report on our recent results on AE from metallic materials.

2. EXPERIMENTAL PROCEDURE

The computer controlled DAKEL-LMS-16 AE facility was used to detect AE during various experiments. A highly sensitive LB10A transducer (sensitivity 85dB ref. 1V/ms⁻¹, flat response between 100 and 500kHz, built-in preamplifier 30dB) was coupled to the quartz rod using silicon grease. The DAKEL AE facility applies a two-threshold-level system of detection and evaluation of AE signals. The AE signals are filtered, amplified and then evaluated at two threshold levels to obtain two AE counts denoted N_{C1} and N_{C2} . The total count N_{C1} at the lower threshold (corresponding to a total gain of 100dB) includes all AE signals detected. The burst count N_{C2} obtained at the upper threshold level (set difference of 20dB, i. e. total gain of 80dB) includes only the AE signals with larger amplitudes (AE bursts). This procedure makes it possible to evaluate the character of the AE signals, i. e. whether they have a small or a large amplitude.

3. EXPERIMENTAL RESULTS AND DISCUSSION

3.1 The Portevin - Le Châtelier Effect in an AlZn Alloy

The Portevin - Le Châtelier (PLC) effect (serrated flow) appears in many Al-based supersaturated alloys if they are deformed at suitable temperature and strain rate. It is well known that prior ageing treatment giving rise to changes in precipitation structure can affect the shape of serrations or determine whether serrations ever appear. Therefore, it is important to study the relation between the alloy precipitation structure and the deformation behaviour. Pink and Król [2] investigated the A-

type of serrations in an Al-10.5wt.%Zn alloy with different size and volume fractions of precipitates. By measuring a correlation between the load drop amplitudes and the precipitation structure they have found that coherent precipitates rather prevent serrated flow provided that their amount exceeds a certain value. Large and incoherent precipitates have not been found to affect the A- type of the PLC effect. Bréchet and Estrin [3] have proposed (mainly theoretically) that an alloy hardened by fine shearable precipitates may exhibit serrated flow with all signs of the PLC effect, (the pseudo-PLC effect), even if no dynamic strain ageing due to solute diffusion is present.

The influence of the precipitation structure on the plastic flow, particularly on the PLC effect, can well be studied by the AE technique. A distinct correlation between AE and the precipitation structure and also between AE and the PLC effect has convincingly been demonstrated by a number of authors [1, 4-6]. The objective of our research was an AE study on how the precipitation structure affects serrated flow in an Al-10%Zn alloy. This alloy is prone to a rapid age hardening thereby matching the assumptions of Bréchet and Estrin [3]. More detail can be found in [7].

An Al-10.5wt.%Zn alloy (solvus temperature at 185°C) was melted, cast and rolled in one direction to sheets of 0.95mm thickness. Tensile samples with a 75mm nominal gauge length were cut parallel to the direction of rolling. The samples were recrystallized at 270°C for 30 min., then homogenized at 450°C for 1h, quenched in oil or water to be aged 6h at 180 or 20°C. The material aged at the elevated temperature was typical of a low amount of coherent precipitates. The material aged at room temperature contained a high amount of coherent precipitates. Immediately after the treatment, the samples were tested in an Instron 1195 testing machine at room temperature and at constant crosshead speed giving an initial strain rate of $4.4 \times 10^{-6} \text{ s}^{-1}$. To determine the strain rate sensitivity of the flow stress, the crosshead speed was increased by certain factors during the tests.

Figure 1a presents the strain dependences of true stress and count rates for the sample with the high amount of coherent precipitates. The offset yield stress of 120 MPa is considerably higher showing significant age hardening. The strain rate sensitivity is positive indicating that the PLC effect leaves its flow controlling role to the precipitate shearing. A detailed analysis shows few load drops

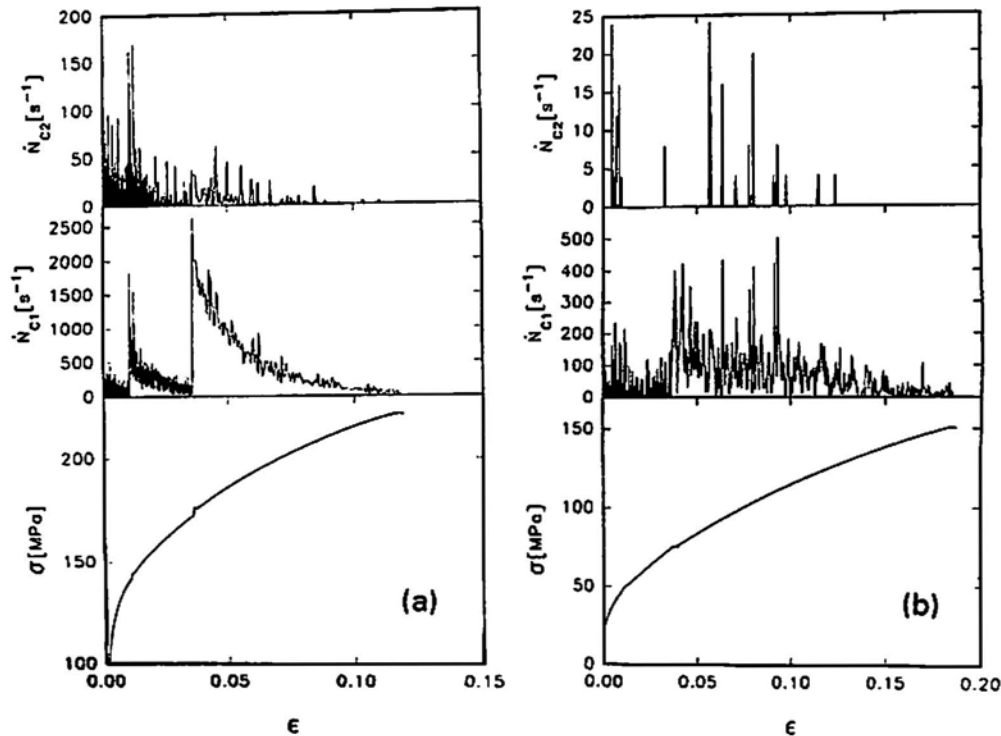


Fig. 1. The effect of strain rate increases from $4.4 \times 10^{-6} \text{ s}^{-1}$ to $4.4 \times 10^{-5} \text{ s}^{-1}$ and further to $4.4 \times 10^{-4} \text{ s}^{-1}$ on stress-strain curves and on count rates for samples of Al-10%Zn with (a) a high amount of coherent precipitates, and (b) a low amount of coherent precipitates.

with an amplitude of 0.03 MPa. The count rates are much higher than in the sample with the low amount of coherent precipitates, especially, many AE bursts appear. This increase can be explained by an intense precipitate shearing that is widely accepted as an effective source of AE [1]. The count rates respond distinctly to strain rate changes by a factor 10 showing an increase by the same factor. This result supports the idea about the precipitate shearing as the main source of AE because one may assume that the number of the precipitates sheared per unit strain should be independent of strain rate (the stress for shearing is independent of the strain rate). Fig. 1b presents the strain dependences of true stress and count rates at two threshold levels for the sample with the low amount of coherent precipitates. The offset yield stress of 26 MPa is consequently low. From the strain rate changes, a negative strain rate sensitivity is visible giving evidence that the PLC effect is the controlling mechanism of the plastic deformation. An inspection of load recordings reveals a jerky character of the plastic flow with sudden load drops of 0.2 Mpa. During the deformation, a more significant AE activity is observed at lower threshold level only, at higher threshold level few AE bursts are found. An increase of the strain rate by a factor ten produces a less distinct response in the count rates that tend to increase by a factor slightly less than ten, i. e. the AE count per unit strain decreases. Such a behaviour has also been observed in other alloys exhibiting the PLC effect [4,6] and is related to another well known experimental fact that the amplitude of load drops often decreases with increasing strain rate.

3.2 Microstructural Changes in Mg-Based Composites Subjected to Thermal Loading

Many Mg-based metal matrix composites (MMCs) have been developed and manufactured during the last decade as prospective light high-performance constructional materials. The microstructure and mechanical properties of MMCs are influenced significantly by the interfaces between the matrix and the reinforcement. When a MMC is subjected to temperature changes, thermal stresses arise at the interfaces owing to a considerable mismatch of the thermal expansion coefficient of the matrix and that of the reinforcement. Even moderate temperature changes may produce thermal stresses which exceed the matrix yield stress, consequently, generating new dislocations at the interfaces causing microstructural changes and plastic deformation of the matrix. It is noteworthy that the effect of temperature variations is similar to creep under non-stationary loading conditions.

Hitherto, the microstructural response of MMCs on changes in temperature has been investigated mainly indirectly (*post mortem*) [8-11]. The generation of new dislocations has been demonstrated by etch pit technique [8], transmission electron microscopy [9,10] and internal friction [11]. However, it is difficult to assess the evolution of the dynamic structure, i. e. to obtain a direct correlation of the structure to the temperature using these methods. *In situ* studies (by transmission electron microscopy - TEM) [12] can establish such a correlation but that is only of a local character and the stress state is most probably influenced by the relatively small thickness of TEM specimens.

AE has been observed during thermal cycling of Mg-based MMCs [13]. It is, therefore, possible by AE measurements to identify and to characterize the microstructural changes and to correlate them with temperature or other parameters. The combination of AE measurements with the dilatometry technique yields non-destructively, at any instant of the test, information on the structure and operating processes over the entire volume of the specimen. The object of our research was to develop combined AE and dilatometry technique and to apply it in a study of structural evolution in Mg-based MMCs subjected to thermal cycling (which corresponds to the typical operating conditions of most structural parts). Detail can be found in [14].

Various short fibre reinforced Mg-based MMCs were prepared by squeeze casting with a subsequent homogenizing treatment followed by quenching in hot water. Thermal cycling for dilatometric and AE measurements was carried out in a dilatometer equipped with a radiant furnace and compressed air for controlled heating and cooling. Up to 60 cycles were carried out on each specimen depending on the experimental requirement. The specimens were in the form of machined rods, 50mm long and 5mm in diameter with the reinforcement plane parallel to the longitudinal axis.

A specimen and a quartz dummy specimen with the same dimensions as the specimen were mounted into the specimen holder of the dilatometer. AE was transmitted by the dilatometer quartz rod in contact with the specimen.

Figure 2 depicts the AE count rate and the specimen elongation during a temperature cycle with an upper temperature of 300°C applied to a Mg-21.1vol.%Saffil MMC. As can be seen, AE appears in certain temperature ranges being much more feeble during heating than during cooling. After the cycle, a residual elongation is measured.

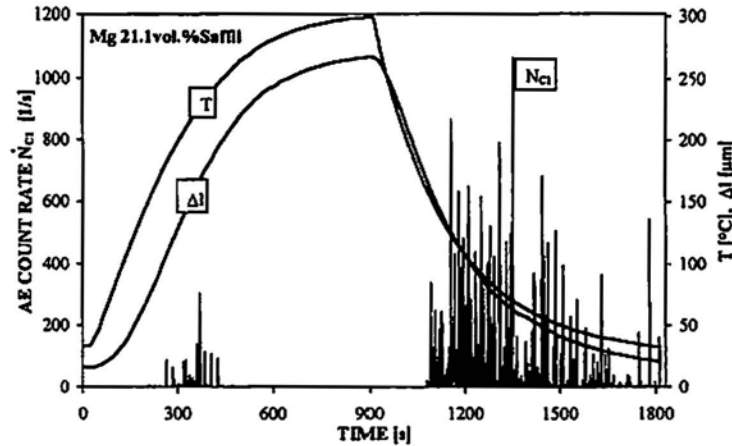


Fig. 2. AE count rate \dot{N}_{C1} , temperature T and sample elongation Δl as measured during the second cycle of the Mg-21.1vol.%Saffil MMC.

Measurements show that there is a minimum upper temperature of cycling necessary for the appearance of AE (AET_{top}). The AET_{top} is considerably lower for the commercially pure (cp) Mg-Saffil MMC than for the Mg alloys-Saffil MMCs. The cp Mg-Saffil MMC is the only case where AE occurs during the heating period. AZ91(Mg-9%Al-1%Zn)- and ZE41(Mg-4.3%Zn-1%Rare Earths)-Saffil MMCs exhibit intense AE bursts during cooling. The residual deformation after the cycle is generally an elongation for lower values of the upper temperature and a contraction for higher upper temperatures. The transition from elongation to contraction takes place for an upper cycle temperature of about 300°C depending on the matrix composition. The behaviour of the Mg-19.5vol.%Saffil MMC during thermal cycling with step by step increase in upper temperature of cycling T_{top} is characterized in Fig. 3. During the entire test an increasing residual elongation is observed. A significant dependence of the total AE count on T_{top} is found. When T_{top} reaches 140°C

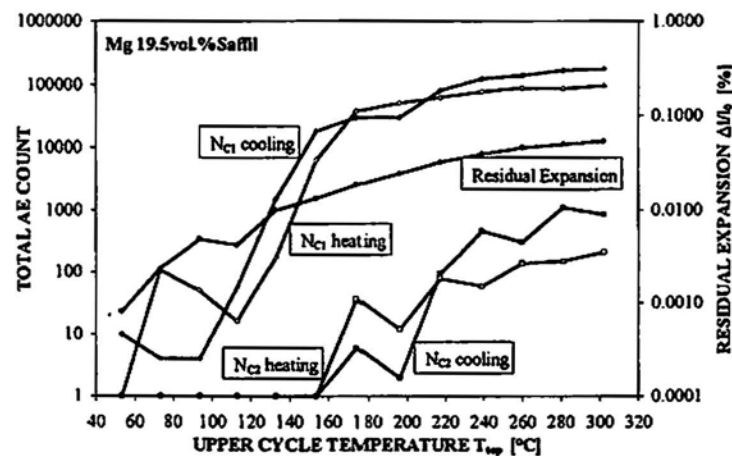


Fig. 3. Total AE count N_C and residual expansion $\Delta l/l_0$ vs. upper cycling temperature T_{top} for the Mg-19.5vol.%Saffil MMC. The total AE count was evaluated for the entire heating and cooling periods of the cycles.

the total AE count increases by several orders. Above T_{top} of 200°C the increase in the total AE count slows down and reaches almost a constant value.

As a consequence of the fabrication at elevated temperatures, all squeeze-cast Mg MMCs exhibit internal thermal stresses at room temperature, whose magnitude should be close to a threshold stress for creep of matrix. The matrix is under tensile stresses and the reinforcement is under compressive stresses. When a MMC is heated up the tensile stress acting on the matrix decreases to zero and on further heating compressive stresses build up. On cooling the MMC the internal stresses will behave in an opposite manner. Evidently, in certain temperature ranges the thermal stresses may exceed the matrix yield stress and relax by generating dislocations in the matrix, which give rise to the matrix structural changes and plastic deformation. Hence, the temperature dependence of the internal thermal stresses during cycling will have the form of asymmetric hysteresis loop. Different deformation mechanisms may appear as dislocation glide, twinning, diffusional creep, and grain boundary sliding. The share of these mechanisms is a result of a complex interplay between the temperature dependences of the thermal stresses and the matrix yield stress and will vary according to the temperature and other parameters of thermal cycling.

AE due to plastic deformation is produced by collective dislocation generation and motion. Hence, a large AE is expected during the deformation of the materials prone to coarse slip and/or twinning, such as hexagonal metals and alloys deformed at lower temperature. On the contrary, diffusional creep, grain boundary sliding and the dislocation glide at higher temperatures, when the dislocations do not move collectively and tend to annihilate, are not typical of large emissions.

When a Mg MMC is cycled (Fig. 2) AE appears in a certain temperature interval during heating. Its onset correlates with the internal stresses acting on the matrix exceeding the matrix yield stress and being relaxed by collective dislocation generation and motion, i. e. localised strain bursts. Increasing temperature renders the dislocation generation more homogeneously and the dislocations do not move collectively and tend to annihilate. Thus, AE disappears before the top cycle temperature is reached. When the specimen is cooled from the upper cycle temperature, the compressive stresses diminish rapidly and tensile stresses in the matrix build up. AE should take place due to relaxation of the tensile stresses but only at lower temperatures and should persist down to the lower cycle temperature. The matrix yield stress of a MMC with Mg alloy matrix is considerably higher (due to alloying) and the initial value of the internal tensile stresses acting on the matrix should consequently be higher. Hence, during heating, the compressive stresses exceeding the matrix yield stress will be built up at a higher temperature, and possibly relaxed by deformation mechanisms that do not produce detectable AE. AE will not appear during heating. However, as in the case of cp Mg MMC, AE occurs at temperatures close to the lower cycle temperature when tensile stresses are relaxed by collective generation and motion of dislocations. Large AE bursts as observed in the Mg, ZE41 and AZ91 MMCs may signalise twinning. It is noteworthy that our results imply that the main changes of the matrix structure should appear in the temperature intervals of the AE events.

3.3 Phase Transitions in a CuAu Alloy

The equiatomic CuAu alloy is a well-known system exhibiting two phase transitions of the first order in solid state [15]. The equilibrium structure is disordered face centred cubic (A1) with a lattice parameter $a = 0.387\text{nm}$ at temperatures higher than $T_{C1} = 410^\circ\text{C}$ and below this temperature a long range order occurs. Between $T_{C1} = 410^\circ\text{C}$ and $T_{C2} = 385^\circ\text{C}$ the product of ordering is the long period superlattice CuAuII phase described by a pseudo-orthorhombic cell with lattice parameters $a = 0.3979\text{nm}$, $b = 0.3963\text{nm}$ and $c = 0.3678\text{nm}$. Below $T_{C2} = 385^\circ\text{C}$ the equilibrium state is ordered face centered tetragonal (L_0) CuAuI phase with lattice parameters $a = 0.395\text{nm}$, $c = 0.368\text{nm}$. The disordered state may only partly be preserved by quenching (due to spinodal ordering), which complicates any *post mortem* investigation. The ordering in the CuAu system is accompanied by lattice shear and volumetric changes. Structure aspects of the ordering mechanisms have been studied e.g. in [16-19]. At lower temperatures, homogeneous nucleation is exhibited, as is typical of

a high occurrence of slowly growing ordered domains. Growth is coherent with the matrix because the slow speed of growth does not produce large internal stresses. Higher temperature accelerates the growth, giving rise to large internal stresses that relax by plastic deformation with a subsequent loss of coherence. The main mechanism of this plastic deformation is twinning but signs of dislocation glide, grain boundary sliding and structural damage may also be witnessed. Under such conditions, large AE may be expected in certain temperature intervals, dependent on the initial sample condition.

AE may well be combined with optical cinematography, i.e. imaging of the surface of a polished specimen by a long distance microscope equipped with a high speed CCD camera. Optical cinematography enables visualizing and recording changes of the surface relief due to plastic deformation (slip steps, twins and cracks). The object of this study was the dynamic correlation of the structure with thermal loading in a CuAu alloy. More detail can be found in [20].

Polycrystalline samples prepared by induction melting of appropriate stoichiometric amounts of Cu and Au were annealed at 750°C for 22 hours and then quenched in water. AE monitoring and optical cinematography were carried out during thermal loading of the CuAu samples. Various regimes (characterized by near linear heating or cooling over large temperature ranges) have been chosen to study the kinetics of the phase transitions and the structure changes in the CuAu system. Specimens for optical cinematography were mounted in a vacuum chamber and heated by focused infrared lamps. Specimen holders were also provided with controlled cooling using water circuits. A flat area on the sample surface was prepared by fine polishing. Observations on this area were effected with a long-distance-microscope QUESTAR QM-100 equipped with a high speed CCD camera and a videorecording facility. The resolution was of 1-2 μ m.

Figure 4a shows the AE count rate \dot{N}_{C_1} for heating a polycrystalline specimen at 4K/min up to 450°C (heating started about 24 hours after quenching so that the initial structure was at least partly disordered). Two distinct AE peaks are seen in this figure. The first peak, occurring between 150 and 400°C with a maximum at 265°C is broad, the second one at about 435°C is very narrow but the peak count rate is two orders of magnitude higher. Fig. 4b illustrates the second AE peak in detail. The high AE count rate starts at 430°C, increases constantly to a maximum at 437°C and disappears abruptly. Fig. 4c shows the subsequent cooling of the specimen down to room temperature. One

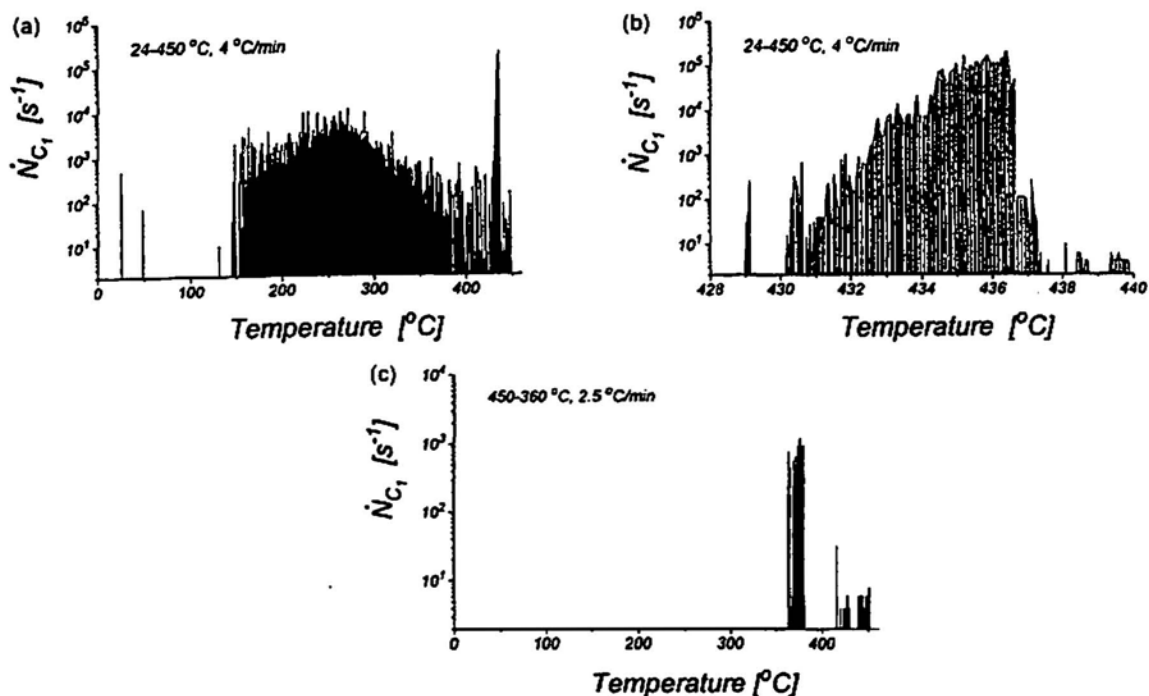


Fig. 4. AE count rate vs. temperature. (a) heating of the polycrystalline specimen (several hours after quenching) at 4K/min, (b) the second AE peak in Fig. 4a in detail, (c) subsequent cooling of the specimen at 2,5K/min.

distinct AE peak at about 375°C may be seen. Figure 5a shows the initial surface morphology of a polycrystalline sample for optical cinematography. The sample was in the same initial condition as the sample for AE measurement. Only fine grinding traces may be seen. On heating, the surface exhibits distinct changes of morphology at temperatures where the AE signal was detected. Fig. 5b shows the surface morphology at 204°C. Several grain boundaries become visible showing characteristic symmetry of triple junctions. The surface becomes shadowed indicating local changes of the relief by plastic deformation. On further heating, these changes become more pronounced as shown in Figs. 5c, 5d. Note systems of dark striae showing a triangle symmetry. This morphology changed considerably between 421 and 430°C. The final situation appears in Fig. 5e. Apart from some grain boundaries, the surface is smooth and the grinding traces become visible again. On subsequent annealing and cooling to room temperature there were no changes of this relief down to about 370°C, where another significant change took place (Fig. 5f).

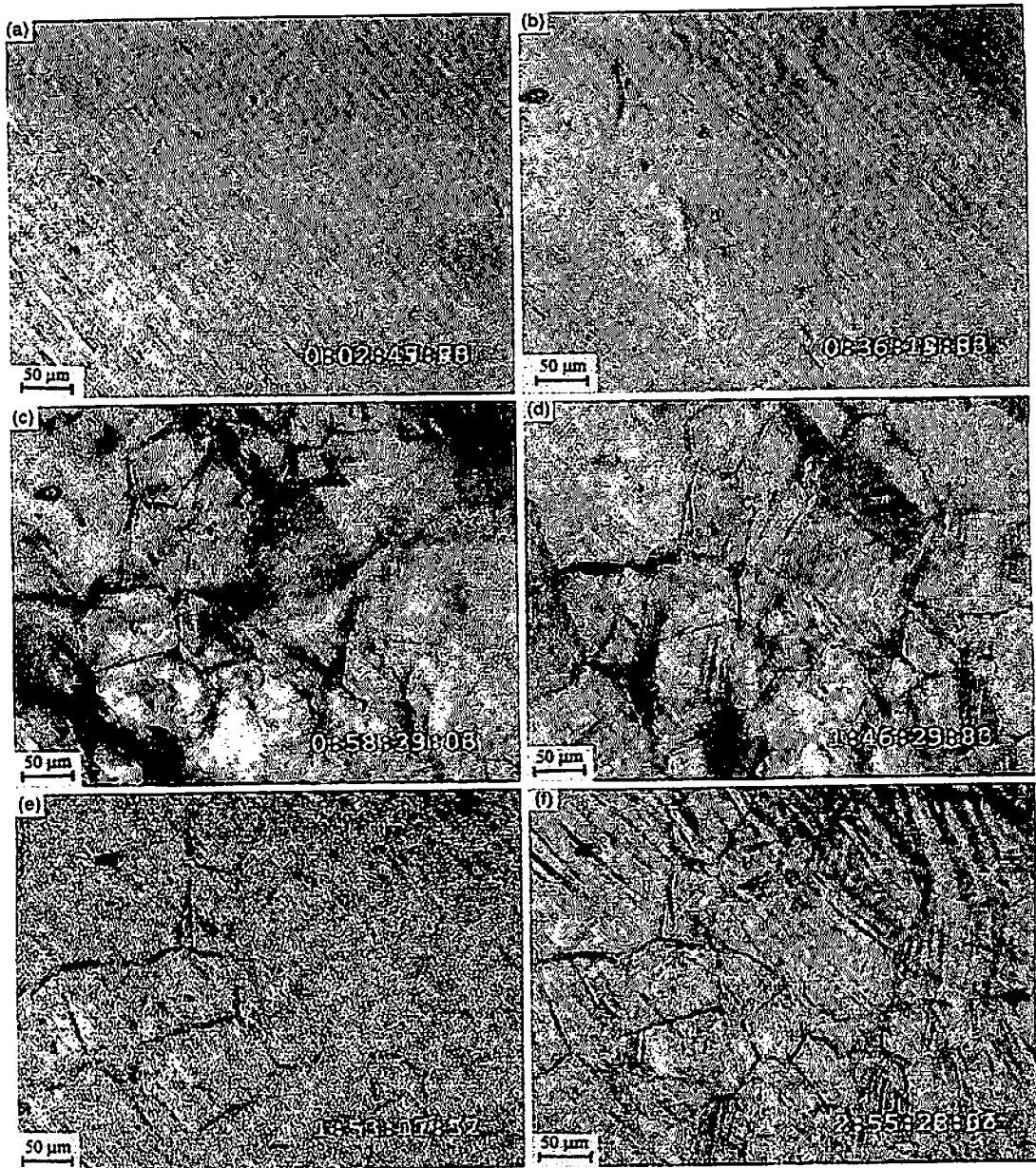


Fig. 5. Optical cinematography of the CuAu sample. (a) the surface relief prior to heating, (b) the surface relief at 204°C, (c) the surface relief at 271°C, (d) the surface relief at 416°C, (e) the surface relief at 430°C, (f) the surface relief on subsequent cooling at 335°C.

The first AE peak occurring on heating is likely due to the transition of the disordered phase produced by quenching to an ordered phase. The changes of the surface relief starting at about 200°C and becoming more pronounced on further heating may be interpreted as plastic deformation relaxing the internal stresses produced by ordering of the sample. The other AE peak occurring on heating at about 430°C correlates very well with considerable changes of the surface relief detected by optical cinematography. Also, the plot of count rate vs. temperature (Fig. 4b) is remarkable. The count rate increases constantly during the peak and then drops rapidly. If we assume the count rate to be proportional to the amount of internal stresses being relaxed, i.e. to the rate of transformation, it may be concluded that the transformation first accelerates and then finishes abruptly. The changes of the surface relief observed at 430°C are very interesting (cf. Fig. 5d to 5e). At this temperature the surface returns almost to the state prior to heating (even with the presence of grinding traces). Hence, the disordering of the sample shows a memory effect. Such effects are very typical for diffusionless martensitic transitions where a correlation exists between old and new phase but they are very unexpected for a diffusion controlled transition. From this point of view our observation demonstrates a martensitic-like character of the phase transitions in the CuAu system, as discussed for e.g. in [21]. On cooling, an AE peak observed at about 380°C corresponds very well to surface changes and may be interpreted as an ordering effect in the sample.

ACKNOWLEDGMENTS

This work has been supported by the Grant Agency of the Charles University (Grant 147/96) and by the Grant Agency of the Czech Republic (Grant 106-99/1717). F. C. acknowledges the financial support from the Alexander von Humboldt Foundation (Germany). This work would never have been possible without extensive assistance of our colleagues mentioned in Refs. [7,14,20].

REFERENCES

- [1] Heiple, C. R., Carpenter, S. H.: *J. Acoustic Emission* 6, 1987, 177.
- [2] Pink, E., Król, J.: *Acta metall. mater.* 43, 1995, 2351.
- [3] Bréchet Y., Estrin Y.: *Acta metall. mater.* 43, 1995, 955.
- [4] Cáceres, C. H., Rodriguez A. H.: *Acta metall.* 35, 1987, 2851.
- [5] Zeides, F., Roman, I.: *Scripta metall. mater.* 24, 1990, 1919.
- [6] Chmelík, F., Trojanová, Z., Lukáč, P., Převorovský, Z.: *J. Mat. Sci. Letters* 11, 1992, 91.
- [7] Chmelík, F., Pink, E., Król, J., Balík, J., Pešička, J., Lukáč, P.: *Acta mater.* 46, 1998, 4435.
- [8] Chawla, K., Metzger, M.: *J. Mater. Sci.* 7, 1972, 34.
- [9] Arsenault, R. J., Fisher, R. M.: *Scripta metall.* 17, 1983, 67.
- [10] Arsenault, R. J., Shi, N.: *Mat. Sci. Eng. A81*, 1986, 175.
- [11] Parrini, L., Schaller, R.: *Mater. Sci. Forum* 210-213, 1996, 627.
- [12] Clyne, W., Withers, P.: *An Introduction to Metal Matrix Composites*, Cambridge University Press, Cambridge 1993.
- [13] Lukáč, P., Chmelík, F., Roos, U., Kainer, K.-U., Mordike, B. L.: In *Innovation '95, Proc. of 2 Int. Symp. on Advanced Materials and Technologies*, Prague 1995, 280.
- [14] Chmelík, F., Kiehn, J., Lukáč, P., Kainer, K.-U., Mordike, B. L.: *Scripta mat.* 38, 1998, 81.
- [15] *Binary alloys phase diagrams* (Massalski T. B., editor-in-chief). ASM International, Materials Park, Ohio, U.S.A., 1990, 362.
- [16] Tanaka, Y., Udoh K.-I., Hisatsune, K., Yasuda, K.: *Phil. Mag.* 69, 1994, 925.
- [17] Arunachalam, V. S., Cahn, R. W.: *J. Mat. Sci.* 2, 1967, 160.
- [18] Hirabayashi, M., Weismann, S.: *Acta met.* 10, 1962, 25.
- [19] Hirabayashi, M., Ogawa S.: *J. Phys. Soc. Japan* 11, 1956, 907.
- [20] Mašek, P., Chmelík, F., Šima, V., Brinck, A., Neuhäuser, H.: *Acta mater.* 47, 1999, 427.
- [21] Muddle, B. C., Nie, J. F., Hugo, G. R.: *Metallurg. Met. Trans. A* 25A, 1994, 1841.

WAVEFORM ANALYSIS OF ACOUSTIC EMISSION DURING PRESSURIZATION OF GLASS-FIBER COMPOSITE PIPES

L. Golaski*, P. Gębski*, I. Baran**, Kanji Ono***

* Kielce University of Technology, Kielce, Poland

** Foundry Research Institute, Krakow, Poland

*** University of California, Los Angeles, California, USA

Keywords: glass reinforced plastics, filament wound pipes, failure criteria, acoustic emission testing, waveform analysis.

Abstract. This report discusses waveform observations corresponding to various stress states, which in turn are related to microfracture processes. Tests were made on two composites. They are composite with epoxy matrix and polyester matrix. Tubular specimens were loaded in different loading modes. During loading AE signals were recorded. Both conventional AE parameters and waveform recordings were obtained using 4-channel Mistras instrumentation and wideband sensors (PAC WD). Results showed that among considered AE parameters only events summation is independent of sensor position and filtration. The most of AE signals which were recorded during smooth pressurization can be clustered into three groups in dependence on their waveforms. The proportions between these groups depend on loading mode and matrix resin. When pipes were loaded in axial tension the waveform of AE signals and relationship between conventional parameters were different in comparison with signals obtained during internal pressurization.

Materials and experimental

We have studied acoustic emission (AE) from glass-fiber composite pipes (with epoxy or polyester matrix) under three different modes of loading to identify AE features and parameters that predict incipient fracture. The glass - fiber composite pipes were filament wound at $\pm 55^\circ$. The internal diameter of pipes with epoxy matrix was $\Phi = 42$ mm while the internal diameter of pipes with polyester resin matrix (more brittle) was $\Phi = 50$ mm. The length of tubular specimens was 300 mm while the wall thickness of all of them was 1.5 mm.

It was assumed that the failure processes depend indirectly only on stress components applied along symmetry direction of composite (i.e. stresses in hoop σ_H and axial σ_A directions). In fact the incipient of fracture depends on stress in single lamina as a part of composite. They are: shear stress $\tau_{\#}$ along fiber direction and normal stress σ_{\perp} perpendicular to fiber direction.

To realize different incipient failure processes tubular specimens were loaded in three modes as listed below:

- stressed in tension axial tension (Mode I),
- internal pressurization with axial stressing (Mode II)
- internal pressurization without axial stressing (Mode III).

For these loading modes the stress components in lamina in reference to fiber direction were calculated using Puck theory [1]. These stress components in dependence on external loading are as below:

- in Mode I - $\sigma_{\perp} = 0.58 \sigma_A$; $\tau_{\#} = 0.50 \sigma_A$
- in Mode II - $\sigma_{\perp} = 0.32 \sigma_H$; $\tau_{\#} = 0.11 \sigma_H$
- in Mode III - $\sigma_{\perp} = 0.03 \sigma_H$; $\tau_{\#} = 0.36 \sigma_H$.

It can be noticed that for M II the incipient failure of single lamina as a part of laminate depends on σ_{\perp} (transverse cracking) while for M III shear cracking as a result of $\tau_{\#}$ is expected. For tension (M I) both stress components may influence the failure. The critical values of normal stress $\sigma_{\perp c}$ and shear stress $\tau_{\# c}$ for single lamina were determined on hoop wound pipes under tension and torsion. During loading of these samples AE activity was recorded to detect the beginning of failure.

Under the assumption that the strength of lamina does not change when it is a part of laminate, the loading corresponding to laminae cracking for different loading modes were estimated. These data are given in Table 1.

Table 1. Loads that can produce cracking in laminae of composite

Loading mode	Epoxy matrix		Polyester matrix	
	Beginning	Final	Beginning	Final
Applied loads which can produce transverse cracking because of high σ_{\perp}				
M I	$\sigma_A=24$ (P=4.76)	$\sigma_A=58$ (P=11.56)	$\sigma_A=25$ (P=5.89)	$\sigma_A=25$ (P=5.89)
M II	$\sigma_H=44$ (p=31)	$\sigma_H=106$ (p=76)	$\sigma_H=46$ (p=28)	$\sigma_H=46$ (p=28)
M III	$\sigma_H=518$ (p=370)	$\sigma_H=1258$ (p=900)	$\sigma_H=540$ (p=320)	$\sigma_H=540$ (p=320)
Applied loads which can produce shear cracking because of high $\tau_{\#}$				
M I	$\sigma_A=72$ (P=14.25)	$\sigma_A=124$ (P=24.54)	$\sigma_A=36$ (P=8.48)	$\sigma_A=96$ (P=22.62)
M II	$\sigma_H=327$ (p=230)	$\sigma_H=550$ (p=390)	$\sigma_H=160$ (p=97)	$\sigma_H=423$ (p=254)
M III	$\sigma_H=100$ (p=72)	$\sigma_H=170$ (p=120)	$\sigma_H=50$ (p=30)	$\sigma_H=130$ (p=78)

The stress components are in *MPa* while, in brackets, the corresponding pressure *p* is in *bars* and axial load *P* in *kN*. The bold data indicated load at which beginning of AE activity is expected.

Conventional AE parameters

During loading AE signals were recorded. Both conventional AE parameters and waveform recordings were obtained using 4-channel Mistras instrumentation and wideband sensors (PAC WD). At each end of the pipe (~20 mm from end) two sensors close each other (No. 1,3 and 2,4) with different low band filters were located. Low band filter for channels No.1 and 2 was 20kHz (LBF20) while for channels No.3 and 4 it was 100kHz(LBF100).

For further analysis selected AE parameters were taken as listed below:

- events/events rate
- counts/counts rate
- duration/ duration rate
- rise time/ rise time rate
- energy/ energy rate

The examples of plots of some AE parameters are given in fig. 1 while values of all recorded AE parameters at failure are given in Table 2 (channels 1, 2 with LBF20 and channels 3, 4 with LBF 100).

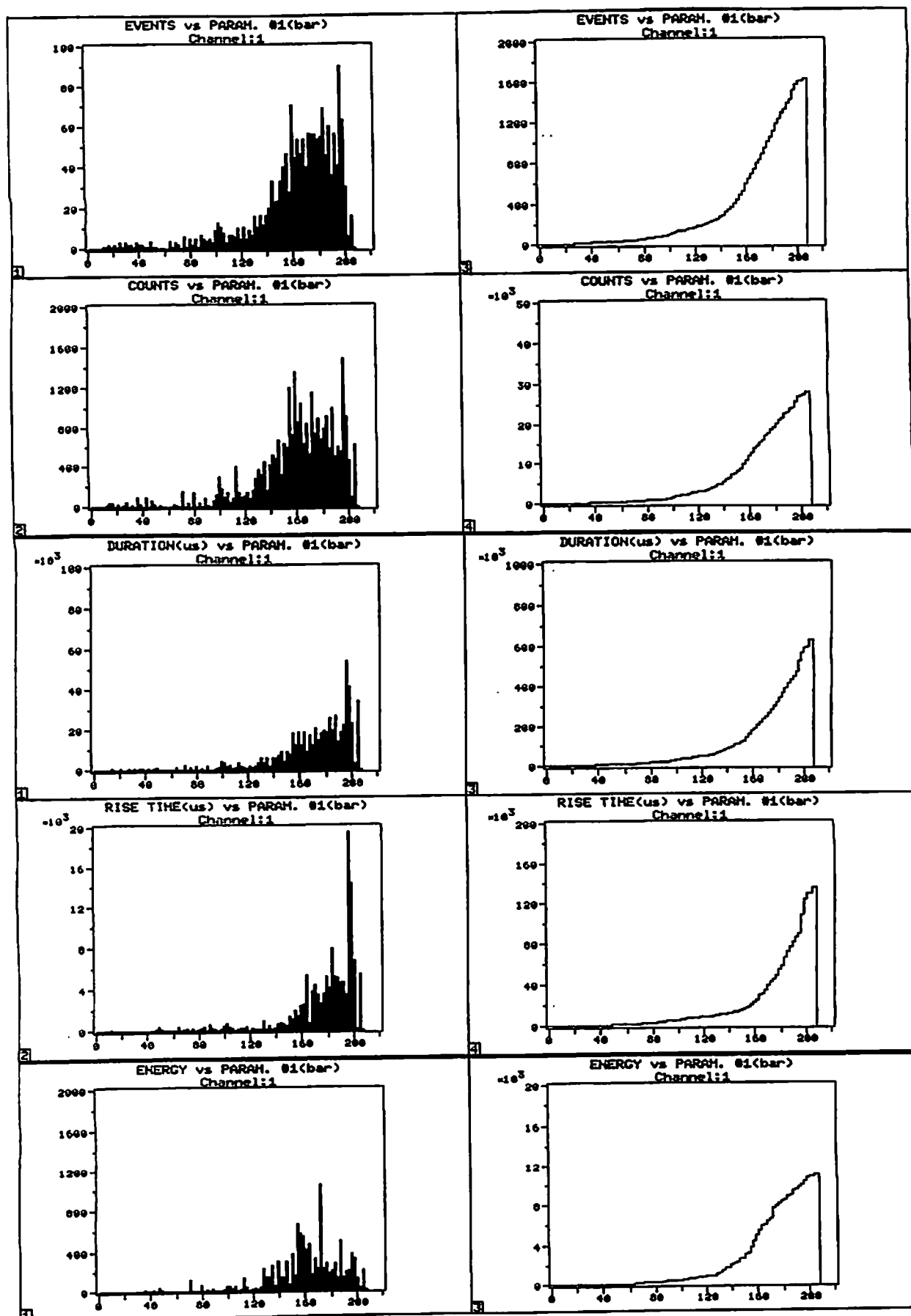


Fig. 1. Conventional AE parameters, M II epoxy matrix

Table 2. AE parameters at failure for pipes loaded in different loading modes

M II epoxy matrix	Channel 1	Channel 2	Channel 3	Channel 4
Events	1230	1240	1420	1400
Counts	$11 \cdot 10^3$	$17 \cdot 10^3$	$24 \cdot 10^3$	$24 \cdot 10^3$
Duration	$360 \cdot 10^3$	$900 \cdot 10^3$	$520 \cdot 10^3$	$520 \cdot 10^3$
Rise Time	$96 \cdot 10^3$	$182 \cdot 10^3$	$138 \cdot 10^3$	$130 \cdot 10^3$
Energy	3400	$11 \cdot 10^3$	$5.4 \cdot 10^3$	$5.1 \cdot 10^3$

M III epoxy matrix	Channel 1	Channel 2	Channel 3	Channel 4
Events	1620	1600	1330	1320
Counts	$28 \cdot 10^3$	$28 \cdot 10^3$	$42 \cdot 10^3$	$37 \cdot 10^3$
Duration	$620 \cdot 10^3$	$1300 \cdot 10^3$	$660 \cdot 10^3$	$710 \cdot 10^3$
Rise Time	$135 \cdot 10^3$	$290 \cdot 10^3$	$144 \cdot 10^3$	$160 \cdot 10^3$
Energy	$11 \cdot 10^3$	$21 \cdot 10^3$	$9.5 \cdot 10^3$	$7.5 \cdot 10^3$

M II polyester matrix	Channel 1	Channel 2	Channel 3	Channel 4
Events	1240	1280	1800	1800
Counts	$140 \cdot 10^3$	$230 \cdot 10^3$	$490 \cdot 10^3$	$340 \cdot 10^3$
Duration	$3300 \cdot 10^3$	$8900 \cdot 10^3$	$5900 \cdot 10^3$	$4000 \cdot 10^3$
Rise Time	$260 \cdot 10^3$	$425 \cdot 10^3$	$470 \cdot 10^3$	$340 \cdot 10^3$
Energy	$345 \cdot 10^3$	$1570 \cdot 10^3$	$310 \cdot 10^3$	$175 \cdot 10^3$

M III polyester matrix	Channel 1	Channel 2	Channel 3	Channel 4
Events	1180	1180	1570	1520
Counts	$41 \cdot 10^3$	$51 \cdot 10^3$	$96 \cdot 10^3$	$72 \cdot 10^3$
Duration	$940 \cdot 10^3$	$2600 \cdot 10^3$	$1300 \cdot 10^3$	$1220 \cdot 10^3$
Rise Time	$96 \cdot 10^3$	$255 \cdot 10^3$	$225 \cdot 10^3$	$220 \cdot 10^3$
Energy	$51 \cdot 10^3$	$160 \cdot 10^3$	$34 \cdot 10^3$	$27 \cdot 10^3$

M I epoxy matrix	Channel 1	Channel 2	Channel 3	Channel 4
Events	3480	3200	$13 \cdot 10^3$	$11.8 \cdot 10^3$
Counts	$355 \cdot 10^3$	$420 \cdot 10^3$	$320 \cdot 10^3$	$360 \cdot 10^3$
Duration	$17000 \cdot 10^3$	$19000 \cdot 10^3$	$8800 \cdot 10^3$	$9100 \cdot 10^6$
Rise Time	$1010 \cdot 10^3$	$890 \cdot 10^3$	$390 \cdot 10^3$	$380 \cdot 10^3$
Energy	$720 \cdot 10^3$	$800 \cdot 10^3$	$540 \cdot 10^3$	$600 \cdot 10^3$

Waveform analysis

There were more than 1000 signals recorded by one sensor during each test. It is almost impossible to find two identical signals. However using MI-TRA software the signals that occurred the most often, had to be clustered in three groups.

The first group (group A) includes signals characterized by low amplitude (up to 30 dB) and a narrow frequency range (up to 300 kHz) (fig. 2a). This type of signals includes the major part of all recorded signals. The second group (group B) is a set of signals characterized by relatively high amplitude (more than 35 dB) and a wider frequency range (up to 600 kHz) (fig. 2b). The third group (group C) includes the signals, which could be placed between type A and type B. The amplitude of

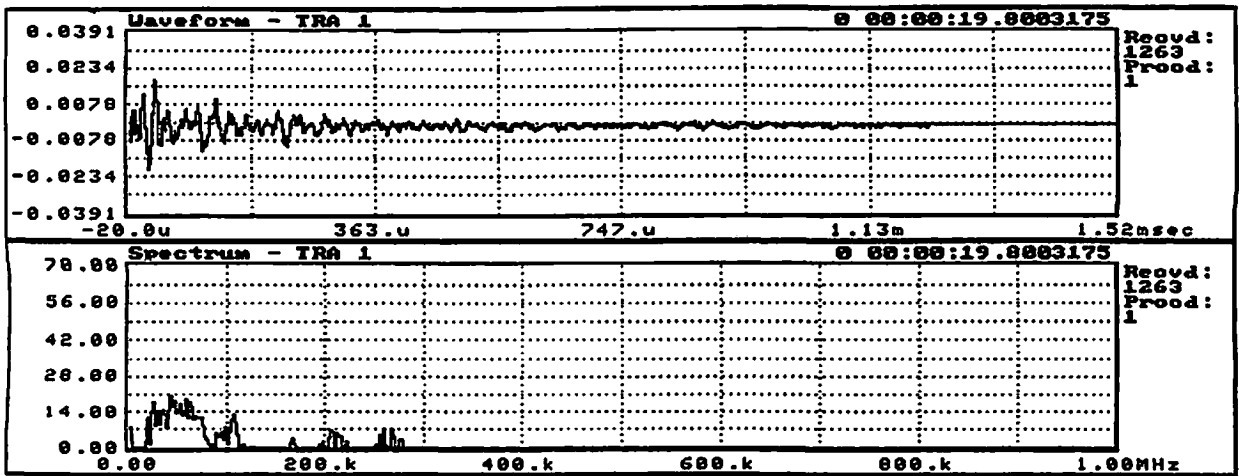


Fig. 2a. Acoustic emission signal - type A

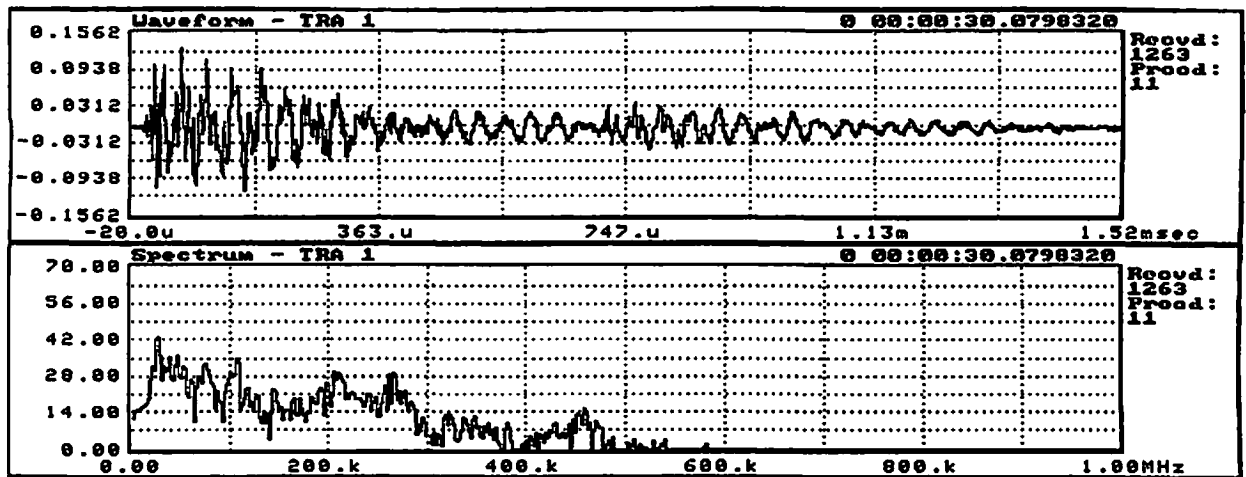


Fig. 2b. Acoustic emission signal - type B

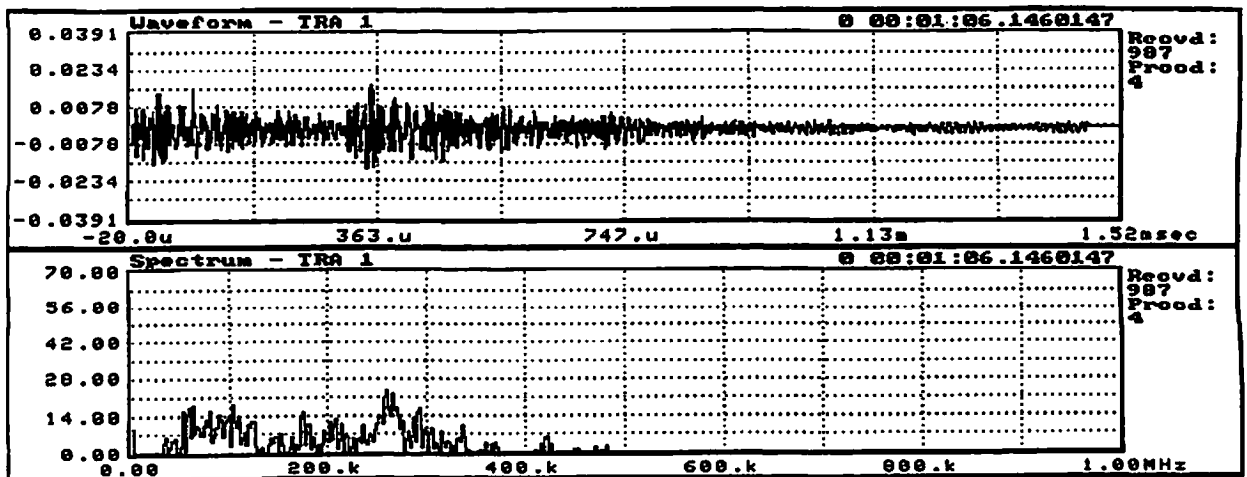
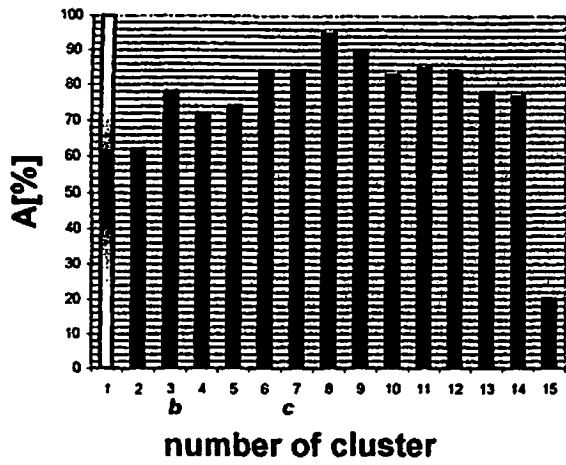


Fig. 2c. Acoustic emission signal - type C

(1) MII-F1A



(2) MIII-F6

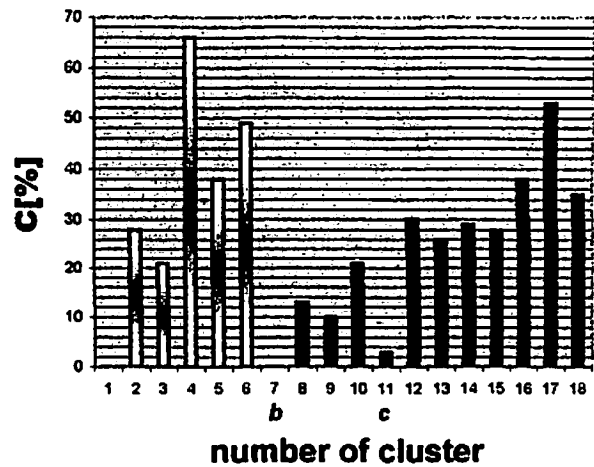
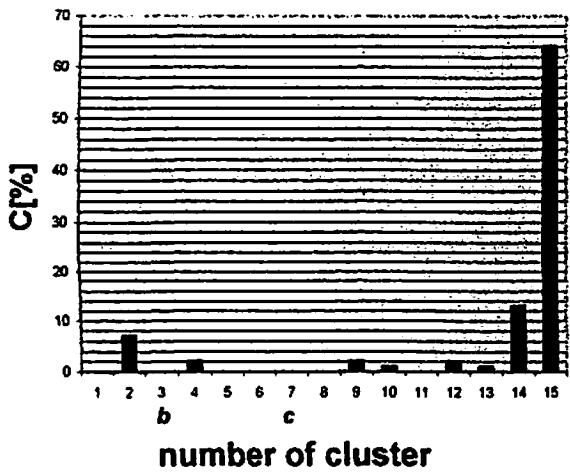
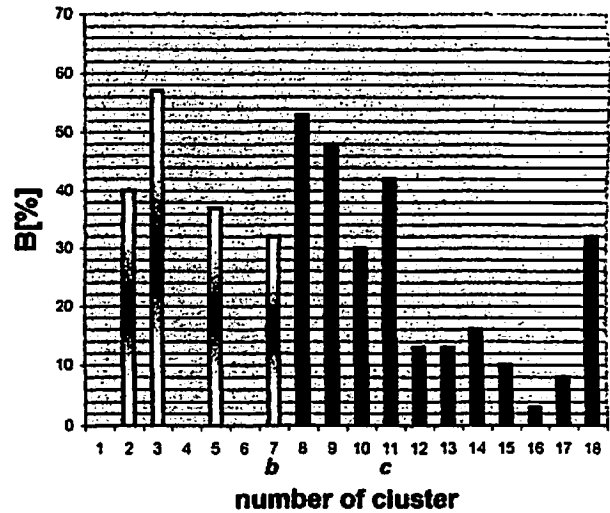
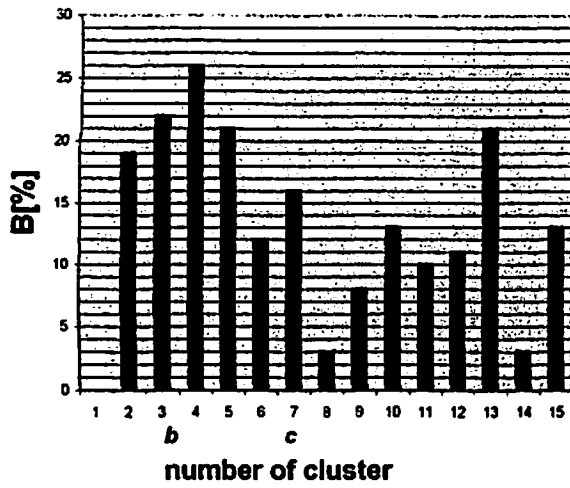
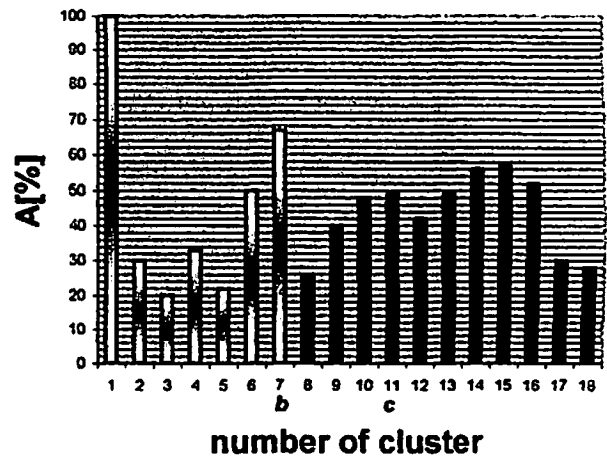


Fig. 3. Percentage of sigals type A, B and C in dependence on loading time

these signals is not much greater than 25 dB and the frequency range is less than 500 kHz (fig. 2c). Another important feature, which enables to differentiate this type of signals is the lack of frequency between 380 kHz and 400 kHz (approximately) on the spectrum graph. These types of AE signals were observed in all internally pressurized pipes independently of resin matrix.

The number and percentage of AE signals in each group in dependence on loading modes and matrix resin are given in Table 3.

TABLE 3. Number and percentage of different types of AE signals

Matrix type	Epoxy				Polyester	
	Mode II		Mode III		Mode II	Mode III
Sample No.	F1A	A11	F6	A2	ANG1	ANG2
Type A	952 (77%)	862 (71%)	619 (38%)	404 (41%)	307 (24%)	350 (30%)
Type B	177 (14%)	172 (14%)	118 (7%)	122 (12%)	471 (38%)	420 (35%)
Type C	26 (2%)	76 (6%)	539 (34%)	428 (43%)	317 (26%)	248 (21%)
Others	85 (7%)	113 (9%)	344 (21%)	33 (4%)	145 (12%)	162 (14%)

The next stage of the analysis required to specify, what types of signals occurred during the individual stages of the pressurization. Two mode M II and two mode M III data files were analyzed. Firstly, the time of the test was divided to several periods - 20 seconds each. Then the percentage of three types of signals (A, B and C) in each period was calculated. The results are shown in fig. 3. On the horizontal axis, there are successive time periods while on vertical axis the percentage of signals in each group. At the beginning of each test, the number of the recorded signals was very low. In some time periods no signals were recorded. Therefore, the results from few records at the beginning of tests may not be reliable. On these graphs they are shaded. On the horizontal axis points are indicated at which stresses referred to fiber direction are enough high to initiate cracking of laminae. For this purposes data from Table 1 were taken. Point indicated as *b* corresponds to beginning of fracture while point indicated as *c* to final fracture.

However when pipe is loaded in axial tension i.e. in Mode I the relationship between AE parameters (see Table 2) and waveform differs from these data which were obtained during internal

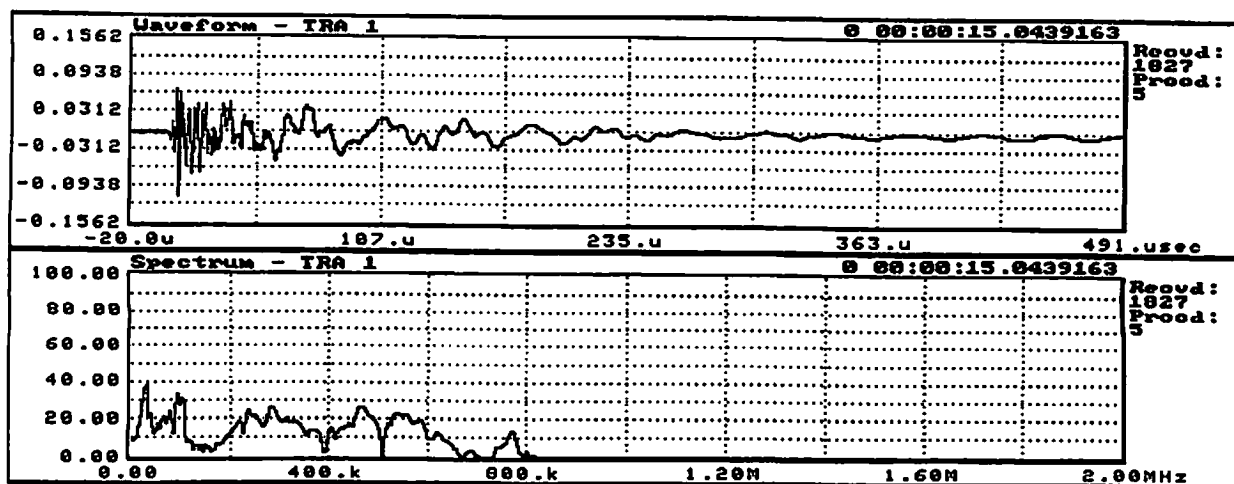


Fig.4. Waveform and spectrum of signals type A from pipes under tension (M I)

pressurization. The AE signals can be cluster into two groups only. About 80% of all signals are in group A. Typical waveform and spectrum is shown in fig.4. Nevertheless AE activity from pipes loaded in M I starts at load which can be predicted from the strength of single lamina.

Discussion of the results

When compare the conventional AE parameters concerning internally pressurized pipes one can concluded:

- the only parameter which does not depend (within few events) on sensor location is AE events
- the AE events depend slightly on low band filter set up
- the number of AE events from channels with higher low band filter (100 kHz) is higher than number of events from channels with 20 kHz low band filter (the only exception from above is epoxy matrix pipe loaded in MIII)
- the recorded AE parameters, but AE events, depend on AE sensor location
- for each couple of sensors with the same filtration all data (but AE events) are not the same; there are no regularity in AE events/ recorded parameters ratio

An exception are pipes with epoxy matrix under tension where:

- the AE events depend on filtration; number of events recorded by filtrate channels are three times the events taken by channels with 20kHz low band filter
- the event/count ratio is significantly higher in comparison with this ratio for pipes under internal pressurization.

The waveform analysis of AE signals recorded during internal pressurization of composite pipes shows, that for epoxy matrix pipes loaded in M II the signals of type A dominate during the whole test and their percentage fraction is the highest at the middle range of the load. The percentage of the signals of types B and C especially is much lower. While the percentage of signals A reaches its maximum, the number of signals B is the lowest. The number of signals C increases during the test and reaches the maximum just before the end of the test. For mode M III, the percentage of the signals A and C are of the same range is lower than for M II and reaches its maximum at the load equal to approximately 80% to 90% of the maximum load. The main difference between modes M II and M III concerns the type C signals. While for pipes loaded in M II their intensity is low and increase just before failure in M III activity this type of signals appeared during large period of test with near constant activity.

For polyester matrix pipes under internal pressurization the frequency of all three type of signals is the near the same for both loading modes however the intensity of their appearance changes during loading.

The beginning of failure process of epoxy matrix pipes, indicated by incipient of AE activity correlate with cracking in single lamina of laminate predicted on the basis of Puck theory and strength of single lamina (hoop wound pipe). This relationship is not observed in polyester matrix pipe where the theoretically predicted load is lower in comparison with load at the beginning of AE activity.

Acknowledgments

This research was supported by the Maria Sklodowska-Curie Fund II

References

1. Puck A., Schneider W., *On failure mechanism and failure criteria of filament-wound glass-fibre/resin composites*, *Plastics and Polymers*, Vol. 37, 1969, s. 33-43.

**ACOUSTIC EMISSION MONITORING DURING
SOLIDIFICATION PROCESSES**

**F.HAVLÍČEK, VŠB TECHNICAL UNIVERSITY OSTRAVA,CZ
J.CRHA, VÍTKOVICE a.s. ,OSTRAVA,CZ**

ABSTRACT

The acoustic emission signal is measured and analysed to show the possibility to distinguish the stages of crack initiation and propagation. They are presented the experiences, which will be used as a base for further research.

KEYWORDS

Solidification, casting, pouring, counts, internal stresses, acoustic emission, tup, thermal treatment, cooling.

INTRODUCTION

The solidification and following cooling down processes of great castings have significant influence on their final quality. The investigation of these processes is very difficult from the reason of high temperatures, which allows the thermal analysis only. According to experiences, gained from our measurements, it seems to be realistic to use acoustic emission method (AE) for the determination of solidification time and for investigation of stress field during cooling down process. The main aim of AE-measurements, during solidification of great castings, is therefore to estimate the solidification time and stage of the development of the stress field in relation to crack initiation and propagation.

PROBLEM DESCRIPTION

AE is generated during many physical and metallurgical processes of non continual characteristic as for example are crack initiation and propagation, phase transformation and many other stresses inducing phenomenas. During all these processes the part of elastic energy is not consumed for own process and it is emitted as elastic wave in frequency range from 50 kHz to 1MHz to the surface of object being tested. Main problem in foundry applications is to realise transmission of the elastic waves from solidificated or cooled down casting to AE sensors. The second problem, which must be solved, is data interpretation (or data acquisition) in relation to structural integrity evaluation. This approach needs to arrange many measurements not only of AE activity but the other parameters such as temperature, internal stresses (or deformation), finally to be supplied by ultrasonic testing methods.

During each physical process of non continual characteristic AE signal is released with its own amplitude and frequency spectrum. The simplest approach for signal evaluation is to use the amplitude criteria for distinguishing of crack initiation and propagation from background noise. This approach was published in the literature (1,2)

but the relationship between counts and the crack size depends on the stress level and is only valid for exactly defined conditions. The reason is the mainly known reality, that for the AE signal output it is necessary to calculate with the geometry of the object. The geometry and the temperature differences induced by fast cooling determine the level of internal stresses, which are „the motion power“ for crack initiation and propagation. The investigation of frequency spectrum was not detailed done. The reason is frequency depending attenuation and hence it follows the wave transformation during propagation to the sensor. For the background noise rejection the used frequency range is 50 kHz to 1 MHz.

The experimental problem might be divided in two parts. The detection of elastic waves from the object being measured is solved in the first part. It must be done by respecting the very high background noise level in the foundry workshop and the high temperature on the surface of casting. Special waveguide was designed for this case, which guaranteed the maximum temperature up to 100°C on the sensor surface and good acoustic contact between sensor and monitored casting. The geometrical size and the location of the waveguide into casting needs many experimental experiences. The last option was done as cylindrical bar with diameter about 25 to 30 mm and length about 1500 to 2500 mm. One end of the bar was put in the riser during casting process, this end was melted and then solidificated in this location. The very good acoustic contact between object being measured and waveguide was done in this way. The other end of bar was grinded to get a good acoustic contact between bar and sensor. The use of suitable couplant for sensor fixed on this end is frequently discussed, each proposed solution should be very carefully tested to prevent sensitivity changes for the detection of elastic waves during long time measurements.

Heavy castings should be „on line“ monitored approximately six days or longer, which depends on the size of casting. For the valuation of extensive data files were used computers, which make possible to draw trends in counts rate versus time in the whole monitored time interval. Quantitative evaluation needs to solve following items:

1. calibration procedure
2. rubbing noise elimination
3. correlation between AE signal and other measured parameters

This can be done after many repeated measurements.

EXPERIMENT

All experiments were performed on a large scale Dunegan-Endevco equipment. Details of the test facility is shown in Figure 1. The waveguide-2 is melted and solidificated into casting-1, two piezoelectric sensors-3 type D 750 are located on the other end of the waveguide-2 using special fixture. The output from sensors is gained in preamplifier-4 type 1801 on 40 dB. The signal is led from preamplifier to DAQ Unit-5 Dunegan-Endevco System 3000, which contains two amplifiers Dunegan-Endevco 320 Dual Conditioner and two counters Dunegan-Endevco type 303. The whole gain for channel A is 76 dB, for channel B is 70 dB. The counts are added in the dual counter type 302 in time interval 10 minutes and the results (rate counts/10 min or 1min) are stored in the digital form on magnetic tape memory-6. The analog data are stored on recorder-7 Hartman-Braun Polycomp 2.

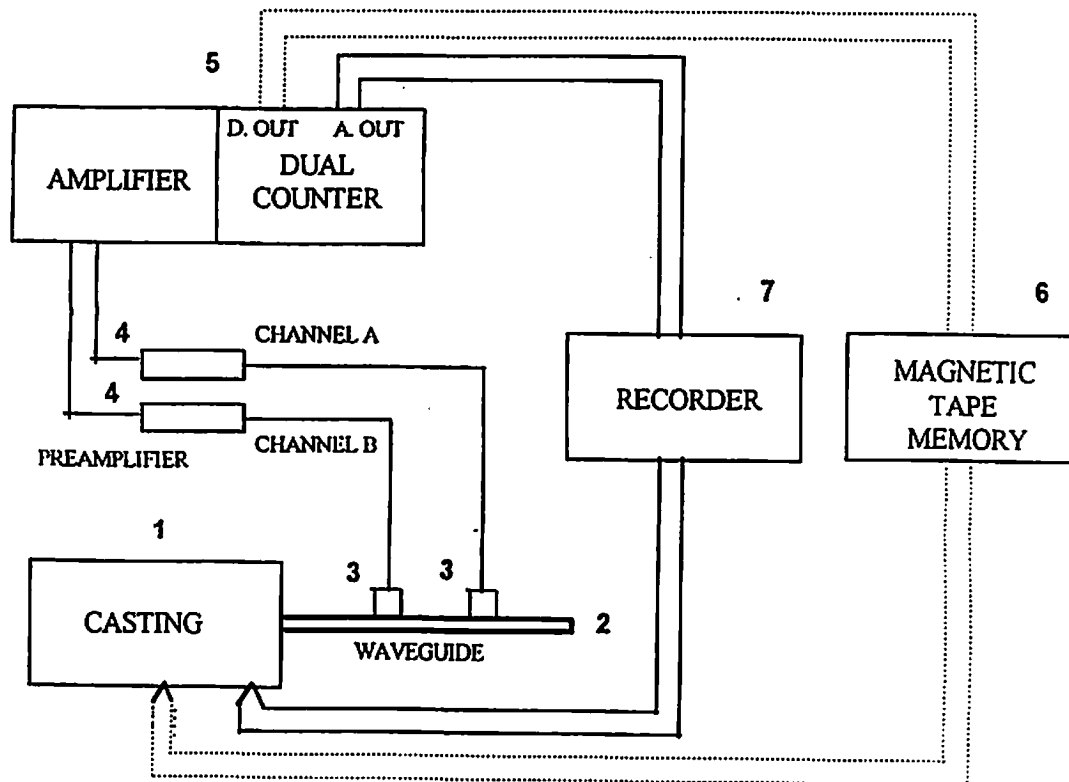


Figure 1

Results

Many measurements of AE were performed during several years on the great scale of castings. The monitoring was focused on solidification and cooling down processes, some parts of work was done by monitoring the machining of great casting before their supply to customer. A typical solidification plot of the roll of diameter 1240 mm, material E85, weight 46t, is in Figure 2. The AE activity was monitored 12000 minutes (200 hours) and has following typical features:

1. negligible AE activity at the beginning of the pouring
2. two peaks on the curve counts versus time in the later time interval

The negligible AE activity lasts cca 660 minutes, that is 11 hour after beginning of pouring. The theoretical (computed) solidification time is about 480 minutes (8 hours). The roll begins release elastic waves after 3 hours in the solid state, what can be explained on the base of physical processes in observed time interval. The high temperature at the beginning of the solid state makes possible to lower stress levels by plastic deformation and the characteristic of processes in this time interval is without sudden changes. The AE plot in the Figure 2 determines the rising of internal stress and its trend. The phase transformation γ to α in the surface layer at temperature 720 C excites the first peak on the plot. After finishing the phase transformation the cooling down continues at the casting surface faster as its internal parts. This phenomena produces the pressure stresses on the

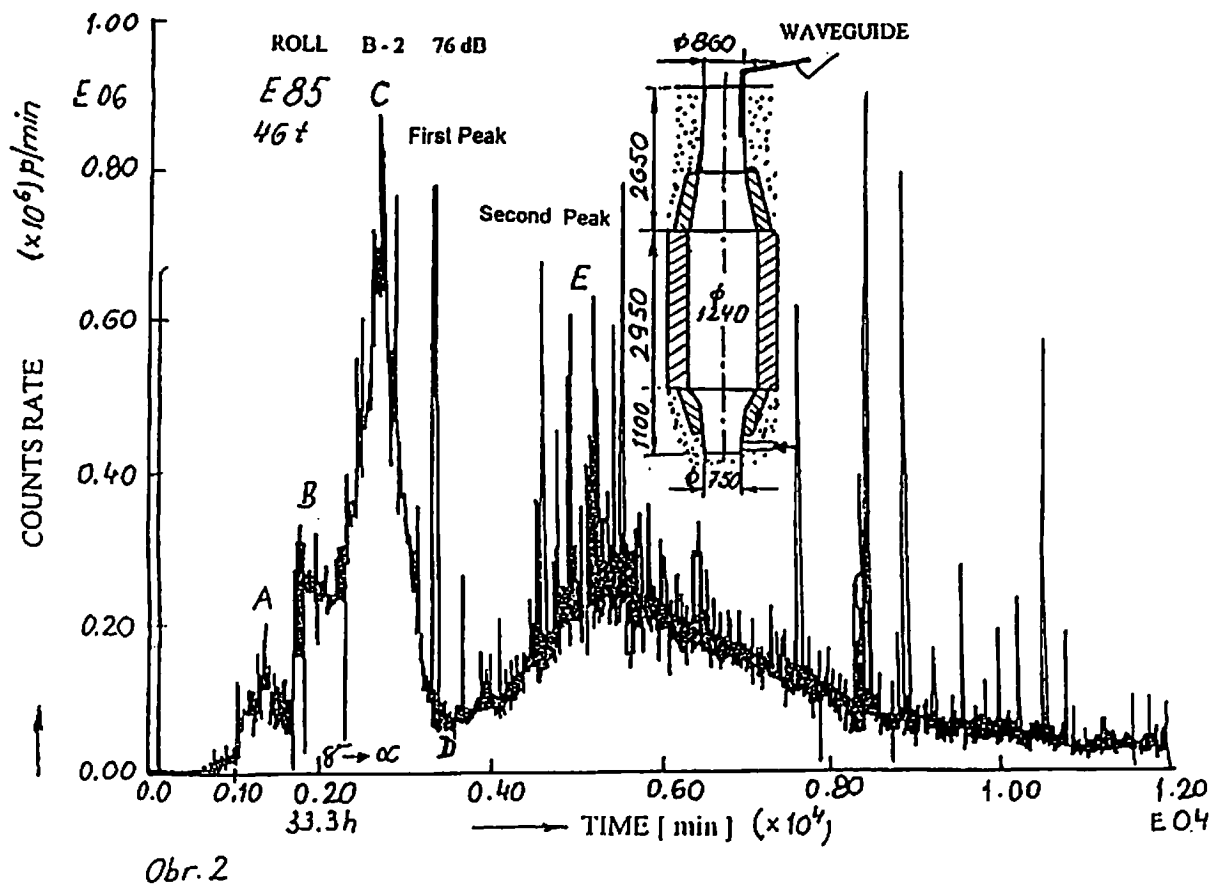


Figure 2

surface and tension stresses inside. The second peak in the Figure 2 responds to the thermal induced stress by cooling the casting down and the plot is the derivation of temperature versus time plot for the internal part of casting.

The crack can be initiated by heat and mechanical treatment in the solid state. The AE and temperature plot for removing of riser by flame -cutting on the top 186 t for the great hydraulic press is in the Figure 3. In the time interval from 13000 to 21000 minutes following activities were observed:

1. temperature range 815-730 C (curve 1), removing the mould top
The AE activity increases from the changes of thermal field
2. temperature range 730-450 C (curve 1)
Preparation the casting for flame cutting
3. temperature range 440 C (curve1)-700 C (curve 2)
Flame cutting
4. temperature range from 700 C to the end of plot
Post flame cutting cooling

As it was described above, in the first part of preparation increases AE activity from changes of the thermal field after removing the mould top from the top. This procedure

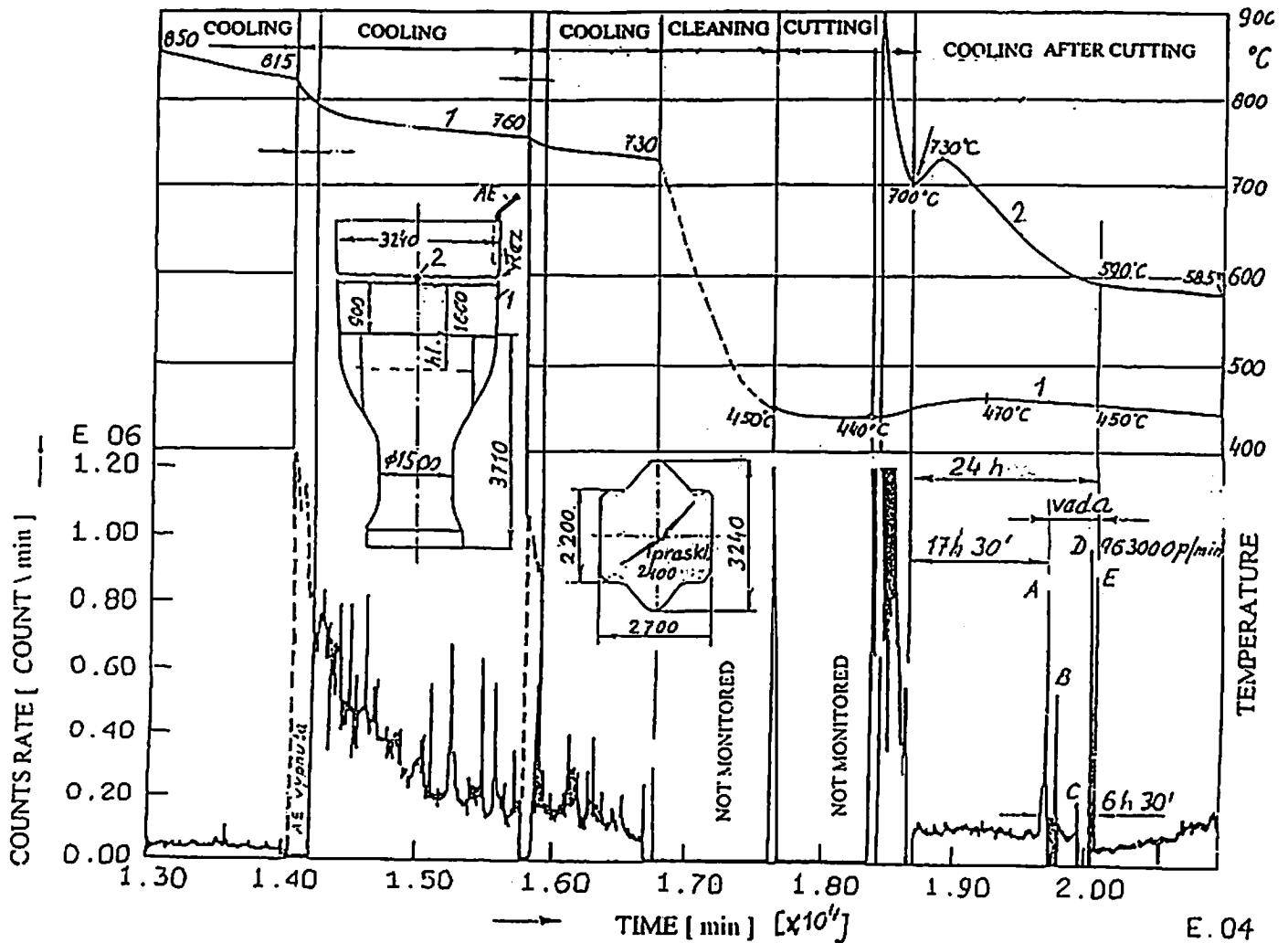


Figure 3

has not influenced the crack initiation from the reason of high temperature inside the tup. The typical AE trend responds to our previous experiences. During the activities in item 2 and 3 the AE was not monitored, the exception is 3,5 hours before finishing the flame cutting only. The five significant peaks, signed in the Figure 3 at A, B, C, D and E, appear from the background noise. The relative silent tup emitted after 17 hours and 30 minutes great elastic energy bursts the seven hours from the first event signed as A. The value of count rates was in range 825 000 counts/min to 936 000 counts/min.

Conclusion

The AE method is suitable for application in foundry as additional method for processing control in these areas:

1. control the poudry sequence time
2. solidification time estimation
3. internal stress development
4. phase transformations in castings
5. crack initiation and propagation

The experimental results confirm the great sensitivity of AE to temperature differences and arising internal stresses. AE shall be especially used for crack initiation and propagation research. Based on the experiences obtained during AE measurement it is possible to take necessary measures such as for example the prevention of fast cooling and the determination of allowed surface temperature. The main deal of these experiments was done in 80th years, new possibilities in casting investigation gives now new AE subsystems (3).

REFERENCES

- 1.Y. Nakamura,C.L. Veach and B.O. McCauley:Amplitude Distribution of Acoustic Emission Signals,Acoustic Emission,ASTM STP 505B, 1972,pp 164-186
2. D.O. Harris, D.L. Dunegan:Continuos Monitoring of Fatigue Crack Growth by AE,Technical Report DE 73-2
3. EMIS_01-technical and application description,1997

**RADIATION OF ACOUSTIC EMISSION WAVES
DURING STRESS CORROSION CRACKING OF THE METAL**

postgraduate st. A. Kotolomov
Prof., Dr.Tech.Sc. G.Budenkov, Ass. Prof., PhD O.Nedzvetskaya,

Izhevsk State Technical University
Studencheskaya st., 7, Izhevsk, Russia, 426069,
E-mail: root imi.udmurtia.su, Tel. (3412) 588852; Fax (3412) 588852

ABSTRACT. The report presents physical models of the process of radiation of Rayleigh waves emitted by different types of cracks which go along the stress-corrosion destruction of pipe walls: cracks growing from the surface deep into the material, surface cracking, and lamination. Directional charts of acoustic emission, pulse spectra and amplitudes in dependence of crack growth rate, its sizes and the crack mouth stratification depth have been calculated.

KEYWORDS: gas pipelines, stress corrosion cracking, Rayleigh waves.

INTRODUCTION

Practice of natural gas pipelines presents frequent cases of pipe destruction due to development of sets of ramified corrosion cracks concentrated on small sections. This phenomenon is known as stress-corrosion. The stress-corrosion damage can be described as local crack initiation which does not necessarily come with surface damage (pipe wall corrosion thinning, scores, scratches, dents etc.). The stress-corrosion is rather a sluggish process, normally occurring on pipelines in extended operation, which also relates this process to fatigue. All initial cracks penetrate deep into the metal perpendicular to the pipe wall surface and having reached some depth they start to expand along the surface, merging with adjacent cracks. Rather often (in up to 60 % of the cases) the center of destruction which may occur in the central part of the pipe wall experiences lamination of the metal [1]. Such lamination normally originates at the production stage of sheet rolling and bending, or at pipe welding and according to SNIP standard 2.05.06-85. is specified as acceptable. However, after an extended period of operation corrosion cracks on the outside wall reach the lamination area bringing about corrosion medium, which results in corrosion depositions and breaking of interpose bonds. The total area of laminated material may expand up to 1 square meter and over. Such defects can be detected by means of intratubular diagnostics. However, to determine whether the lamination is a center of stress-corrosion requires extra research.

Therefore, acoustic emission monitoring of the above defects necessitates a technique and instruments which, with sensors placed on the outer wall, would enable to detect acoustic fields, emitted by the above mentioned cracks and determine the current stage of stress-corrosion development.

At monitoring cracks that develop in plates, Rayleigh or Lamb surface waves are most efficient [2] and it is Rayleigh waves that provide the most reliable information about the destruction process when sensors are placed in the immediate vicinity of a defective spot in the plate.

We have developed physical models of the process of radiation of Rayleigh waves emitted by different types of cracks (cracks developing from the surface deep into of the material, surface cracking, lamination).

These models of the process of acoustic emission waves are based on data obtained by methods of quantitative fractography and X-ray analysis.

SIMULATION OF PROCESSES OF RADIATION OF THE RAYLEIGH WAVES EMITTED BY GROWING CRACKS

The crack (specifically fatigue crack) is assumed to grow by a jump, the value of jump $2a$ is determined from fractograms that correspond to definite modes of material loading [3]. Thus in determining the surface cracking H (fig. 1) we calculate the acoustic field of the linear segment of the mouth of the crack, width $2b$. The acoustic field of a growing (rising) crack is defined as a result of operation of a combination of point sources.

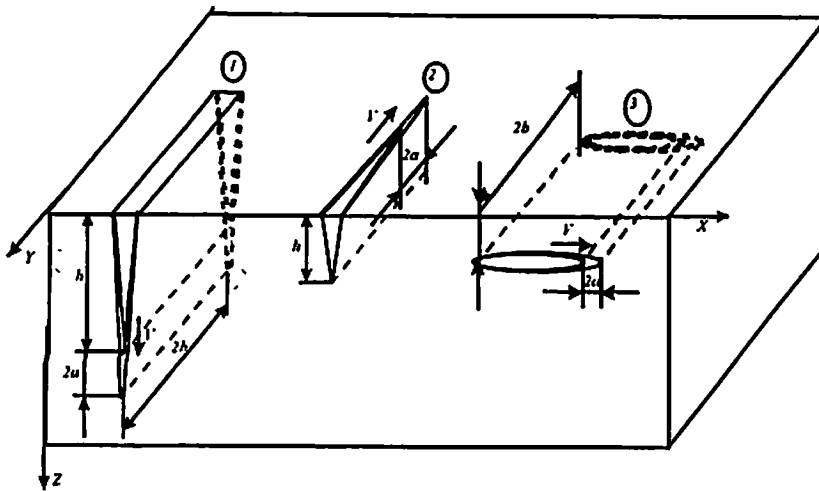


Fig. 1. Physical models of normal separation cracks: crack growing from the surface deep into the material (1), surface cracking (2), lamination (3).

As you know, plastic deformation occurs around the mouth of a crack. We suppose, that the cross-section of a plastic range has the shape of a circle with radius of toughness r_p [4]. Distribution of mechanical stresses around the crack mouth and time function of stresses are similar [5]. Based on expressions for point sources such as a vertical (horizontal) single force we have obtained the equations for amplitudes of displacement of harmonic component in Rayleigh waves [6].

$$U = F_0 H(\omega), \quad (1)$$

where F_0 - amplitude of power effect; $H(\omega)$ - the amplitude-frequency (transmission) characteristic of the process of radiation of acoustic waves emitted by a crack of the given type.

1. Crack growing from the surface deep into the material:

$$H_{zR\uparrow}(\omega) = -\frac{ab\eta_0^2 \sqrt{1-\gamma^2 \eta_0^2}}{4\mu C_0} \sqrt{\frac{2k_0}{\pi\rho}} \frac{\sin x_r}{x_r} \frac{\sin y_r}{y_r} e^{-i(\alpha r - k_0 \rho - \pi/4)},$$

where: $\eta_0 = (0.87 + 1.12\nu)(1 + \nu)$; ν - Poisson's constant; $\gamma = C_1/C_2$; k_0 - Wave vector of the Rayleigh wave; $x_r = a(\omega/V - k_0 \cos \alpha)$; $y_r = bk_0 \sin \alpha$; ρ - distance from the mouth of the crack up to the

view point; $q_0 = k_0 \sqrt{1 - \gamma^2 \eta_0^2}$; $s_0 = k_0 \sqrt{1 - \eta_0^2}$; μ - shearing modulus; α - vectorial angle of cylindrical coordinate system;

$$C_0 = 2(2 - \eta_0^2) - 2 \sqrt{1 - \eta_0^2} \sqrt{1 - \gamma^2 \eta_0^2} - \frac{\sqrt{1 - \eta_0^2}}{\sqrt{1 - \gamma^2 \eta_0^2}} - \frac{\sqrt{1 - \gamma^2 \eta_0^2}}{\sqrt{1 - \eta_0^2}};$$

1. Surface cracking:

$$H_{zR \leftrightarrow}(\omega) = - \frac{2a \cos \alpha \sin(k_0 r_p \cos \alpha) \sqrt{(1 - \gamma^2 \eta_0^2)(1 - \eta_0^2)}}{\mu(2 - \eta_0^2)C_0} \left[\frac{2k_0 \sin y_r}{\pi p y_r} \ell^{i(\alpha - k_0 \rho - 3\pi/4)} f_{\leftrightarrow}(h); \right.$$

$$\text{where: } y_r = a(\omega/V - k_0 \sin \alpha); f_{\leftrightarrow}(h) = \frac{\ell^{-q_0 h} - 1}{q_0} - \left(\frac{2 - \eta_0^2}{2} \right) \frac{\ell^{-s_0 h} - 1}{s_0};$$

3. Lamination:

$$H_{zT}(\omega) = - \frac{ab(2 - \eta_0^2) \sqrt{(1 - \gamma^2 \eta_0^2)}}{2\mu C_0} \left[\frac{2k_0 \sin x_r \sin y_r}{\pi p x_r y_r} \ell^{i(\alpha - k_0 \rho - \pi/4)} f_{\uparrow}(h); \right.$$

$$\text{where: } f_{\uparrow}(h) = e^{-q_0(h+r_p)}(1 - e^{2q_0 r_p}) - \frac{2}{2 - \eta_0^2} e^{-s_0(h+r_p)}(1 - e^{2s_0 r_p}); \quad x_r = a(\omega/V - k_0 \cos \alpha);$$

$$y_r = bk_0 \sin \alpha.$$

The pulse shape of an acoustic wave in a time domain can be obtained, using the formulas of conversion and reconversion of the Fourier transforms.

$$U(t) = \int_{-\infty}^{+\infty} \left[\int_{-\infty}^{+\infty} \sigma(t) \ell^{-i\omega t} dt \right] H(\omega) \ell^{i\omega t} d\omega, \quad (2)$$

where: $\sigma(t)$ - pulse of power effect.

The analytical solution for $U(t)$ is impossible in view of complexity of integrands, therefore the algorithm of the fast Fourier-transform is applied to calculate the time function of a pulse of displacement in an elastic wave [7].

RESEARCH RESULTS

Based on the obtained models we have studied the basic regularities of radiation of Rayleigh waves emitted by cracks growing at subsonic speeds. The obtained regularities allow us to determine the gain of a crack for one jump on pulse amplitudes (Fig. 2,3), the growth rate of cracks on a base frequency and width of the spectrum Δf of the received signals of the acoustic emission (Fig.4), and using the directional diagrams we can determine orientation of a crack, i.e. the direction of development of its mouth. (fig. 5).

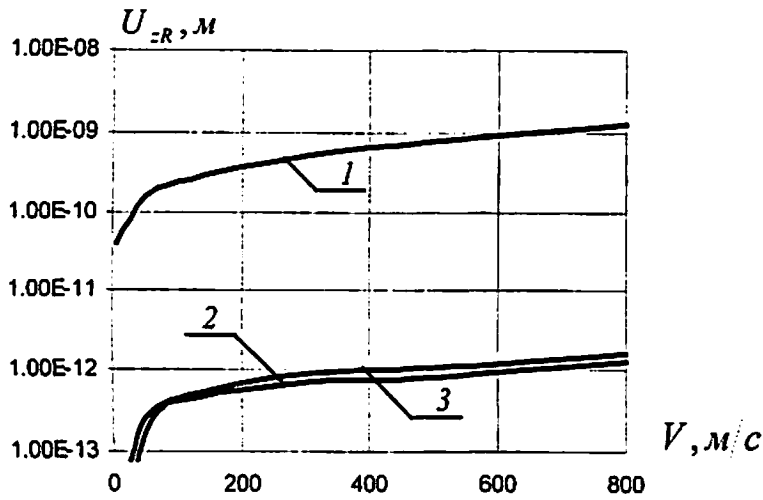


Fig. 2. Relations of amplitudes of displacement in waves of acoustic emission radiated by a crack:

1 - crack growing deep into the material; 2 - surface cracking; 3 - lamination, caused by speed of a crack jump V ($2a=1.0\text{ mm}$; $2b=5\text{ mm}$; $h=5\text{ mm}$; $p=0.1\text{ mm}$).

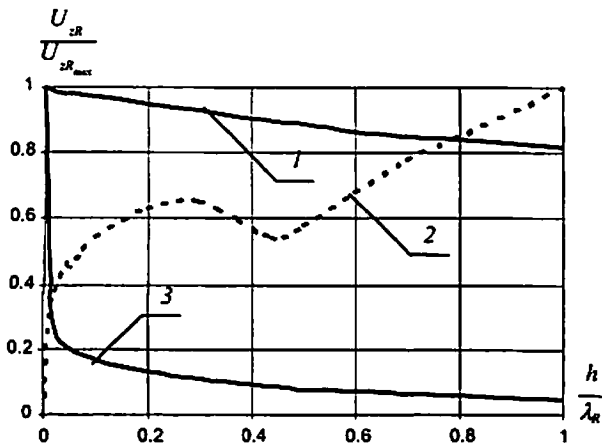


Fig. 3. Amplitudes of displacement in the Rayleigh waves versus stratification depth of the mouth of crack h :

1 - crack growing deep into the material; 2 - surface cracking; 3 - lamination.

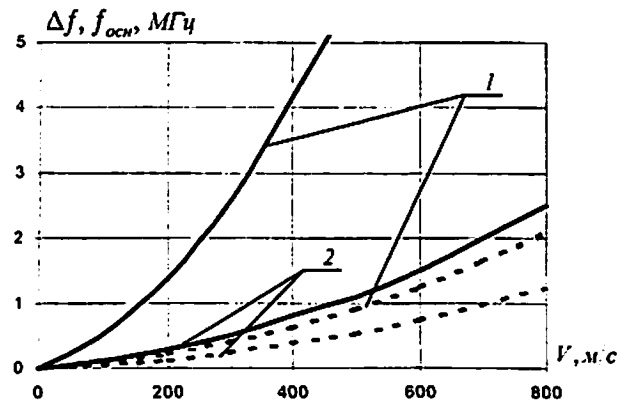


Fig. 4. Width of the spectrum Δf and base frequency of a spectrum f_{OCH} versus Growth rate V of the crack: 1 - crack growing deep into the material; 2 - surface cracking and lamination.

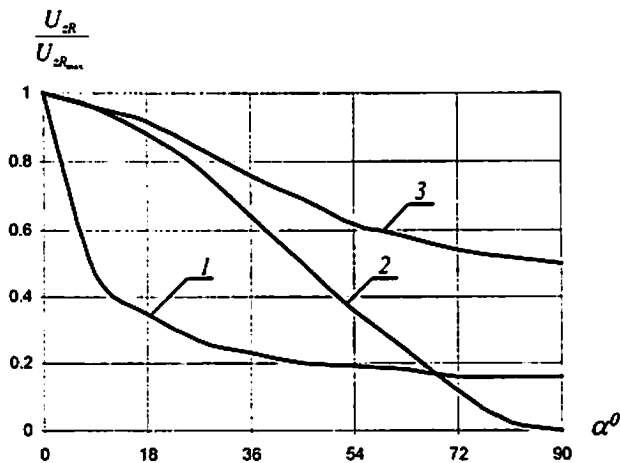


Fig. 5. Directional chart of Rayleigh waves:
 1 - crack growing deep into the material; 2 - surface cracking;
 3 - lamination, ($V=100\text{m/c}$, $2a=1\text{MKM}$, $2b=5\text{MM}$, $h=5\text{MM}$).

Besides, we can determine the type of a crack by the form of pulse spectrum of the Rayleigh wave. Fig.6 shows typical waveforms and spectra of pulses emitted by cracks.

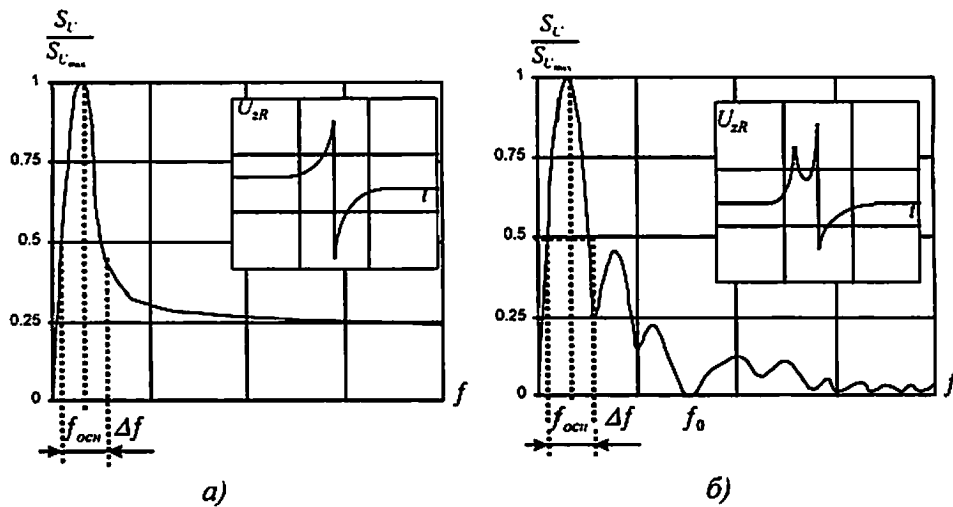


Fig. 6. Typical waveforms and spectrum of an acoustic emission signal, emitted by Rayleigh waves which are excited by: a crack growing deep into the material (a), surface cracking and lamination (b).

The spectrum of a crack growing deep into the material, is shifted into a higher frequencies area (fig. 4). Besides, the amplitudes of displacement in the Rayleigh waves are much higher than in other types of cracks (fig. 2), and the radiation pattern has the highest directivity (fig. 5). Such symptoms are typical of an early stage in the stress-corrosion development. A distinctive feature of the pulse spectrum of a Rayleigh wave excited by cracks, such as surface cracking and lamination, is a harmonic with frequency f_0 , which corresponds to zero amplitude of displacement (fig. 6b). The frequency is definitely related to the stratification depth of the crack mouth h . This dependence is expressed by the equation $hf_0 = Q$ (Q - is constant for the given material and is only determined by the type of a crack, fig. 7).

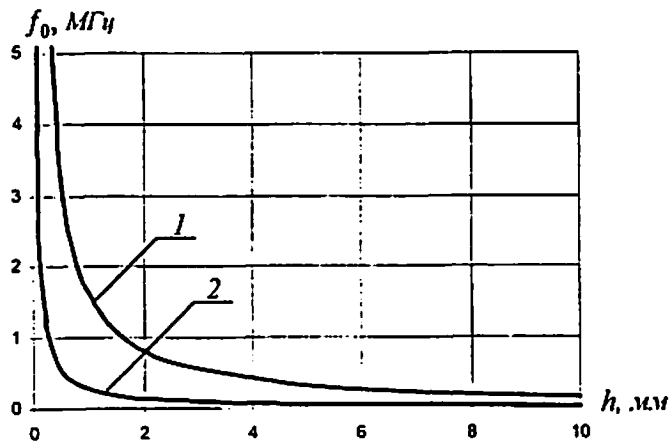


Fig. 7. Frequency f_0 versus the crack mouth stratification depth for low-carbon steel: 1 - surface cracking; 2 - lamination.

The data we have obtained through the discussed models on acoustic fields of Rayleigh waves excited by growing cracks can be applied in monitoring stress-corrosion damages at pitted sections of natural gas pipelines for determining of development stage of the stress-corrosion. In addition, the information on the type a crack and its data (gain, speed, orientation and depth of the mouth) can be used in combination with known acoustic-emission methods of detecting corrosion cracking [8].

REFERENCES

1. V.A. Kanaikin, A.F. Maviyenko. Pipe destruction at main natural gas pipelines. (in Russian), Yekaterinburg, 1997 -102 p.
2. I.A. Viktorov. Sound surface waves in solids. (in Russian), M.: Nauka, 1981. -160 p
3. V.S. Ivanova, A.A. Shanyavsky, Quantitative Fractography. Fatigue Failure (in Russian), Metallurgya, Chelybinsk (1988).
4. V.M. Finkel, The Physics of Fracture (in Russian), Metallurgya, Moscow (1976).
5. G.A. Budenkov, O.V. Nedzvetskaya, A.J. Kotolomov, A.V. Bakhtin. On research of acoustic fields of the Rayleighs waves emitted by growing cracks. (in Russian), Defektoskopia, 1998, No 5, pp 64 -75.
6. G.A. Budenkov, M.S. Boiko, T.A. Guntina, I.A. Usov. Excitation of the Rayleigh waves of by a source such as a harmonic single force which is operational under surface of elastic half-space. (in Russian), Defektoskopia, 1981, No 12, pp 37-42
7. G.A. Budenkov, O.V. Nedzvetskaya, A.V. Bakhtin. On monitoring of acoustic emission waves emitted by fatigue cracks. (in Russian), Defektoskopia, 1997, No 9, pp 61 -70.
8. A.E. Andreikiv, N.V. Lysak. Method of acoustic emission in research of processes of destruction. (in Russian), Kiev, Naukova dumka, 1989. - 176 p.

Nondestructive evaluation of phase transformations in Cu based shape memory alloys by ultrasonic techniques.

M. Landa, M. Chlada, Z. Převorovský

Institute of Thermomechanics CAS, Dolejškova 5, 182 00, Praha 8, CZ

V. Novák, P. Šittner

Institute of Physics CAS, Na Slovance 2, 182 21 Praha 8, CZ

Abstract

This paper deals with the characterization of structure changes during thermomechanical tests of single CuAlNi crystals. The used techniques are based on acoustical properties (wave velocities and attenuation) changes during martensitic transformation (MT). Acoustic emission phenomena seems to be indicative particularly of dynamic of MT. Acoustic waves contain dynamical and orientation information of the mechanism associated with the structural changes that has generated them. The suggested experimental set-up are described. Acoustic properties changes and acoustic activity of forward/reverse MT are presented and identification various types of martensitic phases is discussed.

Keywords : ultrasonic waves, acoustic emission, shape memory alloys, martensitic transformation

1 Introduction

Shape memory alloys (SMA) are generic class of intermetallic alloys that display mechanical memory effects upon stress/thermal cycling. This properties are derived from a solid phase change - thermoelastic martensitic transformation (MT) taking place upon changing external stress and/or temperature, [1].

We have been studying stress-strain response of CuAlNi alloys in a single crystal form under compression at constant (room) temperature. In particular case of Cu-based SMA's , the high temperature austenitic ordered phase of high symmetry bcc structure (β_1) transforms mainly into lower symmetry martensitic phases with 18R monoclinic (β'_1) and/or 2H orthorhombic structures (γ'_1). The ultrasonic nondestructive techniques have a potential to provide (namely bulk) phase information complementary to classical phase identification methods (chemical analysis, TEM, X-ray).

Changes of acoustic wave velocities and attenuation measured during the transformation bring an information about the elastic moduli and structure variations (immediately structure state characterization), [2]. Acoustic emission (AE) accompanying the structure changes, seems to be indicative particularly of the dynamics of the martensitic transformation, [3].

2 Experimental procedure

The two types CuAlNi materials were prepared : The first single crystal (sample C44t) with orientation near [001] has a transition (M→A) temperature ($\approx 40^\circ\text{C}$) above room temperature T_0 and the transition temperature of the second crystal (sample C101t, orientation near [011]) is below T_0 . Typical dimensions of the prism specimen for compression tests is $10 \times 3 \times 3 \text{ mm}^3$.

The $\sigma - \epsilon$ curve of the compression test of the sample C44t is shown in Fig.1a). The strain rate was constant and its typical value was $\dot{\epsilon} \approx 0.8\%/min$. The loading process starts with the elastic deformation of the austenitic monocrystal and continued through $(\beta_1 \rightarrow \beta'_1) \rightarrow \gamma'_1$ transformation to the finish state of the single martensitic crystal. The return process $M \rightarrow A$ may be realized by heating over the transition temperature.

The $\sigma - \epsilon$ curve of the C101t test shows the reversible behaviour of the material structure with the unloading, see Fig.1 b). The unloaded (return) "path" in the $\sigma - \epsilon$ diagram and the hysteresis depend on the maximal value of the strain (ϵ_{max}): If the maximal strain ϵ_{max} is up to 5.5%, then the hysteresis is narrow, crossing this value the hysteresis slowly magnifies and if the transformation process is completed ($\epsilon_{max} \approx 6\%$) then the return path is significantly different.

2.1 Ultrasonic measurement

The pulse transmission technique was used. In the special designed pressure grips were placed ultrasonic transducer (central frequency 10MHz) with respect to the specimen axis. The set-up is schematically drawn in Fig.2 a). The ultrasonic measurements were realized during the selected stops in the loading process. In each loading step the transmitted echo was observed and corresponding rf-signal was recorded by DSO. The actual velocity of longitudinal wave propagation (c_L) was computed from the time delay of transmitted echo and the actual specimen length. The time of flight (TOF) was determined i) from the first signal arrival, ii) from the maximum signal arrival or iii) from the signal phase characteristics. The attenuation coefficient α was determined from the pulse amplitude decay and the rms value of the pulse decay. Attenuation frequency dependence was expressed in the form of spectral ratio (FT) of the actual signal to the reference signal in the zero loading state.

2.2 Acoustic emission measurement

The AE sensor (PZT transducers, frequency band 1.4MHz) are placed in the loading grips. Acoustic emission activity parameters (count rate dN_c/dt , event rate dN_e/dt and amplitude distribution) in equidistant time intervals (0.5s) were monitored during the compression test of the SMA specimen, see Fig.2 b).

Simultaneously, waveforms of selected AE signals were recorded (12bits/10MHz, 16k/chn.) for additional digital signal processing. The signal postprocessing consists of parametrisation of the evaluated AE events from the signal records and statistical analysis of AE parameters ensemble. The 18 parameters were suggested to best characterization of event amplitude/energy distribution in time, frequency and value level domain. The R as well as Q factor analysis were applied, [4]. This approach reveals statistical relations among independently obtained factors. The R-technique gives correlation among AE parameters based on events (measurements) ensemble whereas the Q-technique gives correlation among events based on parameters.

3 Results

3.1 Velocity and attenuation

Specimen C44t

The comparison velocity c_L and attenuation α are measured in the 22 points during the loading, Fig.3 a). The velocity changes during the transformation are relatively small. The velocity values are sensitive on TOF determination technique and the deviations are systematical. This effect may be explained by geometrical dispersion of wave propagation along the specimen. Nevertheless, all used procedures give the weekly increasing trend with respect loading, notable progress in $\epsilon \approx 3\%$ and drop in $\epsilon \approx 4\%$. The total velocity increase is about $\approx 1\%$ (The velocity of initial state is $\approx 4.35mm/\mu s$). The attenuation coefficient α at first rapidly decay, grows at

$\epsilon \approx 2\%$ and then decays relatively slowly. The complete martensite crystal has lower attenuation about $\approx 3\text{dB/mm}$ than initial austenite.

Specimen C101t

The acoustical properties of specimen C101t were measured during two cycles (Fig.3 b)). The first cycle has maximal deformation $\epsilon_{max} = 3\%$ (narrow hysteresis) and the loading of second cycle finishes at $\epsilon_{max} = 6.35\%$. The results are plotted in unrolled form depending on measure number. The total number of measurements is 81. The initial velocity is $5.4\text{mm}/\mu\text{s}$, (higher elastic moduli than in case of C44t). The velocity changes are more eminent and all detection methods give the similar results. The velocity tends to increase and when the slope of the curve $\sigma - \epsilon$ changes, then the velocity decreases. The velocity curve of the return path is symmetrical. The total transformation is reached during the second cycle and the velocity decreases about almost $7\%(5.03\text{mm}/\mu\text{s})$. The peak appears in the end of return path $\sigma - \epsilon$ (Measure No. =72), where the part volume of the specimen does not transform. The rest makes the sharp interface where the ultrasonic pulse scattered and signal waveform dramatically changed. The automatic TOF determination procedures (ii,iii) crashes, see the end of velocity dependence in Fig.3 b). The rest transforms at the final stage of unloading. The attenuation is higher then in case C44t and has a decreasing trend with transformation process and changes from $\alpha = 10.2$ to 3.6 dB/mm .

The acoustical properties of C101t changes more significantly then C44t and velocity dependencies of both materials have an opposite trends.

Frequency dependence of amplitude decay

Amplitude frequency characteristics (*FT*) are shown in Fig.4 in two forms : 3D diagram and gray scale map. Darker shades correspond to higher amplitude of transmitted rf-signal. During transformation process of C44t is important that the local amplitude decay at 2% deformation (point 8) is wideband and the amplitude increasing at the final stage of MT is dominantly localized into lower frequency (6MHz) branch. On the other side, the specimen C101t shows the two main frequency bands of amplitude increase : around 7MHz and the range between 11-12MHz. Visible amplitude growth is also around 9 MHz. The local amplitude decay of measurement upper then No.72 is caused by superposition of reflected wave from the untransformed rest of the material.

3.2 Acoustic emission

The comparison of AE parameters with the stimulate mechanical quantities history are shown in Fig.5 and analysis of sampled data (Fig.6) are plotted in Fig.7-8.

3.3 AE activity versus stimulate quantities

Specimen C44t

The AE activity starts at initial linear stage of $\sigma - \epsilon$ curve. In this moment, the first $\beta_1 \rightarrow \beta'_1$ transformation is expected. The local maximum of AE is "delayed" after the corresponding stress local maximum. The local decay of stress around 3.5% deformation si accompanied with increasing of AE. The final AE growth is at the final stage of MT. The count to event ratio (dNc/dNe) reveals the additional important points (the peak at 2.2% deformation correspond with the local stress decay and the others are at 4.4%, 5.2%).

Specimen C101t

The seemingly continual character of AE activity appears at the close part of compression cycles with higher ϵ_{max} (up to 5.5%). Whether $\epsilon_{max} > 5.5\%$, the AE activity drops after the reverse

and then distributes along the bottom "come-back" way. The important activity accompanying the final stage of unloading when the untransformed rest appear. Thus AE activity of forward and reverse MT process significantly differ.

3.4 Statistical analysis of sampled AE signals

The typical sampled signals for both material testing is plotted in Fig.6. The wide amplitude range and overlapping of the events are notable features of the signals. The great number of composed events may be find in the record ensembles. This composed event consists of a first relatively small fundamental events following the higher amplitude (energy) event (signals: C44t-2, mer=183, C101t-2, mer=300). This character is not able to explain by wave refraction during the wave path trough the specimen and the grip. It is very probable that this feature has origin in the AE source - MT discontinuous spreading.

Only one event is evaluate from each record. From the measurement C44t, 200 events was processed and 1104 events for C101t compression cycling. The parameters : T_r - rise time, T_d - duration time, A - amplitude, T_{am} , ST_{am} - first , second amplitude moment, statistical parameters of amplitude distribution (mean, variance, skewness, kurtosis), energy parameters (RMS, T_{em} , ST_{em} - first, second energy moment), FB -frequency parameters (relative energy contents in the frequency bands: 0-0.3, 0.3-0.6, 0.6-0.9, 0.9-1.2 MHz) and threshold level parameters (peak counts in the interval of the relative amplitude : 1/4-1/2, 1.2-1).

Both ensemble (C44t and C101t) give the same correlation among parameters. In Fig.7, there are compared the results of R-factor analysis. The matrix component (correlation coefficient r_{ij}^2) represents a statistical relation of given parameter to the factor. The set of parameters having the r_{ij}^2 close to 1 for i -th factor, may be just replaced by this factor.

The correlations among the events are determined by Q-factor technique (Fig.8). In the both ensembles the 5 factors is discriminated. Now, the factor matrix is transposed, a row vector contains correlation coefficients of the factor with the measurements. The rows were filtered by moving averaging (9 points) to better clustering of factor to measures. In Fig.8, there are mapped of the Q-factor matrix, the darker shadows represents higher correlation coefficients. The Q-factor matrix maps are drawn with measurement point in the loading curve.

The significance of separated factors change : factors: 1,3,4 in the start stage, 4,1,2 in the central stage and 3,1,5 i the finish stage of MT of C44t, see Fig.8 a). During the transformation of C101t, the importance of the single factors gradually changes, Fig.8 b). The factor 1 is dominant during all load cycles and factors 4,5 are important in the final stage of MT and factors 4,3,2,1 during the wide hysteresis unloading path of MT.

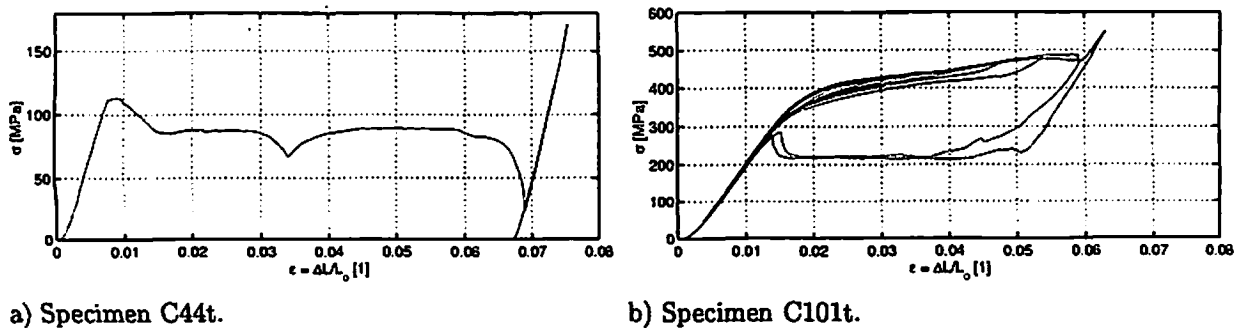


Fig.1 Compression test of CuAlNi crystals.

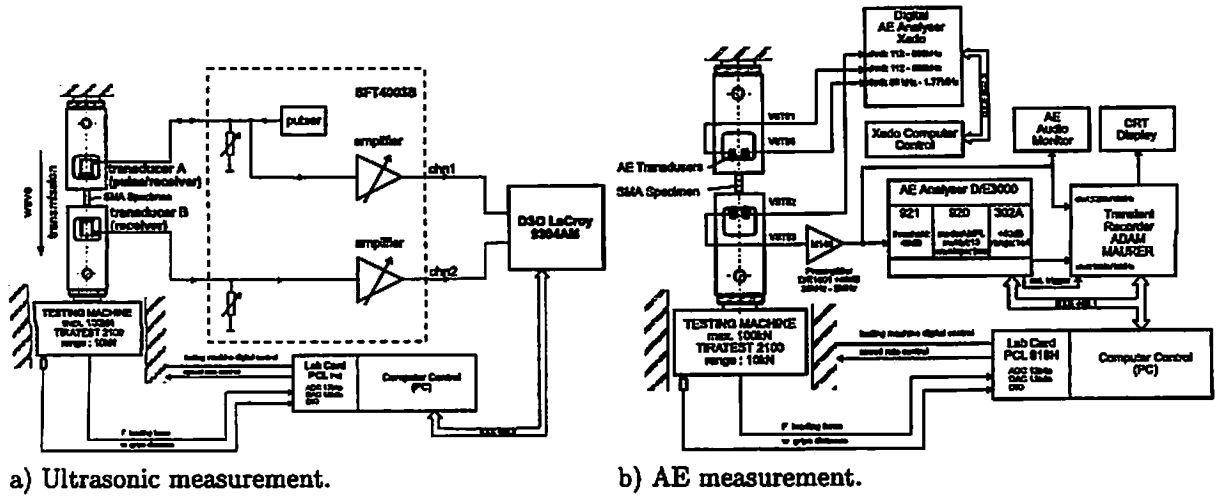


Fig.2 Experimental set-up.

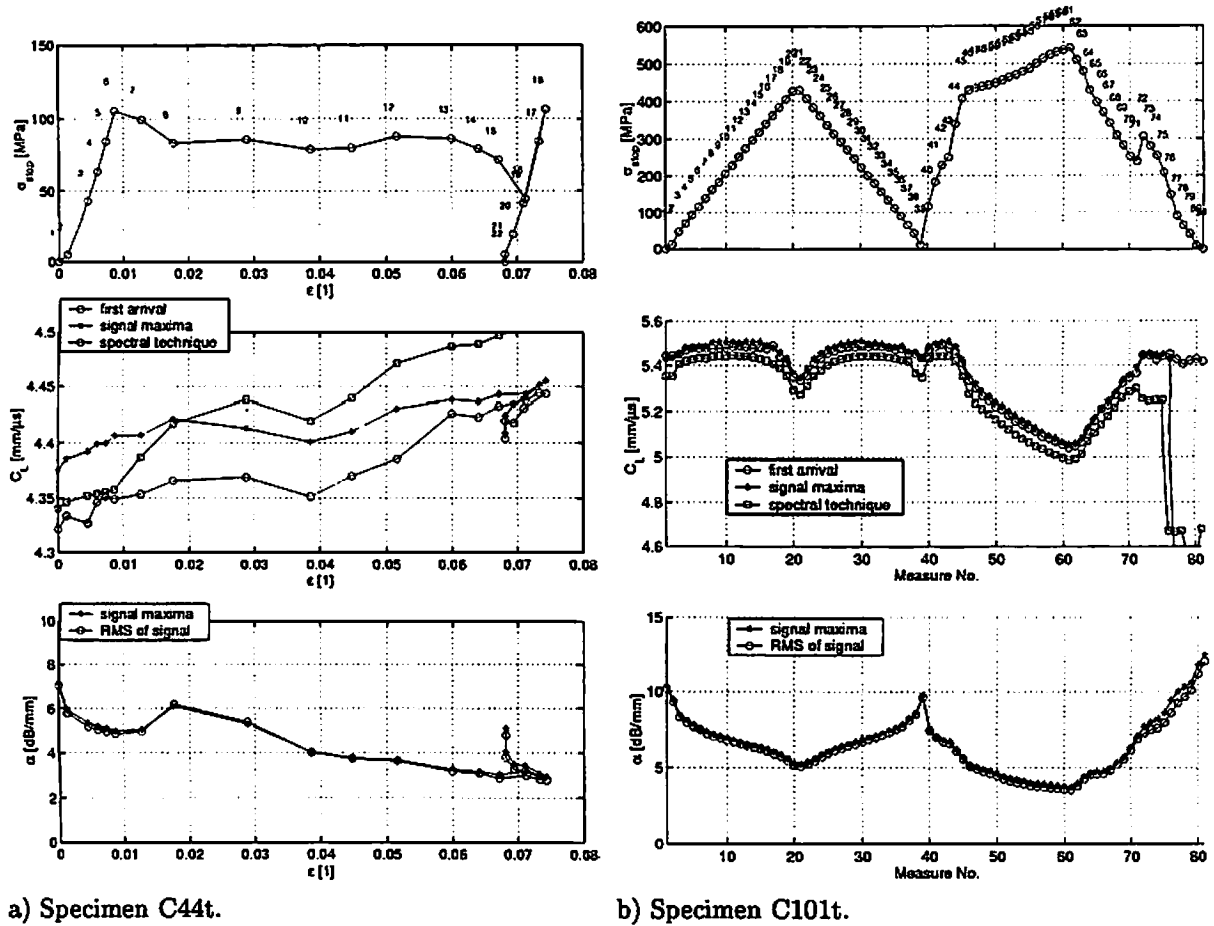
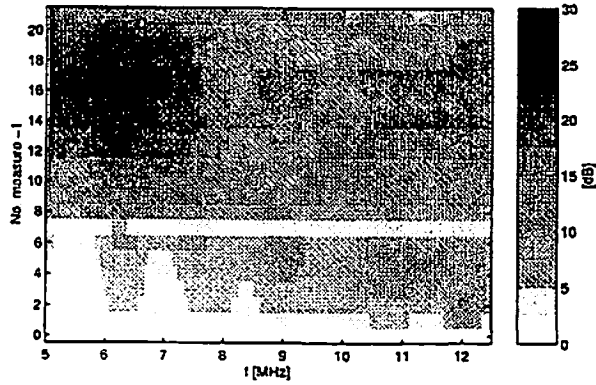
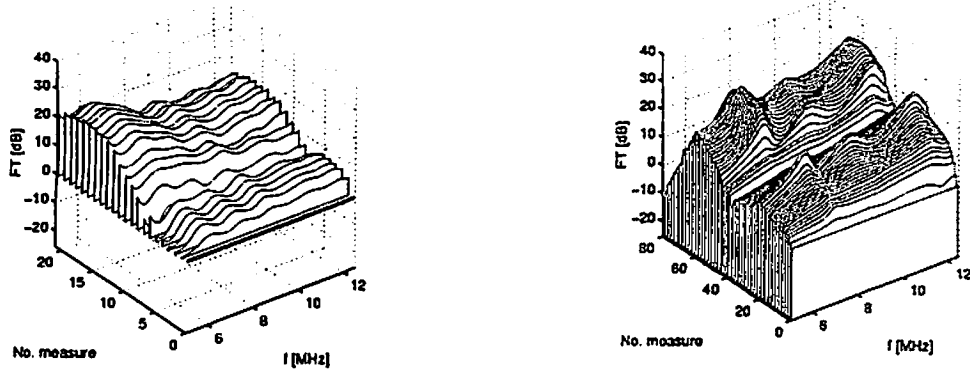
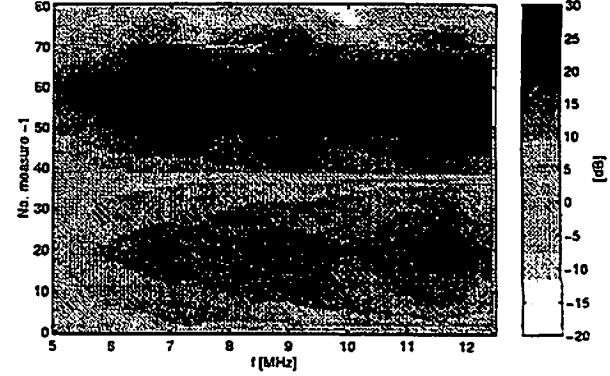


Fig.3 Acoustical properties : longitudinal wave speed c_L and attenuation α .

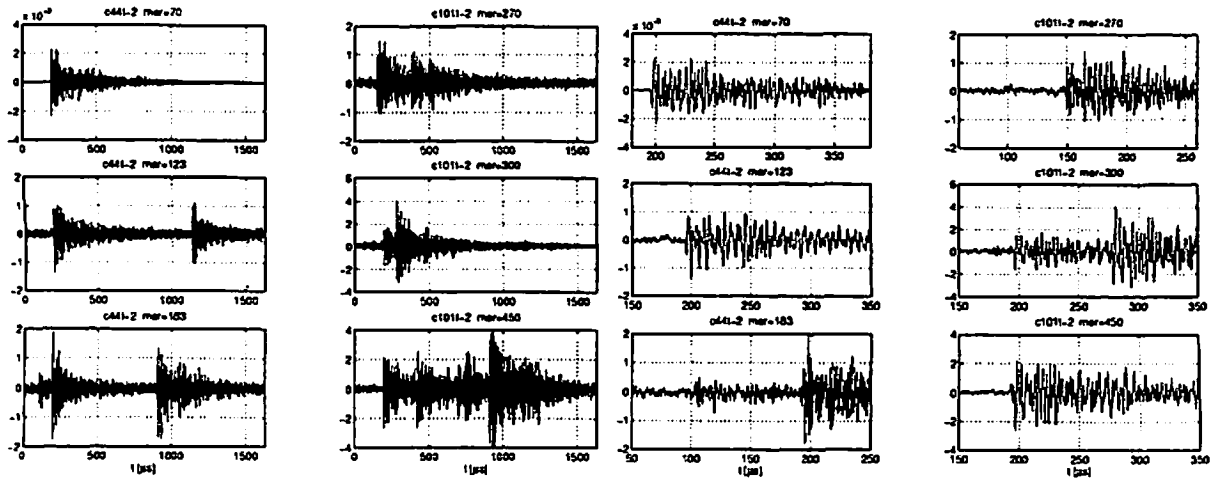


a) Specimen C44t.



b) Specimen C101t.

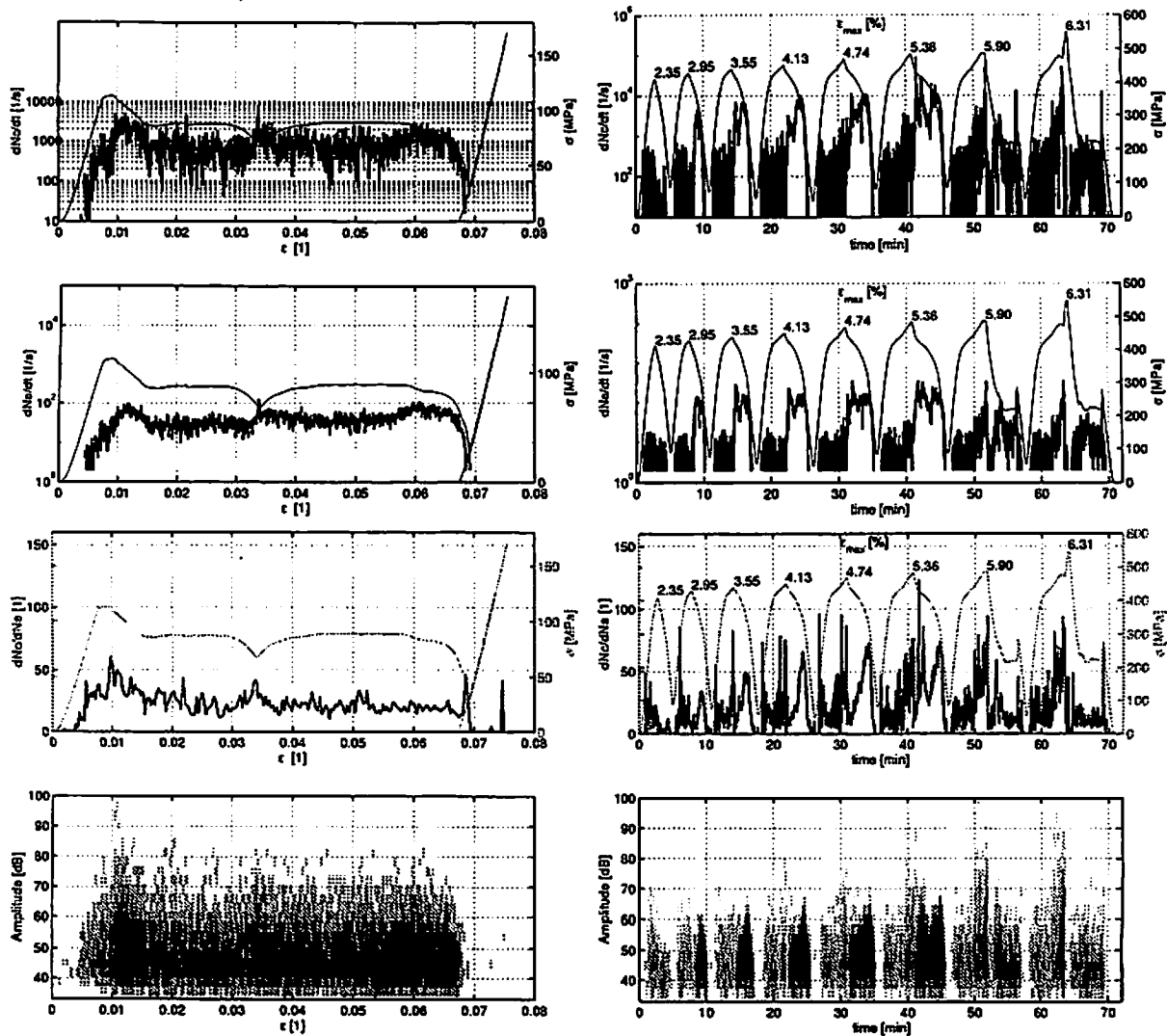
Fig.4 Changes of amplitude frequency spectrum during transformation process.



a) Complete 16k records.

b) Start of events - detailed from a).

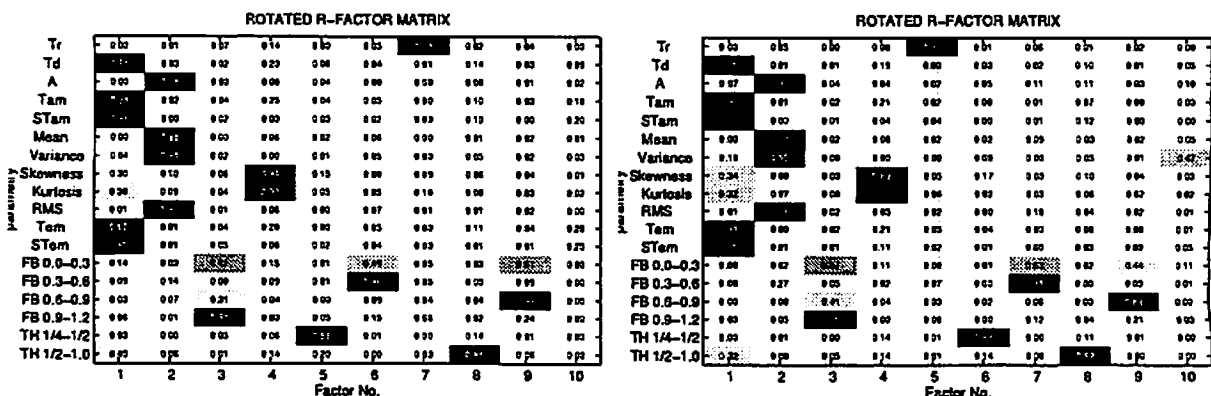
Fig.6 Typical AE signal waveforms.



a) Specimen C44t.

b) Specimen C101t.

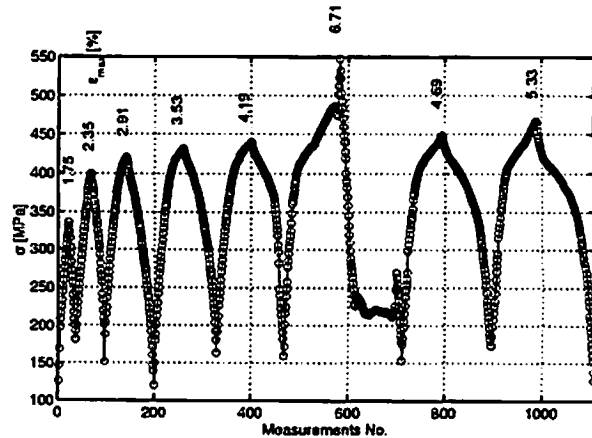
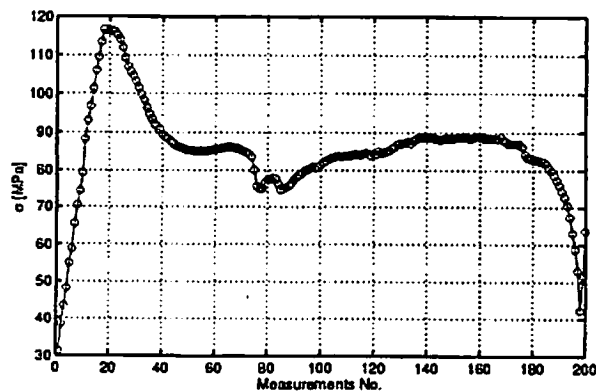
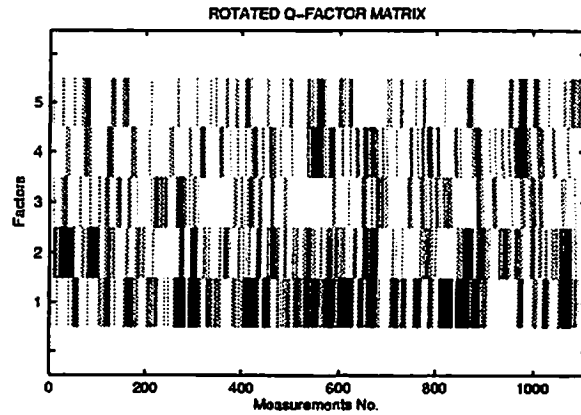
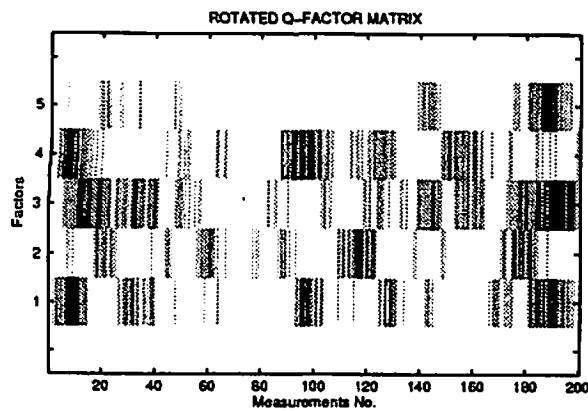
Fig.5 Acoustic activity of specimen C44t and C101t during compression test; count rated dN_c/dt , event rate dN_e/dt , filtered count/event ratio dN_c/dN_e history, amplitude distribution evolution (darker shadows correspond with high number of events in given amplitude class) and unrolled loading curve (thin line).



a) Specimen C44t.

b) Specimen C101t.

Fig.7 Results of R-factor analysis of parametrized sampled signals.



a) Specimen C44t.

b) Specimen C101t.

Fig.8 Results of Q-factor analysis of parametrized sampled signals.

4 Conclusion

During the mechanically induced martensitic transformations of CuAlNi SMA alloys, acoustic wave propagation velocity, attenuation changes was measured and acoustic emission activity was monitored. The material with reversible MT with unloading (C101t) and material with martensitic structure conservation after unloading (at room temperature range) were exposed to compression tests. The differences of acoustical properties both materials, forward/reverse MT are described. The acoustical activity is clustered into 5 classes using factor analysis. Physical meaning of acoustical properties changes and AE activity depends on the knowledge of structural changes and also on the follow wave scattering and AE source mechanical models.

Acknowledgment

This work was supported by the Grant Agency of the Academy of Sciences of the Czech republic under project no. A1010909.

References

- [1] V. Novák, J. Malimánek and N. Zárubová, *Mat.Sci.Eng.* A191 (1995), 193-201
- [2] Ll. Mañosa, J.L. Macqueron and J.C. Baboux, *J. Phys.: Condens. Matter.* 3 (1991), 6257-6266
- [3] Ll. Mañosa A. Planes, D. Rouby and Macqueron J.L., *J. Phys. F:Met. Phys.* 18 (1988), 1725-1731
- [4] M. Chlada , M.Sc. Thesis, Inst. of Thermomechanics CAS, Praha 1999

VVER Steam Generators and Acoustic Emission

Oldřich Matal, Josef Žaloudek, Tomáš Šimo
ENERGOVÝZKUM, spol. s r.o.
Božetěchova 17, 612 00 Brno
Tel: (05) 41214661, fax: (05) 41214659
e-mail: energovyzkum@telecom.cz

1 Abstract

Integrity of primary circuit components of power plants is evaluated by LBB method (Leak Before Break). An acceptable method to detect eventual medium leaks from the primary circuit during plant operation is the acoustic emission method.

Some example of acoustic background emitted in VVER steam generator operation as well as some examples of media leak manifestation in acoustic domain are illustrated and likely limits of detectable leaks with regard to real levels of emitted acoustic background in operation are discussed in the paper.

2 Introduction

A nuclear power plant NPP with pressurized water reactor (PWR, VVER) consists of primary and secondary circuits. From the point of view of power generation the most important primary circuit components are reactor, steam generators (SG), main circulating pumps (MCP), primary pipelines (PP) and pressurizer (PR). The heat generated in reactor is carried out into SGs by pressurized water. At the same time SGs are a barrier between radioactive primary and non radioactive secondary circuits.

One of typical features of the VVER design are horizontal SGs. Six SGs are typical for a VVER 440 unit, four SGs for VVER 1000 unit.

Each of six VVER 440 SGs courts of a horizontal oriented pressure vessel where two vertical oriented primary collectors, a horizontal oriented tube bundle of more than 5000 shaped tubes, a feed water distribution and a water / steam separation systems are inserted.

The SG pressure vessel is of 3210 mm I.D and 11600 mm length and manufactured from carbon steel.

SG design parameters are:

Primary water:	flow rate	1345 kg / s
	average pressure	12,3 MPa
	temperature – inlet	297°C
	temperature – outlet	268°C
Secondary side:	feed water temperature	224°C
	generated steam – flow rate	125 kg/s
	generated steam – pressure	4,6 MPa

Thermal power rate	229,2 MW
--------------------	----------

A number of acoustic emission sensors (AES) was located on the outer SG pressure vessel surface with the aim to monitor and analyze the emitted waves by SG start-up, operating and shut-down periods.

3 Sensor and module specification for VVER applications

Acoustic emission monitoring and evaluation system consist of acoustic emission sensors (AES), preamplifiers, AEM modules, cables and a computer. AES for VVER applications, was selected with a waveguide and designed for frequency range of 100 to 500 kHz. Each AES was connected to a preamplifier by a hard cable. Preamplifier is able to operate in two modes of function and also to amplify signal and to be teleswitched for verification and calibration purposes. Power supply and remote control is provided trough signal coaxial cable. Each amplifier has been connected to AEM module via confinement penetrations by coaxial cables. AEM modules and a computer have been inserted in a cabinet and located in the NPP diagnostic room.

AEM module used in VVER application is of the type AEM – 3000 (manufactured in Energovýzkum Brno). The AEM – 3000 evaluates continuously in the real time actual RMS value of the acoustic signal, RMS value time behavior, counts number of peaks in actual signal over set limit levels and sends this data in to a control computer.

The time interval for RMS integration is short (in milliseconds) and can be flexible changed using software tools. Consequently more information on signal dynamics can be provided.

The AEM – 3000 module is equipped with a programmable source of test signal that enables to test compatibility of measuring channels as well as quality of AES and monitored object surface acoustic feedback's. A sweep generator of square shaped wave with signal programmable magnitude of amplitude, frequency and sweep velocity generates the test signal.

All AEM-3000 module functions are remote controlled by the computer via an interference high resistant serial bus.

Full galvanic separation of channels eliminates channels cross talks and disturbance current ground loop. Acoustic emission monitoring and evaluation system channel lay - out with AEM – 3000 modules provides continual in time monitoring without danger of data losses in contrary to systems with multiplexers.

4 AE system in field operation

The AEM – 3000 modules with connected sensors and preamplifiers save operating self-contained and transferring data in requested time intervals to the control computer in one of system applications at SGs of a VVER 440 units. In this case RMS values of acoustic signals have been evaluated in the real time 100 times per second. It means that in one second 100 evaluations are performed and RMS maximum, minimum and averaged values of the all evaluations as well as continuous number of evaluations performed between two messages to the control computer are being recorded.

5 Selected results monitored and evaluated by the AE system

5.1 Hardware tests after installation at the VVER 440 unit.

A defined test signal from the sweep generator of the AEM-3000 module was sent to one of AESs and responses at the other sensors were monitored and evaluated. The same procedure was applied to test all to the system connected AE sensors.

5.2 Measured AE data in the SG start – up period

Fig 1 illustrates typical RMS value time behavior in comparison to temperature of SG structure and inlet (TH) and outlet (TS) temperatures of SG primary water.

Dominant are:

- Very high RMS values in the range of temperatures of 50 up to 120°C, Increased RMS values at the temperature of approximately 150°C.
- Only small disturbance in RMS values were monitored above SG structure temperature of 250°C.
- RMS values of monitored AE signal are move on less constant in time, when the SG operated at stationary design conditions.
- RMS values differs at different SG on outer surface locations.

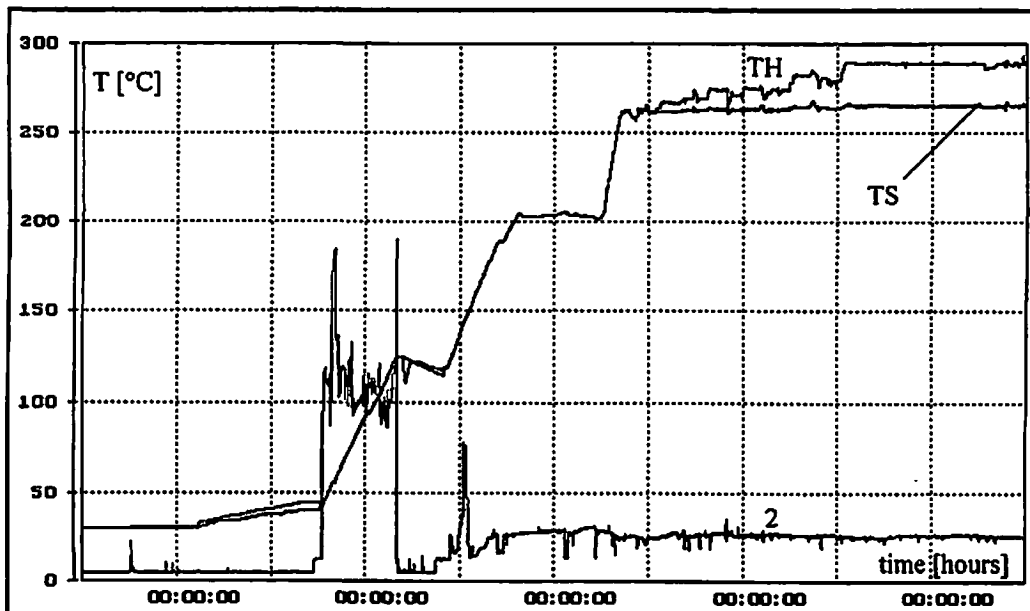


Fig. 1a.

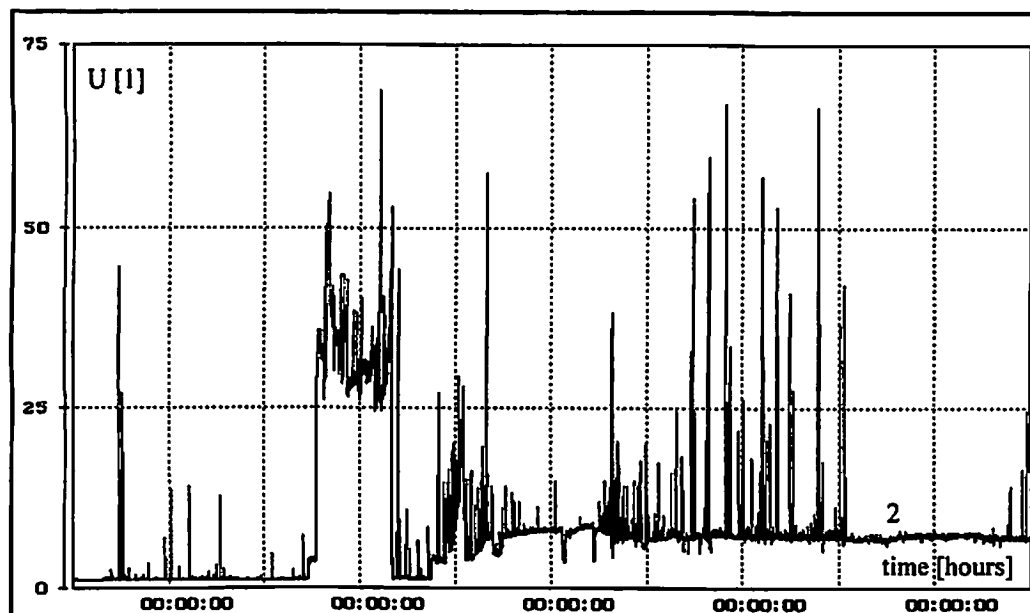


Fig 1b.

Fig.1: RMS values of AE signals and SG temperatures versus time in the unit start-up period.

5.3 High – pressure heat exchanger fall – out

Two high pressure heat exchangers are introduced into the feed water system of SGs at the VVER 440 unit.

Typical responses in SG feed water nozzle temperatures (TNV) and in RMS values of signal of there selected AE sensors located at the SG outer surface are shown in Fig 2

In fact there is no response in RMS of the sensor located in the position 1. On the other hand responses in RMS maximal are intensive for all selected AE sensor locations.

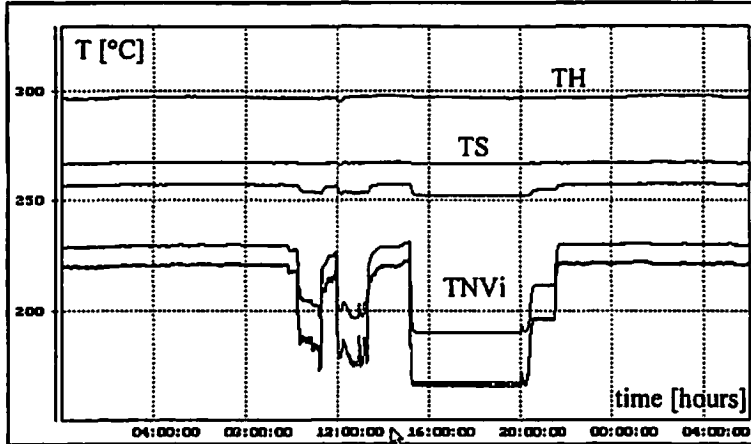


Fig. 2a: SG temperatures in time

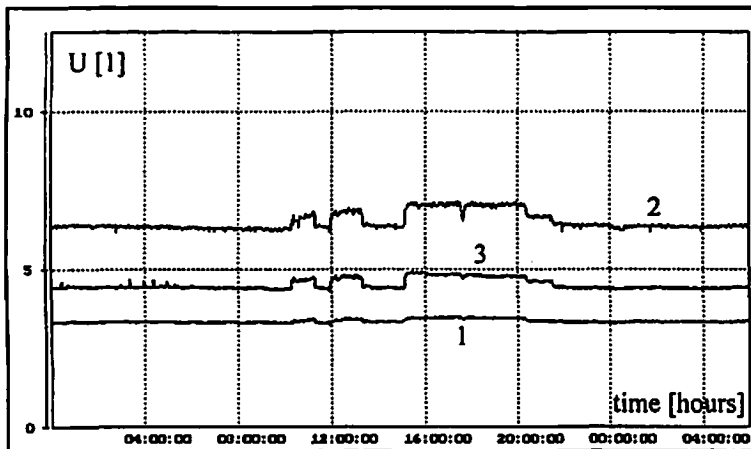


Fig.2b: RMS values in time

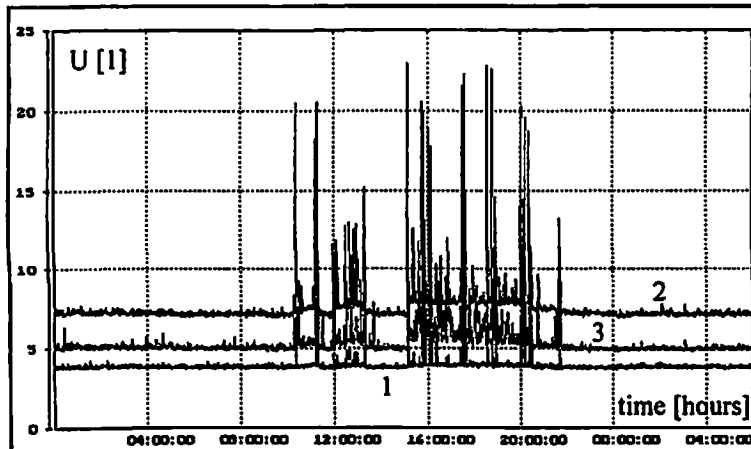


Fig 2c: RMS maxims in time

Fig 2 : Temperatures (TNV), RMS values and RMS maxims responses at SG surface on a high pressure heat exchanger fall-out.

6 Leak detection

Leak before break (LBB) safety concept is based on the assumptions that a loss of integrity of NPP components starts with a crack and small through wall leakage of the pressurized medium. Therefore by early detection of media small leak rates at outer surfaces of components under operation a corresponding safety level can be achieved. The early leak detection in the NPP operation can be realized using acoustic emission methods.

The noise level emitted by a leakage depends on through wall defect shape, cross section, length and also on leak medium physical properties and parameters. The response of AE sensor on a leak depends also on the distance between the leak location and sensor position.

Assuming the distance between the leak location in SG wall and AE sensor position on the SG wall is of 1 m and at the same time a leak rate of the magnitude of about 5 liter per hour. This can correspond in one specific case to the relative RMS level of the AE sensors in a magnitude of 5. If this value is introduced in Fig. 1 and Fig. 2 for the specific case mentioned above then

- no leaks of this magnitude can be detected in the start-up period of the SG,
- the leak can be detected if the SG power level has reached design value and stationary conditions.

7 Conclusions

- Acoustic emission monitoring and evaluation system was installed at SGs of one VVER 440 unit.
- Responses in signal of acoustic emission sensors on SG start-up, power generating and shut-down periods have been recorded and analyzed in real time.
- Specific RMS signal values were registered especially in the start up and shut down periods
- Only in a specific arrangement of sensor at the SG pressure vessel surface and at full and power level of SGs sensors seems to be a chance to detect leak rates below 5 liter per hour.

APPLICATION OF ACOUSTIC EMISSION TECHNIQUE ON FATIGUE TESTING MACHINE RUMUL

Pavel MAZAL, Jan RICHTER, Jiří PETRÁŠ

Brno University of Technology, Faculty of Mechanical Engineering

ABSTRACT

First experience with using acoustic emission method by following of appearance and progressive spreading of fatigue cracks on resonant fatigue testing machine Cracktronic RUMUL have been gathered and commented in this paper.

KEYWORDS

Acoustic emission, fatigue properties, fatigue cracks, surface hardening, fatigue testing machine

1. INTRODUCTION

In the Institute of Design of the Brno University of Technology intensive work has been done on the development of new possibilities of practical application of the acoustic emission technology, namely in the area of cyclic loading of construction materials with the emphasis on materials with surface hardened layers. The biggest experience has been gained especially in the area of contact loading [1,2]. In the last year, we tried to apply our acoustic emission analysers to resonance fatigue testing machine Rumul Cracktronic 8204, which is used for specifying of basic fatigue characteristics of materials - fatigue limit, S-N Curves (Wöhler dependencies) etc.

When describing fatigue characteristics, the basic parameter for technical practice is fatigue limit - which means tension by which the tested sample is not defected even after $1 \cdot 10^7$ loading cycles, possibly the number of cycles to failure under higher tension - so called timed fatigue limit. Studying this problem in details, it is necessary to define the beginning of fatigue damage - the initiation and the beginning of spreading of fatigue crack, possibly to determine roughly the time of spreading of crack. Knowing these parameters, it is possible to guess the time of appearing of crack until the real part is damaged in a real case.

Taking into account the character of fatigue machine Cracktronic (*Fig.1*) and the way of loading it is not possible to watch optically the beginning and spreading of crack during cycling. The only possibility is to stop cycling - in this case it is possible to watch only part of sample or possibly the sample can be taken out and, after measuring of the crack, cycling can go on. This stopping and taking the sample out makes measuring much longer and it can especially cause that the measuring is not very precise.

The development of fatigue damage can be partially followed by indirect method. The whole loading system, sample including, forms resonance system. In case of change of rigidity of the sample the whole system is automatically adjusted which causes change of frequency of loading. The frequency grows by hardening and vice versa, the frequency drops by softening, eventually

by spreading of the crack. It is possible to estimate roughly the course of fatigue failure of the sample by following of frequency changes.

The application of the acoustic emission technology and the analysis of AE signal could in this case importantly extend our knowledge concerning the course of fatigue process. Taking into account the character of the testing machine it is necessary to solve a number of problems. AE technique was employed for the monitoring of the fatigue behaviour in more cases [3,4,5,6] but results are not very clear, yet.

2. DESCRIPTION OF TESTING EQUIPMENT

2.1 PULSATOR RUMUL CRACKTRONIC 8204

Resonance testing equipment load tested sample with both dynamic and static loading. The kinetic condition allow a pure bending between the gripping heads. An electromagnetic driven resonator, built as a rotary oscillator, creates an appropriate bending moment. Independent to the dynamic drive a static moment is possible to be applied to the specimen via a torsion rod. Dynamic stress is developed by vibration system that works together with tested sample in its own frequency. Basic scheme of testing machine RUMUL Cracktronic can be seen in *Fig.1a*. The equipment can work with maximum dynamic bending moment 70 Nm and with static moment up to 35 Nm. In accordance with the rigidity of the sample, we work with frequency of loading up to 300 Hz. In our case, samples with shallow notch have been used (see *Fig.1b*) - in this case the frequency moved from 150 to 120 Hz.

2.2 AE ANALYSERS

Two types of AE analysers have been used for following of AE signal of fatigue loaded sample so far:

1) **AE 10C analyser** - this equipment was made in 1996 - 10 level acoustic emission analyser is controlled by computer PC-AT, which controls its functions. It enables displaying of the activity of output of individual levels of AE signal on the screen of the monitor and the evaluation of experimental data. Of course, the analyser enables output of data, AE signals and their frequency in analogue form. The analyser has 9 levels, firmly adjusted from both sides and the tenth level without any restrictions from above. The gaps between individual levels are 4 dB, the total dynamic range is 40 dB. There is a preamplifier between the AE sensing unit and the analyser (in this case the standard setting was 40 dB). AE signal sensing units type SAE 07 with waveguide with diameter 8 mm is used. The sensing units are based on piezoelectric principle. These differential sensing units have basic frequency capacity 50 - 400 kHz (the advantage of differential sensing units is preventing of getting hampering impulse failures from the surrounding of measured object).

2) **Analyser AED FTA 16** is a modern kit system for sensing and processing of AE signal with 16 identical channels, each of them being controlled by its own 16 bit microprocessor. After filtering of undesirable components, AE signal is fully digitalised and it is processed and evaluated in this digital form. This enables important growth of flexibility and accuracy of measuring of all parameters of AE signal, localisation included, and of important growth of process speed during evaluation. The analyser is equipped by independent channel for measuring of physical quantities, by generator of calibrating impulses etc. Amplitude and time distribution of the signal is done in up to 256 levels, it is possible to follow envelope parameters - lasting of acoustic emission events, data of rise time, number of overshoots, maximum amplitude value, energy of emission signal etc. The analyser is controlled by computer PC Pentium.

In this case piezoelectric sensing units SAE 07 are used - both with and without waveguide.

2.3 ARRANGEMENT OF TESTS

The experiments have been done in two phases so far:

a) with using of one channel system AE 10C. In this case only one sensing unit AE with waveguide is used, which is placed directly on the sample (see **Fig.1b**). In this case only AE signal coming from loaded sample is followed.

b) several experiments have been done with help of 16-channel system AED FTA 16 recently. Four channels are usually used – **Fig.1a** (the first sensing unit with waveguide directly on the sample, second sensing unit on fastening of fixed jaw, the third one inside the fatigue testing machine in the place of fastened torsional rod, the fourth one on plate sample outside machine - etalon).

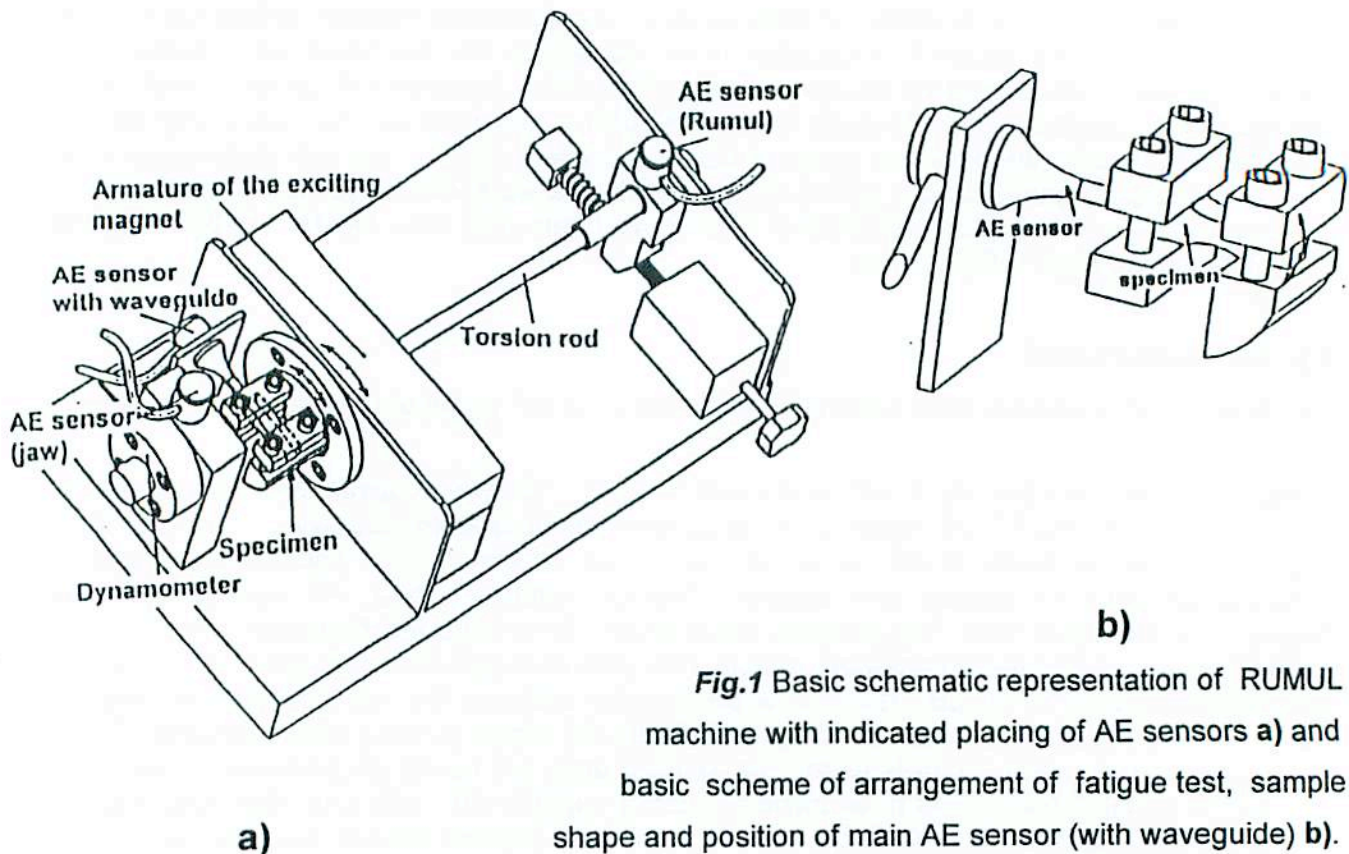


Fig.1 Basic schematic representation of RUMUL machine with indicated placing of AE sensors a) and basic scheme of arrangement of fatigue test, sample shape and position of main AE sensor (with waveguide) b).

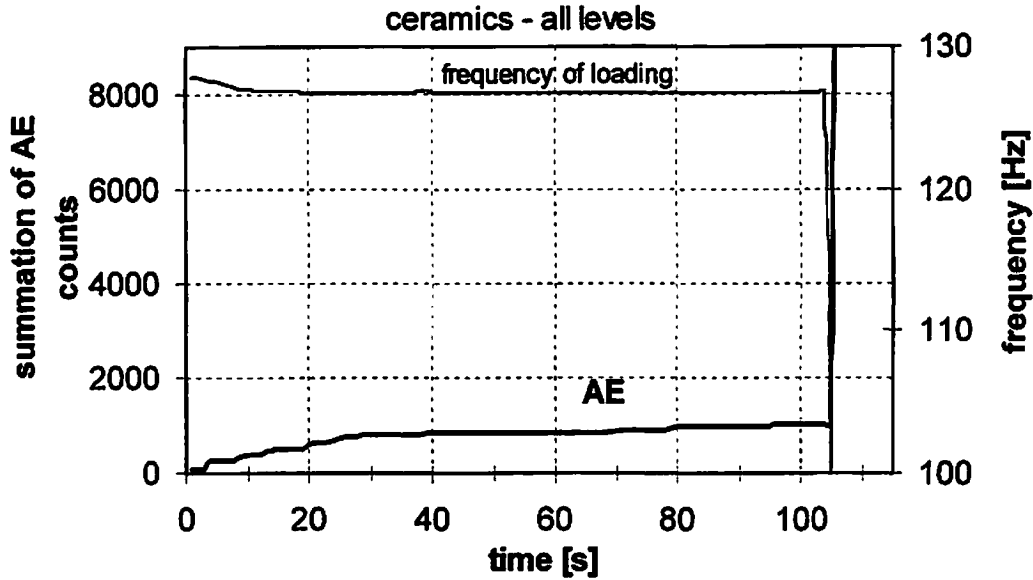
3. MATERIALS USED

Experiments with using AE technology have been done so far as a supplementary measuring by other normally done fatigue tests of materials with modern heat finishing, eventually ceramic materials etc. Most tests have been realised on grey cast iron with laser or plasma nitriding treated surface, on low-alloy carbon steel, middle alloy bearing steel etc.

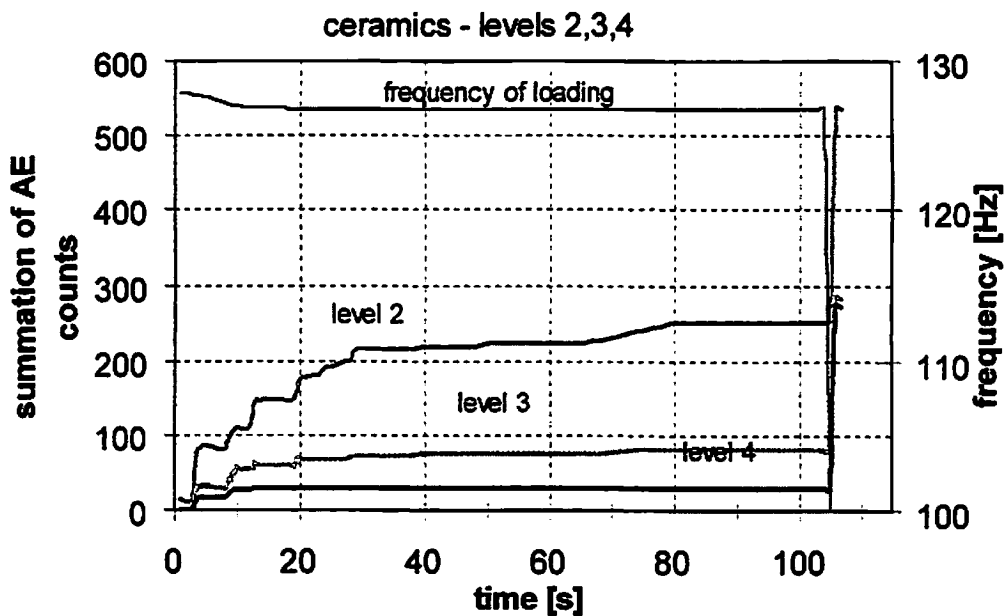
4. EXPERIMENTAL RESULTS

Selected records of frequency of AE count during loading are introduced in further pictures. Examples of records gained by cyclic loading of steel and ceramic material with help of one channel AE analyser 10C are introduced in **Fig.2**. Total sum of recorded AE counts in

dependence of time (number of loading cycles) is shown in these pictures. Measured loading frequency that partially corresponds with changes of the toughness of the sample is shown in the records. The records in **Fig. 2b** and **3b** are elaborated on certain levels, so that the influence of the levels, in which a number of counts, which have no connection with changes in samples, have been put down.

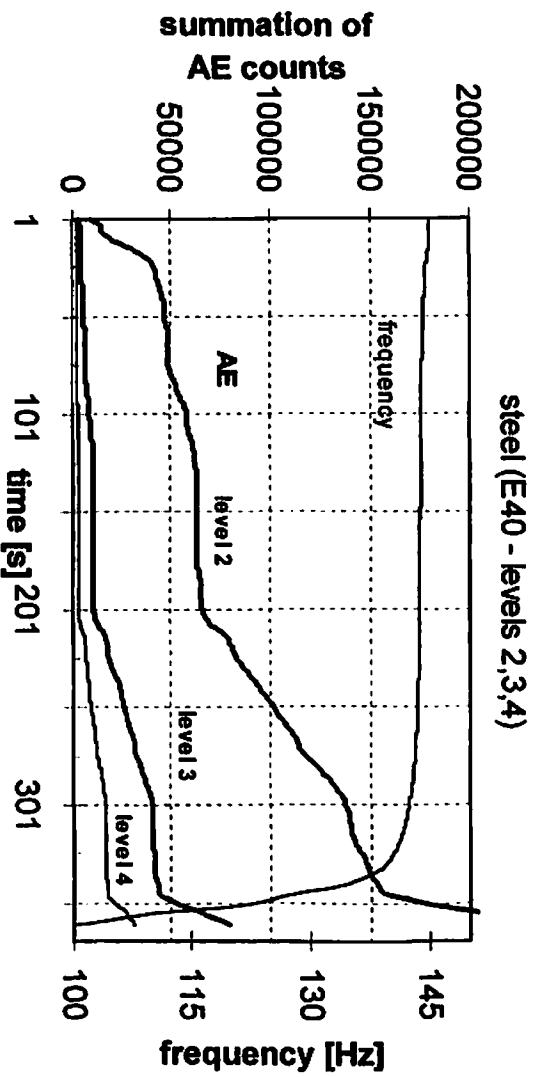
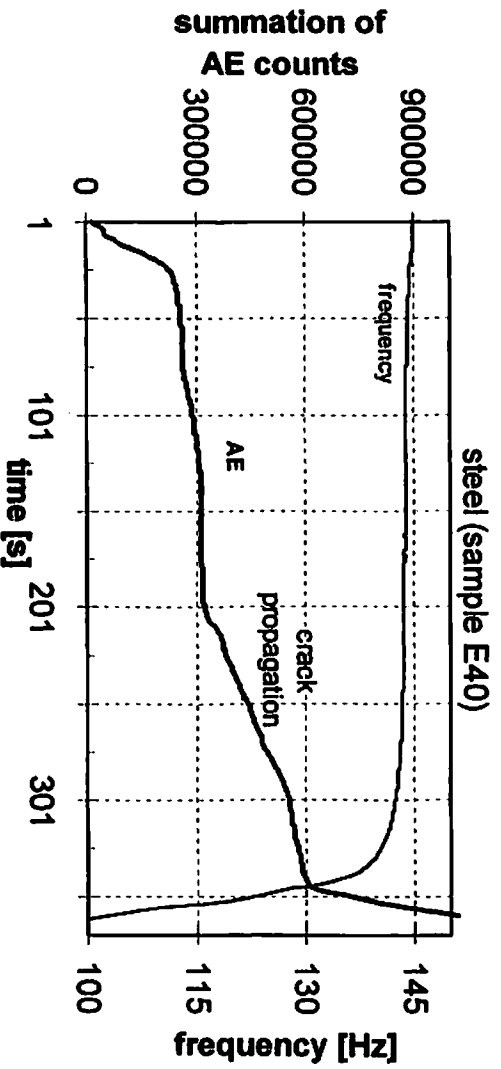
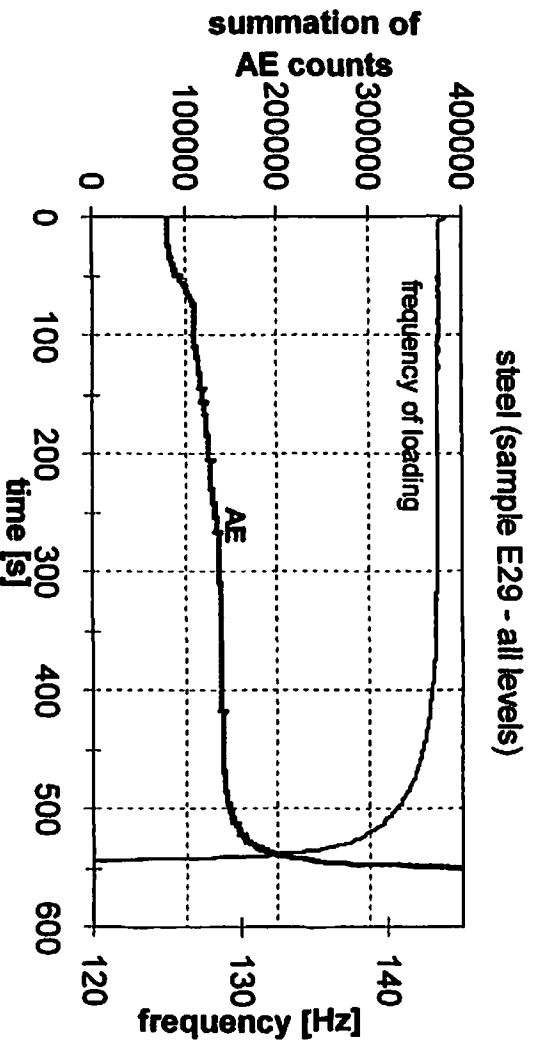


a)



b)

Fig.2 Records of total number of AE counts during fatigue loading of ceramic material:
a) all levels, b) selected levels (AE analyser AE 10C)



Obz.3 Records of total number of AE counts during fatigue loading of steel with nitrided surface: a) lower loading (durability cca 87 000 cycles) b) higher loading (durability cca 60 000 cycles) c) the same plot as b for selected levels

Sample of the first records gained with help of new analyser AED FTA 16 can be seen in following figures. Results from sensing units placed on the sample, fixed jaw and inside the testing machine are compared here. Results obtained on the grey cast iron (CSN 42 2456 – NF A32-401) with surface treated by plasma nitriding are shown in the *Fig.4*.

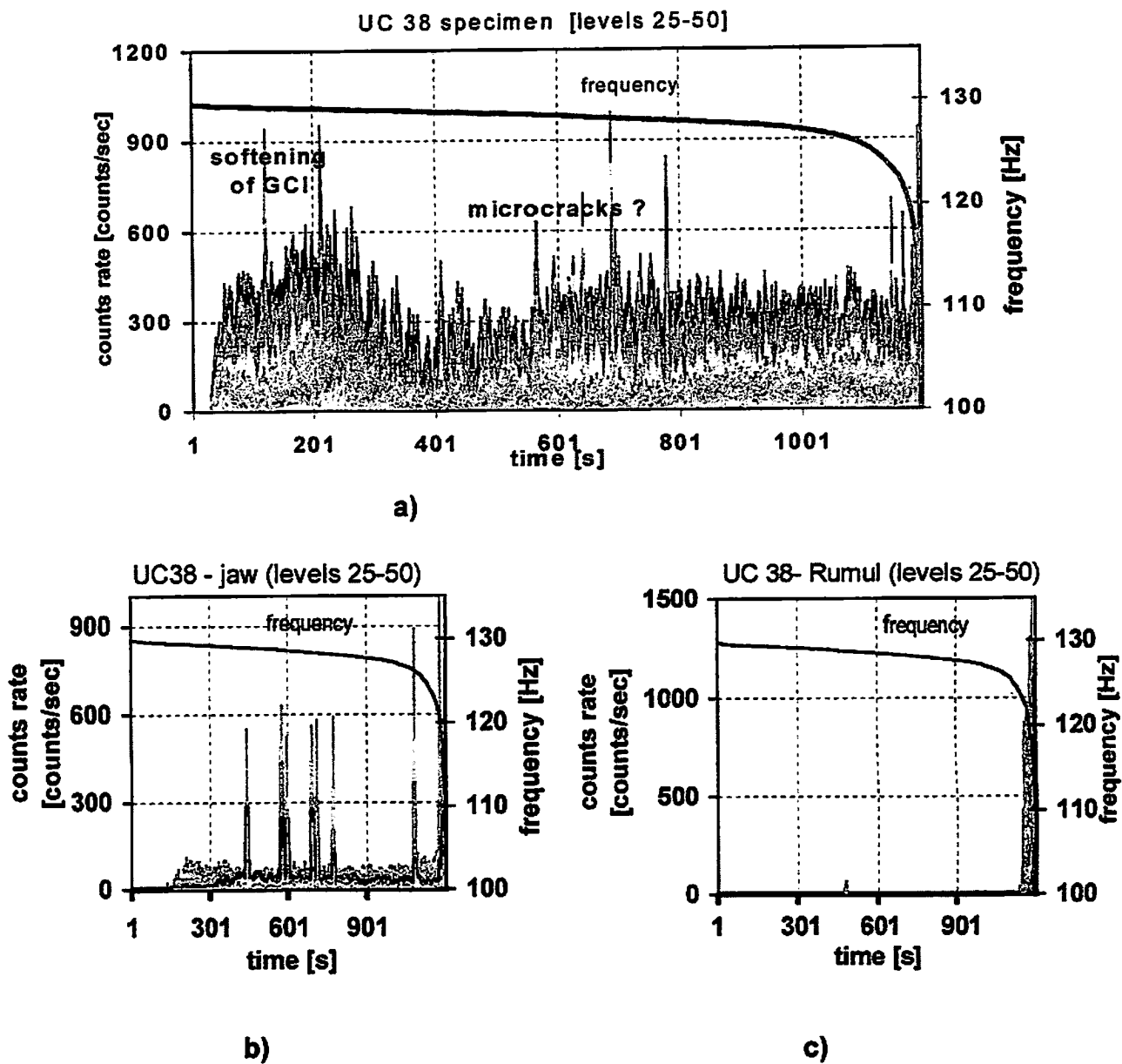


Fig. 4 Differences between counts rates (counts/sec.) measured on different sensors on specimen a), fixed jaw b) and inside the testing machine (near the torsion rod) c) – grey cast iron with surface treated by plasma nitriding – analyser AED FTA 16.

5. DISCUSSION OVER MEASURED RESULTS

Records gained with help of AE technology can show some important changes that are *possibly connected* with the development of fatigue damage of the material. In the area, in which long lasting change of loading frequency appears, increased AE activity of sources appears - see summation curve and records of frequency of overshoots. The stage of macrocrack spreading can be clearly seen. Due to a low number of experiments realised by now it is not still possible to match responses of AE signal with concrete initial stage of fatigue damage.

A number of disturbing influences, which are caused by the principle of the testing machine itself and by the way of fastening the sample obviously appear. These disturbing influences could be possibly identified with help of multi-channel sensing of AE signal from more spots of the fatigue testing machine.

Disturbing influences, which in defined system of loading influence sensed AE signal are before all slippage between fixing jaws and the surface of the samples. The other source of undesirable signals could be torsion rod with tensometers inside the testing machine, which is stressed by torsion. Both these sources will probably change during loading, because, as a result of crack spreading, the rigidity of the sample will drop and the displacement of the moving jaw will grow. Engine with worm gear unit, which adjusts set loading parameters can be further source of disturbing influences. Signals coming from the area outside loading system can have certain influence as well.

Some basic tests for identification and possible elimination of the influence of some above mentioned disturbing influences have been made so far. It is comparatively the easiest to find out the influence of engine with gearbox. The engine can be started separately without starting the whole testing machine. In this case the sensing units placed inside the analyser and on the fixed jaw did not notice any important response in AE signal.

The influence of torsion of torsion rod is being tested at present. The present results imply important possibility of influencing of AE signal. The way of evaluation of slippage between sample and chuck jaw has not been solved yet.

6. CONCLUSION

Basic results measured up to now show, that it will be possible to use the AE technology for following of the development of fatigue crack on the resonance testing machine RUMUL after the methodology is finished and optimum adjustment of analysers is established. It will be possible to identify the length of the stadium of spreading of the crack quite safely. In case that disturbing influences, appearing due to unsuitable fastening of the sample in the fatigue machine, are successfully distinguished, it will probably be possible to try to identify initiation stages - damage cumulation, initiation and initiation spreading of microcrack. The possibility of reliable identification of these actions will be connected with a number of detailed studies in the area of AE signal analysis and in finding connection of its changes with concrete degradation display of tested material. It will be necessary to make a number of repeated measurements in order to find typical changes of the signal and subsequently in beginning of similar changes the sample will necessarily have to undergo detailed metalographic and fractographic analyses. In this way we should manage to match the signal change with individual events in loaded samples.

Managing to use acoustic emission method would considerably extend the possibilities of using RUMUL resonant testing machine. It would make possible to follow the process of fatigue damage in details. It would probably enable to identify the beginning of under surface cracks etc. It offers interesting possibilities in creating of sharp notches (defined length) in notched bodies destined for break toughness testing.

The paper was elaborated in frame of complex Program of the Grant Agency of Czech republic No. 101/96/K264 – Limit states of progressive materials with utilisation of non-standard test methods.

Literature:

- 1) MAZAL,P., DVOŘÁČEK,J., KOLÁŘ,D.: Determination of contact fatigue properties using AE technique. In: 7th ECNDT, Copenhagen, p.2317-2324, 1998.
- 2) DVOŘÁČEK,J., PETRÁŠ,J., MAZAL,P., KOLÁŘ,D.: Acoustic emission and contact properties of surface layers of materials. In:23rd EC on AE Testing, Vienna, p.80-83, 1998.
- 3) TSAMTSAKIS,D.- WEVERS,M.: Fatigue Damage Growth Models for Quasi-Isotropic CFRP Laminates Formulated Using AE Data. In: 23rd EC on AE Testing, Vienna, p.5-8
- 4) DUNEGAN,H.L.: Measuring crack depth of growing cracks by acoustic emission techniques. The DECI Report. www.deci.com/decireport.9.98.html
- 5) DONG-JIN YOON ET AL.: Acoustic emission monitoring of the fatigue crack activity in steel bridge members. Int. Journal on Acoustic Emission
- 6) SIEDLACZEK,J., PILECKI,S. DUŠEK,F.: AE of the 45HNMFA structural steel during low-cycle fatigue. Journal of Acoustic Emission, Vol.10, No3/4, p.1-11, 1992.

ACOUSTIC EMISSION AND STATE OF FATIGUE OF FERROELECTRIC $\text{Pb}(\text{Zr}_x\text{Ti}_{1-x})\text{O}_3$ CERAMICS

Jürgen Nuffer, Doru C. Lupascu and Jürgen Rödel

University of Technology Darmstadt, Department of Materials Science, Petersenstrasse 23, 64287 Darmstadt, Germany

Acoustic Emission (AE) testing is used to investigate the damage mechanisms in ferroelectric PZT ceramics. The AE and macroscopic material parameters like coercive field and remanent polarization were measured simultaneously at different states of fatigue. Fatigue of the samples is artificially generated by bipolar electric cycling. A correlation between the cumulated AE energy and hit data and the macroscopic material parameters is provided. Both the AE data and the material parameters show a maximum value at 10^4 cycles and then decrease during the next 10^8 cycles. The contribution of different AE sources like domain switching and microcracking to the observed AE data is discussed.

KEYWORDS: Acoustic emission, PZT, fatigue, cyclic, ferroelectric

INTRODUCTION

In recent years a strong interest in ferroelectric PZT actuator devices has developed, especially in ultrasonic transducers and multilayer transducers for automobile applications because of their high mechanical coupling factor and prompt response to the applied voltage.

The major obstacle for wide applications is the dielectric fatigue, which is characterized by a change in macroscopic material parameters like remanent polarization, coercive field and generally a degradation of the piezoelectric coupling coefficient. Dielectric fatigue occurs after a large number of switching cycles.

Although described by numerous authors [1 – 3], the mechanisms leading to dielectric fatigue is not yet well understood, partly due to insufficient description of experimental details. Depending on minor changes in microstructure and composition, the PZT materials behave strongly nonlinear, hysteretic and time dependent. Besides a good materials characterization, it is also crucial to accurately determine the cycling conditions. Several attempts have been made for mechanistic description of fatigue. The most important are (1) domain wall pinning due to defect dipoles [1] and (2) microcracks reducing the effective electric field [2,3].

Several authors have used AE testing for the investigation of ferroelectrics [4 - 7]. In ferroelectrics, the most important AE sources are discontinuous domain processes causing sudden strain changes and the onset of microcracks generating elastic waves. The advantage in using AE in ferroelectrics is, that initiation and propagation of cracks can be observed during the electrical driving cycle itself. On the other hand, it is not yet known

at which degree other AE sources, especially discontinuous domain flipping, contribute to the observed AE – data.

Different characteristics of AE-patterns have been attributed to different AE-sources, high AE amplitudes were correlated to microcracking, while amplitudes two magnitudes lower were suggested to originate from domain processes [4]. Distinct AE were found to be due to domain processes, and the onset of continuous AE signals was assigned to microcracking [5]. Another work claims that AE from microcracks only occurs in a small frequency range, and domain processes, in contradiction, lead to AE frequencies scattered in a wide range [6]. To our present understanding none of these assumptions has seen experimental proof. In a previous publication we pointed out that „easy“ domain processes during polarization switching (not hindered by any kind of obstacles like point defects, grain boundaries, other domains or domain system) do not generate any AE [7]. In one previous work cumulated AE from ceramic stack actuators were compared to the state of fatigue by cycling. Rising AE-activity was observed for high cycle numbers [8].

In this work we have correlated the observed AE data with the state of fatigue of the bulk material in ceramic discs, which is characterized by the measurement of remanent polarization and coercive field.

EXPERIMENTAL

Disc – shaped commercial samples (PIC 151, PI Ceramic, Lederhose, Germany) with 10 mm diameter and 2 mm thickness were used. The material consists of the ternary phase system $Pb(Ni_{1/3}Sb_{2/3})O_3 - PbTiO_3 - PbZrO_3$ on the tetragonal side near the morphotropic phase boundary. The average grain size is 5 μm with distribution width of 2 μm standard deviation. The samples were electroded with fired silver on both surfaces.

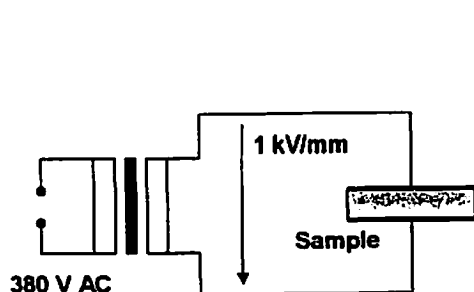


Fig. 1 Setup for bipolar cycling

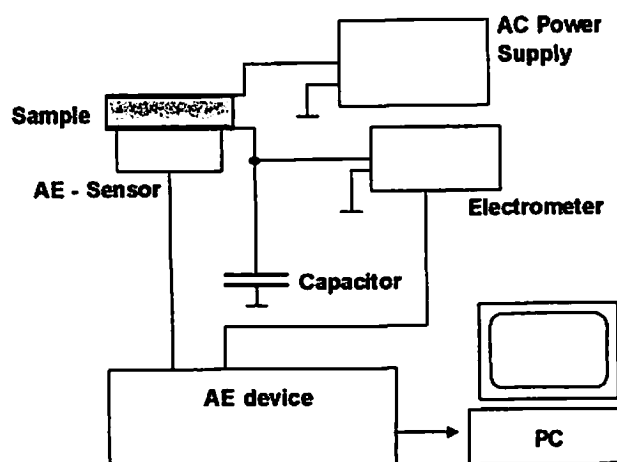


Fig.2 Setup for AE measurement

Bipolar cycling was used for artificially damaging the material. The samples were placed between two metal clamps and a sinusoidal electric field of $E_{max} = 1 \text{ kV/mm}$ and 50 Hz was applied (Fig. 1). The coercive field of an unfatigued sample was determined as 1150 V/mm. After different numbers of cycles the cycling procedure was interrupted and the AE parameters and the macroscopic material parameters were measured (Fig. 2). For this purpose, the samples were driven by a triangular bipolar voltage of $E_{max} = 2 \text{ kV/mm}$ at 0.02 Hz devoid of high frequency noise. During this measuring cycle, the AE events were detected by a 150 kHz resonant transducer (Physical Acoustics) placed on one surface of the sample and then collected and monitored by the AE equipment (AMS 3, Vallent

Systeme). One AE event is characterized by its occurrence (hit) triggered by a threshold crossing, a maximum amplitude, a duration during which the threshold is periodically crossed and the energy per hit, which is the integrated square of the amplitude during the duration. Of these, the AE energy and the number of hits were cumulated during one bipolar measuring cycle. The remanent polarization and the coercive field were determined from the dielectric hysteresis loop detected by a capacitor put in series with the sample.

RESULTS AND DISCUSSION

The results of the AE measurements are shown in Fig. 3, the data of remanent polarization and coercive field in Fig. 4.

The AE data, consisting of the energy and the hits cumulated during a single cycle, both show a maximum value at about 10^4 cycles. The cumulated energy steadily increases until the value has reached two times its initial value. The maximum value of the hits is about three times higher than initially. During the next 10^8 cycles both values decrease down to saturation values markedly below the initial values. The rising AE hits and energy can be correlated to an aging effect, i.e. the material adapts to the external loading conditions, while the subsequent decrease of the parameters can be attributed to a fatigue, a persistent modification of the material properties. During the aging part of cycling, the number of AE-events increases more than the energy and then drops more rapidly than the energy. Two scenarios can explain this behavior. First, two microscopic mechanisms are involved. The number of events of small energy increases up to 10^4 cycles, while the number of events of high energy essentially remains unchanged. The probability of one particular microscopic mechanism of low AE-energy would increase up to 10^4 cycles and decrease or disappear for higher cycle numbers. Secondly, a certain distribution of AE energies, e.g. a Poisson-distribution, is generated by one mechanism alone. During the cycling the whole distribution shifts to higher energies. Due to the fixed threshold value for registering an AE-event, the probability of detecting a small event rises more than proportionally. These arguments hold irrespective of the particular microscopic mechanism leading to the observed AE. A distinction between particular microscopic mechanisms cannot be drawn from these results alone.

The macroscopic parameters P_r and E_c behave in a similar way as do the AE data. Both values show a slight maximum at 10^4 cycles and decrease during the next 10^8 cycles. The behavior of decreasing P_r at high cycle numbers is in agreement with other observations, while E_c usually increases but does not decrease during fatigue [9].

AE-data on stack actuators show a distinctly different behavior from the bulk discs used in this investigation. The AE-hits steadily rise until dielectric breakdown of the device [8]. Thus the damage mechanism will most probably have a different microscopic origin.

The microscopic mechanisms leading to the observed AE data are not yet understood. The purpose of this work was to show the correlation between the AE data and the macroscopic material parameters detected at several states of fatigue.

Further investigations will be necessary to clarify the questions like (1) the exact origins of the observed AE, and (2) the mechanisms leading to fatigue. Furthermore, a detailed comparison of different PZT compositions and microstructures is necessary to correlate the fatigue data to materials properties.

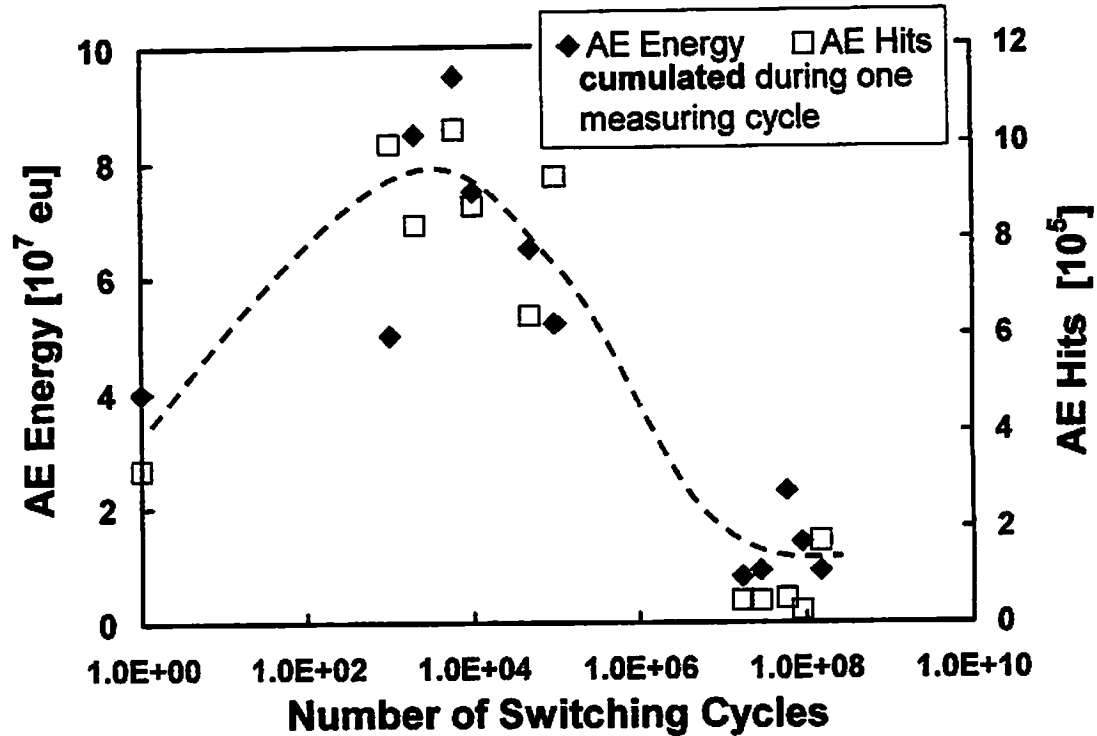


Fig. 3 AE Energy and AE Hits as a function of switching cycles. Note that all values are taken as cumulated values during one measuring cycle.

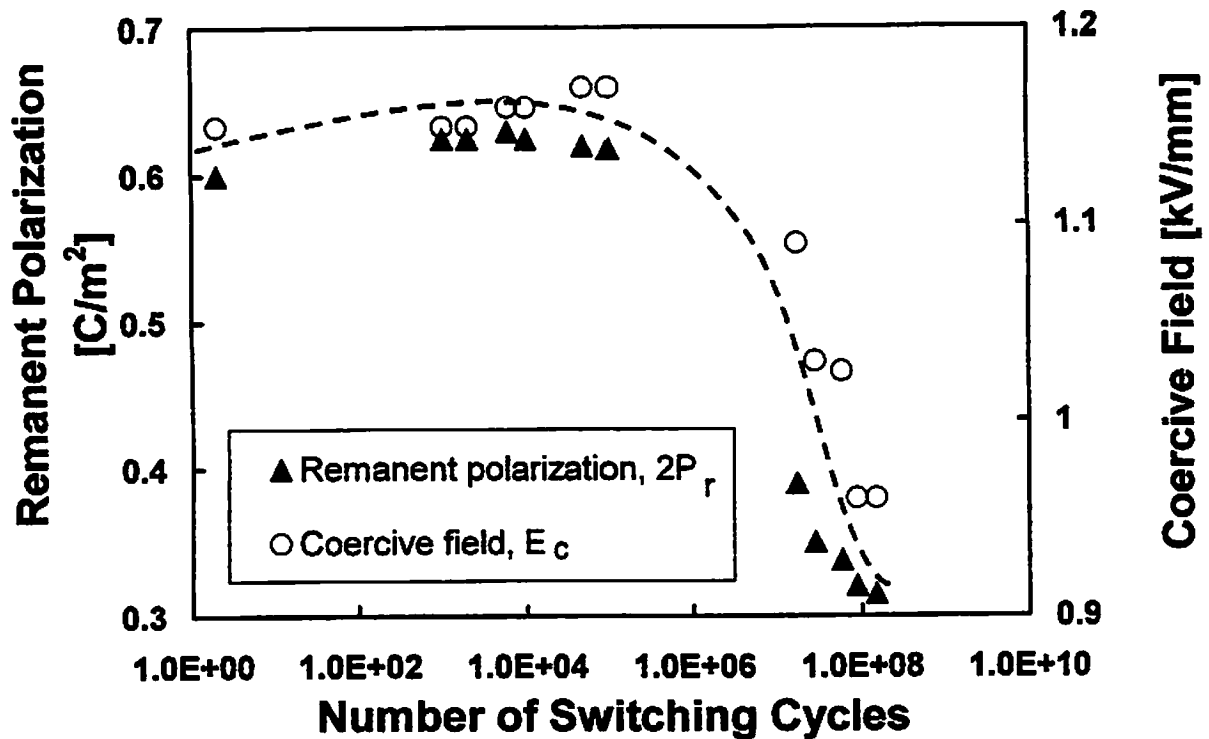


Fig. 4 Remanent polarization and coercive field as a function of switching cycle. The values were determined from the hysteresis loop plotted during the measuring cycle.

REFERENCES

- [1] Q. Y. Jiang, L. E. Cross, Effects of Porosity on Electric Fatigue Behavior; *J. Mat. Sci.* **28**, 4536 – 4543 (1993)
- [2] W. R. Salaneck, Some Fatiguing Effects in 8/65/35 PLZT Fine Grained Ferroelectric Ceramics; *Ferroelectrics* **4**, 97 – 101 (1972)
- [3] K. Carl, Ferroelectric Properties and Fatiguing Effects of Modified PbTiO₃ Ceramics; *Ferroelectrics* **9**, 23 - 32 (1975)
- [4] Q. Jiang, E. C. Subbarao, L. E. Cross, Fatigue in PLZT: AE as a Discriminator Between Microcracking and Domain Switching; *Ferroelectrics* **154**, 113 – 118 (1994)
- [5] E. C. Subbarao, V. Srikanth, W. Cao, L. E. Cross, Domain Switching and Microcracking During Poling of Lead Zirconate Titanate Ceramics; *Ferroelectrics* **145**, 271 – 281 (1993)
- [6] K. M. Rao, D. Aparna, S. P. M. Rao, Frequency Analysis of the AE Signals from PZT Ceramics During the Application of AC Fields; *Ferroelectric Letters* **20**, 45 – 59 (1995)
- [7] D. C. Lupascu, J. Nuffer, J. Rödel, Acoustic Emission from Different PZT's; *Ferroelectrics*, in press
- [8] K. Uchino, H. Aburatani, Destruction Detection Techniques for Safety Piezoelectric Actuator Systems; *Proceedings Int. Conference on Intell. Mater. Struct.*, Williamsburg 2, 1248 – 1256 (1994)
- [9] Q. Jiang, W. Cao, L. E. Cross, Electric Fatigue in Lead Zirconate Titanate Ceramics; *J. Am. Ceram. Soc.* **77** (1), 211 – 215 (1994)

APPLICATION OF ACOUSTIC EMISSION METHOD AT PRESSURE TEST OF BOILER HEADER

**V. Svoboda - Preditest s.r.o., Praha
P. Petrásek - Elektrárny Opatovice a. s.
A. Proust - Euro Physical Acoustic S.A.**

ABSTRACT :

In contribution there is presented application of acoustic emission method on boiler header during hydraulic pressure test. The aims and possibilities of such application as an NDT method are discussed.

By proper location of AE sensors is possible to cover whole volume of header. Special attention was put for area of dropping tubes and other nozzles. Measurement of AE signals was done during whole time of pressure test including pressure drop and during hold period on certain pressure level.

Parallel to this activity was observation of leakage on base of AE data. For AE data evaluation special software MONPAC was used and acoustic emission sources were localised and evaluated.

1. INTRODUCTION

Estimation of residual life time of boiler header after a long period of service is very important task which can result in two possibilities.

- a) to finish the service of a such header with necessity to replace it
- b) to evaluate real technical life of header with possibility to continue his service.

The difference in both approaches is practically in economical value.

To solve this problem is necessary to have a set of basic technical data, time period of header service and consequence of loading conditions, number of starts and cool downs, results of periodic pressure tests and last but not least also the results of NDT methods used during long time of service.

Application of acoustic emission during planned hydraulic test is very promising and investigation of acoustic emission sources which correspond to crack initiation or propagation can be recognised.

Integrity of a header is then evaluated by MONPAC method.

Inspected header was put into the service in year 1958 and had been approx. 270 000 hours in service which represent 40 years of use.

2. PROGRAM OF AE INSPECTION

Suggested program for AE inspection during hydro-test was based on long time experiments done on pressure vessels at various field of industry including fossil and nuclear plants, chemical and petrochemical plants.

18 AE sensors were applied on outer surface of header to cover whole volume. Special attention was put to bottom part of header with tube nozzles. Schematic view of sensor location is on Fig. 1. Sensors were fixed on header surface by magnetic holder.

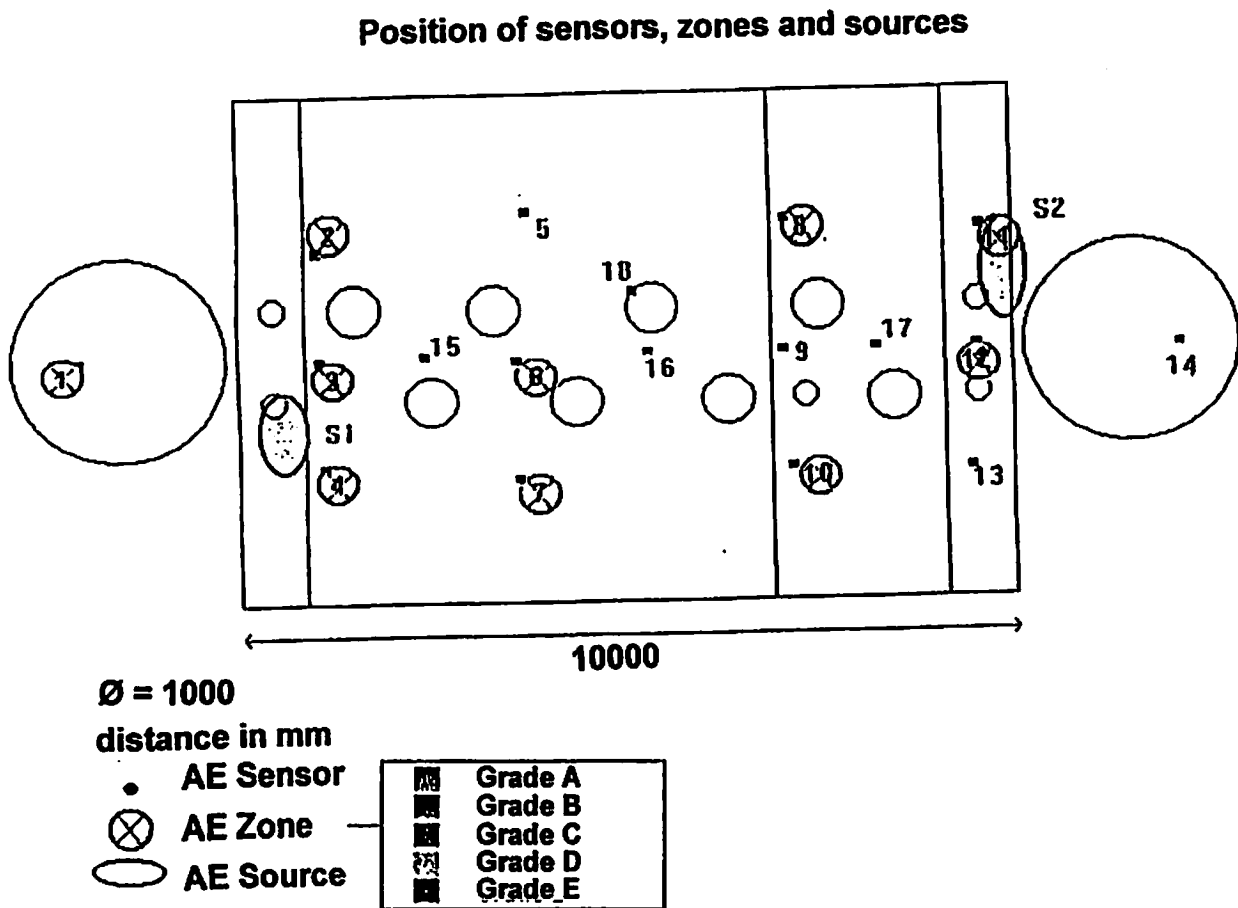


FIGURE 1 : Representation of the structure

3. MEASURING TECHNIQUE

For detection and data acquisition of acoustic emission signal was used multichannel system SPARTAN 2000 . This system provides data evaluation in real time including leak detection during pressure test.

All evaluation of AE data is done according to MONPAC software and emission activity and classification of AE sources is in relation to their activity. Five classes are used for classification.

Parallel to AE the pressure was recorded by special pressure sensor.

4. TEST PROCESSING

Hydraulic test was done according to standard procedure for pressure vessels. During increasing the pressure level individual time period was hold at 90%, 100%, 110% of maximum operating pressure. Time hold period approx. 30 minutes was applied at max. test pressure.

Theoretical course of pressure is on Fig. 2a and practical on Fig. 2b.

5. RESULTS EVALUATION

Registration of acoustic emission signals was done during whole time of pressure test. Acoustic emission activity was compared also during pressure drop.

Results of emission activity are shown at Fig. 1, 2, 3, 4. It can be seen that AE activity is increasing during increasing pressure.

Location of investigated AE sources is on Fig. 4. There are two AE sources by the end of header marked as S1 and S2. They are near sensor No. 4 and No. 11.

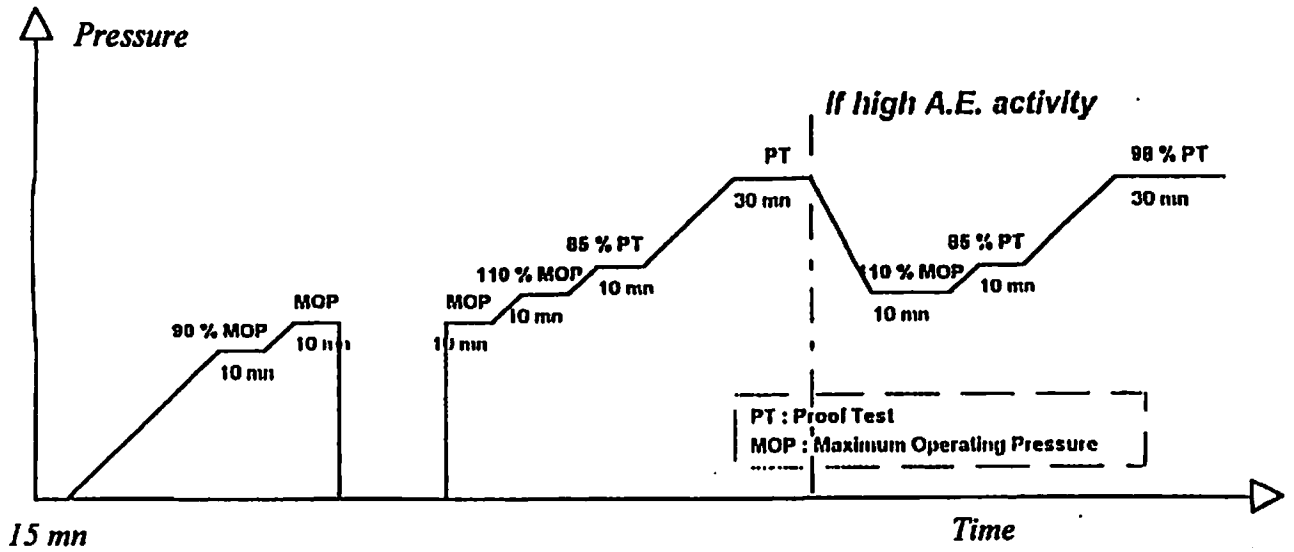
Evaluation according to MONPAC criteria is on Fig. 5 and Fig.6. The header is classified into class - C. Results of such evaluation are at Fig. 7.

6. CONCLUSION

On the base on pressure test on header can be stated:

- a) According to MONPAC analysis the header is classified in category -C-
- b) Next inspection in the short period of time is not needed
- c) Two acoustic emission sources were localised
- d) Both AE sources are located near both end of header

a - Theoretical sequence



b - Really applied

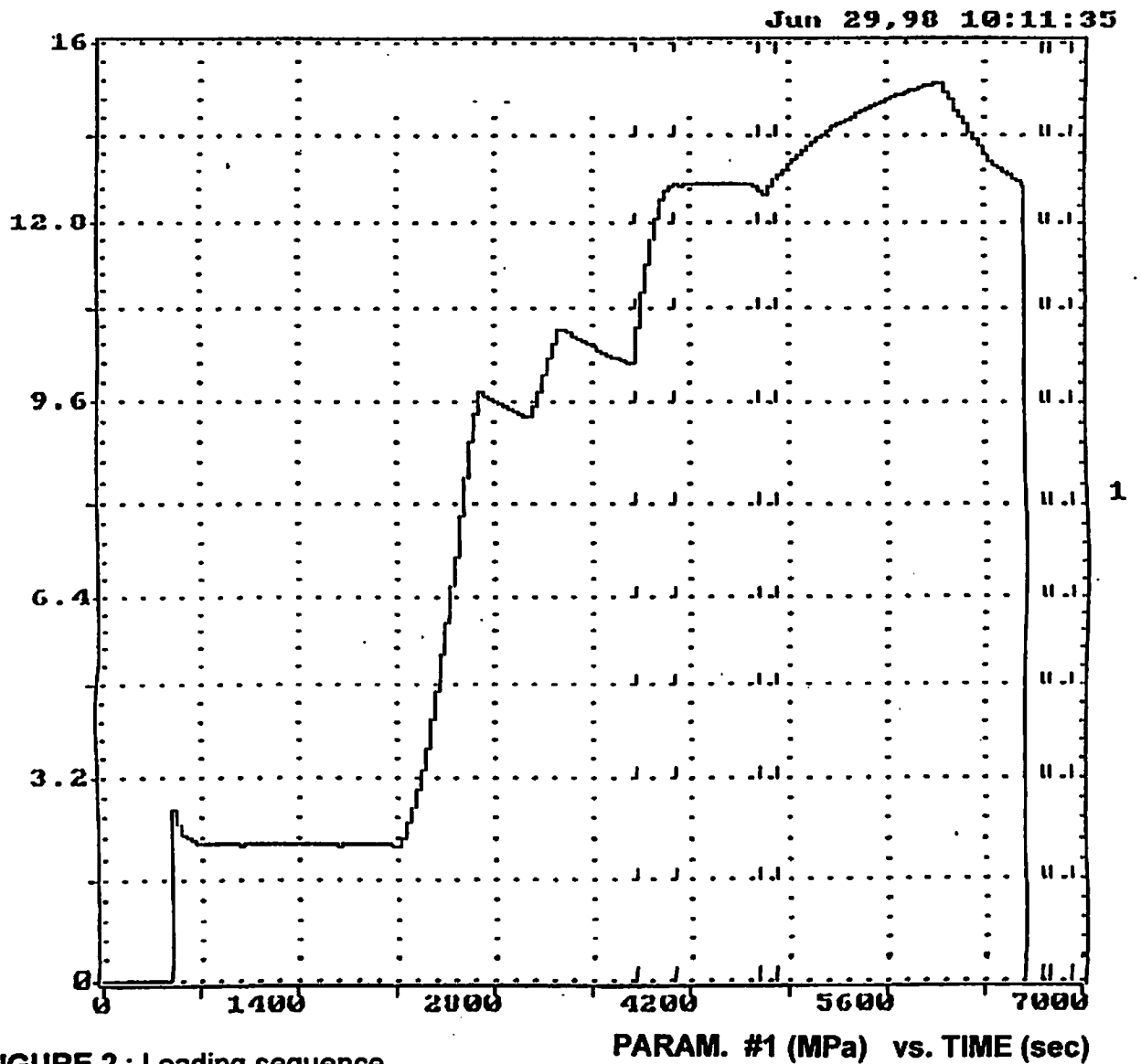


FIGURE 2 : Loading sequence

- Graph 1 : Pressure versus time
- Graph 2 : Amplitude versus time
- Graph 3 : Cumulative Energy versus pressure
- Graph 4 : Cumulative hits versus pressure

AE HITS	EVENTS
13477	833
CUM-CNTS	CUM-ENER
80701	143061
DDD HH:MM:SS	
0 02:03:24	
LOAD #1	CYCLE-C
14.65	

C:\MFC000.DTA

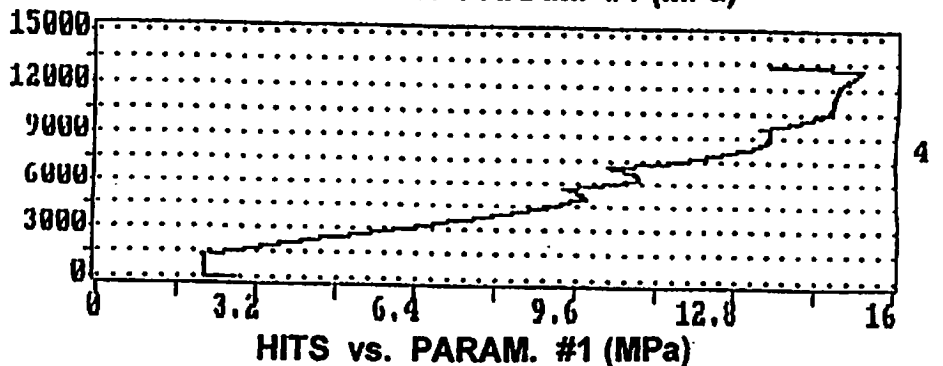
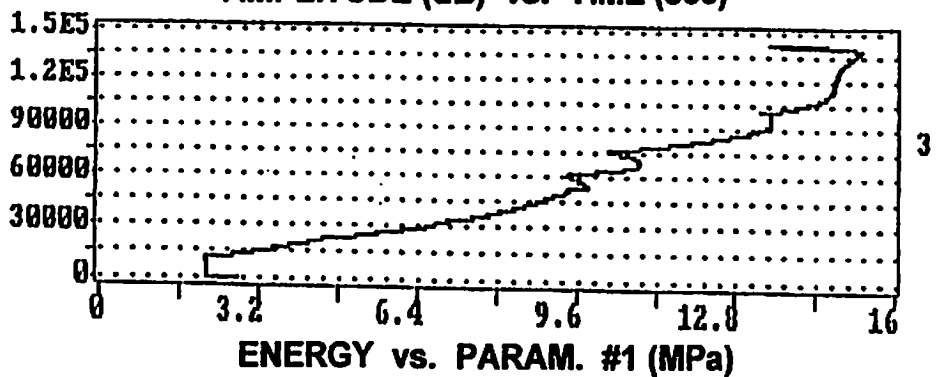
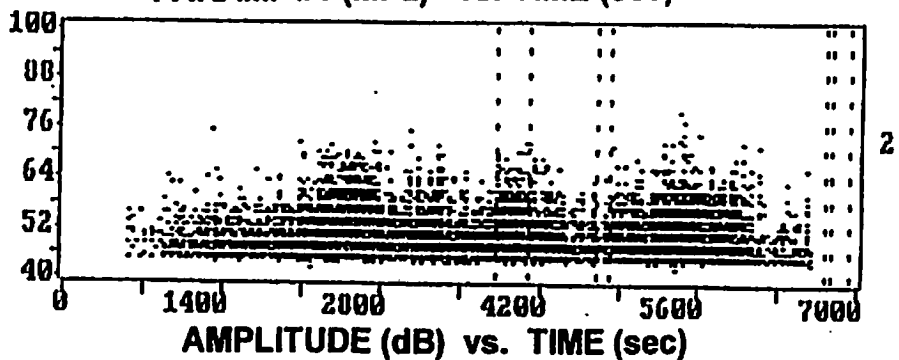
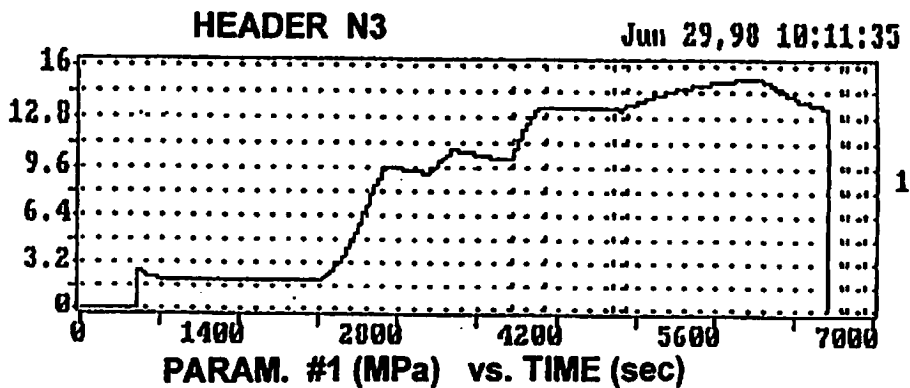
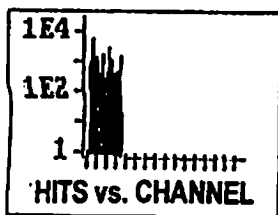


FIGURE 3 : Global activity

RE HITS	EVENTS
13477	833
CUM-CNTS	CUM-ENER
80701	143061
DDD	HHMMSS
0	02:03:24
LOAD HI	CYCLE-C
14.65	

CIME0000 DTA



HEADER N3

Jun 29, 98 10:11:35

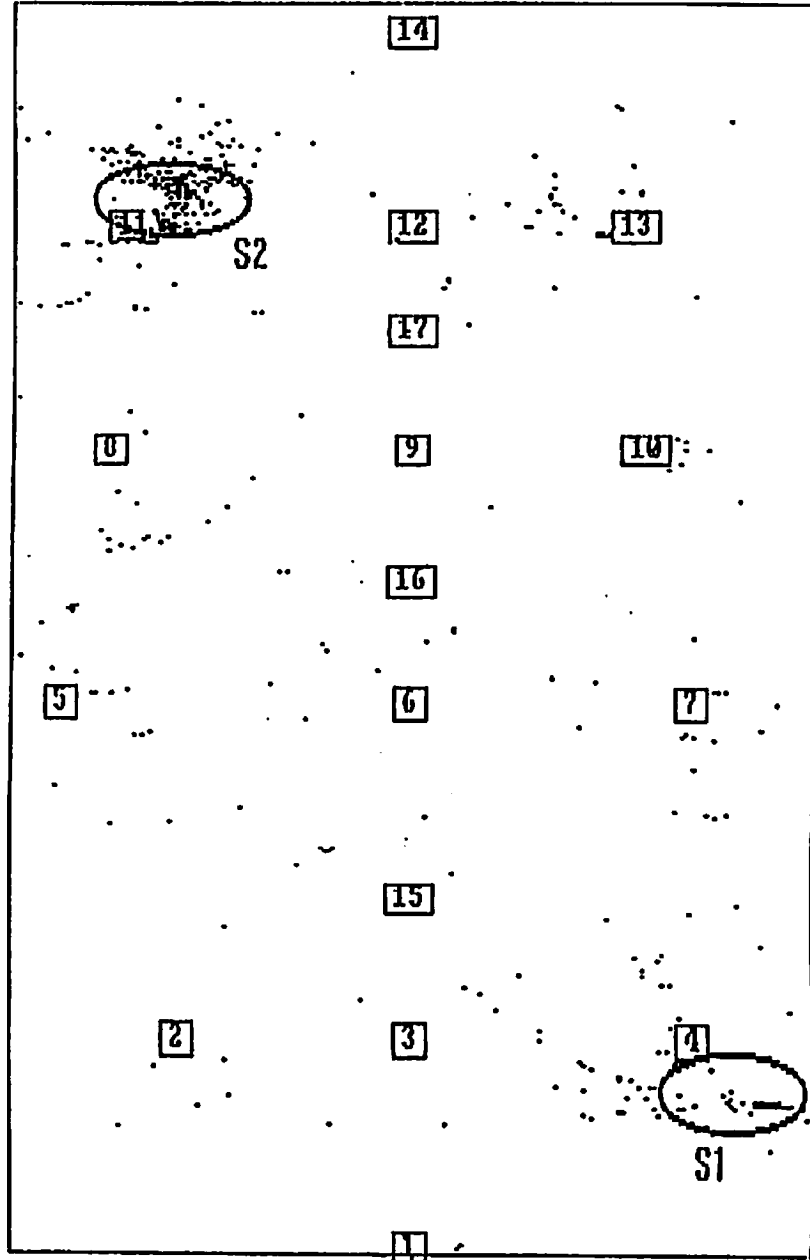


FIGURE 4 : Located activity

Graph 1 : Events position
 Graph 2 : Amplitude versus time
 Graph 3 : Cumulative energy versus pressure
 Graph 4 : Cumulative events versus pressure

AE HITS	EVENTS
13477	833
CUM-CNTS	CUM-ENER
80701	143061
DDD HH:MM:SS	
0 02:03:24	
LOAD H1	CYCLE-C
14.65	

SIMF0000.DTA

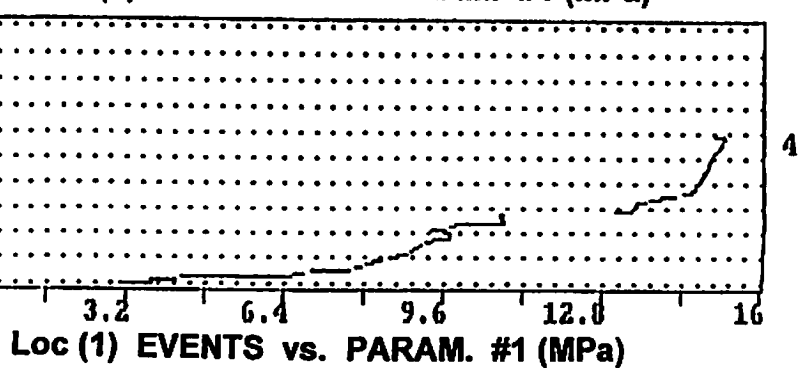
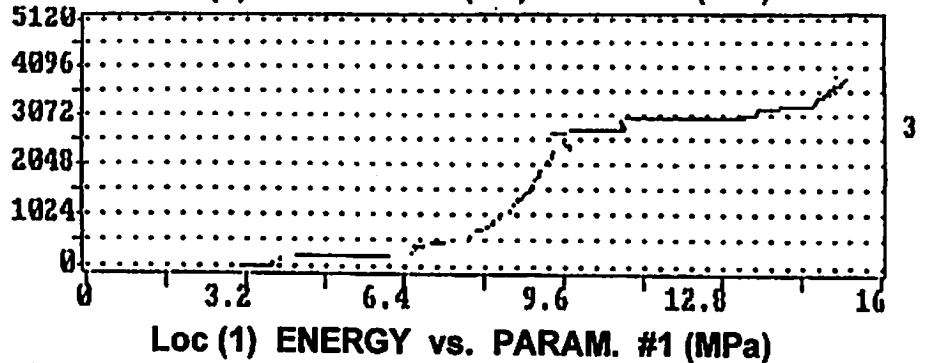
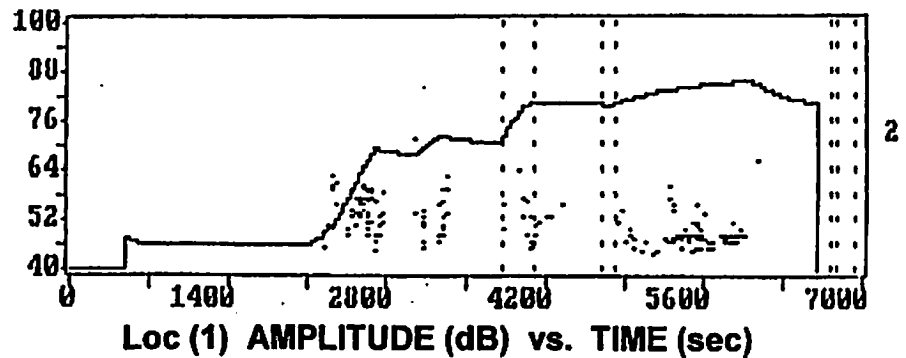
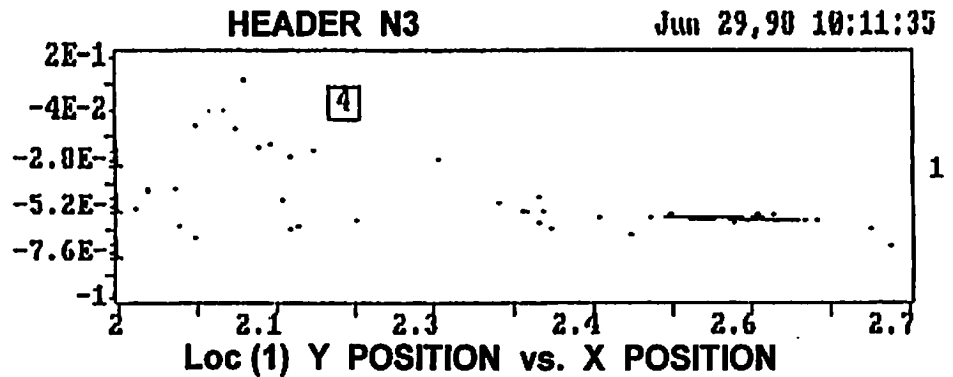
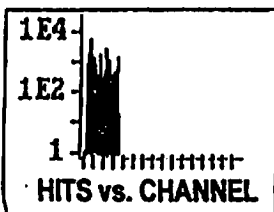
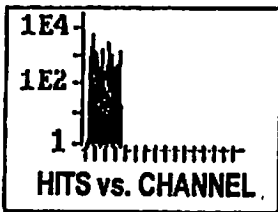


FIGURE 5: Source S1

- Graph 1 : Events position
- Graph 2 : Amplitude versus time
- Graph 3 : Cumulative energy versus pressure
- Graph 4 : Cumulative events versus pressure

PE-HITS	EVENTS
13477	833
CUR-CNTS	CUR-ENER
00701	143061
DDD HHHHHSS	
0 02:03:24	
LOAD #1	CYCLE-C
14.65	

SIHF0000 DTA



HEADER N3

Jun 29, 98 10:11:35

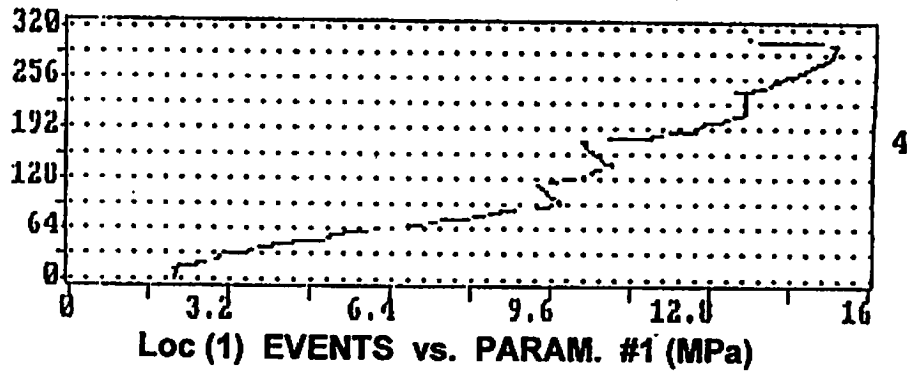
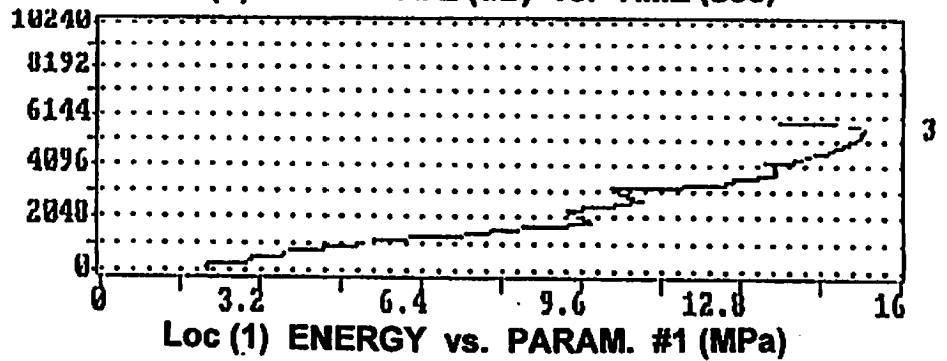
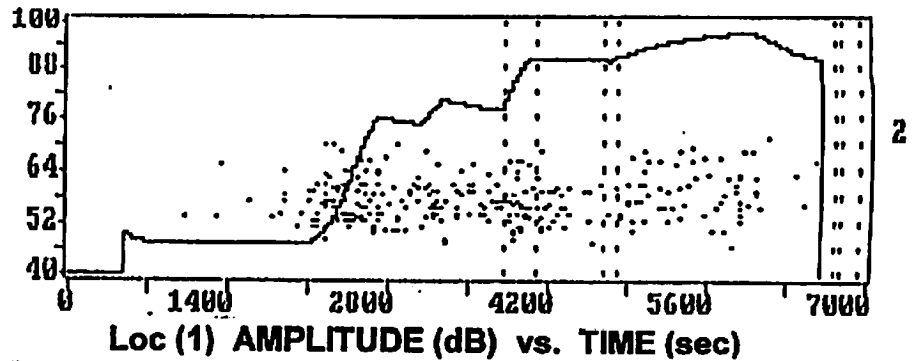
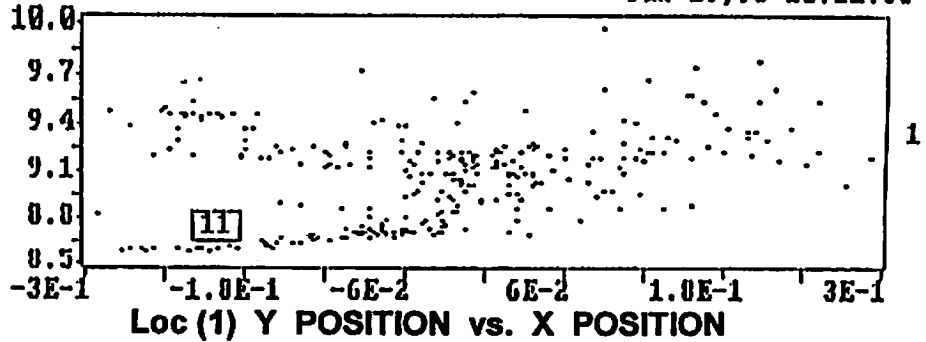


FIGURE 6: Source S2

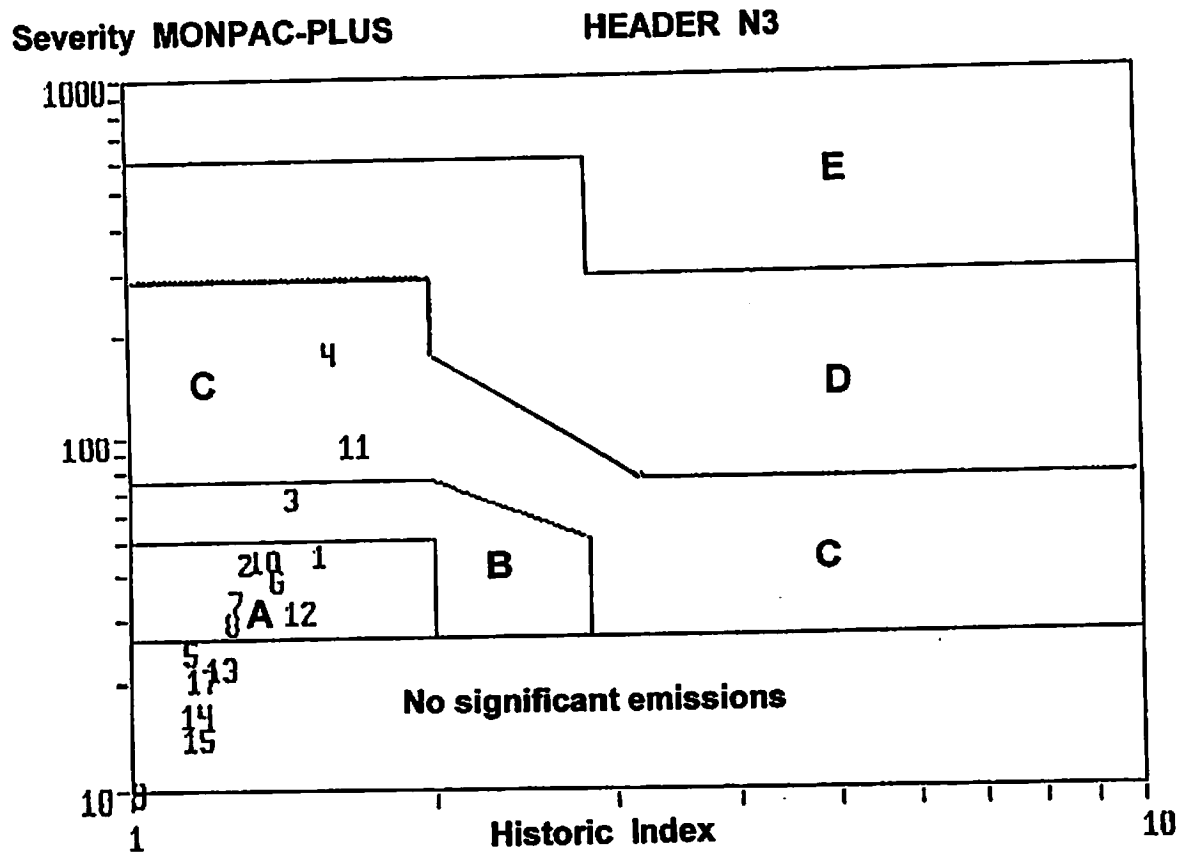


FIGURE 7: MONPAC Classification

ACOUSTIC EMISSIONS OF VESSELS WITH PARTIALLY PENETRATED LONGITUDINAL SEAMS

Franz Rauscher

Institute of Pressure Vessel and Plant Technology

Vienna University of Technology

Gußhausstraße 30, A-1040 Vienna

f.rauscher+E329@tuwien.ac.at

Tel.: ++43-1-58801-32910 Fax: ++43-1-5041588

Keywords:

Acoustic emission, pressure vessels, thin wall, weld failure, incomplete penetration, pressure test, statistical approach

1. Abstract:

Within a European research project three series of pressure vessels (more than 60 vessels) with partial incomplete penetrated longitudinal seams were tested at the Institute of Pressure Vessel and Plant Technology. Within each series at least one burst test was carried out. After a pressure test near to the burst pressure cyclic fatigue tests on the rest of the vessels were carried out.

In all of the tests the acoustic emissions were measured with either two or five sensors. The parameters of the signals and some transients were recorded with the acoustic emission measurement equipment. The process of crack growth is known due to strain gauge measurements during the tests and due to the examinations of the crack surfaces after the vessels had failed. The burst pressure of the vessels, which did not burst at the pressure test, is known via fracture mechanical calculations.

In this paper the acoustic emission signals from pressure tests and burst tests are investigated to answer the following question: How high is the probability to find the investigated failure at the pressure test by acoustic emission measurements?

To be able to answer this question the data measured at the pressure tests of series (BC) were analysed. The pressure test was therefore split in phases. The acoustic emission activity of the different phases was evaluated and statistically analysed. Additionally, the distribution of the amplitudes of the acoustic emission signals over the pressure divided by the burst pressure was investigated.

2. Test Vessels

The base material of the cylindrical shell (figure 1) was St52-3 (DIN 17100) and the wall thickness was 3,5 mm. The vessels were pressurized via a nozzle in the middle of the lower head and the pressure was measured by means of an electronic pressure sensor, which was positioned in the middle of the upper head.

The area of interest was the longitudinal joint, which had a lack of penetration of about 2 mm. It was back welded at the ends (120mm) to guide the failure into the middle section of the seam. In this area the weld was ground off. The resulting rest section (ligament) was about 1 to 2mm.

The circumferential welds were joggle joints. These welds are not the goal of the investigations but they cause a lot of acoustic emission signals.

At all tests strain measurements were performed with at least two strain gauges (length 20mm). On one hand this was necessary to be able to increase the pressure at the pressure test as near as possible to the burst pressure. On the other hand, it allowed for observation of crack growth in the fatigue tests.

3. General procedure

- A burst test was carried out with the first vessel of every series.
- The results of the burst tests were used to determine a suitable break-off criterion for the pressure test, to obtain a hydraulic test pressure close to the limit pressure.
- A pressure test and afterwards a fatigue test were carried out with the remaining vessels in the following way:

At the pressure test the pressure was increased, with a break-off criterion according to a strain limitation criterion near the bursting pressure.

The vessels were pressurized cyclically until failure occurred or a certain number of cycles was achieved.

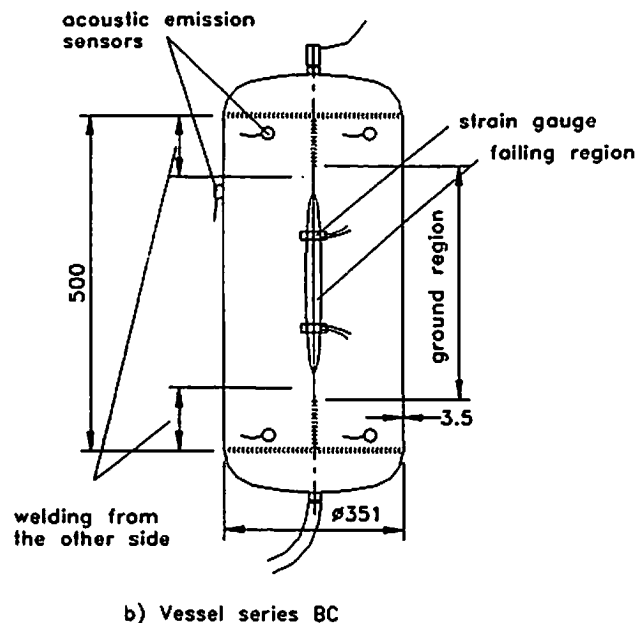


Figure 1: Test vessels

4. Acoustic emission measurements

For measuring the acoustic emissions the AMS3 system of Vallen Systeme GmbH with five channels and three transient recorders were used. Resonance sensors of the type DECI 150-M, which are typical for acoustic emission testing in the pressure vessel field, was used.

At the first series (BB) of experiments the acoustic emissions were measured with two sensors and a fixed, very low threshold (27 dB). During the second series (BC) of experiments five sensors were used and the threshold was higher (about 34 dB). The acoustic emission measurements were carried out both during the pressure test and the cyclic test.

At the series BB some parameters were changed during the testing. At the series BC the procedure of the pressure test was always exactly the same. The used parameters of the acoustic emission measurements were more typical for pressure vessel applications and with the used 5 sensors better

location of the source of the signals is possible (distinction between signals from the circumferential weld and those from the longitudinal weld with the failure). Therefore, the results of series BC are used for these statistical investigations.

The most important parameters for the acquisition of the acoustic signals of Series BC are:

A minimum threshold of 27dB and a crest factor of 6 (6 times RMS) were input to the acquisition program, which effectively caused a minimum threshold of 33.7dB. This resulting minimum threshold results from the program algorithm not due to the noise. In the case of the investigated pressure test the noise level was very low because the pressurisation was done by pressured air via a hydraulic accumulator.

Further parameters for the acoustic emission acquisition:

Peak discrimination time: 0.25ms

Duration discrimination time: 0.5ms

Rearm time: 1.5ms

5. Pressure test

For the pressure tests of the series BC, the pressure history represented in figure 2 was specified. In the tests, phase II was started with a slope of 2bar/min at the pressure of 30bar instead of 80% of p_{max} , because p_{max} was not known in advance. The pressurization was done by means of compressed air via a hydraulic accumulator. If in phase III the pressure drop was greater than 2% of p_{max} , the pressure was increased to p_{max} again. This process was repeated, until the pressure drop within 10 minutes was less than 2% of p_{max} .

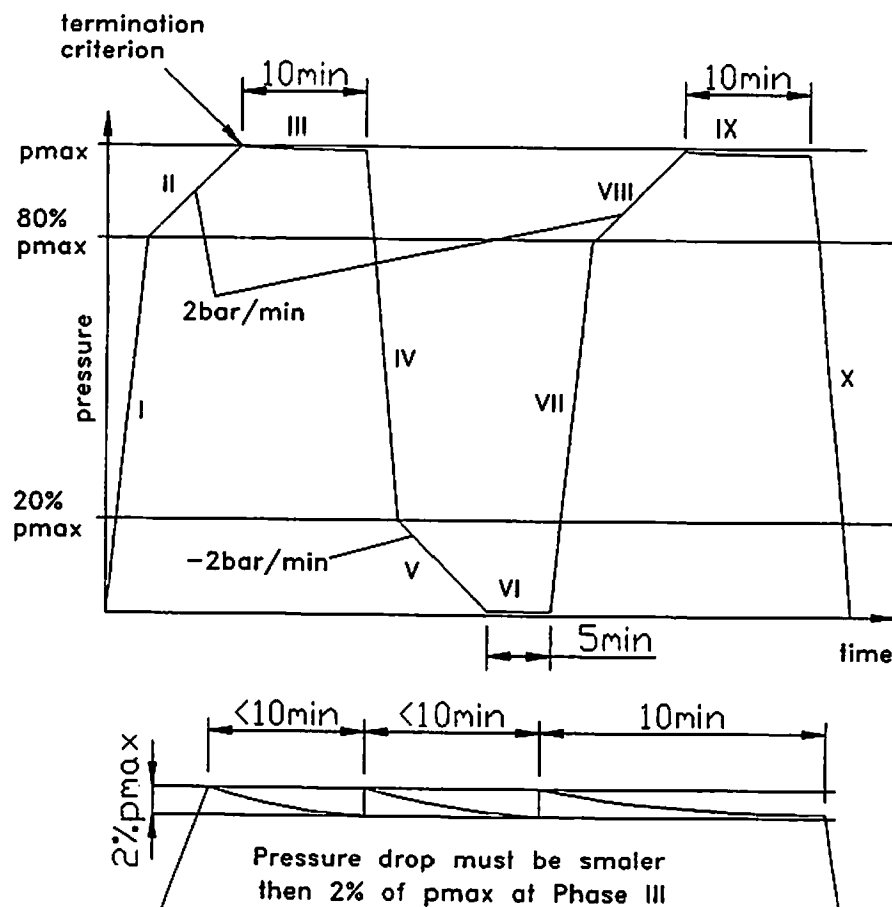


Figure 2: Specification of pressure test

The absolute strain was employed for the termination criterion (first pressurisation). This was determined in the case of the test BC02 with 0,2% (not included in the statistical investigations) and increased to 0,5% for the remaining tests.

6. Location and filtering

For the separation of the hits due to the investigated failure from the hits due to the circumferential weld and due to the welds at the nozzles, a planar location set was used. The sensors were placed as shown in figure 1. For calculation of the location, the time of arrival of the signals (threshold crossing) was used and the circular character of the structure was considered. A velocity of the signals of 4.7m/ms was measured and used for the calculation of the locations. With pencil breaks it was checked that signals from the investigated failure region could be properly located and that signals from the circumferential weld and from the nozzles are not mapped into the investigated region. With this arrangement, signals with amplitudes of more than 40dB at the first hit channel can be properly located.

To filter out signals coming from electrical noise, hits with duration smaller than 30µs and a rise time smaller than 1µs were filtered out.

In the next chapters only the signals from the considered failure, which is 200mm of the defective longitudinal seam, are investigated. Therefore, all signals located outside of the considered failure region ($150\text{mm} < y < 350\text{mm}$; $-50\text{mm} < x < 50\text{mm}$) were filtered out.

7. Acoustic emission activity at the different phases of the pressure test

The numbers of hits coming from the investigated failure (200mm of the longitudinal seam) according to the filter above are investigated. Therefore, the number of hits in five different phases of the pressure test were counted:

1 st up (0.5%)	phases I and II in figure 2 (first pressurisation)
1 st hold	phase III in figure 2 (first holding time)
1 st down	phases IV and V in figure 2 (first unloading)
2 nd up	phases VII and XIII in figure 2 (second pressurisation)
2 nd hold	phase IX in figure 2 (second holding time)

The first phase is the pressurisation up to a measured strain of 0.5% at the strain gauges (maximum measured value of the two 20mm strain gauges). This was the first load for these vessels and the reached maximum load was more than 90% of the burst pressure. At the second pressurisation the load was a little bit lower than at the first pressurisation.

	N	Minimum	Maximum	Mean	Std. Deviation
1st up (0.5%)	21	5.00	85.00	38.0476	21.2120
1st hold	21	.00	29.00	2.6667	6.2316
1st down	21	.00	16.00	2.3333	4.0166
2nd up	21	.00	40.00	2.2857	8.6784
2nd hold	21	.00	35.00	2.0952	7.5690
Valid N (listwise)	21				

Figure 3: Number of hits in the investigated phases of the pressure test

These numbers of hits at the investigated phases can be evaluated for all vessels which survived the pressure test (21 vessels) and which had reached the 0.5% strain at the pressure test. The maximum, the minimum, the mean value and the standard deviations of these numbers of hits are given in figure 3.

Figure 4 shows a box-plot of the same data. In the box plot the median value is marked, the box is drawn over the percentiles 25% and 75%, and lines mark the maximum- and the minimum values. Outliers are marked separately.

In most of the cases only at the first pressurisation a number of hits was received, which would be adequate to detect the failure. At the holding time, the depressurisation and the reloading phases only a few hits were measured in most of the pressure test. The few hits at the second pressurisation demonstrates the Kaiser effect and shows very clear acoustic emission testing does not work well if the failure was loaded before to the same load level than at the test. The hits at the holding times are often very useful, because at this phase almost no noise comes from the circumferencial welds. The problem of using these hits is that in many cases no hits were received in these phases.

It can also be seen that the statistical variation of the acoustic emission activity in tests may be very large even if the failure form and size, the vessel dimensions and material and the acoustic emission measurement equipment is as far as possible the same.

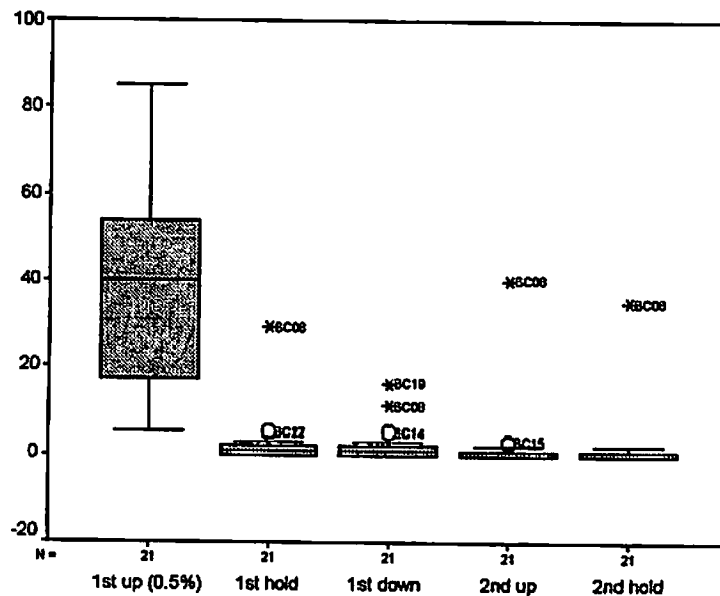


Figure 4: Number of hits at the phases of the pressure test

The figures above show very clearly that the investigated failure can be detected at the first pressurisation (pressure test) in most of the cases, but there are some cases at which this may be very difficult. To get some feeling for the probability of detecting the investigated failure at the pressure test, percentiles of most important parameters of the acoustic emission activity at the first pressurisation are calculated (figure 5). These are the number of located hits (hits), the max amplitude (AMAX) at the first hit channels, the accumulated energy (ENERGY) at the first hit channel and the accumulated counts (COUNTS) at the first hit channels.

It follows that at 5% of the vessels less than 5.25 located hits (from the investigated failure) were received, at 10% of the vessels less than 7.5 hits were received and at 25% of the vessels less than 18.5 hits were received (all at the first pressurisation phase). By looking at the amplitudes it can be seen that all of the tested vessels had at least one hit with an amplitude of more than 66dB and at half of the vessels at least one hit was received which reached more than 94dB.

It was observed that the hits with the maximum amplitude were not received at the maximum pressure; they were received at a rather low pressure. To investigate this phenomenon, the distribution of the hits with different amplitudes over the pressure was investigated.

Percentiles

	Perc	hits	AMAX	ENERGY	COUNTS
Weighted Average(Definition 1)	5	5.2500	68.00	8625.00	11775.00
	10	7.5000	74.50	21750.0	37550.00
	25	18.5000	76.25	132500	95000.00
	50	40.5000	94.00	825000	225000.0
	75	52.7500	100.0	3900000	350000.0
	90	60.0000	100.0	7150000	500000.0
	95	79.2500	100.0	8475000	597500.0
Tukey's Hinges	25	20.0000	76.50	150000	100000.0
	50	40.5000	94.00	825000	225000.0
	75	51.5000	100.0	3800000	350000.0

Figure 5: Percentiles of parameters of the acoustic emission activity at the first pressurisation phase (21 vessels)

8. Distribution of the hits with different amplitudes vs. pressure

To obtain statistical distributions for this investigation, the hit data of 20 vessels were used. To get a compatible value for the pressure, the pressure values at which the hits were received were divided by the estimated burst pressure of the appropriate vessel.

To perform some cross tabulation, the hits were classified in amplitude and pressure classes. From figure 6 it can be seen that most of the hits with high amplitude came at the lower load level (from 20% to 50% of the burst pressure). At higher pressure almost no hits of more than 80dB were received. The hits with lower amplitudes have a maximum at 40-50% of the burst pressure. After this level of pressure the activity of hits with low amplitude decreases and increases again near the burst pressure (more than 80% of the burst pressure). This can also be seen in the three dimensional histogram of figure 7 which was drawn with the same data.

Pressure class * Amplitude class crosstabulation

Count		Amplitude class				Total
		<50dB	50-65dB	65-80dB	>80dB	
pressure class	20-30%	22	35	24	12	93
	30-40%	28	45	31	14	118
	40-50%	30	56	39	26	151
	50-60%	16	40	32	3	91
	60-70%	18	38	24	9	89
	70-80%	24	35	14	1	74
	80-90%	29	48	19	4	100
Total		167	297	183	69	716

Figure 6: Hits at the first pressurisation classified in amplitude and pressure classes (from 20 vessels)

Hits vs. Amplitude and p/burst

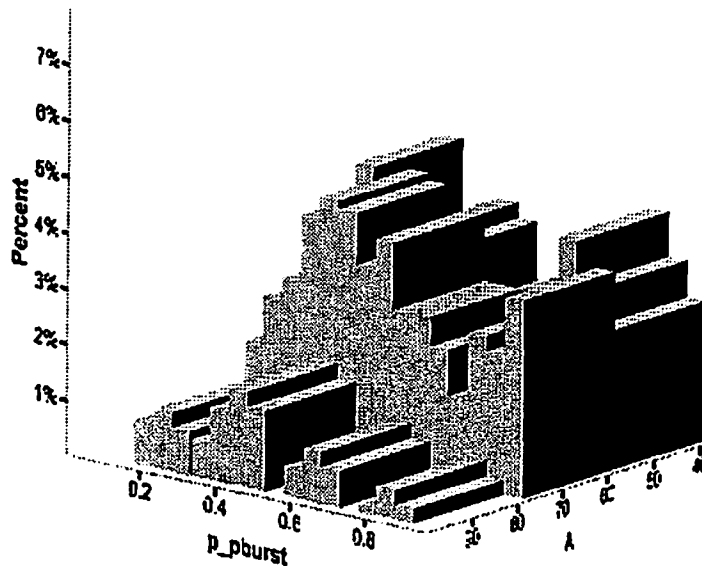


Figure 7: Hits vs. pressure divided by burst pressure and amplitude

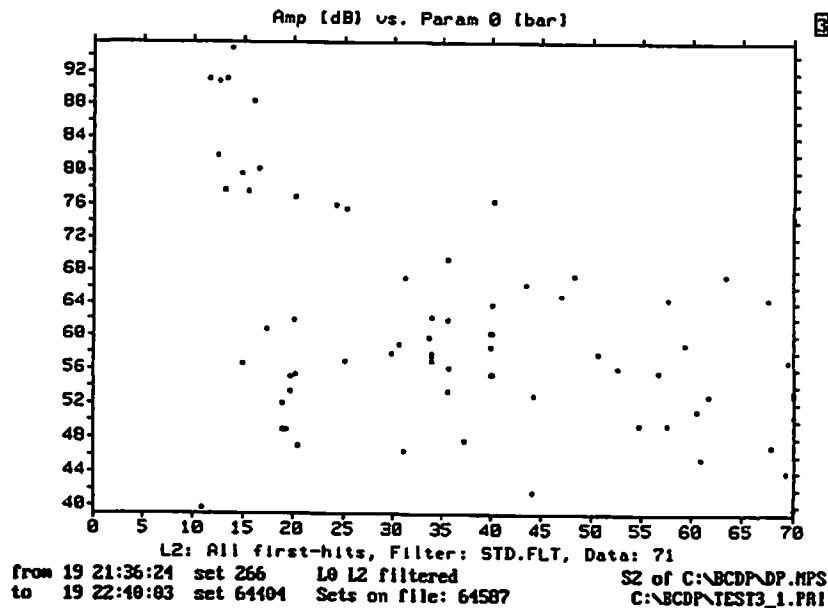


Figure 8: Amplitude vs. pressure at a burst test

The statistical investigation described above considers only the hits, which were received from about 20 to 90% of the burst pressure. To get an idea of the acoustic emission activity from 90% of the burst pressure to the burst pressure, the plot of the amplitudes vs. pressures of the burst test of this series (figure 8) was investigated. At this burst test there is no increased acoustic emission activity near the burst pressure (70bar), but we can see rather high amplitudes at very low pressures. There may also be hits at lower pressures (if pressurise up to this pressure at the beginning) but the vessels were pressurised up to about 10 bar before these tests (to check whether there is a leak). Perhaps there may also be some very useful acoustic emission information beyond 10bar at the first pressurisation. This is also the reason why figures 6 and 7 start at 20% of the burst pressure.

9. Summary

From a large number of tested vessels the measured acoustic emission signals of about 20 vessels were taken to perform statistical investigations. These vessels were fabricated in series production (automatic welding) and the test procedure was the same for each vessel. The topic of the investigation was the longitudinal seam with partial penetration with an investigated length of 200 mm.

Characteristic of the investigated failure:

Thin wall vessels (3.5 mm)

Longitudinal seam with incomplete penetration (about 2 mm) and weld excess ground off
Carbon steel (St52)

- Statistical investigations show a large scattering of the acoustic emission activity within the various vessels. Therefore, it is necessary to investigate a rather large sample of vessels to evaluate the probability of detecting such a failure at the pressure test by acoustic emission analysis.
- Only during the first pressurisation phase (first loading of the failure) there is sufficient acoustic emission activity to detect the failure with good probability.
- Most of the hits with high amplitudes came at rather low pressures (20 to 50% of the burst pressure). Also the hits with the smaller amplitudes have a maximum at 40 to 50% of the burst pressure. Near the burst pressure also an increased number of hits with low amplitude was received. Therefore, the hits over the whole pressure range have to be considered not only at the maximum pressure. Hits with high amplitude at a rather low pressure may help to detect the failure.
- If a number of 18.5 located hits at the failure region (200mm of the weld with the failure) with an maximum amplitude of 76dB is considered to be sufficient to detect the failure, 75% of the failures would be detected at a pressure test with a maximum pressure of 90% of the burst pressure.

Literature:

- [1] Nondestructive Testing Handbook, Volume Five: Acoustic Emission Testing. American Society For Nondestructive Testing. INC. 1987.
- [2] Rauscher F., Schwarz M.: Schallemissionsmessung an Druckbehältern mit fehlerhafter Längsnaht bei zyklischer Belastung sowie bei der Druckprobe. Bericht Nr.5, Technische Universität Wien: Inst. f. Apparate- u. Anlagenbau (1995).
- [3] Leaird J. D.: Acoustic emission training guide. Greensland Publishing Company, Sacramento, California 1997.

ELECTROMAGNETIC EMISSION FROM POLYCRYSTALLINE SOLIDS

J. Šikula, B. Koktavý, I. Košíková, J. Pavelka

Technical University of Brno, Physics Department, Žižkova 17, 60200 Brno, Czech Republic
E-mail: sikula@cis.vutbr.cz Phone +4205 7261 651 Fax +4205 7261 666

T. Lokajiček

Geophys. Institute, Academy of Science of the Czech Republic, Prague, Czech Republic
Boční II - 1401, 141 31 Praha 4 - Spořilov

ABSTRACT

Electromagnetic signals, which are generated in stressed solids, can be used to indicate cracks and defects in solids. When a micro-crack is generated in a solid the faces of the micro-crack make up plates of an elementary capacitor and the charges located on them constitute an electric dipole or quadrupole. The magnitude of the electric charge configuration and the dipole moment depend on the time.

The electromagnetic signal precedes the acoustic emission response and time delay corresponds to the difference of propagation velocities of sound and electromagnetic radiation in the sample.

We may conclude that generation of micro-cracks is accompanied by generation of electric charge, which is measurable by means of a capacitance antenna. The low frequency component of the output voltage is due to a displacement of the charged micro-crack.

INTRODUCTION

Electromagnetic signals and acoustic emission generated by crack creation in mechanically stressed solids is phenomena, which has been known for many years already. This phenomenon was also studied with connection to earthquakes in geophysics [1], [2], [3]. Similar electromagnetic signals were observed, when birth of cracks in hard dielectrics occur [4]. There are many papers related to electromagnetic radiation from rocks and electromagnetic and acoustic emission associated with rock fracture [5] - [14].

Zamada [6], Lokajiček [8] and Mori [10] studied correlation between electromagnetic and acoustic signals. The experimental results are summarised as follows: Electromagnetic signals occur simultaneously with acoustic emission events. EMG signals with large amplitude occurs together with large AE events. EMG and AE signals increases just before the main rupture. Several theoretical models have been proposed for the explanation of these

phenomena, such as piezoelectric effect, the electrokinetic effect or electrification between the newly created surfaces. In previous studies reported measurements of electric potentials related to rock fracture have been carried out under the monotonously increasing compressive stress in laboratory. Mori et al. [10] studied electric potential signals from a rock sample under the cyclic loading and found, that electric potential and AE signals mainly occur in the stage, in which the stress is increasing and reaches the highest level in each cycle. They confirmed, that the electromagnetic signals occur primarily due to a generation of a new crack and its extension. The result, that electromagnetic signals rapidly increase just before the main rupture suggest, that a geoelectric potential may useful as a precursory phenomena.

The current model of electromagnetic signal creation is based on assumption, that at the faces of crack electric charges are created and their configuration builds electrical dipole or quadrupole system. The cracks occurrence is accompanied by generation of phonons and, furthermore, by generation of electric charges at the cracks faces. They are electrically charged due to loose of chemical bonds. The stochastic process of new surfaces creation results in dipole, quadrupole, or more complicates electric charge systems.

This phenomenon is called as an electromagnetic emission and its measurable quantities are:

- i) electric and magnetic field due to the electric charge redistribution
- ii) a generation of electromagnetic radiation.

To give evidence of the mentioned phenomena, two experiments were designed and carried out. In the first experiment we made use of an antenna which consisted of a flat coil. This antenna was sensitive to the magnetic component of the electromagnetic wave. In the second experiment as an antenna the parallel plate capacitor was used to pick up the electric component of electromagnetic emission. This experimental set-up indicates also the electrostatic charge redistribution. The frequency of emitted electromagnetic radiation is given by frequency of mechanical vibration of crack walls. This frequency is about 1 MHz and corresponding length of the crack is of the order of 0,1 mm. Electromagnetic wave of this radiation is much larger (300 m for 1 MHz) than sample size so near-field effects could be observed only.

In our experiments two conducting plates are fitted to the specimen making the parallel plate capacitor (see Fig.1.). The electric voltage measured on this plate capacitor C is time dependent due to sample electrical conductivity and vibration of crack walls. The time dependence is determined by the charge relaxation and phonon field interaction.

The dipole moment depends on the time for two reasons:

- i) as a consequence of the electric conductivity of the specimen,
- ii) because of the crack walls displacement.

THE ELECTROMAGNETIC SIGNAL

Measurable quantity is the electric voltage $V(t)$ on load resistor R connected to parallel plate capacitor C (see Fig. 1). We suppose, that when the crack is produced the electric charges $+q$ and $-q$ appear at the faces of the crack. The charged vibrating crack wall moves with velocity v in electric field E . Then the voltage V on parallel plate capacitor is changed and electric current flow in load resistor R .

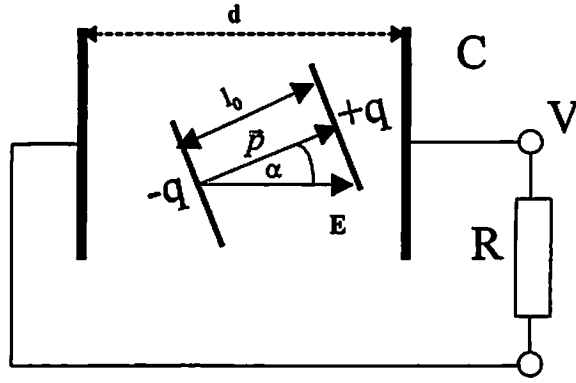


Fig.1. Parallel plate capacitor and dipole moment orientation for a crack.

The electric energy is changed into heat in resistor and into capacitor energy increasing. Using energy balance we find differential equation for voltage $V(t)$ on measuring capacitor

$$\frac{dV}{dt} + \frac{V}{RC} = \frac{q}{CV} E.v. \quad (2)$$

When a crack is produced a certain portion of the mechanical energy is converted into vibrations. The time dependent displacement of the crack faces results in an AC electromagnetic signal component whose frequency corresponds to that of mechanical vibrations of the specimen.

Due to this effect the crack walls are vibrating and crack width l is a function of time. The charges $+q$ and $-q$ are at the equilibrium distance l_0 and their displacement $u(t)$ is given by

$$u = u_0 e^{-\delta t} \sin \omega t \quad (3)$$

where δ , ω are damped harmonic motion constants. The electrical conductivity is discharging the elementary capacitor representing crack walls. We will suppose the electric charge exponential time dependence in the form $q = q_0 e^{-\beta t}$. We have two damping constants, δ due to the mechanical damping and β due to the sample electrical conductivity. Solution of the differential equation (2) was given in [15]. Then we have voltage time dependence in the form

$$V(t) = V_0 e^{-t/\tau} - \frac{g e^{-\gamma t}}{\sqrt{\omega_0^2 + \omega^2}} \sin(\omega t + \varphi) \quad (4)$$

where V_0 is integration constant, $\tau = RC$, $\omega_0 = \gamma - 1/\tau$ is cut off angular frequency and

$$g = \frac{2q_0 v_0 \cos \alpha}{Cd} \quad (5)$$

$\gamma = \delta + \beta$, v_0 is velocity amplitude, d is parallel plate capacitor thickness and α is the angle between electric field intensity E and electric charge velocity v .

EXPERIMENT

The granite samples dimensions of $4 \times 4 \times 1 \text{ cm}^3$ were examined. The samples were loaded with a constant stress rate up to their failure. The capacitor antennas were fixed on DUT (device under test) according to Fig.2. Acoustic emission signal was detected on the sample edges. Corresponding acoustic emission signals are shown in Fig. 3.

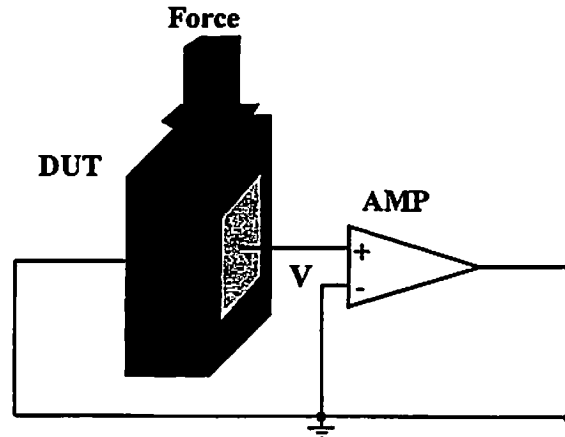


Fig.2. Experimental set-up with a capacitor antenna

Electromagnetic emission signals (EME) are arising across the capacitor antenna and afterward amplified by low-noise preamplifier. Time dependence of recorded signal shown in Fig.3. has two components: first which varies exponentially with time constant given by RC circuit: for $R = 1 \text{ M}\Omega$ and $C = 20 \text{ pF}$ we have time constant $\tau = 20 \mu\text{s}$, which is in good agreement with experiment.

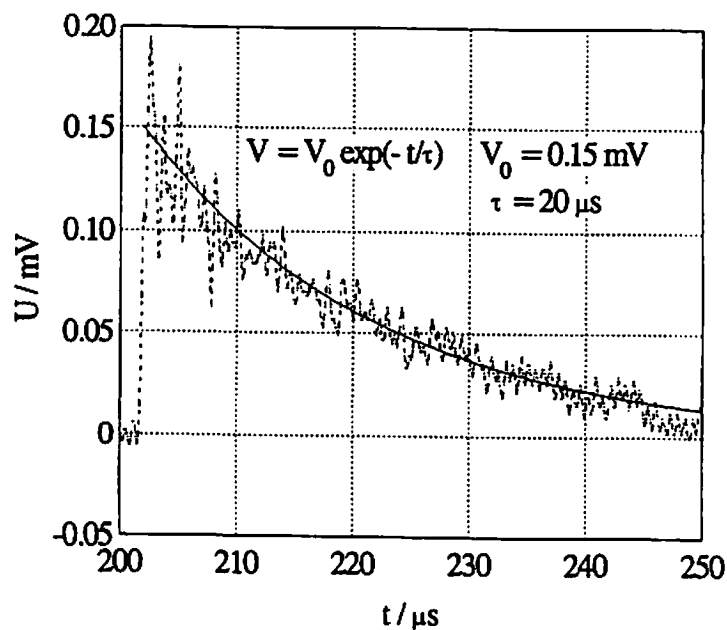


Fig.3. Time dependence of ELMG signal

Electromagnetic signal has second component, which varies with angular frequency ω of crack wall mechanical vibrations. This component has exponentially decreasing amplitude with damping coefficient γ given by (4). Constants in equation (4) can be estimated from time dependence of ELMG signal in Fig.4. Here for sample 4122 we have:

$$\gamma = 0.17 \times 10^6 \text{ s}^{-1}, \quad \omega = 5.6 \times 10^6 \text{ s}^{-1}, \quad \omega_0 = 1.2 \times 10^5 \text{ s}^{-1}, \quad g = 280 \text{ Vs}$$

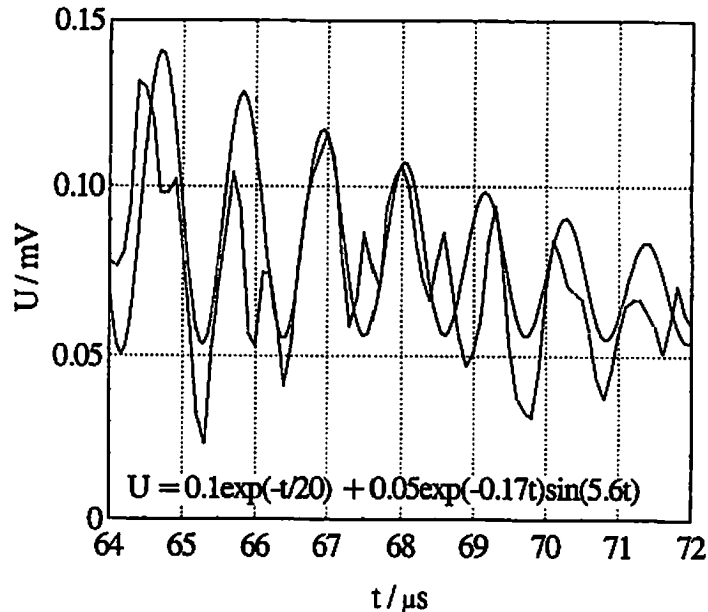


Fig.4. Time dependence of ELMG signal

Crack walls vibrate not only with a fundamental frequency and then in Fig.4. we can see a superposition of different vibrating modes.

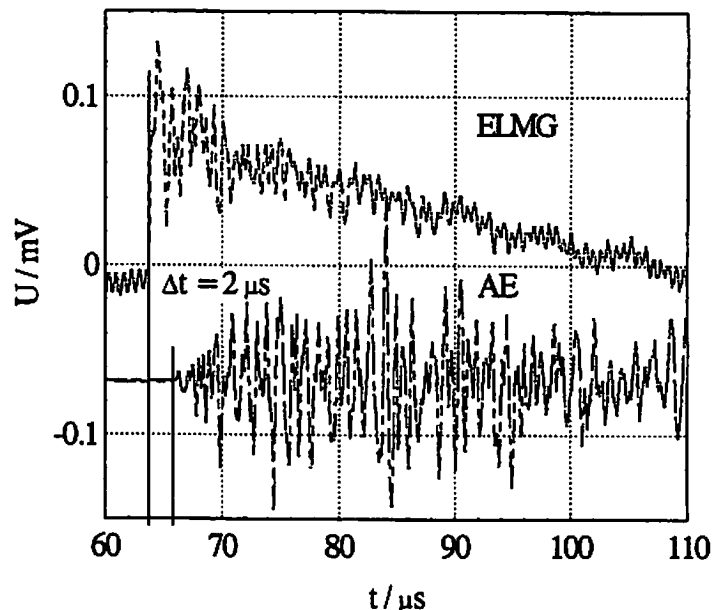


Fig.5. Time dependence of ELMG and AE signals

Time dependence of simultaneously recorded acoustic and electromagnetic signals is shown in Fig.5, 6. and 7. The time delay between EMG and AE signal is ranging from 2 to 10 μs . In Fig.5. the time delay is 2 μs , which correspond to crack distance 1 cm from AE sensor. Electromagnetic signal is propagated with a velocity $c/\sqrt{\epsilon_r}$, where c is velocity of light in free space and ϵ_r is relative permittivity of granite sample. This velocity is much higher than velocity of ultrasonic wave and then we can suppose, that the beginning of ELMG signal give correct information on time for crack creation. This method can improve a crack positioning and give some information on crack orientation and crack dimension.

In our experiment crack length can be estimated from vibrational frequency. For sample 4122 the angular frequency was $\omega = 5.6 \times 10^6 \text{ s}^{-1}$ and corresponding wavelength is 3.3 mm. The crack length is then 1.6 mm.

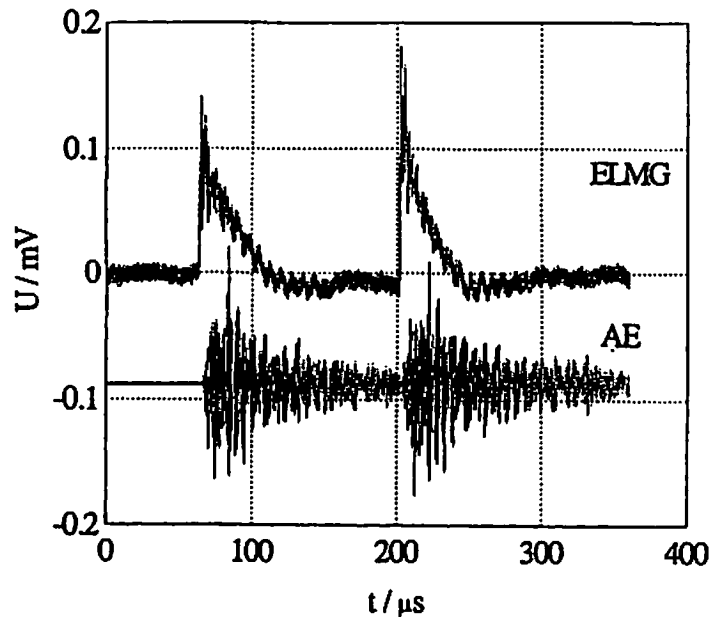


Fig.6. Time dependence of ELMG and AE signals

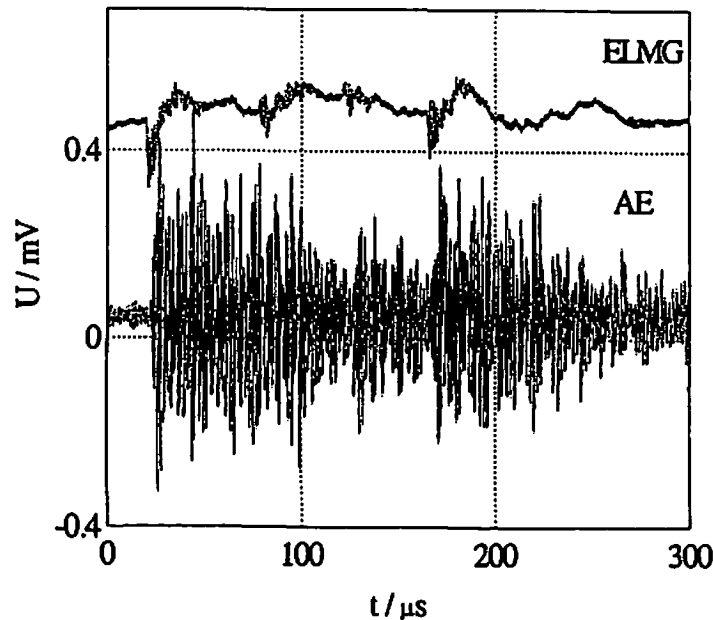


Fig.7. Time dependence of continuous ELMG and AE signals

Time between two cracks is a random variable and sometime we have observed two events separated by time interval less than was a period of damping harmonic motion (see Fig.6.) In Fig.7. crack creation events were appearing with so high frequency, that a near continuous random process was observed.

CONCLUSION

During the process of micro-cracks generation the electric charges appeared. The electric dipole system is a source of voltage induced on metal electrodes. The induced voltage is directly proportional to the crack width and its active area. The simultaneously investigation of acoustic and electromagnetic emission signals enable us to localize the crack position in solid. This phenomenon is based on electric field charge redistribution. The electromagnetic effect is also generated by crack wall vibrations. The recorded electric signal is modulated by an ultrasonic wave. The electric conductivity of solids affects the relaxation of the charge of the elementary capacitor. Both of these effects enable us to improve the sensitivity of cracks detection.

ACKNOWLEDGEMENT

Authors are indebted to the Grant Agency of Czech Republic for support within grant GACR No. 103/97/0899.

This work was also supported as a part of a research project CEZ:J22/98:261100007.

REFERENCES

1. T. Yoshino: Low-Frequency Seismogenic Electromagnetic Emission as Precursors to Earthquakes and Volcanic Eruptions in Japan, *Journal of Scientific Exploration*, Vol. 5, No. 1, pp 121-144, Pergamon Press, 1991
2. N. G. Chatiašvili: Vozmožnye mehanizmy elektromagnitnovo izlučenija pri razrušenii kristallov i gornych porod. *Geofizičeskij žurnal*, 1988, t. 10, s. 45-53.
3. G. Chatiašvili: Elektromgnitnoje izlučenije pri deformacii i razrušenii gornych porod i kristallov. AN Gruzii, Inst. geofiziki. "Mecniereba" Tbilisi, 1991.
4. I. Mirošničenko, V. S. Kuksenko: Izlučenie elektromagnitnych impulzov pri zaroždenii treščiny v tverdyh dielektrikach. *FTT*, Vol. 22, No. 5, s. 1531-1533, 1980.
5. T. Ogawa, K. Oike and T. Miura: Electromagnetic radiation from rocks, *J. Geophys. Res.*, 90, 6245-6249, 1985.

6. I. Zamada, K. Masuda, H. Mizutani: Electromagnetic and acoustic emission associated with rock fracture, *Phys. Earth. Planet Int.*, 57, 157-168, 1989.
7. J. Šikula, B. Koktavý, P. Vašina, Z. Weber, M. Kořenská a T. Lokajiček: Electromagnetic and Acoustic Emission from Solids, *Proc. of 22nd European Conference on Acoustic Emission Testing*, Aberdeen, UK, 1996.
8. T. Lokajiček and J. Šikula, Acoustic emission and electromagnetic effects in rocks, *Progress in Acoustic Emission VIII*, 1996, pp. 311-314
9. Y. Mori, K. Saruhashi and K. Mogi, Acoustic emission from rock specimen under cyclic loading, *Progress in Acoustic Emission VII*, 1994, pp. 173-178
10. Y. Mori, K. Sato, Y. Obata and K. Mogi, Acoustic emission and electric potential changes of rock samples under cyclic loading, *Progress in Acoustic Emission IX*, 1998
11. V. Hadjicontis and C. Mavromatou, Transient electric signals prior to rock failure under uniaxial compression, *Geophys. Res. Lett.*, 21, 1994, pp. 1687-1690
12. I. Yamada, K. Masuda and H. Mizutani, Electromagnetic and acoustic emission associated with rock fracture, *Phys. of Earth and Planetary Interiors*, 57, 1989, pp. 157-168
13. G. O. Cress, B. T. Brady and G. A. Rowell, Sources of electromagnetic radiation from fracture of rock samples in the laboratory, *Geophys. Res. Lett.*, 14, 1987, pp. 331-334
14. U. Nitsan, Electromagnetic emission accompanying fracture of quartz-bearing rocks, *Geophys. Res. Lett.*, 4, 1977, pp. 333-336
15. J. Šikula, B. Koktavý, P. Vašina and T. Lokajiček, Cracks and quality testing by acoustic and electromagnetic emission, *Proc. of the 23rd European Conference on Acoustic Emission Testing*, TUV Austria, Wien 6-8, May, 1998, p. 130-133.
16. J. Šikula, B. Koktavý, P. Vašina and T. Lokajiček, Detection of Crack Position by AE and EME Effects in Solids *Proc. of Acoustic Emission Conf. Bulder, USA*, 1997

THE TESTING OF LPG VESSELS WITH ACOUSTIC EMISSION EXAMINATION (AE)

P. Tscheliesnig

TÜV Austria, A 1232 Wien, Deutschstraße 10

E-mail: tsc@tuev.or.at, Tel.: ++ 43 - 1 - 61091 -13, Fax.: ++ 43 - 1 - 61091 - 21

J. Liska

SKODA JS s.r.o., CZ 316 00 Plzen, Orlik 266

E-mail: jliska@jad.ln.skoda.cz, Tel.: ++42 - 019 -704 - 2262, Fax.: ++42 - 019 - 704 - 2407

ABSTRACT

The conventional repetition tests for LPG vessels are time consuming and expensive. In addition the necessary emptying and the soiled water pollute the environment.

According to today's safety standards a repetition test shall verify a safe situation during the complete following service period. This isn't valid through the only application of a hydrotest and a visual inside inspection. Therefore we are convinced, that a suitable NDT has to be performed during the repetition tests.

It should be demonstrated, that the conventional and regularly used NDT methods are not able to find all specific defects and therefore the AE method even with all boarders is the only possibility to inspect this kind of vessels properly. Even it is very important to establish evaluation criteria based on a clear data base. This evaluation criteria have to be validated by a sufficient number of tested vessels and have to be improved permanently.

The specific application has the advantage, that it is generally in accordance with Annex E „Acoustic Emission“ - „Proposal for the testing and inspection of unfired pressure vessels“ issued by the relevant CEN/TC54/GWE.

It's obvious, that the application of the AE method reduces the risk of the used combined liquid/gas pressure test and is also the only method to increase the safety of the vessels in combination with a reduction of the costs, which reduce the application of the LPG for private houses. This is much more valid also for the specific defects of juggle-joints, which is used for the circumferential welds of LPG-tanks.

We are convinced that the implementation of a verified, reliable and economic AE testing procedure supported by the database of more than 5000 tests is also in Czech Republic the right way to solve the problem of LPG storage tank testing. This reason is the main reason for the co-operation between TÜV Austria and Skoda JS.

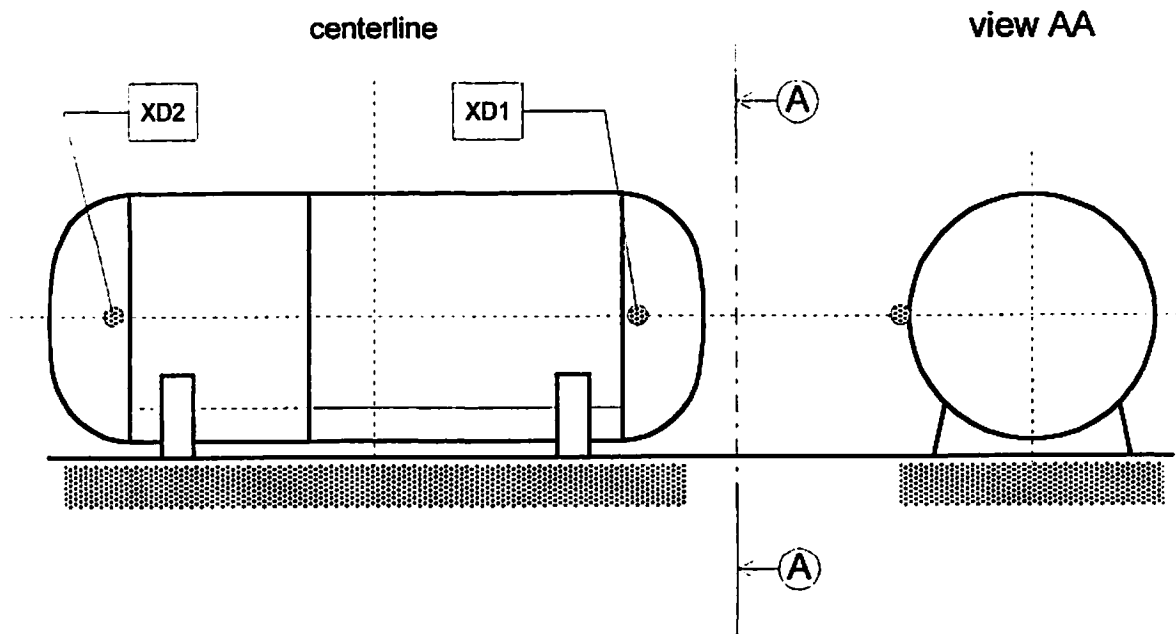
In any case it is important to point out, that for the application of this kind of an expert-system isn't enough to have a high expertise on the field of AE because you need much more a lot of pre-tests for the specific structure in combination with the possible defects (production, material etc.).

KEYWORDS

Acoustic Emission Examination - LPG storage tanks - Repetition tests for pressure equipment - Pattern Recognition Systems - Gas pressure tests according the CEN-standards - Weld defects in juggle-joints

INTRODUCTION

Today beside crude oil gas is the most important basis for the production of energy. Because the establishment of the necessary network of transportation lines for natural gas is expensive the most used alternative is the use of liquefied gas (LPG). This LPG is stored directly at the end user, often private houses or small enterprises, in small storage tanks, between 3 m³ and 15 m³. According the legal requirements these storage tanks (pressure equipments) have to be inspected periodically by a „so-called“ main inspection (hydrotest and inside inspection). This kind of testing is expensive and time-consuming and don't fulfil the today's demand that the periodically repetition tests have to guarantee the security of the pressure equipment for the following service period. Furthermore the performance of a hydrotest causes most time a residual humidity in the vessel and causes a lot of troubles during the winter time and can initiate the corrosion attack of the vessel.



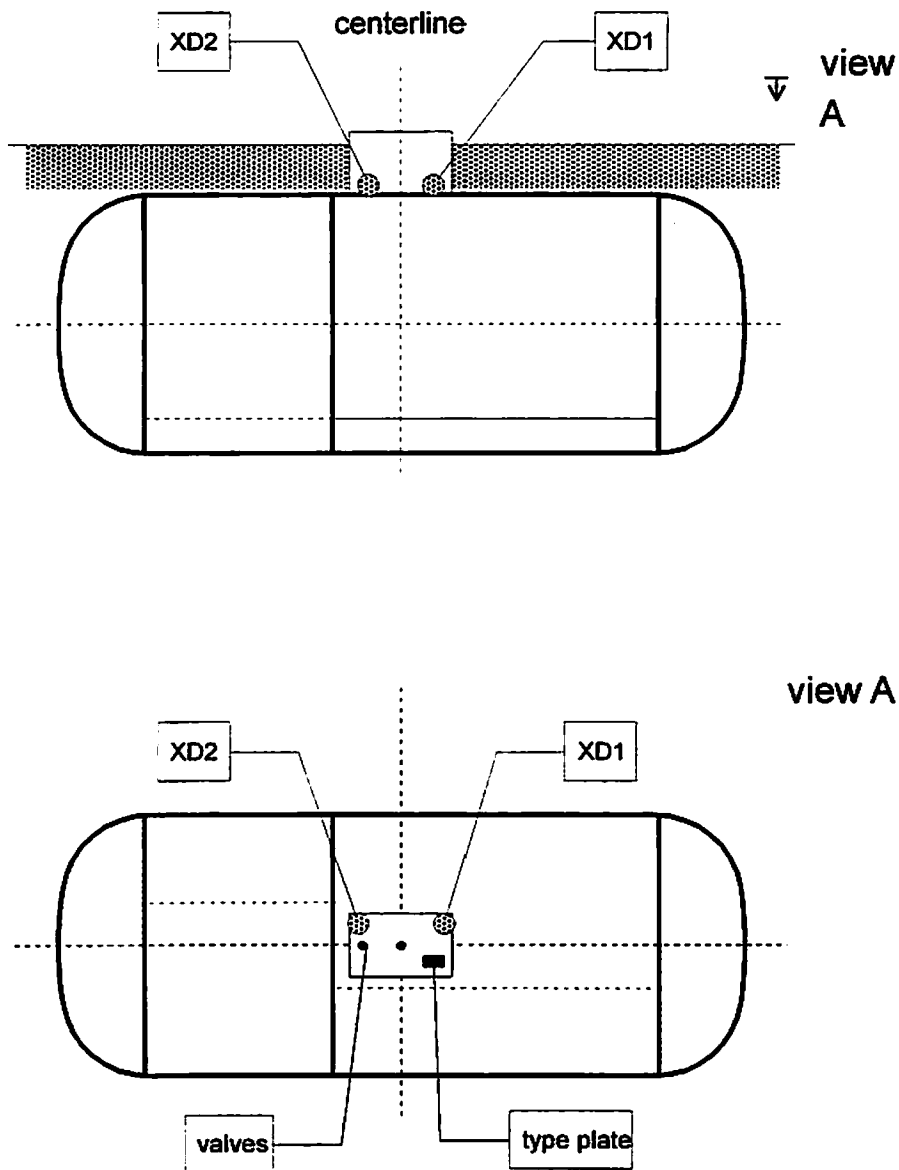
Picture 1: Above ground LPG vessels

Based on these experiences the TÜV Austria started in the year 1990/91 with the first pre-test to replace this conventional method by an Acoustic Emission Examination (AE) during a gas or much more a combined liquid and gas pressure test. The aims of AE here are the prevention of any catastrophic failure (pre-warning system, 1) and a statement about the security of the vessel for the following service period. After extensive lab-tests and the tests of vessels without and with different kind of defects for the establishment of a test-specification with clear evaluation criteria, based on the specific kind of vessels (material, design, production and use), in the year 1992 the TÜV Austria got an exception by the government, department for economical affairs, to replace the conventional main inspection by a combined liquid/gas pressure test controlled by an AE, based on clear and defined rules for the performance and evaluation-criteria (2).

Meanwhile the Austrian law for pressure equipments („Kesselgesetz“) and the adjoining regulations for setting in service and performance of the repetitive inspections („Druckgeräteüberwachungsverordnung“) accept in common the replacement of the hydrotest and visual inside inspection by liquid/gas pressure test monitored by AE. A specific regulation defines the required test-pressure, which is in this case under the safety valve relief pressure.

TEST-PROCEDURE

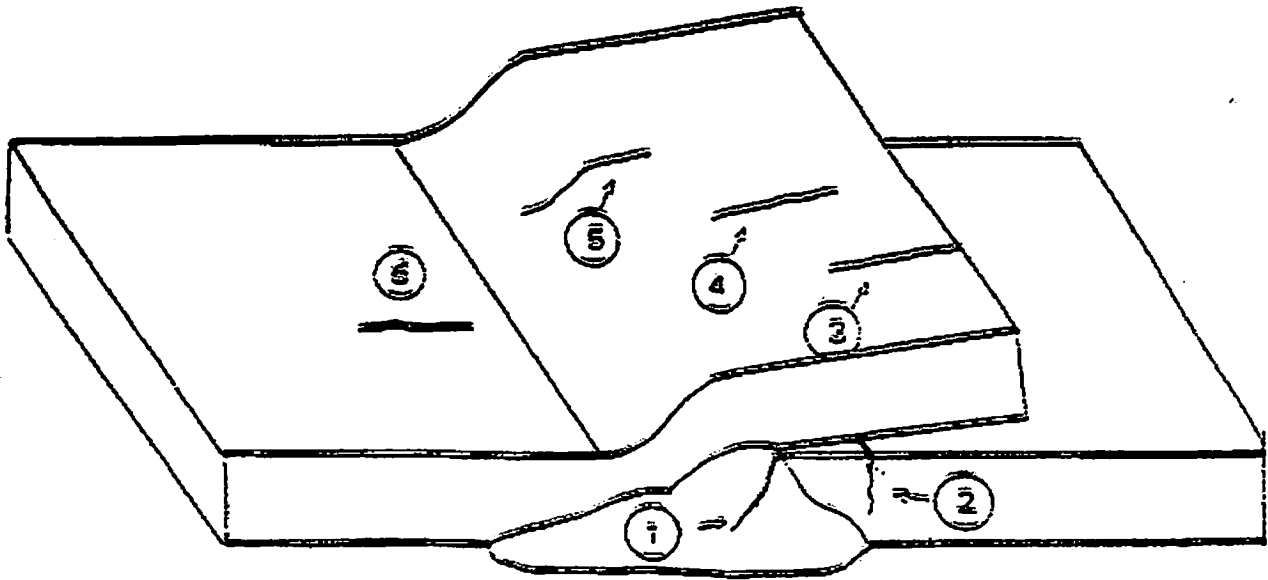
In the beginning the tests were performed with an „one sensor“ system, because our main aim in this period was to avoid any unjustified data reduction by the location. For simple vessels (size and shape) and production (butt-welds) this kind of testing was sufficient and gave good results. The first difficulties appear with the buried underground vessels, where a lot of disturb noise influence the test result. These influences and some doubtful results lead the test-performance together with a new equipment generation to the use of a two and later on partly three channel equipment (3).



Picture 2: examples for the sensor application at underground vessels

In the year 1995 some specific defects, which appeared at the first time in France, within the juggle-joints changed the test-performance completely and required a much more sophisticated application method compared to the roots of the testing method.

The detection of these specific defects (cracks in the juggle-joint, the heat-affected zone and even in the remaining overlapping part of the material) produces much more troubles than the normal weld defects (lack of fusion, slag inclusion, cracks etc.). Due to the specific shape of the juggle-joints and their small slit near to the root this kind of welding is the worst case for AE caused by a tremendous amount of disturb noise by breakage of remaining slag and the specific acoustic behaviour of cracks nearby the weld.



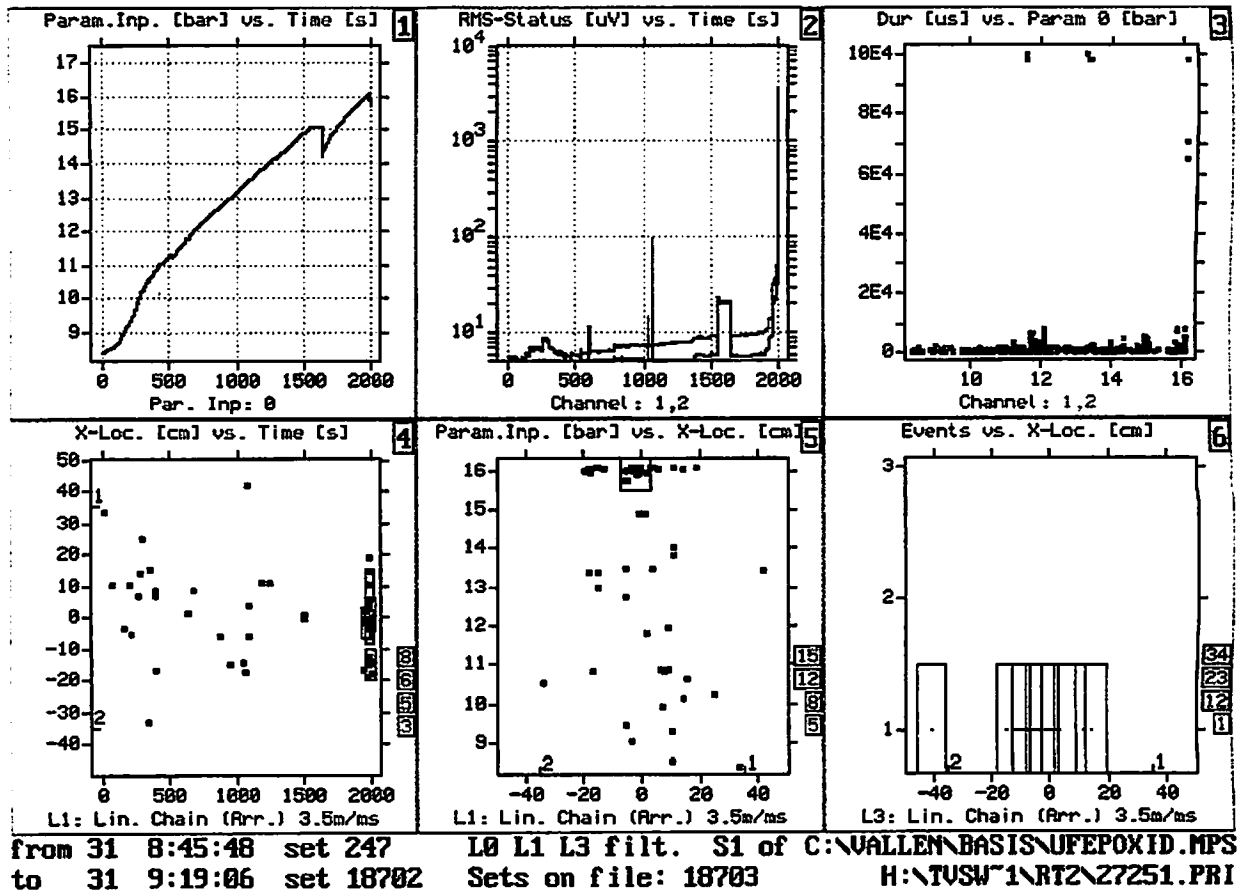
Picture 3: Specific defects in the juggle-joints

The first step was the filtering by a linear location with two sensors, which was very easy for above ground vessels and which result for buried vessels in a correlation cluster instead of a real location, because of the small basis between the two sensors in the dome. With this first step a lot of disturb noise could be excluded and this brought also a better determination between good and bad vessels also for them with exclusive butt-welds.

But a second step became necessary and this resulted in the application of a modern pattern recognition system, which makes it necessary to acquire the complete transient wave form and not only the AE parameters. These transient wave forms, which came from the real defects (cracks within welds and nearby), have to be evaluated in the pre-tests on a lot of different vessels with natural defects. If during the pressurisation a vessel became suspicious and based on the AE parameters no clear decision can be done, the pattern recognition system will be applied. Beside this off-line system a real time decision system for the prosecution of the pressurisation has to be established. This real time decision system is based on the normal AE parameters and has to be on the safe side, this means the evaluation has to be conventional, and the pressure stop criteria have to be very strict (4).

These defects, which appear first time in France, are identical to those, which were identified also in Germany in the year 1997. But those defects in Germany were sometimes much more critical than those in France and it has to be clear, that the detection of this kind of defects touch the borders of AE, although with a well experienced data base and well trained test-inspectors it is possible to find these defects.

The big advantage of AE is on one hand, that these defects will not be detected during a normal NDT (RT,UT) of the vessels, and on the other hand, that for buried vessels the other test-methods require to open the vessel or even more to dig it out.



Picture 4: Cluster report of a defective vessels

TEST EXPERIENCES

Since 1993 the repetition tests of the LPG vessels, which are required in time periods between 6 and 10 years according the level of NDT before the vessels go into service and for underground vessels the installation of a passive cathodic protections system, will be performed regularly with a liquid/gas pressure tests monitored with AE.

The tests were done during test-tours throughout the country. During one weekly tour approximately 25 vessels were tested. Most time during these tours, which will be done in conjunction between the testing and a service company, the tests and necessary maintenance will be done during one visit, which reduce the interference of the use of the vessel to an absolute minimum.

Table 1: Statistical tabulation of the tested vessels

year	tested vessels	above ground	under ground (buried)
1993	1027	665	362
1994	1107	749	358
1995	1000	788	212
1996	897	691	206
1997	720	586	134
1998	910	688	222
total 1993 - 1998	5661	4167	1494
%	100	74	26

During this test-period only 2,5 ‰ real defective vessels were detected (excluding the test tours for a specific production company and period) but compared with the former rejected vessels of less than 1 ‰ we have also here a gain in the safety and in any case a much cheaper method. A further important factor is, that we have detected more than 6 % gas leakages compared to less than 3 % for the normal hydrotest.

I will point out again, that during the upper mentioned time period the proceeding and much more the analysis were developed further and it has to be clear, that based on the new produced and detected defects the one channel technique is insufficient and could be dangerous, if it will be applied on LPG vessels with juggle-joints. This problem was not existing in the beginning, the vessels were produced only with butt-welds, and therefore the experiences from this time can only be transferred with restrictions.

TEST ANALYSIS AND DISCUSSION

The aim of the liquid/gas pressure test, which has to be performed till to at minimum 10 % over the maximum working pressure of the last year, is to classify the condition of the LPG tanks into 4 classes. This classification is done based on two parallel kinds of evaluation,

1. evaluation of the AE-parameters and determination of a „cluster evaluation factor“ and
2. analysis of the transient signals with a frequency domain pattern recognition program „visual class“.

These two steps will be combined at the end and decide in which class the vessel will be filled. This classification into class „A“, „B“, „C“ and „D“ (Tab. 2) has to be done on-line to give the test crew the opportunity to follow the further rules. Even sometimes, especially for doubtful vessels the result has to be rechecked by a post-analysis in the lab.

Table 2: Classification of the vessels and further actions

Vessel-class	status	further action
Class „A“	positive	The vessel is proper for the further service.
Class „B“	suspicious	Further pressurisation till to the test pressure, then further classification into class „A“ or „C“.
Class „C“	negative	Following further tests are required <ul style="list-style-type: none"> • hydrotest and visual inside inspection • 100 % conventional NDT of the welds (UT,RT)
Class „D“	negative with leakage	replacement

For a unequivocal classification of the vessels it is very important to hold all parameters (pressure test, equipment and application) equal, because the smallest alteration can influence the test result (CEF etc.) and consequently the classification.

Beside co-operations in France and also in Germany we have started to establish a co-operation also with Skoda JS, which will apply this technology also within the Czech Republic.

This reason for this is, that in Czech Republic now almost 15 000 LPG tanks are installed and the expected number till the end of the year 2000 is about 20 000. Most of them are small tanks of volume less than 5m³. The idea of implementation AE technology for LPG tank testing in Czech Republic arose after Skoda personally Mr. Liska received the first information about the problem from TÜV Österreich and successive technical discussions between SKODA JS and TÜV Österreich followed in the second half of 1996. In the first half of 1997 SKODA addressed gas distributors in Czech Republic (joined in the Association Propan-Butan), Czech Institute of Technical Inspection and Czech Office for Safety at Work. Because of interest of all these parties in September 1997 a successful demonstration of AE LPG test for Czech experts was performed by TÜV in the locality near Vienna. SKODA continued the contacts with TÜV and in May 1998 the Pre-Cooperation Agreement about the co-operation in the field of AE testing of LPG tanks between SKODA and TÜV was signed. In the near future, this agreement will be followed with full Cooperation Agreement for long-term co-operation including the purchase of license for testing procedure from TÜV.

During the first half of 1998 ŠKODA elaborated set of documents supporting the approval of AE LPG tests in Czech Republic. The main part was the proposal of testing procedure which was submitted to the Czech Institute of Technical Inspection for assessment. The result of assessment was positive. In the second half of 1998 the Association Propan-Butan submitted the proposal of Czech national standard „Inspection and Requalification of LPG Tanks“ based on EU standard. This standard is being discussed and should be approved in the half of this year. In this standard AE test is included as one of the alternative testing modes. In 1999 SKODA in co-operation with TÜV intends to build service truck for AE LPG testing and to perform reference tests needed for approval of testing procedure in Czech Republic. It can be assumed that SKODA will be ready to perform standard AE tests of LPG tanks in the half of next year.

REFERENCES

1. „Proposal for the testing and inspection of unfired pressure vessels“ of CEN/TC54/WG E
2. „Die Anwendung der Schallemissionsprüfung bei der wiederkehrenden Untersuchung von Flüssiggasbehältern“, P. Tscheliesnig, G. Schauritsch, G. Krenn; TÜV Österreich (former Wien) presented at the 9. Kolloquium „Schallemission“ of the DGZfP in Zittau, 1992
3. „Erfahrung und Weiterentwicklung bei der Prüfung von kleinen Lagerbehältern mittels der Schallemissionsprüfung“, P. Tscheliesnig, G. Schauritsch; TÜV Österreich presented at the 11. Kolloquium „Schallemission“ of the DGZfP in Jena, 1997
4. „Testing LPG Tanks By Acoustic Emission“, J.M. Capreau (Institute de Soudure), E. Eberhard (Butagaz), G. Schauritsch, P. Tscheliesnig (TÜV Austria) presented at the 23rd European Conference on Acoustic Emission Testing in Vienna, 1998

Conferences and Symposia

July 10-14, 2000 (Level II)
Aug. 7-11, 2000 (Level I)
Oct. 30-Nov. 3, 2000 (Level II)
Dec. 4-8, 2000 (Level I)

24th EWGAE Meeting (EWGAE 2000)

Held May 24-26, 2000; CETIM, Senlis, France. Program
Chairs: C. Rigault and M. Cherfaoui.

The meeting had over 90 participants from 15 countries.
Proceedings "EWGAE 2000", containing 66 papers, 460
pages, can be purchased from CETIM.
Contact: christel.rigault@cetim.fr

The 43rd Meeting of Acoustic Emission Working Group

To be held at Clarion Hotel, Seattle-Tacoma Airport, WA.
Program Chairs: Allen T. Green and W. Hardrath
Contact: ATGreen1@aol.com

Monday, 17 July, 2000:

Acoustic Emission Primer

Tuesday, 18 July, 2000:

Technical Presentations

AEWG Business Meeting

Wednesday, 19 July, 2000

Technical Presentations

AEWG: Awards Banquet

Banquet Speaker: Jack C. Spanner, Sr.

Thursday, 20 July, 2000

Tour of Boeing Engineering Test Laboratory

Abstracts of presentation can be found at
<http://www.aendt.com>.

15th International AE Symposium (IAES-15)

To be held September 11-14, 2000; The International
House of Japan, Tokyo, Japan. Symposium Organizers: T.
Kishi, Y. Higo, M. Ohtsu, S. Yuyama
Contact: aeyuyama@sh0.po.ijnet.or.jp

Information and titles of presentation can be found at
<http://home.att.ne.jp/green/iaes15>

Short Courses

Acoustic Emission Short Courses for the requirements of
ASNT's TC-1A led by Dr. Adrian Pollock will be offered
by Physical Acoustics Corp. at their corporate headquarters
in Princeton Junction, NJ. Contact: esi@pacndt.com
Dates for the year 2000 are:

For Short Courses by Acoustic Technology Group, contact
ATGreen1@aol.com.

2000 SUBSCRIPTION RATE

Base rate (CD-ROM) for one year	\$ 96.00
Add Postage of U.S. - Priority rate	\$ 8.00
All others - Air mail rate	\$ 8.00
CD-ROM + printed copy, surface mail: add	\$ 32.00

Please note that, beginning with 2000, there is substantial
changes in format and rates. (See page i, vol. 17, nos. 1/2)

VISA and Mastercard orders accepted.

Payment must be in U.S. dollars drawn on a U.S. bank.
Bank transfer accepted. (Account No. 080-03416470) at
California Bank and Trust
San Fernando Valley Office
15250 Ventura Blvd,
Sherman Oaks, CA 91403-3262

One volume of four issues per year through vol. 17. Index
included in the last issue. Back issues available at \$50 per
volume for Vols. 1-3, \$90 per volume for Vols. 4-8, \$96 per
volume for Vols. 9-17. US surface postage \$8 per volume.
For Canada and overseas surface delivery, add \$11 and for
air mail, add \$30 per volume (shipping charges will be
adjusted for multi-volume order).

All orders should be sent to (or Fax 1-818-990-1686):
[Please note the addition of PMB in address. This is a new
US Postal Regulation and mails won't arrive without it.]

Acoustic Emission Group
PMB Suite 106, 16350 Ventura Blvd.
Encino, CA 91436 USA

For inquiry through Internet, use the following address:
ono@ucla.edu

Editor-Publisher	Kanji Ono	Tel. (310) 825-5233
Cover Design	Robin Weisz	(UCLA Publications)
Production	Pace Publication Arts	

Publication Date of This Issue (Nos. 3 and 4): 15 July 2000.

Index to Volume 17

Contents

Numbers 1/2

Page i	Announcement: New Format for <i>Journal of Acoustic Emission</i>
Page ii	Founding members of GLEA, Grupo Latinoamericano de Emisión Acústica (Cover photograph); Color plate for Figure 8 on page 9.
Page 1-13	Classification of Acoustic Emissions in Metallic Glasses A. Vinogradov
Page 15-21	Acoustic Emission Characteristics of Soil and Sand in Response to Simulated Root Growth C. Divaker Durairaj, L. Okushima and S. Sase
Page 23-27	Detection of Defects in Gears by Acoustic Emission Measurements N. Tandon and S. Mata
Page 29-36	Acoustic Emission Signals in Thin Plates Produced by Impact Damage William H. Prosser, Michael R. Gorman and Donald H. Humes
Page 37-47	Reflections of AE Waves in Finite Plates: Finite Element Modeling and Experimental Measurements W. H. Prosser, M. A. Hamstad, J. Gary and A. O'Gallagher
Page 49-59	Classification of Acoustic Emission Signatures Using a Self-organization Neural Network Tinghu Yan, Karen Holford, Damian Carter and John Brandon
Page 61-67	Discussion of the Log-Normal Distribution of Amplitude in Acoustic Emission Signals M. I. López Pumarega, R. Piotrkowski and J. E. Ruzzante
Page 69-81	Unsupervised Pattern Recognition Techniques for the Prediction of Composite Failure T. P. Philippidis, V. N. Nikolaidis and J. G. Kolaxis
Page 83-93	Real-Time Tool Condition Monitoring in Cold Heading Machine Processes Using an Acoustic Approach Henrique L.M. dos Reis, David B. Cook and Aaron C. Voegelé
	Conferences and Symposia
Page 14	Meeting Calendar
Page 22-95	42 nd Meeting of The Acoustic Emission Working Group
Page 96	Available Books on Acoustic Emission/Short Courses

Numbers 3/4

Page 97	Modeling of Buried Monopole and Dipole Sources of Acoustic Emission with a Finite Element Technique M. A. Hamstad, A. O'Gallagher and J. Gary
Page 111	Numerical Assessment of the Quality of AE Source Locations Gang Qi and Jose Pujol
Page 121	Structural Integrity and Remnant Life Evaluation Using Acoustic Emission Techniques Brian R. A. Wood, Robert W. Harris and Elizabeth L. Porter
Page S1	Selected Papers from International Conference Acoustic Emission '99
Page S2	Report on International Conference Acoustic Emission '99 Pavel Mazal and Václav Svoboda
Page S7	Identification of fundamental forms of partial discharges based on the results of frequency analysis of their acoustic emission T. Boczar
Page S13	Technical possibilities of the non-contact acoustic emission method at testing hollow articles integrity G. Budenkov, O. Nedzvetskaya, E. Bulatova
Page S20	Method of AE and possibilities of corrosion degradation detection M. Cerny, P. Mazal, V. Suba
Page S29	Application of acoustic emission in metal physics and materials science F. Chmelík, P. Lukác
Page S37	Waveform analysis of acoustic emission during pressurization of glass-fiber composite pipes L. Golaski, P. Gebski, I. Baran, Kanji Ono
Page S45	Acoustic emission monitoring during solidification processes F. Havlíček, J. Crha
Page S51	Radiation of acoustic emission waves during stress corrosion cracking of the metal A. Kotolomov, G. Budenkov, O. Nedzvetskaya
Page S57	NDE of phase transformations in Cu based shape memory alloys by ultrasonic techniques

Page S65	M. Landa, M. Chlada, Z. Prevorovsky VVER steam generators and acoustic emission	O. Matal, J. Zaloudek, T. Simo
Page S70	Application of acoustic emission technique on fatigue testing machine	Rumul P. Mazal, J. Richter
Page S78	Acoustic emission and state of fatigue of ferroelectric Pb(Zr _x Ti _{1-x})O ₃ ceramics J. Nuffer, D. Lupascu, J. Rödel	
Page S83	Application of AE method at pressure tests of boiler header	V. Svoboda, J. Petrasek, A. Proust
Page S92	Acoustic emissions of vessels with partially penetrated longitudinal seams	F. Rauscher
Page S100	Electromagnetic emission from polycrystalline solids	J. Sikula, B. Koktavy, I. Kosiková, J. Pavelka, T. Lokajíček
Page S108	The testing of LPG vessels with acoustic emission examination	P. Tscheliesnig, J. Liöka
Conferences and Symposia		
Page S116	24th EWGAE Meeting (EWGAE 2000)/ The 43rd Meeting of Acoustic Emission Working Group/ 15th International AE Symposium (IAES-15)/ Short courses	
Page S6	Next EWGAE Meeting / Cover Photograph	
Page I-i	Index to Volume 17	

Authors Index

I. Baran,	S37	O. Nedzvetskaya	S13, S51
T. Boczar	S7	V. N. Nikolaidis	69
John Brandon	49	J. Nuffer	S78
G. Budenkov	S13, S51	A. O' Gallagher	37, 97
E. Bulatova	S13	L. Okushima	15
Damian Carter	49	Kanji Ono	S37
David B. Cook	83	J. Pavelka	S100
M. Cerny	S20	J. Petrasek	S83
M. Chlada	S57	T. P. Philippidis	69
F. Chmelík	S29	R. Piotrkowski	61
J. Crha	S45	Elizabeth L. Porter	121
C. Divaker Durairaj	15	Z. Prevorovsky	S57
J. Gary	37, 97	William H. Prosser	29, 37
P. GebSKI	S37	A. Proust	S83
L. Golaski	S37	Jose Pujol	111
Michael R. Gorman	29	Gang Qi	111
M. A. Hamstad	37, 97	F. Rauscher	S92
Robert W. Harris	121	Henrique L.M. dos Reis	83
F. Havlíček	S45	J. Richter	S70
Karen Holford	49	J. Rödel	S78
Donald H. Humes	29	J. E. Ruzzante	61
B. Koktavy,	S100	S. Sase	15
J. G. Kolaxis	69	J. Sikula	S100
I. Kosiková	S100	T. Simo	S65
A. Kotolomov	S51	V. Suba	S20
M. Landa	S57	V. Svoboda	S2, S83
J. Liöka	S108	N. Tandon	23
T. Lokajíček	S100	P. Tscheliesnig	S108
M. I. López Pumarega	61	A. Vinogradov	1
P. Lukác	S29	Aaron C. Voegelé	83
D. Lupascu	S78	Brian R. A. Wood	121
S. Mata	23	Tinghu Yan	49
O. Matal	S65	J. Zaloudek	S65
P. Mazal	S2, S20, S70		

Notes for Contributors

1. General

The Journal will publish contributions from all parts of the world and manuscripts for publication should be submitted to the Editor. Send to:

Professor Kanji Ono, Editor - JAE
6531 Boelter Hall, MSE Dept.
University of California
Los Angeles, California 90095-1595 USA
FAX (1) 818-990-1686
e-mail: ono@ucla.edu

Authors of any AE related publications are encouraged to send a copy for inclusion in the AE Literature section to:

Mr. T.F. Drouillard, Associate Editor - JAE
11791 Spruce Canyon Circle
Golden, Colorado 80403 USA

Only papers not previously published will be accepted. Authors must agree to transfer the copyright to the Journal and not to publish elsewhere, the same paper submitted to and accepted by the Journal. A paper is acceptable if it is a revision of a governmental or organizational report, or if it is based on a paper published with limited distribution.

Compilation of annotated data files will be accepted for inclusion in CD-ROM distribution, so that others can share in their analysis for research as well as training. ASCII or widely accepted data formats will be required.

The language of the Journal is English. All papers should be written concisely and clearly.

2. Page Charges

No page charge is levied. Twenty-five copies of off-prints will be supplied to the authors free of charge.

3. Manuscript for Review

Manuscripts for review need only to be typed legibly; preferably, double-spaced on only one side of the page with wide margins. The title should be brief. An abstract of 100-200 words is needed for Research and Applications articles. Except for short communications, descriptive heading should be used to divide the paper into its component parts. Use the International System of Units (SI).

References to published literature should be quoted in the text citing authors and the year of publication. These are to

be grouped together at the end of the paper in alphabetical and chronological order. Journal references should be arranged as below. Titles for journal or book articles are helpful for readers, but may be omitted.

H.L. Dunegan, D.O. Harris and C.A. Tatro (1968), *Eng. Fract. Mech.*, 1, 105-122.

Y. Krampfner, A. Kawamoto, K. Ono and A.T. Green (1975), "Acoustic Emission Characteristics of Cu Alloys under Low-Cycle Fatigue Conditions," NASA CR-134766, University of California, Los Angeles and Acoustic Emission Tech. Corp., Sacramento, April.

A.E. Lord, Jr. (1975), *Physical Acoustics: Principles and Methods*, vol. 11, eds. W. P. Mason and R. N. Thurston, Academic Press, New York, pp. 289-353.

Abbreviations of journal titles should follow those used in the ASM Metals Abstracts. In every case, authors' initials, appropriate volume and page numbers should be included. The title of the cited journal reference is optional.

Illustrations and tables should be planned to fit a single page width (178 mm or 7"). For the reviewing processes, these need not be of high quality, but submit glossy prints or equivalent electronic files with the final manuscript. Lines and letters should be legible.

4. Review

All manuscripts will be judged by qualified reviewer(s). Each paper is reviewed by one of the editors and may be sent for review by members of the Editorial Board. The Board member may seek another independent review. In case of disputes, the author may request other reviewers.

5. Electronic Media

This Journal will be primarily distributed electronically by CD-ROM. In order to expedite processing and minimize errors, the authors are requested to submit electronic files or floppy disk copy of the paper. We can read Macintosh and IBM PC formats. On the INTERNET, you can send an MS Word file or the text portion to "ono@ucla.edu".

6. Color Illustration

We can process color illustration needed to enhance the technical content of an article. With the new format, authors are encouraged to use them.

Contents

- Page 97 Modeling of Buried Monopole and Dipole Sources of Acoustic Emission
with a Finite Element Technique
M. A. Hamstad, A. O'Gallagher and J. Gary
- Page 111 Numerical Assessment of the Quality of AE Source Locations
Gang Qi and Jose Pujol
- Page 121 Structural Integrity and Remnant Life Evaluation Using Acoustic
Emission Techniques
Brian R. A. Wood, Robert W. Harris and Elizabeth L. Porter

Conferences and Symposia

- Page S1 Selected Papers from International Conference Acoustic Emission '99
- Page S2 Report on International Conference Acoustic Emission '99
Pavel Mazal and Václav Svoboda
- Pages S7 – Fifteen Papers by various authors
S115
- Page S116 24th EWGAE Meeting (EWGAE 2000)
The 43rd Meeting of Acoustic Emission Working Group
15th International AE Symposium (IAES-15)
Short courses
- Page S6 Next EWGAE Meeting
Cover Photograph
- Page I-i Index to Volume 17